Preliminary result at 180° inclination which are useful in particular for satellite experiments (fig. 3) agree well with other experiment at same latitude but higher energies (4).

4. Conclusion. These preliminary results will be refined by making use of the full informations from the amplitudes and T.O.F.; and also given for other zenital direction monitored during the flights. A first explanation for what concern the discrepancy between trigger-rate and acceptable pictures from track chamber seems to be the large acceptance angle of the counter telescope for low energy gamma-ray. A way to improve this situation could be to locate the particles in the two T.O.F. counters in order to derive an estimate of the incoming direction. More or less sophisticated use of the amplitudes from left and right PM tube on each T.O.F. counter can bring very sensitive improvement (6), it could be used on our telescope at a very moderate cost.

References

1. Lavigne, J.M. et al. Nucl. Instr. & Meth. 199 (1982) 585
2. Ross R.W., Chesney J.R., IEEE Trans on Nucl. Science Vol N 527 n°1 Feb. 1980
3. Lavigne J.M. et al. Ap. J. vol. 261, 720, 1982, October 15
4. Thompson D.J. J.G.R. vol. 79, N°10, p.1309, April 1, 1974
5. Schonfelder V, et al. Ap. J. vol. 240, 350 Aug. 15, 1980
6. D'Agostini et al. Nuclear Inst. & Meth. 185 (1981) 49

C-6

ORIGINAL PAGE IS
OF POOR QUALITY

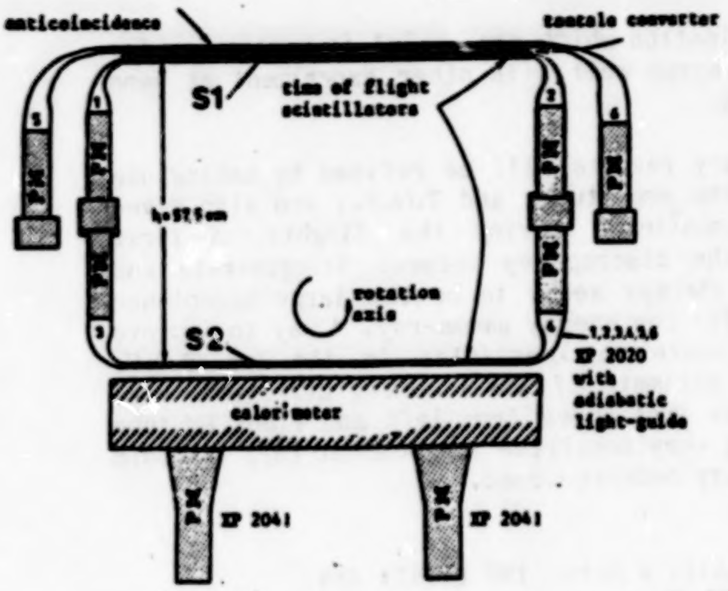
anticoincidence
tantale converter
S1
time of flight scintillators
h=57.5 cm
rotation axis
S2
1,2,3,4,5,6 XP 2020 with adiabatic light-guide
calorimeter
PM
XP 2041
XP 2041

FIG 1

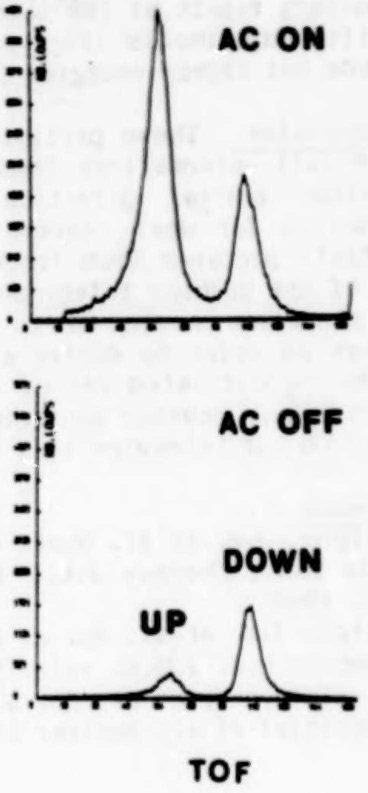

FIG 2

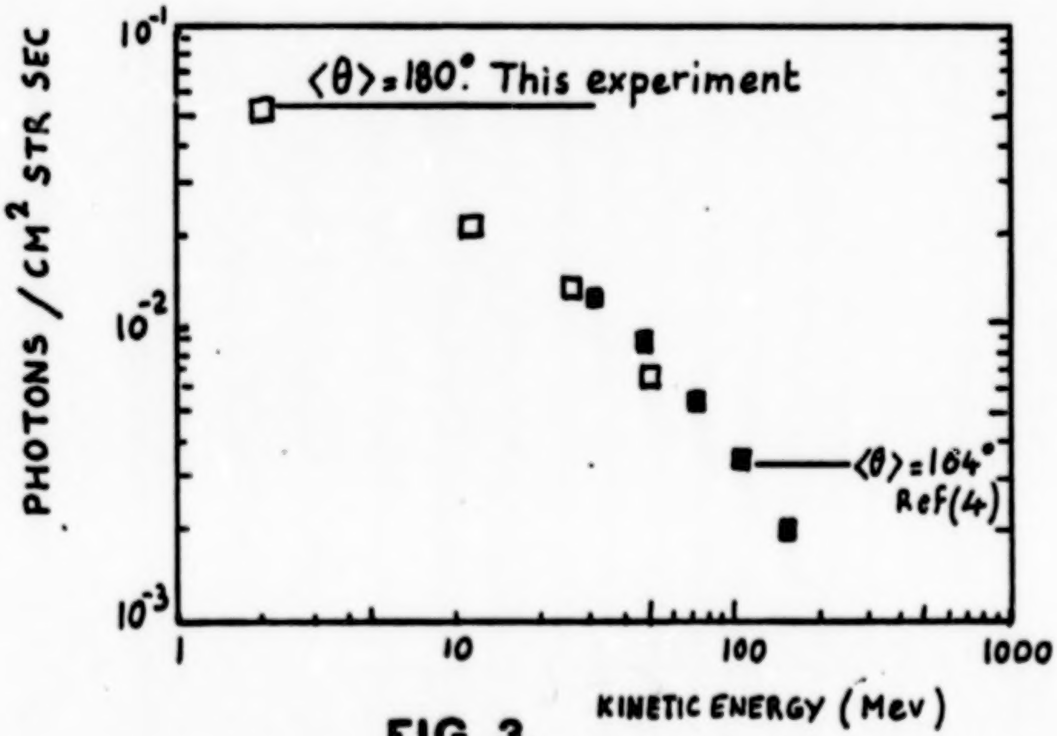

FIG 3

Results of a Study to Build a Gamma-Ray Telescope in an External Tank

N85-34958

David Koch
Smithsonian Astrophysical Observatory
60 Garden Street
Cambridge, MA 02138 USA

Abstract

In response to the ever-present need for a very large gamma-ray detector for energies greater than 100 MeV, a concept to build a telescope of 250,000 cm^2 sensitive area using a Space Shuttle External Tank (ET) is presented. In the Space Station era, for the first time, large detectors can be constructed on-orbit which would otherwise be limited in size by the launch vehicle. The ET will serve both as the spacecraft and the Cherenkov pressure vessel. The significant feature is that the sensitive area will be forty times that of the high energy detector on GRO and will be able to locate even the faintest sources from the GRO survey to a few arc minutes. The detection technique is based upon that originally proposed by Greisen.(1)

1. Introduction

The results to date in high energy gamma-ray astronomy are based primarily upon measurements with instruments of only about 600 cm^2 sensitive area. The next generation high energy detector, EGRET, on the Gamma Ray Observatory (GRO) will have a sensitive area of about an order of magnitude greater. The survey resulting from GRO, in particular from EGRET, should produce a list of sources with the same log N/log S distribution as in previous astronomical surveys. That is, the bulk of the sources should be at the limiting sensitivity of EGRET and due to the detection technique, be of maximum positional uncertainty. Spark chambers have been the workhorse in high energy gamma-ray astronomy since they provide simultaneously a large field of view and positional information which is needed to carry out the survey work. However, spark chambers become impractical if they are substantially larger than EGRET due to complexity and deadtime. In addition, when carrying out discrete source studies, the large field of view is of no advantage. Although GRO does not strain the limits of the Shuttle, a substantial increase in size (more than an order of magnitude) cannot be accommodated as a conventional payload. Therefore new directions must be sought to circumvent the launch capability within the current Shuttle system and a detection technique must be used which can easily be extended to very large areas without also multiplying the complexity.

2. Unconventional Solution

With the advent of the Space Station, unconventional approaches are possible for the construction of large cosmic-ray detectors. The gas-Cherenkov telescope originally conceived by Greisen and proven on several balloon flights(2,3,4) can provide the next advance in high energy gamma-ray detection. It is based upon the principle of imaging the Cherenkov light produced by the created electron pair. The gamma-ray imaging telescope system (GRITS) has 40 times the sensitive area of GRO, thus provid-

ORIGINAL PAGE IS
OF POOR QUALITY

ing among other attendant improvements, measurements of variability one-fortieth as small. An angular resolution of a few arcminutes approaches the ultimate limit imposed by the physics of the pair-production mechanism. The key to this concept is the Space Station, and the availability on-orbit of the currently disposed of external tank (ET). The ET is ideal for this application since it is a large, clean, rigid, thin-walled, insulated, light-tight, gas-tight pressure vessel.

3. Gas Cherenkov Detection Technique

The combination of signatures and constraints utilized in this instrument result in a straightforward detection of gamma rays and inherently excellent non-gamma-ray background rejection. For the energies of concern, greater than 100 MeV, photons interact exclusively to produce an electron-positron pair. Figure 1 illustrates how the ET is to be instrumented. At the top of the telescope a thin converter is tightly sandwiched between two plastic scintillators to form the trigger module. The scintillator on the incident side is used as a veto to reject all singly-charged particles. The one on the exit side is used to detect the two charged particles resulting from the conversion of the neutral gamma ray.

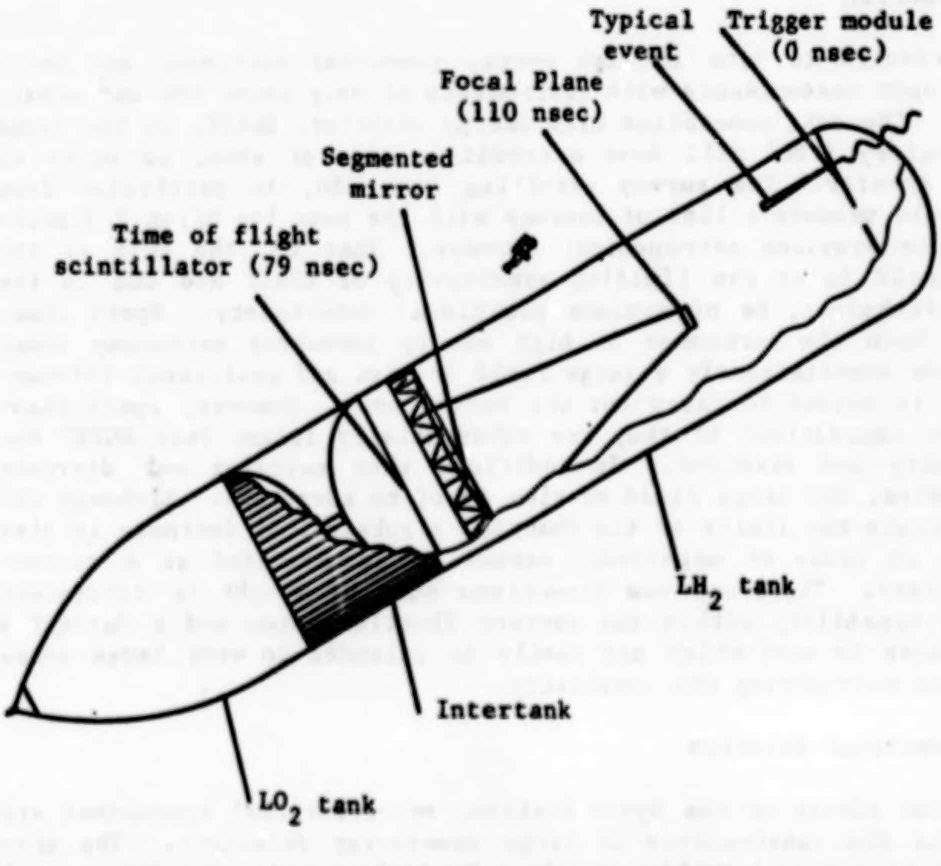

Figure 1. Major elements of the gamma-ray imaging telescope. The numbers indicate the elapsed time in nanoseconds for each signal composing the threefold time-delayed coincidence. In addition, there is a charged particle veto at t = 0. The overall length of the ET is 46.5 meters.

The energetic pair then travels the length of the telescope producing Cherenkov light in the gas-filled ET. For the index of refraction selected, 1.0000726 (air at 1/4 atm), the cone angle of emitted light is 1.4 deg, 5.8 visible light photons are produced per particle per meter of path length and the threshold for emission is at a Lorentz factor of 83. The two cones of light are imaged by a mirror at the far end of the ET onto an array of 127 photomultiplier tubes or a multineedle detector.(5) At the focus the two rings (not filled circles) of light arrive 110 nanosec after the pair creation. Data from the focal plane array are used to determine that the image and the amplitude of light corresponds to two rings of light. A time of flight (TOF) scintillator is placed behind the mirror to detect the passage of the charged pair 79 nanosec after the conversion of the gamma ray.

The electronic signature of an event is a threefold time-delayed coincidence of a pulse from the trigger module with no commensurate veto, 79 nanosec later a pulse in the TOF scintillator and 110 nanosec after the trigger, a pulse at the focal plane. During data reduction, the pulse height data from the light in the focal plane are not only used to validate the detection of two particles, but the location of the rings in the focal plane is used in the determination of the incident direction of the gamma ray. The combination of signatures and constraints make this detection technique naturally immune to all forms of non-gamma-ray background. Table 1 lists various types of background and the method the instrument uses to reject them.

For the converter material, active scintillators are used rather than a passive material such as lead. Measurement of the pulse height in the converter will determine the thickness of material through which the electron pair underwent multiple Coulomb scattering. Non-uniformimities in the light collecting efficiency which would otherwise make the pulse height measurements meaningless can be removed by making the same pulse height measurements in the thin trigger scintillator which will be of the same geometry and mounted directly under the converter scintillator. The amount of scattering in the trigger scintillator and the Cherenkov gas is both constant and smaller than that in the converter. Having determined the amount of scattering to expect in the converter will improve the uncertainties involved in determining the total amount of Coulomb scattering for each event. Knowing the scattering and having measured the angular separation of the particles in the focal plane will determine the energy of the incident gamma ray.

4. Angular Resolution and Sensitivity

Due to implementation constraints, only about half of the cross section of the ET can contain unobstructed trigger modules for a sensitive area of 250,000 cm^2. For converter thicknesses resulting in multiple Coulomb scattering commensurate with the emission angle, the sensitivity is roughly independent of the converter efficiency. To first order a resolution element is proportional to the square root of the converter thickness. Hence, a converter of 0.036 radiation lengths has been chosen to provide the optimum angular resolution with very little loss in sensitivity. This results in an RMS cell size of 1.1 degrees for energies greater than 300 MeV. (The emission angle at 300 MeV is 0.6 degrees.) Since the centroid uncertainty is about one-tenth of the cell size (and is roughly inversely proportional to energy), the error radius for all point sources seen with a signal to noise of ten is 7 arc minutes. Using only events of energy greater than 1 GeV with no loss in sensitivity gives a position to 2 arc minutes. The counting rates for various sources at energies greater than 300 MeV are:

R(Vela) = 70 counts/hour
R(Crab) = 9.8 counts/hour
R(Bkgd) = 0.8 counts/hour/cell (near the Crab and Vela).

Thus a signal to noise of 10 can be reached in 1.4 hours for Vela and in 11 hours for the Crab.

TABLE 1
Methods Of Rejection Of Non-Gamma-Ray Background

EFFECT	REJECTION METHOD
Singly charged primary	Amplitude and shape of light indicative of two rings and veto directly above converter with two-particle trigger directly below
Hadrons	Same as above and require Lorentz factor greater than 83
Chance coincidences	Amplitude and shape of light indicative of two rings and threefold time-delayed coincidence
Backward going events	Same as chance coincidences and not trigger veto
Decaying muons	Amplitude and shape of light indicative of two rings and Lorentz factor greater than 83
Off-axis events	Mirror and focal-plane geometry

References

1. Greisen, K.I. 1966, *Perspectives in Modern Physics*, ed. R. Marshak (New York: Interscience Publishers), p. 355.
2. Koch, D.G. *et al.* 1973, Performance of a Gas-Cherenkov Gamma-Ray Telescope, *Nuclear Inst. & Meth.*, *108*, 349.
3. McBreen, B. *et al.* 1973, Pulsed High Energy Gamma-Rays from the Crab Nebula, *Ap. J.*, *183*, 571.
4. Greisen, K. *et al.* 1975, Change in the High-Energy Radiation from the Crab, *Ap. J.*, *197*, 471.
5. Comby, G. *et al.* 1982, Detector for U.V. Cerenkov Imaging Device, *IEEE Trans. Nucl. Sci.* *NS-29*, 328.

GeV GAMMA-RAY ASTRONOMY TELESCOPES WITH HIGH ANGULAR RESOLUTION

B. McBreen,
Physics Department,
University College,
Dublin 4, Ireland.

N85-34959

ABSTRACT

It is shown that a major improvement in angular resolution for the detection of gamma-rays in the GeV region can be obtained with a single crystal as converter. The electron produced by a gamma-ray incident at a small angle to a major crystal axis or plane is captured into channeling and radiates gamma rays. The channeling radiation and the electron-positron pair can be detected and yield point source locations with a precision of 5 arcseconds at 10 GeV. This is an improvement of three orders of magnitude on the angular precision of telescopes sensitive to gamma-rays above 50 MeV flown on satellites.

1. Introduction. During the past two decades observational gamma-ray astronomy been established as an important branch of astrophysical research. Gamma-ray telescopes flown from high altitude balloons provided the initial detection of the Crab Nebula pulsar. Similar but smaller telescopes were flown aboard the SAS-2 and COS-B satellites. These experiments (1,2) explored the galactic plane emission initially discovered by OSO-3 (3). The SAS-2 and COS-B experiments have detected 26 sources with COS-B making the major contribution (4,5). The identification of the gamma-ray sources with known objects at other frequencies has in all but four cases been unsuccessful. The poor angular resolution of the gamma-ray telescopes flown on satellites, with typical error boxes of a few square degrees, accounts for the failure to identify counterparts for the majority of the gamma-ray sources. The present observational situation emphasises an urgent requirement for telescopes with a major improvement in angular resolution.

2 Pair Production. The most probable opening angle of an electron or positron in pair production is $\theta = 0.8/E_\gamma$ where E_γ is the gamma-ray energy in MeV (6). The limitation results from the scattering in the pair production process due the unobserved momentum of the recoil nucleus. The most probable opening angle of an electron from a 2 GeV gamma-ray is 1.4 arcminutes assuming equipartion of energy between the electron-position pair. For a 100 GeV gamma-ray the opening angle of 1.6 arcseconds is comparable with the resolution of ground based optical telescopes. The cross-section for pair production by gamma-rays incident at small angles to crystal planes and axes has been predicted (7) and verified in experiments at accelerators (8). The cross-section depends on the polarisation of the gamma-rays. The variation of the cross-section above 1 GeV is large and may be used to measure the polarisation of the gamma-rays from cosmic sources.

A new pair creation process has been predicted (9) for high energy gamma-rays aligned with major crystal axes and planes. The crystal assisted cross-section along the <111> axes of heavy elements in equal to the Bethe-Heitler value at 10 GeV and exceeds it by an order of magnitude at 30 GeV. The directional pair creation process, if verified by experiment, predicts a higher efficiency for the detection of gamma-rays incident along major crystal axes and planes.

3 Channeling Radiation. Relativistic electrons and positrons, entering the crystal at a small angle to a major axis or plane and captured into channeling, radiate a characteristic spectrum of x-ray and gamma-rays. The theory of channeling radiation has been experimentally confirmed in experiments at accelerators using single crystals of diamond and silicon (10). The channeling radiation intensity from relativistic electrons is far greater than coherent bremsstrahlung and the bremsstrahlung from electrons travelling at random directions in the crystal. In gamma-ray pair production in a lead crystal the electron-positron pairs are produced near an atomic nucleus except for a small fraction that pair produce in the field of atomic electrons. In a model (11) for axial channeling in high Z materials, like lead, the atomic string is replaced by a tube of charge spread continuously with constant density inside a cylinder whose axis coincides with that of the atomic string. The radius R of the tube is determined by the amplitude of the thermal vibrations of the nucleii. The distance R in high Z materials is comparable with the electron screening radius and small in comparison with the distance d between neighbouring atoms in the string. Electrons with energy
$E = \gamma\ mc^2$ will move inside the tube with angular frequency

$$\omega = \frac{e}{R}\left(\frac{2Z}{md\gamma}\right)^{\frac{1}{2}} \qquad (1)$$

where γ is the Lorentz factor. The positrons, unlike the electrons, will not be channeled as no significant bound states exist. The critical angle for electron capture into channeling is

$$\theta_A = \left(\frac{2Ze^2}{dE}\right)^{\frac{1}{2}} \qquad (2)$$

The values of θ_A, in arcminutes, for the <100>, <110> and <111> axes of lead are 2.4, 2.8 and 3.8 for 1 GeV electron. The electron will be channeled because the opening angle in pair production is smaller than the critical angle. At higher gamma-ray energies the electron will be channeled since θ and θ_A decrease as E^{-1} and $E^{-\frac{1}{2}}$ respectively. The electron may be dechanneled by a single Coulomb scattering through an angle greater than θ_A or by the accumulation of a large number of random scatterings. In lead the length ℓ in which half the electrons will be dechanneled is $\ell = 4\times10^{-7}\gamma$cm.
In the model adopted for crystal planes, the planes are replaced with layers of positive charge of constant density and thickness 2R. The critical angle for electron capture into the layer is

$$\theta_p = \left(\frac{2\pi RZe^2}{Ed^2}\right)^{\frac{1}{2}} \qquad (3)$$

The angle θ_p refers only to the angle perpendicular to the plane since the angle in the plane can take any value. The angle θ_p is typically three times smaller for planes than axes resulting in a higher gamma-ray threshold for electron capture and channeling. The opening angle of an electron with half the gamma-ray energy and the capture angle into the (100) plane of lead are equal to 0.4 arcminutes for gamma-ray energies of 8 GeV.

The transverse oscillations of the channeled particles generate electromagnetic radiation which has been studies for electrons and positrons entering the crystal. The electron energy loss in lead is typically 10^{-1} γ^2 MeV cm^{-1} for the major axes and 10^{-3} γ^2 MeV cm^{-1} for the major planes (11). In the GeV energy range the channeling radiation is far greater than the bremsstrahlung radiation from electrons travelling at random directions in the crystal. The channeling radiation and bremsstrahlung have different spectral and angular properties providing additional discrimination against the bremsstrahlung background from nonchanneled electrons and positrons. The maximum frequency of the channeling radiation is given by $\omega_m = \omega \gamma^2$ (12). The radiation from the channeled relativistic electrons is in the x-ray and gamma-ray regions and the maximum frequency increases as $\gamma^{1/2}$. For the <111> axis of lead the maximum energy of the radiated photons from 2 GeV electrons is about 100 MeV. For very high energy electrons the transverse motion of the electron is relativistic and the maximum frequency increases as $\gamma^{1/2}$. In channeling radiation the crystal governs the motion of the electron and therefore the halfwidth of the angular distribution is not due to multiple scattering but is determined by the radiation and beamed into an angle $1/\gamma$ where γ is the Lorentz factor of the radiating electron. The bremsstrahlung radiation is beamed into a much larger angle which is determined by the multiple scattering of the electron and positron in the crystal converter.

4 Gamma-Ray Telescopes. In almost all detectors sensitive to gamma-rays about 50 MeV flown on balloons and satellites, the direction of the gamma-ray was deduced from the directions of the electron-positron pair produced in a lead converter with an unspecified polycrystalline structure and recorded in a spark chamber (13,14,15,16). Two major changes in the traditional design of gamma-ray telescopes are required to utilise channeling radiation. [1] The converter should be replaced with a single crystal or a mosaic of aligned single crystals to cover the typical telescope areas of 0.1 to 1 m^2. [2] The drift or spark chambers for the detection of the electron-position pair require additional converters for the pair production and detection of the channeled radiation. In addition since this telescope can operate in both survey and pointed modes, the telescope requires a stabilised platform for pointed observations of selected sources.

A telescope of this type would have the following features: [1] As in conventional gamma-ray telescopes, operating in a survey mode with a large field of view, the directions of the electron and positron can be used to establish the incident direction of the gamma-ray to a precision of about 0.5°. [2] The requirement that the opening angle of the electron in pair production be equal to the capture angle into channeling determines the threshold energy of the detector. The gamma-ray threshold energy in lead for axial and planar channeling is about 2

GeV and 8 GeV. The channeled electron will typically radiate a burst of five or more gamma-rays into an angle of halfwidth $1/\gamma$. The number of bremsstrahlung photons radiated by an electron in a random direction in the crystal is

$$N = \frac{4x}{3t} \ln \left(\frac{\omega_2}{\omega_1}\right) \quad (4)$$

where x is the path length, t is the radiation length and ω_2 and ω_1 are the maximum and minimum frequencies of the detected photons. In a typical gamma-ray astronomy telescope, with $x = 0.2$ radiation lengths, N will be less than one for the electron and positron. [3] The capture angle of the electron into channeling determines the angular resolution of the telescope. The beamwidths of the axial and planar channels are different. The planar channel beamwidth is determined perpendicular to the crystal plane but in the crystal plane can take any value. The axial and planar channels may be used in point mode operation to map selected sources. The point source location precision will be about one-fifth of the beamwidth or 5 arcseconds at 10 GeV for planar channeling. [4] The gamma-rays from the channeled electron along with the electron-positron pair must be recorded in a spark or drift chamber which includes additional converters for the gamma-rays.

5 Conclusions. It has been shown that a major increase in the angular resolution of gamma-ray astronomy telescopes can be obtained with a crystalline converter. The characteristic signature of a gamma-ray incident at a small angle to a major crystal axis or plane arises from the radiation from the channeled electron that is beamed into an angle $1/\gamma$. The detection of the electron-positron pair and the gamma radiation from the channeled electron can yield point source locations with a precision of 5 arcseconds at 10 GeV.

6. References.

(1) Fichtel, C.E., et al., Astrophys. J. 198, 163 (1975).
(2) Bignami, G.F., et al., Annu. Rev. Astron. Astrophys. 21, 67(1983).
(3) Kraushaar, W.L., et al., Astrophys. J. 177, 341 (1972).
(4) Swanenberg, B.N., et al., Astrophys. J. 243, L69 (1981).
(5) Hartman, R.C., et al., Astrophys. J. 230, 597 (1979).
(6) Olsen, H., Phys. Rev. 131, 406 (1963).
(7) Uberall, H., Phys. Rev. 103, 1055 (1956).
(8) Palazzi, G.D., Rev. Mod. Phys. 40, 611 (1968).
(9) Kimball, J.C., et al., Nucl. Instrum. Methods, B2,25,1984.
(10) Beloshitsky, V.V., et al., Phys. Reports 93, No. 3, 117 (1982).
(11) Bonch-Osmolovskii, A.G., et al., Yad. Fiz. 29, 432 (1979), Sov. J. Nucl. Phys., 29, 216 (1979).
(12) Kumakhov, M.A., Phys. Status Solidii (b), 84, 41 (1977).
(13) Albats, P., et al., , Proceed. 12th ESLAB Symposium, ESA SP-124, 287 (1977).
(14) McKechnie, S.P., et al., Space Science Instrumentation, (5), 81 (1979)
(15) Parlier, B., et al., Nucl. Instrum. Methods, 148, 483 1978.
(16) Share, G.H., et al., Proceed. of 12th ESLAB Symposium, ESA SP-124, 107 (1977).

N85-34960

OG 9.3-5

AN APPROACH OF REDUCING THE BACKGROUND INDUCED BY NEUTRONS

Shen Changquan Ma Yuqian
Gu Yidong Dai Changjiang
Sun Yangfang Fan Zhenzi

Institute of High Energy Physics,Academia Sinica
P.O.Box 918 Beijing,China

1.Introduction

The background induced by interactions of neutrons with detector material (and shield material) is difficult to be rejected.It is one of the most important factors to affect the sensitivity of a balloon-borne gamma-ray astronomical telescope.

The main component of neutron flux at the major detector of the telescope is incident neutrons,that consists of atmospheric neutrons and neutrons locally produced in the balloon platform. Therefore,shielding the detector from incident neutrons is a possible way to reduce the background. NaI (Tl) crystal is very widely used in gamma-ray astronomical telescope. Our balloon-borne experiment have shown that ^{6}LiF shield is effective to reduce the background in NaI crystal.

2.Methods

The energy range of neutrons which can produce important background effects in gamma-ray telescope goes from thermal energies to several hundred MeV (1,2). For our perpose,the ideal neutron shield is an effective absorber or moderator with little gamma-ray production. The isotope ^{6}Li has large (n,α) cross section,which is 942 barns for thermal neutrons and inversely proportional to the square root of neutron energy. Also both ^{6}Li and F nuclei have very little gamma-ray production in neutron flux. Therefore we use ^{6}LiF as the neutron shield.

We built a balloon payload with two identical 75 mm dia. by 75 mm thick NaI (Tl) crystals. It was launched two times, in June of 1983 and in June of 1984. The block diagram of the experiment is shown in Fig 1. The apparatus consists of two identical parts: A and B. The only difference between them is that crystal A is surrounded by a passive neutron shield but crystal B is naked. For the first flight, the shield was 0.4 $g.cm^{-2}$ thick ^{6}LiF covered by 6.5 cm thick polythene. For the second flight it was o.6 $g.cm^{-2}$ thick ^{6}LiF only. The powdery ^{6}LiF was sticked between two layer of 2 mm thick polythene with silica gel, then this sandwich was shaped as a 12 cm dia.by 16 cm deep cylinder and crystal A was placed in it.

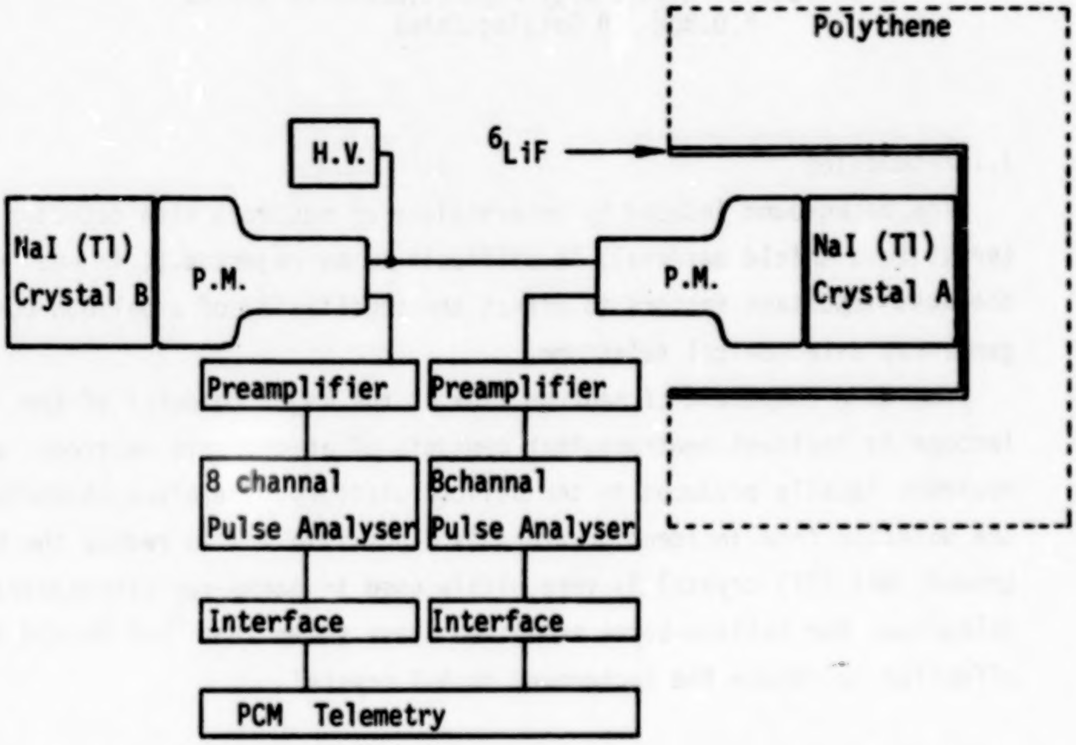
Polythene
H.V.
^{6}LiF
NaI (Tl) Crystal B
P.M.
P.M.
NaI (Tl) Crystal A
Preamplifier
Preamplifier
8 channal Pulse Analyser
Bchannal Pulse Analyser
Interface
Interface
PCM Telemetry

Fig 1. The block diagram of the on board experiment.

3. Result

During the first flight, the background spectra measured by the two detectors with/without neutron shield respectively are different, but they have similar integral background rate in 0.06-2 MeV range.

For the second flight, the integral background rate of the shielded detector in 0.06-2 MeV is about 12% lower than that of the naked one at the altitute 17±1 km where the background rate has its maximum. This value is in excess of 21 times of its standard deviation. The integrated spectra measured there for both detector A and B is shown in Fig 2. In the spectra all counts with energy higher than 2 MeV have been taken off since most of them are contributed by cosmic rays. At other altutute, similar results were recorded.

4.Discussion

Neutrons arriving at a NaI detector may interact by several mechanisms that lead to background counts which have the appearance of the desired gamma-rays events.Firstly,they may undergo radiation capture at either the ^{127}I or ^{23}Na nuclei of the NaI crystal. The ^{127}I has a much larger cross section for neutron absorption than ^{23}Na.

Radiative absorption of ^{127}I leads to a variety of possible prompt gamma-rays via the reaction ^{127}I (n,r)^{128}I. Over an energy range from 60 keV up to about 6.7 MeV,184 different energies were recorded by Archer et al (3).There is also a delayed effect from each neutron absorption on ^{127}I by the beta decay of the product ^{128}I with a half-life of 25 minutes. It makes a continuous spectrum in the energy range less than 2.2 MeV and some gamma-rays e.g. 443 keV gamma-ray.

^{127}I has a resonance region over 15 eV to 1.0 keV in which approximately 75% of absorption events originate,and the strongest resonance region is over 20 eV to 50 eV. Whereas ^{6}LiF can effectively absorbs neutrons in these energy range,for example 0.6 g.cm^{-2} thick LiF layer can absorbs 44% of 15 eV neutrons, 25% of 50 eV neutrons and 7% 1 keV neutrons.This is the reason why ^{6}LiF shield reduces the background.

The second important neutron interaction mecanisms is the inelastic acattering of neutrons at an ^{127}I nucleus. Some energy levels of ^{127}I to be excited by this effect can contribute to the background by emission of gamma-rays at certain energies among which the 58 and 203 keV is the strongest two. Some calculations (2) show that the overall effect of inelastic scattering of the same order as that from prompt effects of neutron absorption and the energy loss spectrum for this mechanisms is roughly a power low of order -1.5 in the energy range 0.2-12 MeV. The background contributed by this mechanisms has not been reduced since we have not found any effective absorber or moderator with little gamma-ray production for fast neutrons.

In our first flight, 6.5 cm thick polythene was used as a moderator. It could slow down some neutrons and make them easier to be absorbed by ^{6}LiF,so that it seems to reduce the background further. But the result is negative, it is similar to Leventhals experimant (4). It indicates that there is some effects in this moderator which increase the background and off set advantage of ^{6}LiF. It seems that it should be careful to add lots of material surround the major detector, since all material could be a background source in the space environment.

In our experiment,since there is no active shield surrounding the NaI (Tl) detectors,the atmospheric gamma-rays are dominant component in background. In this case the value 12% is a significant part of the neutron induced background. Therefore the results are interesting if you also consider 0.6 mm thick ^{6}LiF is neither heavy nor expensive.

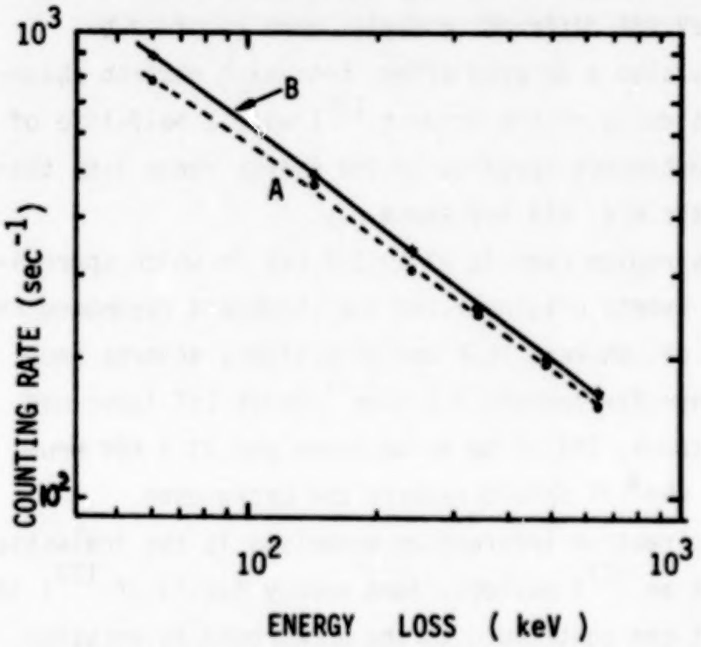

Fig.2.
The energy loss spectrum integrated up to 2 MeV at the altitude 17 km for naked detector B (line) and detector A (dot line) shielded by ^{6}LiF.

References

(1) Chupp E.L., "Gamma-ray Astronomy",Published by D.Reidel Publishing Company (1976),p218

(2) Charalambous P.M. et al.,Nucl.Instr.and Meths (1985),(in Press)

(3) Archer N.P. et al., Nucl. Phys. 83,241 (1966).

(4) Leventhal M.et al.,Ap.J. 240, 338 (1980)

N85-34961

OG 9.3-6

NEUTRON-INDUCED 2.2 MEV BACKGROUND IN GAMMA RAY TELESCOPES

E. M. Zanrosso*, J. L. Long**, A. D. Zych and R. S. White
IGPP, University of California, Riverside, CA 92521
*Xerox Corporation, 125 N. Vinedo Ave., Pasadena, CA 91107
**Hughes Aircraft, P.O. Box 92426, Bldg. R8/2240, Los Angeles, CA 90009

1. Introduction. Neutron-induced gamma ray production is an important source of background in Compton scatter gamma ray telescopes where organic scintillator material is used. Most important is deuteron formation when atmospheric albedo and locally produced neutrons are thermalized and subsequently absorbed in the hydrogenous material. The resulting 2.2 MeV gamma ray line radiation essentially represents a continuous isotropic source within the scintillator itself. Interestingly, using a scintillator material with a high hydrogen-to-carbon ratio to minimize the neutron-induced 4.4 MeV carbon line favors the np reaction.

The full problem of neutron-induced background in Compton scatter telescopes has been previously discussed (1). In this paper we will present results of observations with the University of California balloon-borne Compton scatter telescope (2,3) where the 2.2 MeV induced line emission is prominently seen.

2. Observations. The neutron-induced 2.2 MeV line feature has consistently been present in the background gamma ray spectra measured with the University of California Compton scatter telescope. Figure 1a shows a typical energy spectrum accumulated over a period of 34 hours during a balloon flight from Palestine, Texas in September, 1978. The cutout (Fig. 1b) shows a 1/2 hour accumulation of the line feature at 2.13 MeV with a 0.98 MeV FWHM with the continuum background subtracted. In addition to an expected shift downward in the mean energy from 2.23 MeV due to some loss in event energy from the second scintillator, there was a systematic drift (3.3% or 70 keV) in the mean energy of this 2.2 MeV line feature over the duration of the balloon flight.

Each of the telescope's 56 scintillator cells was calibrated prior to the flight with gamma ray reference sources. During the flight LED light sources in each cell are used to normalize the photomultiplier gains to the pre-flight calibration. The systematic drift referred to above was due to the temperature related drift of the telescope's LED-pulser system which wasn't compensated.

The observed count rates for the 2.2 MeV gamma rays are given in Table 1 for two different geomagnetic vertical cutoff rigidities. With the University of California telescope, the 2.2 MeV line feature is also observed in the upward-moving background spectrum. The upward-moving line feature is approximately four times as intense as the downward moving but is effectively separated from the latter with time-of-flight.

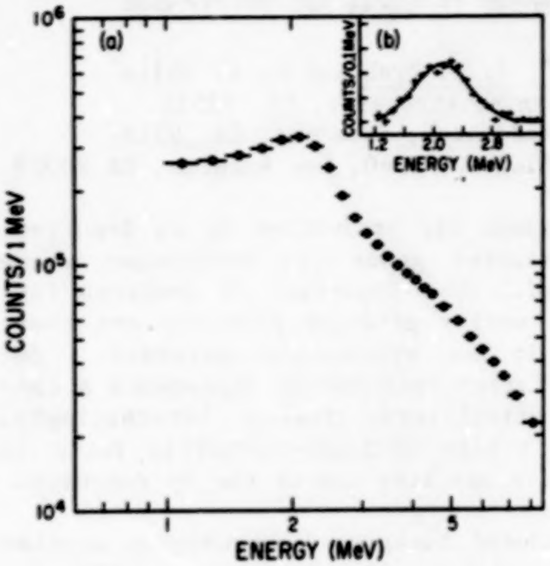

Fig. 1(a) Count rate spectrum of downward moving gamma rays at 4 g/cm^2. (b) Line feature at 2.13 MeV mean energy with continuum background subtracted.

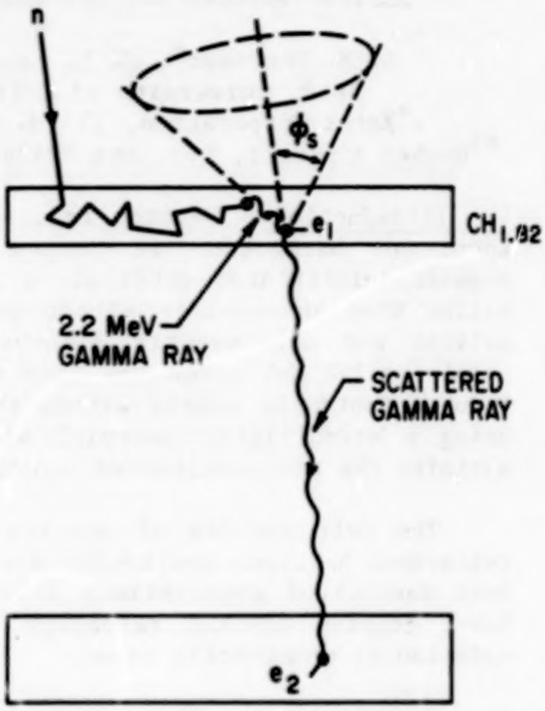

Fig. 2 Typical neutron thermalization and absorption to produce background 2.2 MeV events.

Table 1. Measured Count Rate of 2.2 MeV Induced Gamma Rays

Vertical Cutoff (GV)	Photons/sec
4.5 GV (Palestine, Texas)	2.1
9.0 GV (Alice Springs, Australia)	1.4

3. Calculations. The basic process for detecting a neutron-induced 2.2 MeV photon and misidentifying its direction of origin with a celestial source within the field-of-view of the telescope is shown in Figure 2. First, atmospheric neutrons incident on the large 100 x 100 x 12.5 cm^3 upper scintillator array filled with a mineral oil-based liquid scintillator (H/C = 1.82) are moderated by the hydrogen and carbon until they either escape the boundaries of the array or are absorbed by the hydrogen. Most of the absorbed neutrons are thermalized first (E_n = 0.025 eV).

The fraction of incident isotropic neutrons which actually are absorbed has been calculated with a Monte Carlo code. These results are summarized in Table 2. Typically, about 20% of the incident neutrons are absorbed; they have an exponential absorption time distribution with a mean time of about 140 μsec.

Table 2. Thermalization and Absorption of Isotropic Neutrons Incident on a 100 x 100 x 12.5 cm^3 Scintillator (H/C=1.82)

E_n(MeV)	Percent Thermalized	Percent Absorbed
10	25	14
1	43	23
0.1	42	22
0.01	40	20

Near the top of the earth's atmosphere the cosmic ray albedo neutron flux is relatively insensitive to float altitude changes typical of balloons. Thus the 2.2 MeV gamma ray production rate in the large scintillator array is constant. Using a value of 0.1 neutron/cm^2-sec for this flux (4) at 9 GV, the production rate is approximately 250/sec for the upper scintillator array. At 4.5 GV this rate should be larger by a factor of 2.1. It is primarily neutrons above 10 keV that produce this flux due to the flatness of the albedo spectrum below this energy.

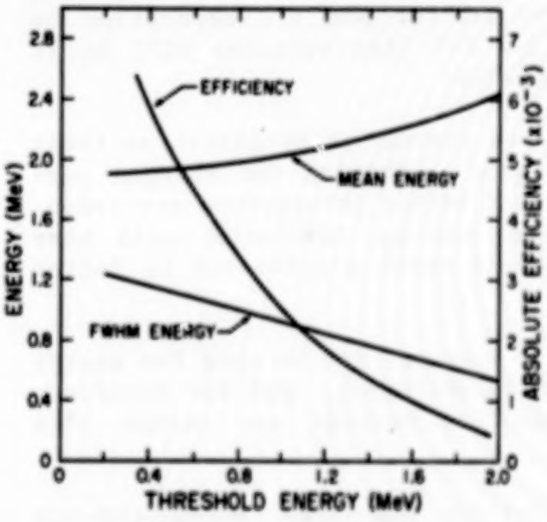

Fig. 3 2.2 MeV gamma ray detection efficiency as a function of energy threshold. Also shown are the variations in mean energy and FWHM.

The actual counting rate for the induced 2.2 MeV γs depends on the double scatter efficiency of the telescope which, in turn, is very sensitive to the energy thresholds in the two scintillator arrays. We have used our gamma ray Monte Carlo transport code to calculate this efficiency for 2.2 MeV photons distributed uniformly throughout the upper scintillator array with an isotropic angular distribution. These results are shown in Figure 3 as a function of the summed energy threshold for the upper and lower scintillator arrays. For a 1 MeV threshold the expected rate is 0.6/sec compared with the observed rate of 1.4/sec at 9 GV. In the above calculation we have neglected the non-negligible downward neutron flux due to the atmosphere remaining above the balloon and any locally produced neutrons in the telescope itself.

The efficiency and, therefore, the count rate is a very sensitive function of the threshold. Also affected by the threshold are the mean energy assigned to the 2.2 MeV peak and the FWHM of the line feature. This is because the threshold energy is comparable both to 2.2 MeV and the energy resolution of the telescope.

Since the production rate of induced 2.2 MeV γs is constant the telescope count rate of these events is a sensitive function of the photomultiplier tube gains. For example, a gain increase of 10%, which is effectively an energy threshold reduction by the same amount, will account for a count rate increase of 16% while the mean energy of the line changes by 7.8% or 160 keV.

The induced 2.2 MeV line emission poses a limitation for observing this same line feature from celestial gamma ray sources. The importance of this line emission in astrophysical processes is illustrated by its dominance in the Sun's solar flare gamma ray emission. Based on our measured count rate of this line feature, our minimum detectable flux for 2.2 MeV line emission is $2.2 \times 10^{-4} \gamma/cm^2$-sec at the 4 sigma level for six hours of observation at 9 GV.

4. Conclusions. The sensitivity for observing 2.2 MeV line emission from celestial sources will be limited by the neutron-induced background at this energy. This will be especially true of gamma ray telescopes which use substantial amounts of organic scintillator materials. This source of background cannot be removed with pulse shape discrimination techniques in the organic scintillator because of the relatively long time delay between the initial neutron scatter and its absorption by hydrogen. Any positive detection of 2.2 MeV line emission will be in addition to the ever-present induced emission.

Gamma ray telescopes which do not use organic scintillator as their primary detection element but do use large quantities for charged particle shields will also see this background unless precautions are taken. Compton scatter telescopes with improved angular resolution will have somewhat improved sensitivity because valid event circles can be better correlated with known source directions.

The 2.2 MeV background line feature, however, can be used for energy calibration purposes if needed or, which is preferred, used for verification that the calibration and gain-control methods are stable with respect to long term drift.

5. Acknowledgments. We wish to acknowledge NASA grant NGR-05-008-022 for support of this research.

References

1. R. S. White and V. Schönfelder, (1977), Astrophys. and Spc. Sci. 38, 19.
2. Herzo, D., et al., (1975), Nuc. Instr. and Meth. 123, 583.
3. Zych, A. D., et al., (1975), IEEE Trans. Nuc. Sci., NS-22, 605.
4. Jenkins, R. W., et al. (1970), Journ. Geophys. Res., 75, 4197.

N85-34962

A COMPARISON OF CALCULATED AND MEASURED BACKGROUND NOISE RATES IN HARD X-RAY TELESCOPES AT BALLOON ALTITUDE

A.J.Dean[1], N.A.Dipper[1], R.A.Lewis[1], F.Perotti[2]

1. Department of Physics, University of Southampton, Southampton, UK
2. Istituto di Fisica Cosmica, Milano, Italy.

ABSTRACT

An actively shielded hard X-ray astronomical telescope has been flown on stratospheric balloons. In this paper we compare the measured spectral distribution of the background noise counting rates over the energy loss range 20-300keV with the contributions estimated from a series of Monte Carlo and other computations. The relative contributions of individual particle interactions aré assessed.

1. Introduction. The sensitivity of hard X-ray telescopes is dependent to a first approximation upon a number of desirable characteristics: a large sensitive area, long observation periods, high photon detection efficiency and a low background noise level. The first two factors are very dependent upon the platform from which the telescope must operate, whilst the effective suppression of background noise requires a detailed analysis of the physical processes involved. We present in this paper the background levels observed in an actively shielded collimated telescope during a balloon flight from Palestine, Texas in 1982. The experimental results are compared with theoretical and computer predictions of the background counting rates.

2. Configuration of the Hard X-ray Telescope. The telescope was composed of 8 NaI(Tl) scintillation crystals (200x200x6mm) shielded over the lower 2π steradians by a 5cm thick NaI(Tl) crystal of the same area. A thin plastic scintillator designed to reject events due to charged particles covered a large fraction of the upper 2π steradians. The aperture of the detectors was restricted to 3 degrees FWHM by a copper collimator. A passive graded shield also surrounded the collimators and the sides of the crystals. A schematic diagram of the telescope is shown in Fig.1. In addition a Sodium Iodide detection crystal, identical to the primary crystal in the telescope, was flown in a completely unshielded configuration in order to determine the efficiency of the

shielding system. The telescope and unshielded crystal were flown on the same stratospheric balloon gondola from Palestine, Texas.

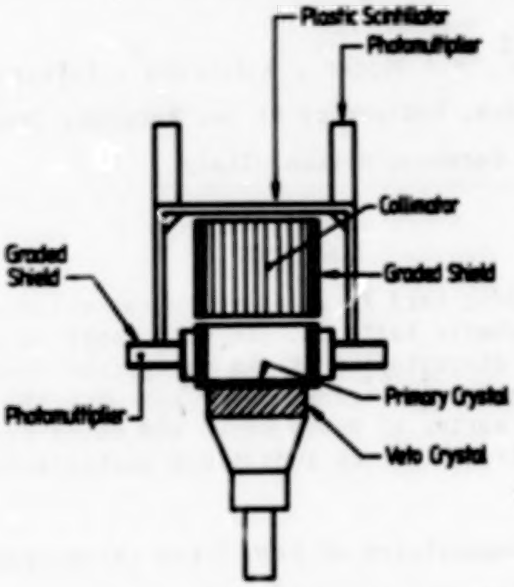
Plastic Scintillator
Photomultiplier
Collimator
Graded Shield
Graded Shield
Primary Crystal
Photomultiplier
Veto Crystal

Fig.1. A schematic view of the X-ray telescope detector units

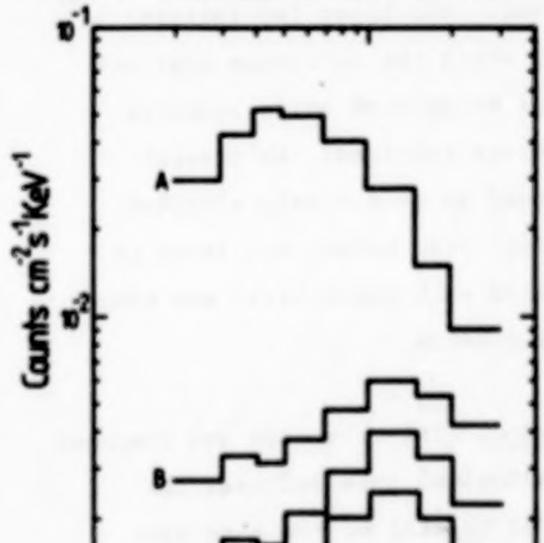

Fig.2. The counting rate in the MIFRASO NaI(Tl) detectors at 4.1mbs residual pressure for four different shielding configurations;
a) counting rate in unshielded det.
b) counting rate in unshielded det. with all active anticoincidence off.
c) counting rate in shielded det. with NaI(Tl) active shield on but with plastic anticoincidence off.
d) counting rate in primary det. with all shielding systems functioning.

Figure 2 demonstrates the effectiveness of each type of shield by showing the counting rates at balloon altitudes for different shielding configurations. It clearly demonstrates that the majority of the reduction in background counting rate is achieved by the passive shield with both sets of active anticoincidence causing roughly similar further reductions in the unwanted background noise.

3. Comparison of measured and calculated background levels. The predicted background counting rate in the detectors of the MIFRASO telescope was computed by a combination of theoretical and Monte Carlo techniques. The photon induced background was determined from the results of an extensive Monte Carlo model of the entire detection system. The program modelled the processes of photoelectric absorption and Compton scattering, but neglected electron transport due to the fact that the path lengths involved for the energy range under consideration are generally small compared to the dimensions of the elements of the telescope. The angular and energy distribution of the gamma-ray fluxes incident over the detector could be varied to suit the particular physical processes under investigation. In each case the energy deposits in all the elements of the telescope were recorded in order to provide an insight into the efficiency of the various shielding systems.

Neutrons arriving at the primary crystal may generate background noise by a variety of mechanisms but the most important are (n,γ) radiative capture and inelastic scattering by the ^{127}I nuclei. Radiative capture by ^{127}I leads to a variety of possible prompt gamma-rays by the reaction $^{127}I(n,\gamma)^{128}I$. The various gamma-ray energies are very extensive and extend from 60 keV up to 6.7 MeV. There is also a delayed effect from the decay of 128 which has a half life of 25 min. The two lowest levels to be excited by inelastic scattering at a ^{127}I nucleus lead to the emission of gamma-rays at energies of 58 and 203 keV.

The neutron flux incident upon the detectors is made up of two components, atmospheric neutrons and those produced within the payload by "boil off" from cosmic ray interactions. The modified neutron flux will depend upon the exact geometry and mass of the payload but may be estimated as described by Charalambous et al (1985) by assuming a uniform distribution of mass and integrating over the volume of the payload. This neutron flux was folded with the cross sections for radiative capture and inelastic scattering to yield an estimate for the background counting rate of neutron induced events. The contribution from charged particles has been estimated from the effect of the plastic scintillator shield. If the shield is assumed to be 100% efficient over the solid angle that it covers, it is possible by considering the effect of switching on and off the shield, to estimate the number of events caused by particles that enter through the solid angle that is not shielded.

High energy cosmic ray protons which are incident upon the material of the detection plane give rise to background events which are derived from the radioactive spallation products produced in the interaction. In general, the veto pulse may be made as long as possible to suppress a number of these types of events. However, since the timescales associated with many of the decay schemes are considerably longer than practicable veto pulse lengths the active shield does not eliminate this type of noise. Calculations of spallation involved background are extremely complex and subject to considerable error so that a reliable estimate of this source of noise is best obtained by experiment. Results of such tests have been reported in the literature (Baker et al 1979) and have been used to yield an estimate for the MIFRASO detectors.

The results of the various calculations are shown in Fig.3. The agreement between calculation and experiment is quite good being within a factor of two and having the same spectral distribution. The similarity in spectral shapes is an encouraging sign that the relative contributions of the various effects as determined by calculation are correct

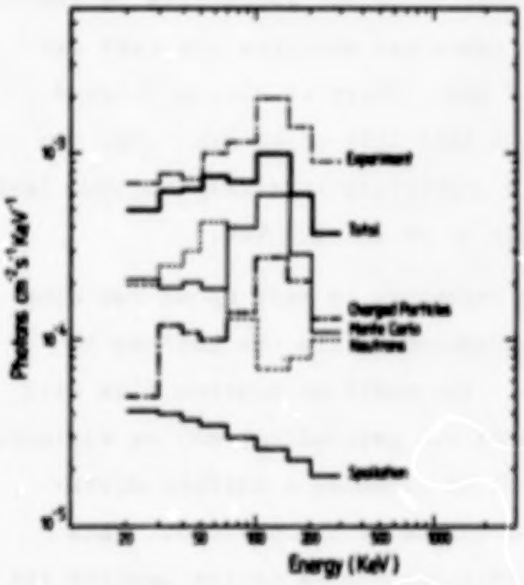

Fig.3. A comparison between observed and calculated background noise events.

References

1. Baker R.E.et al.NIMS, 158. (1979) 595.
2. Charalambous,P.C.et al. NIMS (in press
3. Dean,A.J. and Dipper,N.A. MNRAS (1981), 194, 219.

N85-34963

OG 9.3-8

THE FINAL COS-B DATABASE - NOW PUBLICLY AVAILABLE

H.A. Mayer-Hasselwander[4], K. Bennett[6], G.F. Bignami[2], J.B.G.M. Bloemen[1a], R. Buccheri[3], P.A. Caraveo[2], W. Hermsen[1], G. Kanbach[4], F. Lebrun[5], J.A. Paul[5], B. Sacco[3], A.W. Strong[4]

The 'Caravane' Collaboration for the COS-B satellite:
[1]Laboratory for Space Research Leiden, Leiden, The Netherlands
[2]Istituto di Fisica Cosmica del CNR, Milano, Italy
[3]Istituto di Fisica Cosmica e Informatica del CNR, Palermo, Italy
[4]Max Planck Institut für Physik und Astrophysik, Institut für Extraterrestrische Physik, Garching bei München, Germany
[5]Service d'Astrophysique, Centre d'Etudes Nucléaires de Saclay, France
[6]Space Science Departement of the European Space Agency, ESTEC, Noordwijk, The Netherlands
[a]Sterrewacht Leiden, Huygens Laboratorium, Leiden, The Netherlands

ABSTRACT

The data obtained by the gamma-ray satellite COS-B have been processed, condensed and integrated together with the relevant mission and experiment parameters into the 'Final COS-B Database'. The database contents and the access programs available with the database are outlined. The final sky coverage and a presentation of the large-scale distribution of the observed Milky-Way emission are given. The database is anounced to be available through the European Space Agency.

1. Introduction: Gamma-ray astronomy in the energy range from about 50 MeV up to several GeV is based at present on the data obtained by only two successful satellite experiments, both using the sparkchamber technique: the first flown in 1972-1973 on the SAS-2 satellite of NASA, the second flown on the ESA satellite COS-B. SAS-2 operated ≈7 months and aquired about 8,000 gamma-ray events (1), COS-B was in successful operation from August 1975 until April 1982 and recorded about 210,000 gamma photons. A presentation of part of the COS-B database was given by Mayer-Hasselwander et al. (2).

The two datasets differ in the following respects: a) The low orbit of SAS-2 was well shielded by the earth's magnetic field against the cosmic-ray flux, ensuring a very low instrumental background level; the highly eccentric orbit (due to practical constraints) of COS-B exposed the satellite to the full cosmic-ray intensity, inducing a comparatively high instrumental background level, which is variable with the solar 11-year cycle. b) The COS-B experiment was supplemented by an energy calorimeter, providing good energy information for each recorded photon. c) Due to the differences in experiment configuration the low-energy threshold of SAS-2 was somewhat lower (≈30 MeV), than for COS-B (≈50 MeV). d) The COS-B experiment achieved a complete coverage of the galactic ridge. Its long lifetime, allowing for repeated observations in regions of special interest, enabled detailed analyses of the spatial distribution and of possible time variations of the observed emission.

The databases of SAS-2 (3) and of COS-B will remain for several years the only available gamma-ray survey data, and after the forthcoming experiments GAMMA-1 and EGRET, these databases will remain of interest e.g. in the search for possible secular and periodic time variations of celestial gamma-ray objects. Although considerable analysis effort already has been invested to exploit the data, certainly much more can be done by applying new methods or by using the data together with upcoming new results in other ranges of the electromagnetic spectrum. So it appeared to be mandatory to establish and to make available the COS-B database in a way which will make possible future analysis also by scientists not familiar with the experiment.

2. The COS-B experiment and mission: The European Space Agency's satellite COS-B was dedicated to gamma-ray astronomy in the energy range 50 MeV to 5 GeV and carried a single experiment: a sparkchamber telescope (4), developed in collaboration by six European institutes. The experiment became operational on August 17, 1975 and was switched of on April 25, 1982, when onboard resources were exhausted. During this timespan 65 observations, mostly of a month duration, were performed. The satellite was spin stabilized, with the telescope axis along the spin axis and circular sky regions of about 40 degree diameter were covered in each observation. The majority of the pointings were distributed along the galactic equator, 15 observations were devoted to regions at high (≥20°) galactic latitudes. Several regions of specific interest were repeatedly observed. The overall coverage of the sky is illustrated by Figure 1.

The highly eccentric polar orbit of COS-B with an apogee around 90,000 km, chosen to maximize useful observation time while allowing real-time data transmission, exposed the experiment to the solar modulated interplanetary cosmic-ray flux. The unexpectedly long operational life of the experiment, specifically of the sparkchamber, was acompanied by a long-term degradation and by short-term disturbances of its performance and consequently of the experiment sensitivity. The instrumental background and its variation and the changes in instruments sensitivity were thoroughly investigated. The corrections finally adopted and incorporated in the final database were derived by the method described in a subsequent paper (5). The possible impact of their statistical and systematic uncertainties must be considered in any type of analysis. It is emphasized that the corrections are averages over complete periods.

3. The database content and organisation: The database consists of several parts: A) the observation period, basic dataset, and individual gamma-ray event information, B) the experiment sensitivity, energy dispersion and pointspread functions as derived by accelerator and inflight calibrations, C) programs for easy and efficient access of the database, which produce event lists and skymaps for selected data parameters and time intervals, D) binned skymaps of the galactic disc.

Part A) consists of 3 files: the first one contains a list of the parameters of the 65 observations, including background and sensitivity corrections for each period; the second provides similar information for the 5,943 datasets which correspond to the uninterrupted time intervals during original data recording; the third contains 209,537 entries, one for each accepted gamma-ray event.

Part B) contains the instrument response functions. The sensitivity, energy-dispersion and pointspread-function files are derived from prelaunch calibration; the latter is also based on analysis of the brightest gamma-ray source, the Vela pulsar.

In part C) a collection of Fortran-77 programs is provided, which should allow for easy handling and efficient access of the database. Included are programs to move the database between tape and disc, to make event selections on event parameters and time intervals, and to produce binned skymaps of intensities, counts and exposures. Since these programs access the files in direct access mode, the database has to reside on disc, requiring about 25 Mb of disc space. The system was developed and used under various IBM operating systems (360/OS, MVT, MVS; VM/370, CMS), but also after moderate adaption,

ORIGINAL PAGE IS
OF POOR QUALITY

has been successfully used on a VAX computer.

Part D) contains an atlas in several energy bands of the Milky Way.

Figure 2 gives as an illustration a map of the galactic disc emission (150 MeV), produced by a maximum entropy algorithm (7) using the database.

A more detailed description of the gamma-ray data and instrument response functions is in preparation (6). In view of the complexity of the data it is recommended to consult or to collaborate with members of the 'Caravane' collaboration when detailed analysis of the data is undertaken. It is hoped, that the release of this unique database will promote the full exploitation of the data, which appears mandatory in view of the enormous efforts in acquiring it.

The database is available on tape from the COS-B project scientist, Dr.K. Bennett, at the Space Science Department of ESA.

References:

1. Fichtel, C.E. et al.: 1975, Astrophys. J. **198**,163
2. Mayer-Hasselwander, H.A. et al.: 1982, Astron. Astrophys. **105**,164
3. Fichtel, C.E. et al.: 1978, NASA Technical Memorandum 79650
4. Bignami, G.F. et al.: 1975, Space Science Instrum. **1**,245
5. Strong, A.W. et al.: 1985, Proc. XIX ICRC, La Jolla
6. Mayer-Hasselwander, H.A. et al.: in prep. for Astron. Astrophys. Suppl.
7. Skilling, J. et al.: 1979, Mon. Not. Roy. Astr. Soc. **187**,145

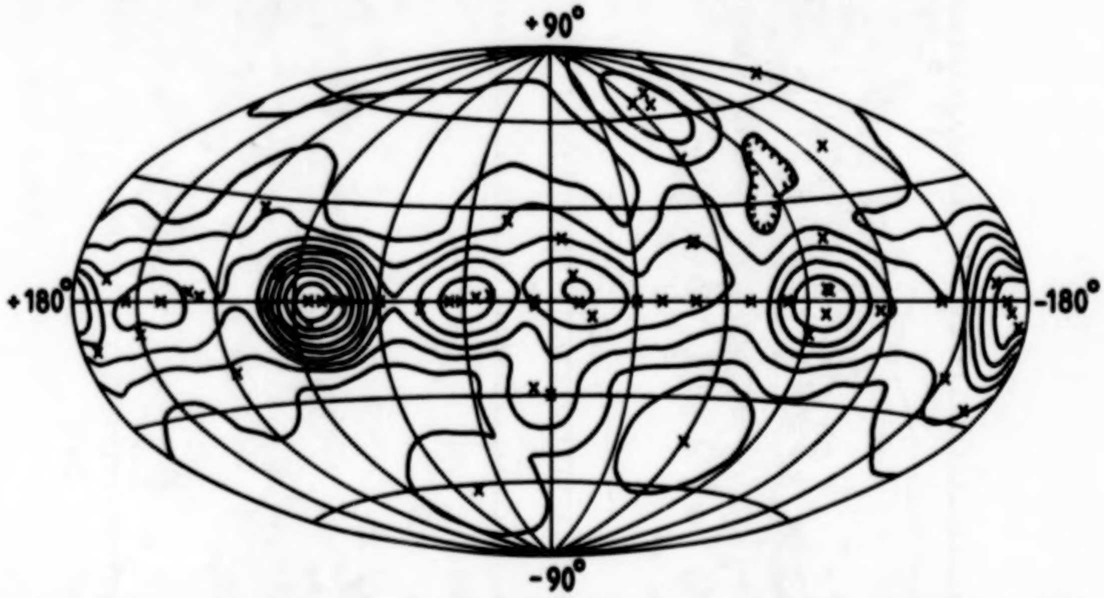

Figure 1: Approximate sky exposure achieved by the COS-B experiment. The contour levels are in 32 d steps, the lowest being 8 d (the exposure time is weighted with the inclination dependance of the sensitivity). The crosses indicate the pointing directions of the 65 observation periods.

Figure 2: Preliminary 'maximum entropy' deconvolved map of the galactic disk, indicating the structure in the emission seen in the energy range 150 MeV to 5 GeV, derived from the database described in this paper. An approximately logarithmic intensity scale was chosen to allow the display of structure in both intense and weak emission regions. This presentation does not give accurate absolute intensities.

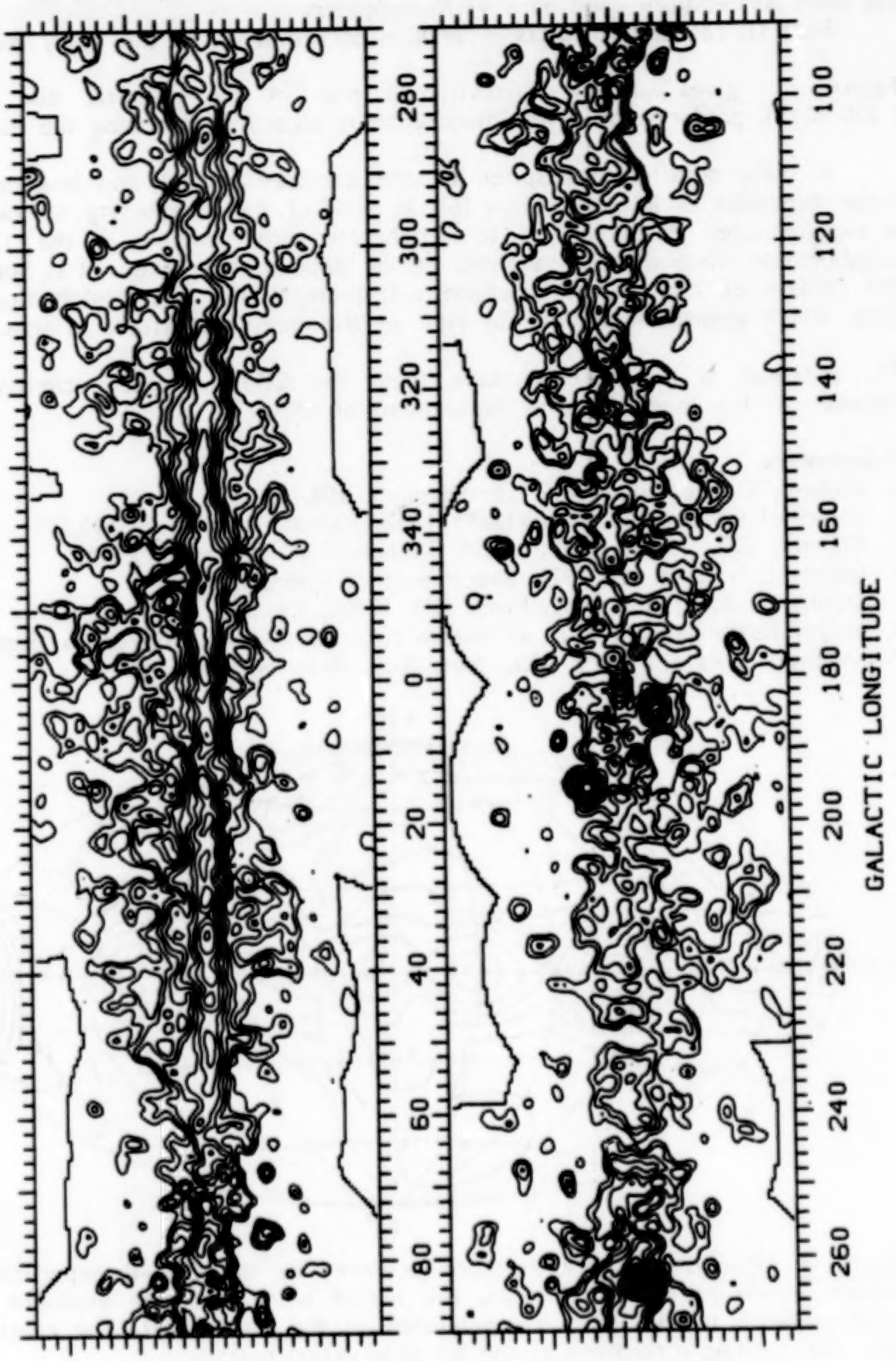
280
300
320
340
0
20
40
60
80
100
120
140
160
180
200
220
240
260
GALACTIC LONGITUDE
20
10
0
-10
-20
20
10
0
-10
-20
GALACTIC LATITUDE

THE FINAL COS-B DATABASE: IN-FLIGHT CALIBRATION OF INSTRUMENTAL PARAMETERS

A.W. Strong[4], *J.B.G.M. Bloemen*[1a], *R. Buccheri*[3], *W. Hermsen*[1],
F. Lebrun[5], *H.A. Mayer – Haßelwander*[4]

The Caravane Collaboration for the COS-B satellite:

1. Laboratory for Space Research, Leiden, The Netherlands
2. Istituto di Fisica Cosmica del CNR, Milano, Italy
3. Istituto di Fisica Cosmica e Informatica del CNR, Palermo, Italy
4. Max-Planck Institut für Physik und Astrophysik, Institute für Extraterrestrische Physik, Garching-bei-München, Germany
5. Service d'Astrophysique, Centre d'Etudes Nucleaires de Saclay, France
6. Space Science Department of the European Space Agency, ESTEC, Noordwijk, The Netherlands

a Sterrewacht Leiden, Huygens Laboratorium, Leiden, The Netherlands

ABSTRACT

A method for the determination of the temporal variation of sensitivity and instrumental background of the COS-B experiment is described, and representative results are presented.

1. INTRODUCTION

The COS-B experiment operated for 6.7 years during which appreciable variations in sensitivity and background occurred. Effective use of these data for scientific analysis requires the determination of the variations and this involves the intercalibration of overlapping observations of the same regions of sky made at different epochs. The final database (described in Mayer-Hasselwander et al. 1985 and this confererence, OG9.3-8) provides ample coverage for such a determination, but owing to the large amount of data involved the problem is not trivial.

Three types of temporal response variation can be distinguished:

(i) long term variations in sensitivity due to degradation in spark- chamber performance

(ii) shorter term period-to-period variations in effective sensitivity due to fluctuations in spark-chamber performance or to the manual editing process

(iii) long-term variations in instrumental background arising from variations in the ambient cosmic-ray intensity.

A method of determination of the variations which uses a non-linear optimisation technique has been successfully applied. The general principle is to use the Galactic diffuse emission as a stable 'calibration source'to compare the response of the instrument at different epochs. The main problem is that observations far apart on the sky are effectively decoupled and this method can give no information on the relative detector response; however the instrument pointing directions were fairly randomly distributed in time so that there should be no correlation between sensitivity and pointing direction, and this can be used as a strong constraint on the solution.

The method is designed to find a set of parameters which lead to maximum consistency between the intensities derived from different observation periods. This will be briefly described and the resulting sensitivity and background variations presented.

2. METHOD

The gamma-ray sky (latitudes $|b| < 30^\circ$) is divided into *subcells* of 1° square, and the field of view of each observation period (20° radius) is divided into *cells* of 100° square by raster scans 1° wide along increasing longitude. For each period i the predicted number of gamma-ray events in subcell j based on the total observations is

$$n_{ij} = f_i e_{ij} \frac{\sum_k (n^o_{kj} - f_k e_{kj} \Delta I_{Bk})}{\sum_k f_k e_{kj}} + f_i e_{ij} \Delta I_{Bi}$$

where the sum is over all periods in which the subcell was observed and

n^o_{kj}= number of events observed in subcell j in period k

f_i= sensitivity relative to the first period ($i = 0$), e_{ij}= nominal exposure (in $cm^2 s$) to subcell j in period i (uncorrected for temporal variations), ΔI_{Bi}= charge in background in period i relative to period 0 .

We define

$$\chi^2 = \sum_i \sum_m \frac{r^2_{im}}{N_{im}}$$

where $N_{im} = \sum_{j \subset cell\ m} n_{ij}$, $N^o_{im} = \sum_{j \subset cell\ m} n^o_{ij}$, and $r_{im} = N^o_{im} - N_{im}$.

The background variation was found from independent studies to correlate with the solar-modulated cosmic ray intensity. This confirmed the expectation that the background is due to γ-rays produced by cosmic-ray interactions with the material in front of the telescope. On this basis the *background variation* was assumed to have the form $\Delta I_{Bi} = b \Delta S_3$ where ΔS_3 is the change in rate of a scaler sensitive to the total charged particle intensity in the detector. The constant b was determined in the analysis along with the sensitivities.

In order to avoid any correlation of sensitivity with position on the sky (see Sec.1), a *fluctuation parameter* S is defined by $S = \sum_i (1 - \frac{f_i}{f^o_i})^2$, where f^o is chosen to fit the temporal smooth long-term trend. The technique then consists of minimising χ^2 subject to the constraint of constant S. Suitable values of S were found empirically and adopted in the final determination of the sensitivity and background parameters. Although the method involves about 60 free parameters the number of constraints is much larger than this and the minimisation can be performed by suitable conjugate gradient methods (see Strong et al. 1985 for details).

ORIGINAL PAGE IS
OF POOR QUALITY

3. RESULTS

Fig 1 shows the variation of sensitivity based on application of the method to data in the range 70 - 5000 MeV. Most evident is the long term variation which causes a 50% reduction over the full time span of the experiment. The method was also applied to the separate energy ranges 70-150, 150-300 and 300-5000 MeV to obtain three independent estimates. The results are consistent with those from the total energy range and show that the period-to-period variations are significant and, further, that the sensitivities are determined with an accuracy which is usually better than 10%. In addition the results in the 3 ranges give an indication of the accuracy of the sensitivity determination in individual periods.

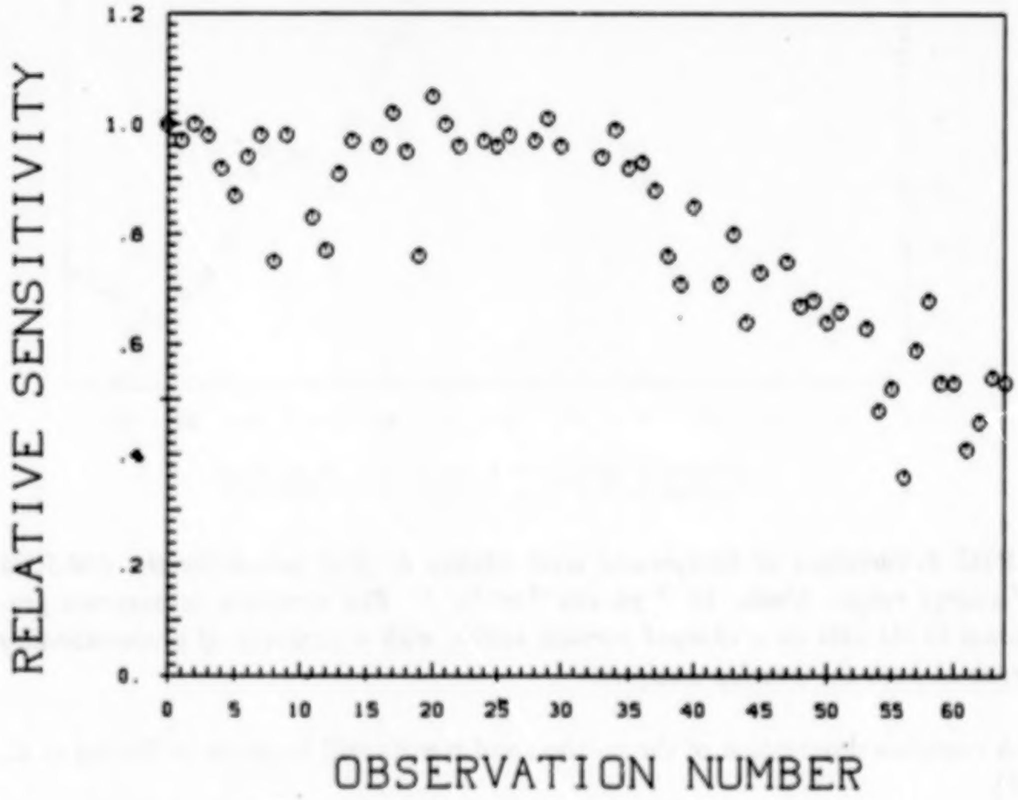

FIG 1. *Relative sensitivity as function of observation period determined for the 70-5000 MeV energy range using the method described in the text. The sensitivity of the first period (Period 0) is taken as 1.0. Periods pointed at high latitudes with insufficient overlap are not displayed.*

There is no trend visible when the sensitivities are plotted as a function of Galactic longitude, demonstrating the success of the technique described above. The larger fluctuations in sensitivity can be identified as originating in known effects such as instrumental malfunctions, and where an independent estimate of the size of the effect can be made the agreement is satisfactory.

Fig 2 shows as an example the background variation in the energy range 300-5000 MeV. The total variation amounts to about 30% of the average absolute background level.

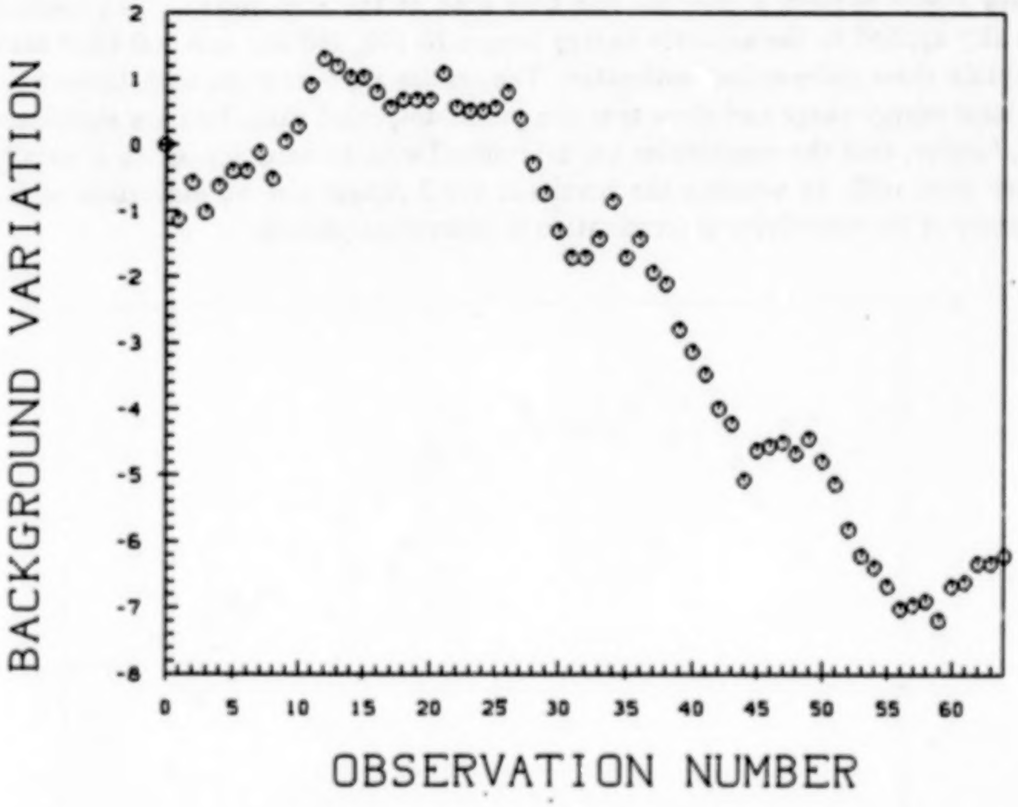

FIG 2. *Variation of background level relative to first period for the 300-5000 MeV energy range. Units:* 10^{-6} *ph* $cm^{-2}sr^{-1}s^{-1}$. *The variation is assumed proportional to the rate in a charged particle scaler, with a constant of proportionality determined from the overlap analysis.*

A complete description of the method and results will be given in Strong et al. (1985).

REFERENCES

Mayer-Hasselwander H A et al. (1985) *in preparation*

Strong A W et al. (1985) *in preparation*

N85-34965

OG9.3-10

A STAR CAMERA ASPECT SYSTEM SUITABLE FOR USE ON BALLOON EXPERIMENTS

S.D. Hunter, R.G. Baker
Code 662, NASA/Goddard Space Flight Center
Greenbelt, Maryland 20771 U.S.A.

1. Introduction. We have designed, built and flown, on a balloon borne experiment, a star camera aspect system. This system was designed to provide offset corrections to the magnetometer and inclinometer readings used to control an azimuth and elevation pointed experiment. The solid state camera used is a General Electric TN2500 CID camera with a Nikkon Noct-Nikkor 58mm f/1.2 lens. The camera is controlled by a Texas Instrument TMS 9995 microprocessor, including commandable exposure and noise rejection threshold, as well as formatting the data for telemetry to the ground. As a background program, the TMS 9995 runs the aspect program to analyze a fraction of the pictures taken so that aspect information and offset corrections are available to the experiment in near real time. The analysis consists of pattern recognition of the star field with a star catalog in ROM memory and a least-squares calculation. The hardware, software and star catalog which make up this system are fully described in reference 1. This paper describes the performance of this system in ground based tests and as part of the NASA/GSFC High Energy Gamma-Ray Balloon Instrument (2).

2. Ground Tests. Ground based tests were performed during 1983 and early 1984 to check the operation of the star camera and aspect program. The TN2500 camera provides an 8 bit digital output, in addition to a standard analog output, which made the camera easy to interface to the microprocessor and provided a convenient measure of star intensities. In the following, ADC counts or counts refers to the digitized output of the pixel or pixels illuminatd by a star.

The intensity of several observed stars in ADC counts for a five second exposure (integration time) as a function of visual magnitude is shown in Figure 1. Each data point represents a lower bound to the intensity because some of the light from a star can fall on the inactive area of the CID chip between the pixels. Stars of magnitude fainter than about 3 illuminate single pixels whereas brighter stars illuminate several pixels. Their intensity is the sum of the response of all the pixels comprising the star image. The observed intensity of brighter stars was fairly constant except for atmospheric effects. The intensity of dimmer stars varied much more dramatically as the star image partially or completely fell on the inactive area between pixels.

For the ground tests, the CID chip was cooled to about 5°C with a thermo-electric cooler. This reduced the thermal noise by a factor of two to between 5 and 8 counts. Thus, from Figure 1, it can be seen that, for a five second exposure, stars of magnitude six were detected with a signal-to-noise ratio of about one. A signal-to-noise ratio of one and the inclusion of a few noise pixels, which are indistinguishable from star images, does not affect the operation of the aspect program other than to slow down the calculation. The aspect program, when provided with the approximate altitude and elevation of the camera, was able to calculate the aspect information for the observations.

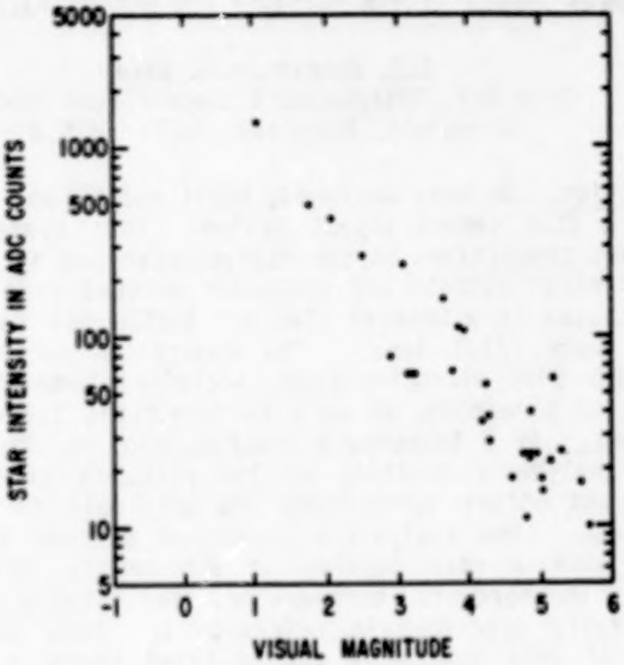

Figure 1 -- CID camera star intensity as a function of visual magnitude for a five second exposure.

3. Balloon Flights. The first balloon borne experiment to use this camera aspect system was flown on May 9, 1984. The first two hours of the flight were dedicated to tests of the aspect system. Three regions of the sky were observed in the constellations of Hercules, Ursa Major and Aquila. During the Aquila observation, 78 pictures were taken. The star Altair (53-α Aqu., Mv = 0.77) was seen in all the pictures. It was so bright that all the pixels which formed the star image were saturated. The star 50-γ Aqu, Mv = 2.7 was seen in almost all the pictures. Its single pixel intensity varied between 25 and 70 counts. The star 60-β Aqu., Mv = 3.7 was seen in only three pictures. The observed intensity was 10, 22 and 33 counts. The only dimmer star observed was 75-Her., Mv = 4.2, which had an average observed intensity of about 8 counts. The signal to noise ratio for these observations was about one although the thermo-electric cooler was not needed due to the low temperature at balloon altitudes.

The azimuth-elevation pointing system of the balloon experiment held the desired azimuth pointing direction within a 0.5° deadband. The elevation drive was powered off during the camera tests. Within the azimuth deadband the experiment moved with an azimuthal velocity between 0.08 and 0.1 degrees per second at all times. This azimuth velocity produced an effective exposure of about 0.5 second per pixel since the star images were smeared over several pixels. Taking into account this effective exposure, the above intensities are consistent with the ground based results shown in Figure 1 if scaled by a factor of ten to correct for the difference between the 0.5 second effective exposure and the 5 second ground based exposure.

ORIGINAL PAGE IS
OF POOR QUALITY

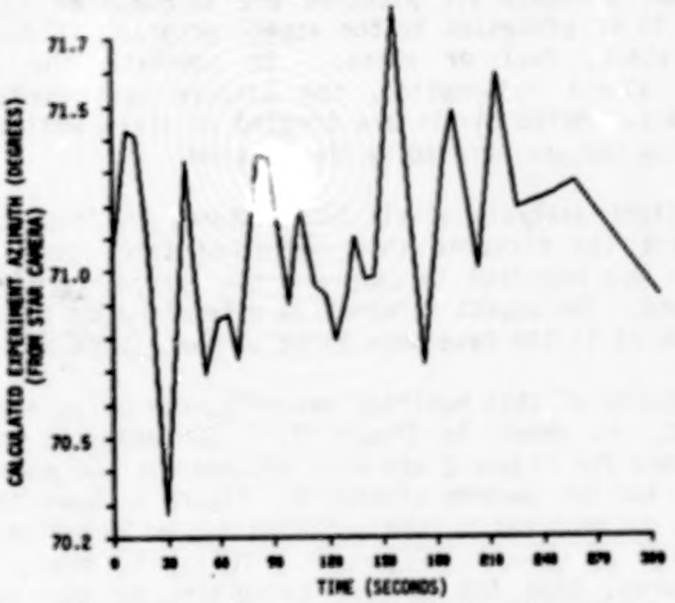

Figure 2 -- The azimuth angle calculated for the experiment by the aspect program.

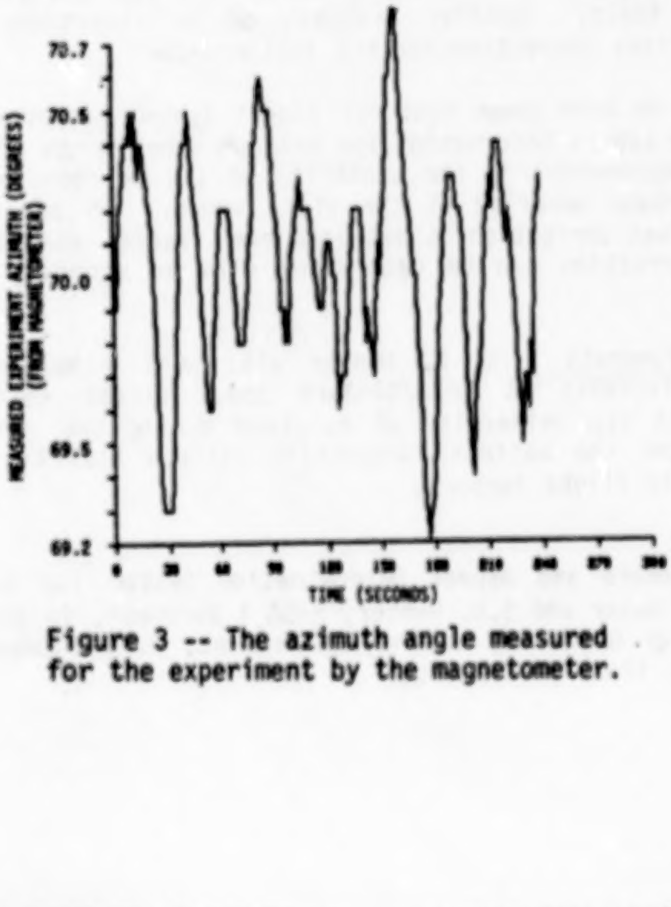

Figure 3 -- The azimuth angle measured for the experiment by the magnetometer.

During the balloon flight the aspect program was not able to analyze any of the pictures because only one in about twenty pictures is processed by the program, although all pictures are telemetered to the ground. For a picture to be processed by the aspect program, it must contain at least three stars, real or noise. To complete the analysis and determine the aspect information, the picture must contain at least three real stars. Noise pixels are treated as stars without a match in the star catalog and are ignored by the program.

During post flight analysis of all the pictures the aspect program was able to analyze the pictures that contained three real stars. The aspect program was modified to complete the analysis if only two real stars were found. The aspect information determined by this analysis is not as accurate as in the case when three or more stars are observed.

Part of the results of this modified analysis, the calculated azimuth of the experiment, is shown in Figure 2. The exposure time for the observations used for Figure 2 was five seconds for the period labeled 0 to 170 seconds and ten seconds afterward. Figure 3 shows the azimuth of the experiment as measured by the pointing system megnetometer for the same time period as shown in Figure 2. It can be seen, by comparing these two figures, that the azimuth calculated by the aspect system shows the same time variations as the azimuth measured with the magnetometer except for a discrepancy of about one degree. This discrepancy between the measured azimuth and the azimuth calculated with respect to the inertial star frame provides the offset correction needed to account for uncertainties in the latitude and longitude of the balloon, the alignment of the magnetometer and the deviation angle of the magnetic field. Similar analysis of th elevation angle would provide the offset correction for the inclinometer

4. Summary. We have shown that our aspect system can provide accurate near real time aspect information for balloon experiments if a factor of two to five improvement in the stability of the balloon experiment can be made to reduce smearing of the star images. In addition, if the calculated offset correction is averaged over several analyzed pictures, the offset correction can be determined with an accuracy of at least 0.1°.

5. Acknowledgements. S. D. Hunter also held a National Research Council Associateship at NASA/Goddard Space Flight Center and was affiliated with the University of Maryland during the period of this work. We thank the National Scientific Balloon Facility, Palestine, Texas, for their flight support.

6. References.

1. A Star Camera and Aspect Determination System for Balloon Borne Payloads, R.G. Baker and S.D. Hunter, NASA X Document, in preparation.
2. High Energy Gamma Ray Balloon Instrument, D.J. Thompson, et al., paper OG9.2-15, these proceedings.

N85-34966
OG9.3-11

Balloon-Borne Video Cassette Recorders For Digital Data Storage

W.E. Althouse and **W.R. Cook**

California Institute of Technology, Pasadena, CA. 91125, U.S.A.

1. Introduction

A high-speed, high-capacity digital data storage system has been developed for a new balloon-borne γ-ray telescope (see paper OG9.2-2). The system incorporates sophisticated, yet easy to use and economical consumer products: the portable video cassette recorder (VCR) and a relatively newer item - the "digital audio processor". The in-flight recording system employs eight VCRs and will provide a continuous data storage rate of 1.4 megabits/sec throughout a 40 hour balloon flight. Data storage capacity is 25 gigabytes and power consumption is only 10 watts.

2. The Digital Audio Processor

The key to rapid development of a VCR based digital data storage system was the availability of the digital audio processor, a consumer product intended to allow the use of a home VCR as a digital audio tape recorder. A simplified block diagram of such a processor, the Sony PCM-701ES is shown in Figure 1. In normal stereo recording operation the incoming left and right audio signals are each digitized with 16 bit resolution at a rate of 44 kHz. The digital data are multiplexed onto a single serial line and input to the "record data processor" at a rate of 1.4 megabits/sec. The processor adds error detecting and correcting codes, interleaves the data, and finally generates a video signal in standard NTSC television format suitable for recording on any home VCR. On playback the digital data are unscrambled, corrected for errors, and sent to 16 bit DACs which reconstruct the original audio waveforms. The powerful "cross interleaved" error correction scheme [1,2] virtually eliminates errors due to dropouts on the VCR tape, as is required for noise-free audio reproduction.

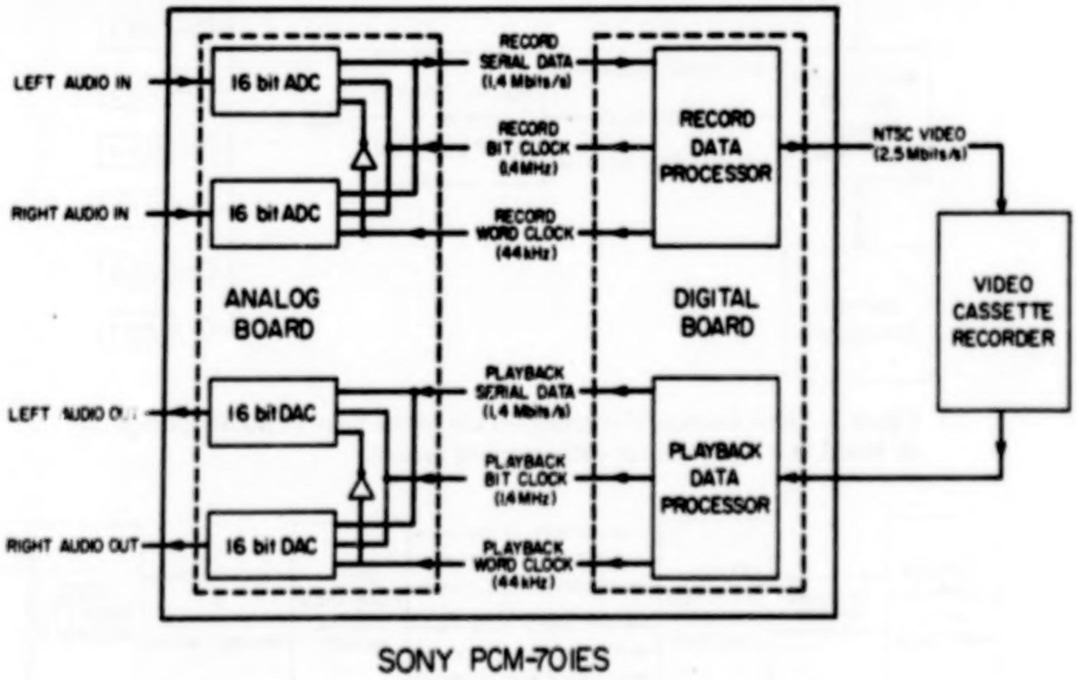
LEFT AUDIO IN
RIGHT AUDIO IN
LEFT AUDIO OUT
RIGHT AUDIO OUT
16 bit ADC
16 bit ADC
16 bit DAC
16 bit DAC
ANALOG BOARD
RECORD SERIAL DATA (1.4 Mbits/s)
RECORD BIT CLOCK (1.4MHz)
RECORD WORD CLOCK (44kHz)
PLAYBACK SERIAL DATA (1.4 Mbits/s)
PLAYBACK BIT CLOCK (1.4MHz)
PLAYBACK WORD CLOCK (44kHz)
RECORD DATA PROCESSOR
DIGITAL BOARD
PLAYBACK DATA PROCESSOR
NTSC VIDEO (2.5 Mbits/s)
VIDEO CASSETTE RECORDER
SONY PCM-701ES

Figure 1. Simplified block diagram of the Sony PCM-701ES Digital Audio Processor.

As shown in Figure 1, the circuitry within the Sony PCM-701ES is conveniently divided into two main printed circuit boards - an analog board and a digital board. For our purpose only the digital board is required. It has been incorporated in our flight recording system (Figure 2) and as part of a record/playback computer peripheral (Figure 3). The digital board is very easy to use. It operates from a single 5 volt supply, is TTL compatible and provides standard 75 ohm video input and output. Power consumption is 3 watts.

The Sony PCM-701ES may be operated in either a 14 or 16 bit mode. In the 16 bit mode the full resolution of the 16 bit ADCs and DACs are used, but fewer error correcting bits are encoded. In the 14 bit mode tape dropouts of up to 32 horizontal television scan lines can be perfectly corrected, while in the 16 bit mode error correction is guaranteed only for dropouts of up to 16 lines [3]. Nonetheless, for the convenience of a simple 16 bit word-aligned format we have used the 16 bit mode. As discused below, the error rate is quite low when high-quality tape is used.

3. Application

In our balloon flight application, γ-ray event data are written into a 2K byte buffer memory while a second buffer memory is read into the PCM-701ES digital board in the format described below. Each buffer can hold 63 events, and buffers are switched synchronously every 11.7 msec, slaved to the PCM-701ES data clock. Thus, ~5400 events per second can be recorded with no deadtime, while the PCM-701ES is supplied with a continuous data stream of 1.4 megabits/sec. The NTSC video signal is fed to eight Sony SL2000 portable VCRs, which are operated sequentially with a capacity of 5 hours recording time for each VCR. Data capacities are summarized in Table I.

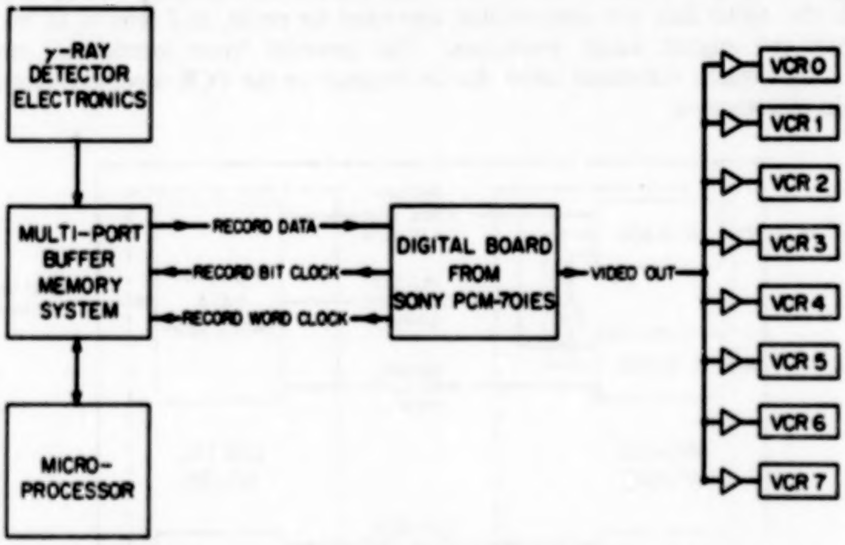
γ-RAY DETECTOR ELECTRONICS
MULTI-PORT BUFFER MEMORY SYSTEM
MICRO-PROCESSOR
RECORD DATA
RECORD BIT CLOCK
RECORD WORD CLOCK
DIGITAL BOARD FROM SONY PCM-701ES
VIDEO OUT
VCR 0
VCR 1
VCR 2
VCR 3
VCR 4
VCR 5
VCR 6
VCR 7

Figure 2. Block diagram illustrating the use of the Sony PCM-701ES digital board in a balloon-borne data recording system.

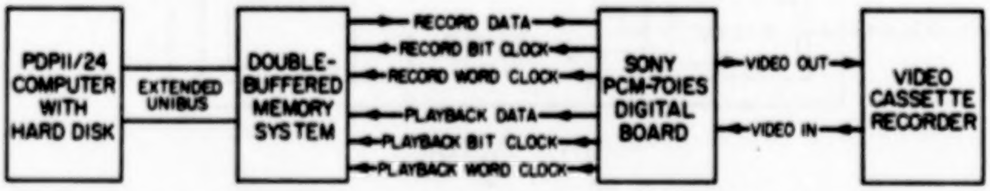
PDP11/24 COMPUTER WITH HARD DISK
EXTENDED UNIBUS
DOUBLE-BUFFERED MEMORY SYSTEM
RECORD DATA
RECORD BIT CLOCK
RECORD WORD CLOCK
PLAYBACK DATA
PLAYBACK BIT CLOCK
PLAYBACK WORD CLOCK
SONY PCM-701ES DIGITAL BOARD
VIDEO OUT
VIDEO IN
VIDEO CASSETTE RECORDER

Figure 3. Block diagram showing the Sony PCM-701ES digital board as part of a mass storage computer peripheral.

Table 1. Balloon-Borne γ-ray Telescope Data Storage System	
Data Rate	**1.4×10^6 bits/sec 175,000 bytes/sec 5400 events/sec**
Recording Time (per tape) (total)	** 5 hrs 40 hrs (8 VCRs)**
Data Capacity (per tape)	** 2.5×10^{10} bits 3.2×10^9 bytes 9.7×10^7 events**
(total)	**2×10^{11} bits 2.5×10^{10} bytes 7.8×10^8 events**
Power Consumption Digital board Portable VCR (total)	** 3 watts 7 watts 10 watts**

We have measured the error rate using Sony L750 Ultra High Grade tape recorded at "βIII" speed on Sony SL2000 portable VCRs. In initial tests approximately 1.5 million 2K byte data blocks were recorded on each of seven video cassettes using seven different VCRs (21 gigabytes total). Each data block contained a 32 bit start code, a 32 bit block count, approximately 1000 psuedo-random 16 bit numbers, a 32 bit stop code and a 16 bit cyclic redundancy check (CRC) code. The tapes were played back on a single VCR and each data block was checked for an accurate start and stop code, CRC error, and sequential block count. Of the 10.5 million blocks checked ~300 were missing (due to "playback muting", where the PCM-701ES simply replaced long stretches of uncorrectable data with a fixed data word), and 19 CRC errors were detected (due to "playback interpolation" where the PCM-701ES replaced isolated uncorrectable data words with the average of adjacent words). The fraction of blocks discarded due to detected errors was $\sim3\times10^{-5}$, a negligible data loss rate for most data acquisition applications. A sample of 600,000 "good" blocks were checked 100% for undetected errors and none were found. Thus the undetected block error rate was less than 2×10^{-6}, acceptable for our present application.

The VCR data systems discussed here were used to record and playback data for the formation of the γ-ray images presented in paper OG9.2-2. In this process 56 megabytes of data were recovered without a single detected error.

This work was supported in part by NASA grant NGR 05-002-160.

4. References

[1] Doi, T.T., Odaka, K., Fukuda, G., Furukawa, S., "Cross Interleave Code for Error Correction of Digital Audio Systems", Audio Engineering Society Preprint, 1979.

[2] Doi, T.T., Tsuchiya, Y., and Iga, A., "On Several Standards for Converting PCM Signals into Video Signals", *J. Audio Eng. Soc.*, 26-9, pp. 641-649, 1978.

[3] Sony PCM-701ES Operating Instructions, 1983.

N85-34967

OG 9.3-12

A POSITION SENSITIVE PHOSWICH HARD X-RAY DETECTOR SYSTEM

A.J.Dean, C.G.Hanson, C.J.Hopkins, R.A.Lewis, J.Fraser-Mitchell
Department of Physics, University of Southampton, Southampton UK

ABSTRACT

A prototype position sensitive phoswich hard X-ray detector, designed for eventual astronomical usage, has been tested in the laboratory. The scintillation crystal geometry was designed on the basis of a Monte Carlo simulation of the internal optics and includes a 3mm thick NaI(Tl) primary X-ray detector which is actively shielded by a 20mm thick CsI(Tl) scintillation crystal. This phoswich arrangement is viewed by a number of two inch photomultipliers. Measured values of the positional and spectral resolution of incident X-ray photons are compared with calculation.

1. Introduction. The use of the coded aperture mask is rapidly becoming a well established technique for the imaging of high energy X/gamma-ray photons ($10\ \mathrm{keV} \lesssim E_\gamma \lesssim 1\ \mathrm{GeV}$) [1,2]. The successful application of this technique and the imaging quality of the final telescope system are related to the development of a suitable position sensitive photon detection plane. The performance of this element must be optimised with respect to a number of factors in order that a high quality astronomical telescope can be constructed. First and foremost, the detection plane must have the best possible positional resolution for the incoming photons so that high definition images can be made. However, to ensure that sophisticated astrophysical information may be extracted from the imaging data it is also important that the detector has good spectral resolution for the detector photons and that the background noise level is reduced to a minimum level in order to maximise the sensitivity of the overall system.

A number of position sensitive detector systems are currently under development for astronomical use in the hard X/gamma-ray region of the electromagnetic spectrum ranging from the thick inorganic scintillators for gamma-ray photons to xenon gas proportional counters at the lower end ($E_\gamma \lesssim 100$ keV) of this spectral range [3,4,5,6]. At the present time the most effective detection system to cover the hard X-ray spectral range $\sim$15-300 keV comprises a thin (few mm) NaI crystal which is actively shielded. The phoswich/collimator arrangement has been extensively used to accumulate hard X-ray astronomical information. Here we describe the development of a prototype position sensitive phoswich system. Apart from eventual use as an imaging syystem such a device has the additional advantage of potential operation as an X-ray polarimeter.

2. The Detector System and Associated Tests. A prototype NaI(Tl)/CsI(Tl) phoswich system was constructed as shown in Fig.1. The dimensions of the assembly were 262mm x 62mm x 33mm. The NaI(Tl) and CsI(Tl) crystals were 3mm and 20mm thick respectively. A thin aluminium entrance window enabled the system to be studied with X-ray photons down to $\sim$15 keV. The 'bottom' face of the arrangement was covered in glass to enable the scintillation light to be detected by a suitable array of photomultiplier tubes which were optically coupled by means

ORIGINAL PAGE IS
OF POOR QUALITY

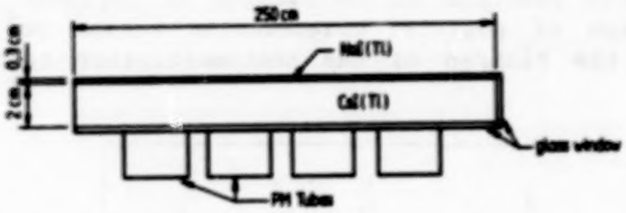

Fig.1. A prototype NaI(Tl)/CsI(Tl) position sensitive phoswich system.

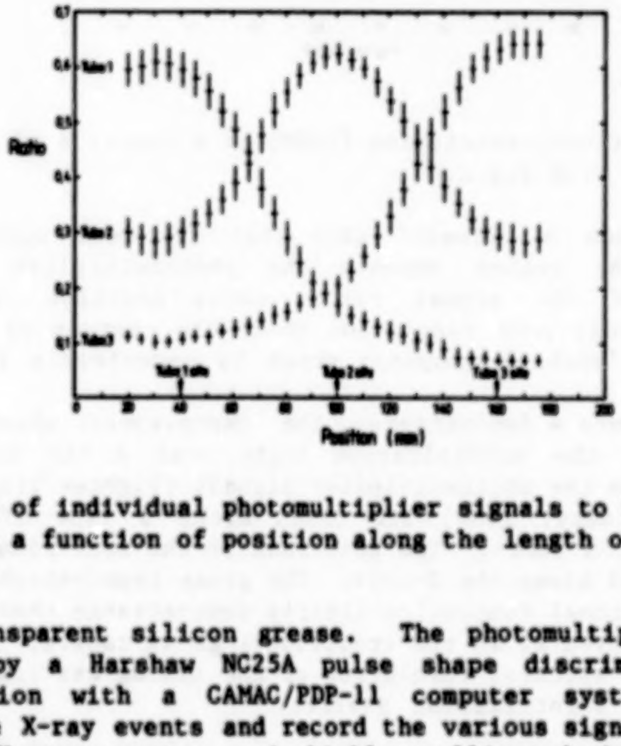

Fig.2. The ratio of individual photomultiplier signals to the total signal as a function of position along the length of the detector.

of a highly transparent silicon grease. The photomultiplier signals were processed by a Harshaw NC25A pulse shape discrimination unit and in conjunction with a CAMAC/PDP-11 computer system in order to select genuine X-ray events and record the various signal amplitudes for individual X-ray events. A highly collimated Am 241 source was used to irradiate a well defined (<2mm) position on the surface of the NaI crystal.

Figure 2 shows the ratio of individual photomultiplier signals to the total signal, as a function of position along the length of the detector. The measurements were taken at 5mm intervals on a line which joins the centres of the phototubes. Approximately 10^4 events were recorded for each position. The positions of the photomultiplier tubes are indicated on the X-axis. The shape of the curves was found to be in excellent agreement with the prediction of a Monte Carlo simulation of the scintillation light collection efficiency for various X-ray interaction positions over the surface area of the detector system.

An appropriate event location algorithm was constructed on the basis of the above experimental data and subsequently used to calculate the position of interaction of incident X-rays. Figure 3 shows a graph of positional resolution versus position along the line joining the centres of the photomultiplier tubes. It can be seen for such a 'linear' case that the best positional resolution occurs in the region between the photomultiplier tubes where the gradients of the signal ratio versus position are at a maximum. The relatively poor resolution above the centres of the photocathodes leads to a 'spikey' response which is undesirable for coded aperture imaging.

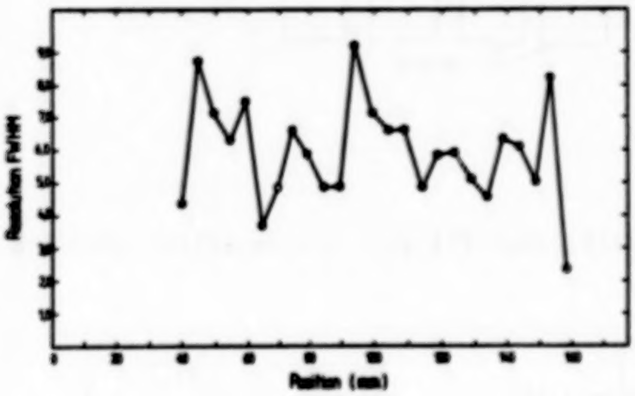

Fig.3. Positional resolution (FWHM) as a function of position using data from Fig.2.

Figure 4 demonstrates the improvement which may be gained by sampling the scintillation light over a two dimensional sample. In this case the photomultiplier signals (lighter lines) and positional resolution (heavy line) are taken along a line of symmetry between two rows of PM tubes. The positions of the individual photomultipliers are indicated along the X-axis. The great improvement in the uniformity of the positional resolution clearly demonstrates that a two dimensional must be employed as in the traditional gamma-camera.

The spectral resolution of the system was found to be competitive the best scintillation devices.

3. Conclusions. The above preliminary tests have demonstrated that a position sensitive phoswich detector can be made to operate in the hard X-ray region of the electromagnetic spectrum with a positional resolution of a few millimetres. For historical reasons the original attempt has been to develop a one-dimensional position sensitive counter. It was found that this device had an extremely non-uniform positional resolution function which is not suitable for the production of good quality coded aperture images. When operated as a two-dimensional device, in a similar manner to the gamma-camera, it was found that

a phoswich device could be made to operate with good spectral and positional resolutions for the incident hard X-rays.

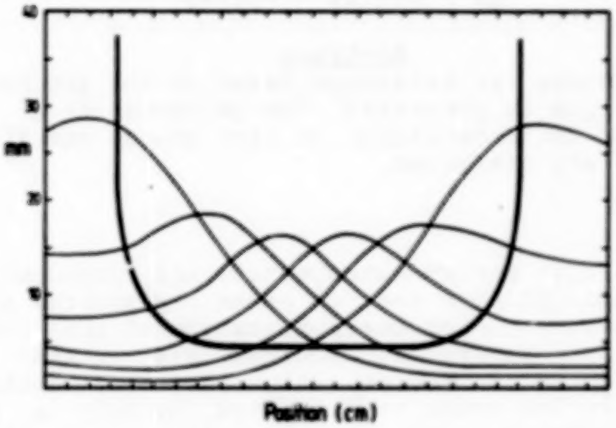

Fig.4. Ratio of individual photomultiplier signals as a function of position along a line equidistant between two rows of photomultipliers (light curves) and arbitrary units). Calculated positional resolution along this line (heavy curve)

References
1. G.K.Skinner, NIMS in Phys.Res.(1969), 221, 33
2. A.J.Dean, NIMS in PHys.Res.(1984), 221, 183
3. P.M.Charalambous et al. NIMS in Phys.Res. (1984) 221, 183
4. A.P.Willmore et al. NIMS in Phys.Res. (1984) 221, 284
5. P. Mandrou. Adv. Space Res. (1984), 3, 525
6. W.R.Cook et al (1983), IEEE Nuclear Science Symp. SRL 83-27

N85-34968
OG 9.3-13

A Cerenkov Imaging Telescope for High Energy Gamma Rays

P. Ferrando and P. Goret
CEN / Saclay - France

Abstract

A large area gamma ray telescope based on the gas Cerenkov imaging technique is presented. The performances of the instrument for the observation of high energy gamma ray point sources are discussed.

1 - Introduction

A new field in high energy astrophysics was opened with the discovery by SAS-2 and COS-B of some 25 gamma ray sources above 30 MeV (see /1/ for a review). After the publication of the COS-B catalog the situation is as follows: (i) sources are located with error radii of a fraction of a degree at best, (ii) detailed energy spectra up to a few GeV could be extracted for only a few sources (Crab, Vela and Geminga), (iii) reliable data on periodicity are available only for the Crab and Vela pulsars. The main limitation in these experiments was the restricted sensitive area of the telescopes which prevented from accumulating a sufficient statistics of photons to provide detailed results for the fainter sources.

On the upper energy side air shower arrays were also successful at identifying gamma ray sources from a few hundreds of GeV up to 10^{16} eV (a review is given in /2/). Hampered by a copious cosmic proton background these experiments typically locate gamma ray sources within a few degrees.

More accurate data will be collected by the GRO /3/ and GAMMA-1 /4/ instruments with sensitive areas of 2000cm^2 and 500 cm^2 respectively. However it is anticipated that the range 1-100 GeV, where the best angular resolution can be reached, will remain essentially unexplored calling for still larger instruments able to bridge the gap between orbiting telescopes and ground based detectors.

A promising technique to reach this goal is to use the Cerenkov light radiated in a gas by the pair electrons. The idea, originally developed by K. Greisen, led to the design of a large balloon borne telescope which was first to detect the Crab pulsar at several hundreds MeV /5/. More recently the concept was revived with two proposals for a gas Cerenkov gamma ray telescope for the Space Station /6/,/7/. In this paper we discuss in more details the expected performances of the large area Cerenkov imaging telescope for high energy gamma rays as proposed in /7/.

2 - The Gamma Ray Imaging Telescope (GRIMTEL)

A preliminary description of a gas Cerenkov imaging telescope was given in /7/ and a more detailed account was presented in /8/. A sketch of the telescope is shown in Figure 1. Briefly the incident gamma ray is converted into a e+/e- pair in the lead target. Both electrons emit Cerenkov light in the radiator gas at a well defined angle to the particle's trajectories. After being reflected by the mirror the Cerenkov photons are detected by a 2-dimensional position sensitive detector at the focal plane. The image pattern consists of 2 circles with fixed radius whose centers give the direction of propagation of each electron in the gas. The incident gamma ray direction is approximated from the bissector of the two electron directions. The physical characteristics of the envisioned GRIMTEL instrument are summarized in Table 1. The electronic signature of a gamma ray is the 4-fold coincidence S1 x S2 x S3 x F with S3 and F being delayed compared to S2 by 16ns and 33 ns respectively. The directionality and high energy threshold of the Cerenkov effect makes the telescope naturally immune to cosmic ray induced background. The difference between the present proposal and the one described by D. Koch in /6/ lies in the granularity of the focal detector. The latter instrument detects individual Cerenkov photons with an angular uncertainty of 0.21 degree compared to 0.017 for the GRIMTEL. We believe that the improved angular resolution will result in a more reliable gamma ray signature and a better angular resolution to individual gamma rays. In addition it opens the possibility to estimate the energy by the amount of Coulomb scattering in the radiator gas.In the next section we present the expected performances of the GRIMTEL instrument.

3 - Performances of the GRIMTEL

The physical effects ultimately shaping the Cerenkov images of high energy gamma rays are as follows:

- the angle at which converted electrons are emitted
- the Coulomb scattering in the remaining target material
- the Coulomb scattering in the radiator gas
- the chromatic dispersion of the Cerenkov effect

Since we are using a thick target (0.5 r.l.) the 1st effect may be neglected compared to the 2nd one. The 4th effect is minute compared to the 3rd one and may also be ignored.

A Monte-Carlo simulation was performed to evaluate the performances of the instrument. Images of gamma ray events are first generated with the above mentioned 2nd and 3rd effects taken into account. We assume that each electron gives 15 Cerenkov photoelectrons on average in the 5 meters long radiator. In a second step each image are searched for 2 Cerenkov circles whose center coordinates are determined. A typical image of a 2 GeV gamma ray is shown in figure 2 together with the fitted circles. In some cases, especially at very high energy, the circles are so close they cannot be disentangled. For those events the gamma ray signature is a number of photoelectrons along a single circle being twice that for singly charged particles. The effective sensitive area of the GRIMTEL as a function of the aspect of the source to the telescope axis is shown in figure 3. It is seen that a figure of 28000 cm^2 at 0° above 1GeV is reached i.e. 14 times larger than in the GRO instrument. The GRIMTEL with a field of view of about 5° is best suited to the observation of gamma ray point sources. The r.m.s. angular resolution to individual gamma rays is estimated as 0.45° at 2 GeV, 0.18° at 5 GeV and 0.10° at 10 GeV. The improvement brought up by the GRIMTEL over the GRO experiment is not with the intrinsic angular resolution which is similar for both instruments. Rather it is that the larger area enables statistically significant observations to be performed at higher energies where the angular accuracy is significantly better.

The energy measurement could be best achieved with using a shower calorimeter. However if restrictions on weight would rule out this possibility an estimate of the energy could still be obtained from a measurement of the Coulomb scattering in the radiator gas. Investigations of the energy resolution attainable with this method are in progress.

4 - Final comments

The feasability of the proposed experiment depends critically on the availability of a photon detector with fine spatial resolution and sensitive areas of several thousands of cm^2. In addition the device should deliver a fast linear response to Cerenkov light in order to take part in the trigger generation. The latter requirement is essential for minimizing the telescope dead time so that the readout of the focal detector, with its large number of cells, be triggered only on those events with an appropriate number of Cerenkov photoelectrons. Gaseous detectors sensitive to VUV light have been used successfully to record the Cerenkov rings of charged particles in accelerator beams (see /9/ for a review). An experiment, using a multineedle detector to record the Cerenkov images of 500 MeV gamma rays, is in preparation at Saclay. Development of multianode photomultipliers with a 3x3 mm^2 pixel size are also currently in progress at Saclay. With these devices a new generation of very large gamma ray telescopes can be envisioned for long exposures on the Space Station. These instruments, with a sensitivity higher by more than one order of magnitude over present day experiments, will undoubtedly increase our present knowledge of the astrophysics associated with celestial gamma ray sources.

References

/1/ G.F. Bignami and W. Hermsen
Ann. Rev. Astron. Astroph. 1983 Vol21 p.67
/2/ R.C. Lamb
Proc. of the Workshop on Cosmic Ray Experiments for the Space Station Era - Baton Rouge 1984
/3/ E.B. Hughes et al.
IEEE Trans. Nucl. Sci. 1980 Vol NS-27
/4/ R. Bazer-Bachi et al.
Proc. 12th ESLAB Symposium - Frascati 1977
/5/ D. Koch et al.
Nucl. Instr. Meth. 1973 Vol 108 p. 349
/6/ D. Koch
' A large area gamma ray imaging telescope system
SAO Report 1983
/7/ P. Goret
' A large area gamma ray telescope for point source studies above 1 GeV ' - idem ref. /2/
/8/ P. Ferrando et al.
' A Cerenkov imaging detector for very high energy gamma rays' 6th Symposium on X and Gamma Ray Sources and Applications Ann Arbor - 1985 - to be published in Nucl. Instr. Meth.
/9/ G.B. Coutrakon
IEEE Trans. Nucl. Sci. 1984 Vol NS-31 p.27
/10/G. Comby et al.
IEEE Trans. Nucl. Sci. 1982 Vol NS-29 p.328

N85-34969

ORIGINAL PAGE IS
OF POOR QUALITY

Converter:
0.5 r.l. lead
Mirror:
spherical f/1.7
Ø = 3 meters
f = 5 meters
Radiator gas:
N2 at STP
Cerenkov angle = 1.5°
Focal detector:
Ø = 60 cm
cell size = 3x3 mm²
# of cells = 31,400

Table 1 - Physical characteristics of the GRIMTEL.

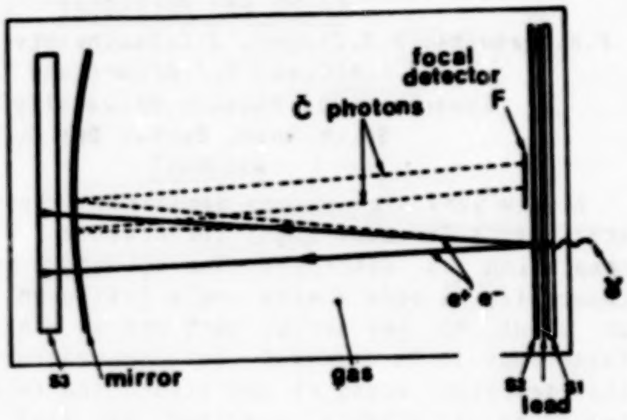

Figure 1 - Sketch of the GRIMTEL.

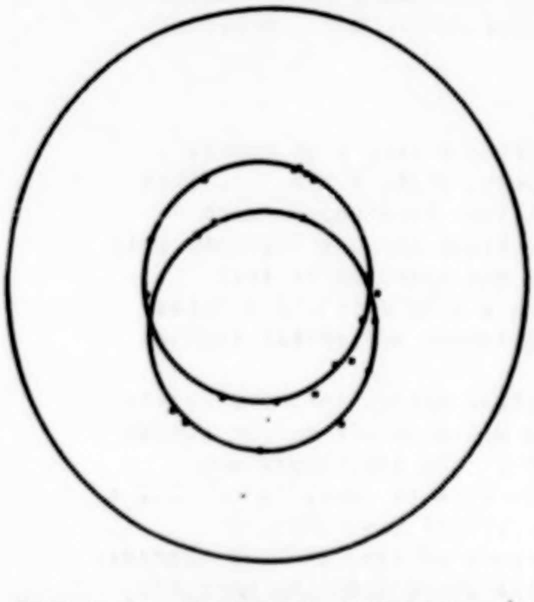

Figure 2 - A simulated Cerenkov image of a 2 GeV gamma ray with fitted circles. Each dot represents a cell lit up by a Cerenkov photon.

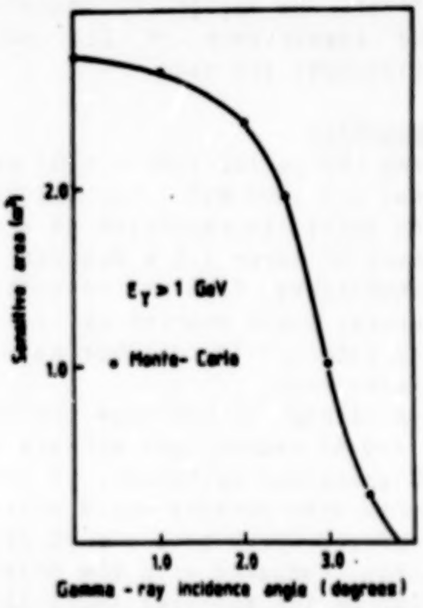

Figure 3 -The effective area of the GRIMTEL as a function of the aspect of the source to the telescope axis.

N85-34969

OG 9.4-2

THE UNIVERSITY OF DURHAM MARK III VERY HIGH ENERGY GAMMA RAY TELESCOPE

P.M.Chadwick, N.A.Dipper, J.C.Dowthwaite, I.W.Kirkman,
T.J.L.McComb, K.J.Orford and K.E.Turver
Department of Physics,University of Durham,
South Road, Durham DH1 3LE, UK.

ABSTRACT

A new very high energy gamma-ray telescope employing the atmospheric Cerenkov light technique and currently nearing completion is described. The telescope is designed to have capability as both a wide angle instrument (4 degree field of view) for sky survey work and as a narrow field of view instrument (1.35 degrees) for conventional drift-scanning and tracking modes of operation. The telescope consists of two 10 sq. m. mirrors operated in fast coincidence with multiple phototube assemblies at the prime focus of each mirror. The design philosophy of the instrument is discussed and comparisons of its performance with our previous telescopes are made.

1. INTRODUCTION

During the period 1981 - 1984 we operated a very high energy gamma-ray (> 1000 GeV) facility at Dugway, Utah, U.S.A (1). This facility initially comprised an array of four telescopes, each consisting of three 1.5 m diameter searchlight mirrors focussed onto three phototubes. Each set of phototubes was operated in fast coincidence, which enabled us to maintain a high gain and singles counting rate (~ 30 kHz) but have a negligible accidental (noise) coincidence rate.

In an attempt to overcome the restrictive optics enforced by the use of f(0.4) searchlight mirrors and to optimise the mirror design for VHE gamma-ray astronomy, in 1983 one of the telescopes was remirrored with purpose-built mirrors. Mirrors of focal length 2.2 m were employed which gave a 1.25 degree field of view using 2" phototubes, compared with the original field of view of 1.75 degrees. Operation of the modified (Mark II) system along side the original (Mark I) system has shown that the narrowing of the field of view has achieved its design objective in improving the ratio of detected gamma-rays to background cosmic ray events for discrete objects. We believe that the geometrical aperture of the Mark II telescope is near optimum, eliminating a maximum number of off-source protons but allowing detection of all gamma-rays from a point source in the centre of the field of view.

The Dugway facility has proved successful during its four years of operation. Numerous sources of VHE gamma rays have been discovered or confirmed. The strongest source detected to date (4U0115 +63,(2)) required observation for 25 hours to give a detection significant at the 4.4 σ level, with proportionally longer periods required for weaker sources. When available observing time is taken into account, this limits the number of thorough examinations of source candidates to 3-4 per year with the original telescopes. Clearly, to fully exploit this energy range of the electromagnetic spectrum, a much more sensitive telescope is required.

2.TELESCOPE DESIGN The Mark III telescope will be capable of operating in three distinct modes:-

(a) Sky survey work where a large solid angle (for reasonable sky coverage), combined with good gamma ray/proton ratio, is required.

(b) Tracking of possible pulsed sources where a small telescope opening angle is desirable giving minimum acceptance of background cosmic rays.

(c) Drift scan mode where a moderate opening angle is required to enable the source to be within the field of view for a reasonable time.

The design philosophy adopted is one of having a ring of six off-axis detector channels surrounding the on-axis one to satisfy requirement (a). Such an arrangement enables seven adjacent areas of sky to be viewed when in sky survey mode with the advantages of background reduction achievable with a narrow angle system. When operating in tracking mode, such an arrangement of seven channels enables six simultaneous off-source measurements to be made, allowing a continuous monitor of the nearby background conditions. The telescope design allows for the addition of a second ring of twelve phototubes, thus allowing a trebling of the area surveyed in a given time. The telescope has been designed so that photomultiplier packages can be easily changed. For example, in drift scan mode of operation we have the option of employing larger phototubes, thus increasing the aperture.

The Mark III telescope comprises a light collector of 20 sq. m. deployed as two 10 sq. m. dishes. A third smaller mirror of 3 sq. m. located between these two allows 3-fold fast coincidence to further reduce accidental noise counts.

A number of different techniques of mirror construction have been investigated. The goal has been to produce mirrors with physical characteristics well suited to the observation of Cerenkov light, which are both light, cheap and easy to produce. Our starting point was the mirrors successfully used on the Mark II telescope which were 0.6 m diameter and machined out of solid aluminium plate and polished. We have investigated pressing and spinning thin aluminium sheet, thermo-forming perspex, bonding thin aluminium sheet to a solid former and pressing thin glass mirrors. The method of manufacture adopted is the bonding of aluminium honeycomb to high reflectivity anodised aluminium sheet after stretching over a former. The method produces mirrors with spot size less than 0.1 degree. The telescope comprises 112 0.6 m diameter mirrors giving 2x10 sq m flux collectors with focal lengths of 2.5 m.

The telescope is mounted on an alt-azimuth mount and is steered under computer control by two DC electric servomotors. Direction sensing is by two absolute digital shaft encoders, giving position resolution of 0.1 degrees.

The main requirement for photomultipliers used in Cerenkov light work is unusual. We require a tube with a low noise performance under conditions of high photocathode illumination. In Figure 1 we show the noise performance of a number of tubes under conditions of photocathode illumination typical of a night sky Cerenkov experiment. The very rapid increase of noise counts with photomultiplier gain noted for the 5" tube (RCA 4522) mitigates against its use although this tube has been extensively used to date. we have selected fast 3" tubes (EMI 9821) as our prime tube when operating in tracking mode.

ORIGINAL PAGE IS
OF POOR QUALITY

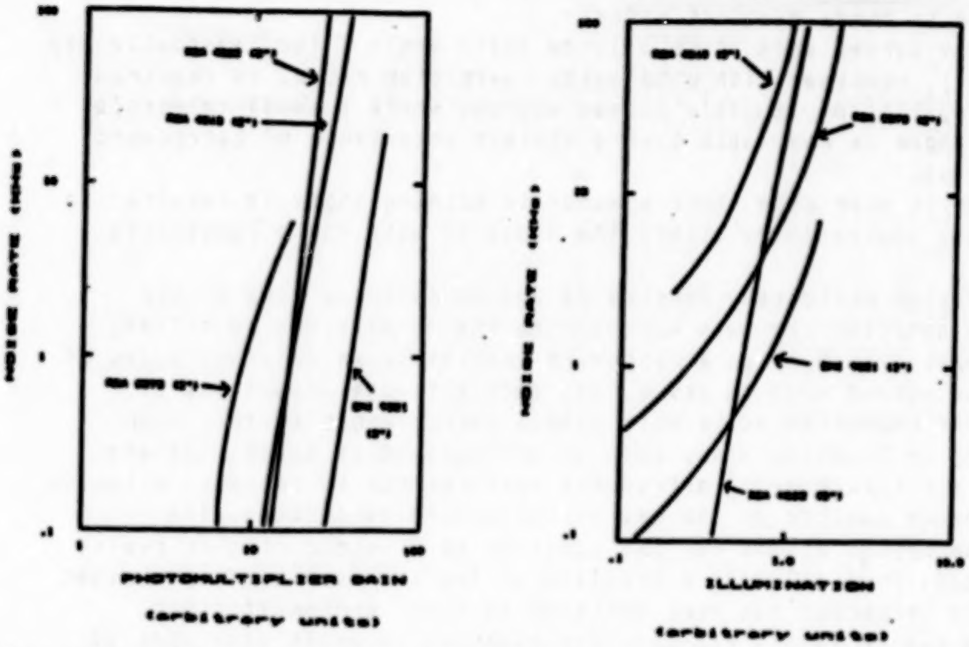

Figure 1. The variation of noise count rate (for a discrimination level typical of our experimental conditions) with phototube gain for constant illumination (a) and illumination level for constant gain (b) for a number of fast photomultipliers. In Fig. 1(b), the RCA 4522 is run at a lower gain than the other tubes.

Our experience with the Mark II telescope and our calculations of Cerenkov emission by gamma-ray showers (3) lead to a best choice of 1.35 degrees for the opening angle of the new telescope. With 3" diameter photomultipliers, this implies a mirror focal length of 2.5 m and an f-number of ~1 for our deployed area. Scaling from the count rates achieved with the Mark I and II telescopes and using our measurements of phototube characteristics leads to an estimation of a counting rate of >200 per minute per phototube pair with a single telescope. This should enable sources of comparable strength to those already established to be detected at the 3σ level in one night's observing time. In addition a useful search for unknown periodicity in e.g. Cygnus X-3 would become feasible.

3.ELECTRONICS

With 15 channels of analogue information to be recorded when operating in survey mode (and the possibility of increasing to ~40 at a later date), the use of CAMAC with its high channel density and high speed as the data recording standard becomes neccessary. Each PMT signal is amplified and discriminated, and fast concidences between the signals from the two mirror units are generated. On each coincidence, the pulse heights are digitized using a fast ADC, and the time of occurrence of the event is recorded. The heart of the data logging system is a purpose built MC 68000-based microprocessor system. In order to have a system dead-time of less than 0.5 ms to avoid possible data loss, it is neccessary to employ a true 16-bit processor to run the CAMAC bus as close to its maximum rate as possible. Total dead-time with this system is 0.3 ms per event.

N85-34970

The data from each event, along with house-keeping information every minute is recorded on a 3M cartridge drive system with a capacity of 68 Mbyte per tape. We have incorporated a system of recording minimum information (event time only) for events occurring within the system dead time to enable recording of very intense short term bursts of events.

We control the telescope with six microcomputers running on a local area network and communicating with the 68000 data logger. One of these computers is responsible for the steering of the telescope, a second acts as master controller for the experiment and the others are responsible for analysing and displaying the status of the experiment on a continuous basis.

ACKNOWLEDGEMENTS

We are grateful to the Science and Engineering Research Council for funding this work, Durham University Microprocessor Centre for the design and construction of the data logging computer, and the staff of the Workshops in the Department of Physics for the construction of the telescope.

REFERENCES

(1) Gibson A.I. et al, (1982), Nature, 296,833.
(2) Dowthwaite, J.C. et al (1985), submitted to Astron. Astrophys. (1985).
(3) Macrae, H. and K.E.Turver (1982) unpublished.

N85-34970

A New Ultra High Energy Gamma Ray Telescope at Ōhya Mine

Aoki T., Higashi S.o), Kamiya Y.n), Kitamura T., Matsuno S.,
Mizutani K.s), Mitsui K., Muraki Y., Okada A., Ohashi Y.,
Sato T.o), Suwada T.o), Shibata S.n), and Takahashi T.o)

Inst. for Cosmic Rays, Univ. of Tokyo, Tanashi, Tokyo
o) Dep. of Physics, Osaka City Univ., Sumiyoshi, Osaka
n) Dep. of Physics, Nagoya Univ., Chikusa, Nagoya
s) Dep. of Physics, Saitama Univ., Urawa

1. Introduction

Search for the ultra high energy gamma rays coming from point sources is one of the main experimental aims of Ōhya project (Fig. 1)[1). A fast air shower timing system has been constructed at ICRR for the study of the angular resolution of the system and operated approximately half a year. This paper describes the characteristics of the surface array of Ohya "air shower telescope".

2. Detail of the System

The array of the 24 channel scintillation counters situated at the campus of ICRR (Tanashi, Tokyo) is shown in Fig. 2. Each scintillator has an area of 0.25 m^2 and a thickness of 5 cm. The scintillation light is observed by the phtomultipliers located at 50 cm above the scintillator. Photomultipliers HAMAMATSU H1161 (R329) are used under a typical high voltage condition ∼1.4 KV. The output signal from the photomultiplier is sent to the preamplifire Le Croy 612A (gain x 10) via 100 m cable (71B/U). The output pulse height for the single particle is ∼30 mV and is discriminated by Le Croy 623B. The discriminator out-put signal is then sent to a coincidence circuit 380A. The delay time of the signal from the input of the preamplifire to the out-put of the coincidence circuit is 35 ns.

The out-put of the coincidence circuit is used for the start signal of the TDC 2228A. Meanwhile one of the output signals of each discriminator is delayed by 20 m cable and is used for the stop signal of the time digitizer. The start pulse arrives ∿15 ns before the stop signal. The time digitizer has a time resolution of 250 ps. The pulse height distribution is also recorded by ADC 2249W. The circuit diagram is shown in Fig. 3.

The liniarity of the phtomultiplier out-put and the time jittering was investigated by the photo-diode. As shown in Fig. 4, in the 3 decades of the pulse height range (from 3 mV to 3 V), the linearity is seen. Typical time jittering of the photomultiplier is given in Fig. 5. For the number of particles $N_e \geq 10$, time jittering becomes ∿1ns (catalogue value is 0.9 ns). The jittering of the electronics is less than 250 ps.

3. Angular Resolution of the Telescope

The trigger pulse is created when the air shower hits more than any 6 scintillation counters. The number of the fired scintillator is presented by the histogram of Fig. 6. The dotted line represents the data in which(digitizer)point deviates less than 3 standard deviation from the least-square fitting plane.

The air shower front is simply approximated by a plane: $Z = a X + b Y + C$. For the vertical shower a and b take zero : $a=b=0$. The shower with zenith angle less than 15° is only used for the present data analysis. The plane determined by the least-square fitting is obtained by :

Define $\chi^2 = \frac{1}{\sigma}\Sigma(Z_i - aX_i - bY_i - c)^2$ and differentiate χ^2 by a,b,c. Then we get:

$$\begin{aligned}
\Sigma X_i Z_i &= a\cdot\Sigma X_i^2 + b\cdot\Sigma X_i Y_i + c\cdot\Sigma X_i \\
\Sigma Y_i Z_i &= a\cdot\Sigma X_i Y_i + b\cdot\Sigma Y_i^2 + c\cdot\Sigma Y_i \\
\Sigma Z_i &= a\cdot\Sigma X_i + b\cdot\Sigma Y_i + c\cdot N \ .
\end{aligned}$$

Parameters a,b and c are determined by

$$a = |A|/\Delta \ , \quad b = |B|/\Delta \ , \quad c = |C|/\Delta \quad \text{and} \quad \Delta = \begin{vmatrix} \Sigma X_i^2 & \Sigma X_i Y_i & \Sigma X_i \\ \Sigma X_i Y_i & \Sigma Y_i^2 & \Sigma Y_i \\ \Sigma X_i & \Sigma Y_i & N \end{vmatrix} .$$

The statistical deviations in a,b and c σ_a , σ_b, and σ_c are given by

ORIGINAL PAGE IS
OF POOR QUALITY

$$\sigma_a^2 = \sigma^2[N\Sigma Y_i^2 - (\Sigma Y_i)^2]/\Delta \quad , \quad \sigma_b^2 = \sigma^2[N\Sigma X_i^2 - (\Sigma X_i)^2]/\Delta \; .$$

The angular resolution of the system $\sqrt{\sigma_\theta^2}$ is defined by $\sqrt{\sigma_a^2 + \sigma_b^2}$.

Fig. 7 indicates the distribution of $\Delta Z_i = Z_i - (aX_i + bY_i + c)$ from the least-square fitting for the data of each scintillator. Fig. 7 shows the fluctuation of shower front σ_z is ± 2.5 m.

Figs. 8 and 9 represent the distribution of the angular resolution σ_θ of each shower. Each curve shows when we take the data with $Z_i \geq 3$, 5 , and the number of total fired scintillators is greater than $\geq$ 6, 10, 15 respectively. From these figures we conclude that our telescope has an angular resolution of 0.5° (at 1σ).

It is interesting to compare present result with the former measurement by Kiel group$^{2)}$ with the use of 1 m^2 scntillators. Their data show on the angular resolution 1°. The data analysis is still continuing for the direction of the Cyg. X-3. The data will be presented at the conference.

References
1) Ōhya group : This conference proceeding, HE 5.1-7.
2) Kiel group : Proceed. of 12th ICRC, 3, 1038 (1971).

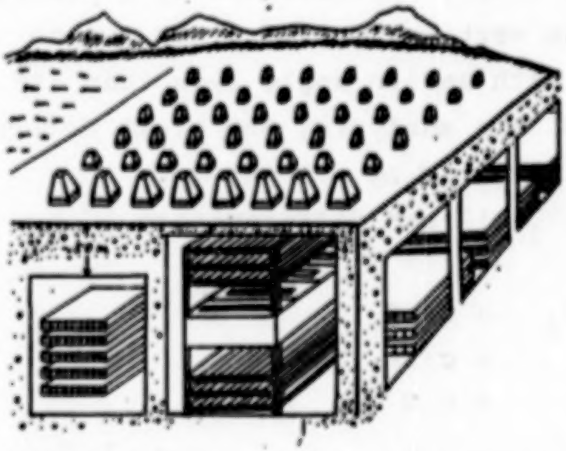

Fig. 1

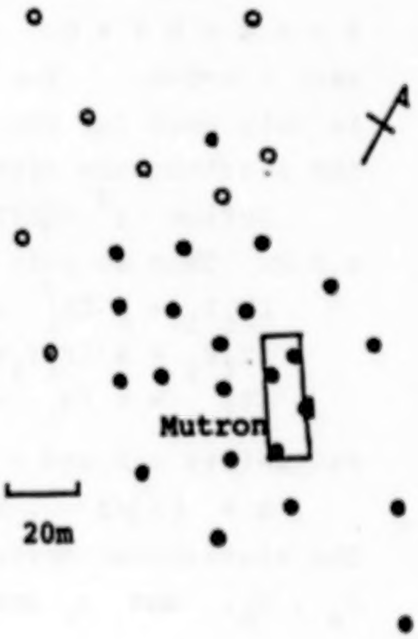

Fig. 2

ORIGINAL PAGE IS
OF POOR QUALITY

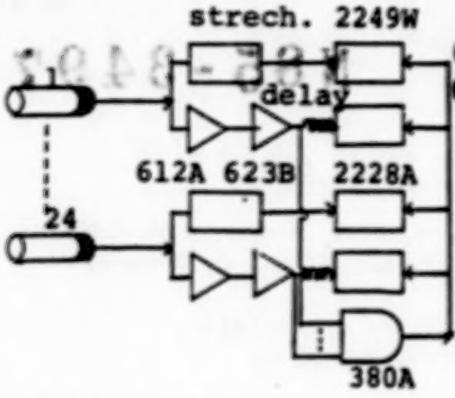
strech. 2249W
delay
612A 623B 2228A
24
380A

Fig. 3

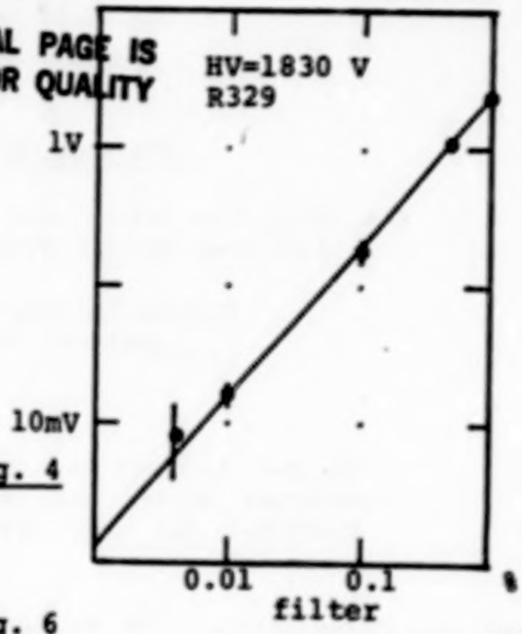

Fig. 4

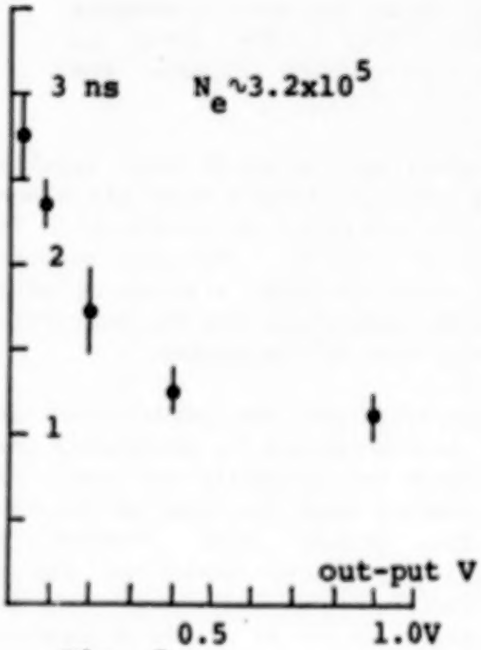

Fig. 5

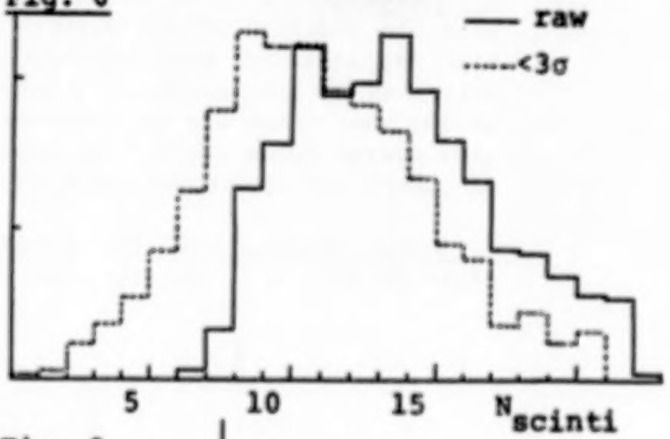

Fig. 6

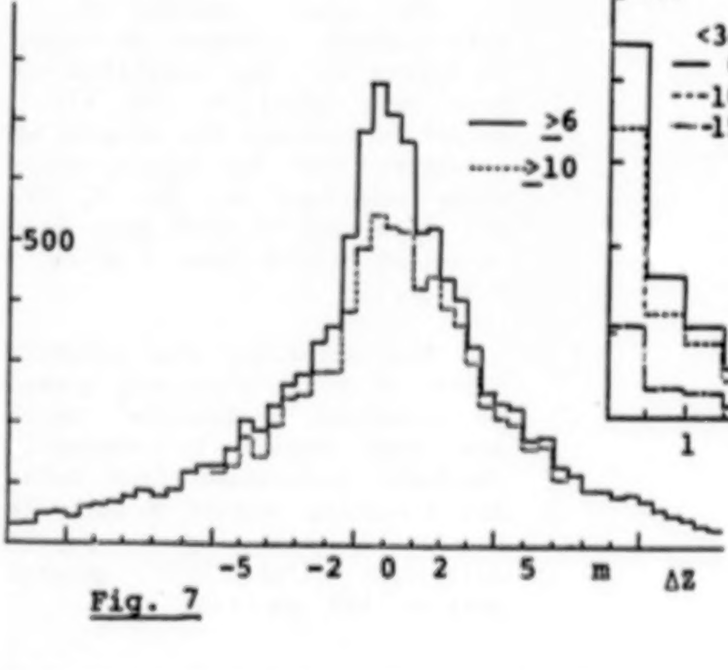

Fig. 7

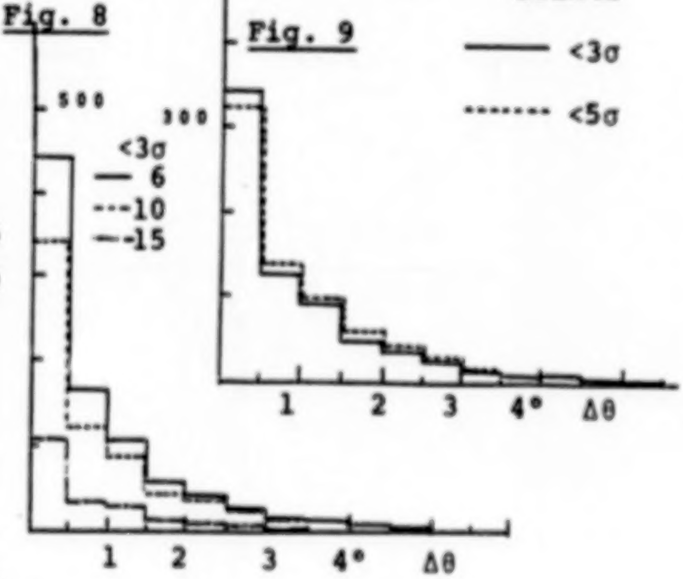

Fig. 8

Fig. 9

414 N85-34971

THE BUCKLAND PARK AIR SHOWER ARRAY

R.W. Clay, C.L. Corani, J.R. Patterson, B.R. Dawson, P.G. Edwards,
A.G. Gregory, J.R. Prescott, S.D. Elton, and D. Ciampa.

Physics Department, University of Adelaide,
Adelaide, South Australia. 5000.

ABSTRACT

The new Buckland Park Air Shower Array has been producing analysed shower data since July 1984. The array is described and some preliminary performance figures are presented.

1. Introduction. The Buckland Park array has recently been upgraded with the addition of new scintillators with the result that its shower size response has been extended to ~ 10^4 particles at threshold. The array now detects events at a mean rate of ~ 1/10s. The main purposes of the new array are to continue the study of point sources of ultra high energy gamma rays[1],[2] in the southern hemisphere and the properties of cosmic ray air showers with sizes less than 10^5 particles.

2. Array Description. The design considerations and predictions are given in ref. 4. Briefly, the major considerations in optimizing the rates of detection of small air showers were the need to increase the ground area covered by closely-spaced detectors and to increase the individual detector areas so as to minimize sampling fluctuations.

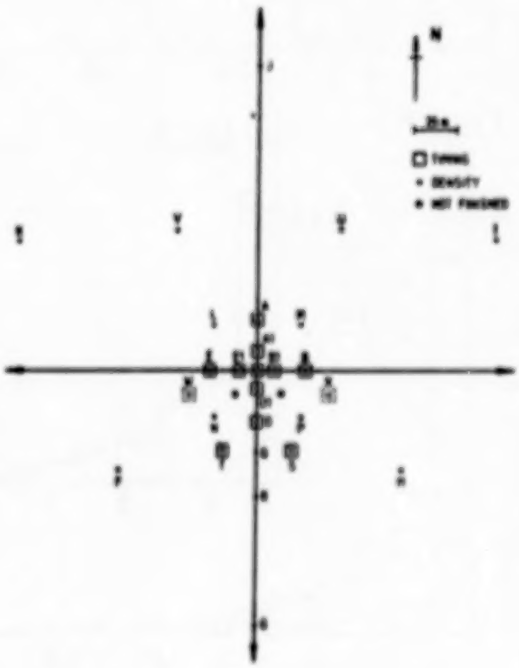

Fig. 1 Array layout

The array consists of 27 scintillators arranged as shown in figure 1. New scintillators have been added to the old array[3] to increase the density of detectors near the centre where eight detectors A1, B1, C, D1, E1, D, S and T have also been increased in size from 1 m^2 to 2.25 m^2.

The detectors are scintillators of 50 mm thickness housed in pyramidal enclosures[4] which are then housed in thermally insulated galvanised iron huts. All detectors contain a particle density measuring photomultiplier (RCA 8055 general purpose 120 mm tube or equivalent) which feeds a pre-amplifier at the detector before signal transmission to the central laboratory. Saturation occurs at ~ 300 particle level Eleven of the detectors have, in addition, a fast timing photo-multiplier (Philips XP2040) which directly drives 50 ohm cable (RG8) to the central laboratory. Fast timing detectors were added at sites S and T to enable directions to be found for small showers falling nearby and to improve the angular accuracy in the north-south plane for medium and larger showers falling near the centre. Two further slow detectors will soon be added as indicated in figure 1 and fast timing introduced in X and W detectors to improve directional measurement of showers in the east-west plane.

An event is recognized when any two of the 19 inner amplitude measuring detectors trigger at the threshold of 2 particles, (each of which has an individual rate ~ 0.5 Hz) and any two of the fast timing detectors also trigger. (Their individual rates are ~ 100Hz). The slow system thresholds are set well above those in the fast system to ensure that, in most cases, the fast detectors trigger as closely as possible to the start of the photomultiplier pulse and reduce timing uncertainties associated with the fast system rise time (σ_t ~ 5ns). A further result is that except for the smallest of showers, there are normally many more than two fast detectors triggered and directions can be found with timing redundancy. The final trigger rate is ~ 8000 events day^{-1}.

The density measuring channels have final pulse shapes which are quite long (rise ~ 100ns, fall ~ 5μs) and these pulses are fed to CAMAC Peak-sensing ADCs (LeCroy 2259A) which are gated by the array trigger. The array data is calibrated and partly analyzed (for angles of incidence) by a Nova mini-computer system. Output is presently recorded on magnetic tape for later analysis and one 2400 foot tape lasts about five days. The resolved single particle peaks of all detectors are monitored regularly, normally when each tape is changed.

The relative times of arrival of the fast timing pulses are measured with ~ 1 ns bit resolution using a CAMAC Time to Digital Convertor (LeCroy 2228A). Our previous practice had been to start the TDC off using a discriminator output from the central detector, the others being delayed a fixed amount to act as stops. With our more loose coincidence system we now do not specify any particular fast channel to be the TDC start channel. Instead the fast coincidence output triggers the TDC start. In order to ensure that all pulses will be within the range of the TDC, there is a further monostable delay of ~ 200 ns in each channel after the discriminator and before the TDC stop. These delays appear to be inherently quite stable and do not suffer from any bandwidth limitations of delay cable.

Any combination of fast timing detectors may trigger on a given event. We need to find one timing detector which has been triggered and calculate all usable (non-collinear) time differences after subtraction of the known delays. It is then straightforward to calculate the zenith and azimuth angles for the shower axis. At the same time, right ascension, declination and Julian time are calculated for the event. The chi-square fitting parameter for a planar shower front is consistent with a directional accuracy ~ 2.5/cos θ degrees where most detectors are triggered. The worst cases will be for small showers triggering only our inner 2.25 m^2 detectors. In these cases, we have a detector spacing of only 8m and directions are expected to have uncertainties $\gtrsim 10°$.

3 Preliminary Results. The array detects showers with analysed sizes down to 10^4 particles and with our present preliminary shower analysis we have a median shower size ~ 0.9×10^5 particles. Figure 2 shows a preliminary graph of the size distribution for analysed showers over the whole array and compares it to the performance of the old array. We are beginning to develop our directional analysis system and Table 1 shows a sky map with the accumulation of events for several sidereal days in which only showers with at least five measured times are used. The map shows the extent of sky coverage available from Buckland Park.

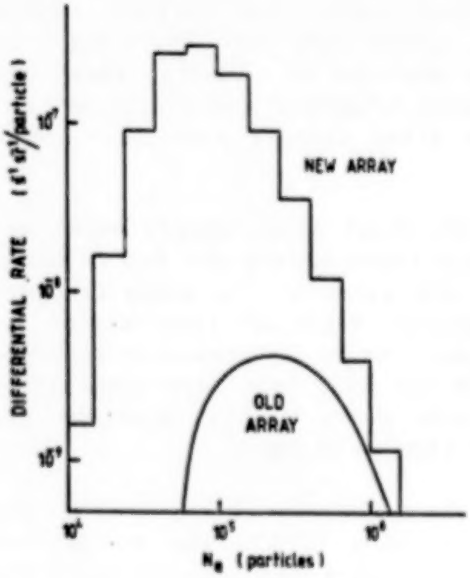

Fig. 2 Size Distribution for all events accepted by whole array. The events are analysed using the NKG function and MINUIT^5 program package.

References

1. Protheroe, R.J., Clay, R.W. and Gerhardy, P.R., 1984, Ap. J. (Lett.) 280, L47.
2. Protheroe, R.J. and Clay, R.W., (1985) Nature (in the press)
3. Crouch, P.C., Gerhardy, P.R., Patterson, J.R., Clay, R.W. and Gregory, A.G. (1981) Nucl. Inst. Meth., 179, 467.
4. Clay, R.W., Corani, C.L., Dawson, B.R., Gregory, A.G., Patterson, J.R., and Prescott, J.R., (1983) Proc. 18th Int. C.R.C. (Bangalore), 6, 257.
5. James, F. and Roos, M., 1975, Computer Phys. Comm. 10, 343.

ORIGINAL PAGE IS
OF POOR QUALITY

RIGHT ASCENSION (HOURS)	-90	-85	-80	-75	-70	-65	-60	-55	-50	-45	-40	-35	-30	-25	-20	-15	-10	-5	0	5	10	15	20	25	30	35	40
0	0	3	8	14	38	43	103	141	187	235	272	287	308	340	197	151	100	88	34	10	7	6	1	0	0	1	1
0.5	0	0	10	16	23	70	108	144	178	231	343	300	237	235	181	152	93	70	33	14	5	3	1	0	0	0	0
1.0	0	3	4	15	39	56	100	138	186	218	270	296	289	256	197	139	102	88	37	28	7	6	3	1	0	0	0
1.5	0	3	4	20	31	67	96	143	203	230	350	285	257	258	189	153	81	61	37	19	9	3	0	1	0	0	0
2.0	0	1	12	8	31	39	102	150	182	229	350	274	355	286	300	137	98	69	24	17	7	4	3	1	0	0	0
2.5	0	3	3	8	36	68	115	153	174	173	253	288	279	237	218	140	113	87	37	18	9	3	0	1	0	0	0
3.0	0	3	5	8	35	69	106	143	177	248	281	272	248	318	205	138	104	57	30	8	6	1	1	1	0	1	0
3.5	0	1	8	18	38	62	87	149	187	237	330	288	350	330	188	143	80	67	25	16	8	2	1	1	0	0	0
4.0	0	1	8	20	38	42	86	144	187	210	358	265	282	259	183	162	89	68	20	13	8	3	0	0	1	0	0
4.5	0	0	5	17	28	80	101	131	184	228	283	348	334	238	184	160	98	53	52	17	8	4	1	0	0	0	0
5.0	1	2	7	18	35	51	96	140	205	253	254	284	294	245	182	156	104	87	29	22	10	3	1	1	0	0	0
5.5	1	4	8	13	35	67	88	141	183	238	248	261	288	229	191	148	88	63	39	14	4	3	1	3	0	0	0
6.0	0	1	3	15	38	48	96	137	210	240	270	281	276	344	181	144	99	59	27	8	11	4	1	0	1	3	0
6.5	0	2	3	14	28	77	81	141	180	234	343	300	358	336	215	145	96	68	27	12	6	1	3	1	0	0	1
7.0	0	3	6	12	38	55	87	153	200	220	272	344	355	358	312	150	84	61	30	13	6	5	1	1	2	0	1
7.5	1	3	3	18	35	50	103	155	188	263	288	361	358	330	181	155	108	54	37	12	8	5	1	0	0	0	0
8.0	0	3	6	18	33	58	102	139	150	349	275	278	348	344	182	158	98	88	30	16	12	1	1	0	0	0	0
8.5	0	1	8	10	38	63	99	118	202	272	374	286	381	330	311	147	100	78	40	18	12	2	1	0	0	1	0
9.0	0	3	3	18	35	65	87	139	182	327	363	365	277	343	216	159	98	83	30	18	8	0	0	3	0	1	0
9.5	0	2	3	18	28	50	100	133	181	328	356	314	388	343	189	145	83	57	29	12	4	8	1	1	0	0	0
10.0	1	3	5	10	34	58	109	188	203	230	363	257	260	250	182	161	94	84	28	12	6	2	0	0	0	0	0
10.5	0	2	4	13	38	57	87	144	181	227	371	283	280	244	313	138	105	83	37	13	3	3	2	1	1	0	0
11.0	0	1	1	18	23	66	106	154	200	225	261	283	280	303	191	148	90	65	48	18	7	3	0	0	1	0	0
11.5	0	8	3	10	39	64	100	148	188	309	380	378	384	385	317	158	89	43	31	14	3	1	0	1	0	0	2
12.0	0	3	2	13	38	48	87	183	174	233	375	249	380	258	184	149	103	41	28	24	5	2	1	0	1	0	0
12.5	0	2	6	13	27	60	93	134	184	238	358	353	300	355	186	178	104	88	35	18	3	4	0	1	0	1	1
13.0	0	3	4	16	30	58	93	144	180	190	367	383	290	318	183	139	106	88	38	17	6	3	3	2	0	0	0
13.5	0	0	6	17	39	45	106	144	193	241	274	288	381	330	189	131	101	82	34	15	7	3	1	0	1	0	0
14.0	0	3	8	13	38	63	74	133	185	329	308	380	272	355	310	134	107	53	38	20	8	3	1	1	0	0	1
14.5	0	2	8	13	34	63	103	151	191	319	344	387	349	348	302	150	93	58	37	18	8	3	1	0	0	1	0
15.0	0	1	3	23	39	58	90	133	207	358	373	384	392	353	310	149	114	84	34	19	3	3	0	0	1	1	0
15.5	0	0	7	15	30	51	104	143	187	308	303	378	383	337	185	144	103	84	31	11	7	8	3	0	0	0	0
16.0	0	1	11	22	30	69	109	138	207	324	333	309	303	348	183	157	100	84	23	19	6	5	3	1	0	0	0
16.5	0	0	5	18	34	65	96	147	305	326	353	387	304	348	189	145	99	80	33	13	1	3	1	0	0	0	0
17.0	0	0	7	10	32	80	103	148	185	331	277	378	294	228	317	187	108	83	38	30	4	3	3	0	1	0	0
17.5	3	3	7	15	34	55	90	133	303	333	383	382	348	337	310	144	98	70	31	18	8	5	1	1	0	0	0
18.0	0	3	4	14	39	63	100	134	178	313	371	363	357	337	180	149	91	69	37	18	3	4	3	0	0	0	0
18.5	0	3	8	8	31	48	93	158	183	336	308	389	380	327	188	154	92	80	35	18	7	1	3	0	0	0	0
19.0	0	3	3	17	38	70	84	138	188	333	337	382	380	353	188	184	107	80	40	15	5	7	0	0	0	0	0
19.5	0	1	7	8	38	63	105	141	180	348	387	378	385	341	300	181	108	85	33	13	6	3	1	0	1	0	0
20.0	1	3	8	13	31	68	98	148	170	318	380	310	381	338	301	141	85	64	33	8	7	3	1	0	0	0	0
20.5	0	3	7	13	34	51	90	139	188	337	349	387	388	349	308	180	110	88	29	14	8	5	3	0	0	0	0
21.0	3	0	8	17	38	53	89	149	183	318	301	378	372	327	187	148	101	58	34	19	5	4	0	0	0	0	0
21.5	1	1	3	14	38	68	105	180	188	333	352	271	351	333	194	181	106	73	37	19	5	4	8	1	0	0	0
22.0	6	3	7	18	31	54	97	147	194	338	390	309	371	381	188	147	113	64	40	23	6	7	0	0	0	1	0
22.5	0	8	7	13	36	61	110	137	188	345	383	309	333	331	319	168	115	57	31	30	4	2	0	1	0	0	0
23.0	3	1	3	18	38	80	106	138	189	313	358	344	389	381	305	145	82	61	28	12	7	3	1	0	0	1	0
23.5	0	1	8	15	37	63	99	135	198	305	348	301	383	347	183	151	104	80	31	18	7	3	3	0	0	0	0

DECLINATION (DEGREES)

TABLE 1

Sky map showing typical coverage of the southern sky. The median shower size is 0.9×10^5 particles.

OG 9.4-5

AN EAS EXPERIMENT AT MOUNTAIN ALTITUDE FOR THE DETECTION OF GAMMA-RAY SOURCES

O.C. Allkofer, M. Samorski and W. Stamm

Institut für Reine und Angewandte Kernphysik,
University of Kiel, Olshausenstr. 40-60, D-2300 Kiel,
West Germany

ABSTRACT.

The plan of an extensive air shower experiment 2.200 m above sea level for the detection of $10^{14} - 10^{17}$ eV gamma-rays from sources in the declination band 0° to +60° is described.

I. INTRODUCTION.

Gamma-ray emission beyond 10^{14} eV has been reported of the sources Cygnus X-3 (Samorski and Stamm 1983a, 1983b, Lloyd-Evans et al. 1983, Baltrusaitis et al. 1985a, Bhat et al. 1985), Vela X-1 (Protheroe et al. 1984), LMC X-4 (Protheroe and Clay 1985), Hercules X-1 (Baltrusaitis et al. 1985b), and the Crab nebula (Dzikowski et al. 1981, Boone et al. 1984). For gamma-ray astronomy in this energy range new EAS experiments are needed meeting special requirements, as for example an improved angular resolution to allow better discrimination against the background of normal showers and larger effective detection areas especially for the lower energy range of showers to be detected.

The Kiel group plans to set up a new experiment dedicated to the detection of gamma-ray sources in the energy region $10^{14} - 10^{17}$ eV, to be run at mountain altitude at a site far south from Kiel.

II. SITE OF THE EXPERIMENT.

A suitable site for the new experiment seems to be the Astronomical Observatory on top of the Roque de los Muchachos at the Canary island La Palma, where a relatively plane area of 200×200 m^2 is available and the electrical power supply requirements are fulfilled. The geographical position is 28.8° north and 17.9° west, at an elevation of 2.200 m above sea level ($x = 780$ g/cm^2).

At the latitude of this site Cygnus X-3 and Hercules X-1 can be detected under better condition than at Kiel (latitude 54.4°), and in addition three further candidate sources are in the observation field of the experiment, the Crab nebula, Geminga (2 CG 195 + 05) and the 1.5 ms pulsar PSR 1937 + 21, all three known as gamma-ray emitters around 10^{12} eV.

Since showers of same primary energy contain more particles at mountain altitude than at sea level, the energy range at this mountain site can be extended to energies below 10^{15} eV.

III. DETECTOR ARRAY.

A plan of the detector array is presented in Fig. 1. In total 56 scintillation counters of 1 m^2 each (scintillators NE 102 A, 5 cm thick) will be distributed over an area of 200×200 m^2 and will be equipped with one photomultiplier VALVO XP 2050 each for particle density measurements. In order to cover the large dynamical range required for EAS particle density measurements the signals will be picked up at three different points of successively decreasing gain on the resistor chain of the photomultipliers, giving $3 \times 56 = 168$

analog informations per shower handled by the same number of analog to digital converters (ADCs).

Fast timing measurements will be performed with the quadratic grid of 6 x 6 scintillation counters in the centre of the array (grid width 10 m). Each of these 36 detectors will be equipped with an additional fast photomultiplier VALVO XP 2041. Since timing modules containing 8 time to digital converters (TDCs) each with common start and individual stops will be used, the 4 x 4 central counters of the 6 x 6 array will provide common start signals for the respective 8 adjacent counters, so that 16 x 8 = 128 time differences will be available for each event. The high redundancy of fast timing channels will ensure reliable operation over long periods.

From the central section of the 6 x 6 counters 25 hard-wired 4-fold coincidences between each 4 adjacent detectors will be formed. Any of the 25 possible 4-fold coincidence signals will trigger the array.

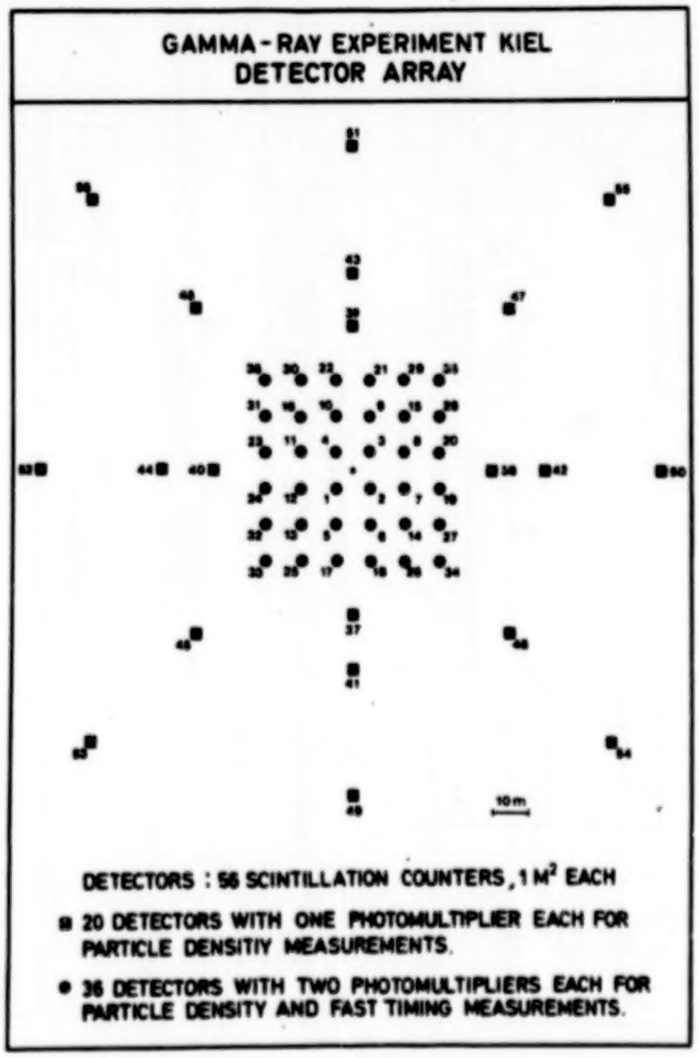

GAMMA-RAY EXPERIMENT KIEL
DETECTOR ARRAY

DETECTORS : 56 SCINTILLATION COUNTERS, 1 M^2 EACH

- ■ 20 DETECTORS WITH ONE PHOTOMULTIPLIER EACH FOR PARTICLE DENSITIY MEASUREMENTS.
- ● 36 DETECTORS WITH TWO PHOTOMULTIPLIERS EACH FOR PARTICLE DENSITY AND FAST TIMING MEASUREMENTS.

Figure 1. Plan of the EAS detector array for gamma ray observations.

ORIGINAL PAGE IS
OF POOR QUALITY

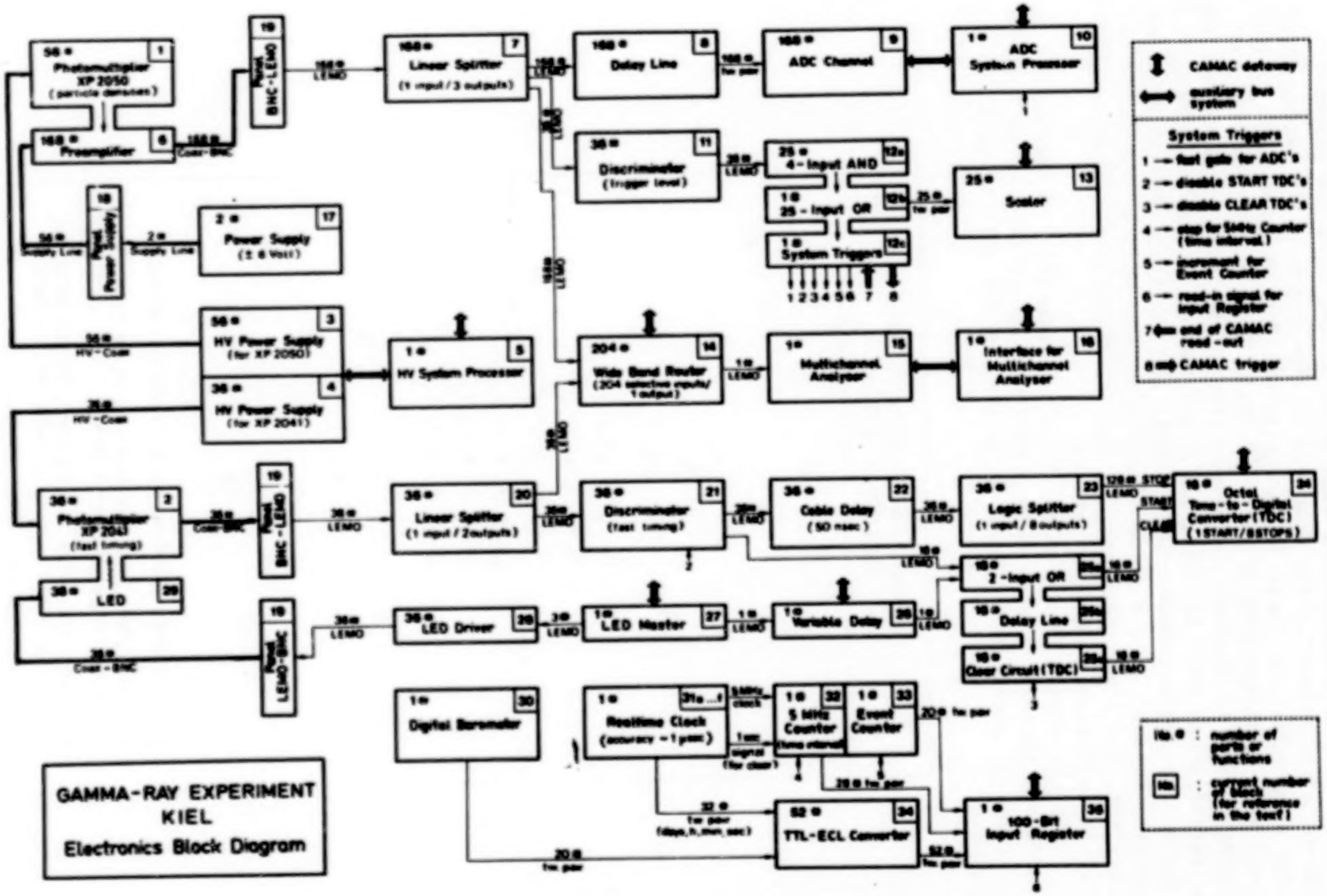
56 ● Photomultiplier XP 2050 (particle detection) 1
168 ● Preamplifier 6
168 ● Coax-BNC
19 Panel BNC-LEMO
168 ● LEMO
168 ● Linear Splitter (1 input / 3 outputs) 7
168 ● Delay Line 8
168 ● tw pair
168 ● ADC Channel 9
1 ● ADC System Processor 10
38 ● Discriminator (trigger level) 11
38 ● LEMO
25 ● 4-Input AND 12a
1 ● 25-Input OR 12b
1 ● System Triggers 12c
1 2 3 4 5 6 7 8
25 ● tw pair
25 ● Scaler 13
18 Panel Power Supply
56 ● Supply Line
2 ● Supply Line
2 ● Power Supply (± 6 Volt) 17
56 ● HV Power Supply (for XP 2050) 3
38 ● HV Power Supply (for XP 2041) 4
56 ● HV-Coax
38 ● HV-Coax
1 ● HV System Processor 5
168 ● LEMO
38 ● LEMO
204 ● Wide Band Router (204 selective inputs/ 1 output) 14
1 ● LEMO
1 ● Multichannel Analyser 15
1 ● Interface for Multichannel Analyser 16
CAMAC dataway
auxiliary bus system
System Triggers
1 — fast gate for ADC's
2 — disable START TDC's
3 — disable CLEAR TDC's
4 — stop for 5MHz Counter (time interval)
5 — increment for Event Counter
6 — read-in signal for input Register
7 end of CAMAC read-out
8 CAMAC trigger
38 ● Photomultiplier XP 2041 (fast timing) 2
38 ● Coax-BNC
19 Panel BNC-LEMO
38 ● LEMO
38 ● Linear Splitter (1 input / 2 outputs) 20
38 ● Discriminator (fast timing) 21
38 ● Cable Delay (50 nsec) 22
38 ● Logic Splitter (1 input / 8 outputs) 23
128 ● LEMO
STOP
START
CLEAR
10 ● Octal Time-to-Digital Converter (TDC) (1 START/8 STOPS) 24
38 ● LED 29
38 ● Coax-BNC
19 Panel LEMO-BNC
38 ● LED Driver 26
1 ● LED Master 27
1 ● Variable Delay 28
10 ● 2-Input OR 25a
10 ● Delay Line 25b
10 ● Clear Circuit (TDC) 25c
10 ● LEMO
1 ● Digital Barometer 30
1 ● Realtime Clock (accuracy ~1 psec) 31a...f
5MHz clock
1 sec signal (for clear)
1 ● 5 MHz Counter (time interval) 32
1 ● Event Counter 33
20 ● tw pair
32 ● tw pair (days, h, min, sec)
52 ● TTL-ECL Converter 34
52 ● tw pair
1 ● 100-Bit Input Register 36
20 ● tw pair
No. ● : number of parts or functions
No. : current number of block (for reference in the text)
GAMMA-RAY EXPERIMENT
KIEL
Electronics Block Diagram

Figure 2. Block diagram of the electronic layout.

According to the relatively small grid width of the detectors in the centre (10 m) and the selected triggering condition all showers of primary energy above 10^{14} eV will be detected, when the core will hit a central area of about 70 x 70 m^2, with an angular resolution of the order of 1 degree at a rate of about 20 events per minute. For primary energies above 10^{15} eV an angular resolution better than 1 degree is expected, at an effective area larger than 100 x 100 m^2.

IV. ELECTRONIC LAYOUT. A detailed block diagram of the electronics is shown in Fig. 2. In all essential parts only reliable commercial micro-electronic systems will be employed. The whole system will be managed and controlled by a PDP 11/24 processor with 256 kB MOS memory and two magnetic disk drives of 28 MB each. The readout and control will be based on standard CAMAC technique. The arrival times of the showers will be determined by means of a high precision real time clock controlled by a Standard Time receiver to allow phase measurements of gamma-rays from pulsars.

Without interrupting or disturbing the air shower measurements the processor will in turn connect via a multiplexer each photomultiplier output to a multichannel analyser, controlling the position of the one-particle-peak and adjusting the PM high voltage, if necessary.

A few times per day the processor will interrupt the measurements at given times for a few seconds for checking the fast timing channels. For this purpose simultaneous test signals will be produced in each fast timing phototube by triggering light emitting diodes (LEDs). By introducing computer regulated time delays between the start and stop signals of all TDCs, the zero point and the linearity of each of the 128 timing channels will be controlled. The various test functions and monitoring of the performance of the experimental equipment will enable a running of the array with a minimum of maintainance.

The authors are gratefully acknowledging the cooperation of Prof. Dr. E. Bagge in the planning phase of this experiment and wish to thank Mr. Ing. K. Sauerland for his engaged support in the electronic design.

REFERENCES.

Baltrusaitis, R.M., et al. 1985a, 1985b, preprints, University of Utah.
Bhat, C.L., et al. 1985, paper submitted to Ap. J. (February 1985).
Boone, J., et al. 1984, Ap. J., 285, 264.
Dzikowski, T., et al. 1981, 17th ICRC (Paris), 1, 8.
Lloyd-Evans, J., et al. 1983, Nature (Letters), 305, 784.
Protheroe, R.J., et al. 1984, Ap. J. (Letters), 280, L47.
Protheroe, R.J., and Clay, R.W. 1985, Nature (Letters), 315, 205.
Samorski, M., and Stamm, W. 1983a, Ap. J. (Letters), 268, L17.
Samorski, M., and Stamm, W. 1983b, 18th ICRC (Bangalore), 1, 135.

AN OBSERVATORY TO STUDY 10^{10} TO 10^{17} EV GAMMA RAYS

Trevor C. Weekes
Whipple Observatory, Harvard-Smithsonian Center
for Astrophysics

Abstract

A facility is described which incorporates many of the best features of existing gamma ray telescopes at a single site. In addition to reducing the flux sensitivity in some energy ranges, it permits the measurement of the energy spectrum over seven decades of energy.

1. Introduction. Ground-based gamma-ray astronomy has matured from a discipline with a small number of detections requiring confirmation to one in which there are several sources that are well-established (Cyg X-3, the Crab, Her X-1) but which now demand more detailed observations before the emission mechanisms can be understood. In at least one source, Cyg X-3, there is some question concerning the nature of the observed particles. All of the sources show evidence for time variability. Since many techniques, whose absolute sensitivities are poorly understood, have been employed and since many of the detections do not have large statistical significance, it is difficult to derive an energy spectrum that can be compared with source models. The energy spectrum in the range 10^{14} - 10^{16} eV is particularly interesting since there is the possibility of detecting the absorption dip caused by pair production on the 3° K microwave background.

A single facility which combines the best features of the many techniques used to cover the energy range from 10^{10} to 10^{18} eV would eliminate the ambiguity arising from the use of different techniques at different epochs. Below we describe in qualitative terms a Very High Energy Gamma Ray Observatory and then list its advantages for each decade of the energy range covered.

2. Physical Description. The observatory will consist of a combination of pointed atmospheric Cherenkov telescopes and all-sky particle detector arrays. It will be located on a mountain plateau at an altitude of about 3.0 km. The array will cover an area of approximately 1.8×10^8 m^2 which must be reasonably flat for ease of construction and access. A central control room will house the recording electronics, the on-line computer, the atomic clocks and the operators.

(a) Atmospheric Cherenkov detectors. This array will consist of a central large reflector (with aperture in the range 15-20m) surrounded by six reflectors of 10m aperture on the corners of a hexagon and at a distance of 75m from the center (figure 1). These atmospheric Cherenkov telescopes will be modeled on the Whipple Observatory 10m

ORIGINAL PAGE IS
OF POOR QUALITY

Optical Reflector. Each will be composed of tessellated segments but the f number will be larger to give a greater depth of focus. Variable focal length segments will be used to improve the optical figure and reduce the light path difference across the reflector. The reflectors will be protected by domes to preserve the mirror coatings and also to permit the reflectors to operate as air Cherenkov muon telescopes under cloudy or brightmoon conditions. Each reflector will be equipped as an imaging device with an array of phototubes at its focus. The number and size of phototubes will be chosen so as to have a pixel diameter of 0.25° and a field of view of 3.4° (e.g. 169 tubes of diameter 4 cm). The telescopes will operate in parallel and will track the position of a suspected source.

The particle detector array will consist of 1m² scintillators with fast timing, arranged in a hexagonal 25m grid spacing as shown in figure 2. The inner seven detectors will be clusters of five scintillators; the total number of scintillators will be 65. When any three adjacent detectors exceed a two particle level, a readout command will be generated. The read out will include the pulse size, the relative time of arrival at each detector and the absolute time.

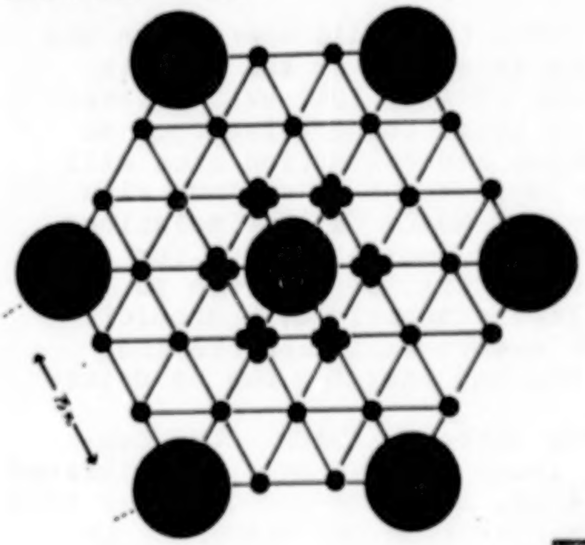

Figure 1. Seven large reflectors with spacing of 75 m.

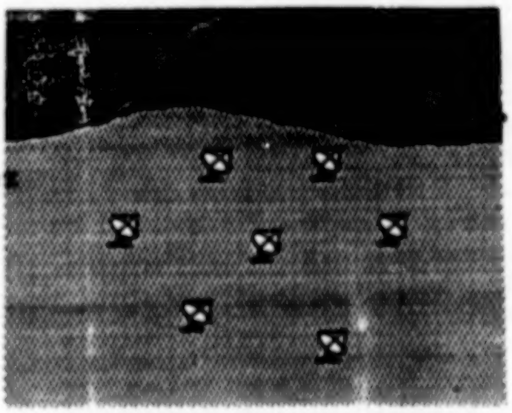

Figure 2. Layout of full array. Large circles are large reflectors; small circles are scintillators. Grid spacing is 25m.

3. Operating Mode. The facility will actually consist of five separate gamma-ray telescopes, which will operate in overlapping energy ranges with the advantage that cross-calibration will be straightforward. The ranges covered are shown in figure 3 and the telescopes are described below.

(a) Low energy atmospheric Cherenkov telescope; (LEACT) in this mode the central light detector will be operated in coincidence with one or more of the outer light detectors at a very low threshold to detect the minimum energy gamma-ray showers. Using fast electronics, small pixels and large mirror areas, it will be possible to achieve an energy threshold close to 10 GeV. This will have two important advantages: (a) it will overlap with the upper end of the coverage available with EGRET on the GRO (b) it opens up a new, and previously unexplored, region of the electromagnetic spectrum in which the background contributions from Cherenkov light deficient proton-initiated air showers will be small (Turver and Weekes, 1978). The light levels will be too low for energies below 100 GeV to permit full use to be made of the imaging technique but the reduced proton background will compensate for the loss of angular resolution.

(b) Imaging Telescope (IT); this will operate on the same principle as the existing telescope at the Whipple Observatory in the energy range 10^{11} to 10^{13} eV. However each shower will be seen by at least three telescopes so that both the angular resolution and collection area will be improved: a factor of ten improvement in minimum flux sensitivity is estimated. Recent Monte Carlo simulations (Hillas, this conference OG 9.5-3) indicate that, for showers that are well sampled, it will be possible to differentiate the primary (electromagnetic or hadronic). High energy (10^{13} - 10^{14} eV) events will saturate the central pixels but their shapes and energies can be determined from the outer pixels.

(c) Wide angle Cherenkov detector (WACD); the centroid of the Cherenkov light image for a gamma ray initiated shower of primary energy 10^{12} eV, with impact parameter 100m from the detector axis, falls 1° from the center of the field. The lateral distribution of Cherenkov light falls off beyond 100m. However a sensitive detector will have a large collection area for showers of energy 10^{13} eV whose impact parameters are in the range 100-250m; the centroid of their light distribution will fall in the ring of phototubes 1.5° from the axis. By triggering on signals in the outer pixels of the adjacent detectors the collection area for air showers is in the range 10^{13} to 10^{15} eV will be $\sim 10^{5}$ m^{2}. This large collection area (a hundred times greater than a small particle array detector) will compensate for the small duty cycle (<10%) of the atmospheric Cherenkov detector.

(d) Gas Cherenkov Muon Telescope (GCMT); the small duty cycle of the atmospheric detectors can be increased by having the reflectors housed in light-tight domes (which can be opened for night-sky use). Under dark conditions, the imaging reflectors can easily detect the Cherenkov light ring from single particles (muons) within the dome. If the dome is large enough to permit the reflectors to track sidereally, then sources can be tracked under cloudy or moonlit conditions (or even during the day if the dome is sufficiently light-tight). The collection area for muons is essentially that of the optical collector 75m^2 This mode would only be justified if it is shown that the directional anisotropies detected in the direction of Cygnus X-3 result from showers with a high component of muons (Samorski and Stamm (1983); Marshak et al. (1985)).

(e) Particle Air Shower Array (PASA); at mountain altitude this conventional array of particle detectors will have an energy threshold close to 10^{14} eV and a high energy cut-off dictated by exposure time and flux levels. Using state-of-the-art fast phototubes and electronics, the angular resolutions will be ~1°. There will be considerable overlap with the atmospheric Cherenkov detectors although the particle array will act as an all-sky monitor and the light-detectors will track specific sources.

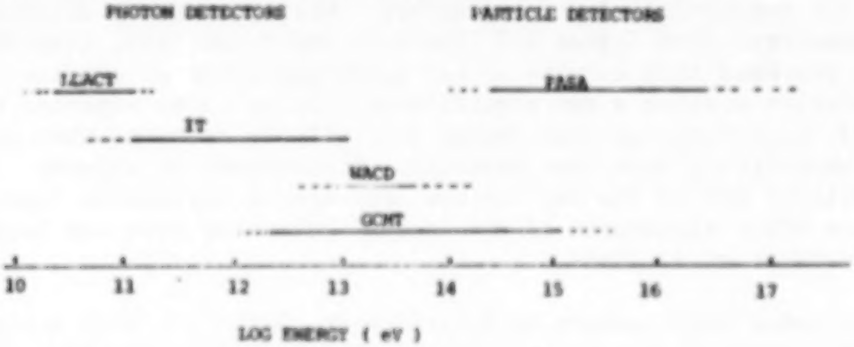

Figure 3. Distribution with energy.

4. Discussion. The facility described above involves no new technology; rather it requires a duplication and concentration of existing telescopes at an optimum site. It also requires an investment on a scale not normally associated with ground-based cosmic ray experiments.

References.

Marshak, M.L., et al. (1985), preprint.
Samorski, M., Stamm, W., (1983), 18th ICRC. 11, 244.
Turver, K.E., Weekes, T.C. (1978), Nouvo Cimento. 45B, 99.

OG-9.4-7

N85-34974

A NEW ARRAY FOR THE STUDY OF ULTRA HIGH ENERGY GAMMA-RAY SOURCES

Brooke G, Lambert A, Ogden P A, Patel M, Perrett J C,
Reid R J O, Watson A A and West A A.

Physics Department, University of Leeds, Leeds LS2 9JT, UK.

ABSTRACT

This paper describes the design and operation of a $32 \times 1\,m^2$ array of scintillation detectors for the detection of 10^{15} eV cosmic rays with an expected angular resolution of $<1^\circ$,[†] thus improving the present signal/background ratio for γ-ray sources. Data are recorded on a hybrid CAMAC and 'in-house' system which uses a laser and Pöckel-Cell arrangement to routinely calibrate the timing stability of the detectors.

1. Introduction. The charged nature of the majority of cosmic ray primaries means that it is not possible to identify their source regions from measurements of the direction of the shower axis and thus most air shower groups have settled for a directional resolution of $\lesssim 5^\circ$ which is adequate for estimation of primary energy. With the recent discovery of pulsed gamma-rays from Cygnus X-3 (Samorski and Stamm 1983, Lloyd-Evans et al 1983), possible only because of its known periodicity, precise angular resolution assumes a new significance. It is to be expected that other sources, less luminous than Cygnus X-3, will be detected when arrays of enhanced sensitivity have been developed; improvement of angular resolution will be one of the key factors here and is especially important as some of the other signatures of the neutral primaries have now been questioned (Marshak et al 1985).

The array now under construction at Haverah Park, GREX, has been designed to trigger on showers with a shower size $N > 10^4$ particles; the full array becoming sensitive at $\sim 3 \times 10^4$.

2. The detector. A Philips 2312B photomultiplier tube (PMT) with a risetime of 2.5 ns and a gain of 3×10^7 at 2 kV, looks up at a $1\,m^2 \times 10$ cm block of NE102 plastic scintillator (Figure 1). The inside of the detector box is painted black to minimize the amount of reflected light reaching the PMT , thus improving the light pulse risetime. This is at the cost of a reduction in the amount of light reaching the tube. We do however use a sheet of aluminized foil above the scintillator to add substantially to the light yield without materially affecting the risetime. With this arrangement a single vertical particle passing through the scintillator produces > 50 photoelectrons in the PMT.

3. Description of the array. The array consists of 32 detectors of $1\,m^2 \times 10$ cm NE102 plastic scintillator positioned on 30 and 50 m grids (Figure 2). The centre of the array is coincident with the 50, 150 and 500 water-Cerenkov array run at Haverah Park by the Leeds University group. Signals from the anode of the photomultiplier (PMT) are transmitted along high bandwidth cable (Aerialite 363) to the recording electronics situated at the centre of the array. The array records a shower coincidence when any three detectors trigger at $> 1\,m^{-2}$ inside a $1\,\mu s$ window. Fast timing, for arrival direction, is started at 1/3

ORIGINAL PAGE IS
OF POOR QUALITY

particle per detector. The contours of log(N) in Figure 2 show the sensitivity of the array to showers of different sizes.

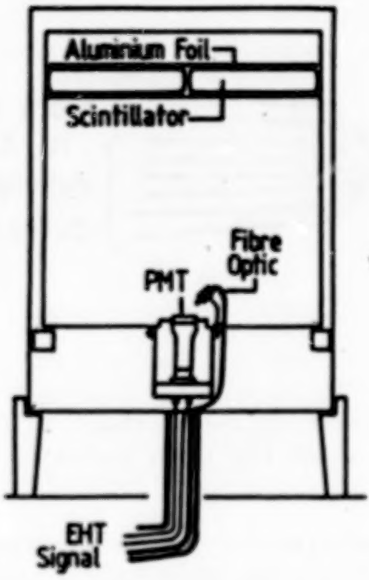

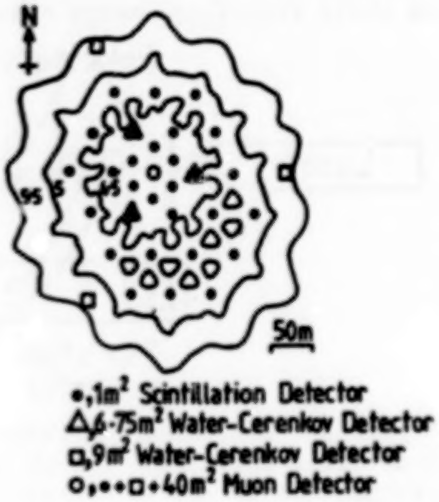
N
5.5
5
4.5
50m
•,1m² Scintillation Detector
△,6·75m² Water-Cerenkov Detector
□,9m² Water-Cerenkov Detector
○,••□•40m² Muon Detector

Figure 1: The GREX scintillation detector showing the arrangement of the PMT, scintillator and Fibre Optic cable.

Figure 2: Disposition of the GREX scintillation detectors in relation to the 50 and 150 m water-Cerenkov detectors and the 40 m² muon detector. The contours show the sensitive area of the array to showers of log(N) > 4.5, 5.0 and 5.5.

The GREX array transmits event triggers to various external arrays:- Nottingham University's 40 m² detector and the 50 and 150 m water-Cerenkov arrays. Every two hours a Timing Stability Pulse (TSP) is applied to monitor the gain and timing stability of the detectors. Figure 3 shows the set-up that is used to do this. The output from a 2 mW HeNe laser is modulated by a Pöckel-cell driven by an externally triggered step generator. The resulting light pulse has a 10 ns FWHM with a 1.5 ns rise-time. This is transmitted to all the detectors via 50/125 graded index fibre optic cable. The detectors trigger on this light pulse and the resulting signals are treated just as if a 32 fold coincidence was recorded.

The GREX system will be capable of supervising 32 detectors each working at a D1 trigger rate of 200 - 300 s^{-1} with only ∿ 1 - 3% deadtime (allowing 2 μs deadtime per background pulse). When the full system is in operation the main contribution to deadtime will be the event processing time or to be more precise the readout time via the slow, but cheap, CAMAC/GPIB interface. The readout time is very software-dependent and for that reason the code will be written in the C-language. The GPIB interfaces to an S100 based machine (North Star Horizon microcomputer) via an IEEE - S100 interface. GREX data will be merged with data from the 50 and 150 m water-Cerenkov arrays and then recorded on magnetic tape. The expected recording rate is ∿ 16 Mb of data per week corresponding to

$\sim$ 10 events min^{-1}. To help merge GREX data with muon data from the Nottingham University group the event time (± 1 ms) will be transmitted to their recording system after every event.

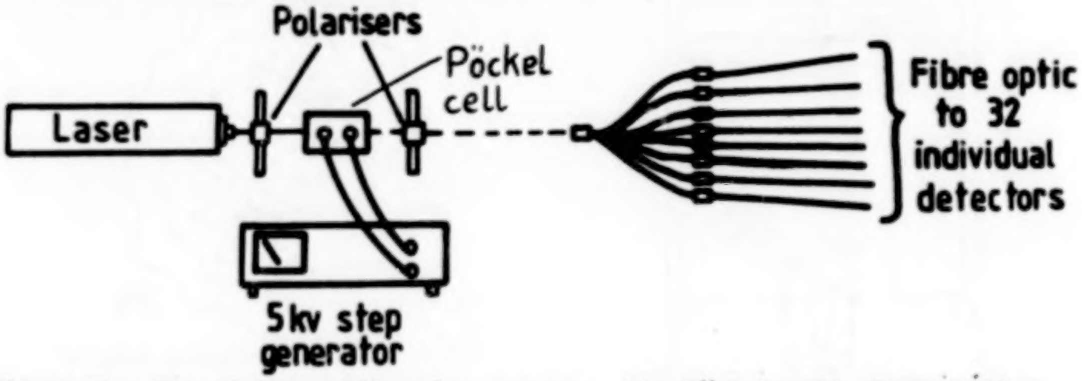

Figure 3: The timing calibration set-up. The Pöckel-cell chops a 10 ns wide light pulse with 1.5 ns risetime. The resulting light pulse is transmitted to all 32 detectors.

4. Recording electronics. The recording electronics in the new Haverah Park gamma-ray experiment, GREX, is a hybrid of commercial LeCroy modules (CAMAC based) and 'in-house' electronics. Figure 4 shows how the various systems are integrated. Signals from the detectors are transmitted to a discriminator board which incorporates the LeCroy MVL407 (quad ultrafast voltage comparator). The signal is split three ways:- one is integrated and input to a LeCroy ADC (4300), while the others are input into two quarters of the MVL407, referred to as the D1 and the D2 discriminators. If the D1 discriminator, set at $\sim$ 1/3 particle threshold, triggers, and if the D1 gate is open the LeCroy TDC (4208) connected to that channel starts counting at 1 GHz. The low D1 threshold is used to keep timing fluctuations to a minimum. If the D2 discriminator triggers, (threshold $> 1\ \mathrm{m}^{-2}$) a 1 μs coincidence window pulse is produced. If the D2 gate is open then the coincidence window pulse is transmitted to the majority logic board.

The majority logic board adds all the coincidence window pulses from the 32 possible D2 discriminators and then discriminates at three times the D2 level giving the 3-fold coincidence and producing a majority logic output pulse. This pulse is transmitted to the coincidence logic board and the event time board which latches the event time to a resolution of 1 ms.

When any TDC triggers the ADC input gate is opened and a fast clear pulse is generated after a 1 μs delay. The fast clear pulse will be 'gated out' if a coincidence is recorded by the majority logic board. If there has not been an event within 1 μs of the first TDC triggering then the fast clear pulse is allowed to clear the 4 TCDs and 2 ADCs. It takes 1 μs to clear all the LeCroy modules; thus there will be 2 μs deadtime per background pulse from any of the 32 detectors.

When a shower coincidence is recorded within 1 μs after the first TDC has triggered (time allowed for the shower to traverse the array) a common pulse is sent to all TDCs. At the end of the 1 μs the CAMAC 'look at me'

N85-34975

ORIGINAL PAGE IS
OF POOR QUALITY

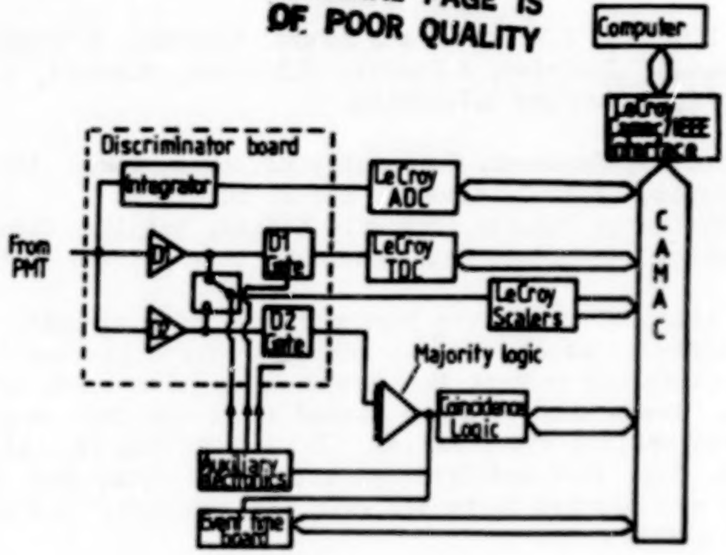
Computer
LeCroy Camac/IEEE Interface
Discriminator board
Integrator
LeCroy ADC
From PMT
D1
D1 Gate
LeCroy TDC
LeCroy Scalers
D2
D2 Gate
C A M A C
Majority logic
Coincidence Logic
Auxiliary electronics
Event time board

Figure 4: Schematic block diagram of the GREX recording electronics. The ADC, TDC, scalers and the GPIB interface are commercial LeCroy modules. The remaining electronics were built 'in-house'.

(LAM) flag is set. The TDCs are capable of recording positive and negative times, i.e. when a TDC triggers before or after the common start/stop pulse. In our system the three detectors that formed the coincidence will have negative times and the remaining detectors which have recorded particles associated with the shower will have positive times. The relative arrival times are recorded to a resolution of 1 ns. The LAM flag is tested by the controlling computer and when detected instructs the 8901 GPIB-CAMAC crate controller to read the data from all the LeCroy modules, event time-board, digital thermometer and barometer. When the event has been processed the TDCs, ADCs and auxiliary electronics are reset; thus the whole system becomes active at the same time.

5. Auxiliary functions. Fast clear pulses are generated on every background pulse, i.e. every time D1 triggers and thus a single noisy detector could result in a large deadtime. Monitoring of detector performance is achieved by recording the D1 and D2 rates. This is achieved with extra electronics, referred to as the auxiliary electronics in Figure 4, which switches the input to the LeCroy scalers (4434) alternately between D1 and D2 pulses. If a detector should become 'noisy' then its contribution to the system can be negated by closing the D1 and D2 gates.

Acknowledgements. We would like to thank the Science and Engineering Research Council for their continued support.

References

†A Lambert and J Lloyd-Evans - this conference, OG-9.5-2.
J Lloyd-Evans et al 1983 Nature 305, 784.
M L Marshak et al 1985 Phys Rev Lett 54, 2079.
M Samorski and N Stamm 1983 Ap J Lett 268, L17.

N85-34975

Akeno 20km^2 Air Shower Array (Akeno Branch)

M.Teshima*, H.Ohoka, Y.Matsubara*, T.Hara, Y.Hatano, N.Hayashida, C.X.He**, M.Honda, F.Ishikawa, K.Kamata, T.Kifune, M.Mori*, M.Nagano, K.Nishijima***, Y.Ohno and G.Tanahashi

Institute for Cosmic Ray Research, University of Tokyo, Tokyo, 188 Japan
*Department of Physics, Kyoto University, Kyoto, 606 Japan
**Institute of High Energy Physics, Academia Sinica, Beijing, China
***The Graduate School of Science and Technology,Kobe University,Kobe,657

As the first stage of the future huge array we have expanded the Akeno air shower array to about 20km^2 by adding 19 scintillation detectors of 2.25m^2 area outside the present 1km^2 Akeno array with a new data collection system. These detectors are spaced about 1km from each other and connected by two optical fiber cables. This array has been in partial operation from 8th, Sep. 1984 and full operation from 20th, Dec. 1984. 20m^2 muon stations are planned to be set with 2km separation and one of them is now under construction.

1. Introduction

The origin of the highest energy cosmic rays is an interesting problem. We have a chance to connect their sources with the astronomical objects, because their propagation becomes simpler than that of lower energies and the possible sources may be limited to some kinds of active astronomical objects. The observation of giant air shower (GAS) produced by cosmic rays above 10^{19} eV have been made at Volcano Ranch[1], Haverah Park[2], Narabrai[3] and Yakutsuk[4]. But there still remain the discrepancies among experiments not only in their energy spectrum but also in their arrival direction distribution.

In order to clarify the present ambiguities on the experiments and to extend the observation to higher energy, a plan of huge surface array of area over 100km^2 is currently under discussion in Japan. In this report we describe about the "Akeno Branch" which is just constructed at Akeno with the intention of being a part of the huge array.

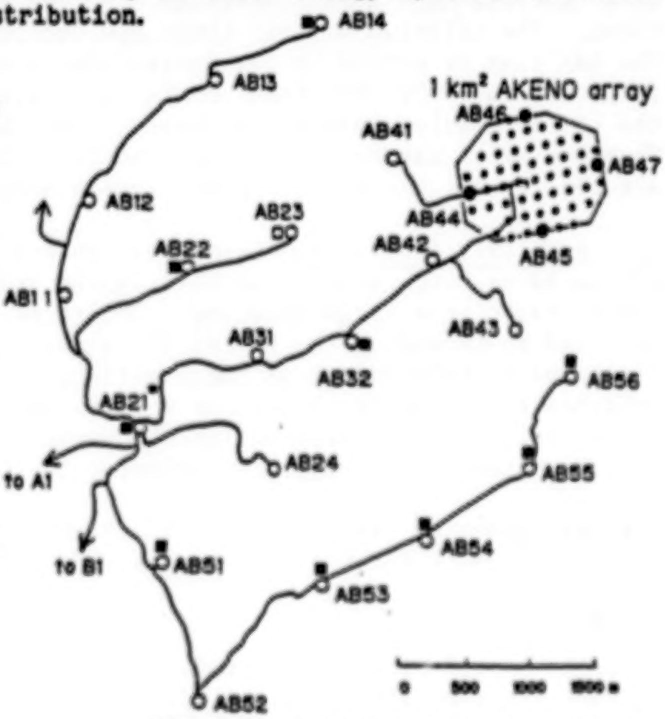

Fig.1 The detector arrangement of the "Akeno Branch".

2. Array of "Akeno Branch"

The detector arrangement of the "Akeno Branch" is shown in fig.1. The open circles are the scintillation detectors of 2.25m^2 each, located at about 1km separation. The closed circles are scintillation counters of 1m^2 area of the existing "1km^2 Akeno array"[5]. The four large ones are also connected to the present new recording system. The open square is a muon detectors of 20m^2 area under construction and the closed ones will be arranged within a few years. Each detector is connected to the next one with two optical fiber cables successively on a string as shown by a solid line. One cable is used for sending the control commands to each module of the detector from the center, and the other is for data transmission.

Inside the 1km^2 array, there are unshielded detectors of total area of 169m^2, shielded detectors of 225m^2 (1GeV for vertical traversing muons) and 75m^2 (0.5GeV), and 53 fast timing channels of 10nsec resolution. These are effective to measure the properties of the large showers at far from the core.

3. Data acquisition system

In each station there is a module called Detector Control Unit (DCU) which is designed with one board micro computer(Z-80A). DCU consists of 3 major parts; communication part, data processing part and detector monitor and control part. Several DCU's are tied to a common string which consists of two directional optical fibers. One fiber of outgoing direction from the center is used to send commands, clock pulses for the timer of DCU and timer frame (clear pulse for the timer). Another one is used to accept the status information of each detector for the trigger conditions and to collect shower data and monitor data from DCU's at the center. The communication data rates on strings are 625kb/s.

Every DCU has a timer which synchronizes to that of the center with 20nsec accuracy. All signals from the detector are digitized and stored in the ring-image-memory of DCU with the incident time of 20nsec accuracy. Each DCU sends the information to the center in every 3.2 μsec period whether the detector is hit by a particle or not. With this status information, coincidence requirements can be set at the center. 6 folds coincidence of neighbouring detectors is required for the trigger. When GAS hits over the array, central unit recognizes coincidence of signals from many detectors and knows its occurence time. Then the central unit issues a command for all DCU's to search for the GAS data in the ring memory with the time information of coincidence. Each DCU which has accepted this command, stops data acquisition and searches for the all corresponding data recorded within 100 μsec before and after the coincidence. Central unit commands DCU's to send the picked out data one by one. These data are sent to micro-computer(NEC 16bit PC9801) at Akeno central laboratory through RS232C line of optical fiber and stored in the 10MB Hard Disk.

With this system not only the air shower data and monitor data are acquired but also detector conditions can be controlled at the center. Supplied voltage to the phototube, temperature, counting rate and pulse height distribution of detectors are monitored periodically. The discrimination level of the amplifier and the high voltage to the phototube can be controlled on request from the center. These functions enable us to maintain the detectors stable for long term and make data reliable. The details of this system are described in Ohoka and Teshima[6].

4. Array response

The response of the present array was examined by analyzing the artificial showers which were simulated by the Monte Carlo method. The fluctuations of electron density and the shower front structure at core distances between 500m and 3000m of 10^{18}-10^{19}eV EAS observed at $4km^2/20km^2$ array[7] were used for the present simulation.

The threshold energy of detectable air shower is found to be about $10^{17.5}$eV and the recording efficiency reaches 100% at $10^{18.5}$eV as shown in fig.2. The histograms show the response and effective area for the showers hit inside the array. The broken line shows the area for all events including outside the array. The sensitivity for shower size and arrival direction in case of showers hit inside the array are shown in fig.3(a),(b) respectively. We can determine the electron size with 30% accuracy, arrival direction with 3 degree and core position with 80m. However for the showers outside the array, these are 150%, 9 degree and 150m, we need much caution to use the outer showers for the discussion of primary energy spectrum and their arrival directions.

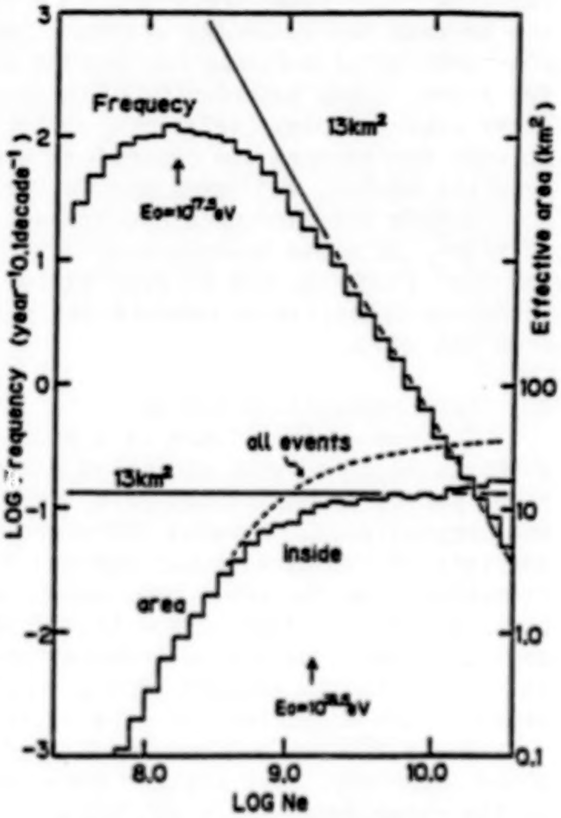

Fig.2 The detection efficiency of EAS with "Akeno Branch".

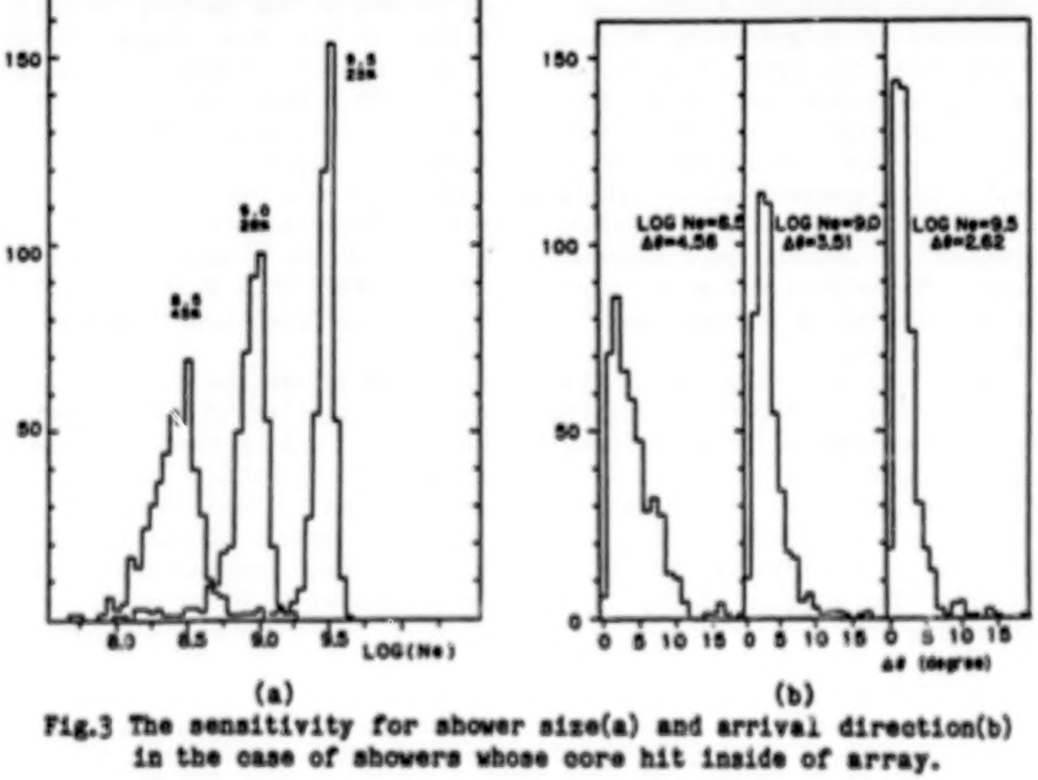

(a)

(b)

Fig.3 The sensitivity for shower size(a) and arrival direction(b) in the case of showers whose core hit inside of array.

ORIGINAL PAGE IS
OF POOR QUALITY

5. Conclusion and future plan

The observation of ultra high energy cosmic rays has started at Akeno. In order to determine their origin, the expansion of array to 100km^2 is under planning. The technical problems for expansion is already solved through the experience under the construction of Akeno Branch.

The schematic diagram of recording system of the future array is shown in fig.4. The whole array is divided into several Branches. Each Branch is managed by BCU(Branch Control Unit) which is connected successively to the next one with two optical fiber cables "String". This structure is exactly the same as that inside Branch. The commands from the center and data from the Branch are put on this "String". The clock pulse is supplied from the central unit SCU(System Control Unit) to each DCU(Detector Control Unit) via BCU (Branch Control Unit). Since the timer of every DCU synchronizes to the central timer, we can manage the GAS hit in the boundary gap between branches, in the same way as ones hit inside a Branch.

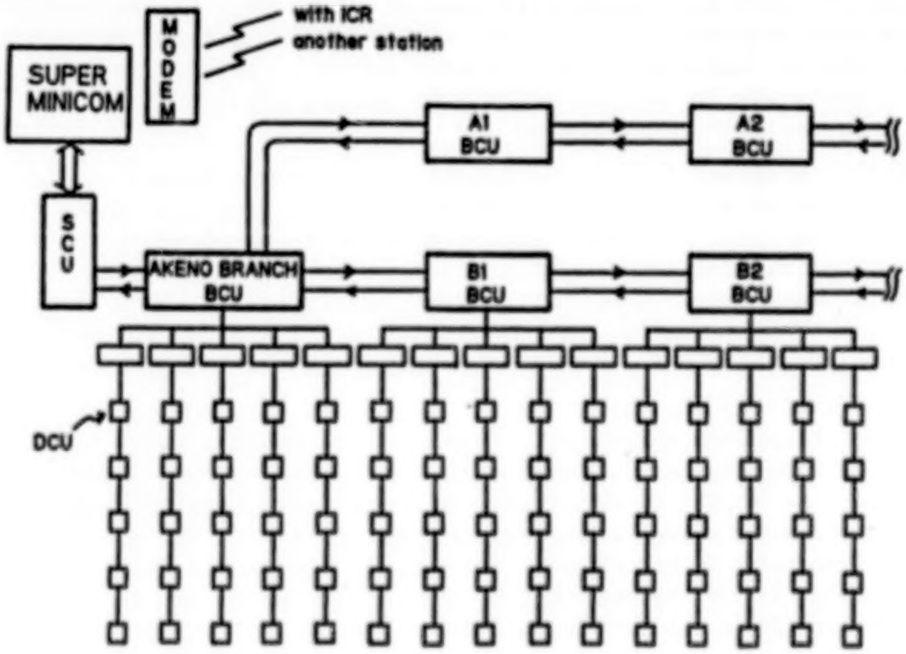

Fig.4 The data acquisition system of future surface array.

Acknowledgements

The authors wish to thank the participants of GAS workshops held in Japan for their fruitful discussions. The simulation was carried out with FACOM M380 at the computer room of Institute for Nuclear Study, University of Tokyo.

Reference

[1] J.Linsley, Proc. 8th ICRC, Jaipur 4 (1963) 295.
[2] D.M.Edge et al., J. Phys. A 6 (1973) 1612.
[3] C.J. Bell et al., J. Phys. A 7 (1974) 990.
[4] O.S. Diminstein et al., Proc. 15th ICRC, Plovdiv 9 (1977) 154.
[5] T.Hara et al., Proc. 16th ICRC, Kyoto 8 (1979) 135.
[6] H.Ohoka and M.Teshima, to be appeared.
[7] M.Teshima et al., This conf. HE 4.7-3

N85-34976

MINI AND SUPER MINI ARRAYS FOR THE STUDY OF HIGHEST ENERGY COSMIC RAYS

John Linsley
Department of Physics and Astronomy
University of New Mexico, Albuquerque, NM 87131
USA

ABSTRACT

The chief difficulty in studying the highest energy cosmic rays is the extremely low intensity, only ~ 5 particles per km^2 sr century above 10^{20} eV. Instead of attacking the problem by assembling all of the available resources in one place, as has been done in the past, I suggest a way that the task can be performed at much less cost per unit sensitive area, by using numerous inexpensive mini arrays operating independently of each other. In addition to the quantities usually observed, each mini array will record shower particle arrival time distributions. At 10^{20} eV the saving in cost per primary particle is estimated to be a factor of 10 or better, compared to methods now in use, even for mini arrays newly built from scratch for just this purpose.

Clearly, however, all of the existing air shower arrays can be made to serve as mini arrays, without interfering with their other functions, by simply adding transient recorders to the existing instrumentation. Giant arrays such as the one at Haverah Park can be made to function as clusters of mini arrays. The new array-telescopes being planned and built for UHE γ-ray astronomy will add further to the number of these installations.

The main difficulty which can be forseen is in determining shower directions accurately. Ideally one would like to be able to identify nearly horizontal but upward moving showers produced by $> 10^{19}$ eV neutrinos, and one would like to obtain information on shower profiles for measuring the interaction mean free path of the primary particles. Compact installations with which it may be possible eventually to carry out these difficult tasks, called 'super-mini arrays', will also be described.

1. Introduction. In the 1950's the empirical upper limit of the cosmic ray energy spectrum was quickly raised from 10^{17} to 10^{19} eV (more than one joule) by using arrays of simple counters to detect extensive air showers. In the 1960's these arrays attained giant size (tens of km^2) and the limit was pushed to 10^{20} eV. Since then detailed studies have shown that the primaries are nuclei mostly as light as hydrogen or helium. Above 10^{19} eV the arrival directions are markedly anisotropic and the energy spectrum has an interesting flattening or bump. But returns are diminishing; in order to make further progress one needs a 100-fold increase in collecting area without a proportionate increase in cost. Methods relying on radio and acoustic signals have their advocates, but they have not yet produced worthwhile results. The Fly's Eye atmospheric fluorescence detector has proven to be useful for studying the structure of very large showers, but it is not cost-competitive for areas as

large as are needed. Mini arrays are low cost counter systems designed to make fuller use of the information carried by air shower secondary particles, especially those with large impact parameters (1-2 km). They can operate practically anywhere--in cities, for example. Super-mini's are an advanced form capable of determining the profile of a shower as well as its energy and direction.

2. Using arrival time spread to measure core distance. My suggestion depends on a well known property of air showers, whose utility has been somehow overlooked, the fact that the longitudinal thickness of the particle swarm increases rapidly with increasing distance from the shower axis, from 1 or 2 m at $r < 10$ m to hundreds of m beyond 1 km.[1,2] This is shown by data on arrival time distributions using as a measure of width the dispersion defined by $\sigma_t = [\int (t-\langle t\rangle)^2 p(t)dt]^{\frac{1}{2}}$, where $p(t)$ is the probability of a particle arriving in dt, and $\langle t\rangle$ is the mean arrival time. In Fig. 1 the points are for single particle distributions built up from observations of individual particles belonging to showers of energies $\sim 10^{17}$ eV and various zenith angles < 45°.[2] The curve represents an empirical formula,

$$\sigma_t = 2.6(1 + r/30)^b \qquad (1)$$

with $b = 1.5$, where σ_t is in ns and r is in m, which fits these results and those for smaller r.[3-6] Can this be used *in individual events*, to determine r from measurements of σ_t? It can, within accuracy limits that depend on 1) the sensitivity of the parameters to primary energy and zenith angle, and 2) the effect on the parameters of hidden variables such as starting depth, primary mass and so forth.

To investigate these limits, and at the same time simulate use of the proposed method, I made use of the original records (oscilloscope photographs) of the Volcano Ranch experiment. Only those for the final year of operation (1962-63) still exist, but in that year 16 showers were recorded which satisfied the condition ($E > 10^{19}$ eV) for inclusion in the *Catalogue of Highest Energy Cosmic Rays*.[7] These are enough for the present purpose. The *Catalogue* lists the observed values of r and particle density S for each detector of the array as well as the size, energy, zenith angle and so forth of the event as a whole. For events such as these most of the 19 detectors were struck by one or more particles. The first step was to select in an unbiased manner one pulse per event. It should not be too small because of statistical errors nor too large because of a technical problem (particle densities > 10 m^{-2} were encoded in such a manner that pulse duration information was lost). The one chosen in each case is the one with greatest S such that $S < 7\ m^{-2}$. Tracings of the selected pulses are shown in Fig. 2, together with tracings of a bandwidth limited (BWL) test pulse and a typical train of 1 MHz timing pulses. The number of particles contributing to the various pulses ($n = AS\cos\theta$

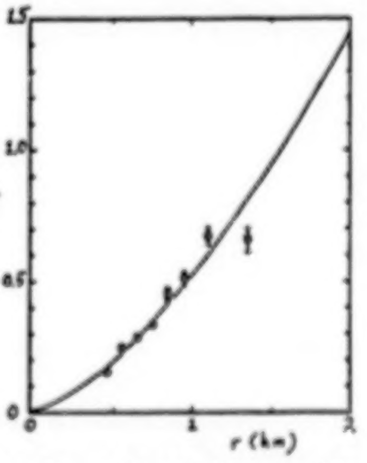

Fig. 1. Dispersion vs distance from AS core. Points from single particle delay distributions (Linsley and Scarsi 1962), curve from (1).

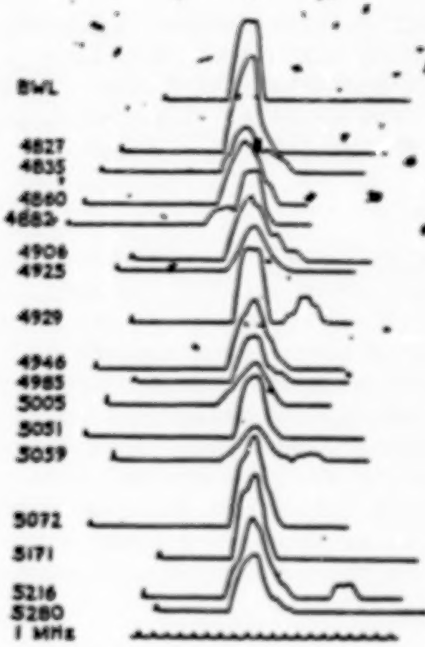

Fig. 2. Selected pulses for 16 AS with E > 10^{19} eV, identified by event No., with a typical bandwidth limited test pulse (BWL) and typical train of 1 MHz timing pulses.

where A is the detector area, 3.26 m^2) ranges from 6 to 22, averaging 12, and the values of r range from 0.9 to 2.0 km, averaging 1.4 km. The average energy of the showers is $3 \cdot 10^{19}$ eV; the zenith angles range from 7° to 55°.

The scintillator pulses and a number of test pulses were digitized and the dispersions were calculated. The dispersion of the input signal was estimated using the relation $\sigma_{in}^2 \sim \sigma_{obs}^2 - \sigma_{BWL}^2$. In earlier work with scintillators it had been found that arrival time distributions are θ dependent, but no energy dependence had been found.[2] In this case, setting the exponent in (1) equal to $b_1 + b_2 \sec\theta + b_3 \log(E/10^{17} eV)$, it was found from the high energy sample that $b_1 = 1.94 \pm .08$, $b_2 = -0.39 \pm .06$. By comparison with the lower energy data of Fig. 1 it was found that $b_3 = 0 \pm .06$. This is consistent with the amount of energy dependence found by Barrett *et al.* using water Cerenkov detectors.[8] Fig. 3 shows the agreement between results of Ref. 2, results for the 16 events from the *Catalogue* (normalized to b = 1.5), and results for another previously published large event (normalized the same way).[1] Core distances denoted by r' were then calculated for the *Catalogue* events, using (1) with θ-dependent b, and compared to the values of r found previously in the usual way.[7] The dispersion of r'/r was found to be 30%.

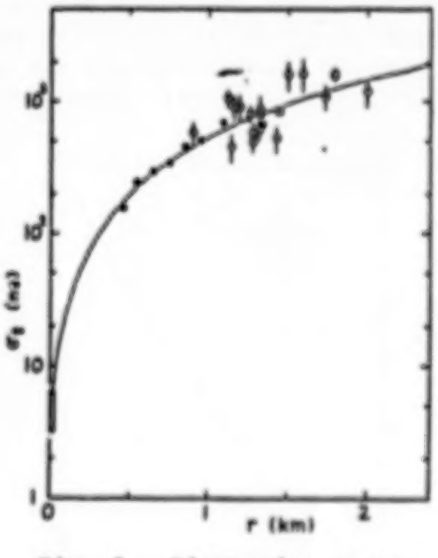

Fig. 3. Dispersion vs core distance. Filled circler and curve as in Fig. 1, open circles for individual events of Fig. 2, squares for event No. 2533 (Linsley Scarsi and Rossi 1961).

3. Determining the energy. The final step in this simulation was to find new energy estimates. I used the Volcano Ranch method, but the Yakutsk method could just as well have been used.[9] Either relies on empirical studies of the way particle density varies with core distance and zenith angle. Letting E' be the energy required to produce the observed density at r', and E the energy found previously, I found that as expected the systematic difference was negligible (10%). Because the structure function is very steep at large distances it was expected that the random errors would be quite large. The

rms deviation from the mean of log(E'/E) was, indeed, 0.3, corresponding to a factor of 2 in the ratio. The largest deviations were a factor of 5 over and a factor of 4 under.

This is not far from being acceptable. In order to provide a sensitive area of 10 km^2 per mini array at 10^{20} eV one must measure r out to 1.8 km. At that range $S = 6\ m^{-2}$, so with 4 m^2 of scintillator, n = 20 particles as compared to 12, the average for these 16 events. Thus the simple statistical errors in σ_t and S would be less even in the extreme case. For a *median* 10^{20} eV event ($r \sim 1.8/\sqrt{2}$ km) I find n = 70, so the improvement would be substantial. One should begin, of course, with mini arrays located at the existing giant arrays (Haverah Park, Yakutsk) so as to calibrate the new method.[10] Work of this kind will lead to refinements in (1) so that more accurate corrections can be made for systematic variations with E and θ. With such improvements and modern instrumentation I am confident that the random error in r can be reduced to 10%, leading to a random error in E of a factor 1.5. This would be entirely adequate for studies of the primary cosmic ray spectrum and anisotropy above 10^{19} eV, which now are limited by inadequate sensitive area, especially in locations where the southern sky is visible.[6]

4. Super mini arrays. The successful operation of the Utah Fly's Eye proves that with the information carried by air shower *photons* one can find shower energies, trajectories and profiles, out to distances of order 10 km. However such an instrument is expensive to build and operate, it must be located in a remote area with a favorable climate, and it can be turned on only 5-10% of the time. The underlying idea of a mini array is making more efficient use of the information carried by shower *particles* at large core distances. Why not go further? The number of particles is adequate even at 1.8 km, about 50 in 10 m^2, half of them muons. Suppose one could record both the direction (within 1 or 2 degrees) and the arrival time (within 10 ns) of each particle. The muons will arrive first; suppose they are separated from the electrons by shielding. Neglecting scattering and geomagnetic deflection, *the muon directions will all lie in the shower-detector plane. Within this plane the muon directions will be distributed in a manner that corresponds exactly to the longitudinal profile of the muon sources.* In the same approximation, assuming v = c as well, the arrival times will be perfectly correlated with the directions. It can be shown, still in this approximation, that *data giving the arrival direction and relative arrival time of just 3 particles are sufficient to determine the shower trajectory: the impact parameter and the direction in space,* albeit the data must be rather precise. Will the advantage of having 25 or more particles rather than 3 be enough to compensate for imperfections of the model and the measurements?[11]

References. [1]LINSLEY *et al.* 1961, Phys. Rev. Lett. 6, 485; [2]LINSLEY and SCARSI 1962, Phys. Rev. 128, 2384; [3]BASSI *et al.* 1953, Phys. Rev. 92, 441; [4]WOIDNECK and BÖHM 1975, J. Phys. A 8, 997; [5]McDONALD *et al.* 1977, Proc. 15th ICRC 8, 228; [6] CLAY and DAWSON 1984, Aust. J. Phys. 37, 309; [7]LINSLEY 1980, in *Catalogue of Highest Energy Cosmic Rays*, ed. M. Wada (Inst. Phys. and Chem. Res.: Tokyo) 1, 3; [8]BARRETT *et al.* 1977, Proc. 15th ICRC 8, 172; [9]BOWER *et al.* 1983, J. Phys. G 9, L53 and Proc. 18th ICRC 9, 207; [10]BROOKE *et al.* 1983, Proc. 18th ICRC 9, 420; [11]LINSLEY 1983, Univ. New Mexico Res. Report UNML-6/26/83.

DETECTION OF 10^{10} GEV COSMIC NEUTRINOS WITH A SPACE STATION

N85-34977

John Linsley
Department of Physics and Astronomy
University of New Mexico, Albuquerque, NM 87131
USA

ABSTRACT

Studies carried out by the author and a colleague in 1980-83 showed the potential value of SOCRAS (Space Observatory of Cosmic Ray Air Showers) for studying the highest energy cosmic rays, including the neutrinos produced in collisions of cosmic ray protons with photons of the 3° background radiation. This instrument would look down at the atmosphere from a space station orbiting the earth at an altitude of 500-600 km. During the night portion of each orbit, air showers would be imaged in the fluorescent light they produce. Progress toward the eventual realization of this scheme is described, including a suggestion by Torii for improving the vertical resolution, measurements of the terrestrial background light by Halverson, and especially an application of the LPM effect, expected to increase the sensitivity for upward moving neutrinos by several orders of magnitude.

1. Introduction. This is a status report on an idea suggested to me by, I believe, Hugh Hudson, at a meeting of a High Energy Astrophysics Advisory Panel at Caltech in September, 1979. I learned later that independently, at nearly the same time, a similar idea for detecting very large air showers with a "Satellite Fly's Eye", was described by S. Torii at a monthly meeting of the Air Shower Division of the Tokyo University Institute for Cosmic Ray Research.

It is well known, of course, that a proposal for detecting air showers from an aircraft by means of atmospheric Cerenkov light reflected from snow was made much earlier, by Chudakov (1972), and showers have in fact been detected using reflected Cerenkov light from a snow field at Plateau Rosa by Castagnoli *et al.* (1981).

Following the meeting at Caltech, on the basis of some crude calculations, I submitted the following in response to a request by the Panel, for 'Projects and Ideas for the 1980's':

Title. Study of 10^{20} eV Cosmic Rays by Observing Air Showers from a Platform in Space.

Description. Record real-time development of air showers produced in earth's atmosphere by cosmic rays, using mirror of very large size but low optical quality (mylar?) with array of fast photoelectric detectors, to sense air scintillation. Mirror pointed downward from satellite in low orbit. Data obtained during half-orbits when sun is hidden.

Purpose. To determine cosmic-ray energy spectrum and arrival direction distribution in the range 10^{18} to $> 10^{20}$ eV with greatly improved statistical accuracy and notable freedom from systematic errors, compared to alternative methods. It is probable that individual primary particles could be sorted according to approximate mass.

C-7

Justification. Goals are the same as those of the Univ. of Utah Fly's Eye project and those of large projects in U.K. and U.S.S.R.—to derive information relevant to astrophysics from a distinct cosmic ray component that appears to be extragalactic in origin.[1]

2. Progress 1980-1983. During the next year I discussed the idea with colleagues, and at length one of them, R. Benson, agreed to help in choosing tentative design parameters and making improved performance estimates. These were reported at an AAS meeting and at the Paris ICRC.[2,3] As indicated above, the plan was to use a single mirror. In order to view what we regarded as a large enough target (100 km diameter circle) with adequate image quality we were constrained to a fairly high orbit (500-600 km). For good enough image quality over such a large field of view the number of sensing elements (photomultipliers) would have to be large, ∿ 5000. We estimated that in order to achieve a good enough signal to noise ratio for energies down to 10^{10} GeV we would need a mirror ∿ 30 m in diameter.

We concluded that the primary advantage of the method we proposed is that *uniformity of response over a very large sensitive area is achieved using a single compact instrument*. Compared to counter arrays it would have equal angular resolution and possibly better energy resolution. It would observe the entire sky, pole to pole, and the counting rate for highest energy cosmic rays would be 50-100 times greater than the combined rate of all ground based arrays then in existence. Compared to a ground based fluorescence detector the counting rate would again be much greater (100 times as great as the Utah Fly's Eye). Moreover, the sensitive area would be *inherently energy independent*, whereas the sensitive area of a ground based Fly's Eye depends strongly on the primary energy, *in a manner that varies with atmospheric conditions*.

In Paris we learned about the work of Torii, whose optical design called for wide angle optics (solid angle ∿ π) appropriate to a lower orbit (200-300 km). He called our attention to the importance of reflected Cerenkov light in this application. This light, strongly collimated in the forward direction, will be diffusely reflected by the earth's surface in the vicinity of the core location, yielding an intensity at our receiver comparable to the maximum intensity of the fluorescent light, *but separated in time and space*. In case of a shower whose fluorescent light had effectively died out before the shower reached earth, this additional component would produce an isolated dot (at a time consistent with $v = c$) so that the composite image would resemble an exclamation point. More often the Cerenkov component would simply add to the intensity from the final image pixel. The additional information from the Cerenkov light will be very helpful in fixing the location of shower trajectories along the line of sight to the detector. This is important for estimating the primary mass, and for accuracy in determining the primary energy.[4]

The initial estimates of SOCRAS sensitivity paralleled the initial estimates made for ground based detectors, estimates which had often proven to be overoptimistic. A painstaking study was made of past shortcomings to locate any weakness or possible oversights that would account for this. It was found that the uncertainty in the initial SOCRAS estimate was large enough to be critical, and some possible errors were identified. It was concluded that it is essential to base further planning on the actual performance of ground based complete systems, especially the Utah Fly's Eye, which at that time was just beginning full operation.[7]

3. Neutrino Astronomy. Two circumstances combine to make SOCRAS attractive for neutrino astronomy. One is the very large mass of atmosphere that can be viewed (10^{11} tons); the other is a feature of the energy spectrum of cosmic neutrinos: there is a shoulder due to photopion production in collisions of cosmic ray protons with photons of the 3° background radiation, making energies $\sim 10^{10}$ GeV relatively favorable for detecting such neutrinos. Consequently the capability of SOCRAS as a neutrino detector was made the subject of a special study.

Three detection modes were envisioned. In all cases the neutrino must interact with a nucleus to produce one or more secondaries capable of initiating an air shower. If its energy is very high ($\sim 10^{10}$ GeV) the shower can be detected by means of air fluorescence in the usual way (mode I). For much lower energies ($\sim 10^{4}$ GeV) the shower could be detected by means of Cerenkov light, provided that the neutrino penetrated the earth, emerging within the target area, and then interacted in the atmosphere (mode II). For intermediate energies ($\sim 10^{6}$ GeV) the neutrino (in this case ν_μ or $\bar{\nu}_\mu$), travelling upward, would have to interact beneath the surface, producing a very high energy muon (mode III). The muon would be detected by means of atmospheric Cerenkov radiation produced by showers from pairs or bremsstrahlung photons.

It was concluded, however, that for modes II and III there would not be a clear enough signature, so that without great difficulty the signals could not be separated from noise. In addition, because the detection solid angle is very small in these modes, the counting rates would not be as great as for an undersea detector (DUMAND) of comparable complexity. In case of Mode I, the signature of a neutrino is a shower propagating in such a direction, and at such a depth, that the primary particle must have penetrated a very large amount of local material (say more than 1000 g/cm^2 of atmosphere or crust) before interacting. Identification would be no problem. However the predicted rate was disappointingly low.[5,6]

4. Progress since 1983. Regarding sensitivity estimates, the continued improvements in over-all performance of the Utah Fly's Eye are very encouraging. A student of Bowen at the University of Arizona has made tests indicating that the intensity of background light for a downward viewing fluorescence detector is several times less than for upward viewing, and he plans a ground based experiment exploiting this result (Halverson 1984). In tests carried out by the Utah group, optical filters were found to improve the signal to noise ratio of atmospheric fluorescence detectors by a factor of 4 (Cady *et al*. 1983). Similar filters have been tried out in work at Srinagar (Bhat *et al*. 1985). An alternative optical system suggested by Garipov (1982), using crossed cylindrical mirrors, might be easier to construct in space and have other advantages.

The most notable new development, however, relates to neutrino detection. Sokolsky (1983) pointed out that because of the LPM (Landau-Migdal-Pomeranchuk) effect, showers initiated in the earth by upward moving neutrinos will emerge with most of their energy intact, for ν_e-rock collisions within several hundred meters of the surface. The result

N85-34978

is an increase of effective target mass by 3 or 4 orders of magnitude (Cady *et al.* 1983b). Even with this much increase, the 10^{10} GeV neutrinos from photopion production may still go undetected by the Utah device. At best the counting rate will be so low that hardly anything can be learned from the neutrino arrival directions (which of course point directly to the site of the initial proton-photon collision) or the zenith angle distribution (from which in principle $\sigma_{\nu h}$ can be learned). The 100-fold greater sensitivity of SOCRAS will result in a counting rate of 2-20 neutrino events per year. For > 10^{10} GeV nuclei the counting rate will be several thousand per year. This is still more than 50 times as great as all existing ground based detectors combined.[8,9]

4. Bibliography

1) LINSLEY, J. 1979, "Study of 10^{20} eV Cosmic Rays by observing Air Showers from a Platform in Space", response to Call for Projects and Ideas in High Energy Astrophysics for the 1980's, Astronomy Survey Committee (Field Committee).

2) BENSON, R. and LINSLEY, J. 1980, "Satellite Observation of Cosmic Ray Air Showers", Bull. Amer. Astron. Soc. 12, 818 (abstract).

3) BENSON, R. and LINSLEY, J. 1981, "Satellite Observation of Cosmic Ray Air Showers", Proc. 17th ICRC (Paris) 8, 145-148.

4) BENSON, R. and LINSLEY, J. 1981, "Astronomical Applications of Large, Aberration-Limited Reflectors on Earth and in Space", Proc. Southwest Regional Conference for Astronomy and Astrophysics, eds. P.S. Riherd and P.F. Gott (Texas Tech Univ.: Lubbock, Texas) 7, 161-168.

5) LINSLEY, J. 1981, "Neutrino Astronomy using SOCRAS, a Satellite Observatory for Cosmic Ray Air Showers", *ibid.*, pp. 169-178.

6) LINSLEY, J. 1981, "Detection of High Energy Cosmic Neutrinos by means of Atmospheric Fluorescence", Bull. Amer. Astron. Soc. 13, 883 (abstract).

7) LINSLEY, J. 1982, "Air Shower Measurements from Space", Proc. Workshop on Very High Energy Interactions in Cosmic Rays, eds. M.L. Cherry *et al.* (Univ. of Pennsylvania: Philadelphia) 476-491.

9) LINSLEY, J. 1983, "Possibilities and Prospects for learning Behavior of Interactions from Extensive Air Shower Data (10^{16}-10^{20} eV Region)", Univ. New Mexico Research Report UNML-9/26/83 (14 pp). See also rapporteur paper, Proc. 18th ICRC (Bangalore) 12, 135.

References. **BHAT *et al.* 1985, "Spectral Differentiation of Atmospheric Fluorescent Events from Background Cerenkov Emission", preprint; CASTAGNOLI *et al.* 1981, Proc. 17th ICRC (Paris) 6, 103; CADY *et al.* 1983, Proc. 18th ICRC (Bangalore) 9, 351; 1983b, *ibid.* 11, 485; CHUDAKOV 1972, Proc. Symposium on Cosmic Rays, Yakutsk; GARIPOV 1982, Izv. Akad. Nauk SSSR, Ser. Fiz. 46, 1839; HALVERSON 1984, "Terrestrial Background for Air Fluorescence Detection", Workshop on Cosmic Ray and High Energy Gamma Ray Experiments for the Space Station Era, Louisiana State Univ., talk; SOKOLSKY 1983, Proc. Utah Cosmic Ray Workshop, ed. T.K. Gaisser (Bartol Foundation: Newark NJ) p. 153; TORII 1981, private communication.**

OG9.5-1

N85-34978

The Longitudinal Thickness of Air Shower Fronts

R.W. Clay, R.J.V. Brissenden, S.D Elton, N.R. Wild
Physics Department
University of Adelaide
Adelaide South Australia 5000.

1. Introduction Linsley (1983) has proposed a technique for the detection and analysis of air showers at large distances from the shower axis based on a measurement of the shower front thickness and the assumption that this thickness is closely related to the core distance. We have been investigating (Clay and Dawson 1984) some of the problems involved with realising such a technique and report here some related observations. We have been particularly interested in the practical problems of how consistent the measurements of the shower front would be, how one would use the measurement, and how the rate of triggered events would depend on the minimum pulse width required.

2. Apparatus We have used two of the 2.25 m^2 detectors (Prescott et al. 1983) of the Buckland Park array (separation ~ 11m) and recorded the pulse shapes from each detector when one of them produced a pulse greater than some specified width (~ 100ns). Any structure related to shower development ought to be reflected by agreement between the observed pulse shapes.

Oscilloscope recording was based on the digitising of an event by a Tektronix 7912 (500ns at 1ns intervals) and photography of a Tektronix 7834 at 50ns/division. Figure 1 includes an example of the single particle response of the 7912. The 7834 system had a rather similar impulse response, limited by the detector impulse response. The 7834 channel was used to trigger the recording system. Recording was triggered by the output of a pulse width discriminator (a coincidence between a prompt and a delayed sample of the waveform) at an amplitude a little below the single particle level. Thus the system triggered when either a broad pulse or a series of pulses was detected. The system also triggered on very large narrow pulses whose reponse at the one particle level still extended to 100ns. These triggers were easily recognisable.

3. Results The system was run first to see to what extent pulses from relatively close-by detectors agreed in terms of their width or pulse shape. 51 events were obtained with signals from both detectors and some of these are shown in figure 1.

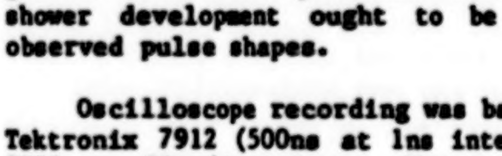

Fig. 1. Examples of pulses triggering the recording system. The outputs of two detectors closeby are shown for two events together with (insert) a single particle impulse response.

If Linsley's expression for the shower thickness against core distance is correct then these events are from showers at core distances of at least 200m and the detector spacing of 11m is rather small in comparison.

Firstly, we make the general observation that the pulses detected by the 7912 system (but triggered by a wide pulse in the other detector) all have widths at the single particle level which are $\gtrsim$ 100ns except for 8 events which showed no signal at all on the 7912 system. The latter events were for small numbers of particles in the triggering detector and we can probably say that these events simply had density fluctuations such that no particles passed through the second detector. In other words, broad pulses in one detector were always associated with broad pulses in a close-by detector.

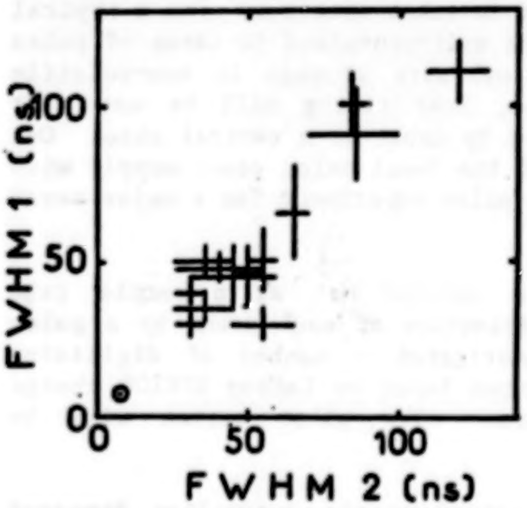

Fig. 2. The relationship between shower front thickness measured by two closeby detectors. The system impulse response is shown by a circle.

Figure 2 shows the relationship found between the full width at half maximum (FWHM) of the signals in the two channels in the cases for which such a parameter could be adequately defined (cases where, for instance, the leading edge of pulses were lost could not be used for this purpose). It would appear that there is a clear and well correlated relationship between measurements made in the two channels so that one can conclude that measurements can be made for such showers ($E_p \gtrsim 10^{17}$ eV, $r \gtrsim$ 200m) which truly represent the local shower width. Alternatively one might say that a measurement of the FWHM using a 2.25m^2 detector appears to make a physically reproducible measurement of shower longitudinal structure, at least over distances of the order of 11m. It does not, of course, indicate necessarily that the shower is not lumpy in its longitudinal distribution over larger distance intervals.

4. Effects of the Pulse Width Discrimination The pulse width discriminator reduces the number of triggers accepted from a scintillator by a very great deal, typically from 2×10^{4}Hz to ~ 10^{-4}Hz. Our system simply checks to see whether or not there is a pulse above the discrimination threshold at a given time after the first trigger. This can be simulated by very high density events due to shower cores falling on a detector which has a low level in its impulse response extending to 100ns. These can easily be eliminated by inspection or probably better by the use of a coincidence system.

If Linsley's expression for width versus core distance is roughly correct, we can determine our collecting area vs energy and using the known energy spectrum we can predict the number of events we expect to detect. This is of the order of 1 event hr^{-1} and such an event rate is found in practice although this depends substantially on the threshold chosen when only a single detector is used.

5. Further Work in Progress A pilot array using the technique is currently under design and construction at Buckland Park. It is expected to consist of five, 2m^2 water Cerenkov detectors with a typical spacing of ~ 500m. Each site will be self-contained in terms of pulse shape discrimination, digitisation, and data storage in non-volatile memory but, in this particular case, fast timing will be used for direction finding with signals carried by cable to a central site. One site will be operated independently of the local mains power supply with solar panels as the power source as a pilot experiment for a major array of stand-alone detectors.

Digitisation is expected to be carried out at a sample rate of ~ 80MHz for up to 4 μs after the detection of each event by a pulse width discriminator. We have investigated a number of digitising systems and are building a pilot system based on LeCroy MVV200 charge coupled cell analog shift registers. The pilot system will be operational by mid 1986.

Acknowledgement This work is supported by the Australian Research Grants Scheme.

References

Clay, R.W. and Dawson, B.R. (1984) Aust. J. Phys., 37, 309.

Prescott, J.R., Clay, R.W., Corani, C.L., Dawson, B.R., Gregory, A.G., and Patterson, J.R., (1983) Proc. 18th Int. C.R.C. (Bangalore), 6, 257.

Linsley, J. (1983) Rapporteur 18th Int. C.R.C. (Bangalore) 12, 135.

CERENKOV LIGHT IMAGES OF EAS PRODUCED BY PRIMARY GAMMA RAYS AND BY NUCLEI

N85-34979

A. M. Hillas
Physics Department
University of Leeds, Leeds LS2 9JT, UK.

ABSTRACT

It is shown that it should be possible to distinguish very effectively between background hadronic showers and TeV gamma-ray showers from a point source on the basis of the width, length and orientation of the Cerenkov light images of the shower, seen in the focal plane of a focusing mirror, even with a relatively coarse pixel size such as employed in the Mt. Hopkins detector.

1. Detection of point sources of cosmic rays

Certain X-ray binaries, pulsars and active galaxies appear to be point sources of TeV cosmic rays – presumed to be gamma-rays. The sources have been detected by observing flashes of Cerenkov radiation from small showers in the upper atmosphere, but these do not stand out clearly against the intense isotropic background of ordinary proton (or nuclear) showers. If the appearance of the Cerenkov flashes differs for the two classes of shower, much of the background might be rejected. In another paper, Cawley et al. (1) describe the modification of the 10m reflector at the Whipple Observatory (Mt. Hopkins, Arizona) to record details of each Cerenkov image on a 0.5° grid, using 37 photomultipliers in the focal plane of the focusing mirror. (A central photomultiplier is surrounded by a ring of 6 others, then by a further ring of 12, and another of 18 – the whole forming a hexagonal grid pattern.) Predictions of the response of this system to air showers will be presented. Even though the r.m.s. widths of shower images are less than 0.5°, the image dimensions should be measured well enough to provide discrimination between types of shower, though the alignment of the short image with the source will be much less clear than with finer angular resolution.

2. Simulation of Cerenkov image patterns

A 3-dimensional Monte-Carlo calculation is used to simulate shower development. The computer program has been used previously for other investigations (2) and is much more detailed than is necessary for calculating Cerenkov processes, following particles down to an energy 0.05 MeV (far below the Cerenkov threshold), although "thin sampling" (3) is used to follow particles below 1/4000 of the primary energy to reduce computing time. The model atmosphere is not isothermal. Hadronic collisions have been simulated both by a radial scaling model with rising cross-sections and by a model with increased production of low-energy secondaries (relative to scaling) at high primary energies (though a less drastic change than proposed by Wdowczyk and Wolfendale, for example, as the important particles in the fragmentation region – high x – are largely retained). However, at TeV energies, there is little difference between the models, being constrained by accelerator data, so the simulation results have been combined together in the presentations below.

Although some loss of Cerenkov light by Rayleigh and aerosol scattering is allowed for (2), scattered light is assumed not to contribute to the spread of the image (size <1°) in a clear mountain atmosphere. The

ORIGINAL PAGE IS
OF POOR QUALITY

light is assumed to be received by a collector of 10m diameter (taken as 2/3 efficient) on the ground, and the directions of arrival of the rays recorded. The rays are traced to see whether they would reach a particular photomultiplier of the 37-tube array as used on Mt. Hopkins, assuming the mirror forms perfect images of stars. (About 50% of the light is lost in gaps between the tubes.) Fluctuations in conversion of photons were incorporated, but not the fluctuations in the electron multiplication process. The altitude (2300m) and geomagnetic field were taken to be the values appropriate for Mt. Hopkins.

All gamma-ray showers were taken to come from the direction of a source in the centre of the field of view, and were sampled from a spectrum $E^{-2.25}dE$ from 0.25 TeV upwards, and impact points were sampled randomly over an area of 250m radius. Showers for analysis had to give signals of at least 40 photoelectrons in at least 2 of the innermost 19 tubes. The proton background showers were sampled from a spectrum $E^{-2.65}dE$, and the images were displaced randomly over a sky area large enough to cover the field of view, to simulate an isotropic background. Some showers initiated by oxygen nuclei were also simulated, using a simplified nuclear breakup representation. As these are easier to distinguish from gamma showers, and as for a given intensity of flash a higher threshold energy is needed than for a proton shower, not so much attention was paid to such showers generated by heavy nuclei.

3. Parameters used to describe Cerenkov images of showers

A typical simulated image is shown alongside in Figure 1. The figures give numbers of photoelectrons in each photomultiplier. (2 TeV gamma-ray from source in centre of field. Impact parameter 60m, zenith angle 30°.) The image axis (dashed line) is determined: this line minimises the signal-weighted sum of squares of perpendicular angular distance of the detectors. (As small distant noise signals can distort the small r.m.s. dimensions, *any individual signal below 1% of the total in all 37 tubes is ignored.*)

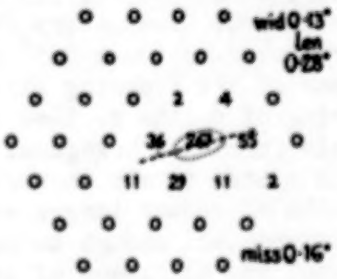

Figure 1.

The r.m.s. spread of light in directions parallel and perpendicular to this axis are referred to as the *LENGTH* and *WIDTH* of the image. *FRAC(2)* (following a suggestion by Weekes) measures the general concentration of light: it is the fraction of light collected by all 37 tubes that is contained in the 2 largest signals. The orientation of the image relative to the (central) source is described by (a) *MISS*, the perpendicular distance of the centre of the field (the source) from the image axis, (b) the *AZIMUTHAL-WIDTH*, the r.m.s. image width relative to a new axis which joins the source to the centroid of the image, and (c) the *DISTANCE* (distance of image centroid from source), to be compared with the distance of the brightest point (tube with largest signal) from the source – thus related to the orientation of the skew images.

Showers aimed directly at the observer will not have distinctive shapes. (The maximum signal will occur in the central photomultiplier – referred to as *ZONE 0*.) Showers having impact parameters at some distance away are viewed partly from the side, and the width and length of the image reflect largely the width and length of the particle cascade. The geometry depends on the impact parameter, so it is important to classify separately shower images having the largest signal in one of the tubes in

ORIGINAL PAGE IS
OF POOR QUALITY

the inner ring of 6 surrounding the centre (these are *ZONE 1* showers), showers with maximum signal in the next ring of 12 tubes (*ZONE 2*), etc.: the latter correspond to somewhat higher energies or impact parameters.

It is found that hadronic showers have longer and more fluctuating images (leading particle effect), and are wider (due largely to emission angles of pions), and are not systematically aligned with the source (if isotropic) — larger *MISS* and *AZIMUTHAL-WIDTH*, smaller *DISTANCE* of centroid for a given *ZONE* (position of peak signal).

4. Comparison of image parameters for different kinds of shower

Figure 2, below, shows the distribution of the widths, lengths, and other parameters of background proton showers, and for showers from oxygen nuclei, compared with those for gamma-ray showers (shaded histogram) from a source placed in the centre of the field of view. Units: degrees — except for *FRAC(2)*, which is dimensionless. The triggering requirement is

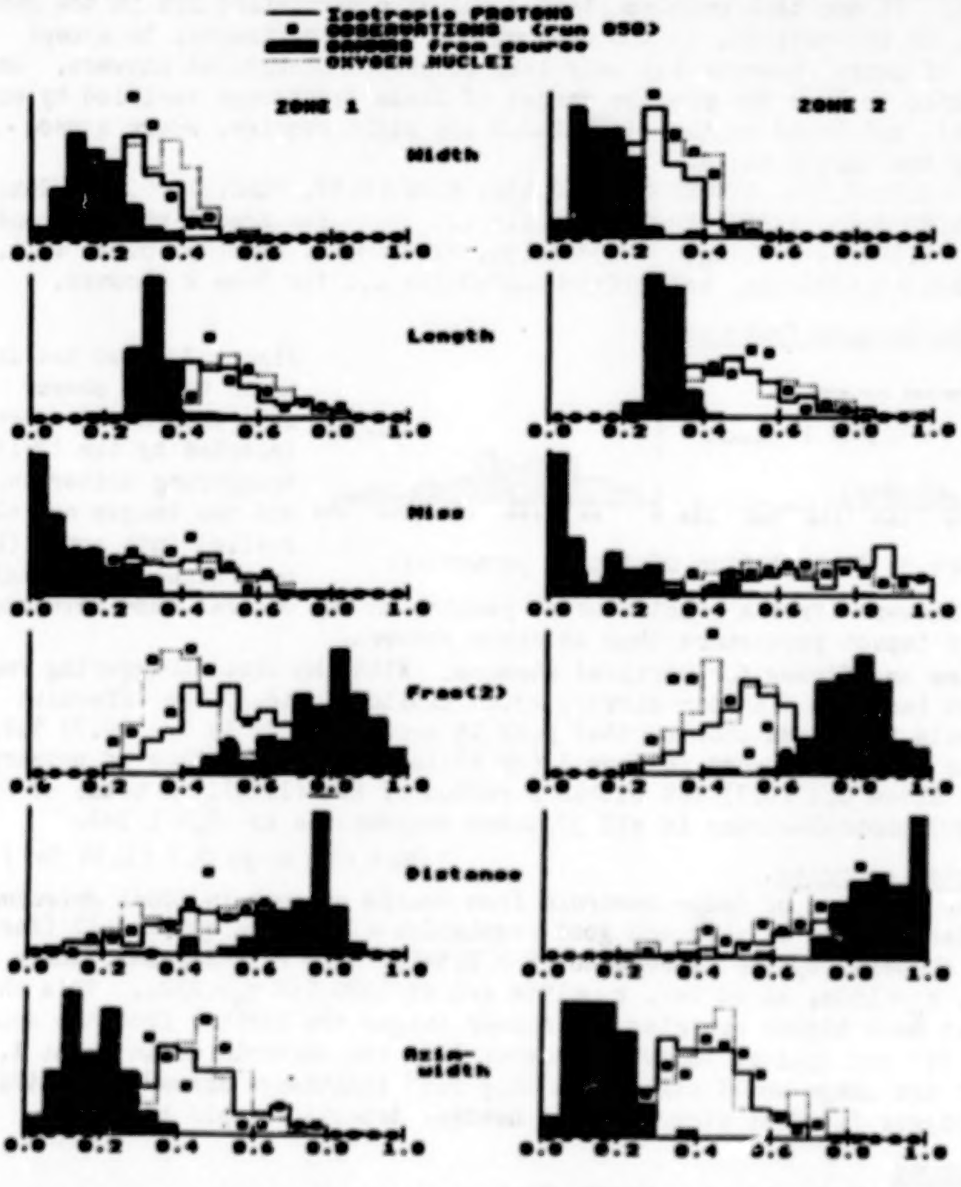

Figure 2: histograms of image characteristics. (vertical showers)

as given above (2/19 at least 40 p.e.). Showers having the brightest signal on the inner ring of 6 tubes (zone 1) or the next ring of 12 (zone 2) are shown in the left and right column. The histograms demonstrate the more concentrated images of the gamma showers. Some real background showers observed in the zenith have been analysed in the same way (using data supplied by M.F.Cawley, D.J.Fegan and N.A.Porter). It seems that the simulations agree well with most features of the observed images, though some additional image spreading may be present in reality. Tests of the predicted image characteristics for gamma showers are not yet available.

5. Selection of gamma-ray showers from the general background

One can define, for each of the 6 image parameters, a boundary marking off the "gamma domain", containing most gamma images, but not many protons. If one then requires that 4 out of 6 parameters lie in the gamma domain, it is possible, in the case of the simulated images, to accept 60-70% of gamma showers, but only 1-2% of proton background showers. One would like to have the precise ranges of these parameters verified by experiment, but based on the simulations one might require, where $x = \sec\phi - 1$, ϕ being the zenith angle,

WIDTH $< 0.21 - 0.17x$, LENGTH $< 0.35 - 0.13x$, MISS < 0.17, FRAC(2) $> 0.72 + 0.28x$,
DISTANCE > 0.65, AZIMWIDTH $< 0.21 - 0.11x$ ... for Zone 1 showers, and
Width $< 0.19 - 0.2x$, Length $< 0.33 - 0.13x$, Miss < 0.22, Frac(2) $> 0.72 + 0.31x$,
Distance $> 0.83 + 0.04x$, Azimwidth $< 0.20 - 0.11x$ ... for Zone 2 showers.

6. Miscellaneous features

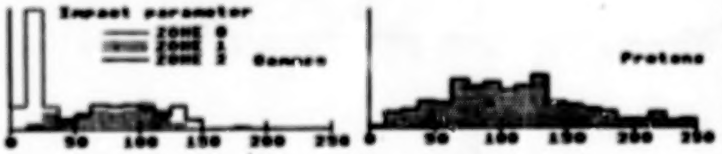

Figure 3: distribution of impact parameter.

Figure 3 shows the distance to the shower axis when showers are selected by the (2/19) triggering criterion, and the images are classified into zones (by peak signal position). Gamma showers (from a point source) peaking in the central tube have much smaller impact parameters than do other showers.

Energies and fluxes for vertical showers. With the above triggering requirement (and 10m diameter mirror, 2300m altitude, etc.), the effective threshold for gamma showers that peak in zone 1 (or 2) is 0.4 (0.7) TeV,* and the rate of showers in zone 1 (or 2) is equal to the flux of primary gammas above 0.4 (0.7) TeV within a radius of 88m (117m). A total of 550 (or 390) photoelectrons in all 37 tubes corresponds to $E_\gamma = 1$ TeV.

* (Median energy 0.7 (1.3) TeV)

7. Higher energies

Angular distance of image centroid from source as seen in ideal detector – i.e. large field of view and good resolution – is given quite well (for gamma showers) by the expression $\theta = 1.5 \times 10^{-5} (r + r_o)^2$ degrees, where at 1 TeV, $r_o = 150$m, at 40 TeV, $r_o = 195$m and at 1000 TeV $r_o = 230$m. This shows that at much higher energies the shower images are further from the source: at 40 TeV and typical impact parameter 110m the centroid would be at 1.5° – but the image would still have only 0.5° lengthways spread about this, so a bigger field of view would be needed: detection would be harder.

References

(1) Cawley, M.F., et al., paper OG 9..
(2) Hillas, A.M. (1982) J. Phys. G 8, 1475-92; 8, 1461-73.
(3) Hillas, A.M. (1981) 17th Int. Cosmic Ray Conf., Paris, 9, 193-6.

N85-34980

SHOWER DISC SAMPLING AND THE ANGULAR RESOLUTION OF γ-RAY SHOWER DETECTORS

A. Lambert and J. Lloyd-Evans[†]

Department of Physics, University of Leeds, LEEDS 2, UK.

[†] Now at NASA/Goddard Space Flight Centre, USA.

ABSTRACT

As part of our design study for the new UHE γ-ray detector being constructed at Haverah Park (1), we have undertaken a series of experiments using scintillators operated side-by-side in $> 10^{15}$ eV air showers. Investigation of the rms sampling fluctuations in the shower disc arrival time yields an upper limit to the intrinsic sampling uncertainty, $\sigma_{rms} = (1.1 \pm 0.1)$ns, implying an angular resolution capability $< 1^\circ$ for an inter-detector spacing of ~ 25 m.

1. Introduction. That an angular resolution of $1.5^\circ - 2.0^\circ$ can be achieved by extensive air shower arrays was shown conclusively by the identification of Cyg X-3 as a source of UHE ($> 10^{15}$ eV) γ-rays (2). Subsequent confirmation (3) and reports of detections of Vela X-1 (4) and LMC X-4 (5) have highlighted the need for a new generation of arrays with a much improved detection signal to noise ratio.

The prospects for detecting a source improve with increasing collecting area, exposure time, or knowledge of source periodicity, but most acutely with improved directional resolution, especially in view of the fact that periodic γ-ray sources are likely to be time variable and lack a constant phase maximum (e.g. (6)), thereby precluding extended observations.

Here we concentrate on an experimental determination of the angular resolution achievable by the new γ-ray detection system in construction at Haverah Park (1).

2. Description of the detectors and the recording system. We have studied the extensive air shower disc at energies $10^{15} - 10^{16}$ eV using two 1 m^2 plastic scintillation detectors in conjunction with a 50 m water-Cerenkov array. Because this work formed the initial stages of the design study for the new array, the scintillation detectors were not identical in construction. The 'start' detector consisted of 1 m^2 type NE102A 7.6 cm thick scintillator, viewed from below at a distance 61 cm by a Philips 2312B 3"ϕ PMT, risetime < 3 s. The 'stop' detector consisted of 1 m^2 type (see (7)) 9 cm thick scintillator viewed from above at a distance 38 cm by an EMI 9821B 3"ϕ PMT, risetime < 3 s. We found it essential to blacken the entire detector interior to eliminate multiple reflections ensuring that the PMT views only the direct light from the scintillator.

The scintillators were situated at the centre of the 50 m water-Cerenkov array used to provide the EAS trigger, and, in subsequent analysis, the shower arrival direction, size, and core position. A block diagram of the arrangement is shown in Figure 1.

A variety of detector configurations, shown schematically in Figure 2 were used to investigate the timing response in EAS and also for a loose

N85-34980

trigger condition (termed "single particles") in which both detectors were required only to exceed the $^1/_3$ particle discrimination level.

3. Detector and recording system limitations. The combined limitation of the detectors and recording electronics was investigated using both the loose trigger and vertical showers at small core distances, experiments (4) and (1) of Figure 2 respectively. A rapid increase in the standard deviation of the time delay, $\sigma(\Delta t)$, at smaller densities was found, due partly to the leading-edge type of discrimination employed and also some electronic cross-talk at low voltage levels which has since been eradicated. For densities>1.6 particles m^{-2} the intrinsic timing resolution of the detector and recording electronics was constant at $\sigma(\Delta t) = 0.89 \pm 0.09$ ns. The identical detector configuration, in response to 50 m shower triggers with zenith angles, $\theta < 10^\circ$, core distances, $r < 25$ m, and both scintillator densities $> 1.6\,m^{-2}$ gave $\sigma(\Delta t) = 0.92 \pm 0.11$ ns, which is not significantly different to the intrinsic resolution. A density threshold of 1.6 particles m^{-2} has consequently been imposed for the remaining analysis.

4. Scintillator timing response in 10^{15} eV showers. Two independent samples of the shower front at the same core distance were obtained with side-by-side detectors (Figure 2, experiment (3)). Separating the detectors by 3 m (experiment (2)) allowed for the effect of small core distance differences to be investigated. Even when side-by-side, the time delay between detectors, Δt, must be corrected to allow for the transit time of the shower disc through the detector centres. The 50 m water-Cerenkov array determines the shower direction to an accuracy of $\lesssim 5^\circ$, which is quite adequate for this correction to be made. Figure 3A shows the mean time delay $\overline{\Delta t}$, before and after correction, for a sample of showers in four azimuth angles defined in Figure 3. After correction the $\overline{\Delta t}$ are consistent with expectation.

5. Time structure of the particle disc. The standard deviation of the time delay distribution, $\sigma(\Delta t)$, is directly attributable to rms fluctuations of the distance into the shower front at which the detectors trigger. We expect $\sigma(\Delta t)$ to increase at larger core distances due to the decreasing particle density and increasing shower front thickness. Figure 4 shows $\sigma(\Delta t)$ as a function of core distance; superposed are lines representing angular resolutions of $\pm 1^\circ$ and $\pm 0.5^\circ$. The results indicate that an angular resolution of $< 1^\circ$ may be achieved. This is in good agreement with the predicted angular resolution obtained from an empirical relationship derived by Linsley (8). Figure 4 also shows that the angular resolution is practically independent of core distance, at least out to 75 m, the improved baseline compensates completely for the effect of a rising $\sigma(\Delta t)$.

6. Discussion. Little, albeit careful, previous work has been done on the sampling of the EAS disc. Bassi, Clark and Rossi (9) obtained thickness ~2-3 m for core distances < 60 m and shower sizes $10^5 - 10^6$. More recent work, by the Kiel group (10,11) aimed to measure the longitudinal profile and curvature of the disc in small air showers. They reported a radius of curvature of 600 m for the electron disc with respect to the muon disc at energies ~10^{15} eV (10). The limitation of the present work is that although $\sigma(\Delta t)$ reveals the magnitude of the timing

fluctuations, we cannot determine the presence of a systematic curvature of the disc. We emphasise this since it is of paramount importance in assessing the attainable angular resolution; the effect of neglecting a curvature of 600 m is to increase the angular uncertainty by ~ 3°. An accurate correction for curvature in individual showers requires many detectors surrounding the shower core. Of the 32 detectors in the new Haverah Park array (1), 14 are located inside a radius of 50 m on a 25 m grid spacing, providing a powerful facility for the future investigation of curvature.

We note that the results discussed are for nucleon-induced showers. The expected absence of a prompt muon front in γ-ray initiated showers may worsen the attainable resolution.

7. Conclusions. We have shown that the scintillation detectors designed for use in the new Haverah Park array (1) have a timing resolution of better than 1 ns. An investigation of their performance in small air showers leads us to expect an angular resolution of < 1° for this array.

Figure 1

BLOCK DIAGRAM OF SETUP

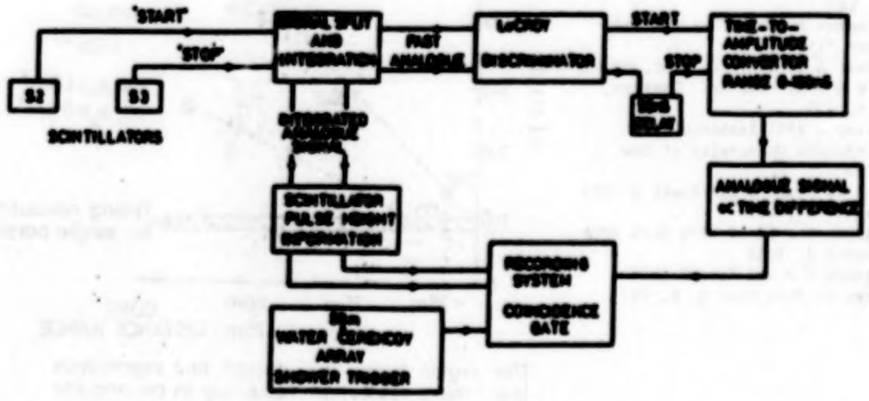
'START'
'STOP'
S2
S3
SCINTILLATORS
SIGNAL SPLIT AND INTEGRATION
FAST ANALOGUE
LeCROY DISCRIMINATOR
START
STOP
DELAY
TIME-TO-AMPLITUDE CONVERTER RANGE
INTEGRATED ANALOGUE SIGNAL
SCINTILLATOR PULSE HEIGHT INFORMATION
ANALOGUE SIGNAL ∝ TIME DIFFERENCE
RECORDING SYSTEM
COINCIDENCE GATE
WATER CERENKOV ARRAY SHOWER TRIGGER

TIME-TO-AMPLITUDE CONVERTER : EG&G ORTEC MODEL TH200A/N

LeCROY DISCRIMINATOR : MVL 407 TB QUAD

Discriminator threshold ~ $^1/_3$ particle m^{-2}.

8. Acknowledgements. We thank Andy West for his valued assistance. The Science and Engineering Research Council (UK) are thanked by AL for the provision of a studentship.

ORIGINAL PAGE IS
OF POOR QUALITY

Figure 2

INVESTIGATION OF TIMING RESOLUTION
ATTAINABLE WITH $1m^2$ SCINTILLATOR

EXPT.	DETECTOR ARRANGEMENT	TRIGGER	PURPOSE
①	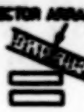	50m ARRAY SHOWER TRIGGERS	DETECTOR LIMITATIONS
and [illegible]	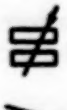	"SINGLE PARTICLES"	DETECTOR LIMITATIONS
②	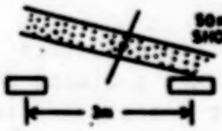 	50m SHOWERS	TIME DIFFERENCES AS A FUNCTION OF SHOWER ARRIVAL DIRECTION
③	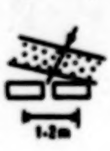 	50m SHOWERS	SHOWER FRONT SAMPLING LIMITATIONS AND RESOLUTION OF ~NANOSECOND TIME DIFFERENCES DUE TO SHOWER ARRIVAL DIRECTION.

Figure 3

VARIATION OF TIME DIFFERENCE WITH SHOWER ARRIVAL DIRECTION

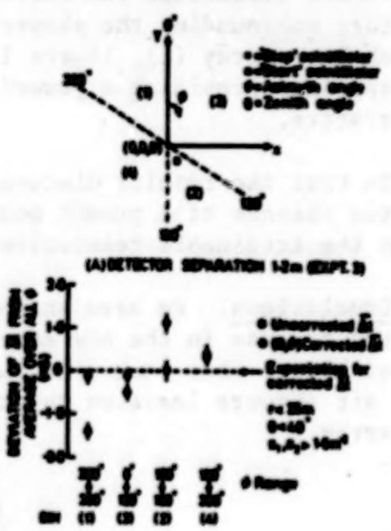

Figure 4

σ(Δt) AS A FUNCTION OF CORE DISTANCE

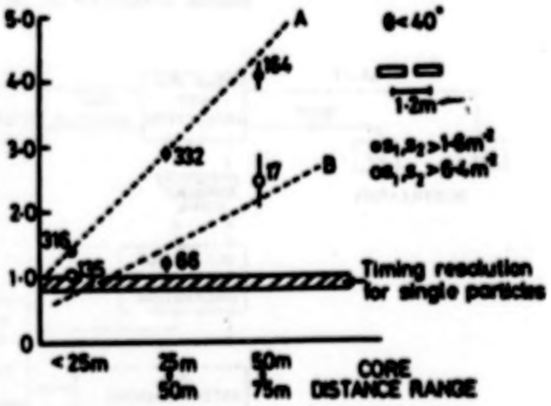

The region below the dotted line represents the timing resolution resulting in an angular error: A±1°, B±0·5°

References

(1) Brooke G B et al, this Conf. OG-9.4-7
(2) Samorski M and Stamm W 1983 Ap J Lett. 268, L17
(3) Lloyd-Evans J et al 1983 Nature 305, 784
(4) Protheroe R J et al 1984 Ap J Lett. 280, L47
(5) Protheroe R J and Clay R W 1985 Nature 315, 205
(6) Lambert A et al, this Conf. OG-2.1-6
(7) Clark G 1957 Rev. Sci. Instrum. 28, 6, 433
(8) Linsley J 1984 Research Note UNML-7/6/84 University of New Mexico
(9) Bassi P, Clark G and Rossi B 1953 Phys Rev 92, 441
(10) Woidneck C P et al 1971 12th ICCR (Hobart) 3, 1038
(11) Woidneck C P and Bohm E 1975 J Phys A: Math Gen: 8, 6, 997

N85-34981

APPLICATION OF IMAGING TO THE ATMOSPHERIC CHERENKOV TECHNIQUE

M.F. Cawley[1], D.J. Fegan[1], K. Gibbs[2], P.W. Gorham[3], A.M. Hillas[6], R.C. Lamb[4], D.F. Liebing[4], P.K. MacKeown[5], N.A. Porter[1], V.J. Stenger[3], and T.C. Weekes[2].

1. Physics Department, University College, Dublin.
2. Harvard-Smithsonian Center for Astrophysics.
3. Physics Department, University of Hawaii.
4. Physics Department, Iowa State University.
5. Physics Department, University of Hong Kong.
6. Physics Department, University of Leeds.

1. Introduction. Turver and Weekes (1977) proposed using a system of phototubes in the focal plane of a large reflector to give an air Cherenkov camera for gamma ray astronomy. A more detailed description of a detector based on the 10m Optical Reflector at the Whipple Observatory was given by Weekes (1981) and Fegan et al. (1983). Preliminary results with a 19 element camera have been reported previously (Cawley et al. 1983). In 1983 the camera was increased to 37 pixels; it has now been routinely operated for two years and some results are presented at this conference (OG 2.3-1, 2.1-11, 2.2-9, 2.7-3, and 2.4-4). In this paper we present a brief physical description of the camera, its mode of operation, and the data reduction procedures; the Monte Carlo simulations on which these are based are also reviewed.

2. The Camera. Each of the 37 camera pixels is a 5cm diameter RCA phototube, 6342A (S11 photocathode). The phototube layout is shown in figure 1; to allow space for the magnetic shields the spacing between centers is 6.25cm. The focal plane scale is 1° per 12.5cm; the useful area of each photocathode is equivalent to 0.36° so that the useful coverage of the full 3.5° diameter field is approximately 50%.

A typical integral pulse height spectrum for a single camera pixel is shown in figure 2 and the trigger level, corresponding to 45 ± 12 photoelectrons, indicated. The absolute gain of each pixel was determined at monthly intervals using an Americium light source which had been previously calibrated against a muon Cherenkov telescope. The relative gain correction was determined by uniformly illuminating all pixels with a pulsed N_2 light source; this was done at the beginning and end of each night's observation.

3. Operating Mode. Observations were only attempted when sky conditions were excellent. Each set of observations consisted of a pair of tracking scans over the same range of azimuth and elevation angles. In one of these, the ON run,

ORIGINAL PAGE IS
OF POOR QUALITY

the reflector was directed at the suspected source. The OFF run was offset by 30 minutes of Right Ascension. The order of ON and OFF runs was interchanged to reduce the possibility of systematic errors.

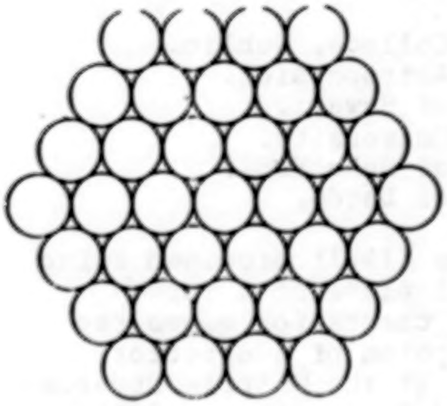

FIG. 1 Phototube Layout

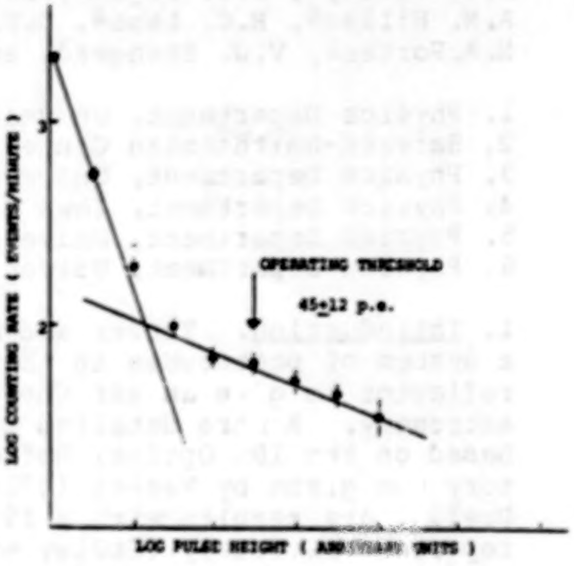

FIG. 2 Integral Pulse Height Spectrum

4. **Simulations**. The original concept of the camera (Weekes 1981) was based on the Monte Carlo simulations of Rieke (1969) which gave the average features of 250 gamma-ray initiated showers. Realistic estimates of the performance of the camera required that fluctuations be taken into account as well as the geomagnetic field. To optimise the selection of gamma rays, hadron-initiated showers must also be simulated.

Three sets of simulations of shower images measured by the Whipple Observatory camera are discussed below; because the conditions assumed are somewhat different, it is not possible to compare these quantitatively. Some large qualitative differences are apparent and are unexplained.

(a) Durham simulations. The Durham Monte Carlo program, which was previously used to evaluate the performance of the 10m reflector in a single detector mode (Browning and Turver 1975), was used to simulate the response of the camera to 300 and 1000 GeV gamma-ray initiated showers (Turver, private communication, 1983). The results were quite different from those expected, with fluctuations dominating the shape and orientation of the shower images. The angular width of the shower was smaller than that of the background events measured by the camera (MacKeown at al. 1983); the orientation of the shower major axis showed little correlation with the position of the shower relative to the optic axis and thus suggested that detailed processing of the shower images would be of limited value.

(b) Altai simulations. Plyasheshnikov and Bignami (1984) have used a compressed Monte Carlo method to evaluate the effectiveness of imaging in improving the sensitivity of the atmospheric Cherenkov technique. They simulated the response of a 10m reflector to both gamma-ray and proton initiated showers for energies from 0.1 to 2.0 TeV. They concluded that there was no difference between the average size of two kinds of images but the orientation i.e. radiating out from the center, would permit the preferential selection of gamma-ray initiated showers. This conclusion is in obvious disagreement with (a). They also suggest that the greater fluctuations along the major axis in proton-initiated showers could be used statistically to discriminate against the proton background.

(c) Leeds simulations. Hillas (this conference OG9.5-3) has simulated the response of the 10m reflector to both photon and proton-initiated air showers taking into account the optical parameters of the 10m reflector. He has simulated the expected response of the system to a proton--initiated background using typical operating parameters. The agreement between the simulated and measured background is good and suggest that the experimental parameters have been realistically accounted for.

Significant differences are found between the gamma-ray and proton shower images; in particular the angular size of the gamma-ray shower is almost a factor of two smaller than that of the proton image. In addition the gamma rays originating from a point source on axis are radially distributed as predicted in (b). Because the angular size of the images is comparable to the pixel size, this radial distribution is difficult to measure with the Whipple Observatory camera.

5. Data Reduction Procedures. All data is reduced off-line using a variety of selection algorithms designed to optimise the detection of a gamma ray signal. Because there is some disagreement between the simulations it is not possible to isolate a single algorithm that will maximise the selection efficiency. Instead the development of an algorithm is an iterative process with the selection criteria initially based on the simulations and modified after feedback from tests on actual data suspected to contain a gamma-ray source that can be regarded as a standard candle.

After calibration, data is sorted according to the following general criterion: (a) all data, (b) data sorted according to total brightness (shower energy), (c) data sorted by size and/or shape, (d) data sorted by orientation, (e) some combination of the above.

An early selection, suggested by the Durham gamma-ray simulations, was the use of the parameter, r to select compact (small angular size) showers as candidate gamma rays. $r = (p_1+p_2)$/total, the fraction of the light intercepted by the camera that is contained in the two highest pixels). This is confirmed by the Leeds simulations which show that the greater angular size of proton showers arises from greater width along the major axis caused by the greater penetration of the proton shower and along the minor axis caused by hadron interactions in the proton shower.

Following the Plyasheshnikov and Bignami (1984) the effectiveness of a selection procedure is the improved signal-to-noise ratio

$$h = \frac{A'_\gamma}{A_\gamma}\left(\frac{A'_p}{A_p}\right)^{-1/2}$$

where A_γ and A_p refer to the collection areas for gamma-ray and proton showers without selection and the dashed values are the post-selection values. h can be evaluated from the simulations where the source and background spectrum must be taken into account. The factor (A'_p/A_p) can be evaluated empirically since it is the ratio of event rate after and before selection. At the zenith this is 0.016. Using the Durham simulations A'_γ/A_γ is 0.5; the Leeds simulations indicate a higher value, so that $h > 4$ at the zenith. It falls off with zenith angle becoming ineffective for $z > 30°$. As discussed in Hillas (1985) the combination of r with other measured parameters can be expected to significantly improve the value of h.

Using the method described in Weekes (1976) and the Durham simulations, we derive the effective energy threshold, E = 200 GeV and the gamma-ray collection area ($A'_\gamma = 9.4\times10^3 m^2$).

6. Acknowledgements. This work was supported by the U.S. Department of Energy, the Smithsonian Scholarly Studies Fund and National Board of Science and Technology of Ireland.

References.

Browning, R, Turver, K.E. (1975), Nouvo Cimento, 38A,223.
Cawley, M.F. et al. (1983), 18th ICRC, 1, 118.
Fegan, D.J. et al. (1983) Nucl. Inst. & Meth. 211, 179.
Plyasheshnikov, A.V. and Bignami, G.F., (1984), preprint.
Rieke, G.H. (1969), 11th ICRC, 3, 601.
Turver, K.E., Weekes, T.C. (1978), Nuovo Cimento, 45B, 99.
Weekes, T.C. (1981). 17th ICRC, 8, 34.

N85-34982

OG 9.5-5

A METHOD TO IMPROVE OBSERVATIONS OF GAMMA RAY SOURCES NEAR 10^{15} eV

Sommers, P. and Elbert, J.W.

Physics Department, University of Utah, Salt Lake City, UT 84112 USA

ABSTRACT

Now that sources of gamma rays near 10^{15} eV have been identified, there is a need for "telescopes" which can study in detail the high energy gamma ray emissions from these sources. We analyze the capabilities of a Cerenkov detector which can track a source at large zenith angle (small elevation angle). Because the observed showers must then develop far from the detector, the effective detection area is very large. During a single half-hour hot phase of Cygnus X-3, for example, it may be possible to detect 45 signal showers compared with 10 background showers. Time structure within the hot phase may then be discernible. The precise capabilities of the detector depend on its mirror size, angular acceptance, electronic speed, coincidence properties, etc. We present calculations for one feasible design using mirrors of an improved Fly's Eye type.

For observing distant air showers, the effective detection area of a Cerenkov detector is determined by its angular aperture according to the formula

$$A = \pi(D \cdot \tan\phi)^2 \tag{1}$$

where ϕ is the 1/2-aperture angle and D is the distance from the detector to the position of Cerenkov light emission. The relevant geometry is indicated in figure 1. A very large detection area can be attained at large zenith angle because the large atmospheric slant depth causes the showers to develop far from the detector. Relatively high primary energies are required in order to yield a detectable photon density at the detector. Our calculations concern showers of 1 PeV ($\approx 10^{15}$ eV) or greater energy. Table 1 shows how the detection area increases with zenith angle for $\phi = 1.7$ degrees. The distance D is the distance from a slant depth of 600 gm/cm^2 (depth of maximum for PeV showers) to a vertical depth of 862 gm/cm^2 (corresponding to the Fly's Eye altitude). The distances are computed using the U.S. Standard Atmosphere and incorporating the (small) effects of the earth's curvature.[1] For quick calculations it is helpful to have an analytic formula which yields approximately correct values. If atmospheric depth is given by $x = 1030 \exp(-h/7)$gm/cm^2, with h the vertical altitude above sea level in km, then one gets

$$D \approx \frac{1}{\cos\theta} \left\{ -7 \ln \left(\frac{600 \cos\theta}{1030}\right) - h_0 \right\} \tag{2}$$

where θ is the zenith angle and h_0 is the detector's altitude in km above sea level.

ORIGINAL PAGE IS
OF POOR QUALITY

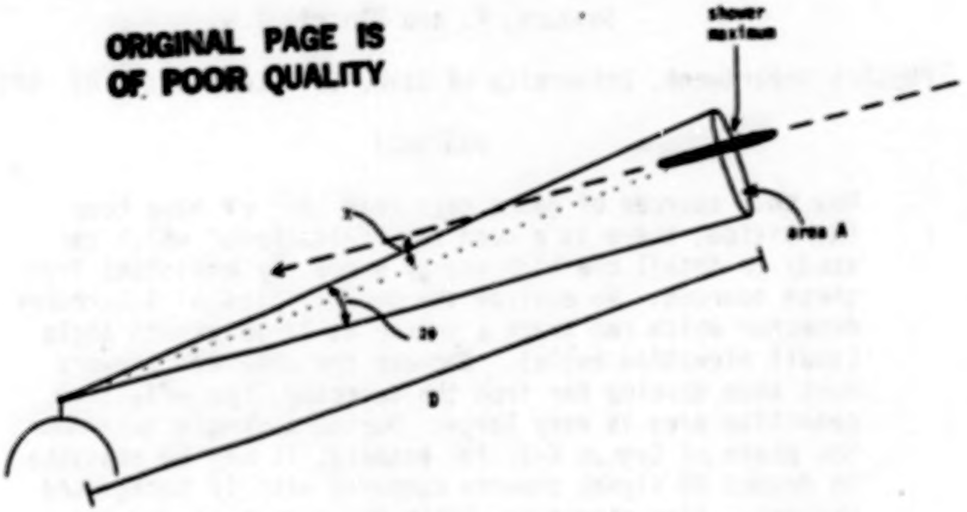

Figure 1

Using numerical simulations of Cerenkov light emission[2] and atmospheric propagation,[3] we have studied the dependence of the detector amplitude on zenith angle and the viewing angle χ (between the shower core and the detector's line of sight to shower maximum). For mirrors of 96 inches diameter (as proposed for an improved Fly's Eye), with 70% reflectivity and for phototube cathodes of the S-11 type with extended UV response, we find the number of photoelectrons to be given approximately by

$$PE = 1.3\text{x}10^7\ E\ D^{-2.5} \times \begin{matrix} e^{\chi_c - \chi} & (\ \chi > \chi_c\ ) \\ 1 & (\ \chi < \chi_c\ ) \end{matrix} \qquad (3)$$

where E is the primary γ-ray energy in PeV, D is the distance as in table 1, χ is measured in degrees, and χ_c is a zenith-angle-dependent critical angle (see table 1). The PE values in table 1 are obtained from this formula with $\chi < \chi_c$. A factor of 1.5 should be applied to the right side of equation 3 for an approximate conversion to photons/meter^2. The formula applies to γ-ray showers; hadronic showers yield an amplitude smaller by a factor of 0.73.

Table 1

Zenith Angle (deg)	D (km)	A [ϕ=1.7°] (km^2)	PE (photoelectrons)	χ_c (deg)
60	16	.71	13000	.8
65	21	1.2	6400	.8
70	30	2.5	2600	.7
75	46	5.9	910	.6
80	84	20.	200	.5

For a fixed amplitude threshold and fixed zenith angle, there is a maximum viewing angle at which a shower can be detected. Suppose the threshold is set at the PE value given in table 1 for a 1 PeV shower. The maximum viewing angle for γ-ray showers is then (from eqn 3)

$$\chi^{\gamma}_{max}(E) = \begin{cases} \chi_c + \ln E & E>1 \\ 0 & E<1. \end{cases} \quad (4)$$

Since this angle is energy dependent, the 1/2-aperture ϕ which optimizes the signal-to-noise ratio depends on the source's spectral index. (In principle, the signal's dependence on ϕ can be used to determine the spectral index.) Table 2 presents some expected results for Cyg X-3 based on the Kiel data (differential spectral index of 2.1 with a cutoff at 20 PeV). The signal rate is computed by

$$\text{signal rate} = \int_1^{20} \frac{dS}{dE} \cdot \text{area}(E)\, dE \quad (5)$$

where $\frac{dS}{dE}$ is the differential flux from Cyg X-3 (taken as a typical hot phase flux of 10 times the time-averaged flux). The area(E) is given by equation (1) with ϕ replaced by $\chi^{\gamma}_{max}(E)$ if $\chi^{\gamma}_{max}(E)$ is less than ϕ. For the background rate we use

$$\text{background rate} = A \int_{1/.73}^{\infty} \frac{dN}{dE}\, \Omega(E) dE. \quad (6)$$

Here A is the area from table 1, $\frac{dN}{dE}$ is the cosmic ray flux (with the spectral index taken to be 2.8) and $\Omega(E) = 2\pi(1-\cos \chi^{H}_{max}(E))$, where the maximum viewing angle for hadronic showers is $\chi^{H}_{max}(E) = \chi^{\gamma}_{max}(.73E)$. The last 3 columns of table 2 give the numbers of showers and signal-to-noise ratio from a single Cyg X-3 observation for 1720 seconds (.1 period).

Because of the strong dependence of rates on zenith angle in this range, careful monitoring of background rates is essential for identification of the signal from a source. Moreover, it may be necessary to operate two or more separated detectors in coincidence in order to reject spurious triggers from stray muons and background light fluctuations. Nevertheless, it appears feasible to detect a source like Cyg X-3 in a single short observation and to see some detail in the light curve. If a neutron star rotation period is modulating the PeV emissions from Cyg X-3, that period should be discoverable using this method.

TABLE 2

Zenith Angle (deg)	Optimal ϕ (deg)	Signal rate (s^{-1})	Background rate (s^{-1})	Signal/noise coefficient ($s^{-1/2}$)	Signal at 1720s (showers)	Background at 1720s (showers)	Signal/Noise at 1720s
60	1.75	.0082	.0019	.19	14	3.2	7.8
65	1.75	.014	.0033	.25	24	5.6	10
70	1.7	.026	.0056	.34	44	9.7	14
75	1.65	.054	.011	.51	92	19	21
80	1.6	.16	.031	.90	270	53	37

Acknowledgement.
This research was supported by the United States National Science Foundation under grant number PHY8415294.

Notes.

1. Based on tables in "An Analysis of the Nuclear Interaction of High Energy Cosmic Rays," Osborne, J.L., Ph.D. thesis, University of Durham (1966).

2. Based on shower properties given in Hillas, A.M., J. Phys. G 8, 1461 (1982).

3. Based on tables in Elterman, L. & Toolin, R.B., Handbook of Geophysics and Space Environments, (Bedford, Mass.: U.S.A.F. Cambridge Research Laboratories), Chapter 7 (1965).

N85-34983

ANGULAR RESOLUTION OF AIR SHOWER ARRAY-TELESCOPES

John Linsley
Department of Physics and Astronomy
University of New Mexico, Albuquerque, NM 87131
USA

ABSTRACT

A fundamental limit on the angular resolution of air shower array-telescopes is set by the finite number of shower particles coupled with the finite thickness of the particle swarm. Consequently the angular resolution which can be achieved in practice depends in a determinate manner on the size and number of detectors in an array-telescope, as well as on the detector separation and the timing resolution. It is also necessary to examine the meaning of 'particle density' in whatever type of detector is used. Results are given which can be used to predict the angular resolution of a given instrument for showers of various sizes, and to compare different instruments.

1. Introduction. Counter arrays for studying air showers are usually multi-purpose installations whose design represents a compromise between many requirements, including limits on construction and operation costs. Ordinarily the requirement for accuracy in measuring shower directions is not very stringent: angular resolving power of a few degrees is adequate. It is a fact of experience that resolving power of this order is achieved almost as a matter of course by applying the 'fast-timing' method of Bassi *et al.* (1953). Arrays which are physically small (diameter < 100 m) need to have 1-10 ns timing resolution, but this is not very difficult to achieve using scintillators. For giant arrays (diameter > 1 km) it might be difficult, but in this case the counter separations (the baselines for time of flight triangulation) are much greater, so the timing doesn't need to be as fast. The angular resolution characteristics of existing arrays have been studied with great care (see for example Clark *et al.* 1961, Linsley and Scarsi 1962, Lloyd-Evans 1982), but this seems always to have been done case by case, after the fact, so when I was asked recently, "What is the limiting precision of determining EAS directions? Is it possible, on a 300 m basis, to see the front within ± 1 ns, so as to achieve an angular resolution of 1 mrad?" (Cocconi 1984), I was unable to find a ready made answer. The question relates to a timely application: observing point sources of $> 10^{15}$ eV γ-rays, in which the signal to noise ratio of an air shower array-telescope depends critically on the angular resolution $\Delta\theta$, being proportional to $(\Delta\theta)^2$.

2. Error in arrival time. For an isolated detector the error in the apparent arrival time will include the instrumental error and the effect of fluctuations due to the finite number of particles producing the signal. The contribution of fluctuations is given by $\delta t = \sigma_t/\sqrt{n}$, where n is the number of independent contributions to the signal and σ_t is the arrival time dispersion. This relation assumes that the fiducial time is the *average* arrival time. In practice it may be more convenient to use instead $t_{\frac{1}{2}}$, the median time, or t_j, the time of the j-th particle, but this makes only a small difference (a factor of order 1) which I will neglect. For vertical showers on a thin scintillator of area A, $n = mSA$, where S is the 'particle density' as it usually is expressed, in units of the signal made by a relativistic muon. The factor m takes into account evidence that the average-size contribution to shower signals may be less than one muon (McDonald *et al.* 1977). For S I will use the NKG formula, $S = (N/r_o^2)C(r/r_o)^{s-2}(r/r_o + 1)^{s-4.5}$, where N is the shower size, s is the age, r_o is the Molière length, and $C = \Gamma(4.5-s)/[2\pi\Gamma(s)\Gamma(4.5-2s)]$. I find empirically that

$$\sigma_t = \sigma_{to}(r/r_t + 1)^b \tag{1}$$

with typical values $\sigma_{to} = 2.6$ ns, $r_t = 30$ m and $b = 1.5$.* Substituting in the formula for δt I obtain

$$\delta t = \frac{\sigma_{to} r_o}{\sqrt{CmNA}} (r/r_o)^{1-\frac{1}{2}s}(r/r_o+1)^{2\frac{1}{2}-\frac{1}{2}s}(r/r_t+1)^b \; . \tag{2}$$

This tells us that one method of improving the angular resolution is to increase the size of the detectors. For primary energies not too great it will also help to increase the altitude, because $\sqrt{N}$ will increase faster than $\sigma_{to}r_o$. To look at typical numbers I assume $s = 1$, which gives me $C \cong 0.4$. Then I take $r_o = 100$ m, $A = 1$ m^2, $N = 10^5$ and $m = 1$. I obtain

$$\delta t = (1.3 \text{ ns})(r/100)^{0.5}(r/100+1)^{1.75}(r/30+1)^{1.5}$$

and find these values:

r (m)	=	10	20	50	100	200
δt (ns)	=	0.8	1.7	8.1	39	267

Thus in order to locate a shower front within, say, 1 ns at greater and greater core distances one must use scintillators of rapidly increasing size. (In this example, whereas 3 m^2 detectors would be adequate up to 20 m, at 50 m the detector area would have to be 65 m^2.)

3. Angular resolution. The exact angular resolution of an array-telescope will depend on details of the layout and the data processing, but if the system is well designed the result will be approximately

$$\Delta\theta = c\delta t(R)/R \; , \tag{3}$$

where the 'effective baseline' R is such that $\delta t(R)$ equals the instrumental timing error, which I will call Δt. The idea is that in a 'well designed' system the separation of the detectors will be small enough in relation to r_o, A, and shower sizes of interest, so that typical useful events will produce several signals with δt approximately equal to Δt. These signals will dominate the usual least-squares fitting procedure for computing the shower direction. Signals with $\delta t \ll \Delta t$ will have little weight because the corresponding baselines will be $\ll R$; signals with δt

---

[*] See conference paper HE4.7-14 for experimental results on $b(E,\theta)$ for $10^{17}<E<10^{20}$ eV, and more references. In that experiment, as in most others, the energy dependence was found to be too small to detect. Parameter b controls the large core distance behavior of σ_t, which is not the main issue here. Measurements near the core are more difficult to make and to interpret; more data are needed. The results of Woidneck and Böhm (1975) favor a smaller value for σ_{to}, around 1.6 ns. See also Clay and Dawson (1984) and McDonald *et al.* (1977).

>> Δt will have little weight in spite of having baselines > R, because δt is such a rapidly increasing function for large core distances.

Moving the radical $\sqrt{mNA}$ to the left hand side of (2), one sees that the right hand side depends only on certain constants and r. Solving for r (graphically or numerically), representing the result as $r = f(\sqrt{mNA}\cdot\delta t)$, and then letting r = R so that δt can be replaced by Δt, one obtains the desired result:

$$\Delta\theta = c\Delta t/f(\sqrt{mNA}\cdot\Delta t) \qquad (4)$$

4. Discussion. Taking the Kiel array as an example (Bagge *et al.* 1979), $\Delta t = 1$ ns and $A = 1$ m^2, so for $mN = 10^5$ the effective baseline R is 13 m (by interpolation in the table above), and the angular resolution is predicted to be 23 mrad. This prediction is in good agreement with what is claimed by the Kiel group: $\Delta\theta$ better than 1° for $N = 10^5$-10^7. I have tested the predictions in other cases (MIT Agassiz, MIT Volcano Ranch, and Haverah Park arrays), each time finding satisfactory agreement.

Fig. 1 shows curves of constant angular resolution in coordinates log(Δt) vs log(mNA), calculated in the way I have explained, using (4). In region A the performance of an array-telescope is *particle statistics limited.* In this region, improving the instrumental time resolution does little to improve $\Delta\theta$. In region B the performance is limited instead by characteristics of the detectors and recording system, so there is room for improvement in $\Delta\theta$ by improving these characteristics.

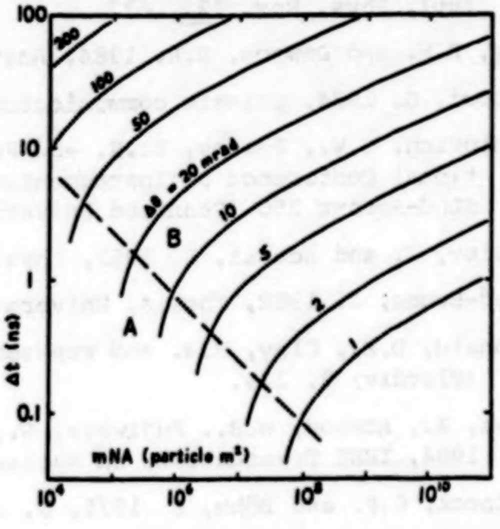

Fig. 1. Curves of constant angular resolution ($\Delta\theta$, mrad) for an array-telescope with given timing error Δt and area per detector A, for showers of size N. See text for explanation of m, and of regions A & B.

For $E = 10^{15}$ eV ($N = 10^5$ at sea level, systems like the one at Kiel are already in region A. The most practical way to improve their performance is by greatly increasing the size (or density) of the detectors, or by moving to a higher altitude. A goal of 5 mrad angular resolution within the next decade seems to be realistic. This can be achieved with scintillation counters, without improving Δt. The improvement in signal to noise ratio for point sources of γ-rays, a factor of $(20/5)^2$, will be substantial.

Improving still further so as to attain $\Delta\theta = 1$-2 mrad at this energy seems to require a radical change, from scintillators to some other kind of device with an intrinsically much faster response. Workers at SLAC have constructed planar spark counters (PSC's) with dimensions of 10 x 300 cm, and these have been tested at PEP giving on-line timing resolution better than 200 ps, as well as position resolution smaller than 4 mm

(Atwood *et al.* 1983, Ogawa *et al.* 1984). The timing resolution of similar 30 x 30 cm units constructed at Novosibirsk is reported to be as small as 24 ps (Fedotovich *et al.* 1982).

References.

Atwood, W.B., Bowden, G.B., Bonneaud, G.R., Klem, D.E., Ogawa, A., Pestov, Yu.N., Pitthan, R. and Sugahara, R. 1983, Nucl. Instrum. and Methods 206, 99.

Bagge, E.R., Samorski, M. and Stamm, W. 1979, Proc. 16th ICRC (Kyoto) 13, 260.

Bassi, P., Clark, G. and Rossi, B. 1953, Phys. Rev. 92, 441.

Clark, G., Earl, J., Kraushaar, W., Linsley, J., Rossi, B. and Scherb, F. 1961, Phys. Rev. 122, 637.

Clay, R.W. and Dawson, B.R. 1984, Aust. J. Phys. 37, 309.

Cocconi, G. 1984, private communication.

Fedotovich, G.V., Pestov, Yu.N. and Putilin, K.N. 1982, Proc. International Conference on Instrumentation for Colliding Beam Physics, SLAC-Report 250 (Stanford University, Stanford CA) p. 127.

Linsley, J. and Scarsi, L. 1962, Phys. Rev. 128, 2384.

Lloyd-Evans, J. 1982, Thesis, University of Leeds.

McDonald, D.M., Clay, R.W. and Prescott, J.R. 1977, Proc. 15th ICRC (Plovdiv) 8, 228.

Ogawa, A., Atwood, W.B., Fujiwara, N., Pestov, Yu.N., and Sugahara, R. 1984, IEEE Transactions on Nuclear Science NS-31, 121.

Woidneck, C.P. and Böhm, E. 1975, J. Phys. A 8, 997.

N85-34984

ASTROPHYSICAL APPLICATIONS OF HIGH ANGULAR RESOLUTION ARRAY-TELESCOPES

John Linsley
Department of Physics and Astronomy
University of New Mexico, Albuquerque, NM 87131
USA

ABSTRACT

The air shower array-telescopes which are currently being used to search for and study point sources of UHE γ-rays have angular resolution ∿ 1°, limited by either the small total area of particle detectors or poor timing resolution. As the signal to noise ratio depends sensitively on the angular resolution, it seems certain that this figure will quickly be surpassed when second generation instruments come into operation. Since the trajectories of galactic cosmic rays with $E > 10^5$ GeV are practically straight lines on scales of 1 A.U. or less, these new instruments will be able to observe a shadow cast by the moon (angular diameter 0.5°). Although the angular diameter of the sun is practically the same, its 'shadow' will be more complex because of its magnetic field. Thus, high angular resolution observations of the sun afford a means of investigating the solar magnetic field, and also the charge composition of cosmic rays, including the ratio of antiprotons to protons.

1. Introduction. The first search for point sources of air shower primaries using fast timing to measure the individual arrival directions was made by Clark, using an array of four 0.13 m^2 scintillators located on the roof of the physics building at MIT. In reporting the results of this search he commented, "The sun and moon must cast a 'shadow' in the flux of high energy primary cosmic rays, and observations of this shadow effect might give new information about the magnetic fields of these bodies." (Clark 1957) With detectors of this size, and the best available electronics, the angular resolution (resolution in zenith angle, θ) was 4°; with a sample of 2660 events no statistically significant evidence of point sources was found. Studies made in the past 3 decades have shown that the sun's large scale magnetic field is weaker than it was thought to be in 1957, and have shown that it is not a simple dipole field. Nevertheless, there is no doubt that the shadow of the sun will show effects of the kind that Clark anticipated. It is known now that the moon has no magnetic field. Therefore the shadow of the moon predicted by Clark will be simply a geometrical shadow.

Regarding the sun, it is still not possible to predict quantitatively, with certainty, what effects will be observed. On the one hand, there is uncertainty about the magnetic field of the sun. "At the present time, very little is known about the actual magnetic field configuration and its changes", according to Zirker, writing in 1981. On the other hand, there is uncertainty about the charge composition of the cosmic rays that produce air showers. One would prefer to address these uncertainties one at a time, but having to deal simultaneously with two interlocking problems is common enough in cosmic ray studies. Despite the complexity some preliminary estimates will be made.

2. The method. The essential variables are:

1) The deficit in counting rate, which determines the statistical errors. This depends on the area A of the array-telescope and the energy E of the cosmic rays. (This is in a regime where E and cp are indistinguishable.)

2) The angular resolution of the array-telescope, and

3) The magnetic deflection.

Regardless of magnetic effects, the counting rate deficit due to particles intercepted by the sun or moon will equal $JA\Omega$, where J is the intensity and $\Omega = 5 \cdot 10^{-7}$ steradian is the solid angle subtended by either of these bodies (Liouville's theorem). I will assume $A = 10^4$ m^2 for second generation array-telescopes. Then using the observed all particle cosmic ray energy spectrum, for primary energy 10^4, 10^5, 10^6 GeV the rate in question amounts to 80,000, 1,500, and 30 counts per year, respectively.

From an analysis of the statistical limitations on the angular resolution of array-telescopes it seems that an accuracy of 5 mrad at 10^6 GeV will be attained in the next few years by second generation instruments. The corresponding practical limits at 10^4 and 10^5 GeV are estimated to be 20 and 10 mrad, respectively. Achieving further improvement will have to await development of large area detectors capable of a much faster response than scintillators (conference paper OG9.6-5). For comparison, the accuracy of direction measurements in a proposed space station magnetic spectrometer facility will be 0.02 mrad (Müller 1985). Thus one can be fairly certain of detecting the shadow of the moon at 10^5 and 10^6 GeV with second generation resolution, but detection at 10^4 GeV seems doubtful, even with the more favorable counting rate.

The arrival direction of cosmic rays affected by the solar magnetic field will also be affected by the interplanetary magnetic field and the geomagnetic field. The latter fields will modify the arrival direction of cosmic rays grazing the moon. To estimate these effects I will use the relation

$$\theta = \frac{300Z}{E} \int B_{\perp} d\ell \, , \qquad (1)$$

where θ is the angular deflection (radian) in a given plane, produced by the perpendicular magnetic field $B_{\perp}$ (gauss) in a region covered by the integration, acting on a cosmic ray with charge number Z and energy E (eV). This holds when θ is not too large. In case of the earth one can use Störmer theory. Here I will use a Störmer-theory calculation of equatorial-plane orbits for illustrating approximately how cosmic ray orbits will be affected by the large-scale solar magnetic field. The illustration is valid to the extent that the heliomagnetic field varies as $1/R^3$ over a sufficient range of distances from the sun.

3. The geomagnetic effect. In this case the field integral is approximately $6 \cdot 10^7$ gauss cm ($=$ 0.1 gauss x $R_{\oplus}$). It is noteworthy that this is nearly 2 orders of magnitude greater than for the spectrometer mentioned above. Substituting in (1), one finds that the deflection will be undetectable using array-telescopes except possibly for Fe nuclei at 10^4 GeV.

4. The effect of the interplanetary magnetic field. Assuming $B_{\perp} = 5 \cdot 10^{-6}$ gauss (Ness 1965), one finds that in case of travel from the moon the effect will be completely negligible. For travel from the sun, the magnetic field integral will be ~ 10^8 gauss cm, so as in the geomagnetic case, the effect will be negligible except for 10^4 GeV Fe nuclei.

5. The heliomagnetic effect. The heliomagnetic field consists of a hierarchy of structures, the largest of which are called active regions. Typical data, given in Table 1, imply values of the magnetic field integral of order $1\text{-}2\cdot10^{11}$ gauss cm over regions with a size of order $R_\odot$, so by a simple scaling argument, comparing the sun with the earth, one expects sizable effects up to proton energies of 10^5–10^6 GeV, and correspondingly higher energies for Fe nuclei. Table 1 shows that above large active regions the field strength decreases with increasing distance about as $1/R^3$, so to at least a crude approximation the field can be modeled as a dipole. Fig. 1 shows trajectories of 20 GeV protons in the equatorial plane of the earth (Hillas 1972). The apparent location of the occulting object for an observer at infinity using protons or antiprotons is also shown. According to Störmer theory the same picture applies to the sun, when its field is approximated by a dipole, provided that the particle energy is scaled upward by a factor $(M_\odot/M_\oplus)^{\frac{1}{2}}$, where M denotes magnetic dipole moment. Choosing $M_\odot = 3\cdot10^{32}$ gauss cm, so that the equatorial surface field will be about 1 gauss, the scale factor comes out 2000. Hence Fig. 1 also illustrates the behavior of $4\cdot10^4$ GeV protons, or 10^6 GeV Fe nuclei, in the vicinity of the sun. Again using Störmer theory, the same picture can be applied to higher energy particles by drawing larger circles to represent the limb of the occulting sphere, the radius being proportional to $\sqrt{E}$. It appears by inspection of the figure that the proton and antiproton images will be separated adequately up to about 10^5 GeV.

Table 1. Magnetic field strength (gauss) vs height (solar radii) above active regions (Dulk and McLean 1978).

height	B
1.02	300
1.1	10
2	0.5
5	0.05

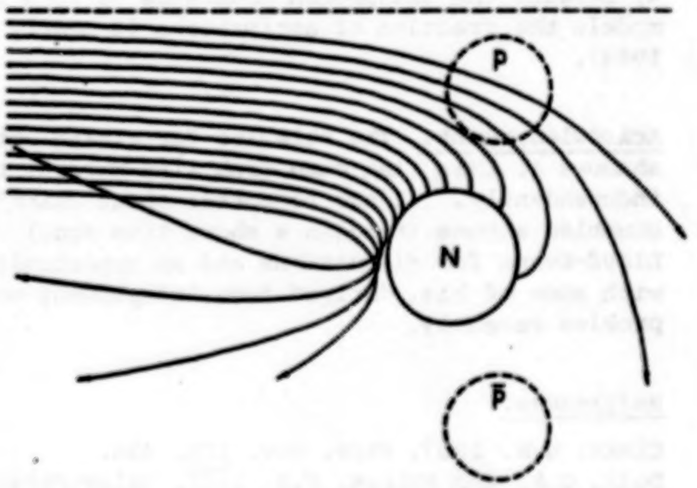

Fig. 1. Trajectories of charged particles in the equatorial plane of the earth's field, with asymptotic direction indicated by the dashed line, and equally spaced impact parameters (Hillas 1972). The solid circle represents the real location of the equator; the dashed circles, the apparent location of the occulting object for protons (p) and antiprotons (p̄) at infinity.

6. Conclusions. Using second generation array-telescopes which I assume will have resolving power of 10 mrad at 10^5 GeV and 5 mrad at 10^6 GeV, it appears that the following can be done:

1) Detect the cosmic ray shadow of the moon. This will be a simple geometrical shadow, undisplaced and undistorted. The detailed character of the shadow will provide an independent test of the instrumental resolution of whatever array is used.

2) Detect the cosmic ray shadow of the sun. This shadow will be complex, made up of partial shadows corresponding to primary charges $Z = 1, 2, \ldots$ The partial shadows will be displaced from the true direction of the sun through angles proportional to Z/E. The larger the angular displacement, the more these partial shadows will be enlarged and distorted. Hence, partial shadows will only be discernable when they are near the true sun; otherwise they will blend into the background.

3) *identify the partial shadows belonging to primary protons, alpha particles, and principal charge groups through Fe, and thus measure the cosmic ray charge spectrum for a fixed rigidity of about 10^5 GeV/c.* The identification can be done in an empirical manner, with only crude information about the strength and character of the heliomagnetic field. At an energy a factor 2-3 lower than pictured in Fig. 1 (and all still lower energies) there will be no discernable shadow, because even the proton shadow will blend with the background. As one goes to higher energies, *the first shadow to appear will be the proton shadow.* As E is increased further, the proton shadow will move inward until it lies in the direction of the true sun. As this happens the shadows belonging to $Z = 2$ and more will successively, for the appropriate value of E, occupy the position where the proton shadow lies in Fig. 2.

4) measure the antiproton abundance up to $\sim 10^6$, where according to some models the fraction of antiprotons is nearly 0.5 (Stecker and Wolfendale 1984).

Acknowledgement. The stimulus for giving attention to the solar-lunar shadows at this time came from Alan Watson, to whom the idea had occurred independently. (I had forgotten about Clark's early comment until I stumbled across it again a short time ago.) I am grateful to Jeremy Lloyd-Evans for discussions and an opportunity to compare my conclusions with some of his, derived from independent work he has been doing on this problem recently.

References.

Clark, G.W. 1957, Phys. Rev. 108, 450.
Dulk, G.A. and McLean, F.B. 1978, Solar Phys. 57, 279.
Hillas, A.M. 1972, in *Cosmic Rays* (Pergamon Press: Oxford) p. 17.
Müller, D. 1985, *A Magnet Spectrometer Facility: Rationale and Science Themes*, preprint.
Ness, N.F. 1965, Proc. 9th ICRC (London) 1, 14.
Stecker, F. and Wolfendale, A.W. 1984, Nature 309, 37.
Zirker, J. 1981, in *The Sun as a Star*, ed. S. Jordan (NASA publication SP-450) p. 135.

N85-34985

ANGULAR RESOLUTION OF AN EAS ARRAY FOR GAMMA RAY ASTRONOMY AT ENERGIES $>5 \times 10^{13}$ eV

Apte, A.R., Gopalakrishnan, N.V., Tonwar, S.C., and Uma, V.

Tata Institute of Fundamental Research
Homi Bhabha Marg, Colaba, Bombay-400 005
India

ABSTRACT

A 24 detector extensive air shower array is being operated at Ootacamund (2300 m altitude, 11.4°N latitude) in southern India for a study of arrival directions of showers of energies greater than 5×10^{13} eV. Various configurations of the array of detectors have been used to estimate the accuracy in determination of arrival angle of showers with such an array. These studies show that it is possible to achieve an angular resolution of better than 2° with the Ooty array for search for point sources of Cosmic gamma rays at energies above 5×10^{13} eV.

1. INTRODUCTION

Interstellar magnetic field causes charged particle trajectories to be tortuous and uncertain for all but the most energetic particles. Therefore information on the highest energy processes occurring in astrophysics can be obtained only from studies of high energy gamma ray photons which travel unscattered and practically unabsorbed through great lengths of galactic and intergalactic space. Observations at energies less than about 10^{10} eV have been carried out with satellite borne instruments which can discriminate efficiently between photons from a source and the isotropic charged particle background. However, studies of photons of energies above 10^{11} eV require very large effective collection areas which are possible with only ground based techniques. Atmospheric Cerenkov radiation technique has been successful for energies above 10^{11} eV and studies of extensive air showers have been carried out to detect sources of very high energy photons of energies above 10^{14} eV. Since most of the Cerenkov photons are produced in the atmosphere near the cascade maximum and suffer negligible scattering before arriving at the detectors placed at sea level or mountain altitude relative timing techniques using detectors spaced few tens of meters apart enable the determination of arrival direction of individual showers to an accuracy[1] of better than about 0.5°. Such good angular resolution of an atmospheric Cerenkov radiation (ACR) telescope allows observation of a small angular region around the suspected source of high energy photons enabling achievement of a large value for the signal to background (S/B) ratio. Studies of extensive air showers (EAS), on the other hand, involve detection of electrons which suffer considerable scattering in the atmosphere. It is therefore expected that angular resolution of an EAS telescope would be much poorer compared to an ACR telescope. However no detailed and systematic studies exist on the possible angular resolution that can be achieved with an air shower array at various energies above 10^{14} eV. In fact, various angular size bins have been used in different experiments[2,3,4] based on approximate estimates of angular resolution of respective arrays, which leads to widely varying values of the S/B ratio causing uncertainities in the estimates of flux of high energy photons from a suspected source.

Since June '84, we have operated an EAS array at Ootacamund (Ooty for short, 2200 m altitude, 11.4° N latitude) in southern India for study of sources of high energy Cosmic ray photons. With data from this experiment we have studied in various ways the time resolution of air shower detectors and the angular resolution achievable with this array. In the next section are presented the details of the array, shower selection and recording system. The observed time resolution of EAS detectors is discussed in section 3 and in section 4 are presented the results on angular resolution achieved with Ooty array for showers of energies $>5 \times 10^{13}$ eV. The conclusions drawn from this study are given in the last section.

2. EXPERIMENTAL SYSTEM

The EAS array at Ooty consists of 24 scintillation detectors of various sizes spread over an area of radius of about 40 meters. 20 detectors are plastic scintillators, each 5 cm thick and the other four called N,E,W, and S,are liquid scintillaters using 10 cm thick column of mineral oil. These four scintillation detectors are only used for selection of showers through a 4-fold coincidence called NEWS. These four detectors are located at the corners of an approximate square around the centre of side length of about 10 m (see figure 1 of paper OG 2.6-8). All the scintillators are viewed by 5 cm diameter fast photomultipliers (RCA 8575) placed some distance above the scintillator giving about 10% uniformity in signal over the area of the scintillator. Showers are first selected with a four fold coincidence of 100 ns wide pulses obtained from discriminators (LRS 623B) for N,E,W, andS. The thresholds for the discriminators have been set at 30 mV while the mean pulse amplitude for near vertical muons is about 100 mV for these detectors. However, this selection with an observed shower rate of about 30 per minute selects many very small size showers which do not trigger many of the other 20 detectors. Since the angular resolution is expected to depend on the number of detectors available for determination of shower arrival direction, showers which trigger only few detectors are not considered to be useful for studies of Cosmic gamma ray sources. In an attempt to optimise the selection of showers which trigger a large number of detectors but at the same time keeping the shower size threshold lower, an additional requirement of at least 3 particles in one of the four selection detectors is included in the final shower trigger. Observed shower rate with this final trigger is about 7 per minute. Each such trigger causes the digitization of the charge collected at the anode for each photomultiplier using fast ADC's (LRS 2248A) and the digitization of the relative delay between the trigger and the output from discriminators for each detector with an accuracy of 0.25 ns by using fast TDC's (LRS 2228A). Pulses from the photomultipliers going to the discriminators are amplified with gain 10 (LRS 612A) to keep the effective threshold low while obtaining a good charge measurement for single particles with the ADC's. For each shower information from all the ADC and TDC channels is transferred to a memory buffer preceding a magnetic tape recording system such that the system can record all the details of showers coming as close as 1.5 ms relative to each other. Real time information is read for each shower from a clock running on a crystal with stability of about 1 part in 10^9 per day which is corrected periodically with ATA time signals broadcast from New Delhi. Data collected on magtape at Ooty are then analysed at Bombay using the CYBER 170/730 computer system at the Tata Institute.

3. TIME RESOLUTION OF EAS DETECTORS

The inherent time resolution of particle detection system used in the present experiment is contributed by the rise time and time jitter in the photomultiplier, amplifier, discriminator and the TDC apart from the scintillator and photon reflections inthe hood on which the photomultiplier is mounted. This resolution has been measured experimentally by mounting two photomultipliers on the same scintillator. The relative time measured between these two channels for showers has a distribution with standard deviation (σ) of about 1 ns which seems to depend only weakly on the particle density over the detector. However the distribution of the relative time between two detectors (N and 6) which are located within 2 m of each other is much broader reflecting the thickness of the shower disk. It is this distribution which is relevant for estimating the accuracy in the determination of arrival angle of showers. The standard deviation for this distribution is 5.2 ns for particle densities of less than 5 particles m^{-2} and 3.8 ns for larger densities. Correcting for the angular distribution of showers and the distance between these two detectors, it is clear that the minimum uncertainity in time measurement by individual detectors, at least for low size showers is about 3 ns. Therefore an EAS array with largest distance span of about 20 m between timing detectors, for example the EAS array at Kiel[2], can hardly achieve an angular resolution better than about 3° for small size showers.

4. ANGULAR RESOLUTION OF OOTY EAS ARRAY

Sine timing information from 24 detectors is available for getting a best fit to a plane shower front passing through all these detectors, it is possible to reduce the effect of timing fluctuations discussed above and achieve a better abgular resolution. In an attempt to estimate the angular resolution of the array, data have been analysed using different sets of detectors and the values of right ascension and declination are compared. In the first instance, the array is split into two arrays, one with odd numbered detectors and the other with even numbered detectors. RA and δ are computed independently with the two arrays. The distribution of the differences between the two RA values as well as the distribution of the differences between the two δ values, show a broad symmetric distribution with σ of about 3°. This suggests a value for σ of about 2° for each sub-array. Another study has been made by comparing the RA and δ values for two arrays, one with all the 20 detectors (excluding the timing selection and reference detectors N,E,W,and S) and the other with only inner 9 detectors. The value of σ for the distribution of the difference in RA values as well as the distribution of the difference in δ values is about 2°. This result suggests that the angular resolution for the array using all the 20 detectors is much better, assuming that the array with only inner 9 detectors has a resolution of about 2°.

These results have been obtained using only those showers which have triggered all the 24 detectors, evidently a sample of same what larger size showers. However similar results have been obtained using showers which have triggered only inner 15 detectors. It should also be noted that showers selected in the manner discussed earlier have on the average 20 out of 24 detectors triggered and nearly 80% of the showers have timing information available from at least 15 out of the 20 detectors, ignoring the selection detectors. The energy threshold for showers triggering at least 15 out of 20 detectors is estimated to be about 5×10^{13} eV.

4. CONCLUSIONS

Ooty air shower array with 24 scintillation detectors, has been used to measure the arrival angles of showers using the relative timing technique. From the computed differences in the values of the right ascension and the declination for showers for various configura-tions of detectors used for calculation of arrival directions, it is estimated that the angular resolution of Ooty array is better than about 2° for showers of energies greater than about 5×10^{13} eV. Results from the search for sources of very high energy gamma rays using data collected with the Ooty array since June '84 is reported elsewhere (OG 2.6-8) in this Conference using the values of angular resolution obtained here.

ACKNOWLEDGEMENTS

It is a pleasure to thank Prof. B.V. Sreekantan for his encouragement and fruitful discussions.

References:

1. Gupta, S.K. et al., preprint (1985).
2. Samorski, M. and Stamm, W., Astrophys. J.(Letters) 268, L17(1983)
3. Lloyd-Evans, J., et al.,Nature 305, 784 (1983)
4. Morello, M.et al.,in 18th International Cosmic Ray Conference, Conference Papers, Bangalore, 1983, Vol.1, p.127

N85-34986

NOTE ON THE DETECTION OF HIGH ENERGY PRIMARY COSMIC GAMMA RAYS BY AIR SHOWER OBSERVATION

KASAHARA,K., TORII,S.*, AND YUDA,T.

Institute for Cosmic-Ray Research, University of Tokyo, Tanashi, Tokyo
**Kanagawa University, Rokkakubashi, Kanagawa*

Basic materials are given which are indispensable to searching for point sources of gamma rays in the PeV energy region by observing air showers. Advantage of a mountain level observation is stressed. The possibility that all the existing Cygnus X3 data for > PeV are of gamma ray origin seems not so high.

1. Introduction

A mountain altitude experiment is being planned at Mt. Norikura(735g/cm^2, latitude 36°) in a form capable of searching for point sources of astrophysical high energy gamma rays in the PeV energy region.

As well known, several groups[1] have reported observations of air showers exceeding PeV (=10^{15} eV) energy that are supposed to be originated by particles coming from Cyg X3. Similar results[2] have also reported on Vela X1 and Crab pulsar. Gamma rays would be the only reasonable candidate which arrives at earth without being deflected from such objects and is detectable by air shower. Should they be other exotic particles, it is rather difficult to conceive such ones without abundant gamma rays.

However, the observations so far seem not to show the characteristics of air showers by gamma rays: for example, showers of the Kiel group contain as many muons as hadronic origin and a shower selection condition of s (age) > 1.1 does not put a substantial weight on gamma primaries. Akeno group selelcted muon poor showers but s is $\sim$ 1 which is, as gamma showers, so young that one may afraid of showers induced by protons penetrating deep in the atmosphere; the number of such showers might not be negligible as the angular resolution is $\Delta\theta \sim 10°$.

In confirming the existence of PeV energy gamma primaries from Cyg X3, in knowing their intensity and spectrum, and in searching for other similar point sources, mountain level observations have advantage. By assuming an observation at Mt. Norikura, we shall show it in many respects by using Monte-Carlo showers.

2. Characteristics of air showers in the PeV energy region

Figure 1 shows a superposition of the transition of the number of electrons (size, N_e) of 1000 simulated air showers, each of which is generated by a 10^{15} eV gamma ray. The effective depths for zenith angles 0, 20, 30, and 45 degrees at observation depths 735 g/cm^2 (Mt. Norikura) and 927 g/cm^2 (say, Akeno) are indicated in the figure. It is to be noted that the fluctuation of the size is minimum at mountain levels.

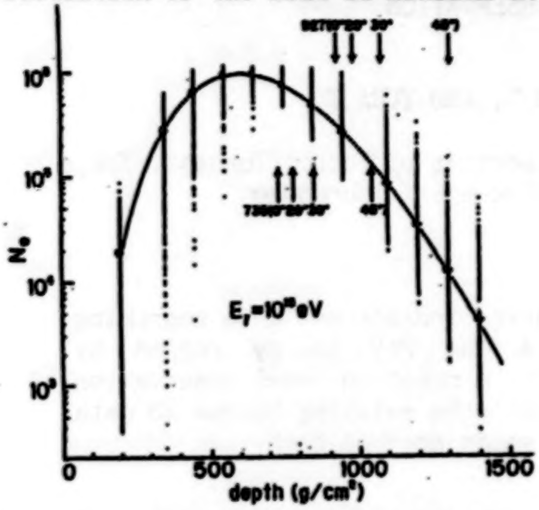

Fig.1 Transition of N_e by 10^{15}eV gamma primary in the atmosphere. 1000 showers are superposed. Effective depths for zenith angles 0,20,30,45° at 735 and 927 g/cm^2 are indicated.

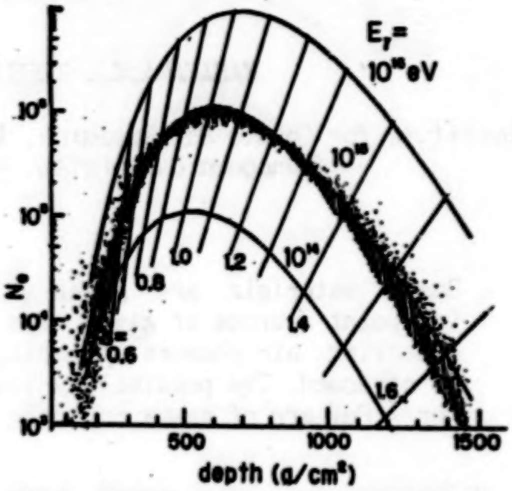

Fig.2 Showers in Fig.1 are superposed by reference to their centre of gravity. Solid lines show analytical result for average N_e and age s.

The apparent large fluctuation is reduced if the showers are shifted and superposed by reference to their centre of gravity (of which the average is 650 g/cm^2) as shown in Fig.2, i.e., each shower has almost the same shape very close to the simple average in Fig.1. The average transition of N_e and age parameter s under approximation B (analytical calculation) is also inlaid. The figure tells that there is almost a unique relation among the primary energy E_0, N_e and s.

Figure 3 shows the distribution of s in the integral form. Note that the fitting of a lateral distribution by NKG function will result in a younger age than here. (see Ref.3). The distribution of the size can well be approximated by log-Gauss form at depth Z=600 to 1500 g/cm^2 and the dispersion is given by $\sigma=\Delta N_e/N_e \sim \sigma_0(Z\sec\theta-735)+\sigma_1$ (%) where $\sigma_0=-0.01\log_{10}(E_0/\mathrm{PeV})+0.04\ g^{-1}cm^2$, $\sigma_1=-4\log_{10}(E_0/\mathrm{PeV})+10$ and θ is the zenith angle.

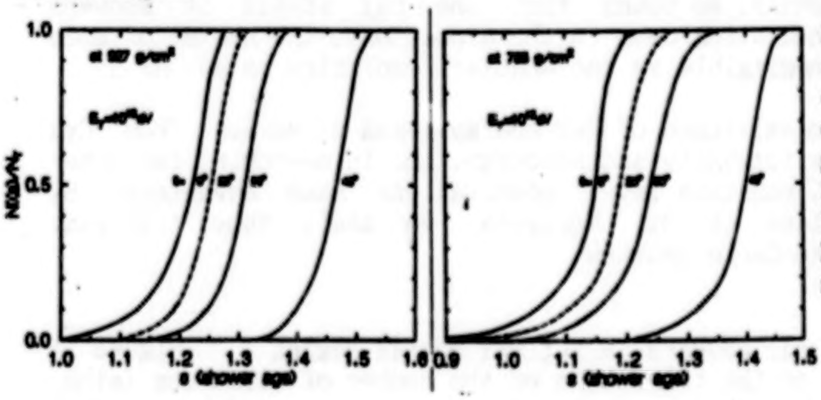

Fig.3 Normalized integral distribution of shower age s. 10^{16} eV primary (at 927 g/cm^2, left). and 10^{15}eV primary (at 735 g/cm^2, right). Parameters are the zenith angle.

ORIGINAL PAGE IS
OF POOR QUALITY

To see characteristics of background showers, 1000 proton initiated showers at 10^{15} eV are superposed in Fig.4 as in Fig.1. The hadronic cases give lower maxima than the gamma case (denoted by dash in this fig.) by ~1/1.5, while at deeper depths they have larger values than the gamma. This means that the background intensity at mountain levels is $(\sim 1/1.5)^2 \sim 1/2$ of the one at the near-sea-level depth.

3. Fast timing efficiency To know the arrival direction of air showers by fast timing (FT) technique within, say, $\Delta\theta \sim 1°$ with time resolution of $\Delta t = 1 \sim 4$ ns, a certain number of electrons must fall in a detector at $r = 10 \sim 40$ m from the air shower centre. We require this number to be more than 30 at $r = 10$ m and 10 at $r = 20, 30, 40$ m. In figure 5 is shown the percentage of the showers that fill such conditions for a primary energy of 10^{15} eV and a 1 m^2 detector. The assumed lateral distribution is the one obtained by our Monte-Carlo calculation and is consistent with Ref. 3.

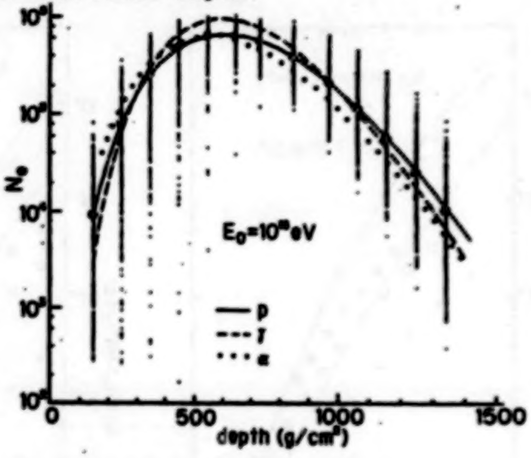

Fig.4 Transition of Ne by 10^{15} eV protons. 1000 showers are superposed. Solid line is average. Average curve by gamma and alfa of the same energy is shown by dash and dot, respectively.

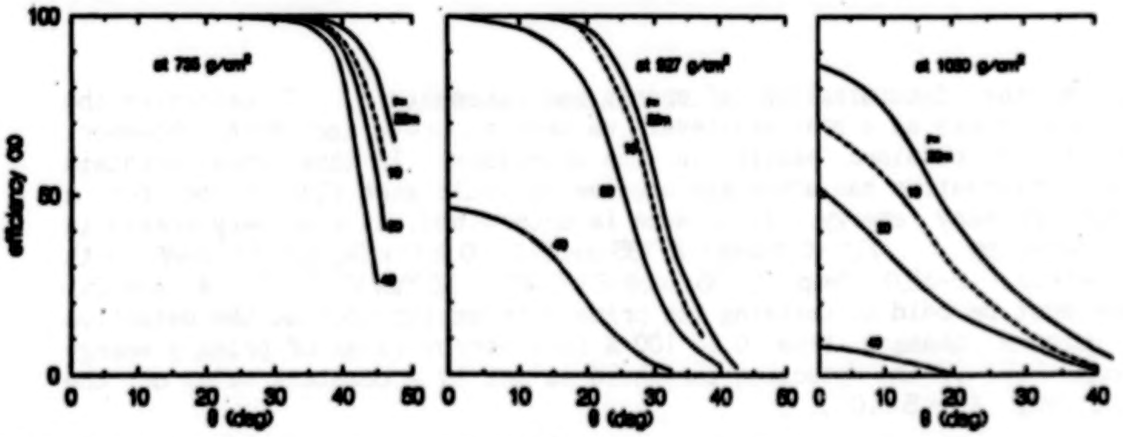

Fig.5 Percentage of showers that satisfy $N_e/m^2 > 30$ at r=10 m from the air shower core, or $N_e/m^2 > 10$ at r=20, 30, or 40 m as a function of zenith angle for primary of 10^{15}eV.

The threshold energy as seen from FT is about 0.3, 1, 3 PeV for depths 735, 930, 1030 g/cm², respectively. An energy three times higher than this would be needed for high quality data at the respective depth.

4. Background showers Assuming an appropriate primary cosmic ray spectra above 70 TeV with compositions ranging from protons to irons, background showers of hadronic origin are computed and the size distribution is shown in Fig.6 where the angular resolution is assumed to

ORIGINAL PAGE IS
OF POOR QUALITY

be $\Delta\theta=1^\circ$ ($=2\sigma$). No cut by muon number or age is imposed here. For reference, the size distribution by primary gamma rays with an energy spectrum $E^{-\beta-1}*(1+E/E_c)^{\beta-\gamma}dE$ is also shown, where $\beta=1, \gamma=2, E_c=10^{16}$ eV and the intensity is adjusted to be compatible with the Cyg X3 observation so far. Cut by the age would not be effective for reducing the background; muon number cut will be needed for further reduction.

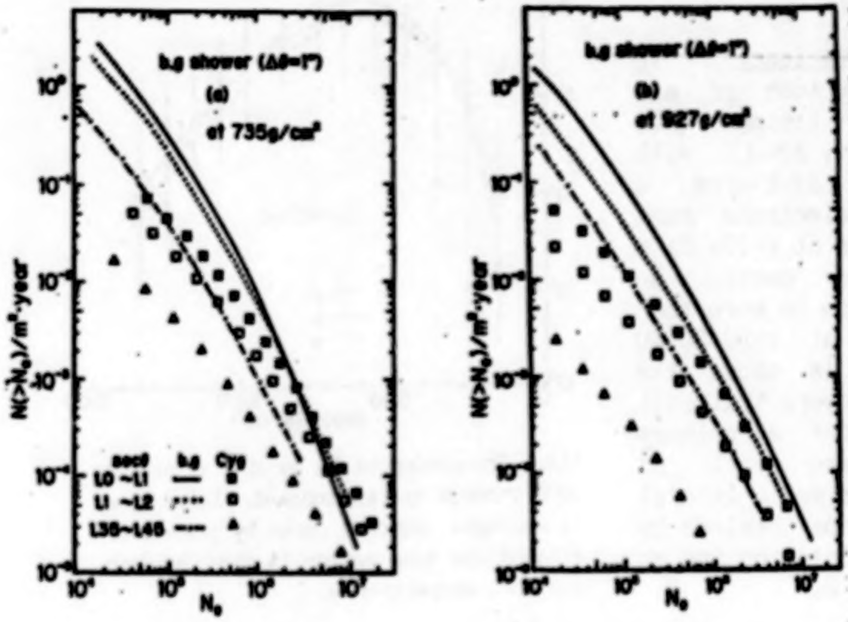

Fig.6 Integral shower size distribution by background hadrons. Solid line for $\sec\theta$=1~1.1, dot 1.1~1.2, dot-dash 1.35~1.45. $\Delta\theta=1^\circ$ is assumed. At 735 g/cm² (left) and 927 g/cm² (right). For reference, a model of signals from Cyg X3 is also shown by symbols in respective range of θ.

5. On the determination of energy and intensity. To determine the primary energy at a near-sea-level, we need accurate age which, however, cannot be obtained easily in the experiment. In this sense, mountain level observation has advantage because of small size fluctuation for a given primary energy. If a size is determined, it's primary energy is estimated by $\langle E_0\rangle \sim 0.14\exp((Z/735+\sec\theta-2)/0.27)\times(N_e/10^5)^{0.84}$ (PeV) with an error, $\sigma=\Delta E/E\sim 9\exp((Z/735+\sec\theta-2)/0.46)\times(E/\mathrm{PeV})^{-0.15}$ (%) A special care must be paid to deriving the primary intensity because the detection efficiency changes from 0 to 100 % in a narrow range of primary energy around PeV, if the detection threshold is set by a constant value of the size (say, $10^5\sim5\times10^5$).

FACOM M380 of INS was used for the present simulation.

References

1. M.Samorsky and W.Stamm, Ap.J.,268,L17(1983).
   J.Lloyd-Evans etal Nature, 305, 784(1983).
   T.Kifune etal, this conference.
2. J.Boon etal, 18th ICRC, Bangalore, XG 57(1983).
   R.J.Protherore and P.R.Gerhardy, Ap.J.,Lett., 280,L47(1984).
3. M.Hillas and J.Lapikens, 15th ICRC, Plovdiv, 8,460(1977).
   A.A.Lagutin etal, 16th ICRC, Kyoto, 7,18(1979).

N85-34987

OG 9.5-10

ON THE STATISTICAL SIGNIFICANCE OF EXCESS EVENTS - REMARKS OF CAUTION AND THE NEED FOR A STANDARD METHOD OF CALCULATION

R.Staubert
Astronomisches Institut der Universität Tübingen, Tübingen, Germany

ABSTRACT

Methods for calculating the statistical significance of excess events and the interpretation of the formally derived values are discussed. It is argued that a simple formula for a conservative estimate should generally be used in order to provide a common understanding of quoted values.

1. Introduction. Substantial nonuniformity exists in the cosmic ray literature with respect to how the statistical significance of features or excess events is being calculated (e.g. point sources, spectral lines, light curves). Consequently, there is no mutual understanding about what the confidence in some result might really be when a number of 'standard deviations' are being quoted. Some of the proposed procedures for calculation need to be taken with caution. On the other hand, there is a clear need for the adoption of a standard method to allow the reliable intercomparison of quoted results and create a common understanding of the associated confidence.

A number of methods and formulae have been proposed together with sometimes extended mathematical derivation or justification (Ref. 1-4). It has become clear however, that some of these methods need to be taken with caution. On the other hand there is a very simple formula which is being widely used by X-ray astronomers providing a common understanding.

2. Statistical Significance. An example for the statistical situation which we like to discuss is given in Figure 1.

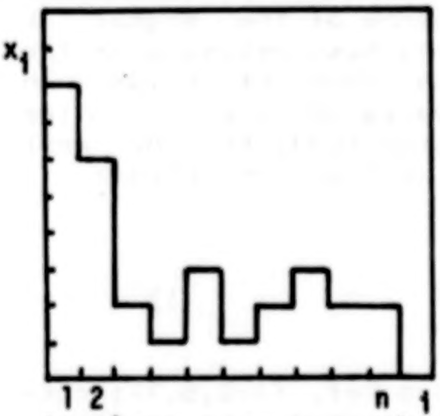

Fig. 1. Statistical example.

Numbers of events x_i are plotted versus bin number $i = 1....n$, corresponding to intervals of some physical variable (e.g. energy, phase, electric charge, time, ...). In the example given there seem to be 'excess events' in bins 1 and 2 as compared to the 'background' defined by the other bihs. The excess is

$$ON - \alpha OFF,$$

when ON and OFF are the integrated counts in channels 1 to 2 and in channels 3 to n, respectively and α is the ratio of the corresponding number of bins, here $2/(n-2)$.

ORIGINAL PAGE IS
OF POOR QUALITY

The general questions then are:
1. Does the excess correspond to the presence of a physical signal?
2. What is the 'significance of the signal'?

It is important to distinguish between these two questions. They correspond to the assumption that one out of two alternative hypothesis is true:
- the null hypothesis H0 is, that there really is only background,
- the hypothesis H1 is, that a true signal exists in addition to background.

When a statement is made about a statistical situation, it should be clear under which hypothesis this statement holds.

The first of the two questions may be answered by giving the probability for a chance occurance of the observed excess by a statistical fluctuation (under H0). It is of course necessary to use the proper statistic (e.g. binomial statistic for small numbers of events). If a low probability for the chance occurance of 'excess events' is found, it is then usually concluded that the presence of a 'physical signal' is likely. From there on hypothesis one is advocated and all statements made should refer to H1.

Only under H1 the term significance should be used. In particular the often used formula $(\mathrm{ON} - \alpha\,\mathrm{OFF}) / \alpha\sqrt{\mathrm{OFF}}$ is useless (as are a number of other formulae, see e.g. (4)). Also the probability which answers the first question should not be converted into a significance (as is sometimes done by using the integrated Gaussian distribution, even in cases where the Gaussian statistic does not apply).

In answering the second question then the presence of a signal is assumed (H1). The 'significance of the signal' k can be defined as the ratio of the best estimate of the signal to its uncertainty. In the case of Poissonian counting statistic for which the variance is equal to the mean a straightforward error propagation leads to the well known formula (in terms of the above defined variables):

$$\text{'significance'} \quad k = \frac{\mathrm{ON} - \alpha\,\mathrm{OFF}}{\sqrt{\mathrm{ON} + \alpha^2\,\mathrm{OFF}}} \qquad [1]$$

in units of standard deviations σ (see Ref. (3,5,6,7); note that in (3) this formula is interpreted incorrectly). Formula [1] may be also derived by using the more complicated maximum likelyhood ratio (6).

A general criticism of the work of (3) and to some extent of (1) and (2) is given in (6). While it is very important, not to overestimate statistical significance, Ref. (3) does too much, leading to an underestimate.

More recently, (5) has contributed significantly to the confusion by trying to show that formula [1] is incorrect and should be replaced by another complicated formula. The main argument is that the new formula fits much better to Monte Carlo simulations than formula [1] does. The whole discussion is misleading and suffers from the fact that no distinction between H1 and H0 is made: while formula [1] refers to H1 the Monte Carlo simulations as well as the new formula refer to H0, so their distributions are necessarily different.

For the example given in Fig. 1 (with a unit of 1 for the scale of counts x_i) the two questions can be answered as follows:

1. The probability (under H0) for a chance occurance of 14 events in bins 1 and 2 whith an average rate of 6 in two bins is ≤10-3, using binomial statistic (note that Poissonian statistic gives the somewhat larger probability of 3.6 x 10-3).
2. If one feels that the probability of 10-3 is low enough to postulate the existence of a physical signal (H1), then the significance of this signal is

$$k = \frac{14 - (2/10)\ 16}{\sqrt{14 + (2/10)^2\ 16}} = 2.6 \text{ standard deviations.}$$

To put it in other words again we consider Figure 2.

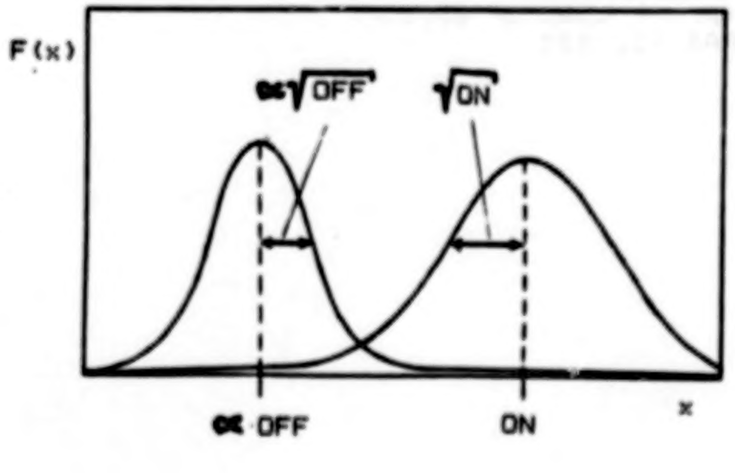

Figure 2. Representation of event number distributions.

If the signal $ON - \alpha OFF$ is compared to the standard deviation of the background $\alpha\sqrt{OFF}$, one gets an estimate for the chance occurance under the null hypothesis H0.
If, on the other hand, $ON - \alpha OFF$ is compared to both the standard deviations of the background and the signal, as is done by formula [1] under H1, one gets a different estimate. This is related to the probability that a second measurement (under identical conditions) will lead to a null result ($ON \le \alpha OFF$). It is this estimate that should be called 'significance of the detected signal'.

3. Final remarks

Values of significances in units of standard deviations are usually quoted when the detection of some signal is claimed. Consequently, a formula refering to H1 (existence of a signal) should be used.

Formula [1] has been widely adopted by X-ray astronomers and has as such served successfully as a standard allowing the reliable intercomparison of stated values of significance. It is up to the individual from what level of significance onward one starts to 'believe' in some reported result. Our personal view is that using formula [1] a minimum significance of 3 standard deviations (better yet 5) should be reached.

References

1. Hearn, D. 1969, Nucl.Instr.Methods 79, 200
2. O'Mongain, E. 1973, Nature 241, 376
3. Cherry, M.L. et al. 1980, Ap.J. 242, 1257
4. Li, T.P. and Ma, Y.Q. 1983, Ap.J. 272, 317
5. Li, T.P. and Ma, Y.Q. 1983, Proc.18th Int.Cosmic Ray Conf., Bangalore, XG 3-7, p.76
6. Nolan, P.L. 1982, preprint UCSD SP-82-15
7. Peterson, L. 1975, ARAA 13, 423

N85-34988
OG 9.5-11

A NEW APPROACH TO EVALUATE GAMMA-RAY MEASUREMENTS

De Jager O.C., J.W.H. Swanepoel,* B.C. Raubenheimer and D.J. van der Walt.

PU-CSIR Cosmic ray Research Unit; PU for CHE; 2520 Potchefstroom; SOUTH AFRICA

* Dept of Statistics; PU for CHE; 2520 Potchefstroom; SOUTH AFRICA

ABSTRACT: Misunderstanding about the term "random samples" and its implications may easily arise. Conditions under which the phases, obtained from arrival times, do not form a random sample and the dangers involved are discussed. Watson's U^2 test for uniformity is recommended for light curves with duty cycles larger than 10%. Under certain conditions, non-parametric density estimation may be used to determine estimates of the true light curve and its parameters.

1. INTRODUCTION: Consider a series of arrival times $t_i, i=1,\ldots,N$, of γ-rays from a certain source direction. The case is studied where the data contains a periodic component of strength p (pulsed counts/total counts) and period T. In the case of detectors with low count rates, the obvious requirement is to determine the significance of p as being due to a periodic source against the possibility that it is only a statistical fluctuation from the uniform background. The deduction of a possible light curve is also important. In this paper the following points are covered: (1) the problem of "random samples", (2) tests for uniformity, (3) non-parametric density estimators of the true periodic light curve and (4) the determination of the light curve parameters from the non-parametric density estimator.

2. THE PROBLEM OF "RANDOM SAMPLES": The measured data are the arrival times with the property $t_i > t_{i-1}$ $(i=2,\ldots,N)$. Assume this process, apart from the periodic component in the data, to be time independent. It is desirable to estimate the true light curve from the arrival times. This is done by folding the t_i's modulo 2π, with respect to a known period T. This results in the "sample" $(\theta_1,\ldots,\theta_N)$, with θ_i the so called phases which are calculated as

$$\theta_i = \frac{2\pi t_i}{T} \pmod{2\pi} = 2\pi\left|\frac{t_i}{T} - k\right|, \quad i = 1, \ldots, N, \ k \in \mathbb{N}^* \tag{1}$$

The choice of 2π is to allow the application of trigonometric functions on the phases. This sample has mostly been treated as being random. This sample would be random if and only if (a) all the θ_i's are identically distributed and (b) if they are statistically independent. If the phases do not form a random sample, then no conclusions about the "true underlying light curve" can be made. The fact is that the phases do not form a random sample! This can be seen as follows:

From eq. (1) the probability density functions (p.d.f) of θ_i and t_i are related by the following wrapping process (Mardia, 1972):

$$f_{\theta_i}(\theta) = \frac{T}{2\pi} \sum_{k=0}^{\infty} f_{t_i}\left(\frac{\theta T}{2\pi} + Tk\right) \tag{2}$$

Since $t_i > t_{i-1}$, it follows that $f_{\theta_i}(\theta) \neq f_{\theta_j}(\theta)$ for every θ and all $i \neq j$, thus proving that the θ_i's are not identically distributed. Furthermore $t_i = t_{i-1} + (t_i - t_{i-1})$, which implies that t_i is a function of t_{i-1}. Since θ_i is a function of t_i, it follows that θ_i is also a function of θ_{i-1}. This shows that the phases are not independently distributed. It should however be noted that if the time differences $v_i = t_i - t_{i-1}$ are used, a random sample would result by folding the v_i's.

From simulations of arrival times the following seems evident (let $b = E(t_i - t_{i-1}) = 1/\text{count rate}$): The distributions become approximately identical when $T < b$. If $T \approx b$, then it suffices to add a constant large time to each t_i, so that $t_i \gg 0$. This will ensure almost identically distributed random phases. If the period T equals the whole period of observation $(T \gg b)$, then

$$\theta_i = \frac{2\pi t_i}{T} \quad \text{and} \quad f_{\theta_i}(\theta) = \frac{T}{2\pi} f_{t_i}(\theta) \tag{3}$$

so that the phases are not identically distributed. The "runs-test" (Lindgren, 1976) was used to determine whether the phases are independently distributed: For $T < b$, the phases seem to be independent random variables and for $T \gg b$ there was strong evidence for dependency, which is also clear from eq. (3). Independency can with a 10% uncertainty be accepted for $T < 3b$. This result seems to be independent of the pulsed fraction.

ORIGINAL PAGE IS
OF POOR QUALITY

Thus, for T>3b, the true light curve cannot be estimated. In γ-ray astronomy this problem amounts to the case of astrophysical objects with periods that is large in comparison with b.

3. TESTS FOR UNIFORMITY: Let θ be a random variable with p.d.f. f(θ), which is assumed to be unknown. An appropriate test in this case would be some non-parametric test:

$$H_o: f(\theta) = U(\theta) = 1/2\pi \text{ against } H_1: f(\theta) \neq U(\theta) \qquad (4)$$

The alternative hypothesis H_1 only suggests that the unknown p.d.f. is different from uniformity. In order to compare tests, the following general form of f(θ), which covers most cases in γ-ray astronomy, was assumed:

$$f(\theta) = p_1 S(\theta;\, \mu_1,\, \delta_1) + p_2 S(\theta;\, \mu_2,\, \delta_2) + \frac{1-p_1-p_2}{2\pi} \qquad (5)$$

The pulsed fraction and phase (mean position) of each peak are denoted for i=1,2 by p_i and μ_i respectively, while δ_i refers to the FWHM of each peak, divided by the period T.

The two most commonly used tests for uniformity in γ-ray astronomy are:

1) χ^2-test: The advantage of this test is that it is a non-parametric test, but its drawback is the choice of the number of bins K (=degrees of freedom+1) and their positions on the phasogram. The best choice for K is $1/\hat{\delta}$, where $\hat{\delta}$ is some estimate of δ. From simulations it was evident that the sensitivity of this test increases with decreasing duty cycles.

2) Rayleigh test (Mardia, 1972): The motivation for the use of this test is its independence of bins. It is however a parametric test that was derived for von Mises alternatives. This corresponds to $p_1=1$, $p_2=0$ and $S(\theta;\mu_1,\delta_1)$ the von Mises distribution $M(\theta;\mu,\kappa)$. In the case of bimodal data (as with certain pulsars), the phase difference is ≈0,42 and the value of the test statistic $\bar{R}$ is small when $p_1 \approx p_2$. This is the result of two nearly opposing vectors, cancelling each other, when the test statistic

$$\bar{R} = \sqrt{(\bar{C}^2 + \bar{S}^2)} \quad \text{with } \bar{C} = \frac{1}{N}\sum_{i=1}^{N} \cos\theta_i;\ \bar{S} = \frac{1}{N}\sum_{i=1}^{N} \sin\theta_i \qquad (6)$$

is computed. Consequently bimodal data may be interpreted by this test as being uniform and real sources could then be discarded.

Two somewhat neglected non-parametric tests in this area of research are Kuiper's V_N test and Watson's U^2 test. Their distributions under H_o with the corresponding critical values are discussed by Mardia (1972). A brief outline of each test's algorithm is as follows:

3) Kuiper's V_N test: Let $\theta_{(1)},\ldots,\theta_{(N)}$ be the ordered phases. With $U_i=\theta_{(i)}/2\pi$, the test statistic is computed by

$$V_N = \max_i\left(U_i - \frac{i}{N}\right) - \min_i\left(U_i - \frac{i}{N}\right) + \frac{1}{N} \qquad (7)$$

so that only the minimum and maximum deviations from the uniform distribution are taken into account. It can intuitively be seen that this test will be sensitive to light curves with narrow duty cycles, but insensitive to those with broad duty cycles.

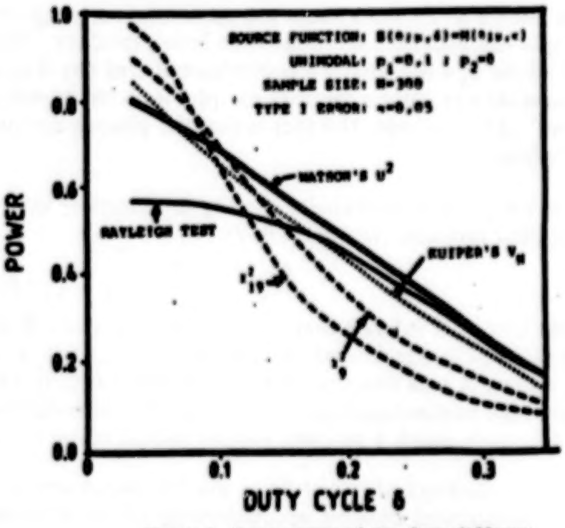

Figure 1 Power curves of the four different tests for uniformity. The light curve is assumed to be unimodal. The subscripts for the χ^2-test refer to the degrees of freedom.

4) Watson's U^2 test: With U_i as above, the statistic is computed as follows:

$$U^2 = \sum_{i=1}^{N} \left[U_i - \bar{U} - ((2i-1)/(2N)) + \tfrac{1}{2}\right]^2 + {}^1/_{12N} \qquad (8)$$

This is a type of a mean square error with respect to the uniform distribution, so that the information of each phase is taken directly into account in the calculation of U^2.

The procedure to determine which of these four tests is the best test, would be to find the test with the largest power. Since these tests are non-parametric, (except the Rayleigh test), one cannot expect to find a single test with the largest power for all choices of parameters in eq. (5). An indication of the relative performances of these tests are given in Figure 1, which was obtained through simulations of unimodal data. It can be seen that Watson's test is the best test for duty cycles larger than 10% and the χ^2-test is best for duty cycles less than 10%. In the latter case it can be seen that the power of the χ^2-test increases if the number of bins is increased. A good choice is $K \approx 1/\delta$. At small duty cycles it can be seen that the Rayleigh test performs badly relative to any other test. These conclusions remain independent of the pulsed fraction p_1.

The question obviously arises whether one may use these tests for uniformity when the phases are not random. The answer is yes, but it applies only to those kind of tests where the distribution of the test statistic is insensitive (robust) with respect to deviations from randomness. This has been investigated for the four discussed tests by looking for a change in the critical values as T increases with respect to b. Fortunately these values did not change, so that these tests may be used for any relation between T and b.

4. *NON-PARAMETRIC DENSITY ESTIMATION OF LIGHT CURVES:* Although a test for uniformity is a first step in identifying a source, the additional estimation of a light curve is very important. The usual method to display a light curve in γ-ray astronomy, is to bin the data into a histogram. The disadvantage of this method is that it is dependent on bin positions and their sizes. A more correct way to display an estimate of the true unknown p.d.f., is through the use of a non-parametric density estimator. This method assumes that the data is random. Since the light curve is a periodic one, a good estimator would be a truncated Fourier series. This estimate and its standard error can easily be computed. The application to estimation on a circle is as follows: Let the random sample be $D=(\theta_1,\ldots,\theta_N)$ with unknown p.d.f. $f(\theta)$. The characteristic function (c.f.) of $f(\theta)$ and its corresponding estimator are

$$\phi_p = \int_0^{2\pi} e^{ip\theta} f(\theta)\,d\theta = \alpha_p + i\beta_p \text{ and } \hat{\phi}_p = \hat{\alpha}_p + i\hat{\beta}_p = \left(\frac{1}{N}\sum_{i=1}^{N}\cos p\theta_i\right) + i\left(\frac{1}{N}\sum_{i=1}^{N}\sin p\theta_i\right) \qquad (8)$$

Using the inversion formula (Mardia, 1972) we obtain

$$f(\theta) = \frac{1}{2\pi}\left(1 + 2\sum_{p=1}^{\infty}(\alpha_p \cos p\theta + \beta_p \sin p\theta)\right)$$

The following asymptotically unbiased estimator of $f(\theta)$ is proposed:

$$\hat{f}(\theta;\, D,\, m) = \frac{1}{2\pi}\left(1 + 2\sum_{p=1}^{m}(\hat{\alpha}_p \cos p\theta + \hat{\beta}_p \sin p\theta)\right) \qquad (9)$$

where m is some "smoothing parameter". Using the method of cross-validation (Bowman, 1984), m can be estimated by $\hat{m}$, where $\hat{m}$ is that value of m which minimizes

$$\sum_{i=1}^{N}\left[\frac{1}{N}\int_0^{2\pi}\hat{f}^2_{N-1}(\theta;D_i,m)\,d\theta - \frac{2}{N}\hat{f}_{N-1}(\theta;D_i,m)\right] \text{ with } D_i=(\theta_1,\ldots,\theta_{i-1},\theta_{i+1},\ldots,\theta_N) \qquad (10)$$

The approximate confidence band of $f(\theta)$ is

$$\hat{f}(\theta;\, D,\, \hat{m}) \pm s\sqrt{(\mathrm{var}\,\hat{f})} \qquad (11)$$

with s=1.96 being the quantity determining the 95% confidence limit. The probability that the true p.d.f will be within the band, will be approximately 95%. Figure 2 displays an example of these bands. One can thus use these bands, in their own fashion, to determine the significance of periodic emission. For $\delta \ll 1$, one may encounter the problem of oversmoothing. Tabulated values of $\hat{m}$ for such cases will be presented by the authors.

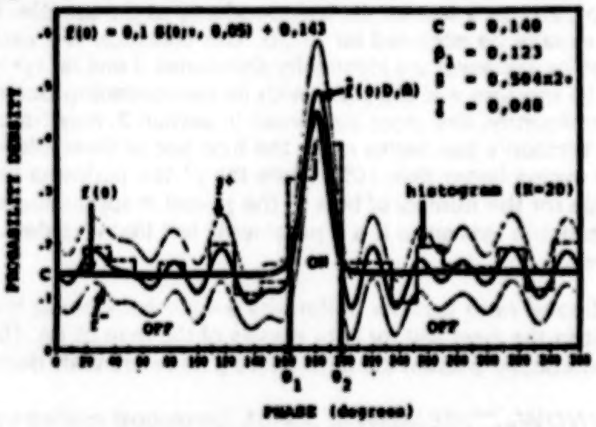

Figure 1 The density estimator $\hat{f}(\theta;D,\hat{m})$ of $f(\theta)$. The 95% confidence band is indicated by $\hat{f}^{\pm}$. The ON- and OFF-source regions are also indicated.

5. *LIGHT CURVE PARAMETERS FROM THE DENSITY ESTIMATOR:* Even if one does not have any knowledge of the true p.d.f $f(\theta)$, it is still desirable to know the light curve parameters. Since the estimator is asymptotically unbiased, one may estimate the desired parameters as follows:: Determine the pulsed region θ_1 and θ_2 roughly. Then determine the uniform background level c:

$$c = \left[\int_0^{\theta_1} f(\theta)d\theta + \int_{\theta_2}^{2\pi} f(\theta)d\theta \right] / \left[2\pi - \theta_2 + \theta_1 \right] \qquad (13)$$

Using this line of height c, determine a better estimate of the pulsed region. This may lead to a small improvement of c. Obtain the light curve parameters:

$$p = \int_{\theta_1}^{\theta_2} (\hat{f}(\theta)-c)d\theta \quad \text{and} \quad \mu = \int_{\theta_1}^{\theta_2} \theta(\hat{f}(\theta)-c)d\theta \;/\; p \qquad (14)$$

The duty cycle (FWHM) can be obtained graphically or numerically from the peak of the light curve. The latter can only be done when a specific source function $S(\theta;\mu,\delta)$ is assumed:

$$\sigma^2(\delta) = \int_{\theta_1}^{\theta_2} \theta^2 \, (\hat{f}(\theta)-c)d\theta \;/\; p - \mu^2 \qquad (15)$$

From these parameters one can obtain the significance of periodic emission in terms of the usual number of standard deviations NSIG from the uniform background. Using a normal distribution for $S(\theta;\mu,\delta)$ and the interval $\mu \pm 1.96\sigma$ (95% area under the normal curve for this interval) for the pulsed region, NSIG was computed for unimodal light curves with a 10% periodic signal. The results are presented in Figure 3. The latter can be used to determine the total number of events that is required to obtain a certain level of significance. From Figure 3 it can be seen that the smaller the duty cycle, the easier it is to identify a source. This method can also be applied to bimodal light curves.

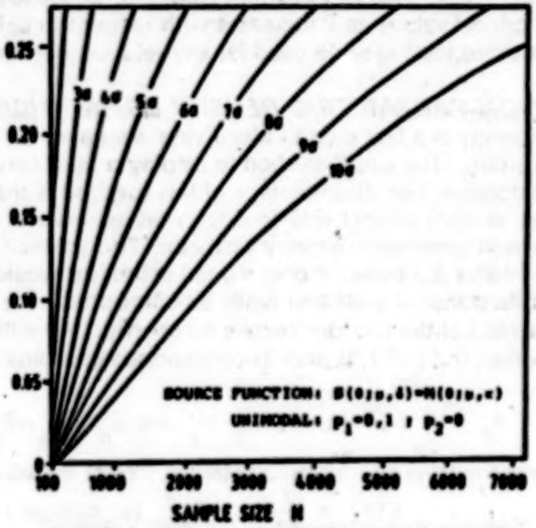

FIGURE 3 Contours of significance of periodic emission as function of the pulse-duty cycle and sample size.

6. CONCLUSIONS: When the phases are formed from the arrival times, great care should be taken if the periodic light curve and the corresponding parameters are to be estimated from the sample. In the first place analysis should be restricted to time independent processes (i.e. the form of the light curve should not change during the observation time). The next step would be to perform a test for the independency of the sample. The null-hypothesis of independency will usually be accepted for T<3b. This condition will usually also ensure that the sample variables (phases) are identically distributed if one let $t_1 >> 0$. Under these conditions the sample will be random and the p.d.f. with its corresponding parameters can be estimated. Certain tests for uniformity, like those discussed in section 3, may be used whether the sample is random or not. Watson's test seems to be the best test of those discussed for unimodal light curves with duty cycles larger than 10%, while the χ^2-test performs better at smaller duty cycles. The best choice for the number of bins in the χ^2-test is approximately $1/\delta$. The Rayleigh test is not a very dependable test since it is a parametric test that was derived for a very limited form of the light curve.

Likelihood ratio tests for uniformity are presently being investigated by the authors. This will result in the best test for light curves of the form of eq. (5). Such an analysis would automatically present the light curve parameters with their corresponding standard errors.

ACKNOWLEDGEMENTS: J.W.H. Swanepoel wishes to thank the South African CSIR for financial support.

REFERENCES:

1. Mardia, K.V. (1972). Statistics of Directional Data.
2. Lindgren, B.W. (1976). Statistical Theory, 3rd ed., p. 498.
3. Bowman, A.W. (1984). Biometrika V71, no 2, pp. 353-360

N85-34989

A NEW STATISTIC FOR THE ANALYSIS OF CIRCULAR DATA IN GAMMA-RAY ASTRONOMY

R.J. Protheroe
Department of Physics, University of Adelaide
Adelaide, South Australia 5001.

1. INTRODUCTION The analysis of directional data (see e.g., Mardia, 1972) is important in many fields of science. In particular, circular data, where each datum may be represented by a point on the circumference of a circle, often occur in astronomy. For example, the arrival of high energy photons from a pulsar recorded as a function of time may be plotted as a function of the pulsar phase and represented by points on the circumference of a circle if the period of the pulsar is known. In this case one would wish to test for evidence of pulsed emission of high energy photons. This would often be done by binning the data into a linear histogram and using conventional statistical tests such as the χ^2 test, etc., although this procedure has disadvantages for circular data. Alternatively, one may use statistical tests designed specifically for directional data. The latter include the Rayleigh test (see e.g. Mardia, 1972), Kuiper's Kolmogorov-Smirnov type test (Kuiper, 1960), Watson's Cramer-von Mises type test (Watson, 1961) and the Hodges-Ajne's test (Hodges, 1955; Ajne, 1968).

The Rayleigh test and the Hodges-Ajne's test are useful where a sinusoidal component is expected or when the excess events are expected to be concentrated over half the cycle (Ajne, 1968). Unfortunately, however, these tests are not powerful for detecting narrow peaked pulses in the presence of a uniform background. Tests for such a situation are highly desirable for testing, for example, for evidence of ultra-high energy γ-ray emission from neutron star binary X-ray sources where the duration of the γ-ray pulses is observed to be a small fraction of the orbital period (~0.007 in the case of Cygnus X-3 [Samorski and Stamm, 1983], ~0.02 in the case of Vela X-1 [Protheroe et al., 1984] and ~0.05 in the case of LMC X-4 [Protheroe and Clay, 1985]). I have recently proposed a new statistic which meets these requirements (Protheroe, 1985). Here, the test based on this statistic is outlined and its power compared with other tests.

2. PREVIOUS TESTS Leahy et al. (1983) have already shown that the Rayleigh test is not as powerful a test for the presence of narrow pulses as the χ^2 test after binning the data. In binning the data however, two decisions have to be made: (a) where to start binning (i.e. at what phase or direction); (b) how many bins to have (or what is the bin size). The optimum bin size will depend on how wide the pulse is, while ideally the bin origin should be chosen such that the pulse lies in the middle of a bin. This information is however usually not known a priori and O'Mongain (1973) has pointed out that re-binning the data would reduce one's confidence in any effect subsequently found. For example, Hillas (1975) has shown that if the bin origin is chosen to maximise the number of events in one bin then the significance of a high count is much less than if the bin origin had been chosen beforehand. An 'educated guess' is

ORIGINAL PAGE IS
OF POOR QUALITY

usually made as to how narrow a pulse could be. No guess can be made about the best bin origin however. This is clearly unsatisfactory and a statistic which requires no binning of the data but still provides a powerful test for narrow pulses will be proposed.

3. THE PROPOSED STATISTIC The requirements of the new statistic are: (i) it should be sensitive to the distance between pairs of points on the circle, having a high value if more points are closer together than expected; (ii) it should be sensitive to grouping of several points in the same region; (iii) the sensitivity to a very small distance between an individual pair of points should not be so great that an "accidentally" close pair dominates the statistic. I will define the distance between two observations x_i and x_j as

$$\Delta_{ij} = 0.5 - |\{|(x_i - x_j)| - 0.5\}|. \qquad (1)$$

Averaging $1/\Delta$ over adjacent pairs would satisfy (i), averaging over all pairs would satisfy (ii) and averaging $(\Delta + 1/n)^{-1}$ over all pairs would satisfy (iii). I have therefore proposed the following statistic:

$$T_n = \frac{2}{n(n-1)} \sum_{i=1}^{n-1} \sum_{j=i+1}^{n} (\Delta_{ij} + 1/n)^{-1} \qquad (2)$$

Its null distribution has been computed using Monte Carlo methods for n ranging from 2 to 200. Crictical values for $\alpha = 0.1, 0.05, 0.01$ and 0.005 are given in Table 1 for several values of n. Coefficients of a 4th order polynomial in $\ell n(n)$ are given in Table 2 to facilitate interpolation for other values of n in this range.

The power function (e.g. Hoel, 1971) of the test for $n=50$ and $\alpha=0.05$ has been calculated by the Monte Carlo method for the alternatives to a uniform distribution in the form of a uniform distribution plus a von Mises distribution (e.g. Mardia, 1972).

$$f(x) = (1-b) + b \exp[\kappa \cos 2\pi(x-x_0))]/I_0(\kappa) \quad (3)$$

where

$$I_0(\kappa) = \sum_{r=0}^{\infty} \frac{1}{r!^2} (\kappa/2)^{2r}, \qquad (4)$$

κ is the concentration parameter and b is the fraction of all events which are not uniformly distributed. The resulting contours of constant power are plotted in Fig 1. The 99% contour for the Rayleigh test has been added to Fig. 1 for comparison. Also shown are 99% contours for tests using Kuiper's V_n and Watson's U^2 statistics and the test based on the statistic Z_1^2 used by Buccheri et al. (1983) in their search for γ-ray emission from radio pulsars. Note that all the tests have very similar powers for broad pulses but that T_n is considerably more powerful than the others for narrow pulses.

4. CONCLUSION I have proposed a new statistic for the analysis of circular data. The test based on this statistic has recently been used in a search for ultra-high energy γ-ray from neutron star binary X-ray sources (Protheroe and Clay, 1985). The statistic is designed

n	α = .10	.05	.01	.005
2	1.82	1.90	1.98	1.99
3	2.24	2.40	2.68	2.78
4	2.60	2.78	3.15	3.28
5	2.91	3.09	3.49	3.65
6	3.17	3.36	3.77	3.94
7	3.40	3.59	4.01	4.18
8	3.61	3.80	4.21	4.38
9	3.80	3.98	4.39	4.56
10	3.97	4.15	4.55	4.72
12	4.27	4.44	4.82	5.00
14	4.53	4.69	5.06	5.23
16	4.75	4.92	5.27	5.44
18	4.96	5.11	5.45	5.62
20	5.14	5.29	5.62	5.78
30	5.86	5.99	6.28	6.42
40	6.38	6.50	6.76	6.89
50	6.79	6.90	7.14	7.26
60	7.12	7.23	7.46	7.57
70	7.41	7.51	7.73	7.83
80	7.66	7.75	7.96	8.05
90	7.88	7.97	8.16	8.25
100	8.07	8.16	8.35	8.43
120	8.42	8.50	8.66	8.74
130	8.57	8.64	8.80	8.88
140	8.71	8.78	8.92	9.00
160	8.96	9.03	9.15	9.22
180	9.19	9.25	9.34	9.41
200	9.39	9.44	9.51	9.58

Table 1. Critical values $T_{n,\alpha}$ for the proposed test of uniformity with the test statistic T_n (equation 2). $\Pr(T_n > T_{n,\alpha}) = \alpha$. (Reproduced from Protheroe, 1985).

α	0.1	0.05	0.01	0.005
A_0	1.368	1.214	0.5523	0.3170
A_1	0.3467	0.8400	2.3416	2.807
A_2	0.4862	0.2436	−0.4819	−0.6597
A_3	−0.07407	−0.02658	0.1155	0.1418
A_4	0.004515	0.001132	−0.009005	−0.01038

Table 2. Polynomial Coefficients for interpolating $T_{n,\alpha}$. The 4th order polynomial $T_{n,\alpha} = \sum_{i=0}^{4} A_i [\ln(n)]^i$ is valid for $2 < n < 200$. . (Reproduced from Protheroe, 1985).

specifically for situations where one requires a test of uniformity which is powerful against alternatives in which a small fraction of the observations are grouped in a small range of directions, or phases.

ACKNOWLEDGEMENTS This work has been supported in part by provision of a Queen Elizabeth II Fellowship and by a grant from the Australian Research Grants Scheme.

REFERENCES

Ajne, B., 1968: Biometrika, 55, 343-354.

Buccheri, R. et al., 1983: Astron. Astrophysics, 128, 245-251.

Hillas, A.M., 1975: Proc. 14th Int. Cosmic Ray Conf. (Munich), 9 3439-3443.

Hodges, J.L., 1955: Ann. Math. Statist., 26, 523-527.

Hoel, P.G. 1971: "Intoduction to Mathematical Statistics" 4th Edition (New York: J. Wiley and Sons).

Kuiper, N.H. 1960: Ned. Akad. Wet. Proc., A63, 38-47.

Leahy, D.A. et al., 1983: Astrophys. J., 272, 256-258.

Lloyd-Evans, J. et al., 1983: Nature, 305, 784-786.

Mardia, K.V. 1972: "Statistics of Directional Data" (London: Academic Press).

O'Mongain, E. 1973: Nature, 241, 376-379.

Protheroe, R.J., et al. 1984: Ap.J. (Lett.), 280, L47-L50.

Protheroe, R.J. 1985: Astron. Expr. (submitted).

Protheroe, R.J. and Clay, R.W. 1985: Nature, in the press; see also these proceedings, paper OG 2.6-10.

Samorski, M. and Stamm, W. 1983a: Proc. 18th Int. Cosmic Ray Conf. (Bangalore), 1, 135-138.

Watson, G.S. 1961: Biometrika, 48, 109-114.

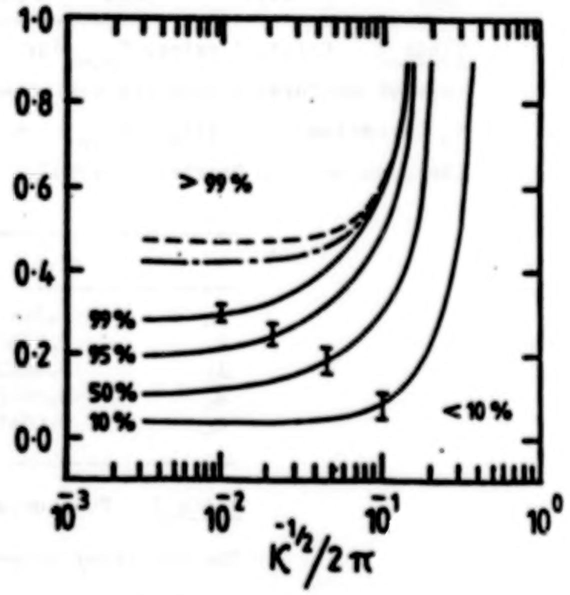

Figure 1. Contour map of the power function P(b, κ) for α = 0.05 for the test based on the statistic T_n. 99% contours for the Rayleigh test (dashed line) and Kuiper's test (chain line) are also given for comparison. (The 99% contours for the Z_2^2 test and for Watson's test are indistinguishable from that for Kuiper's test).

THE ANGULAR RESOLUTION OF AIR SHOWER GAMMA RAY TELESCOPES

C.Morello, G.Navarra (•), L.Periale and P.Vallania

Istituto di Comogeofisica del CNR and
(•) Istituto di Fisica Generale dell'Università di Torino, Italia

A crucial characteristic of air shower arrays in the field of high energy gamma-ray Astronomy is their angular resolving power, the arrival directions being obtained by the time of flight measurements. An approach to the optimization of "air shower array-telescopes" has been recently discussed by J.Linsley (1). By using the small installation operating at the Plateau Rosà station (3500 m a.s.l.) we have studied the resolution in the definition of the shower front as a function of the shower size.

The apparatus (2) consists of four liquid scintillator detectors positioned at the corners of a rhombus (7 x 14 m diagonals, 8 m side). The detectors dimensions are 100 x 100 x 30 cm^3, each of them is viewed by two photomultipliers placed at two opposite corners.
The traversal of a particle is defined by the coincidence of the two photomultipliers and its arrival time by the mean of the two detection times (the discrimination is done in leading edge mode, at a 0.25 particle Level).An EAS is defined by a four-fold coincidence.
The timing resolution is obtained by measuring $\Delta T = T_1 - T_2$ ($\delta T = 50$ ps step), where T_1 and T_2 are the time of flights between the detectors placed at the vertex of two parallel sides.
Different shower sizes are selected by measuring the particle density on a central plastic scintillator (0.5 m^2 area, 15 cm thick), see Fig. 1. For given thresholds in the number of particles (N) on the central detector: the mean number $\bar{n}$ of particles on each 1 m^2 detector, the mean distance $\bar{r}$ from the shower core, and the mean primary energy $\bar{E}_o$, are calculated on the hypotesis of pure electromagnetic cascades.
Due to the tails in the timing distributions we have defined our errors as the half widths of the distributions at half maxima (HWHM). The measured HWHM of the response of an isolated detector to the trasversal of a single particle is $S_{id} = 1.25$ ns and that of the sole electronic syxtem (including the rise time fluctuations of the PM s) is $S_{ie} = 0.59$ ns. Since we don't expect the temporal response of the detector being constant as a function of the number of particles on it, we have used for the instrumental uncertainties (S_i) the two extreme values S_{id} and S_{ie}. After subtracting from the HWHM (S) of the distribution of T_1-T_2

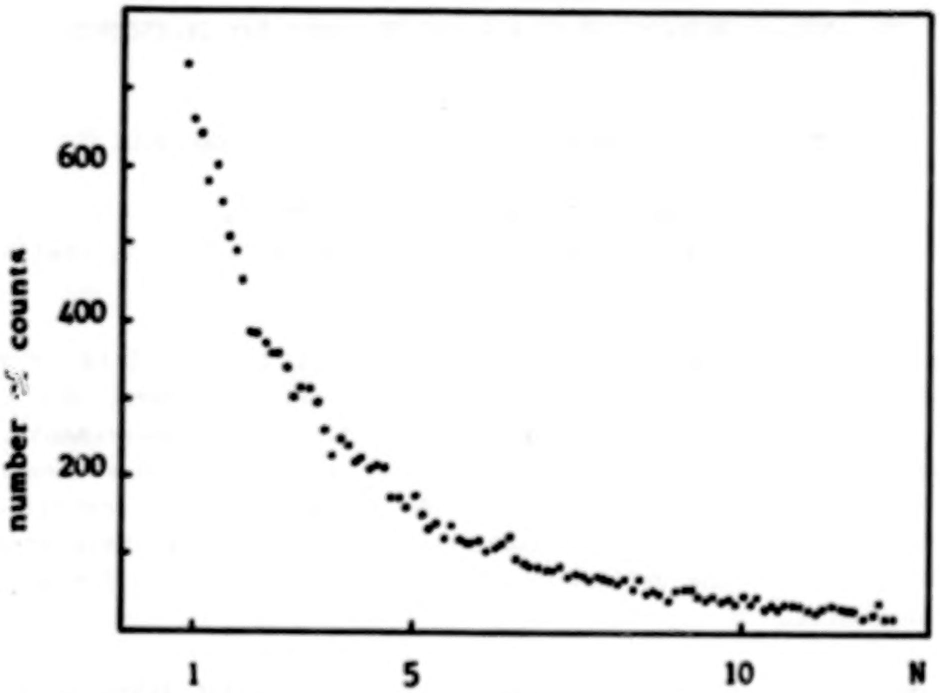

Fig.1: Pulse height spectrum of the central detector triggered by the *fourfold* coincidence. The cut on the left side is due to the ADC threshold.

such instrumental resolution, we obtain the physical limit to the accuracy in the definition of the shower front as a function of N. Fig. 2 shows such accuracies:

a) measured ($\sqrt{(S_N/2)^2 - S_i^2}$);

b) deduced from the resolution measured at the 1 particle level,

scaling by $1/\sqrt{\bar{n}}$ ($S_V/\sqrt{\bar{n}}$, $S_V = \sqrt{2\,(S_o/2)^2 - S_i^2}$);

c) obtained by using the Linsley's formula ($2.6\,(\bar{r}/30 + 1)^{1.5}/\sqrt{\bar{n}}$ ns, $\bar{r}$ in m)
agaist N, $\bar{n}$, $\bar{r}$, $\bar{E}_o$.

It can be seen that the trend of the measured resolutions as $1/\sqrt{\bar{n}}$ is verified inside the uncertainty of the instrumental dispersion and also the absolute values do not move much away from those obtained by using the Linsley's formula.

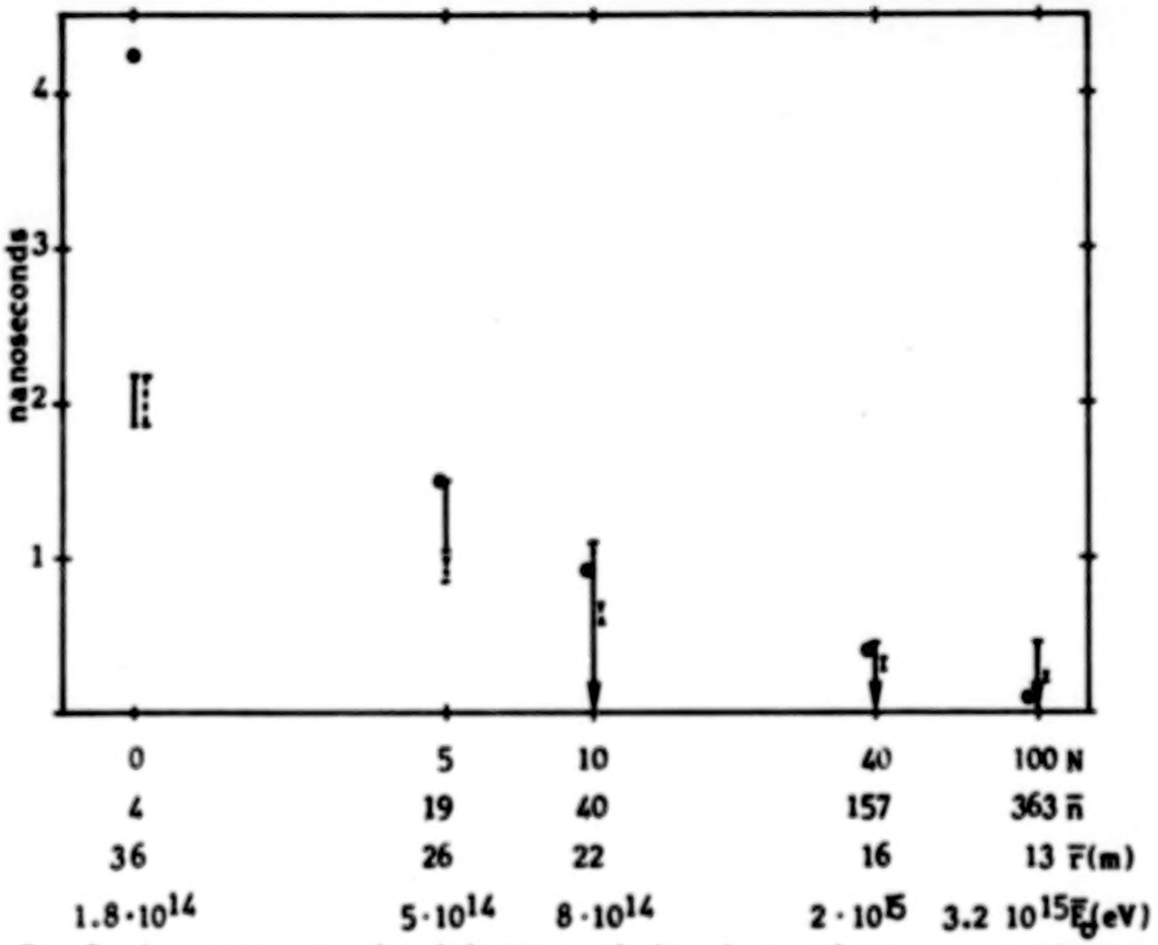

Fig.2: Accuracies in the definition of the shower front: a- continuous line; b- dotted line; c- full dots (see text).

At our atmosperic depth and by using detectors of 1 m^2 area an accuracy in the definition of the shower front $\delta t < 0.5$ ns can be reached at primary energies $\bar{E}_o \sim 2.10^{15}$ eV at a typical core distance $\bar{r} = 16$ m.

References

1. Linsley J. (1984), Research Note UNML - 7/6/84, University of New Mexico, Albunquerque.

2. Morello C. and Navarra G., (1981), N.I.M., 187,533

AUTHOR INDEX

ACHARYA, BS
254,262
278
ADAMS, JH
282
AGNETTA, G
334
AGRINIER, B
314,311
318,359
334
AHLEN, SP
258
AKIMOV, VV
330
ALLKOFER, OC
418
ALTHOUSE, WE
299,395
ANDERSON, KA
326
AN, SY
179
AOKI, T
410
APTE, AR
469
ARCORAGI, JP
167
ARNOULD, M
167
BAKER, RG
391,338
BALASUBRAHMANYAN, VK
254,262
278
BALIBANOV, VM
330
BARWICK, SW
258
BASILI, A
355
BAZER-BACHI, AR
330
BEAHM, LP
282
BECK, R
118,140
BEER, J
99
BENNETT, K
383
BEREZHKO, EG
152
BERTSCH, DL
338
BIELAOUSSOV, AS
330
BIGNAMI, GF
383
BINNS, WR
287,13,13
272,95
BLAKE, JB
21
BLOEMEN, JBGM
387,383
BODIFEE, G
171
BOELLA, G
322
BOGDAN, TJ
144,140
250
BONFAND, E
314,318
BOSTICK, WH
183
BRECHTMANN, C
99
BRETTHORST, GL
58
BREWSTER, NR
1
BRISSENDEN, RJV
442
BROOKE, G
426
BUCCHERI, R
387,383
BUI-VAN, A
359
BUTLER, RC
322
BYKOV, AM
67
CARAVEO, PA
383
CARDINI, D
355
CAROLI, E
322
CARTER, JN
314,322
311,318
CASSE, M
167
CAWLEY, MF

PRECEDING PAGE BLANK NOT FILMED

AUTHOR INDEX

CAWLEY, MF
453
CHABAUD, JP
334
CHADWICK, PM
406
CHARALAMBOUS, PM
322
CHESNEY, JR
338
CHUANZAN, Y
37
CIAMPA, D
414
CLAY, RW
442,414
CLINE, T
347,343
CLINE, TL
307,303
CONNELL, JJ
272
COOK, WR
299,395
CORANI, CL
414
COSTA, E
355,334
COWSIK, R
242
CUMMINGS, AC
299
DA COSTA FEREIRA NERI, A
359
DAI, C
371
DAL FIUME, D
355
DAWSON, BR
414
DE JAGER, OC
481
DE LOORE, C
171
DEAN, AJ
322,379
398
DERDEYN, SM
338
DI COCCO, G
322
DI RAFFAELE, R
334
DIPPER, NA
379,406
DOBRIAN, LB
330
DOGIEL, VA
195
DORFI, EA
115,136
148,121
DOUGHERTY, MK
83
DOWTHWAITE, JC
406
DRACH, J
29
DRECHSEL, H
99
DRURY, LOC
136,148
118,121
140
DUROUCHOUX, PH
326
EDWARDS, PG
414
EHRMANN, CH
338
EICHLER, D
124,124
ELBERT, JW
457
ELLISON, DC
128,124
ELTON, SD
442,414
EMANUELE, A
355
ENGE, W
286
ESPOSITO, JA
262,278
FAN, CY
160
FAN, Z
371
FEGAN, DJ
453
FERRANDO, P
402,61
FICHTEL, CE
338,338
FINGER, MH
295,299
FISHMAN, GJ

AUTHOR INDEX

FISHMAN, GJ
347,343
351
FIXSEN, DJ
287
FRABEL, P
334
FRADKIN, MN
330
FRANCESCHINI, T
355
FRASER-MITCHELL, J
398
FRONTERA, F
355
FRYE, GM
314,311
318
GALPER, AM
330
GARRARA, TL
287
GARRARD, TL
13,95
GEHRELS, N
307,303
GERARDI, G
334
GIBBS, K
453
GILER, M
17,234
GINZBURG, VL
71
GOLDEN, RL
268
GOPALAKRISHNAN, NV
469
GORET, P
268,402,61
GORHAM, PW
453
GOUIFFES, C
314,359
334
GOULD, RJ
207
GRAEME, G
322
GREGORY, AG
414
GREVESSE, N
5
GRIGORIEV, VA
330
GRIMM, G
287
GROS, M
330
GUPTA, M
42
GUREVICH, AV
195
GU, Y
371
HALL, CJ
314,311
318
HANSON, CG
398
HARA, T
430
HATANO, Y
430
HAYASHIDA, N
430
HE, CX
430
HEINRICH, W
230,99,278
HENKEL, M
278
HERMSEN, W
387,383
HIGASHI, S
410
HIGDON, JC
63
HILLAS, AM
449,453
HONDA, M
430
HOPKINS, CJ
398
HUNTER, SD
391,338
HURLEY, KC
326
HUTERS, AF
307,303
IOURKINE, YT
330
ISHIKAWA, F
430
ISRAEL, MH
287,13,272
95

AUTHOR INDEX

ISTOMIN, YAN
195
JACQUES, JS
338
JENKINS, TL
314,311
318
JOKIPII, JR
156,132
KALINKIN, LF
330
KAMATA, K
430
KAMIYA, Y
410
KANBACH, G
383
KASAHARA, K
473
KAZANAS, D
128
KERTZMAN, MP
1,95
KIFUNE, T
430
KIRKMAN, IW
406
KIRRILOV-UGRIUMOV, VG
330
KISH, JC
87
KITAMURA, T
410
KLARMANN, J
287,13,272
95
KOCH-MIRAMOND, L
42
KOCH, D
363
KO, CM
156
KRYMSKY, GF
152
KURNOSOVA, LV
330
KUZNETSOVA, RI
199
L'HEUREUX, J
276
LA PADULA, C
322
LAMBERT, A
426,445
LAMB, RC
453
LANDINI, G
355
LANDREA, MF
334
LAUBENTHAL, NA
338
LAU, KH
91
LAVIGNE, JM
330,359
LAVRUKHINA, AK
199,203
LEBRUN, F
387,383
LEE, MA
144
LERAY, JP
330
LERCHE, I
144,226
222
LETAW, JR
33,46,238
103
LEVENTHAL, M
307,303
LEWIS, RA
379,398
LIEBING, DF
453
LIEKOV, NG
330
LIN, RP
326
LINSLEY, J
434,438
461,465
LLOYD-EVANS, J
445,254
262
LONG, JL
375
LOWDER, DM
258
LUHMANN, JG
79
LUST, R
50
MACCALLUM, CJ
307,303
MACKEOWN, PK
453

AUTHOR INDEX

MAGGIOLI, P
322
MANDROU, P
334
MARGOLIS, AH
38
MARGOLIS, SH
13,21,58
MASNOU, JL
334
MASSARO, E
334
MASSE, P
42,330
MATHIS, KD
230
MATSUBARA, Y
430
MATSUNO, S
410
MATTESON, JL
326,347
343
MAUGER, BG
278
MAY, EN
371
MAYER-HASSELWANDER, HA
387,383
MCBREEN, B
367
MCCOMB, TJL
406
MCKENZIE, JF
83,111
MEEGAN, CA
347,343
351
MEWALDT, RA
91
MEYER, JP
5
MEYER, P
50,276
MITSUI, K
410
MIZUTANI, K
410
MORELLI, E
355
MORELLO, C
489
MORFILL, GE
132
MORFILL, P
50
MORI, M
430
MULLER, D
266,276
MURAKI, Y
410,410
NAGANO, M
430
NARDI, V
183
NATALUCCI, L
322
NAVARRA, G
489
NESTEROV, VE
330
NEWPORT, BJ
287,95
NIEL, M
326,334
NISHIJIMA, K
430
O'NEILL, T
342
OGDEN, PA
426
OHASHI, Y
410
OHNO, Y
430
OHOKA, H
430
OKADA, A
410
ORFORD, KJ
406
ORMES, JF
254,262
278
OSEROV, YV
330
OWENS, A
314,311
318
PACIESAS, W
347,343
PACIESAS, WS
351
PARLIER, B
330
PARNELL, TA
347,343

AUTHOR INDEX

PATEL, M
426
PATTERSON, JR
414
PAUL, JA
383
PEHL, RH
326
PELLING, MR
326
PENDLETON, GN
314,311
318
PERELYGIN, VP
9
PERIALE, L
489
PEROTTI, F
322,379
PERRETT, JC
426
PETERSON, LE
326
POPOV, AV
330
PORRECA, G
307
PORTER, NA
453
POULSEN, JM
355
PRANTZOS, N
167
PRESCOTT, JR
414
PRICE, PB
258
PRILUTSKY, OF
330
PRINCE, TA
295,299
PROTHEROE, RJ
485
PTUSKIN, VS
71,75
RAMSDEN, D
314,311
318
RAUBENHEIMER, BC
481
REBER, JD
303
REFLOCH, A
318
REID, RJO
426
RODIN, VG
330
ROSS, RW
338
ROUAIX, G
334
RUBINI, A
355
RUEDA, A
191
SABAUD, C
359
SACCO, B
383,334
SAKURAI, K
25
SALAMON, MH
29
SALVATI, M
334
SAMORSKI, M
418
SAOAMON, MH
258
SATO, T
410
SCARSI, L
334
SCHINDLER, SM
299
SCHLICKEISER, R
54,226,250
222
SCHULZ, M
79
SERMUND, G
286
SHAPIRO, M
163
SHAPIRO, MM
238
SHEN, C
371
SHIBATA, S
410
SIEGMON, G
286
SILBERBERG, R
33,46,238
103
SILVESTRI, S
355

AUTHOR INDEX

SIMONE, J
342
SIMON, M
230,278
SIMPSON, GA
286
SOMMERS, P
457
SOROKA, F
330
SOUTOUL, A
61
SPADA, G
322
SPIZZICHINO, A
322
STAMM, W
418
STANG, PD
307,303
STARR, CH
299
STAUBERT, R
477
STENGER, VJ
453
STEPHEN, JB
322
STEPHENS, SA
254
STILLER, B
282
STONE, EC
287,299,95
91
STRAUSS, MA
258
STREITMATTER, RE
254,262
278
STRONG, AW
387,383
SUN, Y
371
SUWADA, T
410
SWANEPOEL, JWH
481
SWEENEY, W
342
SWORDY, SP
266,276
SZABELSKA, B
234
TABARY, A
314,318
334
TAKAHASHI, T
410
TANAHASHI, G
430
TEEGARDEN, BJ
347,307
343,303
TESHIMA, M
430
THIELHEIM, KO
210,214
218
THOMPSON, DJ
338
TITTEL, HO
278
TOMOZAWA, Y
187
TONWAR, SC
469
TOPTYGIN, IN
67
TORII, S
473
TSAO, CH
33,46,238
103
TSUIKIN, EI
330
TUELLER, J
307,303
TUMER, OT
342
TURPANOV, AA
152
TURVER, KE
406
UBERTINI, P
322
UMA, V
469
VALLANIA, P
489
VAN DER WALT, DJ
481
VEDRENNE, G
326,359
334
VILLA, G
322
VOLK, HJ

AUTHOR INDEX

VOLK, HJ
148,140
VORONOV, SA
330
WADDINGTON, CJ
287,13,1
95
WATSON, AA
426
WDOWCZYK, J
234
WEBBER, WR
42,286,87
WEBB, GM
144,107
246
WEEKES, TC
422,453
WEST, AA
426
WESTERGAARD, NJ
83
WHITE, RS
342,375
WIBIG, T
17
WIEDENBECK, ME
291
WILD, NR
442
WILSON, RB
347,343
351
WOLFENDALE, AW
234
YADAV, JS
9
YANAGITA, S
175
YELSHIN, VK
152
YOUNG, NGS
322
YOUNIS, FA
322
YU, C
37
YUDA, T
473
ZANK, AP
111
ZANROSSO, EM
375
ZHAN, S
ZHAN, S
37
ZYBIN, KA
195
ZYCH, AD
342,375

BIBLIOGRAPHIC DATA SHEET

1. Report No. NASA CP-2376 Volume 3

2. Government Accession No.

3. Recipient's Catalog No.

4. Title and Subtitle
19th International Cosmic Ray Conference
Conference Papers

5. Report Date August 1985

6. Performing Organization Code 665

7. Author(s) Frank C. Jones, compiler

8. Performing Organization Report No.

9. Performing Organization Name and Address
Laboratory for High Energy Astrophysics
Goddard Space Flight Center
Greenbelt, MD 20771

10. Work Unit No.

11. Contract or Grant No.

12. Sponsoring Agency Name and Address
National Aeronautics and Space Administration
Washington, D. C. 20546

13. Type of Report and Period Covered Conference Publication

14. Sponsoring Agency Code

15. Supplementary Notes

16. Abstract

These volumes contain papers submitted for presentation at the 19th International Cosmic Ray Conference, held on the campus of the University of California, San Diego, in La Jolla, CA., August 11-23, 1985. The conference is held every other year. The present volume contains papers with Paper Codes OG 7.1 through OG 9.5 and deals with cosmic-ray sources, acceleration and propagation through the galaxy. This volume also contains papers on the various experimental techniques used in detecting.

17. Key Words (Selected by Author(s))
cosmic-ray sources, cosmic-ray acceleration, cosmic-ray propagation, shock acceleration, cosmic-ray instruments, gamma-ray telescopes, air-shower arrays

18. Distribution Statement
Unclassified - Unlimited

Subject Category - 93

19. Security Classif. (of this report) Unclassified

20. Security Classif. (of this page) Unclassified

21. No. of Pages

22. Price*

*For sale by the National Technical Information Service, Springfield, Virginia 22161

GSFC 25-44 (10/77)

STAR 22 SEP 11 1985

NASA-CP-2376-vol.4

19TH INTERNATIONAL COSMIC RAY CONFERENCE

LA JOLLA, USA AUGUST 11-23, 1985

CONFERENCE PAPERS

SH

SESSIONS
VOL. 4

(NASA-CP-2376-Vol-4) NINTEENTH INTERNATIONAL COSMIC RAY CONFERENCE. SH SESSIONS, VOLUME 4 (NASA) 543 p HC as boxed set only $200/MF A01 per volum CSCL 03B G3/92
N85-34729 THRU N85-34861 Unclas 20931

19TH INTERNATIONAL COSMIC RAY CONFERENCE

LA JOLLA, USA AUGUST 11-23, 1985

CONFERENCE PAPERS

SH

SESSIONS
VOL. 4

PUBLICATION COMMITTEE

F.C. Jones, Chm.
J. Adams
G.M. Mason

NASA Conference Publication 2376

Published by
Scientific and Technical Information Branch
National Aeronautics and Space Administration
Washington, D.C. 20546

August 1985

For sale by the National Technical Information Service, Springfield, VA 22151

PREFACE

The 19th International Cosmic Ray Conference, under the auspices of the Cosmic Ray Commission of the International Union of Pure and Applied Physics, is being held on the campus of the University of California, San Diego, on 11 through 23 August 1985. In keeping with the tradition begun in 1971 by the Australian organisers of the 12th ICRC, the Proceedings of this conference are appearing in two sets of volumes. The first set, consisting of volumes 1 through 8, is being distributed to all participants at the beginning of the conference. This set contains the contributed papers. The second set, distributed after the conference, contains invited, rapporteur, and highlight papers. The papers are reproduced here exactly as they were received from the authors, without refereeing.

For the 19th ICRC, the scientific program was organised according to three major divisions— OG (cosmic rays and gamma rays of Galactic Origin), SH (Solar and Heliosphere), and HE (High Energy). Technical papers are included in each of the three divisions.

This conference depended on funds from several agencies of the United States government, including major financial support from the National Aeronautics and Space Administration and support from the National Science Foundation, the Department of Energy, and the Air Force Geophysics Laboratory. Important financial support also came from the Center for Astrophysics and Space Sciences of the University of California, San Diego, from the California Space Institute of the University of California, from the Department of Physics and Astronomy of the University of Maryland, College park, from the International Union for Pure and Applied Physics, and from several corporate sponsors who will be acknowledged by name in the post-conference volumes.

We appreciate the confidence placed in the conference organisers by the Cosmic Ray Commission, and acknowledge with thanks the role of the Commission members in setting up the rules for the conference and in advising the organisers during its planning.

We are grateful to all of the members of the various organising committees listed at the front of this volume. The three Program Committees went to great effort to organise a coherent scientific program and to schedule four parallel sessions with a minimum of conflicts. The Local Organising Committee has worked long and hard to ensure efficient and hospitable accommodations for all the participants, both in the scientific sessions and outside them. The Publications Committee not only took great pains to assemble these volumes but also maintained an orderly data base of papers and authors which was extremely helpful to the program committees. The General Organising Committee made important contributions of ideas and efforts to make the conference possible; this committee included international representation from all of North America, thus the departure from the traditional name of National Organising Committee. And the entire effort was coordinated by the dedicated members of the Steering Committee.

August, 1985

Martin H. Israel, Chairman
General Organizing Committee

LETTER FROM THE EDITORS

This conference marks a departure from previous conferences in this series in that the publication of the Conference Papers was carried out an entire continent away from the activities of Local Organising Committee. This posed some problems but, to the considerable surprise of the Publications Committee members, the one that was expected to be the most trouble turned out not to be significant. The overwhelming majority of those submitting papers and abstracts sent them to the correct address, not to La Jolla as was feared. We wish to thank our many authors for their alertness and commend them for handling a complicated situation so well.

There are eight volumes to be distributed to the conference participants in addition to the Conference Program and Author Index: three volumes for OG, two for SH and three for HE. the detailed makeup of these volumes is described in the prefaces written by the Scientific Program chairmen for their respective volumes. Out of some 1100 abstracts that were accepted by the Scientific Program Committees for inclusion in the conference some 929 papers were finally received in time for inclusion in the Conference Papers. This represents a response of approximately 84 percent, a modest improvement. Even if one excludes the 42 one page papers that should be considered as 'confirming abstracts', even though there was no such formal category, the response was somewhat higher than that of recent years. We attribute this to the carrot of a later deadline than before coupled with the stick of there being no printing of post deadline contributed papers. We believe that this decision of the General Organizing Committee was a vise one. Of course invited, rapporteur, and highlight talks will be printed in volumes to be distributed to the participants after the conference as usual.

The Publications Committee had much generous help in performing its duties: from Goddard Space Flight Center we had the help of B. Glasser, L. Harris, E. Schronce, N. Smith, J. Esposito and T. Smith. From the Naval Research Laboratory we were helped by T. Massotta, and at the University of Maryland M. L. Snidow and J. Mucha gave much needed assistance. Special thanks are due to Caryl Short, the lone staff member of the Publications Committee. She maintained the computer data base, organised the abstracts as they arrived, and kept track of the papers themselves to see that the finally arrived in the right place at the right time. Without her help the job would have been far more difficult than it was.

PUBLICATIONS COMMITTEE August, 1985

Frank C. Jones, Chm.
Jim Adams
Glen M. Mason

SH SESSIONS
VOLUME IV

19th INTERNATIONAL COSMIC RAY CONFERENCE
LA JOLLA, USA
AUGUST 11-23, 1985

INTERNATIONAL UNION OF PURE AND APPLIED PHYSICS
MEMBERS OF THE COMMISSION ON COSMIC RAYS OF IUPAP

A.E. Chudakov, Chm.
F.B. McDonald
G.C. Castagnoli
P.H. Fowler
D. Hovestadt
J. Kota
T.O. Montmerle
H. Moraal
J.R. Prescot
B.V. Sreekantan
K. Suga
J. Wdowczyk

STEERING COMMITTEE

F. McDonald, Chm.
G. Burbage
M. Forman
T. Gaisser
M. Israel
F. Jones
R. Lingenfelter
R. Mewaldt
L. Peterson

GENERAL ORGANIZING COMMITTEE

M. Israel, Chm.
M. Bercovitch
P. Freier
R. Gall
R. Jokipii
L. Jones
V. Jones
S. Krimigis
J. Kurfess
J. Lockwood
P. Meyer
B. Price
R. Ramaty
F. Reines
M. Shapiro
M. Shea
J. Simpson
E. Stone
D. Venkatesan
J. Waddington
S. White

PROGRAM COMMITTEES

OG SESSIONS	SH SESSIONS	HE SESSIONS	PUBLICATIONS
R. Mewaldt, Chm.	M. Forman, Chm.	T. Gaisser, Chm.	F. Jones, Chm.
G. Cassiday	H. Hudson	K. Lande	J. Adams
C. Fichtel	G. Mason	J. Linsley	G. Mason
A. Harding	B. McKibben	E. Loh	
J. Matteson	M. Pomerantz	G. Yodh	
D. Muller			
W. Webber			

LOCAL ORGANIZING COMMITTEE

L. Peterson,Chm.
G. Burbidge
R. Lingenfelter
R. Rothschild
J. Arnold
W. Baity
A. Buffington
M. Burbidge
W. Fillius
R. Gall
R. Gould
H. Hudson
J. Linsley
K. Marti
G. Masek
J. Matteson
C. McIlwain
R. Mewaldt
O. Piccioni
M. Thiemens
W. Thompson
H. Ticho
R. White

Sponsored by
National Aeronautics and Space Administration
National Science Foundation
Department of Energy
Center for Astrophysics and Space Science, University of California, San Diego
California Space Institute, University of California
Department of Physics and Astronomy, University of Maryland, College Park

PREFACE TO THE VOLUMES 4 AND 5 (SH)

The category SH includes all papers on solar and heliospheric energetic particle phenomena. SH combines the MG (modulation of galactic) and SP (solar particles) categories used in previous conferences, with papers on particles accelerated in the solar wind. Papers about techniques and instrumentation for science in the SH category are now included in SH. Cosmogenic nuclide studies, formerly in OG (origin and galactic) are also in the new SH category. Papers on particles of strictly magnetospheric origin were not included in this conference.

The SH heading numbers are :

SH1. Particle Acceleration on the Sun and in the Heliosphere
SH2. Composition, Spectra and Anisotropy
SH3. Propagation of Solar and Interplanetary Energetic Particles
SH4. Solar-Cycle Modulation and Propagation of Galactic Particles in the Heliosphere
SH5. Transient Modulations
SH6. Geomagnetic and Atomospheric Effects and Response Functions
SH7. Cosmogenic Nuclides
SH8. Solar Neutrinos
SH9. Techniques
SH10. Others

Papers appear in this volume in a numerical sequence determined primarily by this numbering system. For example, paper number SH2.1-8 is the eighth paper in the first session formed of papers in category SH2.

We thank the SH program committee for devising this numbering system, for reading every abstract submitted and for organizing on the basis of their content coherent sessions with reasonable length for presentation. We thank them also for selecting the rapporteurs and for advice in the selection of invited and highlight speakers. The committee members are: Hugh Hudson (UCSD), Bruce McKibben (U. of Chicago), Glenn Mason (U. of Maryland), Martin Pomerantz (Bartol Res. Foundation, U. of Delaware) and alternate Walker Fillius (UCSD).

These contributed papers are reviewed in plenary session by a team of expert rapporteurs at the end of the Conference. These extremely useful reports can only be prepared during the Conference, and so their written versions will be included in a later volume. We thank the rapporteurs in advance for their willing service.

Miriam A. Forman, Chairman
Solar - Heliospheric Program Committee

This conference is the 19th in a series. Previous conferences in this series were held at:

Cracow, Poland – 1947
Como, Italy – 1949
Bagneres-de-Bigorre, France – 1953
Guanjuato, Mexico – 1955
Varenna, Italy – 1957
Moscow, USSR – 1959
Kyoto, Japan – 1961
Jaipur, India – 1963
London, UK – 1965
Calgary, Canada – 1967
Budapest, Hungary – 1969
Hobart, Australia – 1971
Denver, USA – 1973
Munchen, FRG – 1975
Plovdiv, Bulgaria – 1977
Kyoto, Japan – 1979
Paris, France – 1981
Bangalore, India – 1983

SH 1.1
SOLAR FLARE ACCELERATION

PAPER CODE		PAGE
SH 1.1-3	PROPAGATION OF SOLAR FLARE PARTICLES IN A TURBULENT CORONAL LOOP JM RYAN	1
SH 1.1-4	STOCHASTIC PARTICLE ACCELERATION IN SOLAR FLARES W DROGE,R SCHLICKEISER	2
SH 1.1-5	FIRST-ORDER FERMI SHOCK ACCELERATION IN SOLAR FLARES DC ELLISON,R RAMATY	6
SH 1.1-6	PROMPT ACCELERATION OF IONS BY OBLIQUE TURBULENT SHOCKS IN SOLAR FLARES RB DECKER,L VLAHOS	10
SH 1.1-7	FAST DRIFT KILOMETRIC RADIO BURSTS AND SOLAR PROTON EVENTS EW CLIVER,SW KAHLER,HV CANE,RE MCGUIRE TT VON ROSENVINGE,RG STONE	14
SH 1.1-8	STUDY OF PHOTON EMISSION BY ELECTRON CAPTURE DURING SOLAR NUCLEI ACCELERTION I. TEMPERATURE-DEPENDENT CROSS SECTION FOR CHARGE CHANGING PROCESSES J PEREZ-PERAZA,M ALVAREZ,A LAVILLE A GALLEGOS	18
SH 1.1-9	STUDY OF PHOTUN EMISSION BY ELECTRON CAPTURE DURING SOLAR NUCLEI ACCELERATION II. DELIMITATION OF CONDITION FOR CHARGE TRANSFER ESTABLISHMENT J PEREZ-PERAZA,M ALVAREZ,A GALLEGOS	22

VOLUME 4

SH 1.1-10 STUDY OF PHOTON EMISSION BY ELECTRON CAPTURE DURING SOLAR NUCLEI ACCELERATION: III. PHOTON PRODUCTION EVALUATIONS 26

J PEREZ-PERAZA,M ALVAREZ,A GALLEGOS

VOLUME 4

SH 1.2
FLARE X-RAYS AND ELECTRONS

PAPER CODE		PAGE
SH 1.2-2	STUDY OF NON-THERMAL PHOTON PRODUCTION UNDER DIFFERENT SCENARIOS IN SOLAR FLARES: I. SCENARIOS AND FORMULATIONS J PEREZ-PERAZA,M ALVAREZ,A GALLEGOS	30
SH 1.2-3	STUDY OF NON-THERMAL PHOTON PRODUCTION UNDER DIFFERENT SCENARIOS IN SOLAR FLARES: II. THE COMPTON INVERSE AND BREMSSTRAHLUNG MODELS AND FITTINGS J PEREZ-PERAZA,M ALVAREZ,A LAVILLE A GALLEGOS	34
SH 1.2-4	SPECTRAL AND SPATIAL PROPERTIES OF SOLAR MICROFLARES GM SIMNETT,BR DENNIS	38
SH 1.2-6	TEMPORAL EVOLUTION OF AN ENERGETIC ELECTRON POPULATION IN AN INHOMOGENEOUS MEDIUM. APPLICATION TO SOLAR HARD X-RAY BURSTS N VILMER,AL MACKINNON,G TROTTET	42
SH 1.2-7	QUANTITATIVE ANALYSIS OF FLARE ACCELERATED ELECTRONS THROUGH THEIR HARD X-RAY AND MICROWAVE RADIATION KL KLEIN,G TROTTET	46
SH 1.2-8	AN EXTENDED "SUPERHOT" SOLAR FLARE X-RAY SOURCE HS HUDSON,KI OHKI,S TSUNETA	50
SH 1.2-9	OBSERVATIONS OF SOLAR FLARE PHOTON ENERGY SPECTRA FROM 20 KEV TO 7 MEV M YOSHIMORI,H WATANABE,N NITTA	54
SH 1.2-10	ION ENERGY STORAGE FOR POST-FLARE LOOPS HS HUDSON	58

SH 1.2-11 TWO TYPES OF ELECTRON EVENTS IN SOLAR FLARES 62

EI DAIBOG,VG KURT,YI LOGACHEV
VG STOLPOVSKY

SH 1.2-12 TWO CLASSES OF SOLAR ENERGETIC PARTICLE EVENTS ASSOCIATED WITH IMPULSIVE AND LONG DURATION SOFT X-RAY FLARES 66

HV CANE,RE MCGUIRE,TT VON ROSENVINGE

SH 1.2-13 A DOMINANT ROLE FOR PROTONS AT THE ONSET OF SOLAR FLARES 70

GM SIMNETT

SH 1.2-14 THE ENERGY SPECTRA OF SOLAR FLARE ELECTRONS 74

P EVENSON,D HOVESTADT,P MEYER,D MOSES

VOLUME 4

SH 1.3
GAMMA-RAY FLARES AND INTERPLANETARY PROTONS

PAPER CODE		PAGE
SH 1.3-1	ONSET OF SOLAR FLARES AS PREDICTED BY TWO-DIMENSIONAL MPD-MODELS OF QUIESCENT PROMINENCES J GALINDO TREJO	78
SH 1.3-2	THE STARTING CONDITIONS FOR AN OPTICALLY SMALL SOLAR GAMMA RAY FLARE GM SIMNETT,JM RYAN	82
SH 1.3-5	ON THE DETECTABILITY OF KEV-MEV SOLAR PROTONS THROUGH THEIR NONTHERMAL LYMAN-ALPHA EMISSION RC CANFIELD,CR CHANG	86
SH 1.3-6	OBSERVATIONS OF SOLAR FLARE GAMMA-RAYS AND PROTONS M YOSHIMORI,H WATANABE	90
SH 1.3-7	ENERGETIC PROTONS FROM A DISAPPEARING SOLAR FILAMENT SW KAHLER,EW CLIVER,HV CANE,RE MCGUIRE RG STONE,NR SHEELEY	94
SH 1.3-8	HELIOS 1 ENERGETIC PARTICLE OBSERVATIONS OF SOLAR GAMMA RAY/NEUTRON FLARE EVENTS OF 7, 21 JUNE 1980 AND 3 JUNE 1982 FB MCDONALD,MAI VAN HOLLEBEKE JH TRAINOR	98
SH 1.3-9	INJECTION OF ENERGETIC PARTICLES FOLLOWING THE GAMMA-RAY FLARES ON JUNE 7, 1980, AS OBSERVED ON HELIOS-1 HH NEUSTOCK,G WIBBERENZ,B IWERS	102

SH 1.3-11 ULTRARELATIVISTIC ELECTRONS AND SOLAR FLARE GAMMA-RADIATION 106
PE SEMUKHIN,GA KOVALTSOV

SH 1.3-13 SOURCE ENERGY SPECTRA FROM DEMODULATION OF SOLAR PARTICLE DATA BY INTERPLANETARY AND CORONAL TRANSPORT 110
J PEREZ-PERAZA,M ALVAREZ,F RIVERO

SH 1.3-14 SPECTRA OF SOLAR PROTON GROUND LEVEL EVENTS USING NEUTRON MONITOR AND NEUTRON MODERATED DETECTOR RECORDINGS 114
PH STOKER

SH 1.3-15 GROUND INCREASE OF COSMIC RAY INTENSITY ON FEBRUARY 16, 1984 118
AV BELOV,YAL BLOKH,EA EROSHENKO
VN ISHKOV,VG YANKE

SH 1.3-17 THE SCR FLARE OF 16 FEBRUARY 1984 AS RECORDED BY THE SAYAN SPECTROGRAPH 122
SA KOZLOV,NI PAKHOMOV,LA SHAPOVALOVA
AL YANCHUKOVSKY

VOLUME 4

SH 1.4
SOLAR FLARE NEUTRONS

PAPER CODE PAGE

SH 1.4-1 THE EXTENDED PRODUCTION OF NEUTRONS DURING A SLAR FLARE 126
EL CHUPP,DJ FORREST,WT VESTRAND
H DEBRUNNER,E FLUCKIGER,JF COOPER
G KANBACH,C REPPIN,GH SHARE

SH 1.4-2 FURTHER OBSERVATIONS OF PROTONS RESUTING FROM THE DECAY OF NEUTRONS EJECTED BY SOLAR FLARES 130
P EVENSON,R KROEGER,P MEYER

SH 1.4-3 SUGGESTIONS FOR IMPROVING THE EFFICIENCY OF GROUND-BASED NEUTRON MONITORS FOR DETECTING SOLAR NEUTRONS 134
N IUCCI,M PARISI,C SIGNORINI,M STORINI
G VILLORESI

SH 1.4-5 SEARCH FOR SOLAR NEUTRONS USING NM-64 EQUIPMENT 138
NJ MARTINIC,A REGUERIN,E PALENQUE
MA TAQUICHIRI,M WADA,A INOUE,K TAKAHASHI

SH 1.4-6 A SEARCH FOR SOLAR NEUTRINOS ON A LONG DURATION BALLOON FLIGHT 142
R KOGA,GM FRYE,A OWENS,BV DENEHY,D MACE
J THOMAS

SH 1.4-7 NEUTRAL PION PRODUCTION IN SOLAR FLARES 146
DJ FORREST,WT VESTRAND,EL CHUPP
E RIEGER,JF COOPER,GH SHARE

SH 1.4-8 HIGH ENERGY NEUTRON AND GAMMA RADIATION GENERATED DURING THE SOLAR FLARES 150
GE KOCHAROV,NZ MANDZHAVIDZE

SH 1.4-9 ON THE ANGULAR AND ENERGY DISTRIBUTION OF SOLAR NEUTRONS GENERATED IN P-P REACTIONS 154

✓ YUE EFIMOV,GE KOCHAROV

SH 1.4-10 POSSIBLE DETECTION OF FLARE-GENERTATED POSITRONS BY HELIOS 1 ON 3 JUNE 1982 158

✓ E KIRSCH,E KEPPLER,K RICHTER

SH 1.5
INTERPLANETARY ACCELERATION

PAPER CODE		PAGE
SH 1.5-1	SHOCK AND STATISTICAL ACCELERATION OF ENERGETIC PARTICLES IN THE INTERPLANETARY MEDIUM JF VALDES-GALICIA,X MOUSSAS,JJ OUENBY FM NEUBAUER,R SCHWENN	162
SH 1.5-3	ENERGETIC ION ACCELERATION AT COLLISIONLESS SHOCKS RB DECKER,L VLAHOS	166
SH 1.5-4	ACCELERATION OF IONS AND ELECTRONS NEAR-COSMIC RAY ENERGIES IN A PERPENDICULAR SHOCK: THE JANUARY 6, 1978 EVENT SM KRIMIGIS,ET SARRIS	170
SH 1.5-5	PARTICLE ACCELERATION DUE TO SHOCKS IN THE INTERPLANETARY FIELD: HIGH TIME RESOLUTION DATA AND SIMULATION RESULTS RL KESSEL,TP ARMSTRONG,R NUBER,J BANDLE	174
SH 1.5-6	PITCH ANGLE DISTRIBUTIONS OF 35-1000 KEV PROTONS AT QUASI-PERPENDICULAR INTERPLANETARY SHOCKS A BALOGH,G ERDOS	178
SH 1.5-12	SPATIAL DEPENDENCE OF THE LOCAL DIFFUSION COEFFICIENT UPSTREAM OF THE NOVEMBER 12, 1978 INTERPLANETARY TRAVELING SHOCK G GLOECKLER,FM IPAVICH,B KLECKER D HOVESTADT,M SCHOLER	182
SH 1.5-14	LATITUDE DEPENDENCE OF CO-ROTATING SHOCK ACCELERATION RE GOLD,LJ LANZEROTTI,CG MACLENNAN SM KRIMIGIS	186

SH 1.5-15 ELEMENTAL ABUNDANCES IN COROTATING EVENTS 190

✓ TT VON ROSENVINGE, RE MCGUIRE

SH 1.5-16 SOLAR AND INTERPLANETARY PARTICLES AT 2 TO 4 MEV DURING SOLAR CYCLES 21: SOLAR CYCLE VARIATIONS OF EVENT SIZES, AND COMPOSITIONS 192

✓ TP ARMSTRONG, JC SHIELDS, PR BRIGGS
S ECKES

SH 1.5-17 COSMIC RAY ACCELERATION BY STELLAR WIND. SIMULATION FOR HELIOSPHERE 196

✓ SI PETUKHOV, AA TURPANOV, VS NIKOLAEV

SH 1.5-18 THE ENERGY SPECTRUM OF JOVIAN ELECTRONS IN INTERPLANETARY SPACE 200

✓ SP CHRISTON, AC CUMMINGS, EC STONE
WR WEBBER

SH 1.5-19 THE JOVIAN ELECTRON SPECTRUM: 1978 - 1984 201

✓ P EVENSON, P MEYER, D MOSES

SH 2.1
SOLAR PARTICLES, $Z > 1$

PAPER CODE — PAGE

SH 2.1-1 OBSERVATION OF THE FLUXES OF NUCLEI WITH ENERGIES OF 10-20 MEV PER NUCLEON DURING THE SOLAR FLARE OF APRIL 26, 1984 205

VV BOBROVSKAYA,NL GRIGOROV,DA ZHURAVLEV
MMA KONDRATYEVA,RA NYMMIK,CHA TRETYAKOVA
NV ALEKSEEV,PV VAKULOV,PV VAKULOV
VP SECHINOV

SH 2.1-3 ENERGETIC PARTICLE OBSERVATIONS OF SOLAR GAMMA RAY/NEUTRON FLARE EVENTS OF 3 JUNE 1982 AND 21 JUNE 1980 ISOTOPIC AND CHEMICAL COMPOSITION 209

MAI VAN HOLLEBEKE,FB MCDONALD
JH TRAINOR

SH 2.1-4 PRECISION MEASUREMENTS OF SOLAR ENERGETIC PARTICLE ELEMENTAL COMPOSITION 213

HH BRENEMAN,EC STONE

SH 2.1-5 SOLAR CORONAL AND PHOTOSPHERIC ABUNDANCES FROM SOLAR ENERGETIC PARTICLE MEASUREMENTS 217

HH BRENEMAN,EC STONE

SH 2.1-6 SILICON TO IRON ABUNDANCES IN SOLAR COSMIC RAYS AND IN THE SUN 221

MN VAHIA,S BISWAS,N DURGAPRASAD

SH 2.1-7 VARIATION IN ELEMENTAL COMPOSITION OF SEVERAL MEV/NUCLEON IONS OBSERVED IN INTERPLANETARY SPACE 225

RE MCGUIRE,TT VON ROSENVINGE,DV REAMES

VOLUME 4

SH 2.1-8 ON THE RETENTION OF HIGH-ENERGY PROTONS AND NUCLEI WITH CHARGES Z > OR EQUAL TO 2 IN LARGE SOLAR FLARES AFTER THE PROCESS OF THEIR ACCELERATION 229

✓ NN VOLODICHEV,BM KUZHEVSKY,OYU NECHAEV IA SAVENKO

SH 2.1-9 DIFFUSION IN THE CHROMOSPHERE, AND THE COMPOSITION OF THE SOLAR CORONA AND ENERGETIC PARTICLES 233

✓ S VAUCLAIR,JP MEYER

SH 2.1-10 ANOMALOUS ABUNDANCES OF SOLAR ENERGETIC PARTICLES AND CORONAL GAS: COULOMB EFFECTS AND FIRST IONIZATION POTENTIAL (FIP) ORDERING 237

✓ DJ MULLAN

SH 2.1-11 MEAN CHARGE STATES OF N, NE, MG, SI, AND S DURING SOLAR ENERGETIC PARTICLE EVENTS 241

✓ A LUHN,D HOVESTADT,B KLECKER,M SCHOLER G GLOECKLER,FM IPAVICH,AB GALVIN,CY FAN LA FISK

SH 2.1-12 CALCULATIONS OF HEAVY ION CHARGE STATE DISTRIBUTIONS FOR NONEQUILIBRIUM CONDITIONS 245

✓ A LUHN,D HOVESTADT

SH 2.1-13 ABUNDANCES FROMSOLAR FLARE GAMMA RAY LINE SPECTROSCOPY 249

✓ RJ MURPHY,B KOZLOVSKY,R RAMATY DJ FORREST

SH 2.1-14 SOLAR FLARE GAMMA RAY LINE SPECTROSCOPY 253

✓ B KOZLOVSKY,RJ MURPHY,R RAMATY

SH 2.2
HELEUM-3 RICH SOLAR EVENTS

PAPER CODE — PAGE

SH 2.2-1 ISOTOPIC OVERABUNDANCES AND THE ENERGETIC PARTICLE MODEL OF SOLAR FLARES 257
R PEREZ-ENRIQUEZ,S BRAVO

SH 2.2-2 NUCLEOSYNTHESIS IN THE TERRASTIAL AND SOLAR ATMOSPHERES 261
C YU,R ZHOU,S ZHAN

SH 2.2-3 TYPE III SOLAR RADIO BURSTS AND **3HE-RICH EVENTS 265
DV REAMES,RG STONE

SH 2.2-4 SOLAR SOURCE REGIONS OF 3**HE-RICH PARTICLE EVENTS 269
SW KAHLER,RP LIN,DV REAMES,RG STONE
M LIGGETT

SH 2.2-5 **3HE IN SOLAR NON-RELATIVISTIC ELECTRON EVENTS 273
DV REAMES,RP LIN,DV REAMES

SH 2.2-6 ELEMENTAL ABUNDANCE DIFFERENCES BETWEEN NUCLEI ACCELERATED IN CIR SHOCKS AND SOLAR FLARES3HE-RICH SOLAR FLARES 277
WF DIETRICH,JA SIMPSON

SH 2.2-7 THE HEAVY ION COMPOSITION IN **3HE-RICH SOLAR FLARES 281
GM MASON,DV REAMES,D HOVESTADT
TT VON ROSENVINGE

SH 2.2-8 MEAN CHARGE OF SILICON IN 3**HE-RICH SOLAR FLARES 285
A LUHN,B KLECKER,D HOVESTADT,E MOBIUS

SH 2.2-9 ON THE CONNECTION BETWEEN THE **3HE-ENRICHMENT AND SPECTRAL INDEX OF SOLAR ENERGETIC PARTICLES 289

LG KOCHAROV,YAV DVORYANCHIKOV

SH 2.2-10 THE PLASMA MECHANISM FOR PREFERENTIAL ACCELERATION OF HEAVY IONS 293

LG KOCHAROV,AV ORISHCHENKO

VOLUME 4

SH 3.1
CORONAL PROPAGATION AND ANISOTROPY

PAPER CODE		PAGE
SH 3.1-1	OBSERVATIONS OF SOLAR ENERGETIC PARTICLES AT A SYNCHRONOUS ORBIT T TAKENAKA,T YANAGIMACHI,K ITO,Y OHI T KOHNO,K SAKURAI	297
SH 3.1-2	CORONAL PROPAGATION OF SOLAR FLARE PARTICLES OBSERVED BY GEOSTATIONARY SATELLITE T KOHNO,N NITTA,M WADA,T SUDA	301
SH 3.1-3	CORONAL PROPAGATION OF FLARE ASSOCIATED ELECTRONS AND PROTONS G SCHELLERT,G WIBBERENZ,H KUNOW	305
SH 3.1-5	GEOMETRY OF THE DIFFUSIVE PROPAGATION REGION IN THE AUGUST 14, 1982 SOLAR ELECTRON EVENT P EVENSON	309
SH 3.1-6	PECULIARITIES OF PROAGATION OF CHARGED PARTICLES IN SOLAR CORONA EI MOROZOVA,NF PISARENKO,NA MIKRYUKOVA VV KLIMENKO,VE TIMOFEEV,YUG SHAFER	313
SH 3.1-7	SOME CHARACTERISTICS OF THE SOLAR FLARE EVENT OF FEBRUARY 16, 1984 H DEBRUNNER,E FLUCKIGER,JA LOCKWOOD RE MCGUIRE	317
SH 3.1-8	CONSTRAINTS ON SOLAR FLARE PARTICLE TRANSPORT MODELS FROM ANISOTROPY OBSERVATIONS AT VOYAGER 1 DC HAMILTON,GM MASON,G GLOECKLER	321

SH 3.1-9 LOW ENERGY PROTON BIDIRECTIONAL ANISOTROPIES AND THEIR RELATION TO TRANSIENT INTERPLANETARY MAGNETIC STRUCTURES: ISEE-3 OBSERVATIONS 322

RG MARSDEN,TR SANDERSON,KP WENZEL
EJ SMITH

SH 3.1-10 SECOND-ORDER COMPTON-GETTING EFFECT ON ARBITRARY INTENSITY DISTRIBUTION 326

CK NG

SH 3.1-11 DETERMINATION OF THE PITCH-ANGLE DISTRIBUTION AND TRANSVERSE ANSIOTROPY OF INTERPLANETARY PARTICLES 330

CK NG

SH 3.1-13 PITCH ANGLE DISTRIBUTIONS OF SOLAR ENERGETIC PARTICLES AND THE LOCAL SCATTERING PROPERTIES OF THE INTERPLANETARY MAGNETIC FIELD 334

J BEECK,G WIBBERENZ

SH 3.2
SOLAR PARTICLE PROPAGATION

PAPER CODE PAGE

SH 3.2-1 EXPONENTIAL ANISOTROPY OF SOLOR COSMIC RAYS 335

JW BIEBER,PA EVENSON,MA POMERANTZ

SH 3.2-2 ENERGETIC SOLAR PARTICLE EVENTS 339

KB FENTON,AG FENTON,JE HUMBLE

SH 3.2-3 CHANNELED PROPAGATION OF SOLAR PARTICLES 342

KA ANDERSON,WM DOUGHERTY

SH 3.2-4 THE PROPAGATION OF SOLAR ENERGETIC PARTICLES IN MAGNETIC CHANNELS 346

FB MCDONALD,LF BURLAGA

SH 3.2-5 RADIAL TRANSPORT OF ~ 1 MEV/NUCLEON IONS DURING THE 22 NOVEMBER 1977 SOLAR PARTICLE EVENT 347

GM MASON,DC HAMILTON,G GLOECKLER
B KLECKER

SH 3.2-6 ENERGETIC SOLAR FLUXES OUT TO 3 AU DURING THE MAY 7, 1978 FLARE EVENT 351

JA LOCKWOOD,H DEBRUNNER

SH 3.2-8 THE LOCAL CAHRACTERICTIC FUNCTION OF INTERPLANETARY PARTICLE PROPAGATION 355

G GREEN,W SCHLUTER

SH 3.2-9 INVESTIGATION OF COSMIC RAY PROPAGATION IN INTERPANETARY SPACE 356

EA CHEBAKOVA,EV KOLOMEETS
VN SEVAST'YANOV

SH 3.2-10 DIFFUSION-CONVECTION FUNCTION OF COSMIC RAYS 360

GL YANG,GL ZHANG

VOLUME 4

SH 3.2-11 MONTE CARLO CALCULATIONS OF RELATIVISTIC SOLAR PROTON PROPAGATION IN INTERPLANETARY SPACE 364

M LUMME,JJ TORSTI,E VAINIKKA,J PELTONEN
M NIEMINEN,E VALTONEN,H ARVELA

SH 3.2-13 ON REFLECTING BOUNDARY BEHIND THE EARTH'S ORBIT AT PROPAGATION OF FAST PARTICLES FROM SOLAR FLARES 368

AS NISKOVSKIKH,AT FILIPPOV

SH 4.1
EPISODIC MODULATION

PAPER CODE PAGE

SH 4.1-2 THE DISPERSIVE EVOLUTION OF CHARGED-PARTICLE BUNCHES IN RANDOM MAGNETIC FIELDS 372
VK BABAYAN,MB BAGDASARIAN

SH 4.1-3 NUMERICAL DESCRIPTIONS OF COSMIC-RAY TRANSPORT 376
JA EARL,JR JOKIPII

SH 4.1-4 NUMERICAL AND ANALYTIC DESCRIPTIONS OF COSMIC-RAY TRANSPORT 380
JA EARL

SH 4.1-7 THE ROLE OF SHOCK WAVES IN MODULATION OF GALACTIC COSMIC RAYS 384
R GALL,H DURAND

SH 4.1-9 THE INTENSITY RECOVERY OF FORBUSH-TYPE DECREASES AS A FUNCTION OF HELIOCENTRIC DISTANCE AND ITS RELATIONSHIP TO THE 11-YEAR VARIATION 388
JA LOCKWOOD,WR WEBBER,JR JOKIPII

SH 4.1-10 CUMULATIVE EFFECT OF FORBUSH DECREASES IN THE HELIOSPHERE MODULATION DURING THE PRESENT SOLAR CYCLE 392
SP AGRAWAL,BL MISHRA,AK JAIN
D VENKATESAN

SH 4.1-11 COSMIC RAY MODULATION AND MERGED INTERACTION REGIONS 396
LF BURLAGA,FB MCDONALD,ML GOLDSTEIN

SH 4.1-12 PROPAGATION OF THE PHASE OF COSMIC-RAY MODULATION 400
MA FORMAN,FC JONES

SH 4.1-13 LATITUDE VARIATION OF RECURRENT FLUXES IN THE OUTER SOLAR SYSTEM 404

SP CHRISTON,EC STONE

SH 4.1-14 LONGITUDINAL DISTRIBUTION OF COSMIC RAYS IN THE HELIOSPHERE 405

RE GOLD,D VENKATESAN

SH 4.1-16 THE 1973-1984 SOLAR MODULATION OF COSMIC RAY NUCLEI 409

M GARCIAMUNOZ,KR PYLE,JA SIMPSON
M GARCIA-MUNOZ

SH 4.1-20 COSMIC RAY MODULATION IN A RANDOM ANISOTROPIC MAGNETIC FIELD 413

LI DORMAN,YUI FEDOROV,MI KATZ,SF NOSOV
BA SHAKHOV

SH 4.1-21 EVIDENCE FOR REGIONS OF NEGLIGIBLE COSMIC-RAY MODULATION IN THE INNER HELIOSPHERE (<10 AU) 417

EC ROELOF

SH 4.2
LONG TERM MODULATION AND NEUTRAL SHEET EFFECTS

PAPER CODE PAGE

SH 4.2-3 NOTES ON DRIFT THEORY 421

RA BURGER,H MORAAL,GM WEBB,H MORAAL

SH 4.2-4 DRIFT AND OBSERVATIONS IN COSMIC-RAY MODULATION. I. 425

MS POTGIETER

SH 4.2-5 DRIFT AND OBSERVATIONS IN COSMIC-RAY MODULATION. II 429

MS POTGIETER

SH 4.2-6 COSMIC RAY NORTH-SOUTH ANISOTROPY 1965-1982: 433

JW BIEBER,MA POMERANTZ

SH 4.2-7 NORTH-SOUTH ASYMETRY IN ACTIVITY ON THE SUN AND COSMIC RAY DENSITY GRADIENTS 437

DB SWINSON,MA SHEA,JE HUMBLE

SH 4.2-8 COSMIC RAY INTENSITY AND THE TILT OF THE NEUTRAL SHEET 441

T SAITO,DB SWINSON

SH 4.2-9 DIFFERENTIAL MEASUREMENT OF COSMIC-RAY GRADIENT WITH RESPECT TO INTERPLANETARY CURRENT SHEET 445

SP CHRISTON,AC CUMMINGS,EC STONE
KW BEHANNON,LF BURLAGA

SH 4.2-10 SPATIAL VARIATION OF COSMIC RAYS NEAR THE HELIOSPHERIC CURRENT SHEET 449

JR JOKIPII,J KOTA

SH 4.2-11 EFFECTS OF A WAVY NEUTRAL SHEET ON COSMIC RAY ANISOTROPIES 453

J KOTA,JR JOKIPII

SH 4.2-12 EFFECTS OF SOLAR MAGNETIC FIELD ON COSMIC RAYS 457

GA GONCHAR,EV KOLOMEETS,AKH LYAKHOVA
NV SLYUNYAEVA,NV STEKOL'NIKOV

SH 4.2-13 DETERMINATION OF GALATIC COSMIC RAY LATITUDINAL GRADIENT USING EARTH BASED DETECTORS 461

BADRUDDIN,RS YADAV

SH 4.2-14 THE EXPECTED COSMIC RAY DENSITY AND STREAM DISTRIBUTIONS AT THE HELIOLATITUDINAL ASYMMETRY OF SOLAR WIND 465

MV ALANIA,RG ASLAMAZASHVILI,LI DORMAN
K ISKRA

SH 4.2-16 LATITUDINAL GRADIENTS OF COSMIC RAYS AND THE POLARITY REVERSAL OF THE HELIOSPHERIC MAGNETIC FIELD: A PRELIMINARY EVALUATION 469

G NEWKIRK,JA LOCKWOOD,M GARCIA-MUNOZ
JA SIMPSON

SH 4.2-17 THE INFLUENCE OF NONSTATIONARITY OF THE SOLAR ACTIVITY AND GENERAL SOLAR FIELD ON MODULATION OF COSMIC RAYS 473

AG ZUSMANOVICH,ON KRYAKUNOVA
LF CHURONOVA,YAE SHVARTSMAN

SH 4.2-18 THE EFFECT OF THE NEUTRAL SHEET STRUCTURE OF THE INTERPLANETARY MAGENTIC FIELD ON COSMIC RAY DISTRIBUTION IN SPACE 477

MV ALANIA,RG ASLAMAZASHVILI
TB BOCHORISHVILI,TV DJAPIASHVILI
VS TKEMALADZE

SH 4.2-19 ON THE INFLUENCE OF THE HELIOMAGNETOSPHERIC PERIPHERY ON THE GALACTIC COSMIC RAYS 481

MMB KRAINEV,YUI STOZHKOV
TN CHARAKHCHYAN

SH 4.2-20 SPATIAL DISTRIBUTION OF COSMIC RAYS IN MAGNETIC CYCLES OF THE SUN 485

MV ALANIYA,RT GUSHCHINA,LI DORMAN

SH 4.2-21 11- AND 22-YEAR VARIATIONS OF THE COSMIC RAY DENSITY AND OF THE SOLAR WIND SPEED 489

NP CHIRKOV

SH 4.2-22 DIFFERENCE BETWEEN EVEN AND ODD II-YEAR CYCLES IN COSMIC RAY INTENSITY 493

JA OTAOLA,R PEREZ-ENRIQUEZ
JF VALDES-GALICIA

SH 4.2-23 THE DEPENDENCE OF SOLAR MODULATION ON THE SIGN OF THE COSMIC RAY PARTICLE CHARGE 497

M GARCIA-MUNOZ,P MEYER,KR PYLE
JA SIMPSON,P EVENSON

SH 4.2-24 AN UPDATE ON THE CORRELATION BETWEEN THE COSMIC RADIATION INTENSITY AND THE GEOMAGNETIC AA INDEX 501

MA SHEA,DF SMART

THE PROPOGATION OF SOLAR FLARE PARTICLES IN A TURBULENT CORONAL LOOP

N85-34730

J. M. Ryan
Space Science Center, University of New Hampshire
Durham, New Hampshire 03824 USA

ABSTRACT

Energetic solar flare particles, both electrons and protons, must survive the turbulent environment of a flaring loop and propogate to the lower corona or chromosphere in order to produce hard X-ray and γ-ray bursts. This plasma turbulence, often observed in soft x-ray line widths to be in excess of 100 km/s, is presumably capable of efficiently scattering the fast flare particles. This prevents to some degree the free streaming of accelerated particles and depending on the amplitude of the turbulence, restricts the particles to diffusive propogation along the length of the loop to the target chromosphere. In addition this turbulence is capable of performing additional acceleration of the fast particles by the second order Fermi mechanism. For compact flares with rise times < 10s, the acceleration effect is small and the propogation of the particles is governed by spatial diffusion and energy loss in the ambient medium.

The solution of the time dependent diffusion equation with velocity dependent diffusion and energy loss coefficients yields for the case of non-relativistic protons particle precipitation rates which are necessary for calculating thick target γ-ray emission and also yields the total thin target emissivity. The thick target emission is necessarily delayed with respect to the particle acceleration or injection by more than the mere travel time of the particle over the loop length. Equivalent numbers are calculated for the case of relativistic electrons where in addition the time-dependent electron population at the top of the loop is calculated. This is useful in estimating the resulting μ-wave emission. The results show relative timing differences in the different emission processes which are functions of particle species and energy and the point of injection of the particles into the coronal loop.

STOCHASTIC PARTICLE ACCELERATION IN SOLAR FLARES

N85-34731

W. Dröge, R. Schlickeiser
Max-Planck-Institut für Radioastronomie
Auf dem Hügel 69, 5300 Bonn 1, FRG

ABSTRACT

We propose that particles during the second phase of solar flares are accelerated by stochastic resonant scattering off hydromagnetic waves and first-order Fermi acceleration in shock waves generated in the impulsive phase of the flare. Our solutions allow arbitrary power law momentum dependences of the momentum diffusion coefficient as well as the momentum loss time. The acceleration time scale to a characteristic energy ∿ 100 keV for protons can be as short as 5 s. The resulting electron spectra show a characteristic double power law with a transition around 200 keV and are correlated to the proton spectra evaluated under equal boundary conditions, indicating that electrons and protons are accelerated by the same mechanism. The correlation between the different spectral indices in the electron double power law and between electron and proton spectra are governed by the ratio of first-to second-order acceleration and therefore allow a determination of the Alfvén Mach number of the shock wave.

1. Introduction. We propose that the combination of first- and second-order Fermi acceleration is the mechanism responsible for second-phase acceleration in solar flares. This model has a number of distinct advantages over previous models, in that it gives a natural explanation for the various observed time delays between first and second phase as well as for the dependence of the particle spectra to the strength of the flare and the correlation between electron and proton spectral indices.

2. Theory. Parker and Tidman (1958) have pointed out that Fermi acceleration is an intrinsic property of any sufficiently agitated plasma of energetic particles. The effects of second-order Fermi acceleration due to irregularly moving magnetized fluid elements, first-order Fermi acceleration off strong shocks as well as loss and escape processes can be incorporated into a transport equation in phase space (Ramaty 1979)

$$\frac{\partial f}{\partial t} - \frac{1}{p^2}\frac{\partial}{\partial p}\left[p^2\, D(p)\, \frac{\partial f}{\partial p}\right] - \frac{1}{p^2}\frac{\partial}{\partial p}\left[p^2\,(\dot{p}_G + \dot{p}_L)\, f\right] + \frac{f}{T(p)} = Q(p,t) \qquad (1),$$

where p is the particle momentum, $N(p) = 4\pi p^2 f(p,t)$ the number of particles per unit momentum and unit volume, and $Q(p,t)$ represents sources and sinks of particles. Using the concept of the age distribution (Schlickeiser and Lerche 1985) the effects of spatial diffusion, convection and catastrophic losses have been combined in a momentum-dependent escape time $T(p) = T_0\, p^{-b}$.

In a plasma with a strong MHD turbulence both the momentum diffusion coefficient $D(p)$ and the spatial diffusion coefficient along the mean magnetic field $K_\parallel(p)$ are governed by the turbulence simultaneously. By using quasi-linear theory $K_\parallel(p)$ can be related rigorously to the spectrum of the magnetic field fluctuations (Jokipii 1977). Assuming a power law spectrum for the magnetic irregularities $W(k) = W_o\, k^{-q}$ we may write

$$K_\parallel(p) = \delta\, v(p)\, p^{2-q} = \kappa p^{\eta} \tag{2}$$

(δ, κ = const.) and

$$D(p) = \alpha_2 \frac{V_A^2}{K_\parallel} p^2 \tag{3}$$

(V_A: Alfvén speed, α_2: constant). As gain process, we consider quasi-continuous momentum gain by acceleration at a shock wave moving through the plasma with speed V_S. The momentum gain by first-order Fermi acceleration at a single shock wave has been determined by Drury (1983)

$$\dot{p}_G = \alpha_1 \frac{V_S^2}{K_\parallel} p \tag{4}$$

(α_1: constant). Möbius et al. (1982) pointed out that for conditions in the flare site the rate of systematic acceleration exceeds the rate of momentum loss. Thus we assume that $\dot{p}_G >> \dot{p}_L$ at least at all momenta of interest. Using (2), (3) and (4) in equation (1) and considering the steady-state case ($\partial f/\partial t = 0$) yields

$$\frac{1}{p^2} \frac{d}{dp} [p^{4-\eta} \frac{df}{dp} - a\, p^{3-\eta}] - \lambda p^b = Q(p) \tag{5}$$

($a_1 = \alpha_1 V_S^2/\kappa$, $a_2 = \alpha_2 V_A^2/\kappa$, $a = a_1/a_2$, $\lambda = 1/a_2 T_o$). We assume that the injection takes place at some momentum $Q(p) = q_o\, \delta(p-p_o)$ and we find for the steady-state particle number density $N(p) = 4\pi p^2 f(p)$ (see Dröge and Schlickeiser (1985) for details):

$$N(p) = \frac{8\pi q_o}{a_2 |\eta+b|} p_o^{\frac{\eta-a+1}{2}} p^{\frac{\eta+a+1}{2}} \begin{cases} K_\nu\left(\frac{2\lambda^{1/2}}{|\eta+b|} p_o^{\frac{\eta+b}{2}}\right) I_\nu\left(\frac{2\lambda^{1/2}}{|\eta+b|} p^{\frac{\eta+b}{2}}\right) & p < p_o \\ I_\nu\left(\frac{2\lambda^{1/2}}{|\eta+b|} p_o^{\frac{\eta+b}{2}}\right) K_\nu\left(\frac{2\lambda^{1/2}}{|\eta+b|} p^{\frac{\eta+b}{2}}\right) & p > p_o \end{cases} \tag{6}$$

$\nu = |(3+a-\eta)/(\eta+b)|$. In the limit $\eta+b \to 0$ solution (6) approaches a power law distribution

$$N(p) = \frac{2\pi q_o}{a_2 \sqrt{\frac{(3+a-\eta)^2}{4} + \lambda}} p_o^{\frac{\eta-a+1}{2}} p^{\frac{\eta+a+1}{2}} \begin{cases} (p/p_o)^{\sqrt{\frac{(3+a-\eta)^2}{4} + \lambda}} & p < p_o \\ (p/p_o)^{-\sqrt{\frac{(3+a-\eta)^2}{4} + \lambda}} & p > p_o \end{cases} \tag{7}$$

Equations (6) and (7) are generalizations of the solutions of Ramaty (1979; $b = 0$, $a = 0$, $\eta = 0,1$), Barbosa (1979; $a = 0$), Pikel'ner and Tsytovich (1976; $a = 0$, $b = 0$). The solutions (6) and (7) allow arbitrary momentum power law dependences of the spatial diffusion coefficient (η) and the escape time (b). The parameter $a = (\alpha_1/\alpha_2)(V_S^2/V_A^2) = (\alpha_1/\alpha_2)\, M_A^2$ is of the order of the square of the shock's Mach number and describes the ratio of first- to second-order Fermi acceleration. In the case of no Fermi ac-

ORIGINAL PAGE IS
OF POOR QUALITY

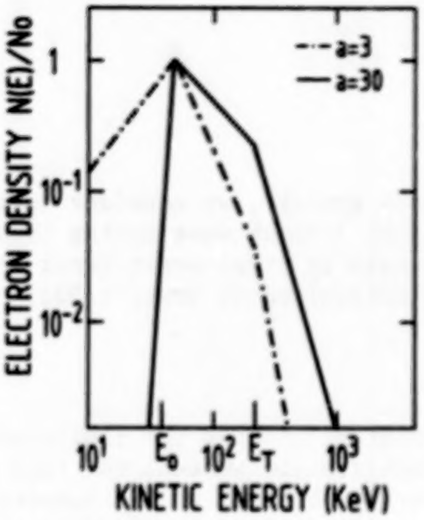

Fig. 1: Normalized steady-state electron number density. Particles are injected at $E_0 = 50$ keV. At $E_T = 200$ keV a transition from solution (6) to (7) occurs.

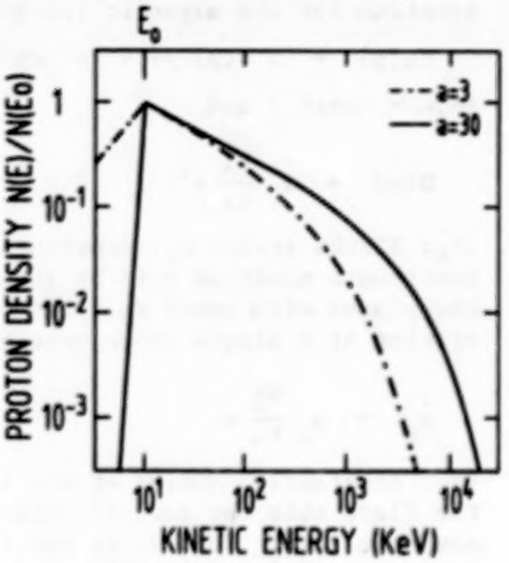

Fig. 2: Normalized steady-state proton number density. Particles are injected at $E_0 = 10$ keV.

celeration at shock waves ($a = 0$) (6) and (7) reduce to the solutions of previous models as quoted above.

3. Discussion. The energy spectra of electrons accelerated in large flares exhibit a characteristic double power law with a break around $E_T \approx 200$ keV (Lin et al. 1982). From this we conclude that for nonrelativistic kinetic energies ($E < E_T$) the Bessel function solution (6) holds, which for small arguments is approximately a power law, whereas for $E > E_T$ the particles are relativistic ($p = mc \mathrel{\hat{=}} E = 200$ keV for electrons) and the distribution function approaches the power law solution (7) (cf. Fig. 1). We take spatial diffusion along the mean magnetic field as the relevant escape process. The escape time then is $T(p) = L^2/K_\parallel = (L^2/\kappa)\, p^{-\eta}$, where L is the length scale of the system and $\eta = b = 0$ in the relativistic and $\eta = b = 1$ in the nonrelativistic case. Thus we may consider the evolution of the particle spectra in the hard-sphere approximation (cf. Möbius et al. 1982), which gives us

$$K_\parallel(p) = \frac{1}{3}\, v(p)\, \ell \tag{8}$$

v(p) is the velocity and ℓ the momentum independent mean free path of the particles. For comparison with data we transform (6) and (7) into energy space where $N(E) = N(p)\,(1/v)$ and $E = (p^2c^2 + m^2c^4)^{1/2} - mc^2$ is the particle kinetic energy. An "effective power law" exponent can be calculated ($E > E_0$)

$$\gamma_{eff}(E) = -\frac{d\,\lg N(E)}{d\,\lg E} = \begin{cases} -\dfrac{a}{4} + \dfrac{a+2}{4}\sqrt{1 + \dfrac{4x^2}{(a+2)^2}\dfrac{2E}{mc^2}} & p < mc \qquad (9) \\[2ex] -\dfrac{a+1}{2} + \dfrac{a+3}{2}\sqrt{1 + \dfrac{4x^2}{(a+3)^2}} & p > mc \qquad (10) \end{cases}$$

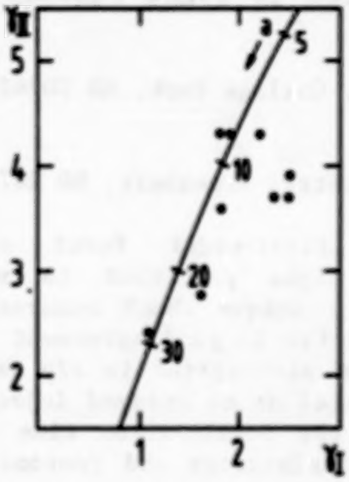

Fig. 3: Correlation between electron spectral exponent below 200 keV γ_I and exponent above 200 keV γ_{II} as a function of a

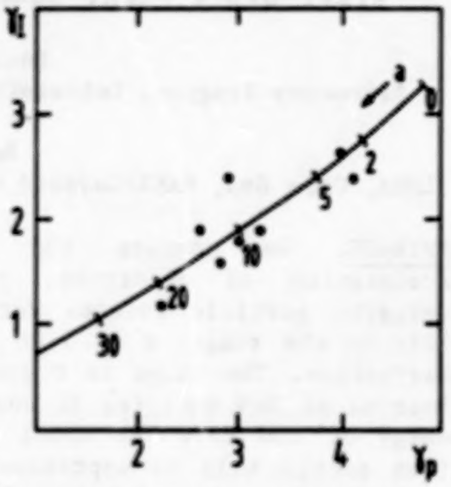

Fig. 4: Correlation between γ_I and proton spectral exponent above 10 MeV as a function of a

$x = \ell_c / L V_A$ is a free parameter which may have different values for electrons and protons and for different flares. Equations (9) and (10) allow us to determine the correlation between the mean spectral index below 200 keV γ_I and above 200 keV γ_{II} for electrons (Fig. 3) as well as the correlation between γ_I and the proton spectral exponent above 10 MeV γ_p (Fig. 4) as a function of a. The curves obtained from (9) and (10) are in excellent agreement with the measurements of Lin et al. (1982), indicating that the strongest shock waves have an Alfvén Mach number $M_A \sim 4$, corresponding to $a \sim 30$ (see Dröge and Schlickeiser (1985) for details).

4. Conclusions. Combining first- and second-order Fermi mechanism in solar flare second-phase acceleration successfully explains the observed ion and electron energy spectra. The model correctly accounts for the sometimes very short delay times, and reproduces quantitatively the correlations of nonrelativistic with relativistic electron spectral indices, and the correlation of nonrelativistic electron with proton indices.

References

Barbosa, D.D., (1979), Astrophys. J. 233, 383

Dröge, W., Schlickeiser, R., (1985), In preparation

Drury, L.O.C., (1983), Rept. Progr. Phys. 46, 973

Jokipii, J.R., (1977), Proc. 15th Int. Cosmic Ray Conf. (Plovdiv), Vol. 2, 429

Lin, R.P. et al., (1982), Astrophys. J. 253, 949

Möbius, E. et al., (1982), Astrophys. J. 259, 397

Parker, E.N., Tidman, D.A., (1958), Phys. Rev. 111, 1206

Pikel'ner, S.B., Tsytovich, V.N., (1976), Sov. Astron. 19, 450

Ramaty, R., (1979), Particle Acceleration Mechanisms in Astrophysics, eds. J. Arons, C. Max, C. McKee, American Institute of Physics, New York, p. 135

Schlickeiser, R., Lerche, I., (1985), this conference, OG 7.2-8

N85-34732

FIRST-ORDER FERMI SHOCK ACCELERATION IN SOLAR FLARES

Donald C. Ellison
Astronomy Program, University of Maryland, College Park, MD 20742
and
Reuven Ramaty
LHEA, Code 665, NASA/Goddard Space Flight Center, Greenbelt, MD 20771

ABSTRACT. We compare the simultaneous first-order Fermi shock acceleration of electrons, protons, and alpha particles to solar energetic particle events. For each event, a unique shock compression ratio in the range, r ~1.5 to 3 produces spectra in good agreement with observation. The range in r predicts that the wide spread in e/p ratios observed at MeV energies is considerably reduced at an assumed injection energy of 100 keV. The model predicts that the acceleration time to a given energy will be approximately equal for electrons and protons and can be on the order of 1 second to ~100 MeV.

1. Introduction. We model the simultaneous acceleration of protons, alpha particles, and relativistic electrons by first-order Fermi shock acceleration (e.g. Axford et al. 1977). Shock acceleration in solar flares has been considered previously (e.g. Achterberg and Norman 1980; Lee and Fisk 1982; Bai et al. 1983; Lee and Ryan 1984). Here, we compare the predictions of Fermi shock acceleration to solar energetic particle events where interplanetary electron, proton and, in some cases, alpha-particle spectra are available (Lin et al. 1982; Evenson et al. 1984; McDonald and Van Hollebeke 1985; R. McGuire private communication) (see also Ellison and Ramaty 1985). In all cases examined, we find that for any given event, a single shock compression ratio in the range ~1.5 to 3 simultaneously produces reasonably good fits to the electron, proton, and alpha-particle spectra.

We also determine the effects of the shock strength and injection conditions on the electron to proton (e/p) intensity ratio. This ratio is sensitive to the injection conditions and large variations in the e/p ratio at MeV energies result from variations in shock strength. We find that these results are in good agreement with the observations.

The acceleration time for shock acceleration is estimated for typical solar conditions. We find that for scattering mean free paths that scale as the gyroradius, shocks can produce rapid acceleration with equal acceleration times for electrons and protons. This result is consistent with the gamma-ray observations (Chupp 1984).

2. Model. In the test particle limit of shock acceleration with no losses, wherein particles gain energy by scattering freely between the converging upstream and downstream plasmas, the accelerated distribution function (at the shock) is a power law in momentum (Blandford and Ostriker 1978). The spectral index depends only on the compression ratio, $r = u_1/u_2$, where $u_1(u_2)$ is the upstream (downstream) bulk plasma flow velocity. The corresponding differential particle intensity is given by

$$\left(\frac{dJ}{dE}\right)_o = n_{inj}(E_1^2 + 2E_1 m_o c^2)^{3/[2(r-1)]} (E^2 + 2Em_o c^2)^{-\frac{1}{2}(r+2)/(r-1)} , \quad (1)$$

where n_{inj} is the density of seed particles injected far upstream and

m_oc^2 is the rest mass energy. Equation (1) assumes that the particles are injected at kinetic energy, E_i, where E_i is much greater than thermal energy. This expression holds, however, for any injected distribution which is steeper, at a given energy, than the resultant power law. For flatter injected distributions, the shock will boost the intensity of the injected spectrum while maintaining its slope. The limiting non-relativistic and ultra-relativistic spectral indexes are $\Gamma_{N-R} = \frac{1}{2}(r+2)/(r-1)$ and $\Gamma_{U-R} = (r+2)/(r-1)$, respectively. The differential intensity steepens in going from the non-relativistic to the ultra-relativistic regime and the spectral index doubles. If, as is normally the case for solar flare events, non-relativistic proton and relativistic electron spectra are observed, acceleration by a single shock of a given r produces an electron spectrum steeper than the proton spectrum (Achterberg and Norman 1980).

The compression ratio can be determined from the Rankine-Hugoniot conservation relations. We find that for typical solar conditions, r lies in the range ~ 1.5 to 3. For example, a coronal shock with $u_1 = 1000$ km s^{-1}, temperature $T_1 = 10^6$ K, density $n_1 = 10^9$ cm^{-3}, and magnetic field perpendicular to the shock normal $B_1 = 10$ Gauss, yields $r = 1.54$. If u_1 is increased to 2000 km s^{-1}, $r = 2.7$.

To model effects such as adiabatic deceleration (Lee and Fisk 1982; Lee and Ryan 1984), finite shock lifetimes (Forman 1981), and finite shock sizes (e.g. Ellison 1984), we assume the spectra will turnover approximately exponentially such that, $dJ/dE \propto (dJ/dE)_o \exp(-E/E_o)$, where E and E_o are energy for electrons and protons and energy per nucleon for ions.

For concreteness, we assume the diffusion coefficient of all energetic particles to be, $\kappa = \kappa_o (v/v_o)(R/R_o)$, where $R = pc/(Ze)$ is rigidity, v is velocity measured in the local plasma frame, and κ_o, v_o, and R_o are constant.

We also assume that the high energy turnover is produced by a shock of finite spatial extent. This implies that the electron turnover energy will be twice that of the protons and that the alpha particle turnover energy will be ½ that of the protons.

If spectra that are power laws in momentum are plotted as a function of energy, the ratio e/p will decrease with increasing energy as the electrons become relativistic. The decrease in the e/p ratio will be greater for smaller r. If shocks of different strengths produce a range of particle spectra, as observed for solar flare accelerated particles, a wide range in e/p will result at MeV energies even if the injection conditions are similar (see Fig. 3).

Estimates of the acceleration time (Ellison and Ramaty 1985) suggest that the solar environment should allow acceleration of electrons and ions to 100's of MeV in times on the order of 1 sec. These estimates assume, of course, that the background turbulence has sufficient power to scatter both electrons and protons from injection energies to 100's of MeV.

3. Comparison with Observations. We have compared the model, using a single set of parameters to simultaneously describe electron, proton, and alpha-particle spectra, to spectra observed in space (see Figs. 1 and 2).

In all cases we choose, for each event, a single compression ratio and E_o that produces the best combined fits to the electron, proton, and alpha-particle spectra. We find that: (1) In all cases, the model provides an excellent fit to the electron spectra above the assumed injection energy of ~100 keV. (2) In all events where multiple species are observed, a single set of parameters (apart from the normalization) provides a fair description of all spectra. (3) The model provides a natural explanation for events with very flat proton spectra such as 3 June 1982 and can be applied over a wide energy range (see Ellison and Ramaty 1985).

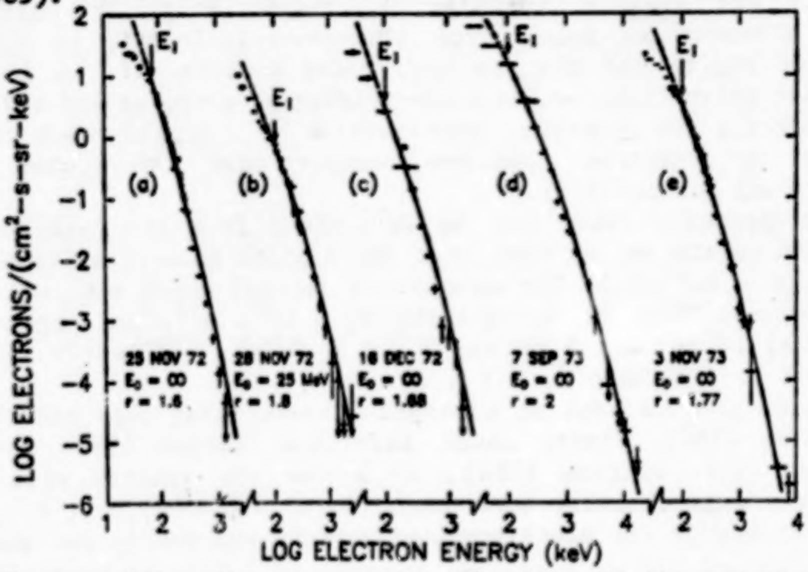

Fig. 1. Electron intensity vs. energy. The line is the spectrum expected from shock acceleration and is calculated for the r and E_0 shown. E_1 is the injection energy of 100 keV. Data is from Lin et al. (1982).

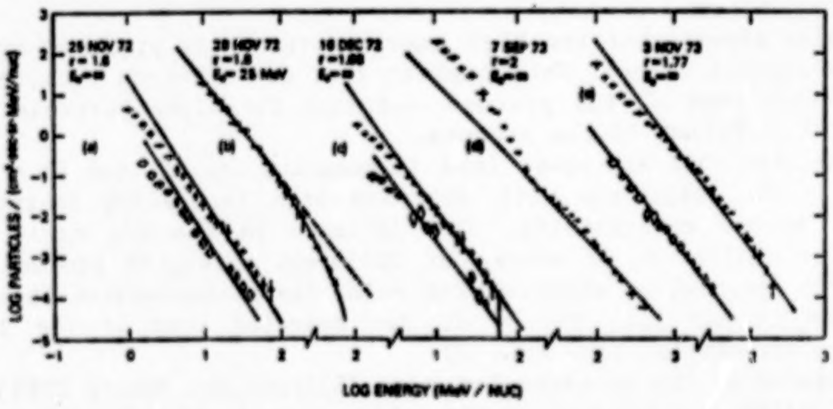

Fig. 2. Proton (crosses) and alpha-particle (diamonds) intensities vs. energy. The data is from IMP 7 and 8 (R. McGuire private communication).

The essential point of the spectral fits is that a single model with a single set of shock parameters produces a reasonable fit to all species. In some cases, in fact, all spectra are fit by a single parameter, r.

A wide range in e/p ratios is observed at MeV energies (Lin et al. 1982; Evenson et al. 1984). Shock acceleration can produce a spread in e/p in two ways. First, steep spectra produce a smaller e/p ratio at high energies than flat spectra assuming the same injection conditions. Second, the injection conditions may vary for electrons and protons.

Using the data of Evenson et al. (1984), we have plotted in Fig. 3 the e/p ratio measured in the energy interval 25-45 MeV (crosses) versus the relativistic electron spectral index, Γ_e. There is a very clear correlation showing that flatter spectra generally produce higher e/p ratios. We also show with the lower solid lines, the predicted correlation between e/p and spectra index or, equivalently, r. The two lines indicate a factor of 10 spread in injection conditions.

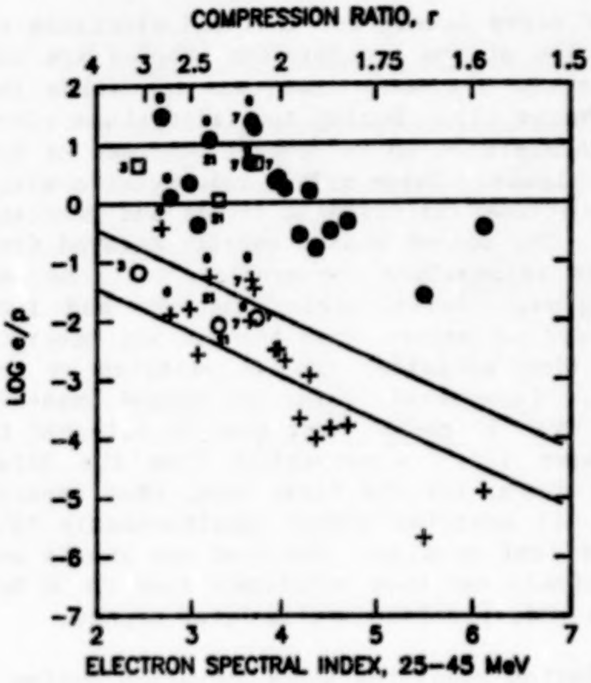

Fig. 3. Crosses are e/p ratios as observed by Evenson et al. (1984). June, 7 and 21 1980 and 3 June 1982 are indicated by open circles and number. These ratios projected to 100 keV are indicated by open squares. Gamma-ray events are indicated by "G". The lower solid lines are the relationship between e/p and r predicted by shock acceleration.

The solid dots in Fig. 3 show the e/p ratios measured at ~ 33 MeV extrapolated to the assumed injection energy of 100 keV. A strong reduction in the spread of e/p results. Gamma-ray events are identified in Fig. 3 with a "G" and it is clear that they tend to have the largest injection e/p ratios and the largest compression ratios.

4. Conclusions. We find that shock acceleration can model many solar flare energetic particle spectra with a single set of parameters for both electrons and protons. The production of power laws in momentum by shocks provides a natural explanation for much of the large spread in the observed e/p ratios at MeV energies. Events that produce gamma rays can be accommodated in this model and do not need to be treated as a distinct class of events. We also find that shocks should allow the acceleration of both electrons and protons to 100's of MeV in seconds.

5. Acknowledgements. We are grateful to Bob McGuire for allowing us to use unpublished data from IMP 7 and 8. This work was supported, in part, by a NASA STTP grant and NSF Grant AST-83-17755.

References

Achterberg, A., and Norman, C.A. 1980, A. A., 89, 353.
Axford, W.I. et al. 1977, 15th ICRC (Plovdiv), 11, 132.
Bai, T. et al. 1983, Ap.J., 267, 433.
Blandford, R.D., and Ostriker, J.P. 1978, Ap.J. Lett., 221, L29.
Chupp, E. L. 1984, Ann. Rev. A. A., 22, 359.
Ellison, D.C. 1984, J.G.R., 90, 29.
Ellison, D.C., and Ramaty, R. 1985, Ap.J., in press.
Evenson, P. et al. 1984, Ap.J., 283, 439.
Forman, M.A. 1981, Adv. in Space Res., 1, 41.
Lee, M.A., and Fisk, L.A. 1982, Sp. Sci. Rev., 32, 205.
Lee, M.A., and Ryan, J.M. 1984, preprint.
Lin, R.P. et al. 1982, Ap.J., 253, 949.
McDonald, F.B., and Van Hollebeke, M. 1985, Ap.J. (Letters), 290, L67.

PROMPT ACCELERATION OF IONS BY OBLIQUE TURBULENT SHOCKS IN SOLAR FLARES

N85-34733

R. B. Decker and L. Vlahos
The Johns Hopkins University, Applied Physics Laboratory
Laurel, MD 20707
USA

1. Introduction. Solar flares often accelerate ions and electrons to relativistic energies. The details of the acceleration process are not well understood, but until recently the main trend was to divide the acceleration process into two phases (1). During the first phase electrons and ions are heated and accelerated up to several hundreds of keV simultaneously with the energy release. These mildly relativistic electrons interact with the ambient plasma and magnetic fields and generate hard X-ray and radio radiation. The second phase, usually delayed from the first by several minutes, is responsible for accelerating ions and electrons to relativistic energies. Relativistic electrons and ions interact with the solar atmosphere or escape from the sun and generate gamma-ray continuum, gamma-ray line emission, neutron emission or are detected in space by spacecraft. In several flares the second phase is coincident with the start of a type II radio burst that is believed to be the signature of a shock wave (2). Observations from the Solar Maximum Mission spacecraft have shown, for the first time, that several flares accelerate particles to all energies nearly simultaneously (3). These results posed a new theoretical problem: How fast are shocks and MHD turbulence formed and how quickly can they accelerate ions to 50 MeV in the lower corona? We address this problem in this brief report.

2. Model. We consider the following model for shock formation during a solar flare. During the flare's impulsive phase, magnetic energy is transferred to plasma particles inside the energy release volume by increasing the random mean square velocity (i.e., heating the bulk plasma) and by accelerating the tail of the velocity distribution. The high plasma pressure inside the energy release expands against the external magnetic field and forms a shock nearly instantaneously (4). The angle $\overline{\Theta}_{Bn}$ between the mean upstream magnetic field and the mean shock normal $\hat{n}$ and the level of magnetic fluctuations in the shock vicinity play a crucial role in accelerating particles to high energies. Since the detailed evolution of energetic ions in a generally oblique turbulent shock is a complex process, we have designed a numerical code that integrates along energetic (i.e., $\gtrsim$ 100 keV) test ion orbits in such an environment (5).

We define K[X, Y, Z] as a system fixed with the shock, with the unit vector $\hat{X} = -\hat{n}$, such that the shock discontinuity coincides with the Y-Z plane and separates the upstream ($X < 0$, subscript 1) from downstream ($X > 0$, subscript 2) regions. The quantities $\vec{U}_1 = U_1 (\cos \delta_1, 0, \sin \delta_1)$ and $\vec{B}_{01} = B_{01} (\cos \Theta_1, 0, \sin \Theta_1)$ denote, respectively, the upstream plasma flow velocity and mean magnetic field (where $\Theta_1 = \overline{\Theta}_{Bn}$). Then, in K the mean electric field on either side of the shock is $-\vec{U}_1 \times \vec{B}_{01}/c$. Given values of the upstream Alfvén Mach number M_{A1} and the plasma beta β_1, the mean downstream conditions are calculated by solving the MHD jump equations (for a ratio of specific heats of 5/3).

We model magnetic fluctuations by superposing upon $\vec{B}_{0i}$ ($i = 1$ or 2) a zero mean, random magnetic field component $\vec{b}_i(z)$ which, in either the upstream or downstream plasma frame, varies only with the coordinate z along $\vec{B}_{0i}$, is transverse to $\vec{B}_{0i}$, and is static, so that scattering is elastic in either plasma frame. We assumed for this study that $\vec{b}_i(z)$ is a superposition of 4096 circularly polarized, parallel-propagating Alfvén waves, each with a random phase, and with the amplitude of each such Fourier component with wave number k derived from a power spectrum P(k) using a technique described by Owens (6). For synthesized realizations of $\vec{b}_i(z)$, the Lorentz force equation was solved for a particle orbit using the field $\vec{B}_i(z) = \vec{B}_{0i} + \vec{b}_i(z)$ in the appropriate plasma frame, and Lorentz transformations were performed between plasma frames at shock crossings. Each particle orbit was followed until a pre-set boundary (spatial or temporal) was crossed.

The source(s) and spectral form of Alfvénic turbulence are, of course, largely unknown in the vicinity of lower coronal shocks. Possible sources upstream include the turbulent pre-flare plasma and Alfvén waves driven by energetic (~ 100 keV) ion beams streaming upstream from the shock following reflection at the shock and/or leakage from the hot downstream plasma. Possible sources downstream include the upstream MHD turbulence convected through and amplified by the shock as well as turbulence excited by the flare release mechanism. We assumed the spectral form P(k) of Alfvén waves shown in Figure 1. The spectrum extends from k_S to k_L, with correlation length $z_c = 10^5$ cm, and slope -5/3 for $k \gg z_c^{-1}$. The integrated power or variance σ^2 assumed was $\sigma_1^2 = 0.19\ B_{01}^2$ upstream and $\sigma_2^2 = 0.38\ B_{02}^2$ downstream. Figure 1 is the upstream spectrum for $B_0 = B_{01} = 50$ G. This spectral form was chosen because it provides power for resonant scattering (gyroradius ~ k^{-1}) of protons (top scale) with energies spanning the range of flare-associated energies from 100 keV to 10 GeV.

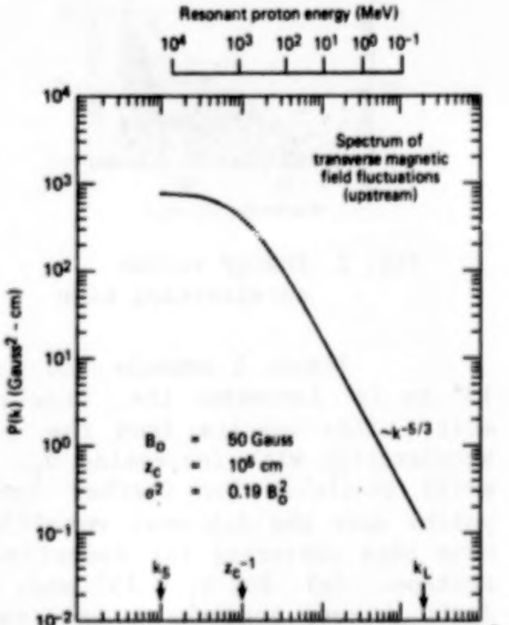

Fig. 1 Power spectrum P(k)

3. Results. Figures 2 and 3 show results for $\delta_1 = 0°$, $U_1 = 3.3 \times 10^8$ cm/s, $B_{01} = 50$ G, $M_{A1} = 3$, $\beta_1 = 0.1$, various values of θ_1 from 0° to 75°, and protons injected upstream of the shock with energy $E_0 = 100$ keV. We define the scale time $\tau_{01} = eB_{01}/m_0c = 1.3 \times 10^{-5}$ sec (nonrelativistic upstream proton gyroperiod). Figure 2 shows the energy E versus acceleration time t/τ_{01} after a total

ORIGINAL PAGE IS
OF POOR QUALITY

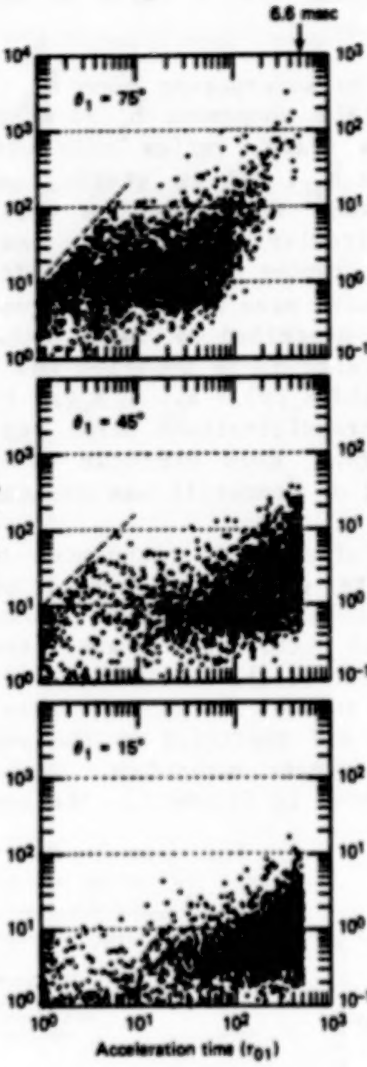

Fig. 2 Energy versus acceleration time

elapsed time of 500 τ_{01} = 6.6 msec for each of 2200 protons injected at shocks with θ_1 = 15°, 45° and 75° (all other parameters held fixed). Plotted is the total energy of each particle against the time taken to reach that energy, or equivalently, the time of the particle's last shock crossing. Points with $t/\tau_{01} <$ 500 imply that these particles spent the time 500 - t/τ_{01} diffusing without net energy change in the upstream or downstream regions.

Particles injected into our turbulent oblique shock model gain energy through both the shock drift and diffusive acceleration processes. Shock drift acceleration, relatively fast and most effective at quasi-perpendicular ($45° \lesssim \theta_1 < 90°$) shocks, results as particles undergo an effective grad-B drift along the $\vec{U} \times \vec{B}$ electric field during shock encounters (7). Diffusive acceleration, relatively slow and most effective at quasi-parallel ($0 < \theta_1 \lesssim 45°$) shocks, results as particles diffuse back and forth across the shock and are compressed between the converging upstream and downstream flows (8). Reference (5) shows a sample orbit.

Figure 2 reveals the following. (a) An increase in θ_1 from 15° to 75° increases the fraction of protons above 10 MeV within 6.6 msec. This results from the increasing contribution from the drift acceleration with increasing θ_1. (b) For θ_1 = 15° most particles are still available for further acceleration (note the high density of points near the 6.6 msec cutoff), whereas for θ_1 = 75° most particles have been convected far downstream and will undergo no further acceleration. (c) For θ_1 = 75° and, to some extent, for θ_1 = 45° the shock drift process produces a spectrum extending from 100 keV to ~ 10 MeV during a super-prompt acceleration phase lasting ~ 0.1 msec, with an apparent upper energy limit indicated by the dashed diagonal lines. Particles in this separate population are those that, through an interplay between pitch angle scattering and drift, remain at the shock and undergo an intensive period of drift acceleration.

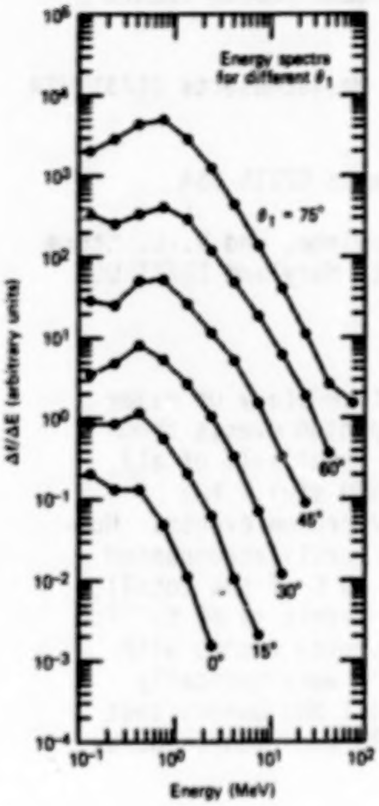

Fig. 3 Energy spectra for various Θ_1

In Figure 3 we show energy spectra for values of Θ_1 from 0° to 75° (all other quantities held fixed), again for a total elapsed time of 6.6 msec. The quantity $\Delta f(E)/\Delta E$ is the fraction of particles with energy E within ΔE centered at the logarithmically spaced plot points. The spectra are separated for clarity and statistical standard deviations are within twice the size of the plot points. Because the drift process produces relatively large and fast energy gains, quasi-perpendicular shocks are clearly most effective in producing power law spectra above ~ 2 MeV (spectral slope ~ 2.1 for 75° and ~ 1.9 for 60°) within ~ 7 msec. Because of the decrease in the drift contribution as well as the slowness of the diffusive acceleration process with decreasing Θ_1, quasi-parallel shocks yield spectra that are steeper and extend to successively lower energies as Θ_1 decreases.

4. Conclusions. We have shown that in solar flares oblique turbulent shocks can accelerate an initial population of 100 keV protons to 50 MeV in less than 7 msec (well below the instrumental resolution of existing instruments) through a combination of diffusion and the shock drift acceleration process. The implication of this prompt acceleration for the overall flare problem is beyond the scope of this brief report.

5. Acknowledgements. This work was supported in part by the JHU/APL Independent Research and Development Program under Navy Contract N00024-83-C-5301 and in part by NSF Grant ATM 83-05537.

References

1. Ramaty, R., et al.: (1980), Solar Flares, (Colorado Press), 117.
2. Frost, K. J. and Dennis, B. R.: (1970), Ap. J., 165, 655.
3. Chupp, E.: (1985), Ann. Rev. Astron. Astrophys., 22, 359.
4. Goodrich, C., et. al.: (1985), EOS Trans. AGU, 66, 331.
5. Decker, R. B., and Vlahos, L.: (1985), Paper SH 1.5-3, these proceedings.
6. Owens, A. J.: (1978), JGR, 83, 1673.
7. Armstrong, T. P., et al.: (1977), "Study of Travelling Interplanetary Phenomena, (Reidel), 367.
8. Drury, L. O. C.: (1983), Rep. Prog. Phys., 46, 973.

14 N85-34734

FAST DRIFT KILOMETRIC RADIO BURSTS AND SOLAR PROTON EVENTS

E. W. Cliver
Air Force Geophysics Laboratory, Hanscom AFB, Massachusetts 01731 USA

S. W. Kahler
Emmanuel College, Boston, Massachusetts 02115 USA

H. V. Cane*, R. E. McGuire*, T. T. von Rosenvinge, and R. G. Stone
NASA/Goddard Space Flight Center, Greenbelt, Maryland 20771 USA

ABSTRACT

We present initial results of a comparative study of major fast-drift kilometric bursts and solar proton events from Sep 1978 - Feb 1983. We find that only about half of all intense, long duration ($>$ 40 min above 500 sfu) 1 MHz bursts can be associated with E > 20 MeV proton events. However, for the subset of such fast-drift bursts accompanied by metric Type II and/or IV activity (~ 40 % of the total), the degree of association with > 20 MeV events is 80 %. For the reverse association, we found that proton events with J(> 20 MeV) $> 10^{-2}$ pr cm^{-2} s^{-1} sr^{-1} MeV^{-1} were typically (~ 80 % of the time) preceded by intense 1 MHz bursts that exceeded the 500 sfu level for times $>$ 20 min (median duration ~ 35 min).

1. Introduction For both scientific and practical reasons, it is useful to identify solar phenomena that typically accompany energetic proton events. Radio signatures identified thus far include metric Type II and Type IV bursts (cf., Cliver et al., 1985). Cane et al. (1981) drew attention to a class of intense, long duration, fast-drift kilometric bursts observed by the low frequency radio experiment on ISEE-3 that occurred in conjunction with metric Type II emission. They suggested that the electrons exciting the fast-drift kilometric emission were accelerated by a coronal shock; subsequently these events were referred to as "shock associated" or SA events. Cane et al. reported that all of the SA events they identified were associated with solar energetic particle (SEP) events while more than half of the proton events detected at 1 AU during the period of their study were associated with possible SA events. Cliver et al. (1983) and Kahler et al. (1985) have recently used the SA signature and the position angle data from the ISEE-3 low frequency experiment to trace SEP events back to atypical origins -- in one case > 500 MeV protons to a weak impulsive phase flare and in the other prompt > 50 MeV protons to a disappearing filament. Thus there is reason to believe that the SA event may serve as an indicator of energetic proton acceleration/escape in flares. To date, however, no detailed comparison of low frequency (< 2 MHz) radio events and SEP events has been made. Thus we do not know whether all major fast-drift kilometric bursts signal the occurrence of a solar proton event or if, conversely, all significant SEP events are preceded by large low frequency

---

*Also: University of Maryland, College Park, Maryland 20742 USA bursts. It is also unclear at present if the so-called SA events can be distinguished from the kilometric extension of long metric Type III bursts (Kundu et al., 1985). In this study, we address such questions.

2. Data Analysis A description of the Meudon/GSFC kilometric radio astronomy experiment on ISEE-3 is given in Knoll et al. (1978). The > 20 MeV proton data were obtained by the GSFC detectors on IMP-8 and ISEE-3. To do the study, we began with a sample of large kilometric bursts and examined their proton associations and then reversed the procedure.

A computer generated list of 658 candidate SAs occurring from Sep 1978 - Feb 1983 was provided by R. MacDowall. This list consisted of all 1 MHz bursts with durations, defined to be the time interval that the intensity (after background subtraction) remained above 500 solar flux units (sfu), of > 20 min. From this list we selected the subset of 110 events with durations > 40 min. We divided these events into two classes: those associated with metric Type II and/or IV bursts and those unaccompanied by such activity. We made the meter-λ associations using data reported only by Ft. Davis, Culgoora, or Weissenau in Solar Geophysical Data (data unavailable for two events). Approximately 40 % (46/108) of the candidate SAs were associated with metric Type II and/or Type IV bursts. For 15 of these 46 cases, either no fresh injection of protons was observed during a time that the > 20 MeV background was enhanced (> 10^{-4} pr cm^{-2} s^{-1} sr^{-1} MeV^{-1}) due to an event in progress (possibly masked event) or an apparently related proton event is more likely to have originated in another solar flare (ambiguous cases). No proton data were available for one low frequency event. Eighty percent (24/30) of the remaining events, originating anywhere on the sun, were associated with a > 20 MeV event at 1 AU. For the non-Type II/IV-associated events (62/108 cases), approximately 30 % (11 of 35 events with "clean" proton circumstances) could have been associated with a > 20 MeV proton event at Earth. Only three of the eleven flare associations are of high confidence and two of these flares had accompanying continuum (but not Type II or IV) metric emission. The non-II/IV events were associated in most cases with groups of metric Type III bursts. There is no marked difference between the durations of the 1 MHz bursts in our sample that were associated with metric Type II/IV bursts and those unaccompanied by such activity. The II/IV-associated events tend to be slightly longer with a median duration ~ 50 min vs. 46 min for the non-II/IV events. A significant difference does exist between the distributions of the time averages of the logarithm of the 1 MHz flux-densities (sfu) for the two groups of events. Obtaining a mean-flux-density value by this procedure reduces the effect of short but intense peaks in the burst time profile. The median value of this parameter is 4.16 for the II/IV-associated events and 3.85 for the non-II/IV group. Thus, for the big events with durations > 40 min, the mean-flux-densities, as defined here, of the II/IV-associated events are statistically higher by a factor of two.

For the reverse association -- beginning with the proton events -- we examined the ISEE-3 low frequency data at the times of the parent flares of all proton events with J(> 20 MeV) > 10^{-2} pr cm^{-2} s^{-1} sr^{-1} MeV^{-1} occurring during this period that could be reasonably well associated with a solar event. Flare associations were made without reference to the low frequency data. For each of the 48 events with available 1

ORIGINAL PAGE IS
OF POOR QUALITY

MHz data, we found associated bursts that had durations above 500 sfu ranging from < 10 min to > 60 min. Approximately 80 % (39/48) of the bursts had durations > 20 min (median duration ~ 35 min). The distribution of durations is given in Fig. 1. Events with lower confidence parent flare associations are cross-hatched. For two higher confidence events the 1 MHz MHz bursts were only ~ 10 min long.

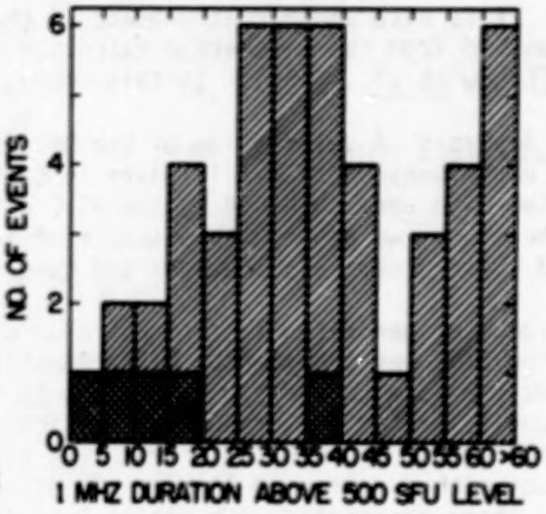

Fig. 1 Histogram of 1 MHz durations (min) for 48 proton events.

In an attempt to gain insight into the question of whether the electrons responsible for the 1 MHz emission in these proton flares were accelerated by shocks or impulsively accelerated in association with metric Type III bursts, we determined the composite fraction of time that the 1 MHz bursts had concomitant metric Type II and Type III emission, respectively. Type II emission covered ~ 45 % of the total combined durations of the 1 MHz bursts while Type III bursts covered anywhere from 32 - 65 %, depending on how weak intermittent activity and storms that may begin well before the kilometric event are treated. An example of good time correspondence between a metric Type II burst and intense 1 MHz emission observed in a major proton flare is given in Fig. 2. Even for this event,

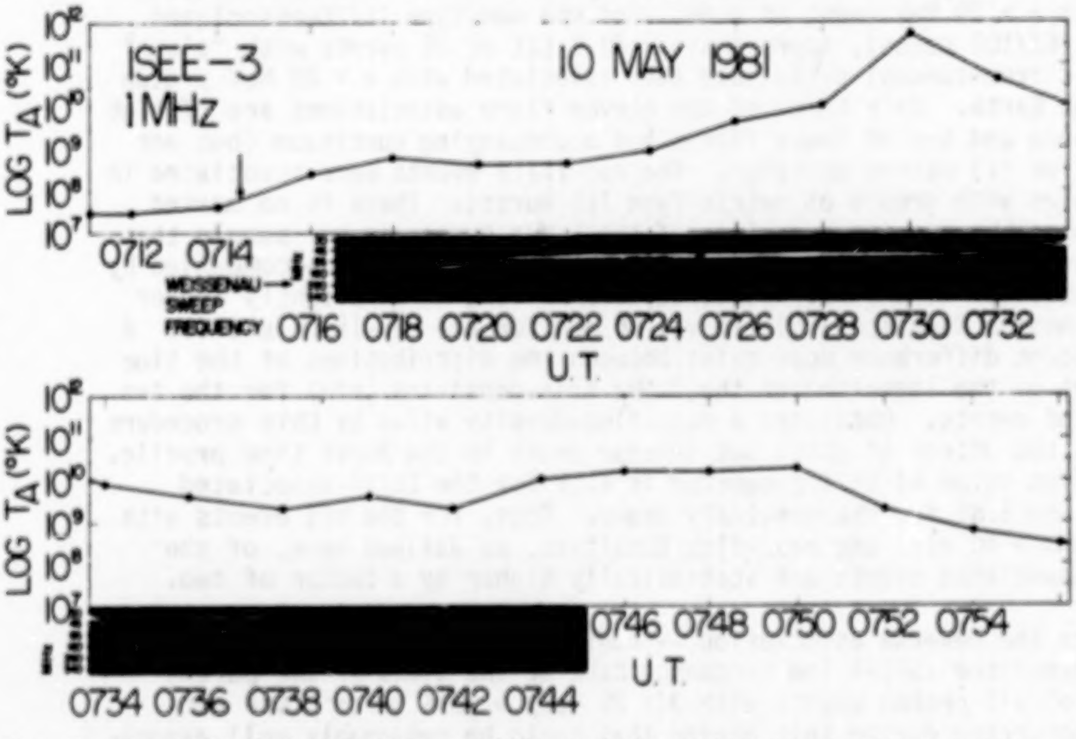

Fig. 2 The ISEE-3 1 MHZ time profile and the Weissenau meter-λ sweep frequency record for the 10 May 1981 proton flare.

however, for which no Type III emission was observed, the 1 MHz event starts earlier (arrow indicates time at which 500 sfu level crossed) than the metric Type II and the possibility of a Type III burst with starting frequency in the 2 - 20 MHz gap between ground-based and ISEE-3 observations cannot be ruled out.

3. Discussion Our preliminary results from this study of the relationship between major fast-drift kilometric bursts and SEP events are as follows: (1) only about half (35 of 65 "clean" cases) of all intense, long duration (> 40 min above 500 sfu) 1 MHz bursts are associated with E > 20 MeV proton events, (2) for the subset of such fast-drift bursts accompanied by metric Type II and/or IV activity (~ 40 % of the total), the degree of association with > 20 MeV events is 80 %, and (3) ~ 80 % of proton events with $J(> 20\ \mathrm{MeV}) > 10^{-2}$ pr $\mathrm{cm}^{-2}\ \mathrm{s}^{-1}\ \mathrm{sr}^{-1}\ \mathrm{MeV}^{-1}$ are associated with 1 MHz bursts with durations of > 20 min above the 500 sfu level (median duration ~ 35 min).

In terms of the well-established impulsive/second phase paradigm for particle acceleration in solar flares (Wild et al., 1963; Lin, 1970; Svestka and Fritzova-Svestkova, 1974), it seems logical to ascribe at least some of the intense 1 MHz emission that typically accompanies significant proton flares to escaping shock-accelerated electrons. At the same time, it appears that the majority of the long duration kilometric events are simply low frequency extensions of "impulsive phase" Type III bursts (cf., Kundu et al., 1985). The 1 MHz bursts associated with proton events were accompanied by metric Type II bursts for ~ 45 % of their composite durations and by metric Type IIIs for 32 - 65 %. The contribution of impulsively accelerated electrons to the kilometric bursts accompanying proton flares will have to be clarified using actual meter-λ sweep frequency records instead of the SGD compilations we have relied on thus far. It remains to be seen if low frequency bursts due to impulsively accelerated electrons can be distinguished from kilometric activity excited by SA electrons on the basis of differences in such parameters as burst time-profiles, spectra, or drift-rates, none of which were addressed herein. We have noted that the Type II/IV-associated events with durations > 40 min had significantly higher (factor of two) mean-flux-densities than non-II/IV-associated events. While this may indicate the presence of an additional acceleration mechanism, i.e., a coronal shock wave, it may also be a Big Flare Syndrome (Kahler, 1982) result in that the larger flares that generate Type IIs and IVs might be expected to have stronger impulsive phases and thus higher mean-flux-densities at 1 MHz.

References

Cane, H. V., et al., 1981, Geophys. Res. Letters 8, 1285.
Cliver, E. W., et al., 1983, Solar Phys. 89, 181.
Cliver, E. W., et al., 1985, J. Geophys. Res. (in press).
Kahler, S. W., 1982, J. Geophys. Res. 87, 3439.
Kahler, S. W., et al., 1985, (these proceedings).
Knoll, R., et al., 1978, IEEE Trans. Geosci. Electronics GE-16, 199.
Kundu, M. R., et al., 1985, EOS, 66, 330.
Lin, R. P., 1970, Solar Phys. 12, 266.
Svestka, Z., and Fritzova-Svestkova, L., 1974, Solar Phys. 36, 417.
Wild, J. P., et al., 1963, Ann. Rev. Astron. Astrophys. 1, 291.

STUDY OF PHOTON EMISSION BY ELECTRON CAPTURE DURING SOLAR NUCLEI ACCELERATION: I.TEMPERATURE-DEPENDENT CROSS SECTION FOR CHARGE CHANGING PROCESSES.

J. Pérez-Peraza * and M. Alvarez *
Instituto de Geofísica UNAM, 04510, C. U. México, D.F.

A.Laville
Instituto Nacional de Astrofísica Optica y Electrónica, Tonanzintla, 72000 Puebla, México.

A. Gallegos
UPICSA, 08400 - México, D. F.

I. **INTRODUCTION**. The study of charge-changing cross-sections of fast ions colliding with matter provides the fundamental basis for the analysis of the charge states produced in such interactions. Given the high degree of complexity of the phenomena, there is no theoretical treatment able to give a comprehensive description. In fact, the involved processes are very dependent on the basic parameters of the projectil, such as velocity v, charge state q and atomic number Z, and on the target parameters Z_t, q_t, the physical state (molecular, atomic or ionized matter) and density. The target velocity, v_t may have also incidence on the process, through the temperature T of the traversed medium. In addition, multiple-electron transfer in single collisions intrincates more the phenomena. Though, in simplified cases, such as protons moving through atomic hydrogen, considerable agreement has been obtained between theory and experiments, however, in general the available theoretical approaches have only limited validity in restricted regions of the basic parameters. Since most measurements of charge-changing cross-sections are performed in atomic matter at ambient T, models are commonly based on the assumption of targets at rest ($T \equiv 0$); however at Astrophysical scales, T displays a wide range in atomic and ionized matter. Therefore, due to the lack of experimental data we attempt here to quantify T-dependent cross-sections on basis to somewhat arbitrary, but physically reasonable assumptions.

II.- **CHARGE TRANSFERT IN FINITE-TEMPERATURE MATTER**. Let introduce the relative velocity

$$V_R = v + v_t \qquad [1]$$

in the kinematics of the collision, where the target velocity, v_t, is the most probable thermal velocity of free electrons or hydrogen atoms in ionized or atomic matter respectively. If v_t is fixed in (1), for instance at $v_t = 0$, the dependence of charge-changing cross sections on the proyectil velocity behaves as is shown in pannel-1, for hydrogenic ions in atomic hydrogen, where σ_{pc}=loss cross-section, σ_{cc}=Coulomb capture cross-section and σ_{cr}=radiative capture cross-section. A rough interpretation of that velocity-dependence may be seen in terms of the idealized "free-collision approximation" (though the Born approximation wich allows for screening effects gives qualitatively the same description): electrons are preferentially captured into states of orbital velocities $u \gtrsim v$ and preferentially lost at $v > u$. Since the impact parameter behaves as qq_t/Mv^2, where M is the reduced mass, σ_{pc} at $v > u$ decreases with v, whereas at $v \lesssim u$, σ_{pc} increases with v because the adiabatic nature of the collision. Similarly, since the capture radius $R_c \sim 1/v^2$, electron capture declines with the projectil velocity. At relatively low v when R_c is large, electrons are readily captured far from the nucleus, where the energetic levels are very closed among them, falling much probably in an allowed state. So, there is photon emission because the electron braking in the capture; this is called Coulomb Capture. When v is relatively high, electron binding takes place at small R_c, where the energetic states are widely separated: the probability is high for the electron to fall in a forbiden state, such that a photon is emitted for the electron to be placed in an allowed orbit; this is known as Radiative Capture. Obviously, σ_{cr} at low v and σ_{cc} at high v are not null. According to [1], at Kinetic Energies $E \gtrsim 9$MeV/n, σ_{cr} becomes predominant over σ_{cc}. It can be seen in (1), from V_R, that Coulomb capture in plasmas (T>>0) becomes a rare process, even at low v, because the electron thermal v_t is quite significant. Now let fix v in (1) to analyze the temperature behavior of cross-sections: for electron capture in atomic gas ($T<T_i$=ionization temperature of the target medium) it is expected that cross-sections increase with the increase of the target T, because the binding energy of the atomic target electrons decline with T, so that when the electronic clusters of the projectil and target come close, it is easier to pick-up a target electron. At $T>T_i$ when the "free-collision approximation" is near to occur, the T-dependence of cross-sections is similar to the v-dependence, because the increase of V_R with the subsequent decrease in R_c. In the limit of high energy particles in high-T plasmas only σ_{cr} is significant. The point $\sigma_{cc}=\sigma_{cr}$ is reached at lower ion energies than 9MeV/n as T increases ($E_{impact}=E_{ion}+E_t=9$MeV/n). For electron loss, the effect of T on σ_{pc} may be seen as a shift in energy, in the sense that, a given value of σ_{pc} is reached at lower ion velocities as T increases. Although it is not expected a noticeable change in σ_{pc} in ionized with respect to atomic H, because the electronic screening of the target nuciei is negligeable relative to the ionization protentials in the projectil ions, however, the increase of the medium-T increase the impact energy, and so σ_{pc} is affected: for a fixed v in the range v>u, σ_{pc} decreases with T because collisions take place at smaller impact parameters, while in the range of adiabatic collisions ($v \lesssim u$), σ_{pc} at a fixed v increases with T. This is rather seen in atomic media, since a relatively high T the Thermal velocities are high, such that $V_R \gtrsim u$, in which case, as we said before the T-dependence show the same behavior as the v-dependence.

---

* On leave for the INAOE,Tonanzintla, A.P.51, 72000-Puebla.

III. METHODS AND RESULTS. Our analyzis here is limited to the case for which projectil ions are accelerated from the background thermal matter, so that their initial velocities and initial charge states correspond to thermal temperatures. For the local charge states, Q_L, we are mainly based on the Solar-System ionization fractions in [2]. We arbitrarely assume that the accelerated ions undergo charge equilibrium in the source (solar flare matter), such that the charge evolves according to the effective charge $q^*=Z[1-\xi\exp(-130\beta/Z^{0.66})]$, with $\beta=v/c$ and $\xi=\exp[-130(kT/mc^2)]$ k=Boltzman constant and m the hydrogen or the electron mass depending on whether $T \lesssim T_i$ or $T>T_i$. Normalization of Q_L with q^* is made by means of

$q=[(Z-Q_L)(q^*-q^*_{th})/Z-q^*_{th}]+Q_L$, where q^*_{th} is the effective charge of the accelerated ions where they are at thermal velocities. For the electron binding in atomic H we assume that the attractive potential is of the form $U_C\psi(T)$, where U_C is the Coulomb Potential and $\psi(T)=1-\exp(1-T_I/T)$. To account for the increase of capture cross-sections with T we divided the prevailing cross-sections in atomic media ($T\equiv0$) by $\psi(T)$, with $T_I=2.5\text{X}10^4\,^\circ\text{K}$. At $T>T_I$ there is an abrupt fall in the capture cross sections because the drastic change in v_t from atomic to electron thermal velocity. For $T\lesssim T_I$ in panels 2-3 we plotted $\sigma_{cc}/\psi(T)$ at $E_{impact}<9\text{MeV/n}$ and $\sigma_{cr}/\psi(T)$ at higher energies. Due to the predominance of σ_{cr} in plasmas, for $T>T_I$ we plotted $\sigma_{cr}/\psi(T)$ with T fixed at $2\text{X}10^4\,^\circ\text{K}$. The cross $\sigma_{cc}=\sigma_{cr}$ is indicated by a transversal solid line. For σ_{pc} we introduced, as in electron canture cross-sections, the normalized charge and V_R instead of v, and we ran it for any T value (panels 4-5). We employed the conventional temperature-independet cross-sections for atomic matter: so, for atomic sources of solar particles we have according to [3] that, for highly charged nuclei $(q\lesssim Z-1)$ $\sigma_{cc1}=\pi a_o^2q^2Z_tZ_t^{*5}2^{10}(v_o/v)^9(1+4Z_t^{*2}v_o^2/v^2)^{-4}$ and according [4] $\sigma_{pc1}=\pi a_oq^{-3}Z^{4/3}Z_t^{2/3}(v/v_o)^2$ if $v\lesssim v_1$, or according to [5] $\sigma_{pc2}=\pi a_o^2q^{1/3}Z_t^2(v_o/v)^3$ if $v>v_1$, where v_1 corresponds to $\sigma_{pc1}=\sigma_{pc2}$. For very high velocities, when nuclei become hydrogenics, according to [5] we have $\sigma_{pc3}=4\pi a_o^2Z^{1/3}Z_t^2(v_o/v)^3$, $(v>Zv_o)$, and according [3] $\sigma_{cc2}=\pi a_o^2Z^5Z_t^{*5}(2v_o/v)^{12}(1+4Z_t^{*2}v_o^2/v^2)^{-4}$. The case of low velocity hydrogenic heavy ions in atomic media has only a meaning when particles are injected into the acceleration region from a preliminary acceleration stage, so it is excluded within the present context. At high T, in sources of ionized H, we used σ_{pc1} and σ_{pc2} with q instead of Z, and according to [6], $\sigma_{cr1}=6.15q_o^2q^4(v_o/c)^3(v_o/v)^2(v_o/v^2+q^2v_o^2)$ if $v\lesssim3qv_o$ and $\sigma_{cr}=9.1\text{X}10^{-21}(q^2v_o^2/v^2+q^2v_o^2)^2(q^2v_o^2/v^2)\exp[-(4qv_o/v)\text{arcT}_g(v/2v_o)]/1-\exp(-2\pi qv_o/v)$ if $v>3qv_o$; for hydrogenic ions (very high T or v) we used according to (5) $\sigma_{pc4}=\pi a_o^2Z^{-5/3}Z_t^{1/3}(v/v_o)^2$ if $v\lesssim v_2$ and σ_{pc3} if $v>v_2$, where v_2 correspond to $\sigma_{pc3}=\sigma_{pc4}$. Obviously, at $E_{impact}>9\text{MeV/n}$ in sources of atomic H, we used σ_{cr} instead of σ_{cc1} or σ_{cc2}. It can be noted that due to continuos changes of the normalized σ, there are oscilations in the cross-section values, that for reason of scale can not be smoothed at high energies as easy as in low energies.

IV. CONCLUSIONS. Under the arbitrary assumption that electronic screening of the target H is not very important compared with the screening of the projectil ions, we extrapolate charge-changing cross sections in atomic matter at $T\equiv0$ to finite temperature media, by introducing the target velocities. Nevertheless, for atomic media we have considered the effect of the target electronic screening on capture cross-sections, as T increases. We feel that the obtained results are of more realistic nature, for astrophysical goals, that the mere extrapolation of the conventional T-independent cross-sections.

REFERENCES

[1] Briggs,J.S. and Detmann,K., Phy.Rev.Letters 33,1123,1974.
[2] Jain,N.K. and Narain,V.,Astron.Astrophys.Suppl.31,1,1978.
[3] Nicolaev,V.S., Soviet Phys.Uspekhi 8,269,1965.
[4] Bohr,N. and Lindhard J., Dan. Mat. Fys. Medd. 28,1, 1954.
[5] Bohr,N.,Dan. Mat. Fys. Medd. 18, 8, 1948.
[6] Bethe,H.and Salpeter,E.E.,Quantum Mechanics of 1-2 electron atoms, Springer Verlag, 1957.

ORIGINAL PAGE IS
OF POOR QUALITY

P-2 →

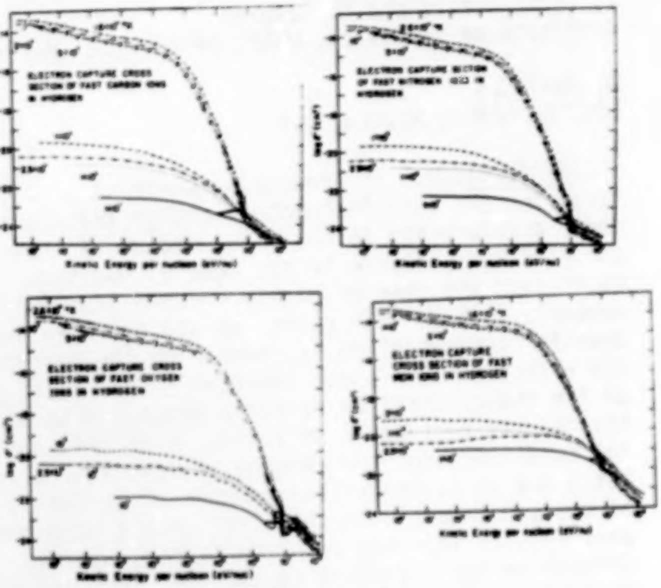

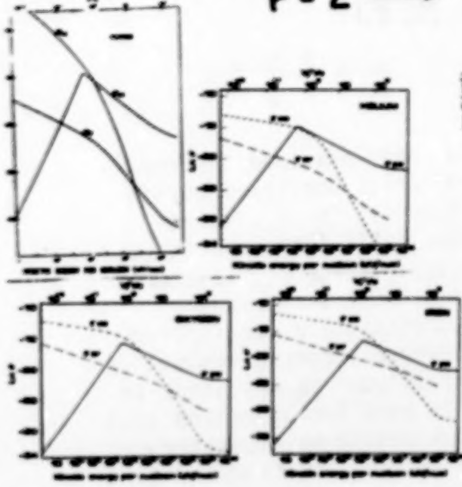

P-1

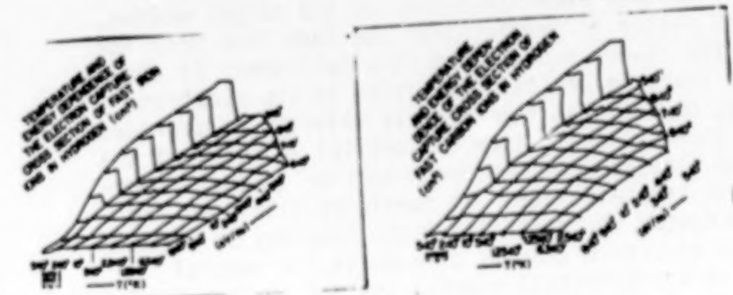

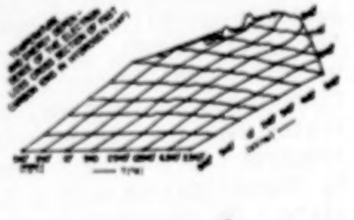

P-3

P-4

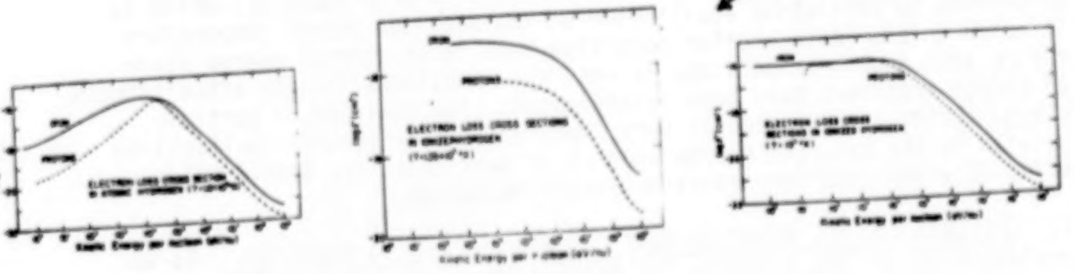

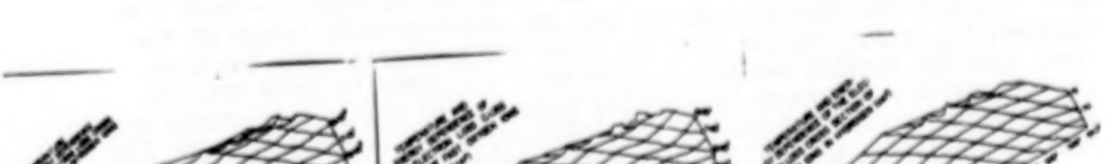

P-5

STUDY OF PHOTON EMISSION BY ELECTRON CAPTURE DURING SOLAR NUCLEI ACCELERATION.II. DELIMITATION OF CONDITIONS FOR CHARGE TRANSFERT ESTABLISHMENT.

N85-34736

J. Pérez-Peraza* and M. Alvarez*
Instituto de Geofísica, UNAM, 04510, C.U. México 20, D.F.

A. Gallegos
UPICSA, 08400, México, D.F.

I. INTRODUCTION. In preceeding works 1 , 2 , we have examined the conditions for the establishment of charge transfert of solar particles during their acceleration in the dense medium of their sources: In 1 , we restricted our analysis to the case of hydrogenic projectil ions, and in 2 we studied the case of highly charged ions (effective charge = $q^*<z$=atomic number). But in both cases, we did not take into account the charge transfer cross-section dependence on the target velocity, i.e. we ignored the effect of the finite temperature of matter. A more occurate evaluation of the charge transfer criteria developed in the previous papers needs of the results derived in SH.1.1-8. With this goal in mind let us remind that the conditions for the passage of fast ions through matter at laboratory scale and in astrophysical sources of energetic particles are to some extent of opposed nature. In the first case a monoenergetic flux of high energy particles is injected into the matter, whereby particles lose energy through energy transfert to the electrons and nuclei of the target medium. When the amount of traversed matter is greater than the mean free path for charge changing processes, the charge equilibrium is established; if the particle velocity is higher than the orbital velocities of its electrons the ion is rapidly stripped, however, as the particle velocity is degraded by collisional losses to a lower velocity than the orbital velocity of the first captured electron, the electron capture cross-section gradually dominates over the electron loss cross-section. As particles slow down and electron capture leads them toward the neutralization, they may be stopped by thermalization with a low effective charge, or even in the neutral state. On the other hand, in astrophysical sources instead of that tendency toward thermalization,particles are accelerated from thermal energies up to high energies, begining with their local charge state Q_L, which is determined by ionization equilibrium at the peculiar source temperature. In order to elucidate whether particles keep their thermal charge state during that acceleration stage or not, the conditions for the establishment of charge transfert have been investigated. The behavior of particle charge during acceleration is very important due to several implications related to the mass and charge spectra of particles, the acceleration efficiency and secondary electromagnetic radiation.

II. CRITERIA FOR THE ESTABLISHMENT OF CHARGE CHANGING PROCESSES. As we explained in 1 the criteria for establishment of charge-changing processes may be seen as an evaluation of the relative importance between the mean free path for charge transfert and the characteristic length of the acceleration step, provided that the later one be shorter than the mean free path for Coulomb inelastic collisions. In order to avoid masking the effects of concurrence between the processes of charge interchange and acceleration, on the behavior of particle charge, it is convenient for the task of simplicity to consider those acceleration mechanisms whose rates are independent of charge: stochastic acceleration (Fermi mechanism) and acceleration by secularly varying magnetic fields (Betatron mechanism), which rates in the non-relativistic range may be expressed as $(dE/dt) = \alpha E^n$, with $n = 1/2$, $\alpha = \alpha_f(2\mu C^2)^{0.5}$ and $n = 1$, $\alpha = 2\alpha_b$ for the Fermi and Betatron mechanisms respectively, $E = \mu v^2/2$, μ = atomic mass unit and α_f, α_b the hydromagnetic acceleration efficiencies. Using $(d/dt) = v(d/dx)$ the above rate becomes $v^{2(1-n)}dv = (\alpha/2)(\mu/2)^{n-1}dx$. Now let define a cross-velocity v_c where both cross-sections for electron capture and loss are equated. So, integrating the acceleration rate from v to v_c in the domain of electron capture ($v \le v_c$) through the thickness L of the traveled matter, and from v_c to v in the domain of electron loss, and introducing the condition of establishment of charge transfert, that the corresponding mean free rath (λ) must be shorter than the amount of traversed matter ($\lambda = 1/n\sigma < L$), where n and σ are the number density and the corresponding cross-section, we obtain the following expressions $\alpha < 2(v_c^{3-2n} - v^{3-2n})n\sigma/(3-2n)\ (\mu/2)^{n-1}$ and $\alpha < 2(v^{3-2n} - v_c^{3-2n})\ n\sigma/(3-2n)\ (\mu/2)^{n-1}$ for the establishment of capture and loss at $v < v_c$ and $v > v_c$ respectively, when an acceleration process of efficiency α is modulating the velocity of the traversing particle through the source matter. However, such an acceleration efficiency must overcome the deceleration efficiency from the rate of inelastic losses in order to produce suprathermal particles. That is, the condition $\alpha/\alpha_c > 1$ must be satisfied, where α_c is the threshold value of the acceleration efficiency above the which the acceleration dominates energy losses. Values of $\alpha_c(n)$ were given in [1] as $\alpha_c = 3.38 \times 10^{-13} nq^{0.5}/A$ and $\alpha_c = 4.5 \times 10^9 nq^{0.16}/T^{0.27}A^{0.78}$ for the Fermi and Betatron processes in atomic H, and $\alpha_c = 3.89 \times 10^{-7} n^{0.98} q^{1.92}/T^{0.96}A^{0.88}$ and $\alpha_c = 0.28 n^{0.97} q^{1.87}/T^{1.45}A^{0.67}$ in plasmas. So,our criteria are reduced to 4 evaluations of $(\alpha_f/(2\mu c^2)^{0.5}\alpha_c) > 1$, two for electron capture (in atomic and ionized H) and two for electron loss, and similarly other 4 evaluations with $(\alpha_b/2\alpha_c) > 1$. On the next figures we have omitted the subfixes f and b, but indicated the considered acceleration mechanism. It must be emphasized that these criteria become independent of number density but strongly dependent on cross-sections and the cross-velocity v_c. Values of v_c for the particular case of targets at rest ($T \equiv 0$) were given in [2]. Here we use the σ values of SH1.1-8 and so the corresponding v_c values were numerically obtained. For the evolution of the charge q appearing in the σ and v_c values, we normalized to the thermal Q_L values as explained in SH1.1-8, when charge equilibrium was found. In the case that the shortness of the characteristic acceleration step only allows for electron capture but not electron loss, we arbitrarely employed in the normalization $q_\xi^* = Q_L \exp\{-130(\beta - \beta_{th})^{0.33}/Z^{0.66}\}$, whereas in the opposite case we used $q_\xi^* = Z\{1 - \xi\exp(-130\beta^{0.33}/Z^{0.66})\}$ where β and β_{th} are the projectil velocity and its thermal velocity respectively and ξ as given in SH1.1-8. The results discused below may be considered as a lower limit in the amount of electron capture and loss, because the main considered target is H. If heavier elements are considered, electron capture becomes much more important, because the employed cross-sections scale as $Z_t Q_L^2$ for Coulomb capture and Z_t for radiative capture; so in evaluating election pick-up with heavy targets we multiplied σ_{crl} and σ_{cr} in SH1.1-8 by Z_t.

---

*On leave for the INAOE, Tonanzintla,A.P.51, 72000-Puebla

III. RESULTS AND CONCLUSIONS. We explored the conditions for establishment of charge transfert during acceleration of nuclei up to Fe, for typical conditions of solar flare regions $T = 5 \times 10^3 - 2.5 \times 10^8$°K. Our results show that such conditions are widely assorted, depending on the acceleration mechanism, the kind of projectil ions and their velocity, the target elements, the source temperature and consecuently on the degree of ionization of matter and the local charge state of the accelerated ions.

Nevertheless, in spite of that assorted behavior, there are some general tendencies that can be sumarized as follows. In atomic H electron capture is systematically established from thermal energies up to high energies, whathever the element and for both acceleration process. For a given element and fixed T, the probability and energy domain of electron capture and loss with Fermi are higher than with Betatron acceleration. For a given acceleration process the heavier the ion the higher the probability and the wider the energy range for electron capture and loss. For a given acceleration mechanism and fixed element the importance and energy domain of capture and loss increase with T: for those reasons, the energy range of charge equilibrium (illustrated with solid lines on the next figs.) is wider with Fermi and increases with temperature and atomic number of projectils. For the same reasons, electron loss is smaller while the lighter the element, the lower the temperature and the Betatron process, such that there are conditions for which electron loss is not allowed at low energies, but only electron capture is established. Consecuently, the energy domain for pure electron capture (illustrated with crosses) is wider the lighter, the element, the lower T and with the Betatron mechanism. On the other hand, at high energies electron capture is not allowed and only electron loss is established (illustrated with small squares) up to high energies, while the heavier the element and the higher the temperature. These results, illustrated through figures (1)-(4) show higher importance of electron capture than that found in [1], [2], because the increase of the cross-section with T in atomic matter described in SH1.1-8. Obviously, the employement of the conventional effective charge expression for charge equilibrium is not adequate when only electron capture is established and particles tend to neutralization, or when pure electron loss is established and particles strip faster. In ionized H electron capture is only established with Fermi acceleration for $T>2\times10^{8}$°K and $Z>10$ provided they are at thermal hydrogenic state ($Q_L=Z$). Under these conditions the heavier the ion the higher the probability and energy domain for electron capture. Electron loss is more important with Fermi than with Betatron and the higher the temperature the higher the probability and the wider the energy domain. At low energies electron loss is more important while the lighter the element and at high energies electron loss becomes more important while the heavier the element as can be understood from the q-dependence of cross-sections in SH1.1-8. We have illustrated these effects on Figs. (5)-(7). An interesting effect that appears with the consideration of the target temperature, in contraposition of the conventional picture described in panel-1 of SH1.1-8, is that in low-T plasmas ($T>T_1$) and low velocities ($v<v_c$), σ_{pc} may become higher than σ_{cr1} because the shift to low velocities of the σ_{pc}-pick and the decrease of σ_{cr1} with the increase of relative velocity v_R. On the other hand, although σ_{cr1} decreases with T roughly as v_R^{-2}, however the reason for which electron capture is established only at high T ($>2\times10^{8}$°K) and that electron loss at low velocities increases with T, is due to the fact that v_c increases with T, in such a way that at high T in our criteria expressions we have, for instance in the Fermi case, that $(v_c^2-v^2)$ increases faster with T than the decrease of σ_{cr1}. Finally, in Fig. 8, we have illustrated the energy domain of charge equilibrium in ionized matter for different ions, when instead of H we consider heavy targets: beyond the end of those curves, at higher energies, only electron loss is established. These cases are very importants in evaluating photon emission from electron capture, since our criteria for charge-transfert establishment are density-independent, and so, only σ and v_c determine the electron capture domain.

REFERENCES

[1] Pérez-Peraza, J., et al., Adv. Space Res. 2, 197, 1983.
[2] Pérez-Peraza, J., et al., 18th Int. Cosmic Ray Conf. 9, 309, 1983.

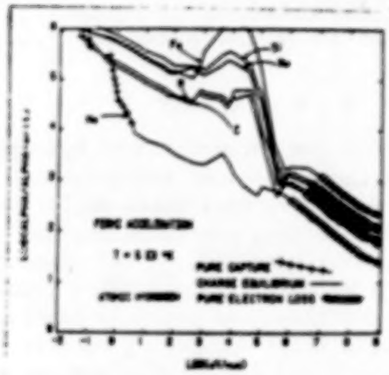

FIG. 1

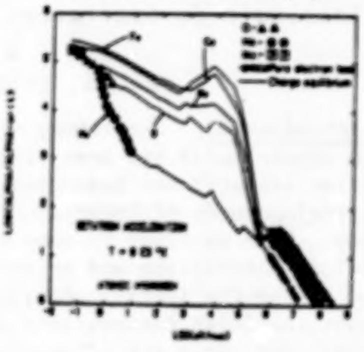

FIG. 2

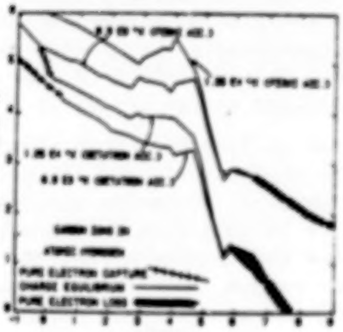

FIG. 3

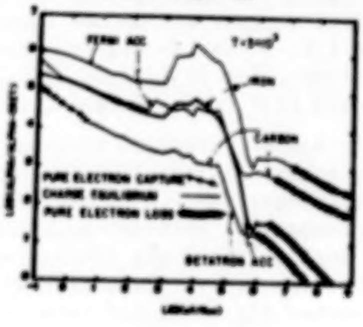

FIG. 4

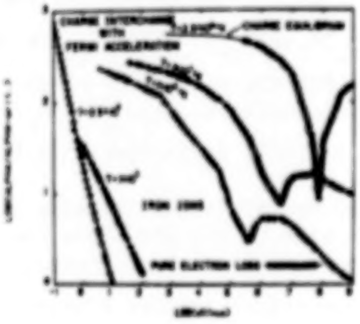

FIG. 5

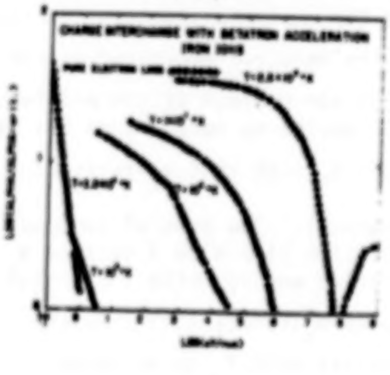

FIG. 6

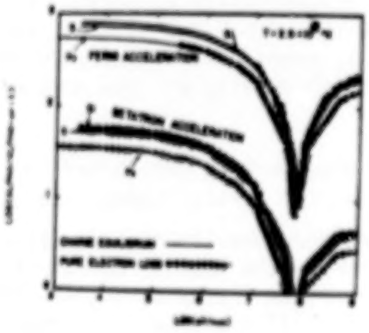

FIG. 7

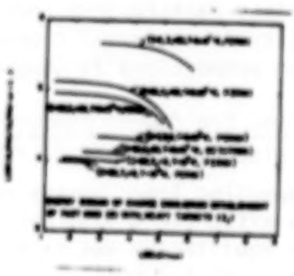

FIG. 8

N85-34737
SH 1.1-10

STUDY OF PHOTON EMISSION BY ELECTRON CAPTURE DURING SOLAR NUCLEI ACCELERATION: III. PHOTON PRODUCTION EVALUATIONS.

J. Pérez Peraza* and M. Alvarez*
Instituto de Goefísica, UNAM, 04510- C. U., México, D. F., MEXICO

A. Gallegos
UPICSA, 08400 - México, D. F., MEXICO

1. Introduction. Electromagnetic emission from the interaction of hydrogenic nuclei with atomic media has been widely studied in Laboratory. At astrophysical scale a similar scenario has been studied: high energy Cosmic Rays (bare nuclei)traversing a certain amount of interestellar matter while loosing energy by Coulomb interactions. Here we study to some extent the opposite scenario, in the sense that particle interaction and emission takes place as particles are being accelerated from the source thermal energies up to high energies. As particle sources we have chosen the Solar chromosphere and corona, where local ions are generally not bare nuclei, and there are often situations for which the amount of traversed matter is enough for the establishment of electron pick-up during acceleration, as was shown in paper SH 1.1-9. Here we limit our calculations to photon emission following electron capture and do not consider emissions following de-excitations. According to SH 1.1.-9 results electron capture is systematically established in atomic H conditions, but in ionized H it is established only at $T>2x10^{6}$°K for nuclei of $Z>10$ and $E<30$ MeV/n; however, since σ_{cr} in ionized matter scales as Z_t= target atomic number, electron pick-up is established at $T>2x10^{6}$°K when the contribution of heavy targets is considered. Actually, since the criteria for charge transfer establishment (SH 1.1-9) are practically independent of matter density, most of the electromagnetic emission expected here appears in this form. It should be noted that such criteria are limited in validity for the condition that the particle flight time within the acceleration volume be enough long for the amoung of traversed matter (X) be higher than the corresponding mean free path (λ) of the charge transfer process ($\rho vt>M/\sigma$): it can be seen that given a density (ρ) and particle velocity (v), since the cross-section (σ) decreases with T, the behavior of the time (t) is fundamental in determining whether ($X>\lambda$) or not: This can be tested from the employed acceleration time $t_f=[2/(2\mu c^2)^{0.5}\,\alpha_f](E^{1/2}-E^{1/2}_{th})$ in the Fermi process, and the betatron acceleration time $t_b=(1/2\alpha_b)\ell_n(E/E_{th})$, where E_{th} is the thermal energy per nucleon of the accelerated ions. For the evaluation of the acceleration efficiencies we recurred to the results of the criteria (α_f/α_c), (α_b/α_c) in SH 1.1-9, such that α_f=(criterium value) α_c(fermi), α_b=(criterium value) α_c (betatron). The general tendency in ionized matter is the increase of the acceleration time with T because α_c decreases with T, so, the above inequality is satisfied easily while the higher T. In atomic matter t_f decreases with T because α_c(Fermi) is T-independent, but the electron capture cross-section increases with T, as we shown in SH 1.1-8, so the inequality is satisfied. With betatron, t_b increases slowly with T as α_c(betatron) decreases with T, however, conditions are such that the inequality is systematically conserved. Similarly, though the electron loss cross-section decreases with T, as t_f does, much of conditions satisfy that inegality. Therefore, even if the density is very low the inegality is conserved because α_c decreases with density and the acceleration times becomes proportionally longer.

2. Method for Photon Production Evaluation. Once we have determined the energy range where electron capture is established, we know the initial charge state q^*_i at the corresponding lower energy value according to the normalization describen in SH 1.1-8 of the effective charge for charge equilibrium to the thermal charge state, when charge equilibrium was established at that particle energy level, or, the arbitrary expresion q^*_c for pure capture given in SH 1.1-9 (if electron loss does not establish). If electron capture begins from thermal energies $q^*_i = Q_L$. Since acceleration is

increasing particle energy, we test at each energy value whether $q_l^*-q_c^*\geq 1$ if charge equilibrium is established, or, $Q_L-q_c^*\geq 1$ if only pure electron loss is established; if not, we iterate to the next energy value with the corresponding q_l^* and q_c^* values in the former case, or $Q_L-q_c^*$, with q_c^* evaluated at the new energy in the 2nd case. When we find that an electron is captured, we evaluate the number of electrons retained by the ion $N_e=Z-q_c^*$. Furhter, we fit this number to the degeneracy condition $2n^2$: if the n-orbit is not still filled, we begin calculating orbit radius $r_n=n^2h^2/Ze^2m_e$ [but, if it is filled we begin to evaluate orbit radius from (n+1)] in order to compare them with the capture radius $(r_c=q^*e^2/m_eV_R^2)$, and in this way to determine at which energy level the electron will be captured; if $r_{n+l}^{-}<r_c<r_{n+l+1}$ we infer that the capture orbit is at $r_{n+l}=r_f$. When $r_c<r_n$ $(n=1)$, we recur to the Sommerfeld eliptic orbits $r_{\kappa}=\kappa n\,^2/m_eZ_e^2$, where κ is the quantic number determining the angular moment, and so, we proceed the evaluation from $\kappa=n-1$ till $\kappa=1$. In the cases that $r_c<r_{\kappa}(\kappa=1)$ we fall in the domain of relativistic mechanics that we have not studied in this preliminar work: this is the case at $T>5\times10^{7}$°K, when V_R becomes extremely high. Therefore, at each energy value we imposed 3 conditions for making possible the evolution of photon emission: (1) electron capture is established, (2) we find $q_c^*\leq q_l^*-1$ (3) $r_c\geq r_{\kappa}(\kappa=1)$. Once these conditions are remplished we evaluate the photon energy $h\nu=E(r_c)-E(r_f)\sim q^*e^2/r_f-q^*e^2/r_c$, and the photon flux at 1. A.U., $F/n_t=N(E)\sigma_c/4\pi R^2$ (photons/eV st/target atom). For our calculations we took the energy spectrum of protons demodulated for interplanetary propagation of the 4-VIII-72 event [1], $N(E)=8\times10^{35}\,E^{-3}$, and typical solar particle abundances [2], such that under the assumption $(O/H)_0=0.77\%$ we built the heavy ions spectra. For radiative capture we did not evaluate photon emission from electron braking as we have done in the case of Coulomb capture.

3. Results and Discussions. As is shown in the next series of pictures, our results are widely assorted depending on T, Z_t, Z, N(E, Z) and the acceleration process. The general tendencies show a frecuency drift toward high photon energies as particles increase their energy during acceleration, because $h\nu\sim 1/r_c$ and $r_c\sim 1/V_R$: oscilations are due to charge changes and the separation between r_c and the quantic level at r_f which is very sensitive to V_R. Typical drifts in atomic matter produces continum radiation from IR to X-ray $(10^{-3}-5\times10^{3})$eV in $\Delta t\sim 1$s, whereas in ionized matter we obtained emission lines from UV to X-rays (50 eV-6.2KeV), with a finite width covered in $\Delta t\leq 0.5$s. It can be appreciated on the drift figures ($h\nu$-E) that the heavy the projectil the emission drifts to higher energies, because $h\nu\sim q^*/r_c^2\sim Z^2$. The range of energy drift widens with T, because the particle energy range for electron capture increases with T. Also the photon energy increase with T because the increase of V_R with T, but with oscilations due to the V_R-sensivity of the separation between r_c and the nearest orbit r_f. On the figures of energy spectra (Flux-$h\nu$) it can be noted that the heavier the target and the projectil the higher the intensity of the emission spectrrum. This follows from the fact that $F/n_t\sim\sigma_cN(E, Z)$ and σ_c increases with Z and Z_t. However, this tendency may also show oscilations because N(E, Z) does not increase always monotonically with Z. Also, the emission intensity increases with T in atomic matter and decreases with T in ionized matter, because the corresponding σ_c increases and decreases with T respectively. Photon fluxes in atomic and ionized matter are in the range $10^{-7}-10^{7}$ ph./eVst/target-atom and $10^{-12}-10^{8}$ph./eVst/target-atom. On the time profiles figures (Flux - t) the t-axis refers to t_f and t_b,

which are increasing functions of particle energy E. Since N(E, Z) is a decreasing function with E, therefore, phothon fluxes decrease with time during acceleration. Photon emission begins faster after acceleration onset with Fermi than with betatron acceleration, and more faster, in atomic than in ionized media, since acceleration efficiencies are higher in atomic matter: for instance, with Fermi acceleration begins $(10^{-5}-10^{-3})$s after acceleration onset, while with betatron begins $(10^{-3}-10^{-2})$s after acceleration onset, whereas in ionized matter corresponding time delays are (0.5-3.5)s and ∿ 2.3s respectively. From the values $\alpha_f \sim (4\times10^{-3}-10^{4})s^{-1}$ and $\alpha_b \sim (3.5 \sim 10^{5})s^{-1}$ in atomic matter, it is realized that acceleration from thermal energies in deep chromospheric layers is restricted to extremely constrained conditions of strong turbulence with extremely short length scales and very high magnetic field gradients, that might only occur in association with fast magnetic field annhilation in active neutral current sheets. On the other hand $\alpha_f \sim (3\times10^{-2} - 0.2)s^{-1}$, $\alpha_b \sim 2.4s^{-1}$ in coronal ionized matter is quite reasonable.

4. Conclusions. We have evaluated lower limits of photon fluxes from electron capture during acceleration in solar flares, because the arbitrary q_c^* assumed in this work evolves very slow with velocity, probably much more slowly than the physical actual situation: in fact, more emission is expected toward the IR region. Nevertheless, we claim to have shown the factibility of sounding acceleration processes, charge-evolution processes and physical parameters of the source itself, by the observational analysis of this kind of emissions. For instance, it would be interesting to search observationallly, for the predicted flux and energy drift of F_e ions interacting with the atomic O and F_e of the source matter, or, even more feasible for the X-ray lines at 4.2 KeV and 2.624 + 0.003 KeV from Fe and S ions in ionized Fe at $T = 10^{7}$°K respectively, the 418 + 2 eV and 20 ± 4 eV lines of Fe and S in ionized Fe at 5×10^{6}°K, which are predicted from Fermi acceleration.

References

[1] Miroshnichenko, L. I. and Petrov, V. M., "Dynamics of Radiation Conditions in Space", Energoatomizdat, Moscow, 1985.

[2] Dietrich, W. F. and Simpson, J. A., Ap. J. 225, L41, 1978.

*On leave for the INAOE, Tonanzintla A.P. 51, 72000-Puebla,MEXICO.

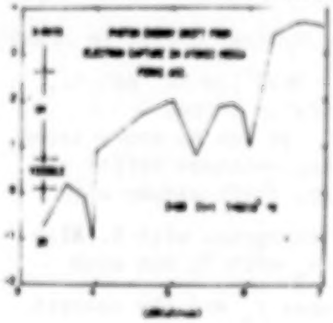

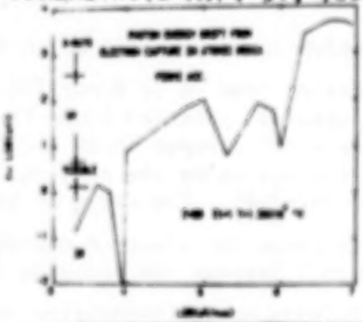

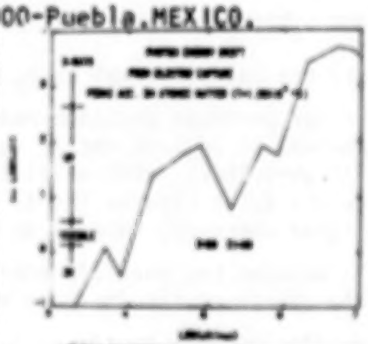

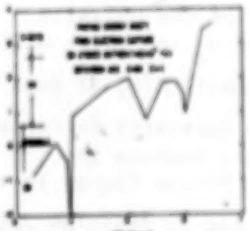

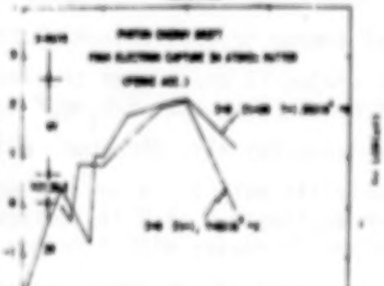

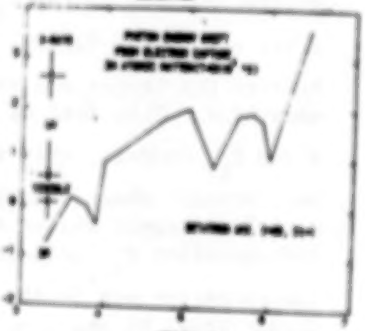

ORIGINAL PAGE IS
OF POOR QUALITY

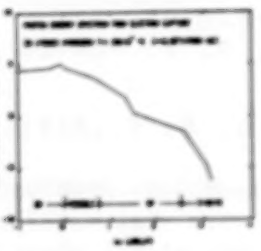

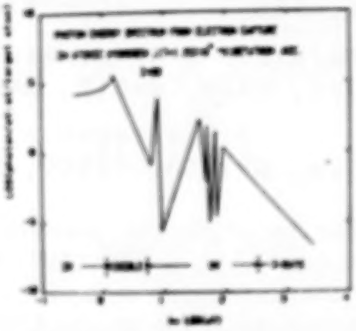

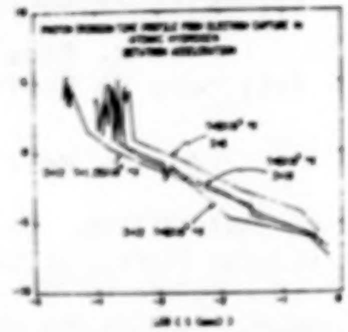

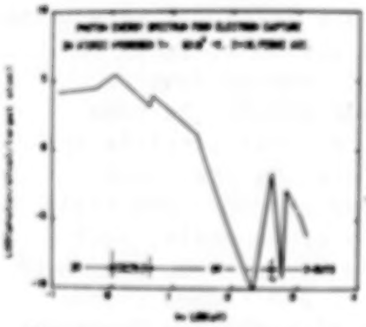

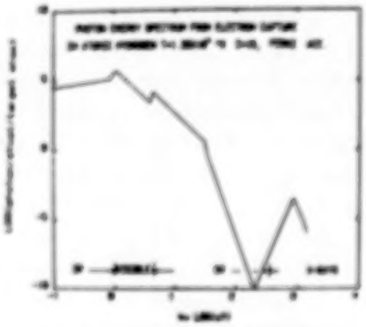

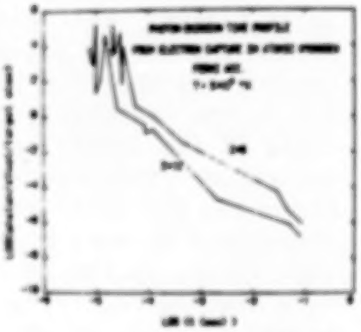

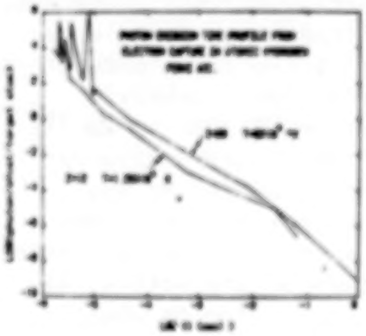

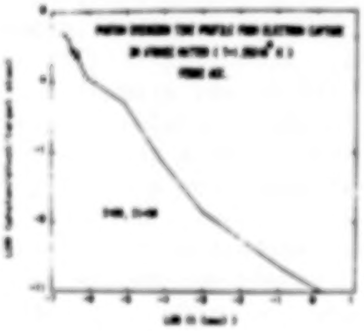

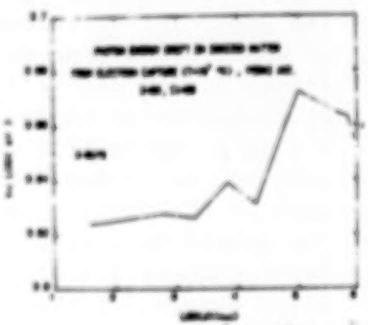

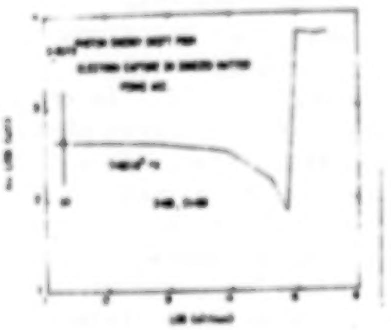

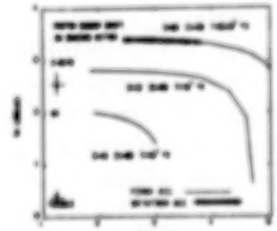

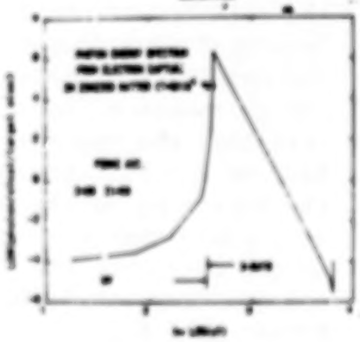

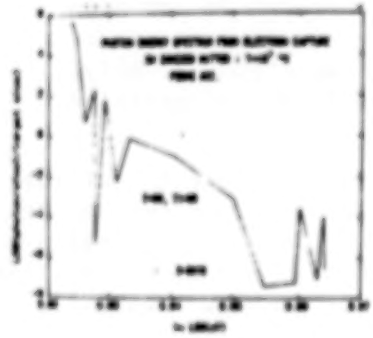

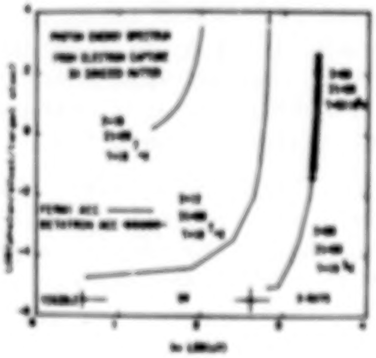

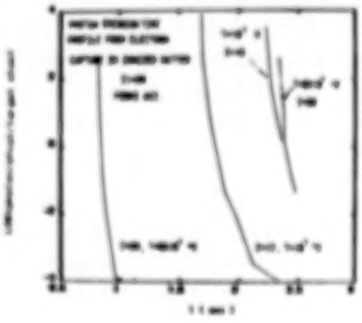

N85-34738

STUDY OF NON-THERMAL PHOTON PRODUCTION UNDER DIFFERENT SCENARIOS IN SOLAR FLARES: I. SCENARIOS AND FORMULATIONS.

J. Pérez Peraza* and M. Alvarez-M.*
Instituto de Geofísica, UNAM, 04510, México, D. F. MEXICO

A. Gallegos
Depto. de Física, UPICSA, 08400, México, D. F.,MEXICO

I. INTRODUCTION. In order to study the overall phenomenology involved in solar flares, it is necessary to understand their individual manifestation before building a corresponding description of the global phenomenon. Here we are concerned with the production of X and γ-rays in solar flares. Following the model in (1), flares are initiated very often within the closed magnetic field configurations of active centers. According (2) when β = kinetic energy density/magnetic energy density ≥ 0.2, the magnetic trap configuration is destructed within the time scale of the impulsive phase of flares (< 100 s). A first particle acceleration stage occurs during this phase as indicated by impulsive microwave and hard-X-rays bursts. In some flare events, when the field strenght B is very high, the broken field lines may close again, such that later, in the course of the flash and main phases more hot plasma of very high conductivity is created, and so, the field and frozen plasma expand outward, as the kinetic pressure inside the closed loops increases. The magnetically trapped particles excite strong Alfvén wave turbulence of small transverse scale. According to (3), small scale turbulence of linear dimensions ∿ (1 - 10) Km may account for effective stochastic acceleration up to relativistic energies. In addition, according to (4) a high pressure piston wich drives a shock within the closed configuration may be formed: magnetized turbulent cells remain bounded in the wake of the "botlle up" shock wave. Since the shock moves faster than the expanding bottle, the stochastic acceleration overcomes the 1st. order Fermi process (adiabatic losses) due to the expansion of the bottle. As discussed in (4) the expanding bottle opens or not depending on whether the duration of the flare induced shock is larger or not than the Raleigh-Taylor instability grow time. Therefore, when the conditions of the opening are satisfied we expect a definite slope change in the energy spectrum, indicating two different particle populations. In the case that the magnetic trap is not destructed during the impulsive phase, because $\beta < 0.2$, the population of the 1st. acceleration stage mix within the expanding bottle with that of the second stage, in which case not a noticeable change in the spectrum slope is expected. On the other hand, in the case that the conditions for the opening of the expanding bottle are not remplished, but the magnetic loop of the impulsive phase was broken ($\beta \geq 0.2$), only the component of the first acceleration stage will be observed. Obviously if the closed magnetic structures do not open during the impulsive phase ($\beta < 0.2$) neither during the subsequent expantion in the main phase, no particle event is expected. Finally, if the flare does not occur within a closed magnetic field configuration, only one main acceleration stage is expected.

II. SCENARIOS FOR X AND γ-RAYS PRODUCTION. Within this context, four scenarios have been examined: (a) Production of the radiation in the source of particle acceleration during the impulsive phase, in a tick geometry context (high amount of traversed matter: high density n and/or long time t); (b) Production of the radiation in the source of secondary particle

(*) On leave for the INAOE, Tonanzintla, 72000 Puebla, MEXICO acceleration (tick geometry); (c) Production of the radiation during secondary acceleration by the superposition, of particles of that stage mixed with the component of the 1st. acceleration stage when $\beta < 0.2$ (tick geometry), and (d) Production of the radiation out of the source of impulsively accelerated particles in a thin geometry context (low amount of traversed matter in the source), either in coexistence or absence of closed field structures. Though particles do not lose energy in the source, they are decelerated by Coulomb collisional losses during transport to the emission volume (dense chromosphere or coronal condensations).

III. ENERGY LOSSES OF SOLAR FLARE ELECTRONS. The main energy losses are: Coulomb-Collisional losses (CC), Bremssthralung (BR), Inverse Compton Effect (IC), Syncrotron Losses (SY) and Adiabatic Losses (AD).The later are negligeable at low energies, becoming gradually important at high energies, however, since the acceleration rates also increase with energy, the predominance of acceleration is conserved. Therefore we have only considered (AD) losses within the frame of scenario (c), with a rate given as $(dE/dt)_{AD} = -(2/3)(V_r/R)\ \beta W$(eV/s), where $\beta = v/c$ is the particle velocity in terms of the light velocity c, W is the total energy, V_r = 2000 Km/s the expansion velocity and $R = 0.7\ R_\theta$ is the expanded distance, with R_0 = the solar radius. For (SY) losses we used the next formula $(dE/dt)_{SY} = -0.98 \times 10^{-3} B^2 (\beta^2/1-\beta^2)$(eV/s), however, they are only important at relatively high energies and strong magnetic fields (Fig. 1); since for the field strength prevailing in flares the electromagnetic radiation produced by syncrotron effects falls very far from the X-ray domain, for the task of simplicity we ignore them in a first approximation. Though (CC) effects do not contribute to X-ray production, energy losses are very important at low energies in determining whether or not the acceleration rate is enough high to generate energetic particles from the thermal solar plasma. Therefore the considered prevailing processes are:

$$(dE/dt)_{CC} = -\frac{K_1}{\beta} \ln \Lambda \{K_2 [0.88 \text{ erf } (X_p) - 1.84 \times 10^3 X_p e^{-X_p^2}] +$$

$$K_3 [0.88 \text{ erf } (X_e) - 2X_e \ e^{-X_e^2}] \} \text{ (eV/s)} \qquad [1]$$

where $K_1 = 1.57 \times 10^{-35} n$, $\Lambda = 4.47 \times 10^{16}\ \beta^2\ (T/n)^{0.5}$, $K_2 = 5.98 \times 10^{23}$, $K_3 = 1.1 \times 10^{27}$, $X_p = 2.33 \times 10^6\ \beta T^{-0.5}$ and $X_e = 5.44 \times 10^4\ \beta T^{-0.5}$, where T is the temperature (°K). For non-Relativistic (BR) we used

$$(dE/dt)_{BR} = -4.74 \times 10^{-11} n\beta \qquad [2]$$

whereas in the relativistic range we have

$$(dE/dt)_{BR} = -1.37 \times 10^{-16} n\ [\ln W/m_e c^2 + 0.36]\ W \text{ (eV/s)} \qquad [3]$$

where $m_e c^2$ is the electron rest energy. For (IC) we have

$$(dE/dt)_{IC} = -1.02 \times 10^{-25}\ \omega_{ph} W^2 \text{ (eV/s)} \qquad [4]$$

where ω_{ph} (eV/cm^3) is the mean photon energy density: for the photon field we have employed the local field in the flare volume due to the flare phenomenon itself, instead of the back ground photospheric field. In fact, if the photon field is computed from the black body low integrated over all frecuencies for a $T \underset{-}{\sim} 6000$ °K, therefore, $\omega_{ph} = 2.7\ akT^5 = 5.5 \times 10^{12}$ eV/cm^3 where a and k are the Radiation Density and Boltzman constants; however when this photon field reaches a distance of $\sim 2 \times 10^9$ cm where flares occur, that value falls to $\omega_{ph} \underset{-}{\sim} 2\times10^{12}$eV/cm^3 due to absorption, mainly from dispersion by electrons. On the other hand, if we considered observed radiative output at flare maximum as a lower limit of the total photon field generated in flare regions, we have according to (5) that for a typical subflare (5/IX/1973) is 10^{27} erg/s, so that adopting as typical time that of 400s for the rise and fall of X-ray data in that event, the radiative output becomes 4×10^{29} erg. Therefore following (6), volumes of this kind of flares are $(0.3\text{-}2) \times 10^{26}$ cm^3, so that $\omega_{ph} \geq 1.2 \times 10^{15}$ eV/cm^3. On the other extreme, class 3 flares show radiative outputs of $\sim 10^{32}$ erg, so that for $V \lesssim 6 \times 10^{32}$ cm^{-3} we obtain $\omega_{ph} \geq 10^{16}$ eV/cm^3. It can be appreciated from Fig. 1, that the preponderant energy loss process are (CC), at least up to 1 MeV, whereas syncrotron losses for $B < 100$ gauss are weaker in relation to the other processes. Also it may be noted that if the photospheric photon field is considered the (BR) process is predominant over the (IC) process for $n \gtrsim 10^{11}$cm^{-3}. If the flare radiation field is considered the (IC) process dominates over the (BR) process for $n \lesssim 10^{12}$ cm^{-3}, however, in the case of small flares in very high density media $n \gtrsim 10^{13}$ cm^{-3} (BR) may become dominant over (IC), (Fig. 1).

IV. ENERGY SPECTRA OF THE FLARE ELECTRONS. Source energy spectra may be derived from a steady-state continuity equation of the Fokker Planck form,

$$\frac{d}{dE}\,(N\ dE/dt) + N/\tau = q\ (E) \qquad [5]$$

for scenarios (a) to (c) we assume that particles are accelerated from the thermal background, so that the injection spectrum $q\ (E) = 0$; in addition, if N is the number of particles per unit energy, the solution of [5] may be reduced to the well known relation of the age-energy analogy for the differential flux

$$N(E) = N_o\ e^{-t/\tau}/\tau\ (dE/dt) \qquad \text{(particles/energy cm}^2\text{sr s)} \ [6]$$

where τ may be identified with a characteristic remain time in the acceleration volume and N_o the number of local particles that participate to the acceleration process. For computation of the thermal flux we integrated the Maxwell velocity distribution from the arbitrary value $V_a = B^2/(4\pi\rho)^{0.5}$ up to ∞, where ρ is the mass-density:

$N_o = 1.63\times10^{-7} nT^{-0.5}(4.79 \times 10^{22}B^4/n + 3 \times 10^{11}T)\ \exp\ (-1.58 \times 10^{11}B^4/nT)$ (particles/cm^{2}sr s). For solving eq. [6] the following equilibrium equations have been employed

$$(dE/dt) = (dE/dt)_{acc} - (dE/dt)_{CC} - (dE/dt)_{IC} \qquad [7]$$

$$(dE/dt) = (dE/dt)_{acc} - (dE/dt)_{CC} - (dE/dt)_{BR} \qquad [8]$$

with the exception of scenario (b) where (AD) losses have been included. Within the frame of scenario (a) two different acceleration mechanisms have been worked out: impulsive acceleration may be provided by the betatron process $(dE/dt)_{acc} = \alpha_b \beta^2 W$ (eV/s) and electric field acceleration processes $(dE/dt)_{acc} = ce\varepsilon\beta$ (eV/s), where α_b is the betatron hydromagne-

ORIGINAL PAGE IS
OF POOR QUALITY

tic acceleration efficiency, ε the electric field, and e the electron charge. For scenario (b) we employed the stochastic Fermi-type process $(dE/dt)_{acc}=\alpha_f\beta$(eV/s). In scenario (c) we use the same acceleration rate that in scenario (b), and for N_o we considered the composition of two components, those of scenario (a) with spectrum N(E) and the thermal spectrum N_o(th), in the site of secondary acceleration. For scenario (d), the general solution of eq.[5], with $dE/dt = -(dE/dt)_{CC}$ gives

$$N(E) = \frac{e^{-t/\tau}}{(dE/dt)_{CC}}\{\int_{E_{th}}^{E_{max}} q(E)e^{t/\tau}dE + N_o(th)(dE/dt)_{th}\} \qquad [9]$$

ENERGY LOSSES OF ENERGETIC ELECTRONS

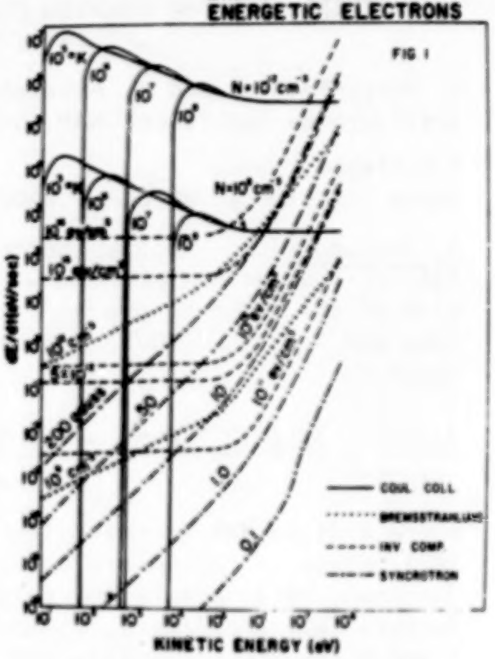

within the frame of this scenario, the 2nd term refers to thermal particles, and so we neglected it because only the impulsively accelerated particles with injection spectrum q(E) travel to the emission region. For q(E) we considered the spectrum of neutral current sheet acceleration derived in (7), per interval time τ', $q(E) = N(E)/\tau'$.

$$N(E)=(9.1\times10^{-2}nV_d/E_o)\left(\frac{E}{E_o}\right)^{-\frac{1}{2}}\exp[-1.12(E/E_o)^{3/4}]\,(\text{part./eV cm}^2\text{sr s}) \qquad [10]$$

where the characteristic energy value E_o and the plasma diffusion velocity V_d depend on the adopted model for neutral current sheet acceleration: for the Priest's model $V_d = 0.057\ V_a$ (cm/s) and $E_o=(2.75\times10^{18}m_e^{\frac{1}{2}}eLV_d\varepsilon)^{2/3}$(eV), where L is the scale length of the neutral sheet. The deconvolution of particle spectra in photon spectra and results are discussed in paper SH 1.2-3.

V. CONCLUSIONS. The consideration of the local photonic field of the flare instead of the conventional photospheric field, gives rise the importance of the Inverse Compton effect for the production of electromagnetic radiation by accelerated particles.

REFERENCES

[1] Pérez-Peraza, J., Invited Talk in Proc. of the 9th. European Cosmic Ray Conference, Kosice, 1984.
[2] Meerson , B. I. and Sasorov, P. V., adv. Space Research 1, 77, 1981.
[3] Pérez-Peraza, J., J. Geophys. Res. 80, 3535, 1975.
[4] Mullan, D. J., Ap. J. 269, 765, 1983.
[5] Canfield et. al., Skylab Workshop on Solar Flares, ed. Sturrock, P., (1979)
[6] Moore et al., Skylab Workshop on Solar Flares, ed. Sturrock, P., (1979)
[7] Pérez-Peraza, J. et. al., Space Research 18, 365, 1978.

^{34}N85-34739 SH 1.2-3

STUDY OF NON-THERMAL PHOTON PRODUCTION UNDER DIFFERENT SCENARIOS IN SOLAR FLARES. II. THE COMPTON INVERSE AND BREMSSTRAHLUNG MODELS AND FITTINGS.

J. Pérez-Peraza* and M. Alvarez*, A. Laville**
Instituto de Geofísica UNAM, 04510-C.U., México, D. F., MEXICO

A. Gallegos
Depto. de Física, UPICSA, 08400 - México, D. F., MEXICO

1. Introduction. Energy spectra of photons emitted from Bremsstrahlung (BR) of energetic electrons with matter, is obtained from the deconvolution of the electron energy spectra derived in SH 1.2.-2. According to Kane and Anderson (1970), the differential photon flux at the earth level is

$$\frac{dJ(h\nu)}{d(h\nu)} = \frac{3.53\times10^{-28}\,E.M.}{n}\int_{E}^{E_m}\frac{d\sigma(E,h\nu)}{dE}\,N(E)\,dE \quad (\text{photons/s KeV cm}^2) \qquad [1]$$

where $d\sigma(E,h\nu)/dE$ is the differential cross-section for electron-proton (BR), given in the non-relativistic range by the Bethe-Heitler formula (Jackson, 1962) and in the relativistic domain by the Koch and Motz formula (Bai and Ramaty, 1976); $E.M. = n^2V$ is the emission measure, with n and V the number density and volume respectively. For Inverse Compton (IC) we followed Sheng (1972), introducing $\sigma(W,h\nu) = \sigma_t\delta[h\nu-(4/3)\bar{\varepsilon}(W/m_ec^2)^2]$ in eq.(1) for $W<(m_ec^2)^2/4\bar{\varepsilon}\sim 290$ MeV, where W=total electron energy, $\sigma_t=6.65\times10^{-25}$ cm^2=Thompson cross-section and $\bar{\varepsilon}=2.7kT$ = mean thermal photon energy, and we obtained at 1 Astronomical Unit.

$$dJ(h\nu)/d(h\nu)=(4.39\times10^{-31}\,E.M.\,\omega_{ph}(h\nu)^{\frac{1}{2}}/n^2T^{3/2})N(E=m_ec^2\{(3h\nu/4\bar{\varepsilon})^{\frac{1}{2}}-1\}) \quad (\text{photons/s KeV cm}^2) \qquad [2]$$

For the evaluation of the electron energy spectra we have explored different combinations of the source physical parameter in the scenarios displayed in SH 1.2-2: $n=10^{10}-10^{13}$ cm^{-3} with $T=10^5-10^7$ °K in scenario (a), $n=10^{10}-10^{12}$ cm^{-3} with $T=10^6-10^7$ °K in scenario (b). For scenario (c) we used the combination of the two previous parameter sets. Values of B were delimited from the thermal flux N_o in SH 1.2-2, for every couple (n,T), by normalization of N_o with the point of maximum flux and minimum energy in the observational photon spectra. For the evaluation of the spectrum [10] of scenario (d) we sweped $n=10^{10}-10^{13}$cm^{-3}, $L=10^8-10^9$cm, $B=10^2-10^3$ gauss and $\varepsilon=10^{-3}-10$ V/cm; in this case two assumptions were worked out for the transport and photon emission regions respectively, first $n=10^{10}-10^{11}$ cm^{-3}, $T=10^5-10^6$ °K with $n=10^9-10^{10}$ cm^{-3}, $T=10^6-10^8$ °K, and on the other hand $n=10^{10}-10^{12}$ cm^{-3}, $T=10^5-10^6$ °K with $n=10^{12}-10^{13}$ cm^{-3}, $T=10^4-10^5$ °K. For the acceleration efficiencies of the Fermi, Betatron and electric field acceleration processes in scenarios (a)-(c) we have required that the net energy change rate $dE/dt>0$ in eqs. [7] and [8] of paper SH 1.2-2. The mean acceleration time τ in eq. [6] is the free parameter of our analysis, however, we have restricted it to physically reasonably values quoted in the literature. Similarly we have proceeded for the selection of the three characteristic times of scenario (d): the characteristic time τ' of the injection rate in eq. [5] of SH 1.2-2, and the mean remain times τ_1 and τ_2 of particles in the trans-

---

** INAOE

* On leave for the Instituto Nacional de Astrofísica, Optica y Electrónica, A.P. 51, Z.P. 7200 - Puebla, México.

port and emission regions respectively. It should be noted that, although electric field acceleration in scenario (a) and neutral sheet acceleration in scenario (d) is basically the same process, in the former case we are adopting a thick geometry, while in the later energy losses in the acceleration volume are neglected (thin geometry), and the spectrum is derived in a quite a different form, by following particle trajectories in the electromagnetic field of the sheet is diffusion region. For the photon field we sweped from $\omega_{ph} = 10^{12}$-10^{18} eV/cm^3.

2. Results. Low energy events and the impulsive phase of high energy events are better described within the frame of scenario (a) rather than with (d)(Figs.1-3). Acceleration in those events is better described by impulsive electric field acceleration in the context of thick geometries, while the dominant radiation process is the (IC) effect, even whithin the frame of the thin geometry of scenario (d). The range of accelerating electrid fields falls between 6.5×10^{-3}-10^{-2} V/cm, whereas in scenario (d) higher fields are required (1-15) V/cm. Similarly, the adequate magnetic field strengths are 50-100 gauss, whereas in scenario (d) it is needed 400-500 gauss. Typical number densities are 10^{11} cm^{-3}, but 10^{10} cm^{-3} in the acceleration region with 10^{13} cm^{-3} in the emission region in scenario (d). Temperatures of 10^6 °K and photon fields > 10^{17}eV/cm^3 prevail in the source. Characteristic acceleration times are 0.03-0.06 s and much higher (30-50)s in scenario (d), where corresponding emission times are ∿80-100 s. Non-impulsive energy spectra of low and high energy events (usually associated to 2nd acceleration stage) are better described by stochastic acceleration from thermal energies, scenario (b), and radiation from (IC) than with injection from a preliminar acceleration phase within the volume of secondary stochastic acceleration scenario (c), in which case radiation appears from (BR). The acceleration efficiency in this kind of events must be very high (α=10-20 s^{-1}), while the corresponding acceleration times are quite shorter ∿ 0.002 s, but if the contribution of a first acceleration step is considered the acceleration efficiency turns to be lower. Typical parameters involved in these events are $n=10^{11}$cm^{-3}, $T\sim10^6$ °K, $B\sim50$ gauss, while ω_{ph} values (10^{16}-10^{17})eV/cm^3 are lower than in impulsive events. On the other hand, the global description of energy spectra composed of two different components (usually associated with two acceleration phases) is better assuming scenario (c) than with (b), in which case radiation from (IC) is dominant, with $\omega_{ph}\geq10^{17}$eV/cm^3, $\alpha \sim 1$ s^{-1}, τ=0.02s, $n=10^{11}$cm^{-3}, $T=10^6$ °K and B=50 gauss. Optimum fits to the observational spectra are sumarized in table 1.

3. Conclusions. From this study it can be infered that the scenario for the production of (X-γ) rays continum in solar flares may vary from event to event, however, it is possible in many cases to associate low energy events to impulsive acceleration, and the high energy phase of some events to stochastic acceleration. In both cases, flare particles seems to be strongly modulated by local energy losses. Electric field acceleration, associated for instance to neutral current sheets is a suitable candidat for impulsive acceleration. Finally we claim that the predominant radiation process of this radiation is the (IC) effect due to the local flare photon field.

TABLE 1

SH 1.2-3

EVENT	BEST SCENARIO	ACCEL. & LOSSES PROCESSES	RAD. PROC.	ω_{ph} (eV/cm^3)	ACCEL. PARAMETERS		FLARE PARAMETERS			BEST FITTING
					ε(V/cm) α(s^{-1})	τ(s) τ', τ$_1$, τ$_2$(s)	n(cm^{-3})	T(°K)	B(gauss)	(FIGS.1-6)
1-III- 970 X-RAYS 35-160 KeV ONE PHASE	(a)	EFA=electric field acceleration	IC	5×10^{17}	$\varepsilon=10^{-2}$	6×10^{-3}	10^{11}	10^{6}	90	EFA-IC
	(a)	BETA= betatron	IC	3×10^{16}	α=1	0.3	10^{11}	10^{7}	100	
	(d)	NSA=neutral sheet acceleration	BR	-	ε=10	50,500,100	$10^{10}-10^{11}$	10^{6}	500	
30-III-1969 X-RAYS 28-254 KeV ONE PHASE	(a)	EFA	IC	10^{17}	$\varepsilon=6.5\times10^{-3}$	6×10^{-3}	10^{11}	10^{6}	50	EFA-IC
	(a)	EFA	BR	-	ε=2	10	10^{11}	2×10^{5}	100	
	(d)	NSA	IC	3×10^{17}	ε=15	50,2000,100	$10^{10}-10^{11}$	10^{6}	400	
4-III-1972 γ-RAYS 0.4-0.7 MeV 1st. PHASE	(a)	EFA	IC	10^{17}	$\varepsilon=5\times10^{-2}$	3×10^{-2}	10^{11}	10^{6}	50	EFA-IC
	(a)	BETA	IC	10^{16}	α=1	0.2	10^{11}	10^{7}	120	
	(a)	BETA	BR	-	α=10	1.	10^{11}	10^{6}	50	
	(d)	NSA	IC	2.5×10^{17}	ε=1	30,400,80	$10^{10}-10^{12}$	10^{6}	400	
4-III-1972 γ-RAYS 0.8-7MeV 2nd. PHASE	(b)	FERMI	IC	10^{17}	α=20	2×10^{-3}	10^{11}	10^{6}	50	FERMI-IC
	(b)	FERMI	BR	-	α=1	1.	10^{11}	10^{6}	50	
	(c)	(BETA-IC)-FERMI	BR	10^{16}	α=1	5×10^{-2}	10^{11}	10^{7}	160	~
30-III-1969 X-RAYS 28-254 KeV 2nd. PHASE	(b)	FERMI	IC	10^{16}	α=10	2×10^{-3}	10^{11}	10^{6}	45	FERMI-IC
	(b)	FERMI	BR	-	α=0.5	0.5	10^{11}	10^{6}	40	
	(c)	(EFA-IC)-FERMI	BR	10^{17}	ε=10	2×10^{-2}	10^{12}	10^{6}	100	~
4-VIII-1972 γ-RAYS 0.4-7 MeV 1st. & 2nd. PHASE	(b)	FERMI	IC	10^{16}	α=10	1.5×10^{-3}	10^{9}	10^{7}	45	~
	(b)	FERMI	BR	-	α=1	0.3	10^{10}	10^{6}	50	
	(c)	(EFA-IC)-FER	IC	10^{17}	5×10^{-2}	2.5×10^{-3}	10^{11}	10^{6}	50	
	(c)	(BETA-IC)-FERMI	IC	2×10^{17}	1.	0.02	10^{11}	10^{6}	50	(BETA-IC)-FERMI-IC
	(c)	(BETA-IC)-FERMI	BR	3×10^{16}	α=10	7×10^{-2}	10^{11}	10^{7}	100	

ORIGINAL PAGE IS
OF POOR QUALITY

References

Bai, T.and Ramaty, R., Solar Phys. 49, 343, 1976
Chung-Chih-Cheng, Space Sc. Rev. 13,3, 1972
Chupp, E. L. et al, Solar γ-X and EUV Radiation, IAU 68, 341, 1975
Crannel, C. J. et al, Ap. J. 223, , 1978
Frost, K. J. and Dennis, B. R., Ap. J. 165, 655, 1971
Jackson, W., Classical Electrodynamics,John Willey & Jons,Chap. 15,1962
Kane, S. R. and Anderson, K.A., Ap. J. 162, 1003, 1970
Suri, A.N. et al, Solar Phys. 43, 415, 1975

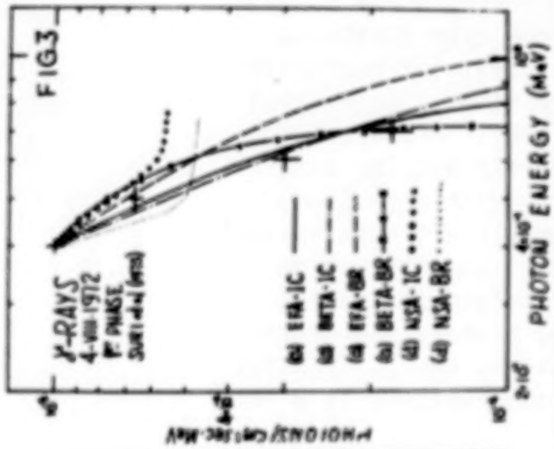
FIG.3

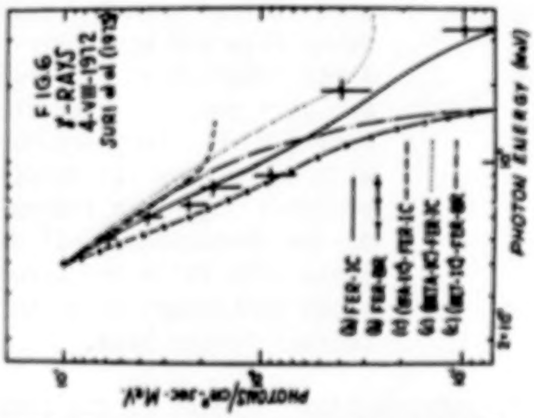
FIG.6

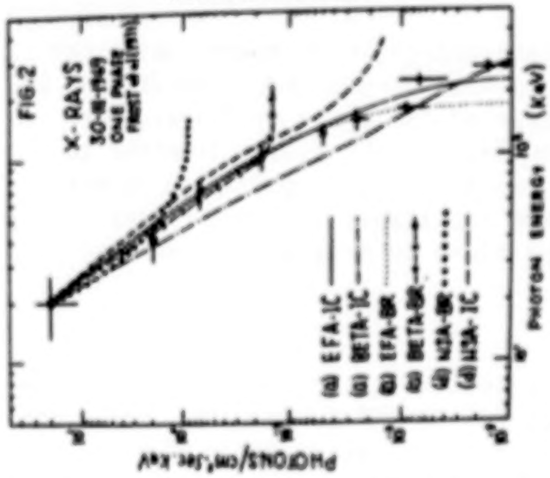
FIG.2

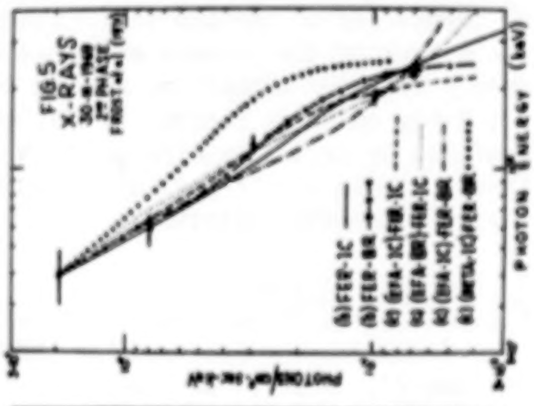
FIG.5

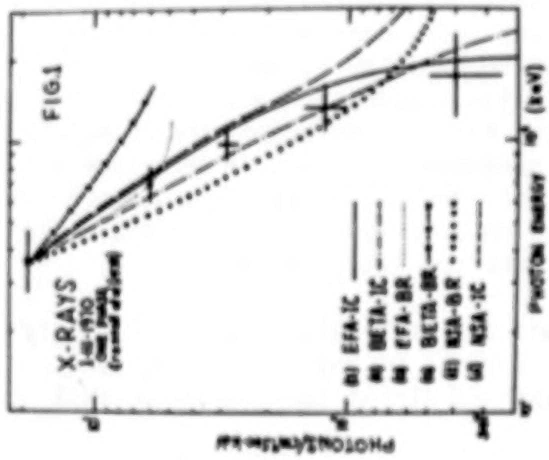
FIG.1

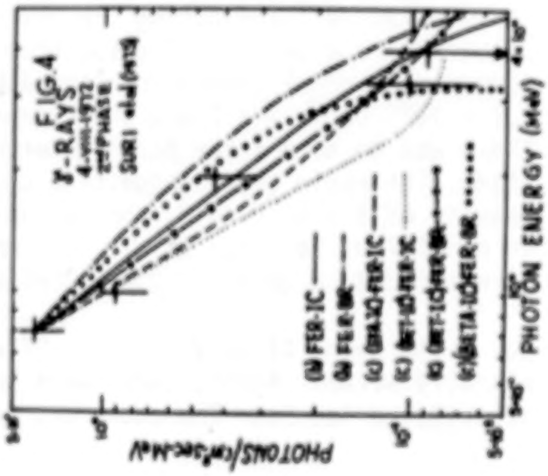
FIG.4

SPECTRAL AND SPATIAL PROPERTIES OF SOLAR MICROFLARES

G.M. Simnett
Department of Space Research
University of Birmingham
England

B.R. Dennis
Goddard Space Flight Center
Code 684, Greenbelt,
MD 20771 USA

ABSTRACT

Solar microflares are studied using both hard (> 28 keV) and soft (3.5-8.0 keV) X-ray observations. The soft X-ray events have durations < 3 m at 0.1x maximum intensity, and typically have similar rise and decay times. The fastest decay observed was < 15 s (1/e). Soft and hard X-ray intensities are uncorrelated. The events are very compact, consistent with a projected area $\leq 8'' \times 8''$. They are normally not associated with Hα or type III emissions and their time profiles suggest a thermal origin at the top of the chromosphere. If the primary energy release site is in the corona, an energy transfer agent consistent with the observations is a non-thermal proton beam.

1. Introduction Studies of the simplest energetic phenomena which can be identified on the Sun should lead to important boundary conditions on the nature of the primary energy release at the onset of flares, the energy transfer mechanism, and the location of the energy transfer to the X-ray emitting plasma. In simple events the interpretation is not confused by secondary effects which are inevitable in large flares. Short, simple soft X-ray spikes may be close to providing answers to these fundamental points.

2. The Observations

Figure 1 shows three examples of fast, soft X-ray spikes observed by the Hard X-ray Imaging Spectrometer (HXIS) (1) on SMM during 1980. The event on June 27, 19:50 UT was seen only in the HXIS coarse field of view (resolution 32") and during the peak was consistent with a source $<< 32''$, but $> 8''$, in dimension. The spectrum was soft, consistent with a two-component thermal source corresponding to 26×10^6 K, emission measure 1.7×10^{46} cm^{-3}, and 6.6×10^6 K, emission measure 5.7×10^{48} cm^{-3}. There was no hard X-ray burst observed, no radio emission, and no Hα flare. The rapid decay suggests a chromospheric origin. If we assume a density of 5×10^{10} cm^{-3}, consistent with the top of the chromosphere in model F of Vernazza et al. (2), and an area $10^4 \times 10^4$ km^2, this would correspond to a depth of 230 km below the transition zone.

The event of July 7, 07:08 UT was qualitatively very similar, only slightly weaker. Again, there were no reports of any other coincident activity on the Sun. The event was confined almost totally to two HXIS

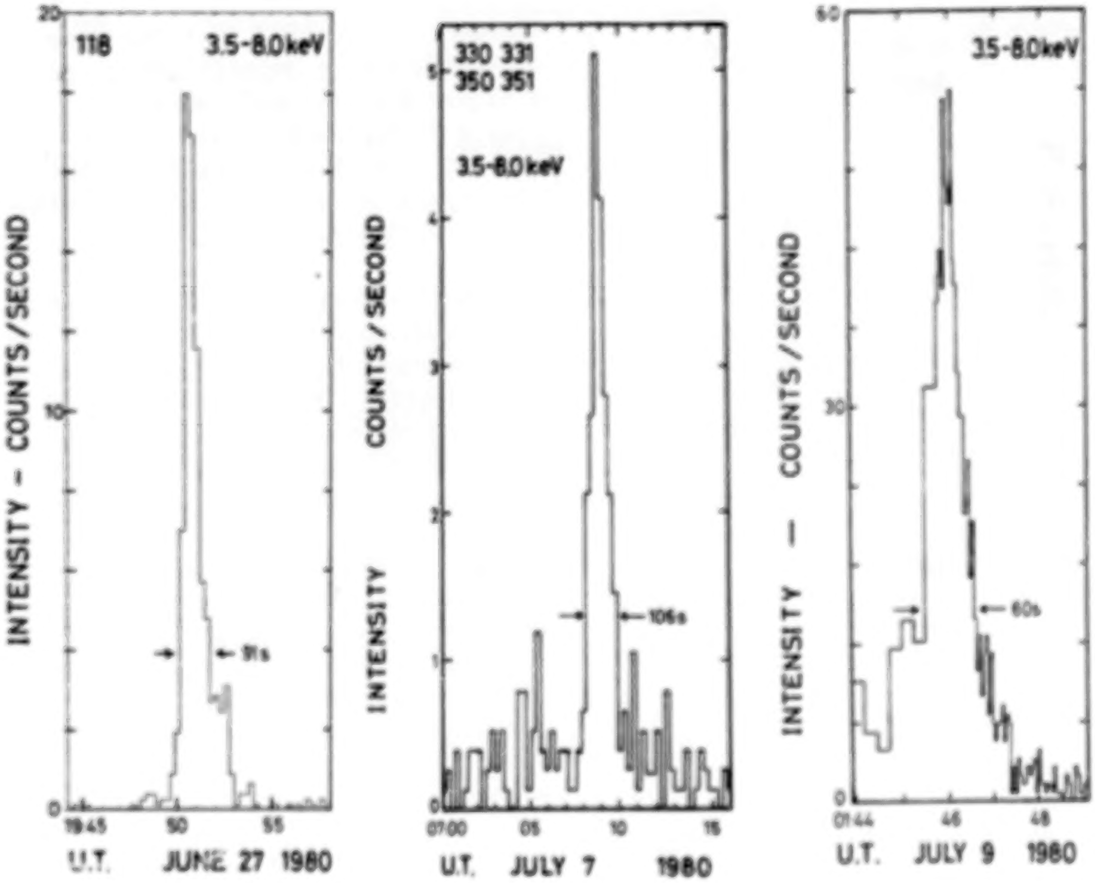

Fig. 1 The 3.5 - 8.0 keV intensity time histories for three events in 1980

fine field of view pixels (resolution 8"), so allowing for the point spread function of the instrument it is deduced that the projected area was < 8" x 8". The spectrum was even softer than the June 27 event, and both events had an e-folding decay time ∿ 40 s.

The third event, on July 9, 01:45 UT was much stronger and started from an already enhanced background associated with a SF flare at 01:40 UT, peak 01:42 UT. The Hard X-ray Burst Spectrometer (HXRBS) (3) on SMM observed an X-ray spike starting at 01:45:35 UT, with a width ∿ 35 s. This is simultaneous within the resolution of the data, with the soft X-ray and microwave onsets. However, the hard X-ray and microwave events ceased at ∿ 01:46 UT, the time of the soft X-ray maximum. If the event has a thermal origin, it would appear that the extremely high temperature required for the hard X-rays cools a factor of 2 or 3 times faster than that required for the soft X-rays. The event is seen close to the solar limb as a compact, < 8" x 8" bright point. The decay time in soft X-rays is ∿ 24 s.

If these events are due to energy deposition from the corona, then

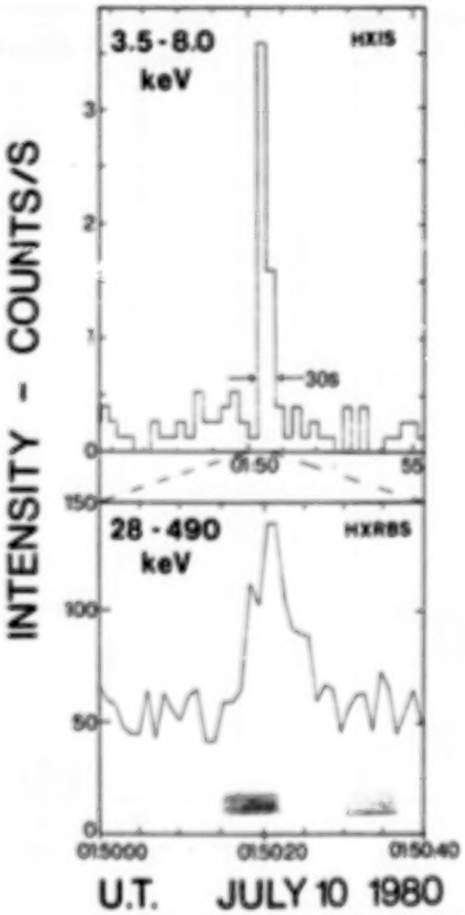

Fig. 2 In the event on July 10,1980 the hard X-ray intensity is shown expanded.

it might be expected that the more energetic events deposit energy at a higher density, and therefore have a faster decay. This is consistent with the observations, but is only one of a number of possible interpretations.

Not all events are as long as that shown in Figure 1. Figure 2 is an example on July 10, 01:50 UT which lasted < 30 s. HXIS data sampling times are shown in black on the hard X-ray enlargement. The data are consistent with a simultaneous start of the hard and soft X-rays, in which case the soft X-ray peak flux would be enhanced; there is a small residual soft X-ray flux from 01:50:30 - 01:50:38 UT. The event was compact and on the limb; there was a type III burst, but no optical or microwave report.

An almost identical soft X-ray event occurred on June 27, 15:24:20 UT, except without any other radiation signatures. Such events occur in isolation, but others are seen on the decay of a normal flare event. Examples are on April 27, 02:23 UT and July 7, 10:17 UT; the latter seen by HXRBS. We suspect that there are many other examples of these events, but a systematic data search has not yet been made.

3. Discussion. From the lack of any consistent correlation with hard X-rays, microwaves, Hα or type III emissions it seems unlikely that the soft X-ray spikes originate in a simple acceleration and impulsive injection of electrons from the corona. The events are all very compact, consistent with a projected dimension ≤ 8". The rapid decay of the soft X-rays suggests that the emission is from a high density thermal plasma, at least of chromospheric densities. However, it does not produce an Hα response, so this suggests the events are confined to the top of the chromosphere.

The July 10 event showed that a notable hard X-ray burst could be associated with a very weak soft X-ray burst (Figure 2). It is possible that this arises because the hard X-rays come from a simultaneous event beyond the HXIS field of view. However, there was no substantial event seen by the GOES full-Sun soft X-ray instrument at this time, so we believe this interpretation is unlikely. It is then significant that events where the soft X-ray intensity is higher by almost an order of magnitude have no observed hard X-rays. This would reinforce the above conclusion that these events did not originate as non-thermal bremsstrahlung from an electron beam accelerated in the corona for the following reason. If the explanation for the lack of hard X-rays is that the accelerated electron spectrum is very soft, it would also mean that the bulk of the energy would be deposited in the corona. The heated coronal plasma would then be expected to have a much longer decay time than that observed (4). Note that the threshold energy for electrons to reach the chromosphere from the corona (e.g. an altitude of $\sim 10^4$ km) is > 30 keV for any reasonable atmospheric model.

As an electron beam is an unattractive explanation for the spikes, a possible alternative is that the events are multithermal, with the energy transfer by means of a non-thermal proton beam. Such a mechanism has recently been suggested as an important feature of the impulsive phase of flares in general (5). The lack of a long decay for these events indicates that there had been no ablation of hot chromospheric plasma into the corona. This is consistent with a recent theoretical model (6) which argues that for a substantial amount of material to be ablated the deposited energy flux should exceed a threshold value. (6) specifically dealt with electron fluxes, but this conclusion should not be significantly different for protons. If the energy flux is below the threshold, most of the power is radiated away by the dense chromosphere with only a small temperature increase. If the events are due to non-thermal protons, they should be in the energy region $10^2 - 10^3$ (5). Such protons will produce none of the radio radiation signatures expected from electrons, and not seen in most of our events, but would produce intense heating at the energy deposition site if it were sufficiently compact. If the heating is sufficiently high and rapid, thermal hard X-rays and microwaves will be observed. The occasional type III burst may arise from run-away electrons from the very hot thermal plasma.

4. Acknowledgements. This work has benefitted from discussions with Dr. A.O. Benz. The author thanks the Institute of Astronomy, ETH, Zurich for their kind hospitality while the paper was completed.

References

1. Van Beek, H.F. et al., (1980), Solar Phys. 65, 39
2. Vernazza, J.E. et al., (1981), Ap.J.Suppl. 45, 635
3. Orwig, L.E. et al., (1980), Solar Phys. 65, 25
4. Moore, R. et al., (1980), in "Solar Flares", ed. P.A. Sturrock, Colorado University Press
5. Simnett, G.M., (1985), Paper SH 1.2 - 13
6. MacNeice, P. et al., (1984), Solar Phys. 90, 357

N85-34741

TEMPORAL EVOLUTION OF AN ENERGETIC ELECTRON POPULATION IN AN INHOMOGENEOUS MEDIUM. APPLICATION TO SOLAR HARD X-RAY BURSTS.

N. Vilmer*, A.L. MacKinnon**, G. Trottet*

* UA 324, Observatoire de Paris, Section d'Astrophysique de Meudon, DASOP, F 92195 Meudon CEDEX, France.
** Department of Astronomy, The University, Glasgow G128QQ, UK

1. Introduction. Energetic electrons accelerated during solar flares can be studied through the hard X-ray emission they produce when interacting with the solar ambient atmosphere. In the case of the non thermal hard X-ray emission, the instantaneous X-ray flux emitted at one point of the atmosphere is related to the instantaneous fast electron spectrum at that point. A hard X-ray source model then requires the understanding of the evolution in space and time of the fast particle distribution. The physical processes involved here are energy losses due to Coulomb collisions and pitch angle scattering due to both collisions and magnetic field gradients.

The evolution of the distribution is properly described by a Fokker-Planck equation (1) which has been solved numerically for steady state or impulsive (δ function) electron injections (2,3). However, its application in cases where the electron collisional lifetime and injection duration are of similar magnitudes has not yet been considered. Such cases are relevant for long-duration events where electrons are injected over a finite period. As a first approximation, a simpler mathematical approach is the use of a first order, non dispersive continuity equation in phase space, taking into account mean rates of change of the phase space variables. Such an equation relates the number of electrons of a specified energy and mean pitch angle at a given point to an arbitrary source function. The angular distribution of the electrons is not correctly described in this treatment, except in a mean sense. However, it includes pitch angle scattering adequatly for purposes of hard X-ray spatial distribution calculations and it has the great advantage of giving analytic, time dependant solutions for arbitrary source functions and ambient density structures. In this contribution, the main properties of the analytic solutions are presented for simple situations in order to illustrate the potential use of such calculations in the interpretation of coronal propagation of energetic electrons and of hard X-ray spatial distribution.

2. Basic characteristics. Energetic electrons are injected into an inhomogeneous, plane parallel atmosphere defined by a density $n(z)$ and a magnetic field $B(z)$ where z is the depth from some arbitrary point. $B(z)$ is assumed to be purely in the z-direction and the electron pitch-angle θ is the angle between the z-axis and the electron velocity ($\mu = \cos\theta$ is positive, resp. negative for an electron moving downwards, resp. upwards.) Electrons are injected for $t \geqslant 0$ at a rate $q(E,t,z,\mu)$ (number of electrons injected per second between z and $z + dz$, with energies between E and $E + dE$ and with $\cos\theta$ between μ and $\mu + d\mu$). The electron population evolves in the medium through different processes such as energy losses (mean rate dE/dt)

and scattering (mean rate $d\mu/dt$). The continuity equation is then given by :

$$\frac{\partial N(E,t,z,\mu)}{\partial t} + \frac{\partial}{\partial E}\left[N(E,t,z,\mu)\,\frac{dE}{dt} \right] + \frac{\partial}{\partial z}\left[N(E,t,z,\mu)\,\frac{dz}{dt} \right] + \frac{\partial}{\partial \mu}\left[N(E,t,z,\mu)\,\frac{d\mu}{dt} \right] = q(E,t,z,\mu) \qquad (I)$$

where dE/dt is the energy loss-rate through electron-electron Coulomb collisions (4) and $d\mu/dt$ is the sum of pitch angle scattering due to Coulomb collisions (5) and to magnetic field gradient (adiabatic invariance of the magnetic moment). Equation I has been solved analytically. The solutions and their physical interpretation are discussed in (6) and (7). The most critical approximation which consists to omit the velocity dispersion due to Coulomb collisions has also been discussed in (6). It has been shown that for mildly relativistic electrons (initial energy below 200 keV), the mean behaviour of the electrons is fairly well described by the analytic treatment.

3. Evolution of the energetic electron population in some specific cases.

We will examine two extreme cases where either pitch angle scattering due to the magnetic field gradient or to Coulomb collisions is negligible. In both cases, a non thermal electron distribution is continuously injected at an arbitrary depth $z = 0$ in a stratified medium with a density scale height H [$n(z) = n_o\, e^{z/H}$] and a magnetic field $B(z)$. We then compute :

$$N(E,t,z) = \int_0^1 d\mu\, N(E,t,z,\mu) \quad \text{for } E < 160 \text{ keV} \qquad (II)$$

For simplicity, $q(E,t,z,\mu)$ is chosen as :

$$\left.\begin{aligned} & q(E,t,z,\mu) = S_o\, E^{-\gamma}\, F(t)\, G(z)\, H(\mu) \\ & \text{where : } F(t) = t\,(2t_o - t) \quad \text{for } 0 < t < 2t_o \\ & \qquad\qquad\quad = 0 \qquad\qquad\quad \text{elsewhere} \\ & \qquad G(z) = \delta(z) \text{ where } \delta(z) \text{ is the Dirac delta function} \end{aligned}\right| \qquad (III)$$

Two extreme cases are considered for $H(\mu)$: a beam distribution [$\delta(\mu-\mu_o)$] and an isotropic one [$H(\mu) = 1$ for $\mu > 0$].

Figure 1 shows electron spectra as a function of depth at $t = t_o$ (maximum of the injection) and at $t = 2t_o$ (end of the injection) for both a beamed injection and an isotropic one, when the magnetic field is assumed to be uniform.

Figure 2 is similar to figure 1, in the case where $B(z)$ is given by : (e.g. 8) :

$$B(z) = \begin{cases} B_o \left[1 + \dfrac{z^2}{z_T^2}\,(R_m - 1) \right] & z < z_T \\ B_o\, R_m & z > z_T \end{cases}$$

where R_m is the mirror ratio at $z = z_T$.

ORIGINAL PAGE IS
OF POOR QUALITY

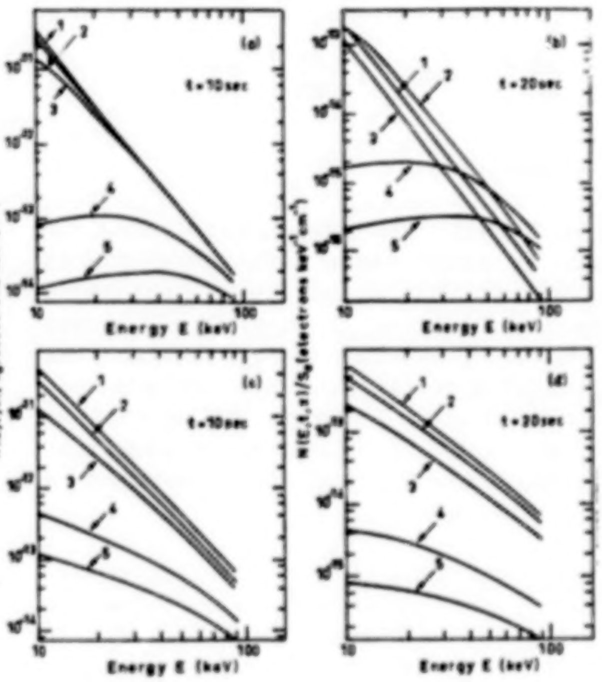

Fig. 1 :
Evolution with depth and time of $N(E,t,z)/S_o$ when the pitch angle scattering is due to collisions alone. Figures 2a and 2b correspond to a beamed injection (μ_o = 0.5). Curves 1, 2, 3, 4, 5 correspond respectively to $z = 5\ 10^7$cm, 10^8cm, $2\ 10^8$cm, $5\ 10^8$cm and $6\ 10^8$cm.
The chosen parameters are : $\gamma = 3$, $t_o = 10$ sec, $n_o = 10^{10}$cm^{-3} at the injection point ($z = 0$).

For both cases, H is assumed to be 10^8cm. The general behaviour of electron spectra with depth is a progressive hardening. However, there are differences between beamed or isotropic injections or between the different scattering processes.

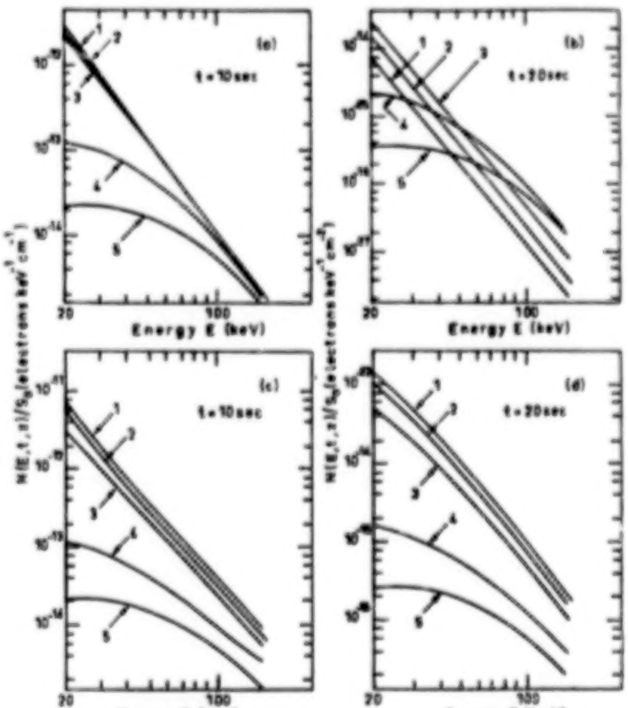

Fig. 2:
Same as figure 1 when scattering is due to a varying magnetic field with $R_m = 2$ and $z_T = 3\ 10^9$cm.

Pitch angle scattering due to collisions : For a beamed injection, there are "humps" in the spectra at large depths, especially at the maximum of the injection. At t = 2 t_o, spectra are softer and "humps" are less pronounced because of the combined effects of the temporal behaviour of the injection and of the electron propagation and energy losses. For an isotropic injection, the hardening of the spectrum is less important and "humps" are no longer visible. At $t = 2t_0$, contrary to the case of a beam, the spectra are harder than for $t = t_0$ at each depth. However, "humps" may develop in that case after the end of the injection. These differences are due to the presence here of electrons with large pitch angles. The results presented here are similar to the ones obtained with steady-state treatments which also predict "humps" in the electron spectra at large depths for both a beamed (8) and an isotropic injection (2). The present treatment generalizes then previous results and allows moreover to study the time appearance of "humps" at each depth. Such a behaviour ("humps") indicates the breakdown of the purely collisional treatment of the evolution of the electron population.

Pitch angle scattering due to magnetic field gradients : The hardening of the electron spectra is smaller with depth and "humps" do not develop during the injection, even for a beam. These differences are due to the combined effects of the scattering process and of the magnetic mirroring. An increase in the magnetic field gradient still enhances this effect and harder spectra are generally obtained at least at low depths.

Calculations made for an extended injection region lead to results similar to the ones presented here for large depths as compared to the source extent. Of course, for both cases, at a given depth, the electron spectrum, as well as the hardness difference between different depths, strongly depend on the injection height.

4. Discussion and Conclusions. The model presented here allows to study the temporal, spatial and spectral evolution of non thermal electrons injected continuously in an inhomogeneous medium and to estimate the X-ray flux produced at each depth. This evolution depends on the characteristics of the electron injection and of the ambient medium. In these conditions, various evolutions with depth of electron spectra may be obtained. This is consistent with stereoscopic observations of partially occulted X-ray flares. Indeed, for coronally occulted events with similar occulting heights, different flux ratios and spectral hardness differences between occulted (observed by the instrument detecting the higher part of the flare) and unocculted fluxes are observed (9). Finally, the present calculations can provide a powerful and convenient framework for the interpretation of spatially resolved hard X-ray observations and the understanding of electron coronal propagation towards the interplanetary medium.

References

1. Rosenbluth, M.N. et al : 1957, Phys. Rev., 107, 1.
2. Leach, J. and Petrosian, V. : 1981, Astrophys. J., 251, 781.
3. Kovalev, V.A. and Korolev, O.S. : 1981, Sov. Astron., 25, 215.
4. Bai, T. and Ramaty, R. : 1979, Astrophys. J., 227, 1072.
5. Brown, J.C. : 1972, Solar Phys., 26, 441.
6. Vilmer, N. et al : 1985, Astron. Astrophys., submitted.
7. Craig, I.J.D. et al : 1985, M.N.R.A.S., submitted.
8. Emslie, A.G. and Smith D.F. : 1984, Astrophys. J., 279, 882.
9. Kane, S.R. : 1983, Solar Phys., 86, 355.

46 N85-34742

SH 1.2-7

QUANTITATIVE ANALYSIS OF FLARE ACCELERATED ELECTRONS THROUGH THEIR HARD X-RAY AND MICROWAVE RADIATION

K.-L. Klein and G. Trottet

UA 324, Observatoire de Paris, Section d'Astrophysique de Meudon,
DASOP, F-92195 Meudon Cédex, France

1. Introduction. A key question of particle acceleration during solar flares is whether electrons and ions are accelerated by a single physical process, or whether a second, distinct step of acceleration must be invoked for the high particle energies attained in some flares. Information on the particles can be inferred from an analysis of their electromagnetic radiation by means of model computations. As far as electrons are concerned, the most direct information is furnished by their hard x-ray ($h\nu > 30$ keV) emission (electron-ion bremsstrahlung), which has been shown /1, 2, 3/ to vary in close temporal correlation with microwaves, although these are produced by a different mechanism (gyrosynchrotron radiation). This correlation is generally interpreted in terms of a common electron distribution /1, 2, 4/ continuously injected into sources at different heights (e.g. /5/). It gives the possibility to test, if the results inferred from hard x-rays are consistent. Gyrosynchrotron radiation does, however, not directly reflect the electron distribution because of various processes of suppression and absorption at low frequencies /6/. Quantitative investigations of the correlation have been carried out by many authors (e.g. /2, 4, 7, 8, 9/). However, on the one hand the radio radiation was often treated in a homogeneous configuration, whereas the gyrosynchrotron mechanism depends strongly on variations of the magnetic field. Furthermore, analytical simplification has often been used, by which the low frequency effects cannot be treated consistently. On the other hand, the analyses were mostly restricted to the instant of peak flux, and no information on the temporal evolution of the injected electrons could be inferred.

Our purpose is to present hard x-ray and microwave modelling that takes into account the temporal evolution of the elctron spectrum as well as the inhomogeneity of the magnetic field and the ambient medium in the radio source. We illustrate this method for the June 29 1980 10:41 UT event and discuss briefly the implication on the process of acceleration/injection.

2. Method of analysis. The model of the x-ray source has been described by Trottet and Vilmer (/10/ and references therein). The radiation is assumed to be produced by non thermal electrons injected continuously with an injection function

$$q(E,t) = q_o \, E^{-\gamma} f(t) \quad (0 < t \le t_o, \;\; 0 \text{ elsewhere}), \qquad (1)$$

with γ being kept constant during each injection. Precipitation is considered in the limits of weak (collisions) and strong (waves) diffusion. Electrons are assumed to loose energy through collisions with ambient electrons. From this model, the injection function, the source density and the total number of energetic electrons are deduced.

The microwve source is represented by a collection of dipolar field lines in an ambient medium with a hydrostatic density model /11/. The electron distribution is composed of a Maxwellian and a non thermal part resulting from the injection function (1).

3. Analysis of the 29 June 1980 flare. The flare has been observed with several SMM and ground-based instruments /12, 13/. Its temporal evolution is shown for a high-energy x-ray channel and one radio frequency in fig. 1. It has been shown in /10/ that the energetic phase of the event between 104130 UT and 1043 UT can be decomposed into five successive electron injections, whose parameters are listed in table 1 of /10/. The hard x-ray source is found to be a high density medium, from which most of the radio frequencies cannot escape. The microwave and hard x-ray sources are then not cospatial. We assume the structure of the microwave source to be identical with the spatially resolved x-ray source below 30 keV (HXIS observations, /12/). Two magnetic loops of different sizes are observed. The geometric parameters of the loops, the x-ray inferred density /12/ and the assumed magnetic field strengths at the top and in the feet of the loop are listed in table 1. In the following we assume the temperature to be identical in both loops, although slight differences are reported in /12/. As the event is a limb flare, we consider in the following magnetic loops in the plane of the sky. They are supposed homogeneous along the line of sight. Following the hypothesis of /12/, we suppose that a quarter of the electron number inferred from hard x-rays is injected into each of the two arches. We compute the microwave spectrum from a simplified form of (1), considering a parabolic f(t) ($t_o = 2\ t_{max}$). Furthermore, the electrons are assumed to be perfectly trapped during each injection, but no particles from previous injections are retained.

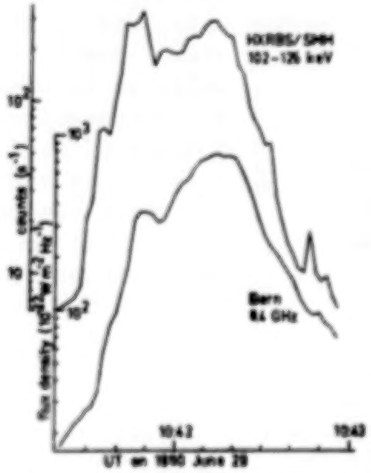

Fig. 1 : Temporal evolution of the observed hard x-ray and microwave fluxes

Table 1

	Loop A	Loop B
height (cm)	$6 \cdot 10^8$	$5 \cdot 10^9$
volume (cm^3)	$1.1 \cdot 10^{27}$	$2.1 \cdot 10^{28}$
temp. (K)	$5 \cdot 10^7$	$5 \cdot 10^7$
dens. (cm^3)	$7 \cdot 10^{10}$	$2 \cdot 10^9$
B_{top} (G)	175	21
B_{feet} (G)	240	240

4. Results. Fig. 2 shows gyrosynchrotron spectra computed at two instants during the injection where the fluxes are greatest, together with microwave observations at four discrete frequencies (5.2 GHz, 8.4 GHz, 11.8 GHz, 19.6 GHz; Bern University, courtesy A.Magun), integrated over 2 s. Because of absorption in the terrestrial atmosphere the measured 19.6 GHz flux represents a lower limit.Both the low and

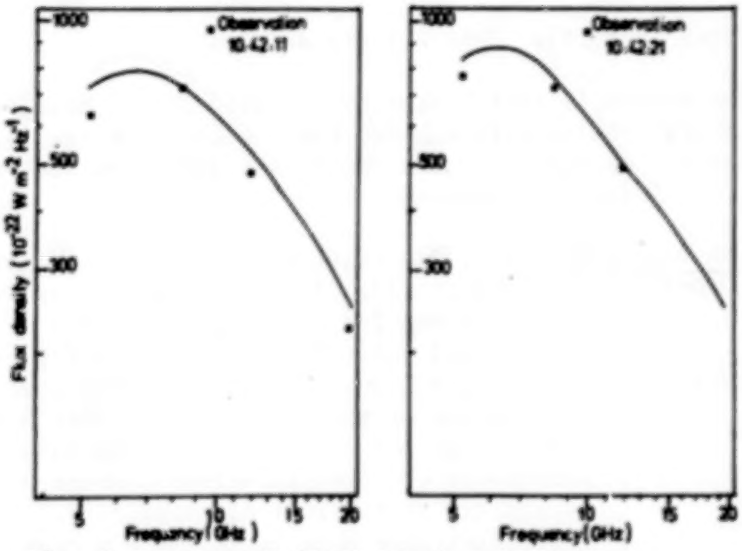

Fig. 2 : Computed (full line) and observed (squares) microwave spectra during injection 4.

the high frequency parts of the spectrum radiated by electrons with the injection function inferred from hard x-rays account for the observations. Emission at the high frequency end is dominated by the small loop A. Its emission is weak at low frequencies because of self absorption by the energetic electrons and a small amount of gyroresonant absorption by the Maxwellian electrons. This part of the spectrum comes predominantly from loop B.

The temporal evolution of the microwave flux during injection 4 is plotted for two discrete frequencies in fig. 3. Up to the end of

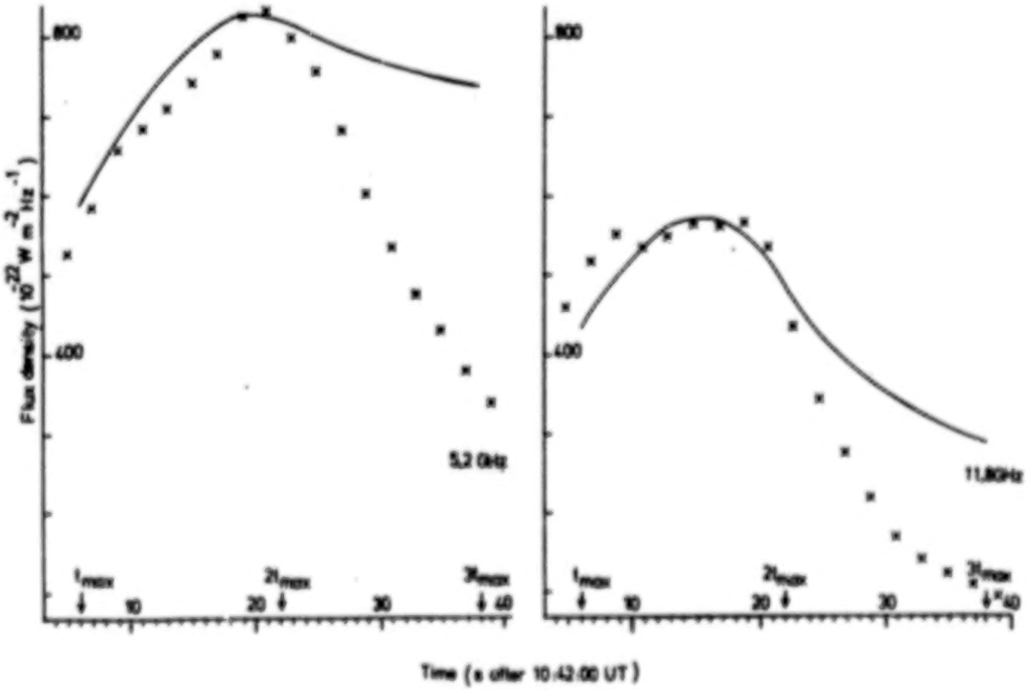

Fig. 3 : Computed (full line) and observed (crosses) evolution of microwave fluxes at a low and a high frequency during injection 4 .

the injection the computed curve fits the observations. Afterwards electron losses through precipitation are revealed by the observed flux decreasing faster than that computed for perfectly trapped particles. The low frequency peak lags that at high frequencies by several seconds both in the model and in observations. This is because growing electron density during the injection increases emission and self absorption. While the latter does not affect high frequencies, it diminishes the low frequency flux, which peaks only in the late phase of the injection, when the instantaneous number density has gone down.

At the very beginning of the event, the computed flux is not compatible with the observated spectrum, which peaks at higher frequencies than afterwards when the flux has grown. This microwave phase might be dominated by thermal electrons, but then a temperature of some 10^8 K is required /14/.

5. Discussion. The analysis of the 29 June 1980 flare has shown that in the most energetic part the hard x-ray inferred injection function and total number of electrons are compatible with microwaves. A long lasting controversy existed, because various authors had claimed the number of radio emitting electrons to be up to four orders of magnitude smaller than that producing hard x-rays (review in /2/, recent discussion in /9/). Account for suppression and absorption, source inhomogeneity and for energy losses during a continuous injection of particles solves this discrepancy and explains spectra and temporal evolution of radiations.

The discussed event is compatible with several electron injections, during each of which the spectral index remains constant. This lends strong support to a single step acceleration process.

Acknowledgements. We wish to acknowledge Drs. A. Magun (Bern) and B. Dennis (NASA) for kindly providing microwave and hard x-ray data. K.-L.K. acknowledges support by an ESA fellowship.

References

1. Peterson,L.E., and Winckler,J.R.: 1959, J.Geophys.Res. 64, 697
2. Svestka,Z.: 1976, "Solar Flares", D.Reidel Publ., Dordrecht
3. Cornell,M.E., et al.: 1984, Astrophys.J. 279, 875
4. Holt,S.S., and Ramaty,R.: 1969, Solar Phys. 8, 119
5. Klein,L., et al.: 1983, Solar Phys. 84, 295
6. Ramaty,R.: 1969, Astrophys.J. 153, 753
7. Takakura,T.: 1972, Solar Phys. 26, 151
8. Böhme,A., et al.: 1977, Solar Phys. 53, 139
9. Gary,D.E.: 1984, submitted to Astrophys.J.
10. Trottet,G., and Vilmer,N.: 1984, Adv.Space Res. 4, 153
11. Klein,K.-L., and Trottet,G.: 1984, Astron.Astrophys. 141, 67
12. Fernandez,A.M.: 1985, in preparation
13. Kundu,M.R.: 1982, Adv.Space Res. 2, 159
14. Batchelor,D.A.: 1984, PhD thesis, NASA Tech.Memorandum 86102

AN EXTENDED "SUPERHOT" SOLAR FLARE X-RAY SOURCE

Hugh S. Hudson
Center for Astrophysics and Space Sciences, Univ. of California, San Diego
La Jolla CA 92093, U.S.A.
K.-I. Ohki
Tokyo Astronomical Observatory, Mitaka-shi, Tokyo, Japan
and
S. Tsuneta
Institute for Space and Astronautical Science
Komaba, Meguro-ku, Tokyo, Japan

ABSTRACT

The *Hinotori* hard X-ray imaging instrument observed a "superhot" (T > 3 x 10^7 K) source during a solar flare occurring beyond the W limb of the Sun on March 28, 1981. Because of the circumstance of occultation by the limb, we determine a height of (3.1 ± 0.8) x 10^4 km. The source extended 4 x 10^4 km along the limb and was smaller than the instrumental resolution perpendicular to the limb. After the disappearance of the X-ray source, weak $H\alpha$ emission occurred at the position if the X-ray sources, suggesting the formation of a loop prominence system. The cooling time estimated for thermal conduction appears to be considerably shorter than the observed time scale of the event, even including a factor of ten to represent suppression of conduction due to possible field-line convergence. We conclude that either stronger forms of suppression, or else extended energy deposition, will be required to explain events of this type.

1. Introduction. The hard X-ray spectrum of a solar flare may give us the key information regarding the basic release of energy. Kane[1] showed that the hard X-rays above about 20 keV[2-3] (the "impulsive" component) have a strikingly different time history from the softer X-rays[4] (the "gradual" component). Recent observations[5] have shown that the spectral evolution exhibits more complexity than had previously been supposed, and that an intermediate spectral component also exists. This new feature, often referred to as the "superhot" component, appears to be thermal but has temperatures considerably above the mean temperature of the bulk of the flare emission measure, typically in the vicinity of 2 x 10^7 K.

The Solar Maximum Mission obtained images of a superhot source in the May 21, 1980 flare; its temperature was initially estimated[6] at 7 x 10^7 K, but later revised downwards to 4 x 10^7K (for a full discussion, see Duijveman[7]). At the present time there appears to have been no systematic study of the HXIS superhot sources, although Duijveman carried out a complete analysis of the 1980 May 21 event. In the meanwhile the *Hinotori* observed many such events including images of five of them[8]. Of the five, three were compact at the *Hinotori* resolution, but two were extended[8].

This paper describes a single superhot source imaged by *Hinotori* in special circumstances: occultation by the solar limb. In this configuration we obtain a clear altitude separation and can make definite statements about the source geometry. The characterization of this source as "superhot" is vague, mainly because of the lack of good spectral data, but the analysis here does not depend upon the classification.

2. Flares in Late April, 1981. In late April, 1981, the *Hinotori* spacecraft observed a sequence of energetic solar flares, including a major one on April 27 (onset about 08:00 UT) that produced γ-ray line emission[9]. The flare to be discussed in this paper occurred on April 28, with an onset in the *Hinotori* data at about 21:10 U.T. Although the April 28 event had a smaller soft X-ray flux than the April 27 event, both had the "long duration event" characteristics described by Kahler[10]. Each produced type II, III, and IV meter-wave radio bursts.

At the time of the April 28 event, the active region responsible for this activity (Hale Region 17590, central meridian passage April 21.1) was already well beyond the limb. From a plot of flare longitudes, we extrapolate to a position 18.8 ± 2.3 degrees beyond the limb. This position corresponds to an occultation height of 31000(±8000) km. An examination of $H\alpha$ data from Big Bear Solar Observatory (S. Martin, private communication) suggests that the faint flare-like brightenings represented late-brightening components of a classical loop prominence system. They initially appeared in the Big Bear films at 21:57 (at disk intensity) and ended at 23:54, with the N component preceding the S component by about ten minutes.

Several other characteristics of these two events are worth mentioning. From the time profiles of hard X-ray emission, little evidence exists for impulsive hard X-ray emission. We believe that the impulsive phase of the April 28 flare occurred while *Hinotori* was in sunlight because of the timing of the meter-wave radio events reported in Solar-Geophysical Data. If so, the April 28 event had a striking deficiency of impulsive hard X-ray emission, consistent with earlier OSO-7[11] and ISEE-3[12] observations of limb-occultation events.

3. The *Hinotori* Hard X-ray Images. A representative hard X-ray image from the SXT instrument on board *Hinotori* appears in Figure 1; many images from different times during the evolution of the event show approximately the same shape and location. The energy range of the the image was nominally 17-40 keV. The smoothness of the time profile and the spectral steepness indicate that this was a "superhot" source, probably with a temperature exceeding 3×10^7 K. The great elongation of the source along the limb suggests that we are viewing the topmost structures of the usual arcade of post-flare loops, a conclusion confirmed by the presence of the $H\alpha$ brightening at the same position later on.

4. Analysis. We analyze these data using the simplest approximation of conductive energy transport, assuming a constant flux-tube cross-section. This gives a cooling time

$$\tau = 1.25^{-10} n_e \ell^2 T^{-2.5}$$

from the Culhane *et al.*[13] estimate. In the absence of accurate parameters for physical conditions in the source, we can evaluate this time constant for the parameter values that would give the fastest and slowest plausible rates as shown in Table 1. To lengthen the "slow" time maximally, we have included a factor of 10 to account for suppression due to field-line convergence[14].

The results of these simple estimates range from 6.8 msec (probably unphysically small) to about 100 sec. The long-limit time does not agree well with the observed event lifetime, although the cooling time properly refers to the decay of source temperature, for which we have no good observational limit. We conclude that the extended lifetime of the event probably requires either (a) a more effective mechanism of suppressing thermal conduction through new physics, or (b) a continued supply of energy to the source.

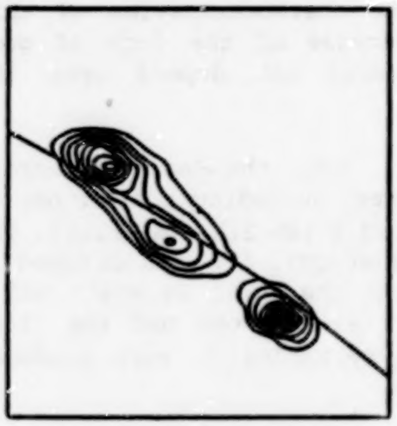

Fig. 1. Image from the *Hinotori* hard X-ray imaging instrument in a nominally 17-40 keV spectral band, taken at 2114 UT, using the ART (algebraic reconstruction technique) method. A smooth time profile, plus the softness of the hard X-ray spectrum, shows that this image comes from a "superhot" source. The appearance of the S component inside the limb may be an artifact.

5. **Conclusions**. We have identified a "superhot" hard X-ray source in a solar flare occulted by the solar limb, and find its hard X-ray image to show great horizontal extent but little vertical extent. An Hα brightening at the same limb position about an hour later suggests a multi-component loop prominence system, so that it appears that a superhot source can evolve in the same manner as a normal solar soft X-ray source. The assignment of plausible values to physical parameters in the source suggests (from the simplest form of classical thermal-conduction theory) that either new physics will be required to suppress conduction, or else that gradual energy release well after the impulsive phase of the flare must occur. In this respect too, the superhot source appears to resemble ordinary soft X-ray sources, except of course that its temperature is higher.

6. **Acknowledgements**. This work was supported by NASA grant NSG-7161 and by the NSF under the U.S.-Japan Cooperative Science Program.

C-2

TABLE 1

Parameters for Conductive Cooling Estimates

	Fast	Slow	
Density	10^8	10^{10}	cm^{-3}
Temperature	5×10^7	3×10^7	K
Length scale	3.1×10^9	6.2×10^9	cm
Convergence suppression	none	10	
Conductive cooling time	6.8×10^{-3}	98	sec

References

1. Kane, S.R., 1969, *Astrophys. J. (Lett.)*, 157, L139.
2. Peterson, L.E., and Winckler, J.R., 1959, *Journ. Geophys. Res.* 64, 697.
3. Frost, K., 1964, in W.N. Hess (ed.), *The Physics of Solar Flares* (NASA SP-50), p. 139.
4. White, W.A., 1964, in W.N. Hess (ed.), *The Physics of Solar Flares* (NASA SP-50), p. 131.
5. Lin, R.P., Schwartz, R.A., Pelling, R.M., and Hurley, K.C., 1981, *Astrophys. J.* 251, L109.
6. Hoyng, P., and 11 co-authors, 1981, *Astrophys. J.* 246, L155.
7. Duijveman, A., 1983, *X-ray Imaging and Interpretation of Impulsive Solar Flare Phenomena*, Thesis (Utrecht), p. 71.
8. Takakura, T., Tanaka, K., and Hiei, E., *Adv. Space Res.* 4, No. 7, p. 143.
9. Yoshimori, M., 1983, *Solar Phys.* 86, 375.
10. Kahler, S.W., 1977, *Astrophys. J.* 214, 891.
11. Hudson, H.S., 1978, *Astrophys. J.* 224, 235.
12. Kane, S.R., 1983, *Solar Phys.* 86, 358.
13. Culhane, J.L., Vesecky, J.F., and Phillips, J.H., 1970, *Solar Phys.* 15, 394.
14. Antiochos, S., and Sturrock, P.A., 1976, *Solar Phys.* 49, 359.

OBSERVATIONS OF SOLAR FLARE PHOTON ENERGY SPECTRA FROM 20 KEV TO 7 MEV

M. YOSHIMORI, H. WATANABE and N. NITTA*
Department of Physics, Rikkyo University, Toshima-ku,
Tokyo 171, JAPAN.
* Tokyo Astronomical Observatory, University of Tokyo,
Mitaka 181, JAPAN.

ABSTRACT

Solar flare photon energy spectra in the 20 keV to 7 MeV range are derived from the Apr. 1, Apr. 4, Apr. 27 and May 13, 1981 flares. The flares were observed with a hard X-ray and a gamma-ray spectrometers on board the Hinotori satellite. The results show that the spectral shape varies from flare to flare and the spectra harden in energies above about 400 keV. Effects of nuclear line emission on the continuum and of higher energy electron bremsstrahlung are considered to explain the spectral hardening.

1. Introduction

The acceleration of electrons and ions during solar flares has been an essential key problem in the study of high energy solar phenomena. Electrons accelerated to the MeV energy range emit radiowaves through synchrotron radiation and hard X-ray and gamma-ray continuum through bremsstrahlung. Solar hard X-rays in the 10 to 200 keV range have been extensively observed, and various problems on the electron acceleration mechanism and the correlation between radiowaves and hard X-rays have been discussed. Most of the hard X-ray spectrum are approximated by a power law spectrum with index of 3.0 to 5.0. However, only a few observations of the photon spectrum extending to gamma-ray energies have been reported. The solar X-rays and gamma-rays were first simultaneously observed from the 4 Aug., 1972 flare (Hoyng et al., 1976; Chupp et al., 1973). The photon spectrum extending to 7 MeV was reported (Suri et al., 1975). The observed spectrum revealed a change in the spectral shape at about 700 keV. Contributions of unresolved gamma-ray lines and new hard component were suggested to explain the spectral change. However, the hard X-ray and gamma-ray spectra were little reported after the observation of the 4 Aug., 1972 flare. It is because of no satellite dedicated to the solar X- and gamma-ray observations. Recently, more data of solar X- and gamma-rays were obtained from SMM and Hinotori observations. These two satellite observations have made it possible to discuss in detail the photon spectrum extending to gamma-ray energies and the hard X- and gamma-ray emission processes. In the present paper, the photon spectra in the 20 keV to 7 MeV range observed from the 1 Apr., 4 Apr., 27 Apr. and 13 May, 1981 flares are presented and the photon spectral shapes are discussed.

2. Observations

The Hinotori satellite is dedicated to solar flare observations and its prime objective is to study high energy flare phenomena in the X- and gamma-ray energies. The hard X-ray spectrometer (8.9 cm dia. x 1 cm thick NaI scintillator) covers the energy range of 17 to 370 keV. The primary data output is a full resolution 7 channel pulse height spectrum every 125 ms (Ohki et al., 1982). The gamma-ray spectrometer (8.9 cm dia. x 5 cm thick CsI scintillator) covers the energy range of 0.3 - 7 MeV range. The primary data output is a full resolution 128 channel pulse height spectrum every 2 s (Yoshimori et al., 1983a). Some of the Hinotori hard X- and gamma-ray data have been already reported (Ohki et al., 1983; Nitta et al., 1983; Yoshimori et al., 1983b). However, no photon spectrum in the 20 keV to 7 MeV range has been presented. The photon energy spectra from the 1 Apr., 4 Apr., 27 Apr., and 13 May, 1981 flares are presented here. Time histories of these flares were described (Yoshimori, 1985).

The 1 Apr., 1981 flare occurred at 0134 UT and lasted for about 26 min. The flare revealed the gradual time history. The Hα importance and the GOES class were 2B and X2.3, respectively. The photon spectrum observed in the interval of 0144:57 to 0156:40 UT is shown in Fig. 1. The photon spectrum is approximated by a power law spectrum with index of 3.75 in energies below about 300 keV, but the spectrum reveals a hardening in energies above about 400 keV.

The 4 Apr., 1981 flare occurred at 0502 UT and lasted for about 80 s. The flare revealed the impulsive time history. The Hα importance and the GOES class were 2B and X1.9, respectively. The photon spectrum observed in the interval of 0502:17 to 0503:05 UT is shown in Fig. 2. The photon spectrum is approximated by the power law spectrum with index of 3.28 or an exponential thermal spectrum with temperature of 7.28×10^8 K in energies above 300 keV. A hard spectral component is apparent in energies above 400 keV.

The 27 Apr., 1981 flare occurred at 0750 UT and lasted for about 30 min. The flare revealed the gradual and multi-peak time history. The Hα importance was not recorded, but the GOES class were 3B. The photon spectrum observed in the interval of 0810:05 to 0814:21 UT is shown in Fig. 3. The photon spectrum is approximated by the power law spectrum with index of 4.00 in energies below 300 keV. The hard spectral component is apparent in energies above 400 keV.

The 13 May, 1981 flare occurred at 0412 UT and lasted for about 18 min. The flare revealed the gradual time history with small increase. The Hα importance and the GOES class were 3B and X1.5, respectively. The photon spectrum observed in the interval of 0419:42 to 0428:13 UT is shown in Fig. 4. The photon spectrum is approximated by the power law spectrum with index of 3.22 in energies below 300 keV. The spectrum reveals the hardening in energies above 400 keV.

3. Discussion

The Hinotori satellite hard X- and gamma-ray observations reveal that the photon spectral shapes do not much vary from flare to flare. The power law spectral indices in energies of the 20 to 370 keV range between 3.22 and 4.00, which is consistent with ones observed previously. These power law photon spectra have been interpreted in terms of electron bremsstrahlung. Further, the present results indicate that the spectral hardening occurs at about 400 keV. This spectral hardening seems to be a common characteristics for the gamma-ray flares. It is known that the instrumental effect sometimes cause a spectral bending. However, such instrumental effect is possibly rejected because the spectral analysis in the 20 to 700 keV range has been correctly made for the 7 Oct. and 14 Oct., 1981 flares (Nitta et al., 1983), and the SMM observations also have revealed the similar spectral hardening for the 4 June and 7 June, 1980 flares (Orwig et al., private communication).

Various physical processes which could produce such observed hardening are considered. Such processes are (1) the effect of observed nuclear gamma-ray line emission on the continuum and (2) the significant contribution of higher energy electron bremsstrahlung. The effect of gamma-ray line emission of positron annihilation at 511 keV, of prompt deexcitation lines of Ne at 1.64 MeV, Mg at 1.36 MeV, Si at 1.78 MeV and Fe at 0.84 and 1.25 MeV and of neutron capture line at 2.22 MeV may be able to explain to some degree the spectral hardening in energies above about 400 keV. The possibility of higher energy electron bremsstrahlung is also considered (Suri et al., 1975). The observed photon spectra probably can not be explained by a population of electrons with a single power law index. Another population of electrons with a harder spectra in energies above a few hundred keV, should be needed to explain the observed spectral hardening. The similar spectral hardening has been reported in large flares such as the 4 Aug., 1972 flare (Suri et al., 1975). The observed spectral hardening represents a characteristics of particle acceleration process in solar flare. The effects of gamma-ray line emission and of higher energy electron bremsstrahlung will be in detail evaluated in near future.

References

Chupp,E.L., Forrest,D.J., Higbie,P.R., Suri,A.N., Tsai,C., and Dunphy,P.P.: 1973, Nature 241, 333.
Hoyng,P., Brown,J.C., and Van Beek,H.F.: 1976, Solar Phys. 48, 197.
Nitta,N., Takakura,T., Ohki,K., and Yoshimori,M.: 1983, Solar Phys. 86, 241.
Ohki,K., Nitta,N., Tsuneta,S., Takakura,T., Makishima,K., Murakami,T., Ogawara,Y., and Oda,M.: Proc. Hinotori Symp. on Solar Flares (ISAS, 1982, Tokyo). p.246.
Ohki,K., Takakura,T., Tsuneta,S., and Nitta,N.: 1983, Solar Phys. 86, 301.
Suri,A.N., Dunphy,P.P., Chupp,E.L., and Forrest,D.J.: 1975, Solar Phys. 43, 415.
Yoshimori,M., Okudaira,K., Hirasima,Y., and Kondo,I.: 1983, Nucl. Instr. and Methods 215, 255.
Yoshimori,M., Okudaira,K., Hirasima,Y., and Kondo,I.: 1983, Solar Phys. 86, 375.
Yoshimori,M.: 1985, J. Phys. Soc. Jpn. 54, 1205

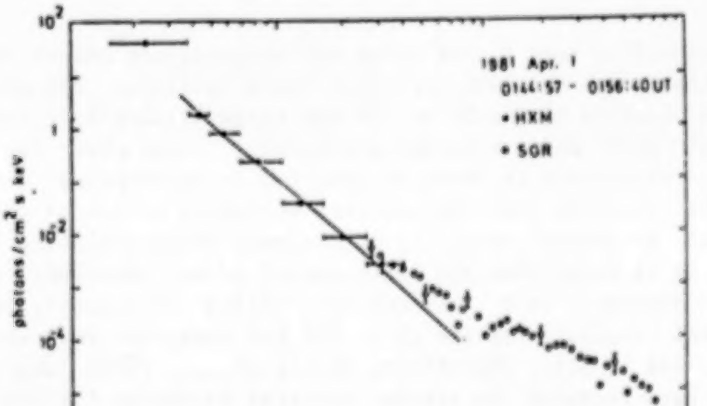

Fig. 1

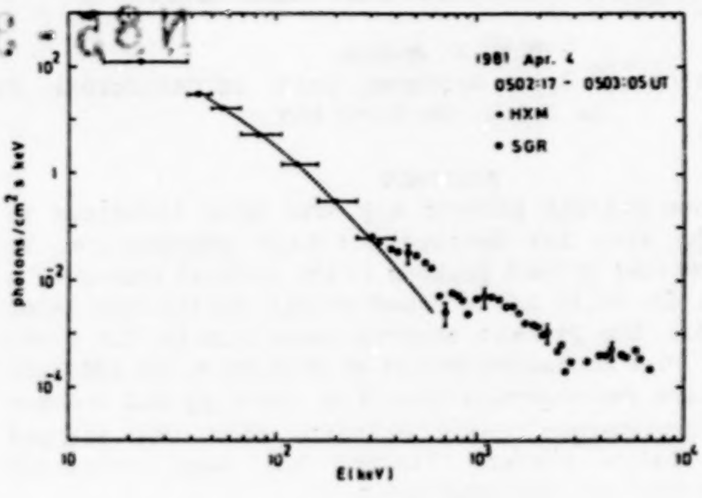

Fig. 2

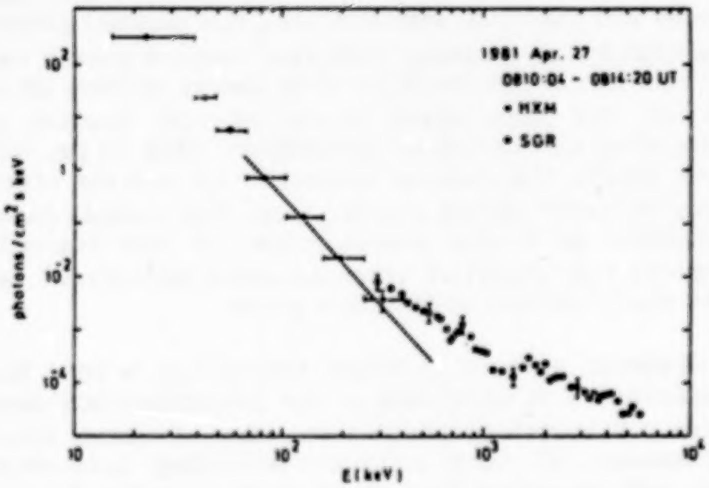

Fig. 3

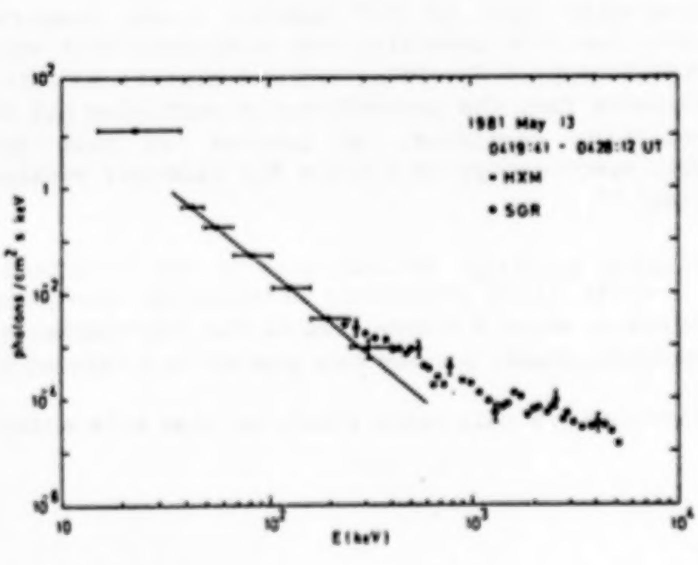

Fig. 4

ION ENERGY STORAGE FOR POST-FLARE LOOPS

N85-34745

Hugh S. Hudson
Center for Astrophysics and Space Sciences, Univ. of California, San Diego
La Jolla, CA 92093 USA

ABSTRACT

Low-energy non-thermal protons may have long lifetimes in coronal loops with low density and high temperature. If energy were stored in such protons in the initial phases of a solar flare, it could be released slowly during the later phases. Within the present observational limits for post-flare loops, this mechanism should be considered in addition to a field-line reconnection theory of the Kopp and Pneuman type. The thin-target γ-ray emission from the trapped protons is below present limits, but more sensitive observations can test the hypothesis.

1. Introduction. Solar flares consist of distinct impulsive and gradual phases[1] plus other associated phenomena. The impulsive phase exhibits powerful energy release and particle acceleration. The gradual phase - the period of main Hα and soft X-ray emission - may also require energy release, although on a slower time scale. The need for this energy release is seen in the gradual growth of the soft X-ray loops of the gradual phase[2] interpreted as a sequential excitation of independent flux loops. Although greater uncertainties exist, theoretical estimates of cooling times also suggest gradual energy release[3] within a given loop. The gradual phase also has a strong association with the acceleration of the coronal mass ejections and the copious production of interplanetary particles[4], so that non-thermal processes must continue during this phase.

The role of energetic protons in solar flares has a long history, stimulated by the observation at Earth and in the interplanetary medium of the "solar cosmic rays." Elliott[5] propounded the idea of energy storage in protons, taking advantage of long Coulomb-scattering lifetimes. The difficult point about understanding the role of protons in the flare proper has remained their essential un-detectability: basically only those particles above thresholds near 10 MeV produce γ-ray spectral line emission, and even this has only generally been diagnostically useful for solar flares since the launch of the Solar Maximum Mission in 1980. Other than theoretical inference from the interplanetary particles and from the high-energy γ-ray-emitting particles, at present we have only the possibility of optical spectroscopy as a means for remotely sensing flare protons at low energies[6-7].

2. An Ion Energy-Storage Scenario. As indicated by the γ-radiation, the impulsive phase of a solar flare powerfully accelerates energetic ions. This acceleration begins at about the same time as the non-thermal electron production of the impulsive phase, but may take place[8] in a "second step".

The scenario discussed in this paper simply is that bulk acceleration of energetic ions in flare loops adjacent to those of the impulsive phase may leave a non-thermal ion population in these loops. Coulomb scattering will then extract this energy from the ions and give it to the electrons, as long as the ions can remain stably trapped. The electrons couple the energy strongly into radiation or conduct it into the chromosphere. The main attractive feature of this scenario, aside from its simplicity, is that the excitation of post-flare loops follows a definite pattern of later loops having lower densities[9], which would have a natural explanation in terms of Coulomb collisions. This scenario of ion energy storage was first proposed by Jefferies and Orrall[10], but has not received much attention in the light of modern data.

3. Coulomb Scattering: Simple Physics. Coulomb scattering describes the physics of charged-particle interactions. The electrostatic force between two particles, one considered as a test particle and the other as a member of the background plasma, will change the energy and momentum of the test particle relative to the background. To apply the Coulomb collision theory, we must specify the velocity distribution functions of the test particles and field particles. In general, flare energy release should result in non-Maxwellian, anisotropic distributions. To avoid this complication, we assume here that the ion and electron components have separately relaxed to Maxwellian distributions characterized by temperatures T_p and T_e respectively. We further assume that the ions are protons. At low proton energies[11],

$$\tau_{pe} = 12.6\ T_e^{3/2}/n_e;$$

note that the equilibriation depends solely upon the temperature and density of the electron distribution. For a typical soft X-ray temperature of 10^7 K and a density of 10^{10} cm^{-3}, we have $\tau = 39.8$ s.

For proton energies exceeding (M/m)kT (1.57 MeV at $T_e = 10^7$ K), the time scale begins to increase approximately as

$$\tau_{pe} = 2.0 \times 10^{11}\ E_p^{3/2}/n_e,$$

with E_p in MeV. For example, at 10 MeV in a density 10^{10} cm^{-3}, we have $\tau = 632$ s.

4. Coulomb Scattering: Complications. The discussion above describes the basic minimum physics of the interactions between differentially heated electrons and protons. Beyond this physics, other processes could play roles important to the question of energy storage: (i) Scattering. The trapped protons may escape by pitch-angle scattering into the loss cone. This scattering could occur as a result of Coulomb collisions or "anomalously" from interactions with waves[12-13]. (ii) Drift. Non-adiabatic motion may lead trapped protons into the loss cone or move them to open field lines[13]; this process depends crucially on the geometry of the flux tubes. (iii) Charge exchange. Low-energy protons can neutralize by picking up a free electron, thus permitting them to cross magnetic field lines and escape from a trap. (iv) Filamentation. If the post-flare loops

contain small-scale filaments, undetectable at present resolution, the higher density in the filaments would shorten the proton Coulomb lifetime.

These processes would in each case reduce the storage time of the protons, making their energy less likely as an explanation for the observed late-phase heating in solar flares. It is likely that pitch-angle scattering from ion-cyclotron waves, driven by the anisotropy of the loss-cone distribution of the mirroring trapped particles, would occur on time scales much shorter than the Coulomb energy losses[12]. Nevertheless the instability calculations are model-dependent and it is worthwhile to consider the Coulomb scattering alone, since this mechanism cannot fail to operate.

From the above estimates of time scales, we can draw the immediate conclusion that proton energy storage would not have long enough time scales for post-flare loops (100 -10000 s) except at low enough densities ($n < 10^8$ cm^{-3}) or for high enough proton energies; in the latter case the protons may be energetic enough to exceed the excitation thresholds and produce γ-ray emission.

5. Comparison with Observations. Gamma-ray Production. To compare the theoretical time scales with the observations, we examine the flare of August 21, 1973, for which MacCombie and Rust[14] have given estimates of the physical conditions in the post-flare loops. Density 5×10^9 cm^{-3} and temperature decay time of 1.7×10^4 s lead to a proton energy of 43 MeV. This energy is high enough to produce γ-ray emission lines from thin-target interactions as the protons bounce between the hypothetical magnetic mirrors.

The total number of trapped protons can be estimated from the total energy of the soft X-ray source. From the emission measure and density quoted by MacCombie and Rust, we find a total energy $W = 5 \times 10^{29}$ ergs. This requires about 7×10^{33} protons at 43 MeV. For the 4.43 MeV γ-ray line of ^{12}C, Ramaty *et al.*[15] give a cross-section of about 40 mb; assuming a carbon abundance of 1.6×10^{-4} relative to hydrogen, we would have a γ-ray flux of about 8×10^{-4} (cm^{2}sec)$^{-1}$. This is about one order of magnitude below the faintest reported solar fluxes[16], so that the energy could be stored in protons and not detected via its γ-ray emission.

6. Conclusions. Elliott[5] proposed the pre-flare storage of energy in energetic protons, based upon their long Coulomb time scales. This idea may still not conflict irreconcilably with observations, although the theoretical question regarding the impulsive nature of the primary flare energy release would remain unexplained. This problem may also exist for the post-flare energy storage hypothesis: experienced observers of Hα line spectra in flares have noted that distinctly unusual Hα profiles occur predominantly at the outer edges of expanding flare ribbons[17]. This implies fairly directly that non-thermal energy release takes place late in the flare development, and provides some of the best evidence in favor of the magnetic flux reconnection[18] as a cause of post-flare heating. These red-shifted or broadened hydrogen emission-line profiles have no simple

explanation in terms of the proton energy-storage hypothesis, since the energy release should occur gradually, but no detailed calculation of the energy transfer between the particle populations presently exists.

I conclude that the proton energy storage hypothesis could work from an energetics point of view. Sensitive γ-ray observations can test the hypothesis directly by observing the thin-target emission of the trapped protons. In the meanwhile, better knowledge of physical conditions in the flare soft X-ray sources would be helpful. Theoretically, further studies of the limits on stable trapping would form part of the necessary treatment of the complete evolution of a flaring loop. Even if ion energy storage turns out to play no role in post-flare energy release, such studies would be well worth while in view of the likelihood that ions and electrons will have different distribution functions.

7. Acknowledgments. This research was supported by NASA under grant NSG-7161. I enjoyed helpful discussions with the Heliobeer participants, plus Bob Lin, Richard Lingenfelter, and Dean Smith.

References

1. Kane, S.R., *Astrophys. J. (Lett.)* 157, L57.
2. Petrasso, R.D., Nolte, J.T., Gerassimenko, M., Krieger, A.S., Krogstad, R., Seguin, F.H., and Svestka, Z., 1979, *Solar Phys.* 62, 133.
3. Moore, R., and 15 co-authors, in P.A. Sturrock (ed.), *Solar Flares* (Colorado), p. 341. 4. Kahler, S.W., Hildner, E., and van Hollebeke, M.A.I., 1978, *Solar Physics*, 57, 429.
5. Elliott, H., 1973, in R. Ramaty and R.V. Stone (eds.), *High-Energy Phenomena in Solar Flares* (NASA SP-342), p. 12.
6. Orrall, F.B., and Zirker, J., 1976, *Astrophys. J.* 208, 618.
7. Canfield, R.C., and Chang, C.-R., 1985, UCSD preprint SP-84-29.
8. Bai, T., 1982a, in *Gamma Ray Transients and Related Astrophysics*, ed. R.E. Lingenfelter, H.S. Hudson, and D.M. Worrall (New York: AIP), p. 409.
9. Svestka, Z., Martin, S.F., and Kopp, R.A., 1980, in M. Dryer and E. Tandberg-Hanssen (eds.), *Solar and Interplanetary Dynamics* (Reidel), p. 217.
10. Jefferies, J.T., and Orrall, F.Q., 1965, *Astrophys. J.* 141, 519.
11. Spitzer, L. Jr., 1962, *The Physics of Fully Ionized Gases* (Interscience), Ch. 5.
12. Meerson, B.J., and Rogachevskii, I.V., 1983, *Solar Phys.* 87, 337.
13. Zweibel, E.G., and Haber, D.A., 1983, *Astrophys. J.* 264, 648.
14. MacCombie, W.J., and Rust, D.M., 1979, *Solar Physics* 61, 69.
15. Ramaty, R., Kozlovsky, B., and Lingenfelter, R.E., 1979, *Astrophys. J. (Suppl.)* 40, 487.
16. Chupp, E.A., 1984, *Annual Reviews Astron. Astrophys.*, to be published.
17. Svestka, Z., Dodson-Prince, H.W., Martin, S.F., Mohler, O.C., Moore, R.L., Nolte, J.T., and Petrasso, R.D., 1982, *Solar Phys.* 78, 271.
18. Kopp, R.A., and Pneuman, G.W., 1976, *Solar Physics*, 50, 85.

N85-34746

TWO TYPES OF ELECTRON EVENTS IN SOLAR FLARES

E.I.Daibog, V.G.Kurt, Yu.I.Logachev, V.G.Stolpovsky

Institute of Nuclear Physics, Moscow State University,
Moscow II9899, USSR

Abstract. The fluxes and spectra of the flare electrons measured on board Venera-I3 and I4 space probes are compared with the parameters of the hard ($E_x > 55$ keV) and thermal X-ray bursts. The electron flux amplitude has been found to correlate with flare importance in the thermal X-ray range ($r \sim 0.8$). The following two types of flare events have been found in the electron component of SCR. (I) The electron flux increase is accompanied by a hard X-ray burst and the electron spectrum index in the $\sim$ 25-200 keV energy range is $\gamma \sim 2$-3. (2) The electron flux increase is not accompanied by a hard X-ray burst and the electron spectrum is softer ($\Delta\gamma \sim 0.7$-I.0).

I. Method and statistics.

The fluxes and spectra of the 25-I500 keV electrons and 55-I00 keV hard (X_h-) X-rays were systematically measured in I98I-I983 on board Venera-I3 and I4 /I-3/. 300 SCR events were selected which could be considered as flare-induced. Only the SCR events which could be identified, using H_α and thermal X-rays, with the flares in the Sun's Western hemisphere were selected in order to study the relationships between the flare electron fluxes injected to interplanetary space and the X-rays. The events were only analysed where the > 70 keV electrons were observed, for it is obvious that the > 55 keV X-rays are produced by the electrons with $E_e > E_x$. Such events amount to I30; out of them only 67 were accompanied by the X_h-bursts; in 63 cases such an accompaniment was not detected. These sets of events will be henceforth designated eX_tX_h and $eX_t\bar{X}_h$.

2. Distribution functions.

We constructed the size distributions of the number of events with given parameter Y: $f(Y) = (I/N)(dN/dY)$, where N is the number of events in a given set. The highest electron fluxes (J_e) and the amplitudes J_{Xt} and J_{Xh} of, respectively, the X_t- and X_h-bursts are used as Y. The functions $f(J_e)$, $f(J_{Xt})$, and $f(J_{Xh})$ are shown in Fig.Ia,b,c where the crosses and the dashed lines relate to the eX_tX_h set. From Fig. I it is seen that, throughout the major part of the interval of the amplitudes J_e, J_{Xt}, and J_{Xh} the distribution functions may be approximated by a power low with index α. It is seen that (I) the distribution functions of various parameters within the same set are alike and have similar indices and (2) the distribution functions of the same parameters within different sets are characterized by different α. We have $\alpha \sim$ I.2-I.4 for eX_tX_h and $\alpha \sim$ I.7-I.8 for $eX_t\bar{X}_h$. Thus, by using the additional indication (the accompanying X_h-burst), we have obtained two sets of events in which the

ORIGINAL PAGE IS OF POOR QUALITY

intensity distributions differ in slopes. This means that two types of electron events are realized in SCR which correspond to different conditions for particles acceleration and leakage in solar flares. We think that the conventional approach (see, for example, /4/) makes it difficult to discriminate the types of flare events in SCR because in this case the distribution function of the events of given parameter is usually constructed, irrespectively of the relationships of these events to other parameters of flare activity.

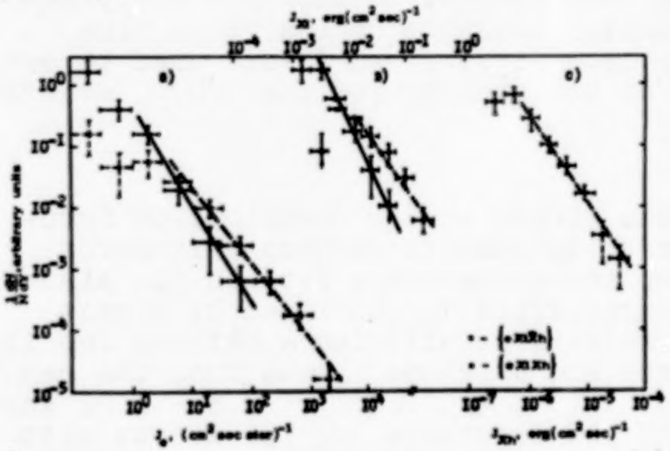

Fig. I

From Fig. I it is seen that the eXtXh to- eXtX̄h events number ratio increases with amplitudes J_e and J_{Xt} and that, starting from certain values of the amplitudes, only the eXtXh events occur. This is understandable in terms of the big flare syndrome /5/ according to which, as the power of a flare rises, the probability for the flare to be accompanied by the entire spectrum of flare events rises also. However, two types of the SCR events can hardly be accounted for only by the difference in the power of parent flares. From Fig. I it is seen that there exists the interval of the J_e and J_{Xt} amplitudes where the SCR events of both types are realized.

The electron spectra

Fig. 2 shows the results of comparing between the differential electron energy spectra in the eXtXh and eXtX̄h events. In the energy range $E_e \sim$ 25-2I0 keV the electron spectra were approximated by a power law with exponent γ_e. The values of γ_e presented in Fig.2 have been obtained by averaging over the number of the events of given type in the intensity interval $[J_e, J_e + \Delta J_e]$. The dots relate to the eXtX̄h events, and the crosses to the eXtXh events. According to Fig.2, the eXtXh events differ from the eXtX̄h events in the electron spectrum slope ($\Delta\gamma_e \sim$ 0.7-I.0) and in the dependence of γ_e on J_e. Nevertheless, the differences in the spec-

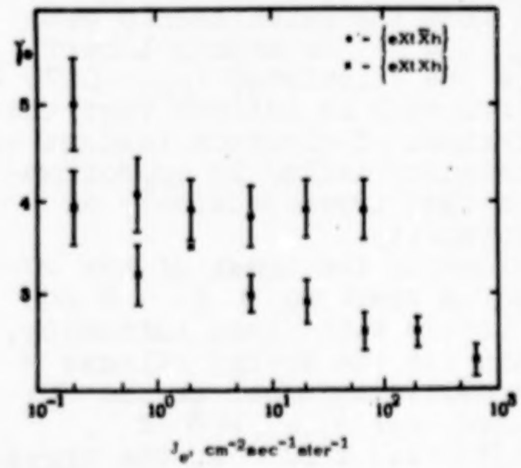

Fig. 2

tral characteristics of electron fluxes cannot account in all cases for the X_h-burst accompaniment of the SCR events. It is easy to verify that the identical electron fluxes at $\Delta\gamma_e \simeq 2$ produce the quantum fluxes differing by a factor of less than 3. In some cases, therefore, we must have seen both an X_h-burst and a SCR electron event.

The most probable condition for the $eX_t\bar{X}_h$ events to be realized consists in that the plasma density n in the acceleration region is low and all the accelerated electrons or the majority of them, are ejected to interplanetary medium within a period smaller than the Coulomb loss time. The values of J_e and γ_e from Figs. I and 2 were used to estimate the upper limit of the density for the $eX_t\bar{X}_h$ events: $< 5\times10^{9}-10^{10}\ \text{cm}^{-3}$.

Correlations

The coincidence of the slopes of the distribution functions of events for the amplitudes of various parameters (see Fig. I) ensues from the correlation between the electron events and X-ray bursts:This is confirmed by direct calculations of the correlation coefficients between the intensities of X-ray bursts and electron fluxes from the central and western flares. $r(\lg J_e, \lg J_{Xt}) \sim 0.8 \pm 0.02$ for I47 events with the > 25 keV electrons and I30 events with the > 70 keV electrons. Such value of r_{eXt} means that (I) the energy lost for SCR electron acceleration is approximately proportional to the flare energy because the energy release in the X_t-range is proportional to the energy realized in the flare /4/ and (2) the X_t-flux may be also a measure of the power of a SCR event. We have also obtained that $r(\lg J_e, \lg J_{Xh}) \sim 0.69$. Partly, this may be relevant to the fact that the electron flux must be compared with the total number of quanta or with energy release in a burst $\varepsilon = \int J_{Xh}\,dt$ rather than with the J_{Xh}-burst amplitude, because it is ε that is proportional to the particle number in the generation region of the X_h-rays in terms of the nonthermal model. Fig. 3 shows the correlation between ε and J_e. It is seen that the relationship between J_e and ε is nearly linear and that the calculated $r_{eXh} \sim 0.79 \pm 0.03$. From this it follows that the effectiveness of electron leakage to interplanetary medium is approximately constant irreespectively of flare intensity.

Considering the index of the X_h-ray quantum spectrum δ is ~ 4 and varies little with flare intensity, we obtain for the energy release ε and the particle number at the X_h-ray source n_s: $n_s = k(\delta)\,\varepsilon$, where $k(\delta) \simeq 1.3 \times 10^{41}$ at the threshold values $E_x = 70$ keV and $E_e = 55$ keV in case of thick target or trap

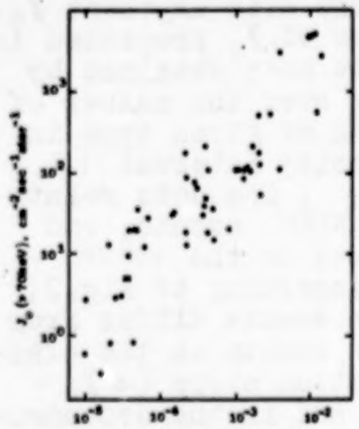

Fig. 3

model /6/. Considering that $\varepsilon = bJ_e$ (see Fig. 3) and turning to the number of particles injected from the source, n_{inj} , we obtain the following relation between n_s and n_{inj} in terms of the diffusion model: $n_s = A n_{inj}$ and $A \approx 10^3$.

References

I. Daibog E.I. et al. Kosm issl., I983, v.2I, p.574.
2. Daibog E.I. et al. Izv. Akad. Nauk SSSR,ser.fiz., I984, v.48, No.II, p.2I58.
3. Belyakov S.A. et al. Kosm issl., I984, v.22, p. 906
4. Hudson H.S. Solar Phys. I978, v.57, p.237.
5. Kahler S.W., J. Geophys.Res., I982, v.87, p.3439.
6. Merlose D.B., Brown J.C. Mon. Not. R.astr.Soc., I976, v.I76, p.I5.

N85-34747

SH 1.2-12

TWO CLASSES OF SOLAR ENERGETIC PARTICLE EVENTS ASSOCIATED WITH IMPULSIVE AND LONG DURATION SOFT X-RAY FLARES

H. V. Cane, R. E. McGuire and T. T. von Rosenvinge
Laboratory for High Energy Astrophysics
Greenbelt, MD 20771
USA

ABSTRACT

Solar energetic particle events observed in space have different properties depending on the class of associated flare. Impulsive flares, which occur low in the corona in regions of high energy density, are associated with particle events which are deficient in protons. These events are rarely associated with coronal mass ejections and interplanetary shocks. The vast majority of large, high energy proton events are associated with long duration flares, many of which are also associated with fast coronal mass ejections and strong interplanetary shocks. Such flare events originate relatively high in the corona.

1. Introduction. Recently it has been pointed out from two different viewpoints that there may be more than one class of interplanetary solar energetic particle (SEP) event. In the first study [1] it was found that there were SEP events which showed high abundances of electrons relative to protons at energies near 35 MeV and which were well correlated with gamma ray events. Previously it had been found that there was a poor relationship between particle fluxes inferred from gamma ray observations and fluxes measured in space [2,3]. In another study [4] a few examples of SEP events were found which were not associated with coronal mass ejections(CMEs). In this work it was noted that these rare events were associated with impulsive flares. It had been previously established that the flares associated with CMEs and interplanetary shocks (and by inferrence SEPs) [5,6,7,8] tend to be predominately of a different class, namely 'long duration'. A study in 1977 [9] showed that impulsive and long duration flares, as observed in soft X-rays, occurred in different regions of the corona. Long duration flares occur higher in the corona than impulsive flares.

We have made a study of SEP events and find that there are two classes. Although in one class the events tend to be 'proton poor' and are not, in general, associated with CMEs, the important distinguishing feature is their association with impulsive flares.

2. The Data. We have used data from Goddard Space Flight Center detectors on IMP-8 and ISEE-3 to assemble a list of solar flare events which produced relativistic electrons (>3 MeV) above approximately 5x10-4 electrons/(cm2.ster.sec.MeV) during the interval September 1978 to December 1983. Only events with a confident source association were included. For the majority of the events, this meant that there were H-alpha, soft X-ray and

ORIGINAL PAGE IS
OF POOR QUALITY

metric radio phenomena that occurred at the same time. The events were divided into two classes depending on the durations of the associated (1-8 A) soft X-ray events.

We term "long duration" those particle events associated with soft X-ray flares which lasted for more than 1 hour at greater than 10% of the peak intensity. "Impulsive events" were associated with X-ray flares with a duration of less than 1 hour at greater than 10% of the peak intensity. Four further events without X-ray observations were included in this group on the basis of the short duration of the associated H-alpha activity. It is important to note that the terminology "impulsive" and "long duration" refers to the soft X-ray profiles and not to the particle time histories. However, the SEP events associated with impulsive flares do tend to have short durations relative to 'normal' proton events as can be seen in Figure 1.

The 73 events of our study are listed elsewhere [10] along with a more detailed description of the selection criteria. There are two lists corresponding to the two classes. The information provided is as follows; a) flare timimg and location, soft X-ray intensity and duration; b) timings and intensities of associated metric bursts of Types III, II and IV; c) average speed to earth of any associated interplanetary shock; d) electron onset and peak fluxes in two energy bands (~1 and 10 MeV); e) peak proton fluxes

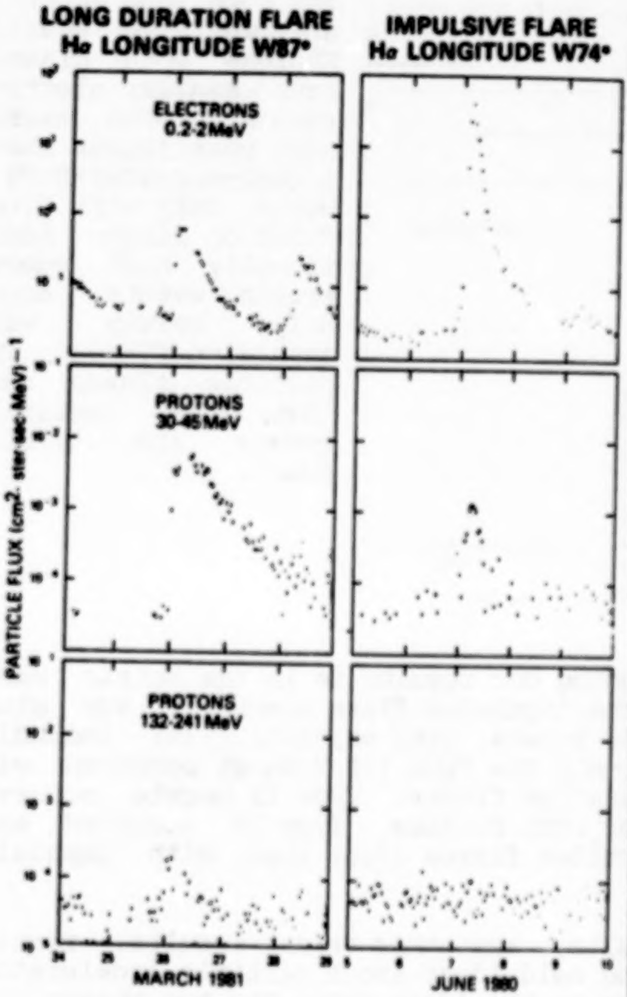

Fig.1 Proton and electron fluxes as a function of time for three events. There were two events on June 07, 1980 but they are unresolved in these figures.

in two bands (~10 and 60 MeV), f) the ratio of the high energy electron flux to the low energy proton flux; and g) approximate electron and proton spectral indices based on the ratios of the high to low energy fluxes of each specie.

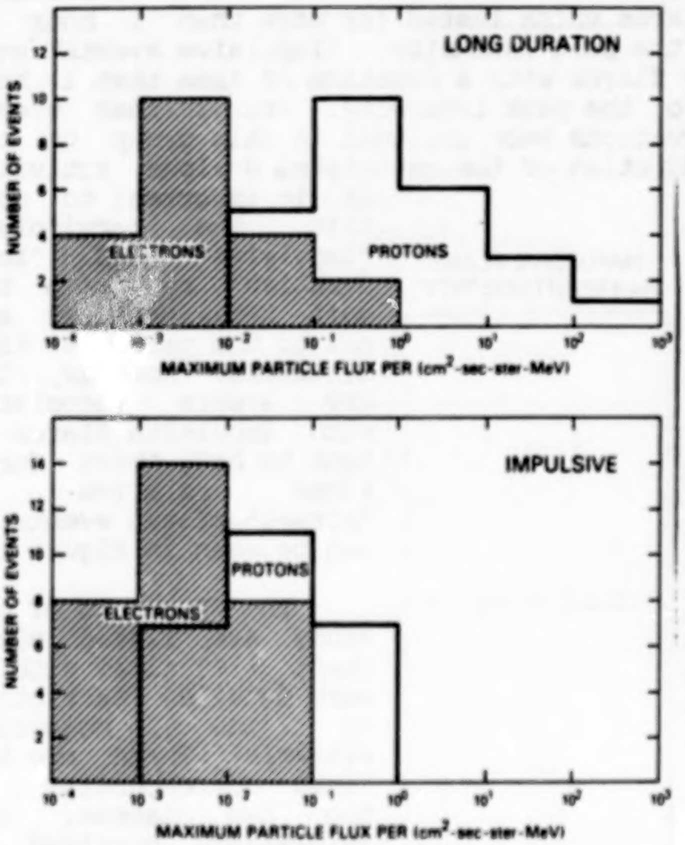

Figure 2 shows event size distributions for electrons (4-19 MeV) and protons (9-23 MeV) for both long duration and impulsive events. Whereas both classes have similar electron events, proton events with peak fluxes above 1/(cm2-sec-ster-MeV) occur only with long duration flares. Additionally high energy proton events occur only rarely with impulsive flares. The particle fluxes show that the impulsive events are 'proton poor'.

The key to understanding our results is in the metric radio bursts. We find that the impulsive flare events of our study produced strong Type III bursts, the majority (77%) including Type V continuum. Conversely the Type III/V burst occurred with only 15% of the long duration flares. Type II bursts occurred about equally (~80%) for both classes. Type IV occurred more frequently with long duration flares (72%) than with impulsive flares (23%).

3. Discussion. Our results, and other recent results, require modifications to many long held ideas about particle acceleration in flares, in particular to the ideas about the two phases. It was originally proposed [11] that in the first phase only non-relativistic electrons were accelerated. Observations of gamma-rays and the association of a class of proton and relativistic electron events with strong Type III bursts show that this is incorrect. Acceleration at coronal shocks was assumed necessary for the production of protons and high energy electrons. Since Type II bursts (the signatures of shocks) always follow

associated Type III bursts it was assumed that the first phase was necessary for the generation of shocks and the subsequent second phase acceleration. We find that there is a good correlation between high energy proton events and Type II and Type IV bursts but note that some events are not preceded by Type III bursts. Proton events with weak impulsive phases have been discussed before [12]. We believe that the relationship between the two phases is the following: A shock can form as a consequence of the initial impulsive energy release in energetic solar events. At essentially the same time beams of high energy particles can be created but the probability is greatest low in the corona. When the coronal shock strengthens (relatively high in the corona) it can accelerate high energy particles which escape to the interplanetary medium. In this scenario there is no relationship between the intensity of the first phase and that of the second. However in very 'big' flares both phases will be strong.

4. Conclusions. Our results suggest that energy releases that take place high in the corona are most likely to be associated with a CME and the particles observed in space may include substantial fluxes of both electrons and protons. Energy releases in the low corona occur rapidly and are most likely to produce fluxes of particles that in the interplanetary medium are deficient in protons.

5. Acknowledgements. This work was supported in part by NASA grant NGR 21-002-316.

References

1. Evenson, P. et al., (1984), Astrophys. J., 283, 439.
2. von Rosenvinge, T. T. et al., (1981), 17th ICRC, 3,28.
3. Cliver, E. W. et al., (1983), 18th ICRC, 10, 342.
4. Kahler, S. W. et. al., (1984), J. Geophys. Res., 89, 9683.
5. Sheeley, N. R. ,Jr., et al., (1983), Solar Wind 5, 693.
6. Sheeley, N. R., Jr., et al., (1985), J. Geophys. Res., 90, 163.
7. Cane, H. V. and Stone, R. G., (1984), Astrophys. J., 282, 339.
8. Cane, H. V., (1985), J. Geophys. Res., 90, 191.
9. Pallavicini, R., et al., (1977), Astrophys. J., 216, 108.
10. Cane, H. V. et al., (1985) to appear in Astrophys. J.
11. Wild, J. P., et al., (1963), Ann. Rev. Astron. Astrophys., 1, 291.
12. Cliver, E. W., et al., (1983), Astrophys. J., 264, 699.

N85-34748

SH 1.2-13

A DOMINANT ROLE FOR PROTONS AT THE ONSET OF SOLAR FLARES

G.M.Simnett
Department of Space Research, University of Birmingham, U.K.

ABSTRACT

We suggest that recent observations have cast considerable doubt on the generally accepted explanation that non-thermal electron beams transfer most of the flare energy during the onset of solar flares. In this paper we argue that non-thermal protons in the energy region 10^2-10^3 keV are a more probable energy transfer mechanism. An important consequence of this hypothesis is that the hard X-ray burst must be thermal.

1.Introduction It was shown many years ago(1) that the energy released in a solar flare was consistent with the total energy in non-thermal electrons above 20 keV, assumed to be responsible for the hard X-ray burst via non-thermal bremsstrahlung in a thick target. Since that time support for this hypothesis has grown to the extent that many regard it as an established fact. For example, it has recently been stated(2) that to account for many large flares no significant energy input, other than electrons $>$ 25 keV, needs to be invoked. In another recent paper(3) it was argued that over 10^{36} electrons.s^{-1} were required during the impulsive phase of the 1981 April 24 flare.

We believe that improved observations made during the last solar maximum have cast doubt over this interpretation of the impulsive phase of flares. Among the more significant observations are the following:

a) The high plasma turbulence seen in heavy ions, eg CaXIX, prior to the onset of the hard X-ray burst, including in some cases significant mass upflows(2,4).

b) The presence of high energy protons at the onset of the impulsive phase of some gamma ray flares(5,6).

c) The complete absence of metric/decimetric radio emissions during many large flares including the impulsive phase of the 1981 April 24 flare(7).

When the energy inputs required for a) and b) are taken into account, together with the energy in the whole electron spectrum, the total flare energy budget becomes heavily oversubscribed. In addition, if the efficiencies of the acceleration processes are also considered, which are quite probably less than 50%, the situation is even worse. Thus another significant point is:

d) When the energy in the pre-impulsive phase plasma turbulence and upflows is added to the energy in the non-thermal electrons and ions, together with an efficiency factor, the flare energy budget appears to be exceeded.

To overcome these problems an alternative hypothesis is suggested, namely that the primary energy release results in the coronal acceleration of non-thermal protons which have the bulk of their energy in the 10^2-10^3 keV region. We shall show that this offers an attractive alternative to both the non-thermal electron hypothesis discussed above and the alternative thermal models suggested recently(8,9). Our model is essentially a non-thermal proton model which results in excessive heating of the chromosheric plasma to produce the hard X-ray burst by thermal bremsstrahlung.

2.The Non-Thermal Proton Hypothesis We now consider the four points a)-d) mentioned above in more detail.

a) The plasma turbulence and upflows observed before the onset of the hard X-ray burst cannot be caused by the impact of electron beams on the chromosphere without producing X-rays. As soon as an electron beam is accelerated a reverse current will be set up to avoid charge separation. Emslie(10) has shown that when reverse current losses of the beam are taken into account the electron energy must exceed ~60 keV to penetrate below the transition zone for any reasonable atmospheric model. Theory has shown(11) that energy must be dumped below the transition zone for significant mass to be ablated.

Protons in the region 10^2-10^3 keV can do this readily. Depending on the atmospheric model the threshold energy for penetration to the top of the chromosphere from the corona is 400 ± 150 keV, with the lower limit probably more appropriate to the onset of a flare. Reverse current losses are largely eliminated by having accompanying electrons of the same velocity as the protons. The energy content of such electrons is negligible compared with the protons.

b) Gamma ray production at the flare onset is accounted for by a slightly more efficient acceleration process which raises the high energy tail of the proton energy spectrum. This need only have a minor effect on the total energy of the accelerated protons, which explains in a natural way why many gamma ray flares are optically small, with relatively low total energy. On the conventional model, if the typical flare is dominated energetically by non-thermal electrons then the gamma ray flares must invoke a proton acceleration process which suddenly becomes important. We believe such a scenario is unattractive.

c) Radio emission is an important electron signature. In a magnetic field relativistic electrons emit gyrosynchrotron radiation, which in the flare situation appears in the microwave region. An electron beam with a velocity distribution increasing towards high energies will emit plasma radiation; such beams are frequently observed as type III bursts and only $\sim 10^{29}$ electrons $>$20keV are required for these to be detectable by modern radio-telescopes. Correlation of microwave bursts with hard X-rays is very high; virtually 100% for bursts $>$1000 counts.s^{-1} detected by the Hard X-Ray Burst Spectrometer on SMM. Yet 15% (7) of the same flares have no metric/decimetric radio emission.

It might be argued that the required velocity distribution in the electron beam builds up too slowly for a type III burst to be produced. However, observations(12) of very fast ($\ll 1$s) hard X-ray fluctuations argue just the opposite, namely that the release must be impulsive unless the acceleration site is very close, $\sim 10^3$km, to the chromosphere. Hard X-ray imaging observations from SMM suggest that such small distances are unlikely in a typical flare(13).

The impulsive phase of the white-light flare on 1981 April 24 had 35 GHz emission of $\sim 5000.10^4$ Jy(3). Microwave emission at this level occurred in only nine flares during 1979-82, so this is truly a major event. However, it produce no metric/decimetric emission until the onset of the gradual phase some 5m after the impulsive phase maximum. On the non-thermal electron hypothesis over 10^{36} electrons.s^{-1} are required to produce the X-rays and the impulsive phase lasts for over 100s. It is very surprising that during this time enough electrons to produce a type III burst - 10^{29} - did not escape into the corona.

d) It has been proposed recently(2) that electrons >25 keV may provide the energy for the entire flare. This, however, neglects the energy in electrons <25 keV and there is no basis from observations to suggest that these electrons are negligible. In fact, to the contrary. Lin et al(14)made high spectral resolution observations of a flare which showed that the electron spectrum extended to 13 keV (the low energy cut-off of the measurement) without a change in spectral index. As the spectral index was -4.5 this implies an order of magnitude increase in energy content going from 25 keV to 10 keV. We have no way of estimating the proton energy spectrum at the Sun below ~ 5 MeV. However, analysis of the 1972 August 4 flare(15) indicated over two orders of magnitude more protons than electrons at 5 MeV and extrapolation of the spectrum produced equal numbers of protons and electrons at 40 keV. While there is no basis in this flare for such an extrapolation, it shows proton energy should not be disregarded. The accelerator is presumably $<100\%$ efficient at producing non-thermal particles. Even if we assume 50% efficiency, it appears that we would have no difficulty in estimating a total energy which is a factor of 20-40 higher than that contained in electrons above 25 keV.

From the above there is no doubt that the arguments for the total flare energy residing in non-thermal electrons >25 keV are weak and that there is substantial evidence against their existence in any energetically-dominant form at all. It now remains for us to show that non-thermal protons can explain the phenomena better. Protons of a few 100 keV can readily drive the plasma turbulence and ablation without producing hard X-rays. They are necessary for the gamma rays, and they can easily heat the chromosheric plasma to produce the soft X-ray emission. The principal difficulty with a proton beam is in hard X-ray generation. To do this there must be rapid heating in a way that produces electron temperatures significantly above ion temperatures. Such a mechanism has been suggested in the context of Tokomaks(16), which invokes plasma instabilities in fine-scale filamentary structures where electron temperatures are enhanced by 10^2 or more. While this is probably not directly applicable to the flare situation, it indicates that anomalous effects are likely in plasmas with high beam currents and that extremes in temperature might occur.

In terms of energy, thermal hard X-ray production is ~30 times more efficient than a non-thermal process(17). In addition our model only requires one acceleration mechanism to be operating to account for all flares. There are other important observations, such as the insensitive way O$\underline{V}$ emission correlates with hard X-rays and the negative results from polarization studies that also argue against non-thermal electron dominance(18,19).

3.Conclusions. We have shown that there is considerable evidence against non-thermal electron beams as the dominant energy transfer mechanism during the impulsive phase of solar flares. Instead we suggest that non-thermal protons in the energy region 10^2-10^3 keV are a more likely energy carrier. The advantages of protons are that they can account for the plasma turbulence and upflows seen before the hard X-ray burst, they can produce gamma ray emission from optically weak flares and they can account for the lack of metric/decimetric emission in many large flares. In addition, only one acceleration process need be advocated to account for all flares provided it is approximately velocity dependent. Such a process is the MHD shock, which certainly has all the right properties when observed in interplanetary space. An important consequence of our model is that the hard X-ray burst must be thermal in the impulsive phase.

References

1)Lin R.P. and Hudson H.S.(1976) Sol Phys 50,153
2)Antonucci E. et al (1984) Ap J 287, 917
3)Kane S.R. et al (1985) Ap J 290, L45
4)Antonucci E. et al (1982) Sol Phys 78,107
5)Chupp E.L. et al (1982) Ap J 263, L95
6)Forrest D.J. et al (1981) Proc 17th Int Cosmic Ray Conf 10,5
7)Benz A.O. and Simnett G.M. (1985) (in preparation)
8)Brown J.C. et al (1979) Ap J 228, 592
9)Smith D.F. and Lilliequist C.G. (1979) Ap J 232, 582
10)Emslie A.G. (1980) Ap J 235, 1055
11)MacNeice P. et al (1984) Sol Phys 90, 357
12)Kiplinger A.L. et al (1984) Ap J 287, L105
13)Hoyng P. et al (1981) Ap J 246, L155
14)Lin R.P. et al (1981) Ap J 251, L109
15)Ramaty R. et al (1980) in "Solar Flares" ed P.A.Sturrock, Colorado Univ Press
16)Haines M.G. and Marsh F.J. (1982) J Plasma Phys 27, 427
17)Smith D.F. and Harmony D.W. (1982) Ap J 252, 800
18)Poland A.I. et al (1984) Ap J 280,457
19)Tramiel L.J. et al (1984) Ap J 280, 440

N85-34749

SH 1.2-14

THE ENERGY SPECTRA OF SOLAR FLARE ELECTRONS[*]

Paul Evenson[+], Dietrich Hovestadt[‡], Peter Meyer[x], and Dan Moses[x]

[+]Bartol Research Foundation, University of Delaware
Newark, DE 19716 USA

[‡]Max-Planck Institute for Extraterrestrial Physics
8046 Garching, West Germany

[x]Enrico Fermi Institute and Department of Physics
University of Chicago, Chicago, IL 60637 USA

__ABSTRACT__. A survey of 50 electron energy spectra from .1 to 100 MeV originating from solar flares has been made by the combination of data from two spectrometers onboard the ISEE-3 (ICE) spacecraft. The observed spectral shapes of flare events can be divided into two classes through the criteria of fit to an acceleration model. This "standard" two step acceleration model, which fits the spectral shape of the first class of flares, involves an impulsive step that accelerates particles up to 100 keV and a second step that further accelerates these particles up to 100 MeV by a single shock. This fit fails for the second class of flares that can be characterized as having excessively hard spectra above 1 MeV relative to the predictions of the model. Correlations with soft x-ray and meter radio observations imply that the acceleration of the high energy particles in the second class of flares is dominated by the impulsive phase of the flares.

I. __INTRODUCTION__. Previous surveys of electron flare spectra with energies extending up to 10 MeV have been conducted by Datlowe (1971), Simnett (1974), Lin __et al__. (1982), and Evenson __et al__. (1984). The study presented in this paper has the advantage of nearly continuous coverage over a four year period of high solar activity in the absence of magnetospheric effects due to the orbit of the spacecraft. Two independently well calibrated instruments on the same spacecraft are used to cover two adjacent energy ranges. The total energy range and the resolution are well suited to explore the spectral regime characteristic of the second step of acceleration. The combination of improvements in this study yield results not identified in previous surveys.

2. __METHOD__. Measurements of solar flare electrons in the energy range of .075 to 1.30 MeV were obtained from the ULEWAT spectrometer (Hovestadt __et__. __al__. 1978) and electron spectra in the range of 5 to 100 MeV were measured with the MEH spectrometer (Meyer and Evenson, 1978). No attempt was made at normalization of the two sources of data as each instrument was judged to be adequately calibrated by independent methods. The time interval of the survey extends from launch of ISEE-3 in August 1978 through December 1982.

---

[*] Supported, in part, by NASA contract NAS5-26680 and NASA grant NGL-14-001-005.

Two requirements for inclusion of a flare in the survey were applied: first, all energy bins in the ULEWAT data must have an impulsive (~ 1 day rise time) enhancement over background and, second, all energy bins in the MEH data through the 10 MeV bin must also have an impulsive enhancement over background. The majority of events observed with ULEWAT has no measurable counterpart in MEH. To relate the interplanetary particle spectrum to the source spectrum, the assumptions were made that the spectrum of particles escaping from a flare is identical to the spectrum of particles accelerated in that flare and that the propagation of particles from the flare is a simple diffusion process which does not change the energy of the particles. With these assumptions the spectrum at the source is obtained by subtracting the pre-flare background flux from the flare maximum flux in each energy bin (Lin et al. 1982).

The classification of spectral shape by comparison with the prediction of a single shock acceleration is equivalent to comparison with a spectral shape which is a power law in momentum (Blandford and Ostriker, 1978). Following Ellison and Ramaty (1985), the loss of efficiency in acceleration of the highest energy particles due to effects such as the diffusion length of the particle being greater than the size of the shock is modeled by an exponential roll-off in energy above a characteristic energy, E_o. A good power law in momentum fit to an energy spectrum is shown in the example of Figure 1, and replotted as a function of rigidity in Figure 2. The case of a spectrum that deviates from a power law in momentum (rigidity) predicted by the single shock model is obvious on a rigidity plot (Figure 3).

3. **RESULTS**. A detailed list of the properties of the individual flares in this study will be presented in a full paper now in preparation. Of the 50 events included in the survey, 31 can be modeled by the single shock mechanism and these will be referred to as class II events. The events which deviate from a power law in momentum will be referred to as class I events. Sixteen of the class I spectra are consistent with a power law shape in kinetic energy while 3 spectra are flatter at high energies. Events with an identified source position on the sun show a selection effect in favor of well connected flares which is more pronounced in the class I events. The average 25-45 MeV proton flux from the class II events is higher than that of the class I events while the average electron to proton ratio at 25-45 MeV of the class II events is lower than that of the class I events.

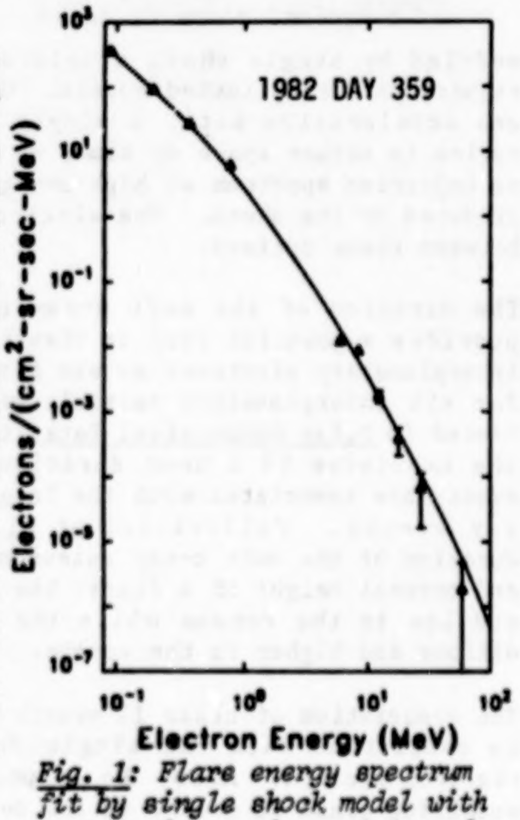

Fig. 1: Flare energy spectrum fit by single shock model with compression ratio, r=2.3, and e-folding energy, E_O=60 MeV.

4. **DISCUSSION**. While the spectra of class II electron flare events are well

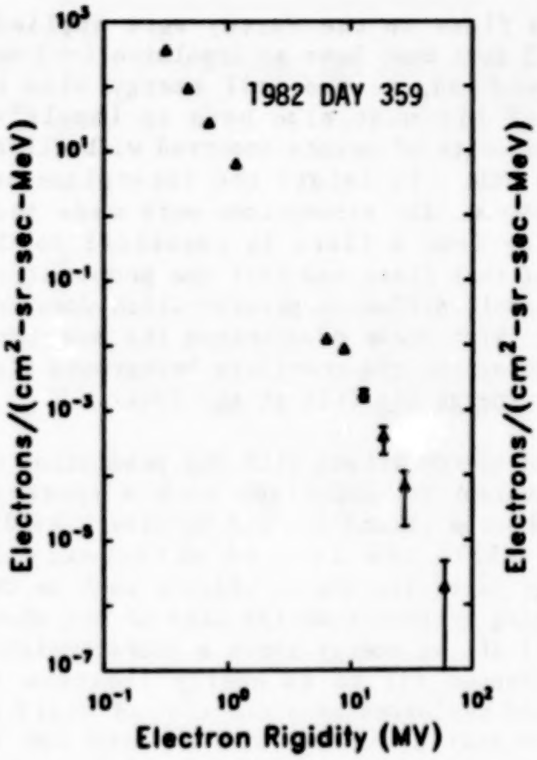

Fig. 2: Flare rigidity spectrum of a typical class II event.

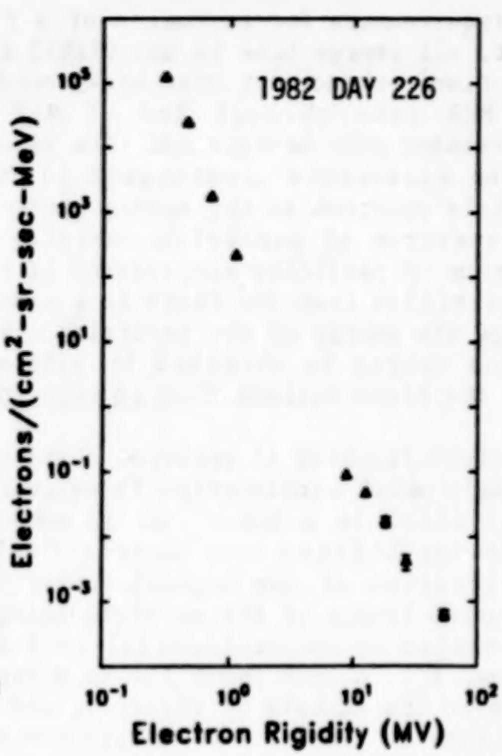

Fig. 3: Flare rigidity spectrum of a typical class I event.

modeled by single shock acceleration, the spectra of class I events require more complicated models. Obvious candidates include more than one acceleration site, a single shock with a compression ratio which varies in either space or time, an energy dependent escape mechanism, and an injection spectrum at high energies which is flatter than the spectrum produced by the shock. The electron spectra alone cannot distinguish between these options.

The duration of the soft x-ray thermal emission (1-8 Å) of flares provides a powerful tool in classifying flares associated with energetic interplanetary electrons as was first recognized by Cane et al. (1985). For all interplanetary particle events associated with soft x-ray events listed in Solar Geophysical Data, the class I events are associated with the impulsive (< 1 hour duration) soft x-ray events while the class II events are associated with the long duration (> 1 hour duration) soft x-ray events. Pallovicini et al. (1977) have demonstrated that the duration of the soft x-ray emission is further associated with the volume and coronal height of a flare: the impulsive flares (class I) are compact and low in the corona while the long duration flres (class II) are diffuse and higher in the corona.

The association of class II events with diffuse events high in the corona is consistant with the single shock acceleration model used to fit the electron spectra. Also, in support of the single shock acceleration model for class II events is the correlation by Cane et al. (1985) of the long duration x-ray events with interplanetary shocks and coronal mass ejections. The duration of gamma-ray emission bursts (Chupp, 1984) in

N85-34750

the class II events is also consistent with a shock of velocity 10^3 km/s traversing the $10^{13}-10^{14}$ km^3 volume associated with the long duration soft x-ray events. The relative height in the corona of class II flares results in less coronal diffusion than of class I flares and predicts less sensitivity to the degree of connection with the flare site.

The association of class I events with impulsive, compact events low in the corona is inconsistant with a single shock model with a compression ratio which varies in time or space. Multiple acceleration sites would be expected to produce multiple soft x-ray impulses which are not seen. The spectral shape of the gamma-ray continuum for the impulsive 1972 August 4 flare suggests that the electron spectrum at the acceleration site has a class I spectral shape (Ramaty et al. 1975) and thus the escape mechanism is not energy dependent.

A model of class I flare acceleration dominated by the impulsive (magnetic reconnection) phase of the event is consistant with both the observed electron spectral shape and the soft x-ray emission by a compact and impulsively heated volume of plasma. One might expect evidence of beaming along the direction of the electric field resulting from magnetic reconnection and Cane et al. (1985) have found a correlation of the impulsive soft x-ray events with strong type III radio bursts which accompany streaming electrons. Tentative association of the directivity of gamma-rays described by Vestrand et al. (1984) with class I events provides further evidence for electron beaming. The component of shock accelerated particles appears to be restricted to the lower energies by the size and density of the heated plasma region and the shape of the electron spectrum is consistant with such a component.

5. ACKNOWLEDGEMENTS. We would like to thank Mr. Leo Krawczyk and Ms. Judith Fontana-Kroeger for assistance in preparing this paper. We would also like to thank Mr. Richard Kroeger for helpful discussions.

REFERENCES

Blandford, R. and Ostriker, J. 1978, Ap.J. 221, L29.

Cane, H., McGuire, R. and von Rosenvinge, T. 1985, submitted to AP.J.

Chupp, E. 1984, Ann. Rev. Astron. Astrophy., 22, 359.

Datlowe, D. 1971, Solar Phys. 17, 436.

Ellison, D. and Ramaty, R. 1985, accepted in Ap.J.

Evenson, P., Meyer, P., Yanagita, S. Forrest, D. 1984, Ap.J. 283, 439.

Hovestadt, D., Gloeckler, G., Fan, C., Fisk, L., Ipavich, F., Klecker, B., O'Gallagher, J., Scholer, M., Arbinger, H., Cane, J., Hofner, H. Kunneth, E., Laeveranz, P. and Tums, F. 1978, IEEE Trans. GE16, 166.

Lin, R., Mewaldt, R. and Van Hollebeke, M. 1982, Ap.J. 253, 949.

Meyer, P., Evenson, P. 1978, IEEE Trans. GE16, 180.

Pallavicini, R., Serio, S. and Vaiana, G. 1977, Ap.J. 216, 108.

Ramaty, R., Kozlovsky, B. and Lingenfelter, R. 1975, Space Sci. Rev. 18, 341.

Simnet, G.M. 1974, Space Sci. Rev. 16, 257.

Vestrand, W., Forrest, D., Chupp, E., Rieger, E. and Share, G. 1984, Bull.of AAS. 16, 475.

N85-34750

SH 1.3-1

ONSET OF SOLAR FLARES AS PREDICTED BY TWO-DIMENSIONAL MHD-MODELS OF QUIESCENT PROMINENCES

J. GALINDO TREJO
Instituto de Geofísica,UNAM, 04510 - México, D. F., MEXICO

1. Introduction. It is well known the close connection between the sudden disappearance ("disparition brusque") of the quiescent prominences and the two-ribbon flares (see e.g. [6]). During this dynamic phase the prominence ascends rapidly (typically with a velocity about 100 Km/sec) and disappears. In another later stage is observed material falling back into the chromosphere. The impact of this downfalling matter on the chromosphere produces the H_α-brigthening, which shows the symmetric double pattern. The occurrence of the "disparition brusque" is thought to be a consequence of a plasma instability of magnetohydrostatic structures (see e.g. [11]). Two-dimensional MHD-models for quiescent prominences have been worked out since the fifties. They describe the prominence in magnetohydrostatic equilibrium under the action of Lorentz forces, gas pressure gradients and the gravitational force. However, the stability properties of most of these models are not yet determined. We analyze by means of the MHD-energy principle [2] the stability properties of four prominence models. We show that all considered models undergo instabilities for parameters outside of the observed range at quiescent prominences. We consider the possibility that such instabilities in the flare parameter range may indicate just the onset of a flare.

2. Equilibrium and Stability Theory. We define a coordinate system with x-axis along prominence, y-axis perpendicular to the prominence sheet and z-axis vertical (opposed direction of the gravity acceleration). We take into account only plasma structures, which are independent on x. In a two-dimensional theory the magnetic field can be expressed as:

$$\underset{\sim}{B} = \nabla A(Y,Z) \times \underset{\sim}{e}_x + B_x(Y,Z)\,\underset{\sim}{e}_x \qquad (1)$$

where A is the x-component of a vector potential. The equilibrium condition, which A must satisfy reads:

$$\Delta A = -4\pi \frac{\partial \Pi(A,\phi)}{\partial \phi} \quad , \quad \Pi(A,\phi) = P(A,\phi) + \frac{1}{8\pi} B_x^2(A) \qquad (2)$$

where P is the plasma pressure, the external gravitational field and $\rho = -\partial\Pi/\partial\phi = -\partial P/\partial\phi$ the mass density. Any two-dimensional prominence model corresponds to a particular choice of the functions $P(A,\phi)$, $B_x(A)$ and the boundary conditions. In order to analyze the stability properties of

ORIGINAL PAGE IS
OF POOR QUALITY

prominence models we use the MHD-energy principle of Bernstein et al. (1958), according to which the stability of an equilibrium configuration is determined by the behaviour of the potential energy functional $\delta W(\xi,\xi^*)$ resulting from a perturbation $\xi(\underline{r},t)$ to the system. For the two-dimensional equilibrium class the functional $\delta W(\xi,\xi^*)$ may be written in the form:

$$\delta W(\xi,\xi^*)=\frac{1}{2}\int\!\!\int\Big\{\frac{1}{4\pi}|\nabla_\perp a|^2-\frac{\partial^2\Pi}{\partial A^2}|a|^2+\frac{1}{4\pi}|\underline{B}_\perp\cdot\nabla_\perp\xi_x-B_x\nabla_\perp\cdot\underline{\xi}_\perp|^2+K^2\Big[\frac{1}{4\pi}|B_x\underline{\xi}_\perp-\xi_x\underline{B}_\perp|^2+$$
$$+\gamma P|\xi_x|^2\Big]+\frac{1}{4\pi}|\underline{B}_\perp\cdot\nabla_\perp\xi_x-B_x\nabla_\perp\cdot\underline{\xi}_\perp|^2+\gamma P|\nabla_\perp\cdot\underline{\xi}_\perp|^2-2\mathrm{Re}\Big[\rho(\nabla_\perp\cdot\underline{\xi}_\perp)\underline{\xi}_\perp^*\cdot\nabla_\perp\phi\Big]-\frac{\partial\rho}{\partial\phi}|\underline{\xi}_\perp\cdot\nabla_\perp\phi|^2+2k\,\mathrm{Im}\Big[\frac{1}{4\pi}\cdot$$
$$\cdot(\nabla_\perp a\times\underline{e}_x)\cdot(B_x\underline{\xi}_\perp^*-\xi_x^*\underline{B}_\perp)-\frac{\Delta A}{4\pi}\xi_x a^*-\gamma P\xi_x(\nabla_\perp\cdot\underline{\xi}_\perp^*)+\rho\xi_x(\underline{\xi}_\perp^*\cdot\nabla_\perp\phi)-\frac{B_x}{8\pi}\Delta A(\underline{\xi}_\perp\times\underline{\xi}_\perp^*)\cdot\underline{e}_x\Big]\Big\}\,d^3r \qquad (3)$$

where $\nabla_\perp=\underline{e}_y\frac{\partial}{\partial y}+\underline{e}_z\frac{\partial}{\partial z}$, $a=-\underline{\xi}_\perp\cdot\nabla_\perp A$, $\underline{B}_\perp=\nabla_\perp A\times\underline{e}_x$. We have supposed complex three-dimensional displacements of the following generalized form:

$$\underline{\xi}(\underline{r},t)=\underline{\xi}(\underline{r})e^{i\omega t}=\big[\xi_x(y,z)\underline{e}_x+\underline{\xi}_\perp(y,z)\big]\,e^{ikx+i\omega t} \qquad (4)$$

It is assumed periodic boundary conditions along the prominence axis (x-direction) and $\underline{\xi}=0$ on the edge of the plasma region in the y,z-plane. The x-integration in equation (3) is to be carry out over one period. If δW is positive for all displacements which satisfy the boundary conditions, then the equilibrium is stable. The MHD-energy principle is a necessary and sufficient criterion for stability. The stability problem reduces therefore to analize the sign of the minimum of δW. It is interesting to note that to the variational problem which implies the minimisation of δW, is associated the Euler-Lagrange equation:

$$-\rho\omega^2\underline{\xi}(\underline{r})=\underline{F}(\underline{\xi}(\underline{r})) \qquad (5)$$

where $\underline{F}$ is a self-adjoint differential operator with time independent coefficients (see e.g. [1]). We use the normalization constraint: $\frac{1}{2}\int\rho|\underline{\xi}|^2d^3r=1$ and obtain the spectrum of eigenvalues further one has $\omega^2_{min}=\mathrm{Min}\,\delta W(\xi,\xi^*)$.

3. Stability Results for Prominence Models. We have evaluated the energy principle for four prominence models: Menzel, (M), [10]; Dungey, (D), [3]; Kippenhahn and Schlüter, (KS), [7]; Lerche and Low, (LL), [9]. One obtains generally stability statements by two procedures: (a) analytically, by manipulating the energy functional δW to recognize a definite sign and so to infer about the stability properties, (b) numerically, by carring out the minimisation of δW with the aid of a computer code. Our analytical results concerning to these models are reported elsewhere [4]. We obtain global stability for the KS-model in case of arbitrary 3D-displacements [5]; for the other models the stability statements are restrictive to special

classes of displacements (2D, long wavelengths, etc.). In order to obtain more general results concerning to broader class of displacements we have developed a numerical code based on the finite element-method. This procedure provides, besides qualitative stability statements, the largest growth rate in case of instability and the frequency of the fundamental oscillations of stable systems. Our code was tested successfully by applying it to simple systems, whose dynamic properties are well known (e.g. Alfvén waves, current sheets and sound waves in a constant gravitational field). We obtain numerically a stable behaviour for the four models in the parameter range of the observations of typical quiescent prominences ($T=7.10^3\,{}^\circ K$, $n_e=5.10^{10} cm^{-3}$, $B=5G$, thickeness $Y=5.10^3$ Km, height $Z=1.5-5.10^4$ Km). All models describe horizontal large-scale oscillations with periods between 16 and 80 min (see Table 1). Reported data indicate that quiescent prominences undergo actually horizontal oscillations from and towards the perturbation, which is originated in solar flares. The observed periods range from 6 to 80 min. [2], [8], [1].

Table 1. Periods of horizontal oscillations in quiescent prominences.

Model	Period (min)
M	40
D	55-80
KS	16
LL	17-50

Unstable behaviour is found only out of the observed parameter range. When one considers typical parameters of flares (e.g. $T\sim 10^7\,{}^\circ K$, $n_e \sim 10^{11} cm^{-3}$, $B \sim 50$ G) one obtains $\beta = \frac{8\pi n_e kT}{B^2} \gtrsim 1$. Just for these parameters we get instability only in case of LL model. The other models continue stable around these parameters. Figure 1 shows function of $\alpha = \beta/2$ (we use dimensionless variables, so that ω^2_{min} is normalized by g/h, where $g=2.74 x 10^4 cm/sec^2$, $h=kT/mg$ is the density scale height and m is the proton mass). We have separated the different physical effects (electromagnetic, compressional and gravitational parts) in the energy functional $\delta W(\xi_{min}, \xi^*_{min})$, so that it is possible to infer about the nature of the instability. For the situation illustrated on Fig. 1 we find that the instability is driven mainly by electromagnetic forces. Gravitation provides also an instabilizing effect. In opposition to this, the compression has continually a stabilizing effect. Such a gravitational-electromagnetic mixed instability has a typical growth rate $\Gamma = \sqrt{g/h}\,|\omega_{min}|/2\pi \sim 4.77 \cdot 10^{-5} sec^{-1}$, i. e. a growth time $\tau \sim 5.8$ h. On the other hand, the impulsive phase of a flare elapses within few minutes, so that the found

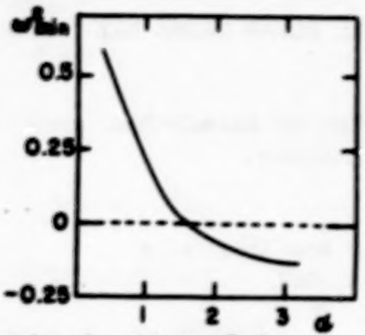

Fig.1. LL-Model: minimum eigenvalue ω^2_{min} as function of $\alpha=\beta/2$.

growth time may explain rather the evolution of the flare ribbons and the associated loop system which last several hours. The cause of the parameter shift in the quiescent prominence may reside in an external perturbation in form of a shock wave generated by a distant flare or in an internal perturbation in form of a newly emerging flux in the same active region. Our results can be considered as preliminaries because the studied two-dimensional models are still very simple to describe the complexity of quiescent prominences. However, further applications of our stability method to more realistic models give the possibility of a better description of the impulsive phase of solar flares.

References.

[1] Bashkirtsev et al.: 1983, Solar Phys., 82, 443.

[2] Bernstein, I. B. et al.: 1958, Proc. Roy. Soc., A244,17.

[3] Dungey, J. H.: 1953, MNRAS, 113, 180.

[4] Galindo Trejo, J.: 1985, to be published.

[5] Galindo Trejo, J. and Schindler, K.: 1984, Astrophys. J., 277, 422.

[6] Hyder, C.: 1967, Solar Phys., 2, 49.

[7] Kippenhahn, R. and Schlüter, A.: 1957, Z. f. Astrophys., 43, 36.

[8] Kleczek, J. and Kuperus, M.: 1969, Solar Phys., 6, 72.

[9] Lerche, I. and Low, B. C.: 1980, Solar Phys., 67, 229.

[10] Menzel, D. H.: 1951, Proc. Conf. on Dynamics of Ionised Media, London.

[11] Priest, E. R.: 1983, Solar Phys., 86, 33

[12] Ramsey, H. E. and Smith, S. F.: 1966, Astron. J., 71, 197.

N85-34751

SH 1.3-2

THE STARTING CONDITIONS FOR AN OPTICALLY SMALL SOLAR GAMMA RAY FLARE

G. M. Simnett
Department of Space Research, University of Birmingham
Birmingham B152TT, United Kingdom

J. M. Ryan
Space Science Center, University of New Hampshire
Durham, New Hampshire 03824 USA

ABSTRACT

We suggest that optically small γ-ray flares result from gradual pre-flare acceleration of protons over $\sim 10^3$s by a series of MHD shocks in the low corona. A fraction of the accelerated protons are trapped in the corona where they form a seed population for future acceleration. If the shock acceleration is sufficiently rapid proton energies may exceed the γ-ray production threshold and trigger γ-ray emission. This occurs without the total flare energy being necessarily large. Magnetic field geometry is an important parameter.

1. Introduction

Now that the statistics of γ-ray flares have improved to the point where meaningful comparisons can be made with other flare data it has become clear that not only the large, spectacular Hα flares are associated with prompt nuclear line emissions (e.g., ^{12}C and ^{16}O). Such flares require the presence of protons $>$ 10 MeV and generally exhibit the p(n,γ)d neutron capture line requiring protons $\gtrsim$ 30 MeV. Results from SMM [1] have shown that a significant portion of the γ-ray events have onset times of γ-rays and hard X-rays ($>$ 28 keV) coincident to within $\sim$ 1 s with the total hard X-ray integrated flux well correlated with that of the γ-rays [2]. A process for producing hard x-rays from γ-ray producing protons is discussed in another paper [3]. Our model for such flares must be capable of producing such quasi-simultaneity, and it should also be capable of delaying γ-ray production without having to resort to a separate model. In extreme cases there is evidence of proton (ion) acceleration up to 1 GeV within a few s of the hard X-ray onset [4].

If we concentrate on the more common case where protons only up to 30 MeV are required, this still represents a significant energy gain if the protons start with a thermal distribution at $\sim 10^7$K (1 keV). Although mechanisms have been examined theoretically to achieve such rapid accelerations [5], the necessary physical conditions for the required acceleration efficiency are very severe and appear to be improbable at the Sun. We suggest that such rapid acceleration is not necessary, and that γ-ray emission represents the end product of a much more gradual ($\sim 10^3$ s) acceleration process.

2. The Acceleration of Protons

There are few observational constraints on proton acceleration up to $\sim$ 1 MeV, somewhat below the γ-ray production threshold. However, we know from range/energy considerations that the acceleration cannot take place at high densities, thus restricting the acceleration site to the high corona. For example, at a density of 2×10^9 cm^{-3}, which is representative of the base of the corona [6], a 100 keV proton has a range of only 4×10^9 cm, which it would cover in ∿ 8 s. Therefore not only would any acceleration process at these densities result in excessive heating - most of the available energy would be dissipated as heat - but protons which did manage to get accelerated to 100 keV would have a short lifetime. However, a 400 keV proton has a range of 10^{12} cm at a density of 10^8 cm^{-3}, and therefore a lifetime ∿ 10[illegible] s. From these considerations we suggest that any proton acceleration region should be at a density at least as low as 3×10^8 cm^{-3} corresponding to an altitude of ∿ 10^5 km. We believe the most plausible mechanism for proton acceleration is coronal shock acceleration. The basic theory of particle acceleration in shocks has been given by Bell [7] and most subsequent work has developed from his suggestions.

Fig. 1 outlines the scenario that appears most appropriate for the development of γ-ray flares. The magnetic field configuration is likely to be complex, with a series of small scale loops (shown left inset), plus some overlying magnetic structure with an overall size ∿ 10^5 km. We suggest that evolution of the lower lying loop structure, possibly caused by emerging flux, causes small energy releases, heating and a succession of small shocks. A fraction of the protons accelerated in these shocks are trapped in the overlying field and are available for further acceleration as seed particles in subsequent shocks . The acceleration we believe requires and is enchanced through the development of resonant turbulence, illustrated schematically in the center inset of Fig. 1. Throughout the whole process there is feedback between the accelerated particles, the MHD waves and shocks. This drives the energy release process harder. The latter is probably due to induced additional magnetic field reconnection. In the γ-ray

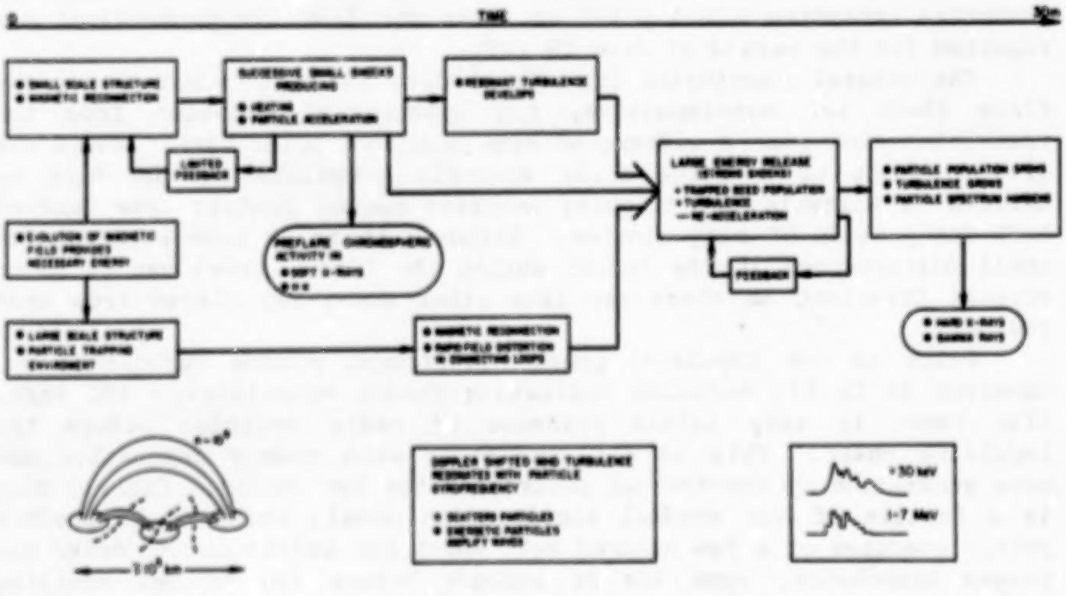
0
TIME
30m
SMALL SCALE STRUCTURE
MAGNETIC RECONNECTION
SUCCESSIVE SMALL SHOCKS PRODUCING
HEATING
PARTICLE ACCELERATION
RESONANT TURBULENCE DEVELOPS
LIMITED FEEDBACK
LARGE ENERGY RELEASE (STRONG SHOCKS)
TRAPPED SEED POPULATION
TURBULENCE
RE-ACCELERATION
PARTICLE POPULATION GROWS
TURBULENCE GROWS
PARTICLE SPECTRUM HARDENS
EVOLUTION OF MAGNETIC FIELD PROVIDES NECESSARY ENERGY
PREFLARE CHROMOSPHERIC ACTIVITY IN
SOFT X-RAYS
FEEDBACK
LARGE SCALE STRUCTURE
PARTICLE TRAPPING ENVIRONMENT
MAGNETIC RECONNECTION
RAPID FIELD DISTORTION IN CONNECTING LOOPS
HARD X-RAYS
GAMMA RAYS
DOPPLER SHIFTED MHD TURBULENCE RESONATES WITH PARTICLE GYROFREQUENCY
SCATTERS PARTICLES
ENERGETIC PARTICLES AMPLIFY WAVES
>30 MeV
1-7 MeV

Figure 1. Schematic of pre-flare and flare particle acceleration and activity.

flare the build up of the proton population is eventually sufficient for a significant precipitation of protons near or below the transition zone, producing the signature of a γ-ray flare. This is illustrated schematically in the right inset of Fig. 1. The whole process takes ∿ 10^3 s. This is consistent with the coronal acceleration model discussed by Lee and Ryan [8].

There are some observable consequences of the scenario we have outlined. First, some of the more energetic protons from the early accelerations will not be stably trapped but will impact the top of the chromosphere, causing heating but little else. This heating should be visible prior to the flare as small soft X-ray and EUV brightenings from the appropriate impact points along the base of the loops indicated in the left inset (Fig. 1). Second, the protons that are stably trapped will, in fact, continue to lose energy to the coronal gas, thereby heating it. It has recently been suggested [9] that such heating may destablize a coronal mass ejection, thus opening the magnetic field and releasing the trapped protons. This would also drive the energy release harder, causing a flare but probably not a γ-ray flare because the particle trapping environment has been lost.

3. Supporting Observations

The model is well supported by observations of the M4 γ-ray flare near the solar limb on 1980 June 29, 10:41 UT. Fig. 2 shows the intensity-time profile of 3.5-8.0 keV X-ray, emission from 10:20-10:45 UT. The onset of the impulsive phase we take to be 10:40:10UT. It is obvious from the soft X-ray observations that there was considerable pre-flare activity for some 20 m before the impulsive phase. The OV transition region UV line intensity exhibits the same general behavior while hard X-rays and γ-rays are undetectable until after 1041 and peaking at about 1042. Spatially resolved data show that there were a number of resolved bright points in OV over a region of the limb covering a projected distance of > 10^5 km. A large X-ray emitting structure extending ∿ 1.5 x 10^5 km above the limb (in projection) was reported for the period of June 29 [10].

The general conclusion from these data is that before the γ-ray flare there was non-impulsive, but substantial emission from the transition zone over a widespread area near the solar limb. There was also evidence of a large scale magnetic structure of the type we believe is suitable for trapping moderate energy protons (few hundred keV) for periods of many minutes. Although there is some evidence for small disturbances in the corona during the flare, there was no major coronal transient as there was from other non-γ-ray flares from this region.

Prior to the impulsive phase significant plasma turbulence was observed in Ca XIX emission indicating random velocities > 150 km/s. Also there is very little evidence of radio emission before the impulsive phase. This is all consistent with energy deposition and wave generation by non-thermal protons in the low corona. Clearly this is a feature of our gradual acceleration model, which would predict proton energies of a few hundred keV, which are sufficient to drive the plasma turbulence, some 10s of seconds before the 10 MeV energies required for the γ-rays.

ORIGINAL PAGE IS
OF POOR QUALITY

4. Conclusions

We believe that the mechanism resulting in γ-ray emission from an otherwise optically small flare is the slow build-up of particle energy over a time scale of 10^3 s before the impulsive phase. The magnetic field configuration is very important and requires the presence of stable magnetic structures in the corona reaching to altitudes in excess of 10^5 km. Such magnetic structures are used to trap accelerated particles. During the pre-flare period energy is transferred to non-thermal protons by a series of small MHD shocks, gradually reaccelerating the surviving protons. A signature of this acceleration is the excitation of weak EUV and soft X-ray emission where some of the accelerated protons impact the chromosphere.

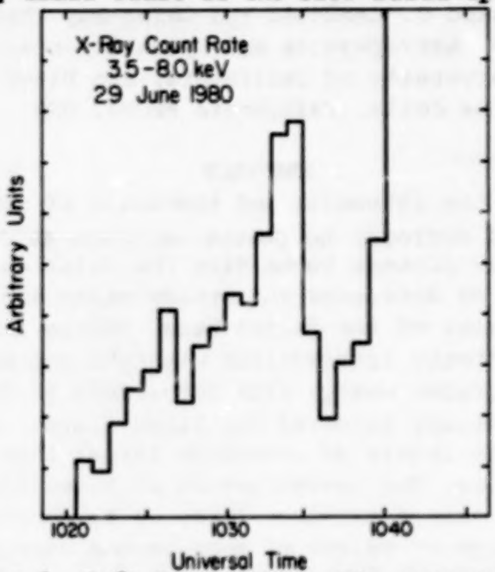

Figure 2. Soft X-ray count rate measured by HXIS on SMM. The impulsive phase is well off scale.

5. Acknowledgements We are grateful to Drs. D.J. Forrest, B.R. Dennis, J. Lemon and R.A. Shine for SMM data.

6. References

1. Forrest, D.J. and Chupp, E.L., 1983, Nature, 305, 5932, 291.
2. Forrest, D.J., 1983, AIP Conf. Proc. No. 101 (Ed. M.L. Burns et al.) 3.
3. Simnett, G.M., 1985, Proc. Intl. Cosmic Ray Conf. (LaJolla), SH 1.2-13.
4. Chupp, E.L., et al., 1982, Ap. J., 263, L95.
5. Achterberg, A., and Norman, C.A., 1980, Astron. & Astrophys. 89, 359.
6. Vernazza, J.E, et al., 1981, Ap. J. Suppl., 45, 635.
7. Bell, A.R., 1978, MNRAS 182, 147 and 443.
8. Lee, M.A. and Ryan, J.M., 1985, submitted to Astrophy. J.
9. Simnett, G.M. and Harrison, R.A. 1985, Adv. Sp. Res., 4, 7, 279.
10. Harrison, R.A., et al., 1984 Proc. STIP Symp. on Sol. Interplanet. Intervals (Eds., M.A. Shea, D.F. Smart and S.M.P. McKenna-Lawlor) 287.

N85-34752

ON THE DETECTABILITY OF KEV-MEV SOLAR PROTONS THROUGH THEIR NONTHERMAL LYMAN-ALPHA EMISSION

Richard C. Canfield and Ching-Ray Chang
Center for Astrophysics and Space Sciences, C-011
University of California, San Diego
La Jolla, California 92093, USA

ABSTRACT

We investigate the intensity and timescale of nonthermal Doppler-shifted hydrogen Lα photon emission as diagnostics of 10 keV-10 MeV protons bombarding the solar chromosphere during flares. We determine the steady-state excitation and ionization balance of the proton beam, taking into account all important atomic interactions with the ambient chromosphere. For a proton energy flux comparable to the electron energy flux commonly inferred for large flares, we find Lα wing intensities orders of magnitude larger than observed nonflaring values. Our investigation of timescales for ionization and charge exchange leads us to conclude that over a wide range of values of mean proton energy and beam parameters, Doppler-shifted nonthermal Lα emission is a useful observational diagnostic of the presence of 10 keV-10 MeV superthermal proton beams in the solar flare chromosphere.

1. Introduction. Gamma-ray and hard X-ray observations of solar flares imply that, at energies $\gtrsim$ 10 MeV, the number of of energetic protons exceeds that of energetic electrons by several orders of magnitude [6]. This is currently understood [4] to be the consequence of an acceleration mechanism (e.g., a stochastic Fermi mechanism) in which the acceleration rate is proportional to momentum, acceleration takes place in a tenuous medium (the corona), and the emission is produced when the energetic particles are stopped fully in a thick target (the chromosphere and photosphere). However, this mechanism operates effectively only if some particles are already accelerated above a threshold energy by some other mechanism. Orrall and Zirker [5] have shown that charge-exchange Lα emission may be useful for the detection of relatively low energy ($E < 1$ MeV) superthermal protons, which do not produce a significant level of nuclear emission. In this paper we extend the work of Orrall and Zirker to energetically significant values of beam flux, and address the question of the range of values of beam flux for which the intensity and timescale of Lα charge-exchange emission may fall into observationally relevant ranges.

2. Atomic Physics. To simplify our study of the emission of Lα by superthermal protons we represent the protons injected into the chromosphere by a vertical beam directed away from the observer. Some superthermal protons become superthermal hydrogen atoms in excited states, and subsequently radiate before they stop. Potentially relevant atomic processes that we have examined include charge exchange between beam protons and ambient hydrogen atoms, excitation of beam hydrogen atoms by collisions with ambient electrons, hydrogen atoms and protons, spontaneous radiative de-excitation of beam hydrogen atoms, stimulated radiative de-excitation of beam hydrogen atoms, collisional ionization of beam hydrogen atoms by ambient electrons, protons and hydrogen atoms, and spontaneous radiative recombination of beam hydrogen atoms.

We have examined the relative importance of these various competing atomic processes, with the following conclusions. The dominant destruction process for superthermal beam protons is charge exchange with ambient chromospheric hydrogen atoms. Ionizing collisions of superthermal hydrogen atoms with ambient electrons, protons, and neutral hydrogen atoms are of comparable importance in creating superthermal protons. The main source of Lα emission is charge exchange from the proton beam. The dominant slowing process is Coulomb collisions with ambient electrons [7].

3. Computed Lα Spectra. Our chosen value of the hydrogen ionized fraction in our uniform chromospheric model atmosphere is guided by Orrall and Zirker, who used a detailed empirical model [8] to show that 10-1000 keV proton nonthermal Lα emission originates in the chromosphere. Our assumed 10% ionized fraction is an appropriate mean value. We have adopted a simple monoenergetic proton beam at input. The values of the input energy E_0 and the total input energy flux $F_E(0)$ are free parameters.

In Figure 1 we show the computed nonthermal Lα spectrum generated by monoenergetic proton beams of input energy flux $F_E(0) = 10^{11}$ erg cm^{-2} s^{-1} (an upper limit to plausible values), for values of E_0 ranging from 3 keV to 30 MeV. If we examine a single curve, say for $E_0 = 30$ keV, we see a sharp

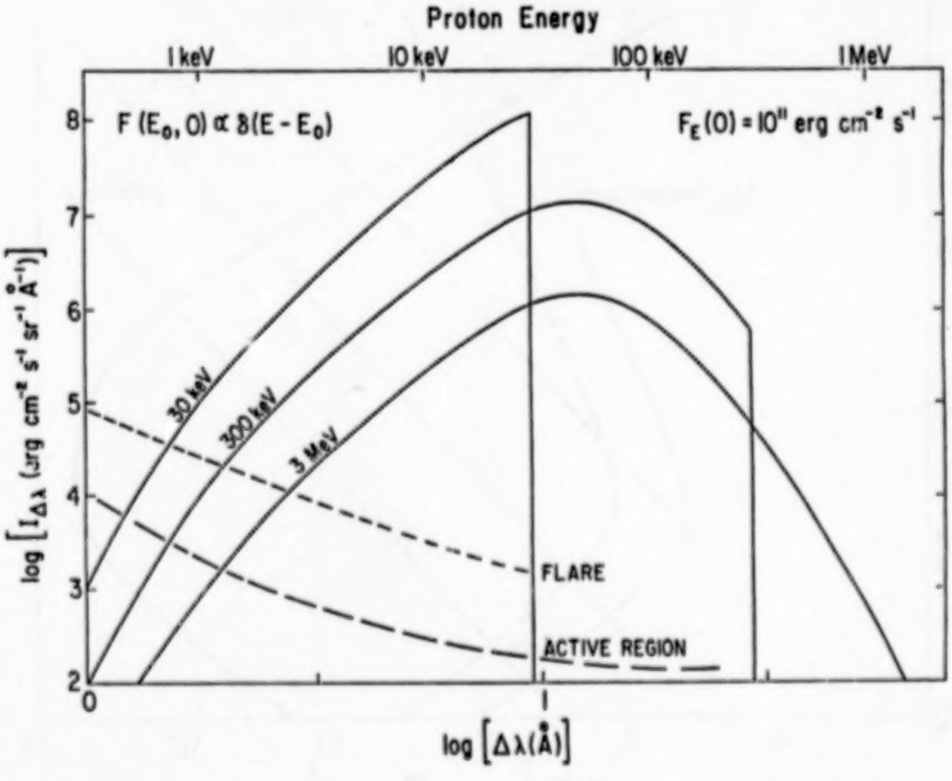

Fig. 1. - Theoretical nonthermal Lα spectra for protons of initial energy E_0.

peak in the spectrum at the wavelength shift $\Delta\lambda$ appropriate to the velocity of protons of initial energy E_0, corresponding to emission from near the top of the chromosphere. At lesser values of $\Delta\lambda$ the emission comes from slower protons that have penetrated some distance z into the target, where their velocity (and hence Doppler-shift) has dropped. If we consider the spectra in Figure 1 for E_0 = 300 keV and 3 MeV, we see that the curves peak somewhat below E = 100 keV (somewhat above $\Delta\lambda$ = 10 Å). This peak Lα intensity corresponds to the peak in the charge-exchange cross-section in this same energy range. It is interesting to compare the computed spectra to an observed solar active region Lα spectrum [3] and an observed (presumably thermal) solar flare Lα spectrum [2]. Throughout much of the energy range considered in Figure 1 the intensity of the computed nonthermal Lα emission exceeds the observed active region emission by several orders of magnitude.

4. Timescales. Our equilibrium computations of Lα emission will not be applicable unless the ionization structure of the chromosphere remains substantially unchanged within the time required for charge exchange. If the chromosphere becomes highly ionized within the collisional range of the protons, little charge exchange between superthermal protons and ambient hydrogen atoms can take place. Because recombination is several of orders of magnitude less efficient than charge exchange, per ambient particle, much less nonthermal Lα emission will be created if the atmosphere becomes ionized.

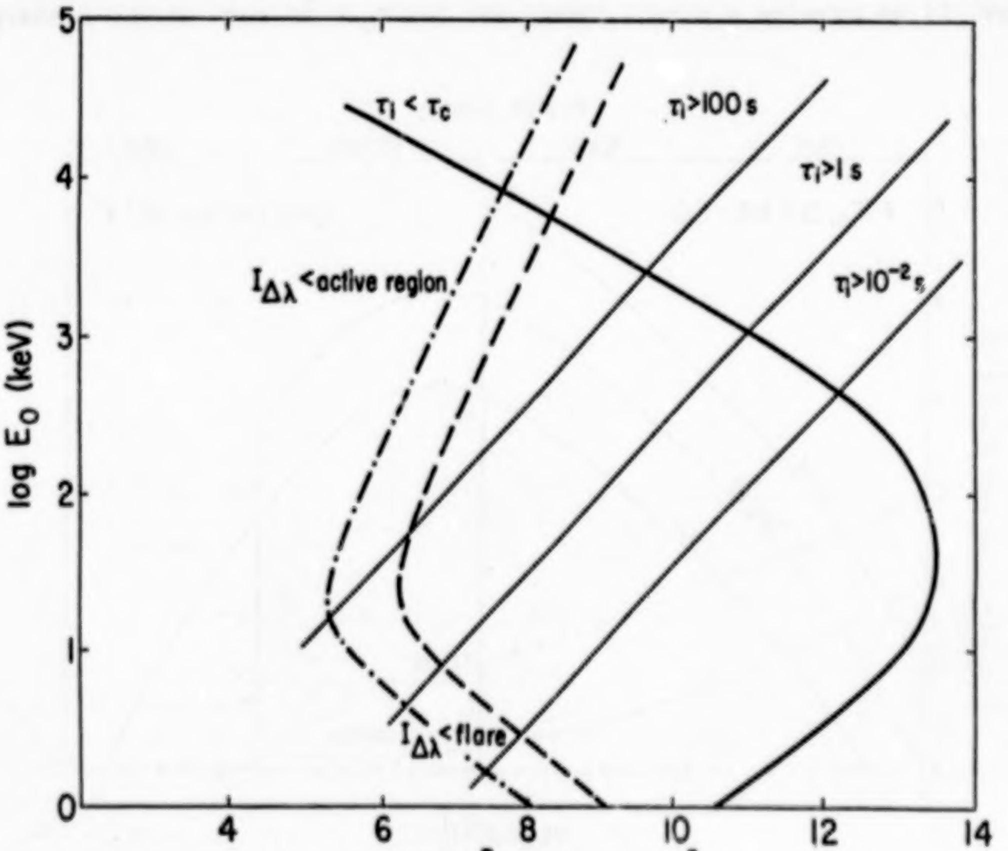

Fig. 2. - The range of relevance of the equilibrium Lα spectra in Figure 1.

The range of relevance of the Lα spectra of Figure 1 is explored in Figure 2. The thick solid curve is that for which the ionization timescale τ_i equals the charge exchange timescale τ_c. The thin lines indicate various values of τ_i. On the long-dashed curve the peak intensity of nonthermal Lα emission equals that of observed flare Lα-wing emission. On the dot-dashed curve the peak computed intensity of nonthermal Lα emission matches that of observed active-region Lα-wing emission. We see that at an energy of interest (say 100 keV), the intensity of nonthermal Lα emission exceeds the observed active-region background for all $F_E(0)$ values above about 10^6 erg cm^{-2} s^{-1}, and the charge-exchange mechanism is effective up to around $F_E(0)$ - 10^{13} erg cm^{-2} s^{-1}. Over this range of $F_E(0)$ values the ionization time ranges from about 1000 s to very small values. Obviously at the lowest detectable intensities the equilibrium calculation given above is physically relevant throughout the duration of typical flares; at the high end of the $F_E(0)$ range, the duration of validity becomes inconsequentially small. Figure 2 also serves to show that at input proton energies above about 10 MeV and below about 1 keV the equilibrium calculation is not both physically and observationally relevant at any value of the total energy flux.

5. *Conclusions*. We conclude that if the sun's chromosphere is bombarded suddenly from above by superthermal protons of energy 10 keV - 1 MeV, with energy fluxes consistent with the hypothesis that such protons are a significant component of the population of superthermal particles in flares, charge exchange would lead to an intense but brief burst of Doppler-shifted Lα emission. At much lower proton flux levels the emission would still exceed preflare background, but last much longer. In other work [1] we consider power-law and thermal forms of the input proton energy spectrum, the generation of emission in the hydrogen Hα line, and the details of the atomic physics.

6. *Acknowledgements*. We thank Edward Shoub, William Thompson, and Jack Zirker for stimulating discussions. This research has been supported by NASA grant NSG-7406 and National Science Foundation grant AST 83-20306.

References
1. Canfield, R. C., and Chang, C.-R. 1985, *Astrophys*. *J*., 295, in press.
2. Canfield, R. C., and VanHoosier, M. E. 1980, *Solar Phys*., 67, 339.
3. Cohen, L. 1981, *An Atlas of the Solar Spectrum Between 1175 and 1950 Angstroms Recorded on Skylab with NRL's Apollo Telescope Mount Experiment*, NASA Reference Publication 1069 (Washington: U. S. Government Printing Office).
4. Heyvaerts, J. 1981, in *Solar Flare Magnetohydrodynamics*, ed. E. R. Priest (New York: Gordon and Breach Publ.).
5. Orrall, F. Q., and Zirker, J. B. 1976, *Astrophys*. *J*., 208, 618.
6. Ramaty, R. et al. 1980, in *Solar Flares*, ed. P. A. Sturrock (Boulder: University of Colorado Press), p. 117.
7. Trubnikov, B. A. 1965, *Reviews of Plasma Physics*, Consultants Bureau, New York, 1, 105.
8. Vernazza, J. E., Avrett, E. H., and Loeser, R. 1981, *Ap*. *J*. *Suppl*. *Ser*., 45, 619.

N85-34753

OBSERVATIONS OF SOLAR FLARE GAMMA-RAYS AND PROTONS

M. YOSHIMORI and H. WATANABE
Department of Physics, Rikkyo University,
Toshima-ku, Tokyo 171, JAPAN.

ABSTRACT

Solar flare gamma-rays (4 - 7 MeV) and protons (8 - 500 MeV) were simultaneously observed from six flares on 1 Apr., 4 Apr., 27 Apr. 13 May 1981, 1 Feb. and 6 June, 1982 by the Hinotori and GMS satellites. The relationship between 4 - 7 MeV gamma-ray fluences and peak 16 - 34 MeV proton fluxes for these flares are analyzed. It does not reveal an apparent correlation between these two parameters. The present result implies that the protons producing gamma-rays and the protons observed near the Earth do not always belong to the same population.

1. Introduction

The particle acceleration mechanism in solar flares has been studied through observations of radiowaves, X-rays, gamma-rays, neutrons and flare particles. The energetic photon observations provide a clue on the particle acceleration through interaction processes in the flare region. On the other hand, the particle observations provide the clue through propagation effects in the corona and interplanetary space. Hence, we need simultaneous observations of the photons and the particles to understand deeply the particle acceleration mechanism and the photon emission processes in solar flares. To study the acceleration of nuclei, it is important to investigate the relationship between the particles producing gamma-ray lines and the particles observed near the Earth. This investigation provide diagnostics for the following question: Are these two kinds of accelerated particles the same population ? In addition, it provides the clue on the interaction model (thin-target or thick-target interaction model), together with observations of fragments such as deuterons, tritons and He-3 nuclei.

The gamma-ray observations were successfully performed during the solar maximum period from 1981 Feb. to 1982 June by the Hinotori satellite (Yoshimori et al., 1983). The Hinotori satellite observed 8 gamma-ray line flares during the above period. On the other hand, the GMS (Geostationary Meteorological Satellite) observed 23 solar proton events during the same period. Several observations of solar particles associated with gamma-ray line flares have been reported so far by the ISEE-3 (Pesses et al., 1981) and the IMP-8 (McGuire et al., 1981) satellites. These observations indicated that the solar proton fluxes were not always correlated with the gamma-ray line fluxes. Furthermore, Cliver et al.(1983) showed a lack of correlation between the peak 10 MeV proton fluxes and the 4 - 8 MeV gamma-ray excesses for western hemisphere flares.

In this paper, we analyze the relationship between flare-associated gamma-ray lines and interplanetary proton events observed from Apr., 1981 to June, 1982. The gamma-ray data are from the gamma-ray spectrometer on board the Hinotori satellite. The proton data are from the solid state Si detector on board the GMS.

2. Gamma-Ray and Proton Observations

The flares in which gamma-rays and protons were simultaneously observed are listed in Table 1. The flare date, maximum time, location, Hα importance and GOES X-ray class are presented there. The detailed characteristics of these flares were described by Yoshimori (1984).

The time histories of gamma-ray count rate in the 4.0 - 6.7 MeV band were observed for the 1 Apr., 4 Apr., 27 Apr., 13 May, 1981, 1 Feb. and 6 June, 1982 flares. The 4.0 - 6.7 MeV gamma-rays are mostly dominated by prompt nuclear deexcitation lines of C-12 at 4.44 MeV and of O-16 at 6.13 MeV (Yoshimori, 1984). A few additional gamma-ray lines were reported for these flares. Of these flares the Feb. 1, 1982 flare did not reveal an apparent gamma-ray emission. The corresponding time histories of proton fluxes in the 8 - 500 MeV bands were observed.

The 1 Apr., 1981 flare showed the gradual time history with a long duration of 26 min. The 4.0 - 6.7 MeV gamma-ray fluence and the peak 16 - 34 MeV proton flux were (20 ± 4) photons / cm^2 and (2.5 ± 0.3) protons / cm^2 s sr, respectively. This flare is considered to be magnetically well-connected to the Earth; this flare occurred within the so-called preferred connection helio-longitude range. Protons with high energies of 200 - 500 MeV also were observed (Yoshimori, 1985). These 200 - 500 MeV protons revealed a fast rise and fall time history.

The 4 Apr., 1981 flare showed the impulsive time history with a short duration of 80 s. The 4.0 - 6.7 MeV gamma-ray fluence and the peak 16 - 34 MeV proton flux were (25 ± 5) photons / cm^2 and (3.4 ± 0.4) protons / cm^2 s sr, respectively. This flare is also considered to be magnetically well-connected to the Earth.

The 27 Apr., 1981 flare showed the gradual time history with long duration of 25 min, but the Hinotori satellite was eclipsed by the Earth at 0815 UT. This flare revealed the intensive gamma-ray line emission (Chupp, 1982, 1983; Yoshimori et al. 1983). However, this flare did not reveal the apparent proton increase in the 8 - 500 MeV band, in spite of the magnetically well-connected flare. Further, three large proton events which occurred in the same sunspot were reported on 24, 26 and 28 Apr., 1981. These results may imply that protons accelerated in the 27 Apr. flare could not escape into interplanetary space. The 4.0 - 6.7 MeV gamma-ray fluence is (30 ± 5) photons / cm^2, and the upper limit of the peak 16 - 34 MeV proton flux is 3 protons / cm^2 s sr.

The 13 May, 1981 flare showed the gradual time history with long duration of 18 min. This flare revealed a small increase of gamma-ray emission, but did not reveal the increase of proton flux. The absence of the apparent increase of proton flux may be due to the bad propagation condition in interplanetary space; this flare did not occur within the preferred connection helio-longitude range. The 4.0 - 6.7 MeV gamma-ray fluence is (50 ± 9) photons / cm^2 , and the upper limit of the peak 16 - 34 MeV proton flux is 2 protons / cm^2 s sr.

The 6 June, 1982 flare showed the impulsive and multi-peak time history with duration of 6 min. The proton flux revealed the very gradual increase and the peak reached on 9 June. In addition, protons with energies above 68 MeV were not observed with statistical significance. It implies that protons could not be accelerated to energies above 70 MeV during the flare. The 4.0 - 6.7 MeV gamma-ray fluence and the peak 16 - 34 MeV proton flux are (35 ± 6) photons /cm^2 and (6.0 ± 0.7) protons / cm^2 s sr, respectively.

An unusual event was the 1 Feb., 1982 flare, in which intensive proton flux was observed, but gamma-ray line emission was not significant. The 16 - 34 MeV peak proton flux is (80 ± 9) protons / cm^2 s sr, and the upper limit of 4.0 - 6.7 MeV gamma-ray fluence is 13 photons / cm^2 . This flare shows an opposite trend to the 27 Apr., 1981 flare, although this flare is also considered to be magnetically well-connected to the Earth.

3. Discussion

As shown in the previous section, the Hinotori and GMS data do not always reveal the apparent correlation between the gamma-ray line fluences and the peak 16 - 34 MeV proton fluxes. The scatter diagram of the 4.0 - 6.7 MeV fluence versus the peak 16 - 34 MeV proton fluxes is shown in Fig. 1 to see the correlation between these two parameters. The most of the 4.0 - 6.7 MeV gamma-rays consist of the C-12 line at 4.44 MeV and of the O-16 line at 6.13 MeV. The 16 - 34 MeV protons should contribute greatly to the production of these prompt gamma-ray lines. As shown in Fig. 1, there is no compelling evidence for the correlation for both eastern and western hemisphere flares. It is easily understood that there is not good correlation for the eastern hemispher flares of 13 May, 1981 and 6 June, 1982. It is because the bad propagation condition in interplanetary space. Furthermore, the correlation is neither always found for the western hemisphere flares, which occurred within the preferred connection helio-longitude range. The present result is consistent with the Cliver et al's result (1983). These results seem to suggest that the protons producing the gamma-ray lines in the flare site and the protons observed near the Earth do not always belong to the same population.

Two gamma-ray line production models (thick- and thin target interaction models) have been proposed (Ramaty et al., 1975). If the gamma-ray lines are produced from the thin-target interaction, the gamma-ray line fluence should be nearly proportional to the 16 - 34 MeV proton flux. On the other hand, the thick-target model should predict that there is not always apparent correlation, because the gamma-ray lines are produced by the accelerated nuclei streaming down to the denser chromosphere and photosphere. The thick-target model is also supported from the absence of spallation products such as deuterons, tritons and He-3 nuclei (McGuire et al., 1977; Mewaldt et al., 1983). In the thick-target model, the spallation products that accompany the production of gamma-ray lines, are slowed down in the denser solar atmosphere and hence are not expected to be observed in interplanetary space.

The scattering diagram suggests that the directivity of accelerated nuclei in the flare site varies from flare to flare. The directivity may depend on the configuration of magnetic field of the flare region. If the directivity is isotropic, both gamma-ray lines and accelerated nuclei should be observed. However, if most of the accelerated nuclei stream down to the chromosphere, only gamma-ray lines will be observed. For example, the 27 Apr., 1981 flare showed the significant gamma-ray line fluences, but did not show the apparent solar proton flux. No increase of solar protons associated with this flare was interpreted in terms of some particle confinement mechanism (Sakurai, 1983). This confinement mechanism asserts that most of accelerated nuclei were trapped for long time in the acceleration region and were little released into interplanetary space. On the contrary, if most of the accelerated nuclei move upward, only solar particles will be observed. For example, the 1 Feb., 1982 flare showed the appreciable solar proton flux, but did not show gamma-ray line emission. Another similar result was reported from the 9 Dec., 1981 flare (Cliver et al., 1983). These two flare data may indicate that the upward moving protons are so dominant that gamma-ray lines are not observed. Much more data of solar gamma-rays and protons are needed to establish the detailed relation between the gamma-ray line fluences and the peak solar proton fluxes.

The authors wish to acknowledge the Meteorological Satellite Center for providing the solar proton data. The authors thank Dr. T. Kohno for his analysis of solar proton fluxes.

References

Chupp,E.L.: 1982, Gamma-Ray Transients and Related Astrophysical Phenomena, ed. R.E.Lingenfelter, H.S.Hudson and M.M.Worrall (American Institute of Physics, New York, 1982) p.363.

Chupp,E.L.: 1983, Solar Phys. 86, 383.

Cliver,E.W., Forrest,D.J., McGuire, R.E., and von Rosenvinge,T.T.: 1983, 18th Int. Cosmic Ray Conf., Bangalore, 4, 84.

McGuire,R.E., von Rosenvinge,T.T., and McDonald,F.B.: 1977, 15th Int. Cosmic Ray Conf., Plovdiv, 5, 54.

MuGuire,R.E., von Rosenvinge,T.T., and McDonald,F.B.: 1981, 17th Int. Cosmic Ray Conf., Paris, 3, 65.

Mewaldt,R.A., and Stone,E.C: 1983, 18th Int. Cosmic Ray Conf., Bangalore, 4, 52.

Pesses,M.E., Klecker,B., Gloeckler,G., and Hovestadt: 1981, 17th Int. Cosmic Ray Conf., Paris, 3, 36.

Ramaty,R., Kozlovsky,B., and Lingenfelter,R.E.: 1975, Space Sci. Rev. 18, 341.

Sakurai,K.: 1983, 18th Int. Cosmic Ray Conf., Bangalore, 4, 93.

Yoshimori,M., Okudaira,K., Hirasima,Y., and Kondo,I.: 1983, Solar Phys. 86, 375.

Yoshimori,M.: 1984, J. Phys. Soc. Jpn. 53, 4499.

Yoshimori,M.: 1985, J. Phys. Soc. Jpn. 54, 1285.

Table 1

No.	Date	Maximum Time (UT)	Location	Hα/ GOES
1.	1 Apr., 1981	0154	S43 W52	2B/X2.3
2.	4 Apr., 1981	0502	S44 W85	3B/X1.9
3.	27 Apr., 1981	0813	N15 W90	--/X5.5
4.	13 May, 1981	0418	N11 E58	3B/X1.5
5.	1 Feb., 1982	1402	S14 W09	3B/X2.6
6.	6 June, 1982	1633	S09 E25	3B/X12

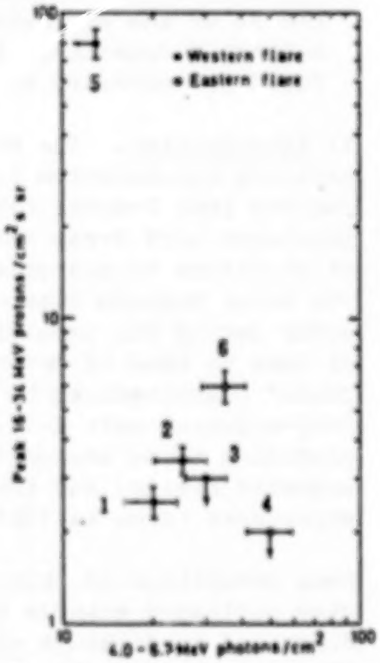

Fig. 1 Numbers attached to data correspond to flare numbers in Table 1.

ENERGETIC PROTONS FROM A DISAPPEARING SOLAR FILAMENT

S.W. Kahler
Emmanuel College, Boston, Massachusetts 02115 USA

E.W. Cliver
Air Force Geophysics Laboratory, Hanscom AFB, Massachusetts 01731 USA

H.V. Cane* and R.E. McGuire*
Laboratory for High Energy Astrophysics, Goddard Space Flight Center
Greenbelt, Maryland 20771 USA

R.G. Stone
Laboratory for Extraterrestrial Physics, Goddard Space Flight Center
Greenbelt, Maryland 20771 USA

and N.R. Sheeley, Jr.
Naval Research Laboratory, Washington, D.C. 20375 USA

ABSTRACT

A solar energetic ($E > 50$ MeV) particle (SEP) event observed at 1 AU began about 1500 UT on 1981 December 5. This event was associated with a fast coronal mass ejection observed with the Solwind coronagraph on the P78-1 satellite. No metric type II or type IV burst was observed, but a weak interplanetary type II burst was observed with the low frequency radio experiment on the ISEE-3 satellite. The mass ejection was associated with the eruption of a large solar quiescent filament which lay well away from any active regions. The eruption resulted in an Hα double ribbon structure which straddled the magnetic inversion line. No impulsive phase was obvious in either the Hα or the microwave observations. This event indicates that neither a detectable impulsive phase nor a strong or complex magnetic field is necessary for the production of energetic ions.

1. Introduction. The conventional view of energetic (tens of MeV) solar particle acceleration is that it occurs only during flares in active regions (see Svestka (1981) for a general review). In many flares impulsive hard X-ray and microwave bursts indicate a rapid acceleration of electrons to energies of tens of keV. The γ-ray observations from the Solar Maximum Mission have shown that MeV ion production can also occur during the impulsive phase (Forrest and Chupp 1983). Acceleration of ions to tens of MeV then sometimes occurs in a subsequent "second phase" characterized by metric type II and type IV radio bursts and long-enduring soft X-ray and microwave events. The active regions producing these energetic flares are characterized by strong and complex magnetic fields, and the flares themselves are usually Hα double ribbon structures (Svestka 1981).

Some exceptions to this conventional picture are known. The most convincing published example of a nonflare source for a prompt SEP event was discussed by Sanahuja et al. (1983). They attributed a $1 < E < 15$ MeV SEP event to the disappearance early on 1979 April 23 of a large filament

---

*Also: University of Maryland, College Park, Maryland 20742 USA

ORIGINAL PAGE IS
OF POOR QUALITY

at least partially located in a small and weak active region. A pair of double-ribbon flares, one in McMath region 15956, accompanied the filament disappearance. However, they argued that the filament eruption, rather than the flares, was the important factor in this SEP event.

2. Observations. The SEP event of 1981 December 5 was observed with the GSFC cosmic ray experiment on the ISEE-3 spacecraft (Figure 1). The MeV electron onset was between 1415 and 1430 UT, followed by the proton onset between 1500 and 1530 UT. The velocity dispersion and rapid rise to maximum are evidence of an impulsive injection of particles from a well connected solar longitude. The 11-22 MeV proton flux measured by the Helios 1 spacecraft (~ 13° behind the west limb) on December 6 was a factor of 10 lower than that measured simultaneously by the GSFC experiment on IMP-8 at the Earth, consistent with our association of the SEP event with the disappearance of the disk filament, rather than with a source from behind the limb.

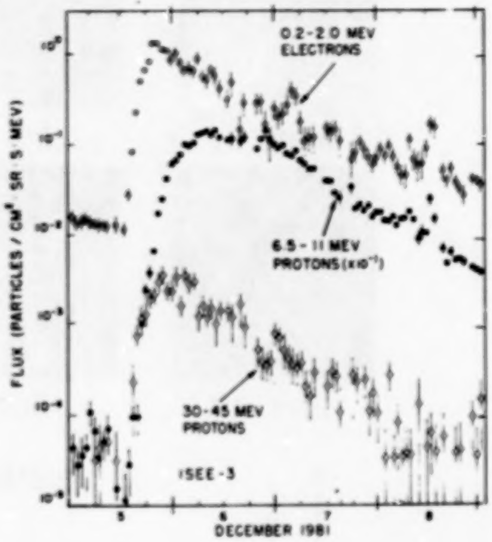

Figure 1. Flux-time plots of energetic particles for the SEP of 1981 December 5.

Several Hα filtergrams obtained by the Haute Provence Observatory (provided courtesy of P. Simon) and reproduced in Figure 2 show the key times in the eruption of a large filament on 1981 5 December. The filament, located at ~ W35-45°, N15-30° became active and began to erupt at ~ 1215 UT. Hα brightenings were first observed at 1315 UT, forming a classic double-ribbon pattern along the filament channel. The filament was not at the location of a former active region, and it lay at least 25 heliographic degrees from the nearest plage region.

Figure 3 shows the ejected filament and coronal material observed by the NRL white-light coronagraph (SOLWIND) on the P78-1 satellite. The first of these difference images shows that the coronal disturbance was not yet visible at 0658 UT, but was in progress during the next available image at 1447 UT. At this time the leading edge of the coronal material was already located at 6.2 R_0 in the northwest quadrant while the much smaller prominence was near the edge of the occulting disk at 2.5 R_0. During the subsequent images the ejected coronal material left the 2.5-10.0 R_0 field of view, and the prominence moved uniformly outward in the plane of the sky. Its apparent latitude 30° north of west is consistent with the original location of the filament on the disk. From these observations, we found that the prominence was moving with a speed of 305 ± 20 km/s in the plane of the sky. Extrapolated back to the 0.65 R_0 location of the disk filament, this speed gives a starting time of 1329 ± 0010 UT, or approximately 1 hr after the disk filament began to disappear. This 1-hr time delay suggests that the erupting filament accelerated during the first hour after its initial disappearance from the Hα spectral bandpass, as is usually observed for erupting prominences.

ORIGINAL PAGE IS
OF POOR QUALITY

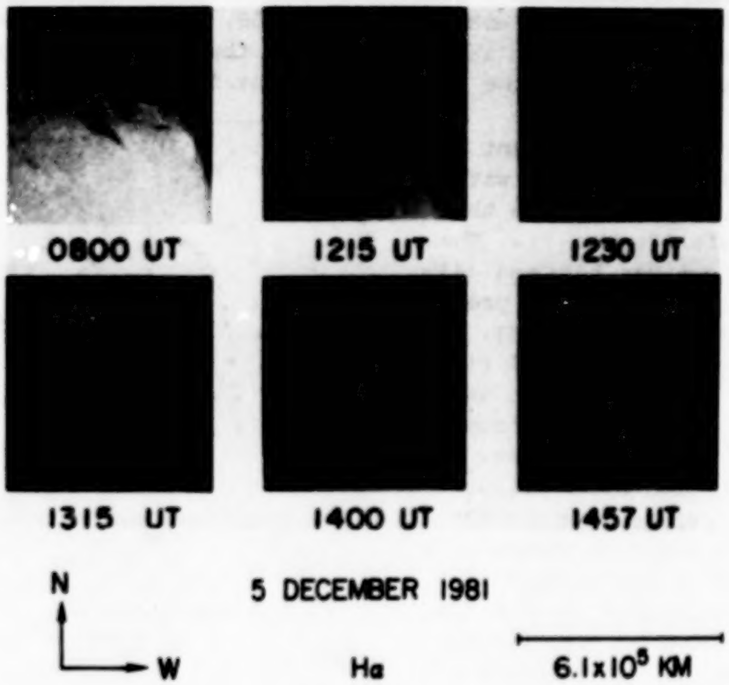
0800 UT
1215 UT
1230 UT
1315 UT
1400 UT
1457 UT
N
W
5 DECEMBER 1981
Hα
6.1x10⁵ KM

Figure 2. Hα images from the Haute Provence Observatory showing the filament disappearance (top) and subsequent two-ribbon brightening (bottom) on 1981 December 5. Comparison of the top three images shows a clear outward motion of the northernmost part of the filament.

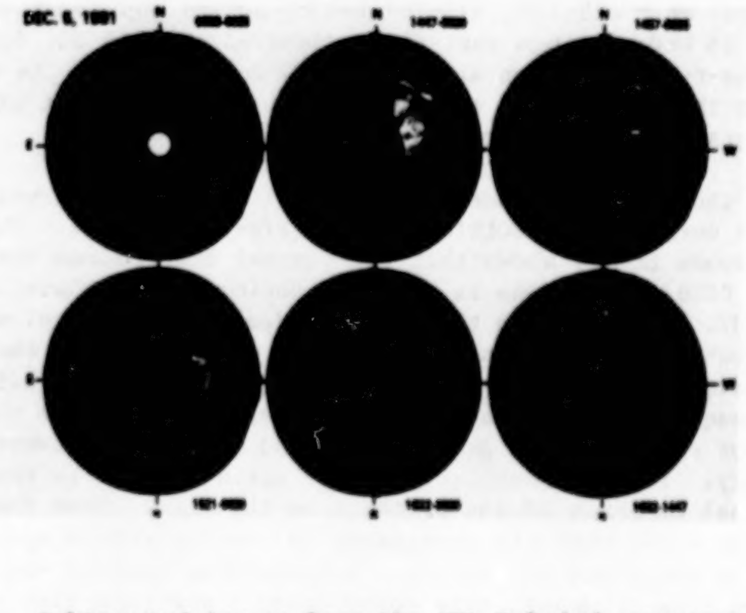
DEC. 5, 1981
N
E
W
S

Figure 3. Subtracted images from the NRL Solwind coronagraph showing the CME of December 5. The Hα filament can be seen as the small bright structure at the inner core of the CME.

No impulsive microwave or hard X-ray bursts accompanied the filament disappearance. There were, however, weak gradual soft X-ray and microwave events that appeared to accompany the eruption. A faint and very gradual GOES 1-8 Å enhancement began shortly after 1300 UT, rising from a C2.5 background to a peak level of only C3.5 at 1430-1450 UT. A gradual rise-and-fall event was observed in the Sagamore Hill Observatory 4995 MHz record beginning at ~ 1300 UT with a peak flux of 21 ± 3 s.f.u. at ~ 1400 UT. Metric type III bursts observed from 1316 to 1326 UT were also detected in the ISEE-3 radio data, but these were not due to the filament activity because the deduced position of the 1980 kHz position was east of central meridian. An apparent shock-associated (SA) event (Cane *et al.* 1981) was observed at 1980 kHz in the ISEE-3 radio data from the end of the type III emission at about 1328 UT until 1352 UT. By tracking the centroid of the emission out to about 0.7 AU, we estimate that the source longitude for this event was in the range W10°- W40°, indicating a spatial as well as temporal association with the filament disappearance and CME. The SA event was followed by a weak interplanetary type II burst (Cane 1985).

3. *Discussion and Conclusion.* The E > 50 MeV SEP event of 1981 December 5 has been associated with a filament disappearance well removed from any active region. The motion of the filament was observed in Hα as shown in the second and third images of Figure 2 and later in the coronagraph images shown in Figure 3. Besides the filament disappearance, the prominent solar signatures of the December 5 event were the Hα double-ribbon emission shown in Figure 2 and the accompanying weak gradual thermal soft X-ray and microwave event. The Hα ribbons appear to be the footpoints of cool loop arcades overlain by hot soft X-ray loops.

In addition, we found no evidence of any impulsive phase microwave emission from this event. This indicates that neither active regions nor obvious impulsive phase phenomena are necessary for energetic particle production (cf. Cliver *et al.* 1983). The good association of SEPs with Hα flares and with flare impulsive phase bursts is most likely not a direct cause-and-effect relationship but rather a manifestation of the Big Flare Syndrome (Kahler 1982), which states that, statistically, energetic flare phenomena are more intense in larger flares, regardless of the detailed physics.

Acknowledgements. This work was supported at Emmanuel College by AFGL contract AF 19628-82-K-0039, at NRL by NASA DPR W 14,429, and at GSFC/University of Maryland by NASA grant NGR 21-002316.

REFERENCES

Cane, H.V. 1985, *J. Geophys. Res.*, *90*, 191.
Cane, H.V., *et al.* 1981, *Geophys. Res. Letters*, *8*, 1285.
Cliver, E.W., *et al.* 1983, *Astrophys. J.*, *264*, 699.
Forrest, D.J., and Chupp, E.L. 1983, *Nature*, *305*, 291.
Kahler, S. 1982, *J. Geophys. Res.*, *87*, 3439.
Sanahuja, B., *et al.* 1983, *Solar Phys.*, *84*, 321.
Svestka, Z. 1981, in *Solar Flare Magnetohydrodynamics*, ed. E.R. Priest (New York: Gordon and Breach), p.47.

N85-34755

SH 1.3-8

HELIOS I ENERGETIC PARTICLE OBSERVATIONS OF THE SOLAR GAMMA RAY FLARE EVENTS OF 7, 21 JUNE 1980 and 3 JUNE 1982

Frank B. McDonald, NASA Headquarters/Code P, Washington, DC 20546
M.A.I. Van Hollebeke, Musee National des Sciences, Technique et Industrie
PARC de La Villette, Paris, France
James H. Trainor, NASA/GSFC, Code 600, Greenbelt, MD 20770

ABSTRACT

The observed characteristics of the energetic particles associated with the solar γ-ray events of 3, 21 June 1980 and 3 June 1982 differ in several important aspects from the typical solar particle increases. They have flat energy spectra, are electron rich and have small precursor increases that begin some hours before the impulsive flare increase.

1. Introduction. Solar flare γ-rays and neutrons provide a direct means of determining the flux and energy spectra of those energetic particles accelerated by the flares which impact the lower coronae and photosphere (Ramaty et al., 1982, 1983; Chupp, 1984). The γ-ray time histories, when compared to those of x-rays, establish limits on the time required for particle acceleration. The flux and energy spectra of those flare accelerated particles which escape from the Sun can be determined by interplanetary observations. Comparing these two complimentary particle populations provides further understanding of the particle acceleration and transport processes in the flare region.

The Solar Maximum Mission Gamma Ray experiment of Chupp and his co-workers have made detailed observations of a number of solar γ-ray events (cf Chupp, 1984). Three of these flare increases are of special importance: 3 June 1982 and 21 June 1980 which are large intense γ-ray events that also produced a detectable flux of solar neutrons at 1 AU (Chupp et al., 1982, 1983); the 7 June 1980 event was more moderate in size, was accompanied by a small $H\alpha$ flare, but the near simultaniety of the onset of γ-ray and soft x-ray emission implies that the particles are accelerated on a time scale of less than 2 seconds.

The Helios I spacecraft was in a favorable location at the time of each of these flares (Table 1). The small heliocentric distance

TABLE 1

SOLAR EVENT	FLARE LOCATION & $H\alpha$ CLASS	PEAK TIME FLARE IMPULSIVE PHASE (1)	HELIOS I HELIOCENTRIC DISTANCE	HELIOLONGITUDE SEPARATION (2)	PROTON SPECTRAL INDEX γ	ELECTRON/PROTON	Fe/O	He/H	^{3}He/He^4
3 June 1982	S09 E72 2B	1143.5	0.57 AU	3°	1.2 (3-200 MeV)	1 (3-6 MeV)	2.5±.5	132	.02±.014
21 June 1980	N19 W88 1B	0118	0.54 AU	33°	2.6 (8-200 MeV)	0.25 (3-6 MeV)	0.9±.02	29	.03±.013
7 June 1982	N12 W74 1B	0312	0.37 AU	14°	2.3 (3-30 MeV)	0.7 (1-2 MeV)	NOT OBSERVED	4	<.02

(1) Earth Observed Time
(2) Heliolongitude Separation Between Helios I and Nominal Field Line (Based on measured plasma velocity) Connecting to the Region of the Flare Site.

between the spacecraft and the flare site significantly enhances the observations of the source region characteristics. The detailed observations of the energetic particles associated with these γ-ray flare events by the Goddard cosmic ray experiment on Helios I are presented in the following discussion along with their implication for the acceleration process. This present study builds on the previous reports based on both ISEE-3 and Helios I energetic particle data (Evenson, et al., 1980; Pesses et.al.,1979; von Rosenvinge et al., 1981; McDonald and Van Hollebeke, 1985).

2. Helios-I Energetic Particle Observations. Both the 3 June 1982 and 21 June 1980 proton and electron data exhibit a "classical form" with a rapid rise to peak intensity followed by a relatively smooth exponential decay (Fig. 1). The peak fluxes at 50 MeV of 10.5 and 0.3 MeV protons mark these as moderate sized increases. For both events there is a definite precursor increase that begins some 3 hours before the major flare (McDonald and Van Hollebeke, 1985).

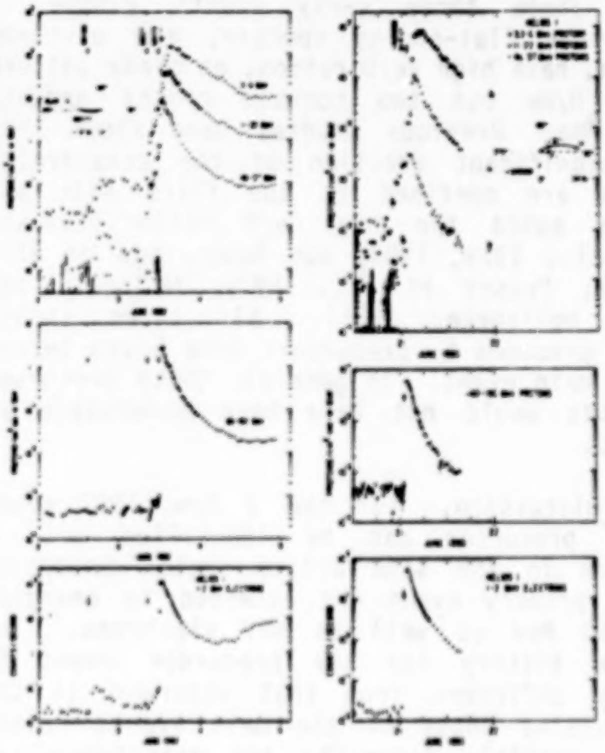

Fig.1 Energetic particle time histories. Vertical lines with arrows represent flare on-set times. The top insert shows the separation between Helios 1 and the nominal field line connecting to the flare site based on the measured plasma velocity.

The time history of the 7 June 1980 event is remarkably different from those of the other two increases (Fig 2). The solar energetic particle time histories are complex and the peak intensities are small (Fig. 2). The 1-2 MeV electrons arrive promptly at ∿0307 (Helios time), have a step increase at ∿0400 and there is a new injection at ∿0715. The integral electron channel for electrons > 250 keV is a single parameter measurement which also responds to x-rays and γ-rays. The time history of these electrons indicate flare activity at ∿ 0120, 0307 and 0715. The dashed line at 0300 (Helios time) is before the onset of the Hα flare producing the gamma-rays observed by SMM. The 1.25-6 and 3.7-21 MeV proton channels both show a precursor event in progress at the time of the flare (Fig. 2a, 2b). Unlike the MeV electrons, the onset time for protons appears to be delayed until ∿0400 (the transit time is ∿17 minutes for 15 MeV protons and 31 minutes for 3.6 MeV protons). The sharp decrease that occurs in all proton channels between 0400 and 0500 appears to be produced by a change in declination of the interplanetary magnetic field of ∿22°. The proton anisotropies from

ORIGINAL PAGE IS
OF POOR QUALITY

3-20 MeV and 6-20 MeV are remarkably high from 0300-0900 so the observed proton intensities are very sensitive to the field direction. Fortunately the IP magnetic activity is usually quiet for this period and the field is in the plane normal to the spacecraft spin axis except for this deviation. There is also a new injection of 1.2-20 MeV protons at ~0720.

These three γ-ray events (Table 1) have flat-energy spectra, are electron rich, have high Fe/O ratios, no clear pattern for H/He but two contain modest amounts of ^{3}He. Previous studies have shown that a significant fraction of the accelerated ions are confined at the flare site and have noted the high e/P ratio (Evenson et al., 1979, 1983; von Rosenvinge et al., 1979; Pesses et al., 1979; McDonald and Van Hollebeke, 1985). All three events are preceded by precursors some hours before the main event. In general, these precursor events would not have been observable at 1 AU.

3. Discussion. For the 3 June 1982 event the precursor can be identified with a flare in the same active region producing the primary event and extended to energies > 60 MeV as well as MeV electrons. The time history for the precursor event is very different from that observed in the impulsive phase of the main event. Since the particle intensity and anisotropy are still increasing at the onset of the large flare and in view of the short transit time of the 1.5 MeV electrons, it is unlikely that there were significant changes in the interplanetary propagation conditions between the precursor event and the large event at 11:34. The slow continuing increase in energetic particles between 8:40 and 11:30 must reflect the effects of leakage from a coronal source region. For the June 21, 1980 event, the time history or the precursor proton increase is remarkably similar to that of 3 June 1982. The 7 June preflare increase resembles a pulse-like injection feature.

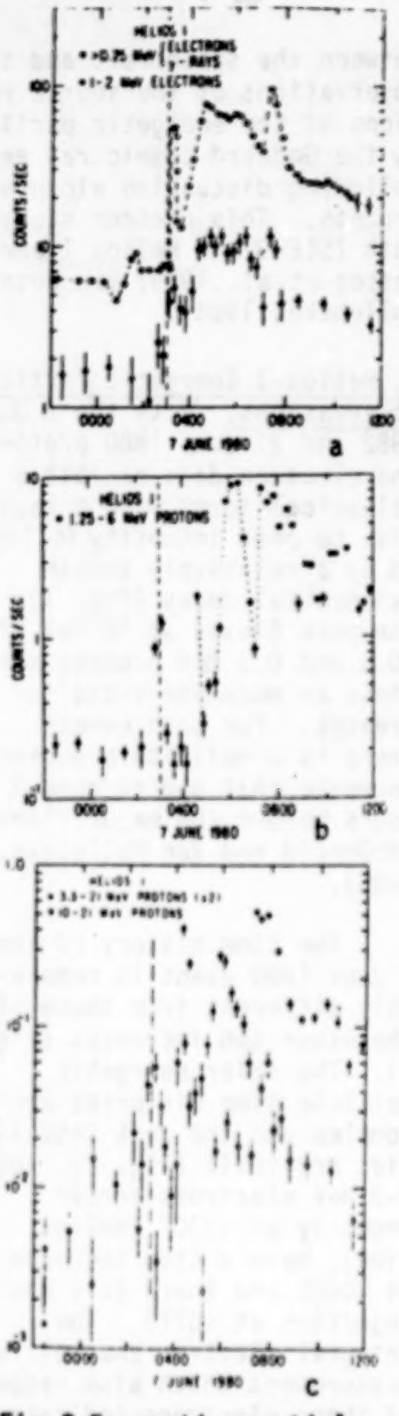

Fig.2 Energetic particle time histories for 7 June 1980 events. The DASHED line represents the flare on-set time

The precursor events described here imply that MeV ions (with energies extending to above 60 MeV along with MeV electrons in one case) are present in the corona prior to the onset of the main flare.

The presence of these energetic particles allows the consideration of models where the impulsive phase and the resulting shock both further accelerate and precipitate this existing reservoir of stored energetic particles. The possibility of a continual acceleration process over the 3 hrs. prior to the main flare cannot be ruled out.

The problem of the storage of ions in magnetic loops has been examined by Zweibel and Haber (1983). They found that particles with small pitch angles at the top of the loop, i.e., particles that mirror closer to the photosphere, will be lost much more rapidly. Using their calculations, it is found that an average electron density, $n_e < 10^8$ cm^{-3} is required if 5 MeV protons, mirroring near the top of the loop, are to lose < 2 MeV in 2 hr. On this time scale, particle drifts become important but may be reduced by twisting the loop. The shock acceleration of these particles in a closed loop structure will preferentially increase the velocity component along the field line and lead to enhanced particle precipitation.

References

1. Block, G.M., and Kuzhevskii, B.M., (1979), Proc. 16th Internat. Cosmic Ray Conf. (Kyoto), 5, 1.
2. Chupp, E.L., et al. (1982), Ap.J. (Letters), 263, L95.
3. Chupp, E.L., Forrest, D.J., Kanbach, G., Share, G.H., DeBrunner, H., and Fluckiger, E. (1983), Proc 18th Internat. Cosmic Ray Conf. (Bangalore), 4, 75.
4. Chupp, E.L., (1984), Ann. Rev. Astr. Ap., 22, 359.
5. Evenson, P., Meyer, P., and Yanagita, S., (1981), Proc. 17th ICRC 3, 32.
6. Evenson, P., Meyer, P., and Pyle, K.R. (1983), Ap.J., 274, 875.
7. Forrest, D.J., and Chupp, E.L. (1983), Nature, 305, 291.
8. McDonald, F.B. and Van Hollebeke, M.A.I., (1985), Ap.J., 290, L67.
9. Pesses, M.E., Klecker, B., Gloeckler, G., and Hovestadt, D., (1981), Proc. 17th ICRC, 3, 36.
10. Ramaty, R., Lingenfelter, R.E., and Kozlovsky, B. (1982), in Gamma Ray Transients and Related Astrophysical Phenomena, ed. R. E. Lingenfelter et al. (New York: AIP), p.211.
11. Ramaty, R., Murphy, R.J., Kozlovsky, B., and Lingenfelter, R.E., (1983), Ap.J. (Letters), 273, L41.
12. Reinhard, R., and Wibberenz, G. (1974), Solar Phys., 36, 473.
13. Van Hollebeke, M.A.I., Ma Sung, L.S., and McDonald, F.B., (1975), Solar Phys., 41, 189.
14. von Rosenvinge, T.T., Ramaty, R., and Reames, D.V., (1981), Proc. 17th ICRC (Paris), 3, 28.
15. Zweibel, E.G., and Haber, D.A., (1983), Ap.J., 264, 648.

N85-34756

SH 1.3-9

INJECTION OF ENERGETIC PARTICLES FOLLOWING THE GAMMA-RAY FLARES ON JUNE 7 , 1980, AS OBSERVED ON HELIOS-1.

Neustock, H.-H., Wibberenz, G., Iwers, B.
Institut für Reine und Angewandte Kernphysik, Universität Kiel
Olshausenstr. 40 - 60, 2300 Kiel, FR Germany

ABSTRACT

On June 7, 1980, two flares with impulsive gamma-ray emission were observed at 0117 UT and 0312 UT. We present measurements of the University of Kiel cosmic-ray experiment on HELIOS-1. The first ∿0.5 MeV electrons escaped from the sun to interplanetary space simultaneously with the hard X-ray burst. For the 0312 UT flare the protons and α-particle in the 3 - 20 MeV/nucleon range were injected from the sun with a delay of ∿40 min, followed by two subsequent new emissions.

1. Introduction. For a long time it was postulated in most models that the ion and relativistic electron acceleration takes place in the "second phase" of a flare, some ten seconds after the impulsive phase. But gamma-ray observations on SMM demonstrated (1) that these particles can be accelerated very rapidly and appear almost simultaneously with the non-relativistic electrons within time scales of seconds.

Correlations between the emission of hard electromagnetic radiation and the escaping energetic charged particles should give important clues for the acceleration mechanism. However, first studies showed that the number of nucleons escaping into space is only a small fraction of the number required to explain the observed gamma emission (2). A lack of correlation was found between the nuclear gamma emission of the flare and the size of the interplanetary proton events (3). These observations were explained by a highly variable ratio of particles moving upwards and downwards after acceleration, or by the existence of two independent populations.

In this paper we study the injection of energetic electrons, protons, and helium nuclei following a series of flares on June 7, 1980. The small distance of the HELIOS spacecraft to the sun and the unusually smooth interplanetary magnetic field allow a temporal resolution of the solar injection process which has not been reached before.

2. Observations. Energetic particle data were obtained with the University of Kiel cosmic ray experiment on HELIOS-1 (4,5). The instrument measures electrons with energies ≳ 0.3 MeV, nucleons above 1.3 MeV/N in eight sectors each 45° wide in the ecliptic plane. For selected energy channels pulse height analysis allows particle identification and precise energy measurement for a representative sample of all incoming particles.

HELIOS-1 was in an ideal position to study the solar events on June 7, 1980, which occurred in Hale plage region 16886. The spaceprobe was located at 0.37 AU distance from the sun and was magnetically connected to a coronal region about 2 - 11° apart from the active region. Solar wind data indicate that HELIOS-1 was inside a "hole" in the solar wind (Schwenn, private communication). The interplanetary magnetic field (courtesy F.M. Neubauer, G. Musmann) was exceedingly smooth. As a consequence, solar energetic particles arrive totally collimated and were practically confined to the sector which contained the magnetic field direction leading towards the sun. This allows to reduce the isotropic background considerably and to reconstruct directly the injection profile at the sun.

Figure 1 shows three minute averages of the particle intensities from the solar oriented sector for a 12 hour period on June 7. Time and location of the three solar flares are given in the inserts in the upper panel. The first two flares are also observed at $\gtrsim$ 0.3 MeV gamma energies, the third one is not. It is remarkable that this event shows the largest intensity in electrons. Because of the scatter free interplanetary propagation we can directly construct the total number of injected particles by integrating the observed directional intensities over time. The total electron numbers for the three events vary as 1:6:29. In contrast, the X-ray emission in the 1.6 to 12.4 keV range varies as 1:3:0.2.

In Figure 2 we have corrected for the interplanetary travel time of each particle group by subtracting $t = s/v$ from the time of observation. Here s is the curved path length along the smooth interplanetary magnetic field spiral, as determined from the measured solar wind speed. The velocity v is determined from identification and energy measurements of the various particles. Results are plotted as a function of "solar release time" (SRT). Earth bound electromagnetic observations have been corrected accordingly. On this scale, the emission of electrons and X-rays occurs simultaneously, whereas for the first two flares the protons are delayed. In case of the 0315 flare we also find a multiple injection, with the first proton injection starting at 0345 SRT, the second at 0440 SRT. The last release at 0635 SRT is superimposed by a fresh injection of particles from the 0725 flare. In this case, protons and electrons are injected simultaneously and also coincident with the optical flare.

The temporal relation between X-ray and electron emission for the three flares is shown on an extended time scale in Figure 3. It shows that within about one minute the electron injection onset matches the impulsive X- and gamma-ray emission of the flare which marks the particle acceleration. The number of injected electrons has reached their maximum (I_{max}) in several minutes, but the injection lasts in any case much longer than the electromagnetic emission (see Figure 2). The steps in the electron onset in Figure 3 correspond to the temporal resolution of the data transmission of HELIOS at the time of observation. The uncertainty in fixing the release time by uncertainties in the path length is below one minute.

Figure 4 shows the injection of nucleons of different energy/nucleon, ordered from top to bottom with decreasing velocity. For the three separate injections following the 0315 flare we find that higher energy nucleons are injected later. This inverse velocity dispersion is not observed for the 0725 flare. Here nucleons are released simultaneously with the electrons.

Energy spectra can be fitted by power laws in kinetic energy over the range of observation (see Table 1). The electrons resulting from the gamma-flares show a harder spectrum. This is in accordance with results in (6). We see that also the proton energy spectrum for the 0725 flare which was not accompanied by gamma-rays is steeper than the first injections for the other cases. For the three consecutive injections following the 0315 flare the spectrum steepens from one injection to the next.

In summary, we find the following observations:

(1) The $\sim$0.5 MeV electrons are released simultaneously with the hard X-ray bursts for all three events, within the temporal uncertainty of about one minute.
(2) The electron injection continues for 15 - 20 minutes, much longer than the duration of the X-ray bursts.
(3) There is no correlation between the number of electrons in interplanetary space and the emission in 1 - 8 Å X-rays or $\gtrsim$ 0.3 MeV gamma-rays.
(4) For the flares at 0118 and 0315 nucleons are released from the sun with a considerable delay.
(5) We find repeated injections of nucleons after the 0315 flare. For each of the three subsequent injections the proton spectrum gets steeper.
(6) After correcting for interplanetary travel times we find that the injection starts later for nucleons of higher energy/nucleon.

3. Discussion. The delayed emission of nucleons confirms the view that the nucleons observed in interplanetary space need not be identical with the component responsible for the gamma-ray generation. Nevertheless the emitted nucleons may have been accelerated simultaneously with a gamma producing component, followed by storage in closed magnetic field regions with subsequent repeated release, possibly connected to the bird cage model (7). However, in this model the immediate release of electrons would be hard to understand. An alternate explanation for two independent populations is the acceleration of nucleons by a coronal shock wave. A type-II radio burst suggestive for a coronal shock had been observed after the 0312 flare, but not for the 0725 flare. In this event not accompanied by gamma-ray production the release of electrons and nucleons occurs simultaneously.

4. Acknowledgements. We are grateful to all members of the HELIOS team at the University of Kiel, principal investigator H. Kunow, who contributed to the success of the cosmic ray experiment. Unpublished X-ray data from the SMM gamma-ray experiment (see Figure 3) have been kindly supplied by E. Rieger, Garching. This work was supported by the German Bundesminister für Forschung und Technologie.

References

(1) Chupp, E.L. et al., Ap. J. 244, L171-L174, 1981.
(2) Von Rosenvinge, T.T. et al., Proc. 17th ICRC, 3, 28-31, 1981.
(3) Cliver, E.W. et al., Proc. 18th ICRC, 4, 84, 1983.
(4) Kunow, H. et al., Raumfahrtforschung 19, 253-258, 1975.
(5) Kunow, H. et al., BMFT-FB-W81-016, 1981.
(6) Evenson, P. et al., Ap. J. 283, 439-449, 1984.
(7) Newkirk, G., and Wentzel, D.G., J. Geophys. Res. 83, 2009-2015, 1978.

ORIGINAL PAGE IS
OF POOR QUALITY

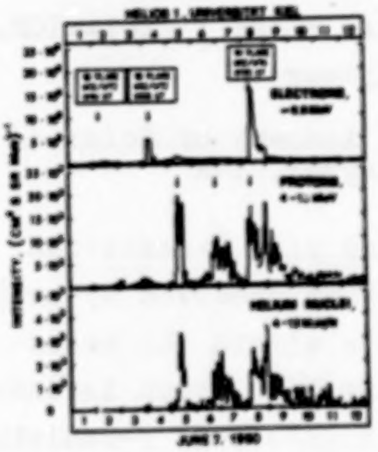

Figure 1: Particle intensities from the solar direction on a linear scale.

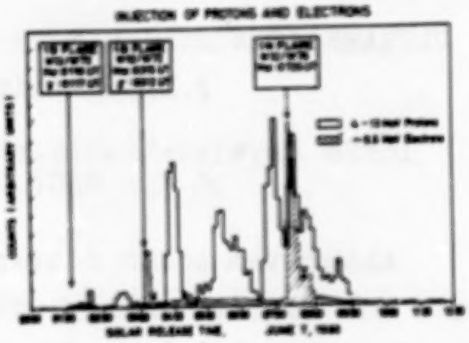

Figure 2: Solar injection of electrons and protons after correction for interplanetary travel time along the smooth interplanetary magnetic field. Solar Release Time (SRT)= UT - s/v.

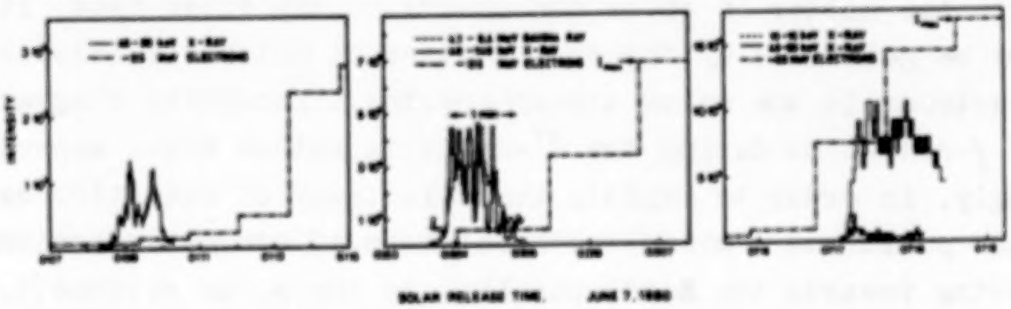

Figure 3: Temporal correlation between hard electromagnetic radiation and the release of relativistic electrons.

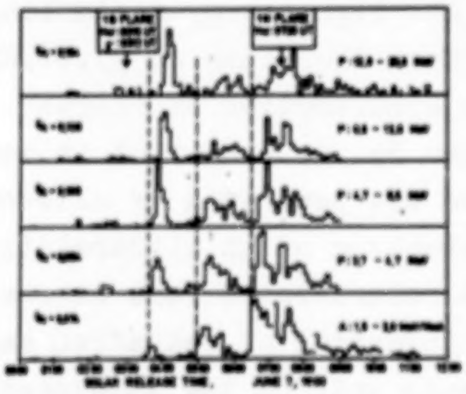

Figure 4: Energy dependence of solar release of protons (P) and Helium nuclei (A). The energy range is indicated on the right side. The dashed vertical lines give the injection onset for the lowest velocity channel.

Particle type	time interval	spectral index
electron (0.3 to 4 MeV)	0113 - 0154 UT 0307 - 0330 UT 0720 - 0804 UT	3.50 ± 0.11 3.48 ± 0.07 3.93 ± 0.05
proton (4 to 37 MeV)	0138 - 0317 UT 0416 - 0449 UT 0513 - 0646 UT 0712 - 0745 UT 0745 - 0858 UT	2.29 ± 0.25 2.67 ± 0.13 3.04 ± 0.15 3.66 ± 0.24 3.18 ± 0.13

Table 1: Spectral indices for a power law fit of the measured spectra. Proton spectra: The second to fourth time interval represent the three injections following the 0315 flare.

N85-34757

ULTRARELATIVISTIC ELECTRONS AND SOLAR FLARE γ-RADIATION.

P.E.Semukhin, G.A.Kovaltsov

Ioffe Physico-Technical Institute Academy of Sciences
of the USSR,194021 Leningrad,USSR

About ten solar flares accompanied with γ-radiation with the quantum energy >10 MeV have been observed by now[1]. Practically all these flares took place within the heliolongitude $\lambda>60^\circ$,i.e. close to the solar limb,which is indicative of an essential anisotropy of high-energy γ-radiation. Such radiation may be generated on one hand,by the decay of π^0, produced by nuclear interactions of accelerated protons with the matter of solar atmosphere.On the other hand, it may be generated by the deceleration of ultrarelativistic electrons in the solar atmosphere.The directivity diagram of γ-radiation during the π^0-decay is rather wide. Accordingly, in order to explain the anisotropy of radiation we must postulate a monodirectional beam of energetic protons moving towards the Earth parallel to the solar surface [2,3]. It is evident that in a major flare,the spectrum of accelerated protons being hard enough,the radiation produced by the π^0-decay may be predominant for high-energy radiation, the instance of which must have been the flare on 3.06.82 [3,4]. However,we think that the distribution of flares along heliolongitude is determined by the fact that in most cases the major part of radiation was generated by ultrarelativistic electrons.The bremsstrahlung of an ultrarelativistic electron with an energy E is concentrated in a narrow cone $\sim E/m_ec^2$. Accordingly the intensity of radiation emitted in a definite direction depends only on the thickness traversed by electrons in this direction.It is common knowledge the evolution of solar flares starts in closed magnetic arcs.Such arcs are the traps for energetic charged particles.Accelerated electrons will oscillate between two bottoms of the arc.They move parallel to the solar surface near the mirror points traversing maximum thickness in unit time,because ambient density increases with depth. Thus the accelerated electrons regardless of its pitch-angle at the arc top generate γ-radiation of maximum intensity along the solar surface tangential line. For this reason the radiation will be anisotropic provided that the acceleration of electrons at the arc top is isotropic.

For the quantitative analysis of the model in question we have calculated the γ-radiation of ultrarelativistic electrons decelerating inside the magnetic arc. The coronal part of the arc was assumed to be semitoroidal with the radius of the axis line R, a magnetic field B_0 and the ambient density n_a. At either bottom of the arc the field is directed along the solar radius and increases with depth: $B=B_0(1+Z/Z_0)$; the density is $n=n_0 \exp(Z/h)$. Z being equal to 0, the density goes up ($n_0 \gg n_a$) which corresponds to the transition region "corona-chromosphere". The calculation include ionization and synchrotron energy loss of electrons. To simplify the calculation a loss cone α_{min} was introduced (α is the pitch-angle at the arc top). Its value is so large that the electron trapped in the arc lose a minor part of its energy at one bouce. Fig. 1 gives an example of the calculation of the temporal behaviour of radiation with the quantum energy $\varepsilon = 10$ MeV in the case of isotropic instantaneous injection of accelerated electrons at the arc top. The spectral index of power law injection spectrum $\gamma_e = 3,5$. It is evident that the radiation is highly anisotropic during the first 10-20 sec. Within this period the intensity falls by 10-50 times and the radiation becomes unobservable at the contemporary level of experimental technique. This result corresponds to the observed duration of γ-ray impulses [1,5]. It is worth mentioning that the decrease of the loss cone increases the anisotropy of γ-radiation and steepness of the impulse fronts. Fig. 2 shows the radiation directivity at the moment of impulse maximum, the model parameters varying in value. It is evident that the radiation intensity from the limb to the center of the solar disk falls by 20-100 times. The radiation intensity of a major

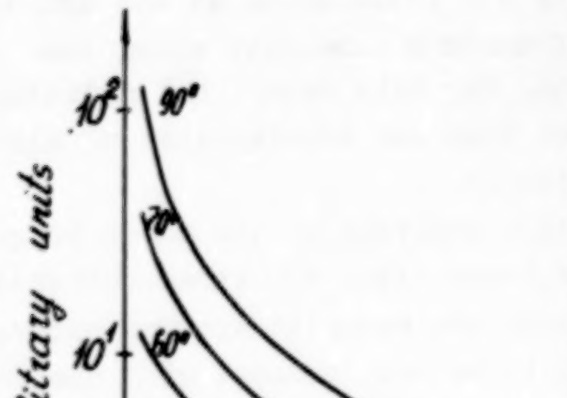

Fig. 1
Temporal behavior of γ-radiation with the quantum energy of >10 MeV for an instantaneous injection of accelerated electrons into the arc with the parameters: $h = 2 \cdot 10^7$ cm, $Z_o/h = 4$, $R = 10^9$ cm, $n_d = 10^{11} cm^{-3}$, $n_o = 10^{12} cm^{-3}$, $B_o = 500$ the loss cone $\cos\alpha_{min} = 0,8$. Heliolongitude of the flare is indicated above the curves.

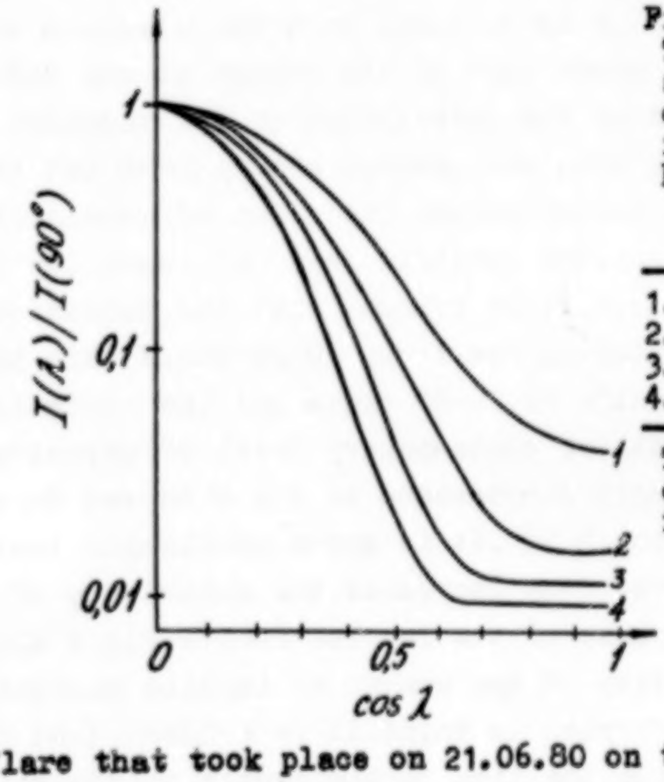

Fig. 2
The radiation intensity at the moment of impulse maximum in variation with heliolongitude.

	Z_o/h	$\cos\alpha_{min}$
1.	1	0,94
2.	4	0,8
3.	8	0,68
4.	12	0,6

The other parameters correspond to those in Fig. 1.

flare that took place on 21.06.80 on the limb, would have been lower or comparable on the disk with the threshold of response of modern equipment.

In calculating the γ-radiation of the flare on 21.06.80 within the range of 0,2-1 MeV a complete number of accelerated electrons was obtained, $N_e(>1\ \text{MeV})=5\cdot10^{33}$, the index of spectrum being $\gamma_e=3,5$ [6]. Extending this spectrum into higher energies, γ_e being constant, we calculated the γ-ray fluence with the quantum energies >10 MeV which corresponds to the observed value $F_\gamma(>10\ \text{MeV})=18\ \text{cm}^{-2}$ [1], the model parameters being equal to those in figure 1. The electron spectrum in interplanetary space during the flare on 21.06.80 was power low, γ_e being constant within the range of energies 0,5-20 MeV [7]. This fact justifies our extrapolation of the electron spectrum. During this flare only ~10% of high-energy electrons escaped the solar atmosphere [7], which confirms our assumption that electrons are trapped by the magnetic arc in the solar atmosphere.

Thus the observation data of high-energy γ-radiation of flares can be explained by the specific features of the bremsstrahlung of ultrarelativistic electrons trapped within the magnetic arc even if the acceleration of electrons is isotropic.

References.

1. E.Rieger et al. Proc. 18-th ICRC, 1983, v.4, p.83.
2. G.E.Kocharov, N.Z.Mandzhavidze, Pis'ma v AZh, 1984, v.10, p.771.
3. G.E.Kocharov, N.Z.Mandzhavidze, Izv.ANSSSR, ser.fiz., 1984, v.48, p.2212.
4. R.Ramaty, R.J.Murphy, Proc. Plasma Astrophysics school and workshop, Varenna, 1984, p.83.
5. E.L.Chupp, Solar Phys., 1983, v.86, p.383.
6. G.A.Kovaltsov, G.E.Kocharov, Preprint FTI AN SSSR, 1982, N.799.
7. P.Evenson et al. Astrophys.J., 1984, v.283, p.439.

N85-34758

SOURCE ENERGY SPECTRA FROM DEMODULATION OF SOLAR PARTICLE DATA BY INTERPLANETARY AND CORONAL TRANSPORT

J. Pérez-Peraza*, M. Alvarez-Madrigal*, and F. Rivero*
Instituto de Geofísica, UNAM, 04510- C.U., México 20, D. F., MEXICO

L. I. Miroshnichenko
IZMIRAN, Troitsk, Moscow Region, 142092, USSR

1. Introduction. The data on source energy spectra of solar cosmic rays (SCR), i.e. the data on the spectrum form and on the absolute SCR are of great interest at least for three reasons: 1) the SCR contain the energy comparable to the total energy of electromagnetic flare radiation ($\le 10^{32}$ ergs); 2) the source spectrum form indicates to a possible acceleration mechanism (or mechanisms); and 3) the accelerated particle are efficiently involved in nuclear electromagnetic and plasma processes in the solar atmosphere. Therefore the data on SCR source spectra are necessary for theoretical description of the processes mentioned and for the formulation of the consistent flare model. Below it is attempted to sound solar particle sources by means of SCR energy spectrum obtained near the Sun, at the level of the roots of interplanetary field lines in the upper solar corona. We consider data from ∿ 60 solar proton events (SPE) between 1956-1981 [1]. These data were obtained mainly by the interplanetary demodulation of observed fluxes near the Earth. Further, we used our model of coronal azimuthal transport to demodulate those spectra, and to obtain the source energy spectra.

2. Interplanetary Demodulation. Several methods are used for the interplanetary demodulation of SCR fluxes observed near the Earth. Most of them are traditionally based on the different modifications of the diffusion model of the full transport equation. In addition, at present the possibility exists to reconstruct the source spectrum by the gamma-ray and flare neutron data. The diffusion methodics of interplanetary demodulation was described in detail in another works [2, 3]. This methodics rest upon the extrapolation of intensity time profiles of SCR fluxes observed near the Earth to the momentum of their injection from the solar corona. Each of modifications of such a methodics is applicable only to a limited time interval or to a limited range of particle energy. Besides that, our Catalogue [1] contains some discrepancies and gaps in spectrum parameter estimations obtained by the different researchers. Because of these reasons we were able to use for the coronal demodulation only the data of 26 events.

3. Coronal Demodulation. The coronal transport model of solar flare particles was discussed in [4] and extensively described in [5]. Basically two transport steps take place in azimuthal coronal transport of particles: (a) a velocity-independent transport in a fast propagation region (FPR) which is associated with an expanding magnetic structure, (b) an energy-dependent transport in a low propagation region (LPR), dominated by transversal diffusion, drifts and gradual escape into the interplanetary space. The initial condition for the 2nd transport state, when particles are globally liberated from the FPR, at t=0 is $N(X,0)=N_a(E)/X_0$, if X is within the width X_0 of the FPR centered at the flare site, and $N(X, 0)=0$ elsewhere, where $N_a(E)$ is the flare source energy spectrum. The azimuthal evolution of the number density of particles at time t and position X during the 2nd transport step is [4, 5].

---

*On leave for the INAOE, Tonanzintla, A.P. 51. 72000-Puebla.México

$$N(X,t)=2.5N_a\exp\left(-\Gamma t-\frac{(X-v_dt)^2+(X_\circ/2)}{8\kappa_\ell t}\right)\left\{\exp\left[\frac{(X-v_dt)(X_\circ/2)}{4\kappa_\ell t}+\frac{(X-v_dt-X_\circ/2)^2}{8\kappa_\ell t}\right]\mathrm{erf}\left(\frac{X-v_dt-X_\circ 2}{(4\kappa_\ell t)^{0.5}}\right)-\exp\left[-\frac{(X-v_dt)(X_\circ/2)}{4\kappa_\ell t}+\frac{(X-v_dt+X_\circ/2)^2}{8\kappa_\ell t}\right]\mathrm{erf}\left(\frac{X-v_dt+X_\circ/2}{(4\kappa_\ell t)^{0.5}}\right)\right\} \tag{1}$$

where κ_ℓ and v_d are the transversal diffusion coefficient and drift velocity. Here after we will refer our results to the flare position (X_f), such that $X_i=X-X_f$. For coronal demodulation we adopted the following procedure. We assume that the observed particle flux proceeds from a coronal longitude at ∿ 60°W; so, at the coronal level the observed flux corresponds at the position $X_c=X(60°W)-X_f$, and an ejection time from the corona (t_e) given as $t_e=0$ if $|X_c|\leq X_\circ/2$ and $t_e=|X_c|/v_d$ if $|X_c|>X_\circ/2$; next we equate (2) with the demodulated energy spectra N(E) from [3], [that for the task of simplicity we translated from rigidity to kinetic energy, Figs.(1) and (2)]:

$$2.5N_a(E)f[\chi_c,t_e,v_d(E),\kappa_\ell(E),X_\circ] = N(E)\ \text{(part/MeV)} \tag{2}$$

so that the source energy spectrum $N_a(E)=N(E)/2.5f[X_c,t_e,v_a,\kappa_\ell,X_\circ]$, where the function f has been normalized. Once we have determined $N_a(E)$ (part/MeV) we build the time-profiles by fixing the positions X_i and energy E_i in eq.(1), and making vary time relative to t_{on}, $(t-t_{on})$, where $t_{on}=(|X_i|/v_d)-X_\circ/2$ is the onset time of particle arrival at that particular position X_i, so that the time-origin occurs at $t=t_{on}$. The coronal time-profiles were built for several coronal positions and energy values. To build the particle azimuthal distributions we fixed energy and time in eq.(1) and evaluated for $X_i\leq\pm180°$ taking the flare position as the coordinate-origin. Further, we evaluated for other times and different energies. For calculations we assumed for the FPR, an azimuthal width at its opening of 80° at 0.9 R_θ above the photosphere. For $v_d=(60-250)\beta^2/(1-\beta^2)^{0.5}$(cm/s) depending on whether the observational peak intensity was very late or early respectively, where $\beta=v/c$, v and c are the particle and light velocities. We used $\kappa_\ell=6.7\times10^6 v(\mathrm{cm}^2/\mathrm{s})$. For the task of illustration we have chosen an event which FPR contains the connecting position X_c(23/VI/1956) and other which FPR does not contain X_c(22/VIII/1958). On the next figures we have illustrated linear azimuthal positions X_i in terms of angular coordinates Ψ_i; on Fig.(2) we show along with the demodulated spectrum the energy spectra that we have built for two others coronal longitudes. On figures(3)-(8) it is shown the azimuthal distributions of both events for several times at three different energies. It can be observed that the observational W-E asymmetry is confirmed by our results: the higher the particle energy the sharped the effect. Theoretically this is the translation of particle drift in the model. On figs. (9)-(11) it is show the time profiles of

ORIGINAL PAGE IS
OF POOR QUALITY

the event for which X_c is outside of its FPR, for 3 different energies and several longitudinal positions: out of the FPR profiles show the characteristic diffusive shape, whereas at locations within the FPR they show a peculiar decreasing shape. On Fig. (12) it is shown the regression in time from the corona back to the top of the FPR: since regression in time is equivalent to regression in distance to the FPR, for a given value of Ψ any other Ψ' such that $\Psi_f<\Psi'<\Psi$ can be seen as a time regression toward the time of particle liberation from the FPR. In fact time profiles at $\Psi_f \pm 40°$ begin at t=0. Out of the FPR the onset is delayed proportionally to the distance from the flare site, such as indicated by observations. Fig.(13) shows the west-asymmetry effect relative to the profile on Fig. (9): at 50°-distance from the flare on the East side there is more of 10^2 time less particles than at the same distance an the West side, and at 60°-distance the flux has fallen to negligeable levels relative to the West side. On figs. (14)-(16) we show time profiles for the 23/11/1956 event. Concerning source energy spectra, it is obvious that according to the coronal transport model the observational and the source spectra are basically the same when the FPR contains the connection longitud. So, among the studied 26 events, only in 8 events the FPR does not contain X_c. We have tabulated on Table 1, the source spectra characteristics of these 8 events along with one (23/11/1956) of the remaining 18 events where $N_a=N(E)$. On Fig.(17) we show the source spectrum $N_a=D_o E^{-\gamma}=4.18\times10^{45}E^{-6.36}$ (part./MeV) of the 22/VIII/1958 event. Finally, on Fig. (18) it is illustrated the source spectrum $N_a/\delta\Psi_f$ (part./MeV cm) under the assumption of a finite flare width $\delta\Psi_f=8°$ and the spectrum at the top of the FPR at t=0, $N(X,t,E)=N_a/X_o$ (part./MeV cm).

4. Conclusions. Though results are model-dependents they furnish a clear picture of the evolution of particle energy spectra from the source till their ejection into the interplanetary space, for those events where the observational-connecting-longitude is out of the FPR: it can be seen in Table 1 that energy spectra flattens at the coronal level relative to the source spectra; when particles move in the W-E direction, as in the 1/IX/1971 event, the change in spectrun slope is more important. It is interesting to analyze our results within the frame of the observational effects and model predictions sumarized in [5]. We believe that this approach must be taken into account within the frame of solar particle acceleration theory and solar flare phenomena, such as for the evaluation of flare neutrons and electromagnetic radiation of non-thermal origin.

References

[1] Miroshnichenko, L.I., Preprint IZMIRAN, 15, 548, 1985.

[2] Miroshnichenko, L. I., Geomagn. and Aeron, 13, 26, 1973.

[3] Miroshnichenko, L. I. et al., Dynamics of Radiation Conditions in Space, Energoatmizdat, Moscow, 1985 (with Petrov V.M.)

[4] Pérez-Peraza, J. and Martinell, J., Proc. 17th Int. Cosmic Ray Conf. 3. 55, 1981.

[5] and Pérez-Peraza J. in Invited Lecture, 9th European Cosmic Ray Simposium, Kosice, 1985.

		CORONAL			SOURCE Na	
EVENT	LONGI-TUDE	RANGE MeV	Dc PART/MeV	γ_E	Do PART/MeV	γ_E
23/02/1956	23N80W	35 - 480	2.10E37	1.27	2.1E37	1.27
22/08/1958	18N10W	15 - 115	5.77E39	3.74	4.1E45	6.36
03/09/1960	18N89E	10 - 410	2.91E36	2.02	1.4E53	8.76
29/09/1961	13N29E	15 - 470	1.97E39	3.20	4.6E53	8.76
28/01/1967	150E	75 - 410	5.16E34	1.25	1.1E40	3.11
29/09/1968	13N13W	10 - 160	1.04E34	1.18	2.8E43	5.76
01/09/1971	12S130W	10 - 55	1.43E39	2.25	4.9E45	6.33
28/05/1972	09N30E	30 - 75	1.22E37	2.62	4.1E40	4.14
--'--'----	-'--'-	30 - 120	1.00E3[illegible]	2.20	2.6E38	4.03

ORIGINAL PAGE IS
OF POOR QUALITY

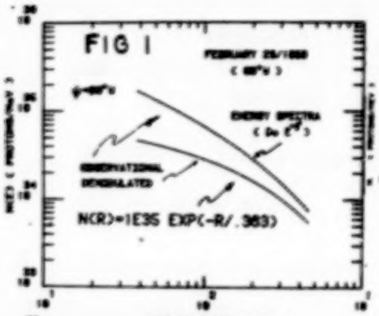
FIG 1

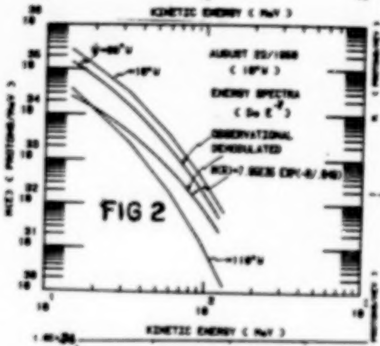
FIG 2

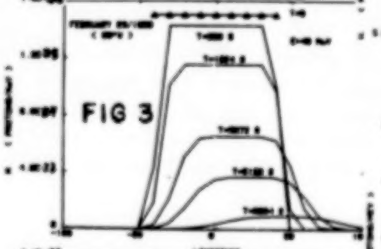
FIG 3

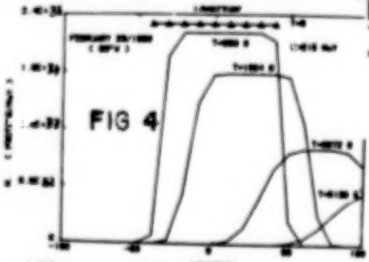
FIG 4

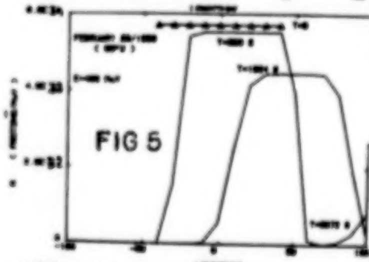
FIG 5

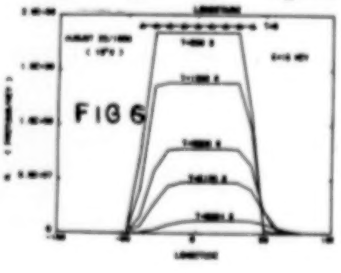
FIG 6

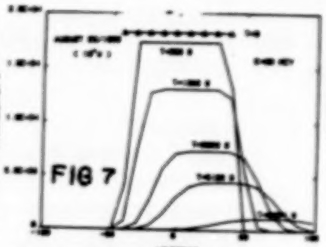
FIG 7

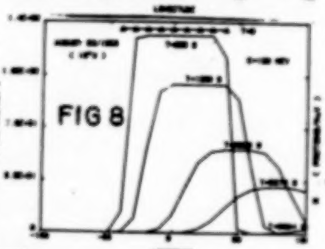
FIG 8

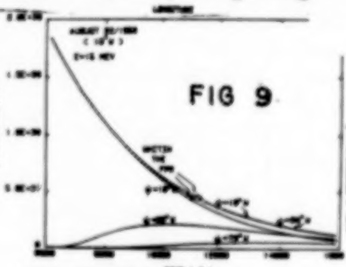
FIG 9

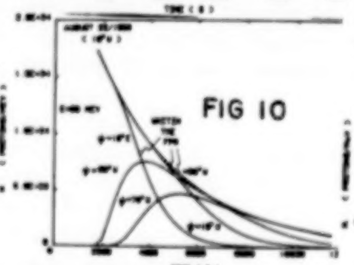
FIG 10

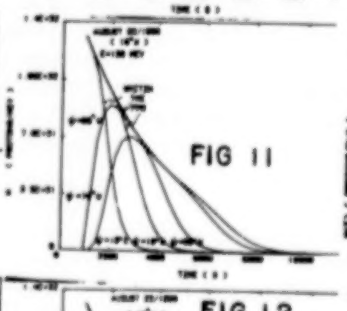
FIG 11

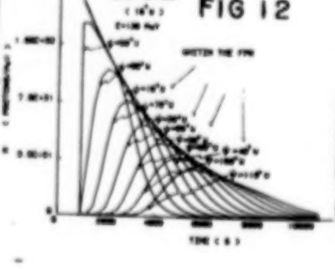
FIG 12

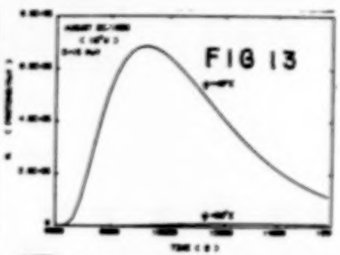
FIG 13

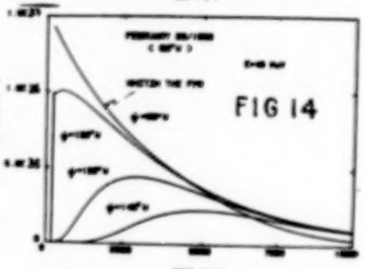
FIG 14

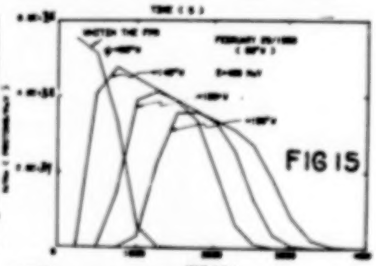
FIG 15

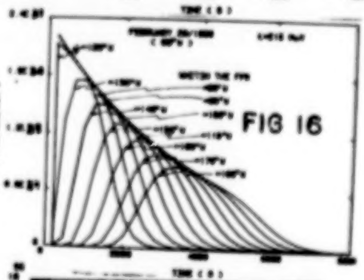
FIG 16

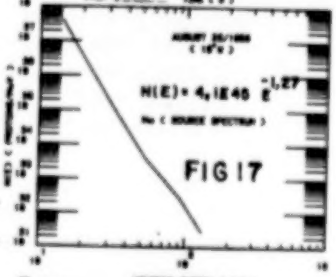
FIG 17

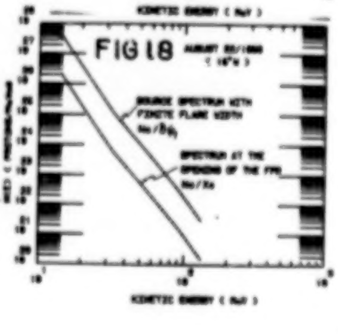
FIG 18

N85-34759

SH 1.3-14

SPECTRA OF SOLAR PROTON GROUND LEVEL EVENTS USING NEUTRON MONITOR AND NEUTRON MODERATED DETECTOR RECORDINGS

P.H. Stoker
PU-CSIR Cosmic Ray Research Unit
Department of Physics
Potchefstroom University for CHE
POTCHEFSTROOM 2520
South Africa

ABSTRACT

Recordings on relativistic solar flare protons observed at Sanae, Antarctic, show that the percentage increase in counting rates of the neutron moderated detector (4NMD) is larger than the percentage increase in counting rates of the 3NM64 neutron monitor. These relative increases are described by solar proton differential spectra $j_s(P) = AP^{-\beta}$. The power β is determined for each event and the hardnesses of the temporal variations of β, found for the GLE's of 7 May, 1978 and 22 November, 1977, are related to the results of Debrunner et al. (1980).

1. Introduction. Neutron monitors record at ground level solar protons of energies $\gtrsim$ 0.5 GeV, while satellite data generally covers the energy range below 0.5 GeV. Debrunner et al. (1984) combined the two sets of observations for the solar proton events on 7 May, 1978 and 22 November, 1977, and deduced for various phases the solar proton energy spectra from 50 MeV to about 10 GeV.

These two events and several other solar proton events were recorded during the present solar cycle at Sanae with a cutoff rigidity of 0.86 GV in Antarctica. When looking at an event from only a single position on Earth, a particular spectral function has to be assumed in order to deduce the spectrum of solar protons entering the atmosphere. Since rigidity is the appropriate parameter for the combined effect of protons, α-particles and heavier particles for earth bound recordings, a rigidity dependent spectral function was considered. A power law rigidity spectrum $j = AP^{-\beta}$ appears to fit the spectra given by Debrunner et al. (1984) in the rigidity range ~ 0.5 GV - 10 GV better than the exponential rigidity spectrum $j = A \exp(-P/P_o)$.

The neutron moderated detector 4NMD and super neutron monitor 3NM64 record at Sanae primary cosmic rays with different rigidity dependent sensitivities. In order to derive solar proton spectra for ground level events from these recordings, the specific yield functions of these two detectors have to be obtained accurately for rigidities $\gtrsim$ 1 GV. Solar proton ground level events recorded at Sanae during the present solar activity cycle are analyzed accordingly in this paper.

2. Method. A specific yield function was computed for each detector from $S(P) = n(P,t)/j(P,t)$. The primary differential rigidity spectrum $j(P,t)$ was obtained from the 1965 cosmic ray proton and helium particle spectra compiled by Webber (1973), while the differential response functions $n(P,t)$ were deduced from a least square fitting (Van der Walt, 1983) of the Dorman function $N(P) = N_o(1-\exp(-\alpha P^{-k}))$ to the data of the 1976 sea level survey (Potgieter et al., 1980). The differential response functions for the NMD

and NM64 thus obtained were applied to reproduce correctly the relative counting rates recorded for the 15 February, 1978 Forbush decrease (Stoker and Louw, 1983).

If $j_s(P,t)$ represents the primary solar proton differential spectrum, the enhanced counting rate due to a solar proton GLE is given by

$$\Delta N_s(P,t) = \int_{P_c}^{\infty} S(P) j_s(P,t) dP$$

with $j_s(P) = AP^{-\beta}$. The ratio of the enhanced counting rates recorded by the two detectors then becomes

$$\frac{\Delta N_s^{NMD}}{\Delta N_s^{NM64}} = \frac{\int_{P_c}^{\infty} S^{NMD} P^{-\beta} dP}{\int_{P_c}^{\infty} S^{NM64} P^{-\beta} dP}$$

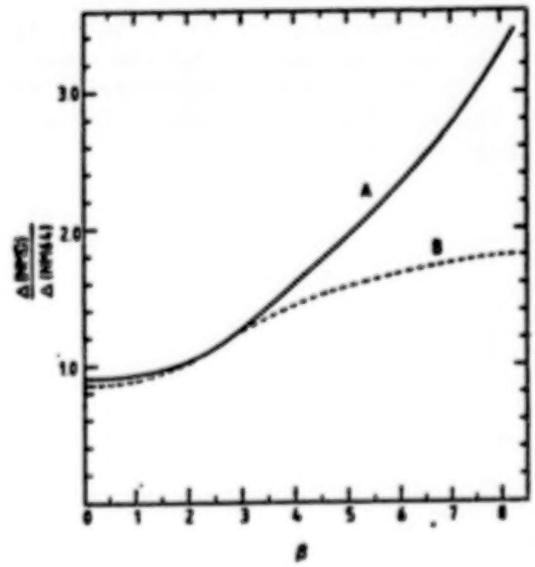

Figure 1

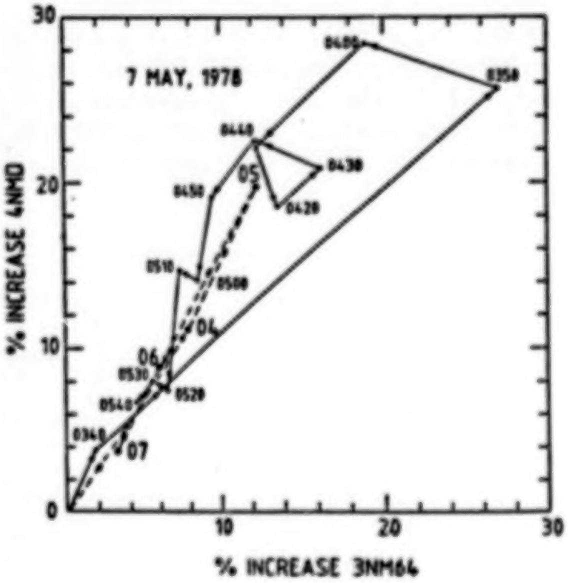

Figure 2

In Figure 1 the calculated ratio of enhanced counting rates is shown as a function of the power β, with P_c = 0.86 GV. The constants of the Dorman function used in calculating S(P) are N_o = 151.67, α = exp 2.13 and k = 0.894 for the 3NM64, while for the 4NMD the values are N_o = 157.68, α = exp 1.99 and exp 2.06, k = 0.898 and 0.940 respectively for the solid and broken lines A and B in the Figure. For both of these two sets of constants the Dorman functions lie within the statistical regression limits determined from fittings to latitude survey data for the NMD. The ratio of enhanced counting rates is not 1.00 for β = 0 because the two differential response functions for the 4NMD and that of the 3NM64 are normalized at P = 17 GV. The two curves in Figure 1 are considered to present the upper and lower limits of the ratio of the enhancements at a particular power β.

3. The GLE of 7 May, 1978. In Figure 2 the enhanced pressure corrected ten minute and hourly counting rates for the 4NMD are plotted as a function of the similar counting rates of the 3NM64, for the GLE of 7 May, 1978. The galactic contributions have been normalized to 100. From this Figure it follows that the first particles arrived at Sanae in the time interval 0335-0340 UT (signified by 0340) followed by a fast rise in counting rates during 0340-0350 UT. With ΔNMD/ΔNM64 = 0.95 for the enhancement until 0350 UT, $\beta \approx 1.3$, suggesting a flat initial spectrum, which presumably is the result of the earlier arrival of the more energetic protons. Subsequently the intensity of the slower particles are increasing, causing the displacement in the plot from 0350 to 0400, with the ratio ΔNMD/ΔNM64 changing to 1.49, giving $\beta = 3.4-3.5$ from Figure 1 for curves A and B respectively. After 0400 the solar proton spectrum becomes even softer. The average of the enhanced counting rates for the hour 0400-0500, indicated by 05 in the Figure, represents a ratio ΔNMD/ΔNM64 1.63, giving $\beta = 3.8-4.2$. At 0450 UT ΔNMD/ΔNM64 = 1.99, and $\beta = 4.9$ for the upper curve A in Figure 1.

When the 7 May, 1978 solar proton spectra of Debrunner et al. (1984), for the rigidity interval of about 0.8 - 5 GV, are represented by the power law $J_s \propto P^{-\beta}$, the power values are $\beta \approx 3.3$, 3.6, 4.0 and 4.9 respectively for the time periods 0335-0345, 0345-0400, 0400-0415 and 0430-0500. These values are about the same as we have obtained from Figure 1.

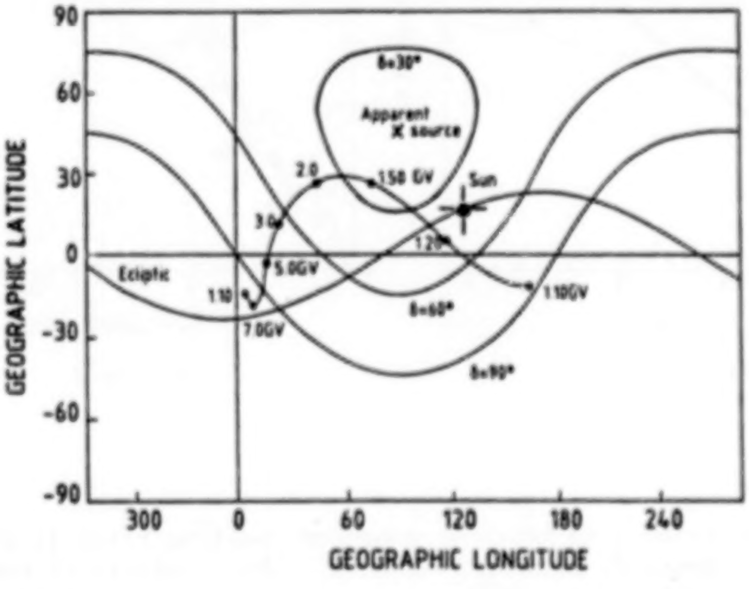

Figure 3 is in part a reproduction of Figure 3 of Debrunner and Lockwood (1980). The apparent source position and contours for angular distances of 30°, 60° and 90° are shown for the 7 May, 1978 event. Added to the Figure are the asymtotic directions of vertical incident particles for Sanae (Shea and Smart, 1971). From this Figure follows that the proton spectrum incident on top of the atmosphere at Sanae should be equivalent to the free space spectrum at 1 AU.

N85-34760

4. The GLE of 22 November, 1977. In Figure 4 the enhanced pressure corrected ten minute and hourly counting rates for the 4NMD are plotted as a function of corresponding counting rates of the 3NM64 for the GLE of 22 November, 1977. Here again the spectrum appears to soften from the eleventh to the twelfth hour UT. The ratio ΔNMD/ΔNM64 for the first ten minutes 1010-1020 UT is ~0.9, suggesting $\beta \lesssim 0$, presumably again due to the earlier arrival of the more energetic protons. The ratio ΔNMD/ΔNM64 = 1.30 at 1030 which is also the average for the hour 1000-1100, implies $\beta = 2.7 \pm 0.1$. At 1040 the ratio of the enhancements = 1.41, with $\beta = 3.1$. For the decaying phase of this event the ratios of the enhancements show fluctuations around these values. For 1050-1100, ΔNMD/ΔNM64 = 1.23, and $\beta = 2.5$; 1100-1110, the ratio increased to 1.48 and β to 3.4. For the twelfth and thirtienth hour, the average ratio = 1.38 and $\beta = 3.0$.

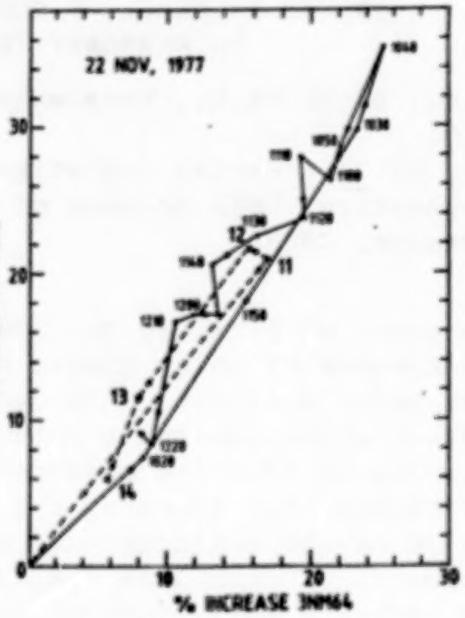

When representing the 22 November, 1977 solar proton spectra of Debrunner et al. (1984) by a power law for the rigidity range ~ 1 - 6 GV, the power values are $\beta = 5.5$, 4.6 and 4.9 respectively for the time periods 1035-1046, 1055-1105 and 1200-1215. These values are larger than we found, but the fluctuations in hardness follow the same trend as we are observing. The lower power values deduced for Sanae may be attributed to an apparent source direction to the left 0° geographic longtitude in Figure 3, favouring the higher rigidity protons to enter the atmosphere. Thus a harder solar proton rigidity spectrum was possibly incident at Sanae comparing to the free space spectrum as 1 AU.

5. Conclusions. Spectra of relativistic protons recorded at Sanae may be deduced from the relative enhancements in counting rates of the 4NMD and 3NM64 detectors. For GLE solar proton spectra of 23 September, 1978, 8 December, 1982 and 16 Februarie, 1984 average powers $\beta = 4.5 \pm 0.2$, 2.8 ± 0.1 and 2.6 ± 0.1 were obtained respectively.

Acknowledgements. The financial controbution and logistic support by the Department of Transport for Antarctic research are gratefully acknowledged.

References

Debrunner, H., Flückiger, E., Lockwood, J.A. and McGuire, R.E., J. Geophys. Res. 89, 769, 1984.
Debrunner, H., and Lockwood, J.A., J. Geophys. Res. 85, 6853, 1980.
Potgieter, M.S., Raubenheimer, B.C., Stoker, P.H., and Van der Walt, A.J., S. Afr. J. Phys. 3, 77, 1980.
Shea, M.A., and Smart, D.F., AFCRL-TR-75-0247, May, 1975.
Stoker, P.H., and Louw, P.A., 18th ICRC, Bangalore, Conf. Papers 4, 181, 1983.
Van der Walt, A.J., 18th ICRC, Bangalore, Conf. Papers 10, 287, 1983.
Webber, W.R., 13th ICRC, Denver, Conf. Papers 5, 3568, 1973.

N85-34760

GROUND INCREASE OF COSMIC RAY INTENSITY ON FEBRUARY I6, I984

Belov A.V., Blokh Ya.L., Eroshenko E.A., Ishkov V.N., Yanke V.G.
Institute of Terrestrial Magnetism, Ionosphere and Radio Wave Propagation, USSR Academy of Sciences, I42092 Troitsk, Moscow Region, USSR

The event of February I6, I984 is one of the two largest ground increases of solar cosmic rays (CR) in the last two cycles of solar activity. This event happened at a decrease of the 2I-st cycle against a quiet background. Although at the beginning of I984 the observed indices of solar activity /I/ were higher than those at the end of I983, the day of February I6 may be characterized as very quiet. On that day the geomagnetic perturbance ($\sum K_p$=I4, A_p=7) was the lowest in February. After a small Forbush decrease due to the magnetic storm of February I2-I3, the CR intensity almost completely recovered by February I6. Thus, the solar particles that came to the Earth on February I6 got into a practically unperturbed magnetosphere, and the variations of secondary CR induced by these particles were nor superimposed on any other substantial variations of extraterrestrial or magnetospheric origin.

In the first half of February I984 the solar flare activity was determined mainly by two active regions and was at a rather low level. This activity was somewhat hightened beginning from February 9, when the two active regions, AR 4408 (CD 25: S I2 L 340) and AR 44I3 (CD 30: S I4 L 264) increased sharply in size and within 3 days each gave two flares of medium force. The second of the active regions rapidly lowered its activity and went beyond the western disk on February I9, I984 and practically died away. The region AR 4408 went behind the disk increasing its area, it was in the phase of increasing activity. The activity of the region AR 442I on the eastern disk did not give noticeable effects in CR observed on the Earth.

The solar flare responsible for the ground increase of solar CR on February I6 occurred most probably in the region AR 4408 three days after it went behind the western disk. That the flare occurred far beyond the disk is probably the most important specific feature of this event. Due to this, besides the CR from the indicated flare, it was only radio emission that reached the Earth, no emission at all being observed in the optical, UV, X-ray and γ -ranges.

According to radio data, the flare of February I6 occurred not later than 0858 T and was accompanied by intensive bursts of types IV, III, and II. For this event the western disk is a screen for all emissions that occur below ~150 10^3km. The microwave burst was therefore small, whereas in the metric wave band, for which the radiation source is high in the corona, the event was rather powerful.

Figure I presents ground increases of February 16 for a number of neutron monitors of the world-wide net (five-minute data). The time of the beginning of the increase differs strongly for different stations. But within the second five-minute interval of the tenth hour (0905-0910 UT) a large effect was observed already for several stations. Analizing the time variation of the counting rate for different monitors, one can obtain the following estimate of the time of arrival of first solar particles to the Earth: t_i=(0906 ± 01) UT. Thus, if one does not assume the existence of an essential delay of radio bursts relative to the time of CR generation, one may state that having rapidly overcome the 60-degree's difference between the heliolongitude of the flare and IMF lines passing near the Earth, the first flare protons came to the Earth, in fact, without any delay.

Figure 2 presents the data of the neutrino monitor onthe ship "Academician Kurchatov" which was at that time in the Atlantic Ocean at the point with coordinates (at 0900 UT) 46° 11'N, 53°02'W. By means of interpolation of the calculations made by Shea and Smart /2/, we estimated the vertical cutoff rigidity for this point to be R_c = 1.62 GV.

By many characteristics the flare of February 16, 1984 turned out close to the largest ground increase of the last cycle, to the event of May 7, 1978. In both cases one should note a rapid arrival of particles from the Sun, a small duration of the increase, a fast rise (< 10 min. for stations with a large cutoff rigidity) and a sharp decrease of intensity. The decrease of intensity on the ship "Academician Kurchatov" can be represented in the period 0915-1015 UT in the form exp $(-t/\tau)$, where τ = 15 m (Fig.2).

The increase of February 16, 1984, the same as the increase of May 7, 1978 is characterized by a large (close to 100 %) degree of anisotropy. The anisotropic phase of the flare was positive and occupied almost the whole period when the increase was large. The largest effect was observed in the stations, which at 9 h UT "looked" along the IMF lines towards the Sun. North-American stations and the research ship "Academician Kurchatov" appeared to be in an advantageous position for recording the ground increase. The dependence on the longitude and latitude of the point of observation turned out to be even stronger than the dependence on the cutoff rigidity, and the value of the increase (57.4 %) on the research ship "Academician Kurchatov" (R_c = I.62 GV) exceeded, in particular, the value of the increase in high-latitudinal stations Alert and Thule (R_c = 0.00 GV) situated in the same longitudinal zone /I/.

The large anisotropy of the effect and the large duration of its anisotropic phase do not allow us in this case to determine the form of the energy spectrum of the solar CR which came to the Earth by analyzing the dependence of the increase on the cutoff rigidity. In this case the analysis of the distribution of the effect on neutrons of different multiplicity /4/ may prove to be the most effective means for determining the slope of the energy spectrum. The observations of multiple neutrons were carried out in an expedition on the research ship "Academician Kurchatov".

It seems to us that the arrival to the Earth of charged particles from a flare beyond the disk can be explained by a particle drift in the neutral layer of heliomagnetosphere. By the indirect magnetospheric data /I/, on February I6 the Earth was in the positive sector of IMF, and the neutral layer was crossing the helioequator plane 40-50° to the west. The line of force which goes out of the flare region of heliolatitude ~s IO can come closer to the neutral layer, which at this heliolongitude must be projected onto the southern hemisphere of the Sun. Having drifted about 60° eastward (the drift of protons in I984 in the neutral layer near the Sun must have just this direction), the protons could get (already in the northern hemisphere) onto the IMF line which was coming to the Earth. The hypothetic way of charged particles from the flare of February I6 to the Earth is shown in Fig.3.

REFERENCES

I. Solar Geophysical Data, 476, Part I, I984, Boulder, Colorado, USA 80303.

2. Shea M.A., Smart D.F., Proc. I8-th ICRC, v.3, 4I5, I983.

3. Belov A.V., Blokh Ya.L., Gushchina R.T., Dorman L.I., Eroshenko E.A., Inozemtseva O.I., Kaminer N.S. Libin I.Ya. Izv.AN SSSR, ser.fiz., 43, I2, 25I2, I979.

4.Dorman L.I. Experimental and Theoretical Bases of Cosmic Ray Astrophysics. Moscow, Nauka, I975.

ORIGINAL PAGE IS
OF POOR QUALITY

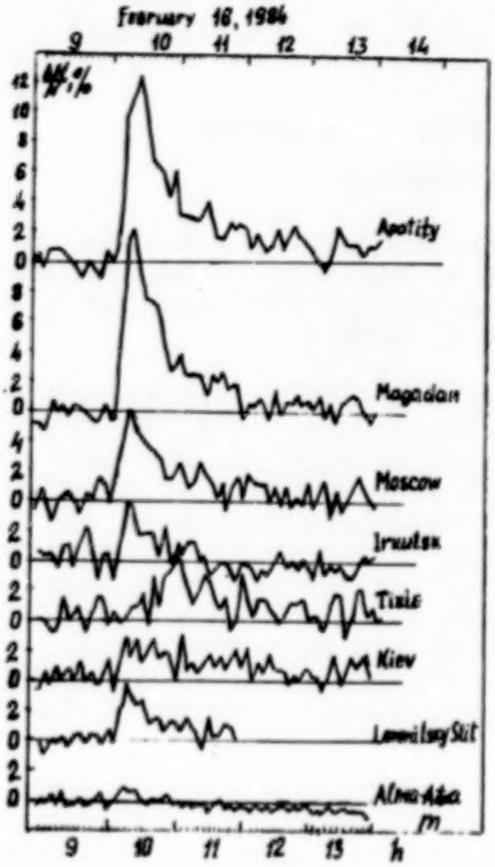

Fig. 1

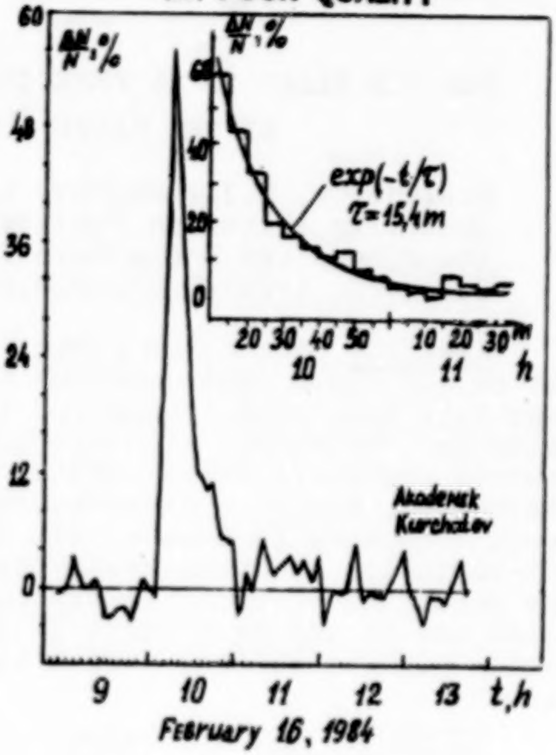

Fig. 2

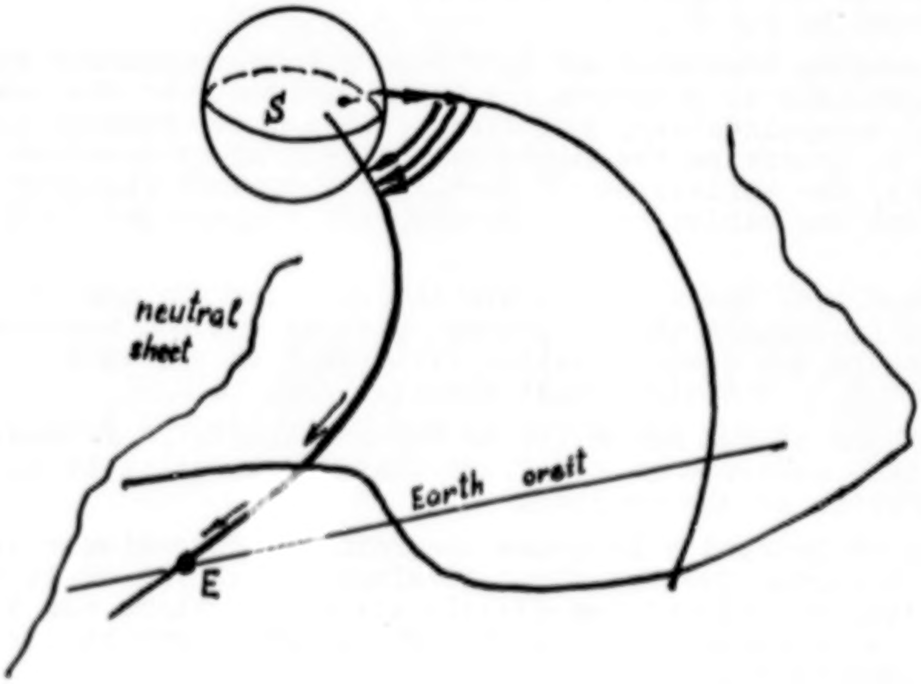
S
neutral sheet
Earth orbit
E

Fig. 3

N85-34761

SH 1.3-17

THE SCR FLARE OF 16 FEBRUARY 1984 AS RECORDED BY THE SAYAN SPECTROGRAPH

S.A.Kozlov, N.I.Pakhomov, L.A.Shapovalova, A.L.Yanchukovsky (Siberian Institute of Terrestrial Magnetism, Ionosphere and Radio Wave Propagation, USSR Academy of Sciences, Irkutsk 33, P.O.Box 4, USSR)

ABSTRACT. The Sayan cosmic ray (CR) spectrograph recorded an SCR flare that occurred on 16 February 1984. We present data from both 1-hour and 10-minute duration measurements in 10 channels with different energy sensitivity (of neutron monitors HM-64 located at different depths in the atmosphere, and of a neutron, multiple neutron and rigid mu-meson component lead-less detector). The parameters of the SCR variation spectrum are evaluated and it is shown that the recording of multiple neutrons at the same geographic point and at the same level in the atmosphere provides information similar to that from a spectrographic complex of instruments.

INTRODUCTION. The Sayan CR spectrograph /1/ is designed to provide data on the CR variations in different portions of the primary spectrum. This is achieved through: recording two components of secondary cosmic radiation (nucleon and muon), spacing the detectors in the depth of the atmosphere and the different geometry of neutron detectors. The CR geomagnetic cut-off rigidity at the site where the detectors are located is 3.9 GV.

A complex treatment of spectrographic measurements makes it possible to separate the CR variations into the components of interplanetary, magnetospheric and atmospheric origin and to determine the parameters of a primary spectrum ($\Delta D / D$), the variations of geomagnetic cut-off rigidity (ΔT) and the variations of atmospheric temperature (ΔR_c) /2/.

Since 1983 the spectrograph incorporates the 6HM-64-selector instrument that provides multiple neutron records according to two discrimination criteria " $\geq m$ " and " $= m$" (m - neutron multiplicity) /3/.

RESULTS OF THE RECORDING OF THE SCR FLARE. In February 1984, there occurred an SCR flare that was recorded by all the detectors of the complex.

The CR intensity increase according to five-minute measurements lasted for the first 10 minutes 10:00 UT on 16 February 1984 and almost immediately afterwards there was the onset of a decrease which, within 25 minutes, reached 1/2 its maximum value.

Table 1 summarizes the results of measurements of SCR flare amplitudes.

In order to intercompare the values of the amplitudes recorded, these are also plotted in Fig. 1. Straight line "A" indicates the values of flare amplitudes with five-minute intervals of averaging. These are recorded data on the neutron component obtained by three detectors HM-64 located at 3000, 2000 and 435 m above sea level and results of measurements of multiple neutrons at 3000 m according to the discrimination criterion of $m \geqslant 1$ and $m \geqslant 2$. The values of amplitudes for one-hour intervals of the neutron component measurements as recorded by the lead-less detector and HM-64 instruments at different depths of the atmosphere, the values of multiple neutrons according to the discrimination criteria of $m \geqslant 1$, $m \geqslant 2$, $m = 1$, $m = 2$, and $m = 3$ and of the values of the rigid mu-meson component are indicated on straight line "B".

Table I

Instrument (component)	Height above sea level of detector, m	Flare amplitude (in %) at different times of data averaging		
		5 minutes	10 minutes	1 hour
Lead-less detector	3000	-	-	3.3±0.2
6HM-64	3000	5.2±0.4	4.8±0.3	2.6±0.1
12HM-64	2000	4.7±0.4	4.5±0.3	2.4±0.1
18HM-64	435	4.0±0.5	4.0±0.4	2.2±0.2
Rigid mu-meson	435	-	-	0.0±0.2
6HM-64	3000	-	-	2.6±0.1
$m \geqslant 1$	3000	5.0±0.4	4.8±0.3	2.5±0.1
$m \geqslant 2$	3000	4.6±1.0	4.6±0.7	2.2±0.3
$m = 1$	3000	-	-	2.6±0.1
$m = 2$	3000	-	-	2.5±0.3
$m = 3$	3000	-	-	1.5±0.8

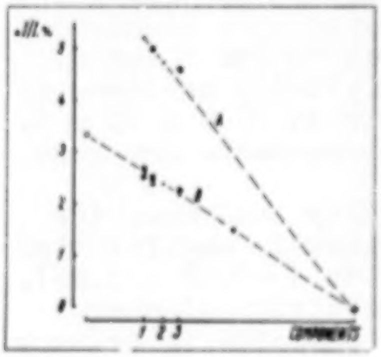

Fig. 1. Dependence of the recorded amplitudes of the SCR flare for five-minute (A) and one-hour (B) data of averagings. • - flare amplitude in the neutron component, as recorded by standard instruments at different depths in the atmosphere: 1 - 3000 m, 2 - 2000 m, 3 - 435 m; ○ - amplitude in the neutron component, as recorded by the lead-less detector; ● - amplitude in the total count rate of neutrons, as measured by the instrument 6HM-64-selector; flare amplitudes in multiple neutrons:

● - $m \geq 1$, ⬟ - $m \geq 2$, ▶ - $m = 1$, ▲ - $m = 2$, ◀ - $m = 3$; ✚ - flare amplitude, as measured in the rigid mu-meson component).

EVALUATION OF PRIMARY SPECTRUM PARAMETERS DURING THE FLARE. The analysis of the ratio of increase amplitudes averaged over a one-hour interval to those recorded by different detectors of the complex reveals that the energy spectrum of the variations for particles incident on the atmospheric boundary over Irkutsk cannot be represented by a simple exponential function. Thus, from the ratio of the amplitudes recorded by the neutron exponent of the exponential spectrum γ must be ~ 0.35 while for detectors 6HM-64 (3000 m) and 18HM-64 (435 m), $\gamma \sim 0.7$. With such values of γ, the effect of CR intensity increase was to be observed in the rigid mu-meson component. However, no such effect was recorded. It is interesting to note that according to the ratio of the amplitudes in 6HM-64 (3000 m) and 18HM64 (435 m) averaged over the five-minute interval for a maximum SCR flux, the exponent of the spectrum was found to be ~ 1.7.

The observed peculiarities of the variation spectrum seem to be due to a significant anisotropy of the SCR flux density. In this case, because the particles of various energies have different asymptotic directions, the energy spectra of the particles arriving at the boundary of the atmosphere will depend on the location of the recording point, on local time and on SCR anisotropy characteristics. Within these considerations it is possible to explain both the anomalies in the spectrum of particles at some or another point of the Earth's surface and their dependence on the time interval of data averaging (on account of the anisotropy dynamics).

COMPARATIVE ANALYSIS OF THE MEASUREMENTS FROM THE SAYAN SPECTROGRAPH AND THE INSTRUMENT 6HM-64-SELECTOR. The instrument 6HM-64-selector is designed to record multiple neutrons of up to $m \geq 6$ and $m = 6$.

An increase in CR intensity in the channels recording multiple neutrons during the flare was observed up to $m = 3$ (channel $m \geq 3$ was not operative during this period).

A comparison of the amplitudes recorded during the flare by the Sayan spectrograph and the instrument 6HM-64-selector reveals that the amplitude measured by a standard neutron monitor 18 HM-64 at 435 m is equal to the value of the intensity increase of secondary multiplicity neutrons as measured by the instrument 6HM-64-selector at 3000 m ($m \geq 2$, see Fig. 1). Temporal profiles of these components are also quite similar (see Fig. 2).

For the recording of third-multiplicity neutrons, the amplitude value is 1.5 % which is significantly smaller than that measured by a standard neutron monitor ($\Delta J/J = 2.6\%$). This indicates a shift of the energy sensitivity of channel "$m = 3$" towards the region of larger energies of primary particles.

N85-34762

ORIGINAL PAGE IS
OF POOR QUALITY

CONCLUSIONS. The SCR flare of 16 February 1984 showed a significant CR anisotropy which makes it difficult to represent the primary CR variation spectrum using a simple exponential function.

The SCR amplitude as measured at 3000 m and by recording multiple neutrons according to the discrimination criteria of $m \geqslant 1$, $m \geqslant 2$, $m = 1$, and $m = 2$, correspond to those recorded by standard neutron monitors at 3000, 2000 and 435 m.

The energy sensitivity of third-multiplicity neutrons (as compared with measurements of the neutron component by standard detectors HM-64) is shifted towards the region of larger energies of primary CR.

The recording of multiple neutrons at 3000 m provides information about CR variations similar to that from the Sayan CR spectrograph.

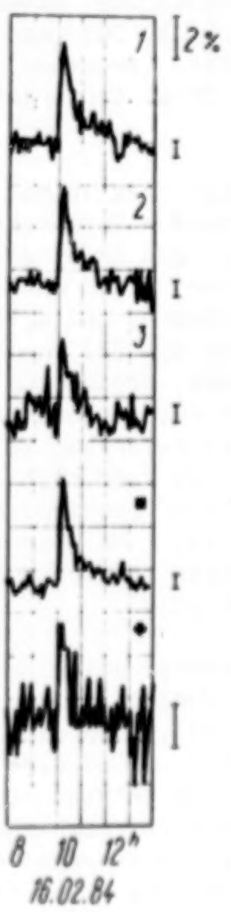

Fig.2. Results of recording the 16 February 1984 SCR flare from five-minute duration measurements with the Sayan spectrograph and the instrument 6HM-64-selector. 1, 2, 3 - neutron component as measured by standard neutron monitors at 3000, 2000 and 435 m, respectively; ■ ◆ - multiple neutrons as measured at 3000 m according to the discrimination criterion of $m \geqslant 1$ and $m \geqslant 2$, respectively (measurement errors are shown at right).

REFERENCES

1. A.L.Yanchukovsky, A.A.Luzov, A.V.Sergeev. A spectrographic complex of instruments for studying the cosmic ray intensity variations. - In: Issl. geomagn., aeron. fiz. Solntsa, v.20, Irkutsk, Nauka, 1971, p.389-395.

2. V.M.Dvornikov, Yu.Ya.Krestyannikov, V.E.Sdobnov, A.V.Sergeev. Informativity of the spectrographic method. Izv. AN SSSR, 44, 1980, p.2640-2644.

3. A.L.Yanchukovsky, V.L.Yanchukovsky. An adaptive method of recording cosmic ray variations. - In: Issl. geomagn., aeron. fiz. Solntsa., v.68, Moscow, Nauka, 1984, p.201-210.

TIME EXTENDED PRODUCTION OF NEUTRONS DURING A SOLAR FLARE

Chupp, E. L., Forrest, D. J., Vestrand, W. T.
University of New Hampshire, Durham, NH 03824, USA

Debrunner, H., Flückiger, E.
Universität Bern, Bern, Switzerland

Cooper, J. F., Kanbach, G., Reppin, C.
Max-Planck-Institute für extraterrestriche Physik, 8046 Garching, FRG

Share, G. H.
E.O. Hulburt Center for Space Research, Naval Research Laboratory,
Washington, D.C. 20375, USA

1. Introduction. The most energetic neutral emissions expected from solar flares are γ-rays (>10 MeV) from relativistic primary and secondary electron bremsstrahlung, from π^0 meson decay, and from neutrons (>50 MeV). Bremsstrahlung photon energies extend to that of the highest energy electron present, but the shape of the the π^0 γ-ray spectrum, peaking at 69 MeV, does not depend strongly on the proton spectrum above threshold, which is ~292 MeV for meson production on protons. The highest energy neutrons observed indicate directly the highest energy ions which interact at the Sun, and the presence or absence of an energy cutoff in the acceleration process. The high-energy proton spectrum shape can be determined from the neutron spectrum.

Detection of solar neutrons at the Earth with energies from 10 MeV to 1000 MeV have been reported from observations by the Gamma-Ray Spectrometer (GRS) on the Solar Maximum Mission (SMM) satellite (1,2), and from ground level neutron monitors (3), and through observations of the neutron-decay protons (4,5,6). By the use of new Monte Carlo calculations of the neutron and γ-ray responses of the SMM GRS (7) we have reevaluated the GRS neutron observations taking into account the effect of continuous production of rays and neutrons. This analysis has been carried out for two intense major solar flares; on 1980 June 21 and 1982 June 3, hereafter referred to as event I and II. The γ-ray results are given in (8). We find that the revised neutron efficiencies and background determination require some modification of the neutron results reported for event I (1). We also find that when continuous production of neutrons is taken into account that previous interpretation regarding event II must be revised (2,3).

2. Methods. We first reestablish that the SMM GRS high-energy detector has detected a neutron flux in the delayed phase of the 1980 June 21 impulsive limb flare. The high-energy detector portion in the SMM GRS, described in (9), consists of the 7 NaI elements and a single 24 cm X 7.5 cm CsI element, and records energy loss events in all elements, in 4 windows between 10 MeV and 100 MeV. In Figure 1 we show the excess GRS count rate in high-energy elements for energy losses > 10 MeV. These excess rates are averaged over 65.54 s and are found by subtracting a measured background from the total GRS counts obtained during the flare. The principal characteristic in this plot is that the high-energy excess count rate rises steadily after the impulsive phase has fully terminated at 0122 UT. Since there is an absence of excess counts after this time at all energy losses (< 10 MeV), we

ORIGINAL PAGE IS
OF POOR QUALITY

attribute these excess counts to the arrival of solar neutrons at the SMM GRS. If a short burst of neutrons were released at the Sun during the impulsive phase, the count rate grows with time as progressively lower energy neutrons arrive at the Earth. This interpretation is the same as given earlier for this event (1) but we can now compare the GRS observations with the results of the Monte Carlo calculations of the GRS response (7), which predict that energy loss events due to high-energy neutrons should be confined to individual detector elements rather than produce simultaneous losses in both NaI and CsI. On the other hand, any γ-ray spectrum will produce a significant fraction of "mixed" events; that is, energy loss in both the NaI and CsI detector elements.

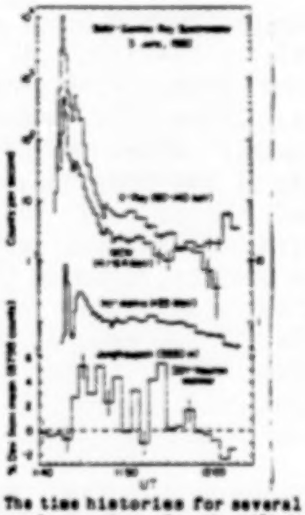

Fig. 3. The time histories for several GRS data channels are shown for the 1982 June 3 flare (event II) at 1143 UT and the corresponding response from the Jungfraujoch neutron monitor.

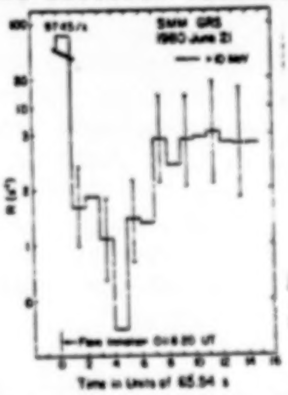

Fig. 1. GRS High-Energy detector average excess count rate during and after the impulsive limb flare at 0118:20 UT on 1980 June 21. The main impulsive phase at all energies occurs within the first time interval indicated but extends for about 3 minutes for all events > 10 MeV. The neutron event commences in interval 5.

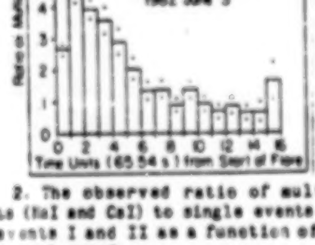

Fig. 2. The observed ratio of multiple events (NaI and CsI) to single events (CsI) for events I and II as a function of time during each event.

In Figure 2 we show, for events I and II, the observed behavior of the ratio of "mixed" high-energy events to those in the CsI element alone (above 25 MeV energy loss) from the impulsive phase until the end of the daylight portion of the flare orbit. During event I this ratio is initially about (0.3-0.4), but during the delayed phase it falls to 0.047 ± 0.023 when averaged over a full 10 minutes of delayed emission. For a spectrum due only to π^0 γ rays and the associated meson decay electron bremsstrahlung, this ratio is expected to be rather large, 0.5-0.6, while primary electron bremsstrahlung spectra give a ratio ranging from 0.4-0.1 for power laws with exponents 1 to 5, respectively. As mentioned above, Monte Carlo calculations show this ratio is essentially zero for a pure flux of neutrons, and we conclude that the neutron interpretation for the delayed phase of event I is valid. No other reasonable explanation has been found for the delayed emission in this event.

3. Results. Observations of solar neutrons at the Earth were first reported for event II on 1982 June 3 from neutron-decay proton observations (4). Further reports came from GRS observations (2), and from ground level neutron monitors (3). In Figure 3 we show the count rate time histories for several GRS data channels, and for the Jungfraujoch neutron monitor which has a one minute sampling time.

It has been previously reported (3) that the Jungfraujoch neutron monitor recorded high-energy neutrons in the time interval > (1144-1155) UT. Two other European neutron monitors, at Lominicky Stit and Rome, also recorded simultaneous increases, averaged over five minutes. Since the neutron monitors have an efficiency that increases continuously above 300 MeV but falls sharply below this energy, the early response of the Jungfraujoch monitor at 1144-1145 UT must be due to neutrons of GeV energy, if they were produced at the Sun at the time of the impulsive 1143 UT γ-ray peak shown in Figure 3. It should be noted that the neutron monitor response (Figure 3) above background, continues until $\sim$1155 UT. This observation requires that significant production of high-energy neutrons (> 300 MeV) at the Sun must have continued well after the initial impulsive burst, since arriving neutrons from this emission would have energies well below that required to develop a significantly large atmospheric nucleon cascade (10).

In the case of the GRS rates, during event II the ratio of "mixed" to single events is initially large ($\gtrsim$0.4) and falls to $\sim$0.1 at $\sim$1149 UT (Figure 2). Based on the GRS response to neutrons in event I, and assuming that the Monte Carlo calculations are correct in predicting no "mixed" events for neutrons, we would conclude that the GRS is responding to a combined flux of photons and neutrons. This circumstance alone indicates that photon production also continues throughout the post-impulsive phase. Earlier it was suggested (2) that the GRS was responding to a combined flux of γ-rays and neutrons between 1144-1147 UT, and that from 1147-1206 UT the energy loss spectrum was basically characteristic of high-energy neutron interactions in the GRS scintillators. We must now reevaluate the earlier conclusions on neutron observations in event II using a model for combined high-energy photon and neutron production throughout the event.

We have used several approaches to study the neutron and γ-ray contributions to the GRS rates in the post-impulsive phase. One approach assumes that γ-ray and neutron production rates are proportional throughout the flare and that spectral shapes do not change with time. Using this assumption, and π^0 fluence versus time, (8), we can test any assumed neutron spectrum against the Jungfraujoch and GRS data. As an example we have used a neutron production spectrum at the Sun (11), based on a Bessel function accelerated proton spectrum (parameter αT). To perform this test we calculate the expected unnormalized count rate of the Jungfraujoch neutron monitor versus time using its known neutron sensitivity (3). This rate is then normalized to the observed monitor rates (Figure 3) by a χ^2 minimization for a given neutron production spectrum. Each best fit absolute continuous production solar neutron spectrum shape is then used to predict the GRS count rate versus time using the Monte Carlo results for the GRS sensitivity. Because of the limited statistics of the 1 minute neutron monitor rates, the normalization of the predicted curves is not better than a factor of 2.

Figure 4 shows a comparison of the predicted GRS count rate versus time for αT = 0.03 and 0.05, compared with the GRS total high-energy detector rates averaged over 65.54 sec. Calculations of predicted rates for other αT spectral shapes are in progress.

4. Discussion We have confirmed that the delayed emission observed by the GRS in event I is due to neutrons with energies from 50 MeV to > 250 MeV,

ORIGINAL PAGE IS
OF POOR QUALITY

assuming a delta function emission of neutrons at the Sun. Over this limited energy range, a neutron spectrum at the Sun of power law form ($\alpha = 3.6$), or that produced by a proton Bessel function spectrum ($\alpha T = 0.02$) is sufficient to fit the observed neutron flux at the Earth. This result is not changed significantly if the neutron emission is spread over the short time interval of the impulsive emission (1).

In the case of event II, we have confirmed that a time extended production of neutrons at the Sun is required to account for the response of the GRS and the Jungfraujoch neutron monitor throughout the delayed phase. Therefore a delta function production in the impulsive phase cannot account for the observations of the neutron monitors and the GRS to solar neutrons. As a consequence there is not a one to one correspondence of arrival time to neutron energy, and this complicates the determination of a neutron spectrum. Also, a neutron production spectrum at the Sun resulting from a Bessel function flatter than $\alpha T = 0.05$ may be required to pull the predicted neutron count ratio down to that required for the GRS simultaneous response to both neutrons and γ rays. This is indicated by the dashed curve in Figure 4. As previously pointed out (11, 12) a power-law spectral shape which is constant from 1 GeV down to 50 MeV is not viable.

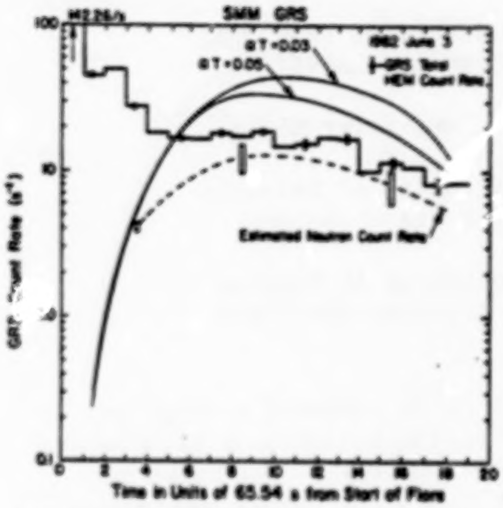

Fig. 4. The total GRS high-energy count rates for energy loss > 10 MeV compared with predicted αT fits determined from a time extended production of neutrons and normalised to Jungfraujoch neutron monitor rates. The estimated neutron count rate (dashed) is based on subtracting meson γ-ray contributions from the total rate (8). Error ranges are 1σ - count statistics only.

5. Conclusions. Reanalysis of the GRS neutron observations taking into account time extended production of γ rays and neutrons and the neutron monitor results has led to a reinterpretation of event II. Theoretical results we have used here had assumed isotropic production of neutrons and an invariant spectral shape with time. It may be necessary to consider the effects of nonisotropic neutron production and a time varying spectral shape to satisfy all observational constraints including those provided by the neutron-decay protons.

6. Acknowledgements. We wish to thank Mary Chupp for and Robin Tuttle for preparation of this manuscript; Karen Dowd, Sabrina Kirwan, and Bao Li for data analysis assistance. This work was partially supported by contract NAS 5-28609 at the University of New Hampshire; NASA contract S.70926A at NRL; contract 010K017ZA/WS/WRK 0275:4 at the MPI, FRG; and the Swiss National Science Foundation Grant 2.876.80 at the U. of Bern.

References

1. Chupp, E. L., et al. (1982) Ap. J. (Letters) 263, L95.
2. Chupp, E. L., et al. (1983) Proc. 18th ICRC, 10, 33.
3. Debrunner, H., et al. (1983) Proc. 18th ICRC, 4, 75.
4. Evenson, P., et al. (1983) Ap. J. 274, 875.
5. Evenson, P., et al. (1983) Proc. 18th ICRC, 4, 97.
6. Meyer, P., et al. (1985) Bull. Am. Phys. Soc. 30, 780.
7. Cooper, J. F., et al. (1985) This Conference SH 9.1, 1.
8. Forrest, D. J., et al. (1985) This Conference SH 1.4-7.
9. Forrest, D. J., et al. (1980) Solar Physics 65, 15.
10. Debrunner, H., et al. (1984), Presented at the 9th European Cosmic Ray Symposium, Kosice.
11. Murphy, R. J. and Ramaty, R., (1985) Advances in Space Research 4, 127.
12. Ramaty, R., et al. (1983), Solar Physics 86, 395.

FURTHER OBSERVATIONS OF PROTONS RESULTING FROM THE DECAY OF NEUTRONS EJECTED BY SOLAR FLARES*

Paul Evenson[+], Richard Kroeger[x], and Peter Meyer[x]

[+] Bartol Research Foundation, University of Delaware
Newark, Delaware 19716 USA

[x] Enrico Fermi Institute and Department of Physics
University of Chicago, Chicago, Illinois 60637 USA

ABSTRACT. The solar flare of 1984 April 24 produced a large γ-ray fluence with energy >2MeV. The time profile of the interplanetary proton flux from this flare indicates the presence of decaying solar neutrons. This makes a total of three neutron flares so far observed by this method. The three flares are used to place constraints on the fluence and spectra of neutrons emitted by the sun.

1. INTRODUCTION. Neutrons emitted from the sun by large solar flares have been observed by two methods; direct detection as the neutrons pass the earth[1-3], and detection of protons which result from the decay of the neutrons [4,5]. The first unambiguous identification of decay protons was made during the 1982 June 3 event[4]. More recently, on 1984 April 24 at 2354 UT, another solar event occurred showing a similar behaviour that fully confirms the earlier interpretation. This flare was located on the sun at S12 E43 and had the largest gamma ray fluence (>2MeV) thus far detected by ISEE-3. A third neutron flare occurred on 1980 June 21[5].

In this paper, we use the decay proton method to interpret data collected from the University of Chicago experiment onboard the ISEE-3 spacecraft. The energy of the decay protons is essentially the same as that of the parent neutrons. Thus, we can obtain precise neutron energy spectra near 1 AU in the range 25-138 MeV. These results yield information on the propagation of charged particles in the inner heliosphere as well as the fluence and spectrum of emitted neutrons.

2. MEASUREMENTS. The signature of neutron production is a flux enhancement prior to the expected arrival of the flare protons. Neutrons travel in straight lines from the flare site, hence their travel time is simply distance divided by velocity. Protons are influenced by the solar and interplanetary magnetic field. On a scale large compared with the proton gyro radius, their motion appears diffusive resulting in significant travel time delays. In flares which are poorly connected magnetically to the spacecraft these delays can be on the order of several hours. This is evident for the flares of 1984 April 24 (located at E55 relative to ISEE-3) and 1982 June 3 (located at E72). The measured proton rates from 25.7-47.5 MeV for these two flares are in figures 1 and 2. In both flares we observe a large initial gamma ray burst followed by a rise in the proton flux approximately 20-30 minutes later - the expected delay

---

*Supported, in part, by NASA contract NAS 5-26680 and NASA grant NGL 14-001-005.

* C-3

for the arrival of neutrons. The initial rise in the proton flux is rapid, corresponding to the time when the expanding shell of neutrons passes the instrument. This is followed by a slow decline in flux as the decay protons diffuse away. Protons produced directly by the flare cause the flux to rise again about 4 hours after the initial gamma ray burst in the 1984 flare, 16 hours in the 1982 flare, and only 1 hour in the neutron flare of 1980 June 21 (not shown here). The solid line in these two figures is a result of modeling proton propagation in the inner heliosphere using a mean free path of 0.3 AU and an isotropic emission of neutrons.

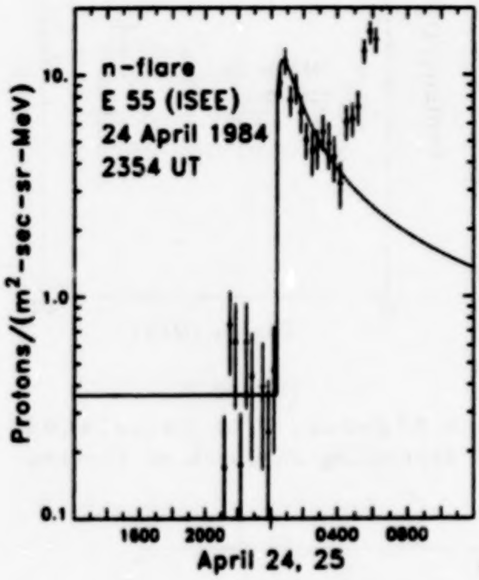

Figure 1

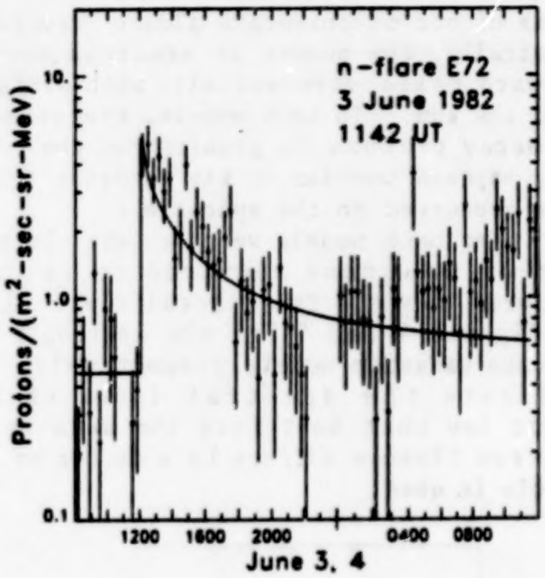

Figure 2

The intensity at the onset of the decay proton flux depends only on the number of neutrons emitted in the direction of the spacecraft. This flux is determined by decay protons which were produced in the vicinity of the spacecraft. In figure 3 we show the spectrum of decay protons collected from 30 to 90 minutes after the initial gamma ray burst. During this time the flux of decay protons is expected to vary by less than about 30% from its initial value. Most of the protons have undergone several scatterings and are nearly isotropic in their pitch angle distribution.

3. __DISCUSSION__. We consider two models which both are able to describe the profile of the decay proton fluxes. In one model, the neutrons are emitted from the sun isotropically in all directions . The sun blocks all downward moving neutrons. The remaining neutrons form an expanding hemispherical shell. In the other model, the neutrons are all emitted in the plane parallel to the local horizon at the flare site, half of which escape the sun. The models are referred to as the isotropic and the pancake model. For both models, we assume that the neutrons are produced impulsively at the time of the gamma ray burst. As they move outward they decay to form energetic protons in the inner heliosphere. We assume

ORIGINAL PAGE IS
OF POOR QUALITY

that these protons rapidly become isotropic in pitch angle. Propagation is treated using a spherically symmetric diffusion model with negligible cross field diffusion.

The rate of decline in the decay proton flux depends primarily on the scattering mean free path for protons along the direction of the solar magnetic field. We find that the same mean free path fits our data in both models and that it is impossible to distinguish between them on the basis of our measurements alone. Described physically, the number of neutrons moving outward falls exponentially with distance from the sun. In both models, the density of decay protons is greatest at the inner most exposed portion of the magnetic field line connected to the spacecraft.

For both models we calculate the number of neutrons required to fit our measured fluxes. These results are shown in figures 4 and 5 for the isotropic and pancake emission models respectively. We indicate the spectral index of the power law that best fits the data in both figures. The calculated neutron fluence differs by a factor of 2.3 depending on which of the two models is used.

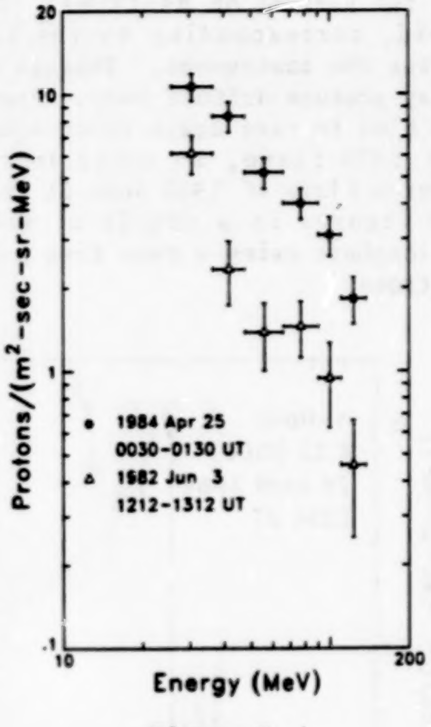

Figure 3

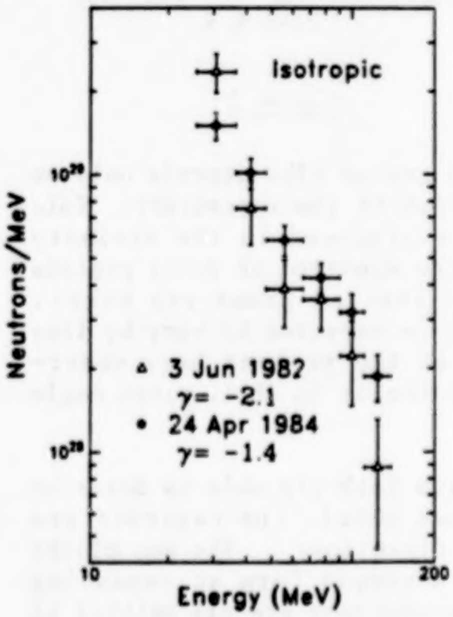

Figure 4

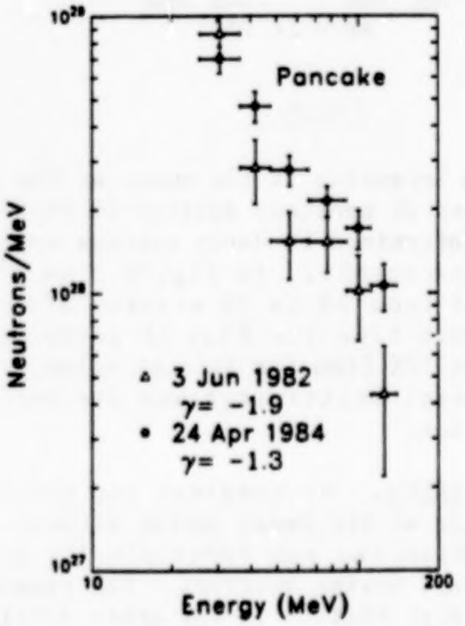

Figure 5

Figure 6 relates the neutron fluence (25.7-47.5 MeV) to the gamma ray fluence (E >2MeV). We have not observed neutron emission from small gamma ray flares. Results from all large gamma ray flares are included in this figure except for one when the proton background was very high due to a previous flare. The 1983 flare occurred at 2217 UT on May 7.

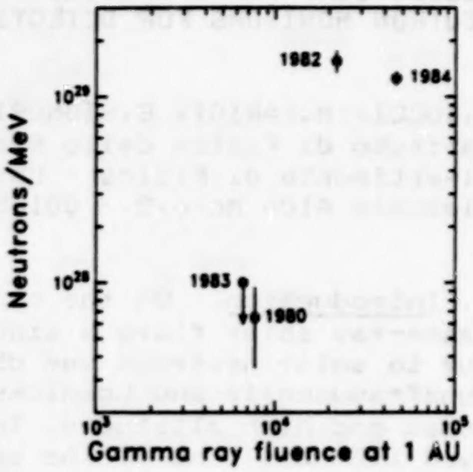

Figure 6

4. CONCLUSION. All three neutron flares have similar neutron emission spectra. Neutrons, along with γ-rays, result from a primary population of particles accelerated in the flare which most likely interact in the solar corona[7]. Since the neutrons result mostly from higher energy particles than the γ-rays, the correlation in figure 6 is related to the shape of the primary particle spectrum. Our results suggest that the shape of this spectrum is relatively invariant in the three flares though possibly somewhat harder in the larger flares.

The scattering mean free path of protons in the inner heliosphere does not depend strongly on the isotropy of the neutron emission. Therefore, the 1982 and 1984 neutron flares offer a unique and clean chance to study charged particle propagation in the inner heliosphere without being affected by phenomena that occur near the sun. A mean free path of roughly 0.3 AU fits the decay proton profile in both flares quite well suggesting this value may be applicable to other propagation problems too.

5. REFERENCES.

1. E. L. Chupp, D. J. Forrest, J. M. Ryan, J. Heslin, C. Reppin, K. Pinkau, G. Kanbach, E. Rieger, and G. H. Share, 1982, Ap. J., 265, L95
2. H. Debrunner, E. Fluckiger, E. L. Chupp, D. J. Forrest, 1983, 18th ICRC (Bangalore), 4, 75
3. E. L. Chupp, D. J. Forrest, G. H. Share, G. Kanbach, H. Debrunner, E. Flueckiger, 1983, 18th ICRC (Bangalore), 10, 334
4. P. Evenson, P. Meyer, K. R. Pyle, 1983, Ap. J., 274, 875
5. P. Evenson, R. Kroeger, P. Meyer, D. Müller, 1983, 18th ICRC (Bangalore), 4, 97
7. R. J. Murphy and R. Ramaty, Advances in Space Research, Proc. of the Solar Maximum Analysis Symposium, COSPAR, Graz, Austria, (1984)

N85-34764

SH 1.4 - 3

SUGGESTIONS FOR IMPROVING THE EFFICIENCY OF GROUND-BASED NEUTRON MONITORS FOR DETECTING SOLAR NEUTRONS

N.IUCCI, M.PARISI, C.SIGNORINI, M.STORINI and G.VILLORESI
Istituto di Fisica dello Spazio Interplanetario del CNR
Dipartimento di Fisica - Universita' 'La Sapienza'
Piazzale Aldo Moro,2 - 00185 ROMA, ITALY

1. Introduction. On the occasion of the June 3, 1982 intense gamma-ray solar flare a significant increase in counting rate due to solar neutrons was observed by the neutron monitors of Jungfraujoch/1/ and Lomnicky Stit/2/ located at middle latitudes and high altitudes. In spite of a larger detector employed (12-NM64) and of the smaller solar zenith angle, the amplitude of the same event observed at Rome (see Figure 1) was much smaller and the statistical fluctuations of the galactic cosmic ray background higher than the ones registered at the two mountain stations, because of the greater atmospheric depth at which the Rome monitor is located.
We will study here the efficiency for detecting a solar neutron event by a NM-64 monitor as a function of the Sun zenith angle, atmospheric depth and threshold rigidity of the station; some suggestions for improving remarkably the detection efficiency will be given.

2. The efficiency of a standard neutron monitor for the detection of solar neutron events. The increase $\Delta I(X_\Theta)$ produced by a solar neutron event in the neutron monitor counting rate will depend on the amount of atmospheric matter in the Sun's direction, $X_\Theta = X/\cos\Theta$, where X is the actual atmospheric depth in g/cm^2 and Θ the solar zenith angle (see Figure 2). The observed relative amplitude is $\Delta I(X,\Theta)/I(X,P_T,t)$, where the nucleonic intensity background $I(X,P_T,t)$ is a function of atmospheric depth, threshold rigidity P_T and modulation level at the observation time t.
The standard error σ of the relative amplitude is produced by the fluctuations in the cosmic ray background $[\sigma(X,P,t) = = \bar{m}(X,P_T,t)/\sqrt{I(X,P_T,t)}$ where $\bar{m}$ is in first approximation the mean detected multiplicity], therefore will depend also on the size and type (IGY or IQSY) of monitor employed. In Figure 3 we show the expected change of the relative amplitude $\Delta I/I$ for a solar neutron event registered at the rigidity threshold of Rome ($P_T = 6.3$ GV), as a function of X and Θ .
For this computation we used the attenuation lengths $\lambda(X)$ of the nucleonic component estimated by BACHELET et al./3/ for a modulation level I(1033,0,t)=0.9 I(1033,0,May 1965). For the secondary neutrons of the solar neutron event a tentative attenuation length $\lambda_n = 110\ g/cm^2$ was used. This value of λ_n was derived from the June 3, 1982 solar neutron event (see Figure 3). The expected change of the relative amplitude for a change $\Delta X = (X'' - X')$ in atmospheric depth as a function of Θ is comp-

uted by

$$\frac{\Delta I(X',\theta)}{I(X')} \Big/ \frac{\Delta I(X'',\theta)}{I(X'')} = \frac{\exp[\Delta X/(\lambda_n \cdot \cos\theta)]}{\exp[\int_{X'}^{X''} dX/\lambda(X)]}$$

In Figure 3 the variation of the inverse of the standard error of the relative amplitude is also plotted. From this plot we may estimate that the value of the signal to noise ratio $[\Delta I/I] \cdot \sigma^{-1} \simeq 3$ obtained for the June 3, 1982 event registered at Rome ($\theta \simeq 20^\circ$) becomes $\simeq 14$ for the same NM-64 placed at an intermediate altitude of 750 g/cm^2. In Figure 3 the computations relative to $\theta = 0^\circ$ are also reported because the results obtained here for $P_T = 6.3$ GV can be applied to any rigidity threshold by simply taking into account the latitude effect of the nucleonic component.

3. Modifications of the standard neutron monitor for improving the efficiency of detecting solar neutron events. The relative amplitude of the event $\Delta I/I$ for a given X, θ, t and P_T can be increased by decreasing the background cosmic ray intensity I. This could be done in two different ways: (a)- by changing the energy response of the standard neutron monitor towards lower energies and (b)- by modifying the omnidirectional property of the standard neutron monitor in order to have the maximum response for particles approaching the monitor from the Sun direction. A simple way to increase the low energy response and decrease the cosmic ray background is suggested by the energy dependence of the number of neutrons emitted by the nuclear disintegration in lead /4/ ; the number of detected correlated neutrons (multiplicity) will be also function of the energy of the colliding neutron /5/. It is expected that the secondaries produced by solar neutrons of energy < 1GeV /6/ should influence mainly the intensity I_1 of the channel of detected multiplicity 1; for this channel the relative amplitude of a solar neutron event can be estimated as:

$$\frac{\Delta I_1(X,\theta)}{I_1(X)} \simeq \frac{\Delta I(X,\theta)}{I(X)} \cdot K(X) \quad \text{where } K(X) = I(X)/I_1(X) \;;$$

$$\sigma_1(X) = 1/\sqrt{I_1(X)} = \sigma(X)[\sqrt{K(X)} / \bar{m}(X)]$$

The signal to noise ratio increases by a factor $\bar{m}(X) \cdot \sqrt{K(X)}$, which is $\simeq 2$ for a NM-64 at sea level. In Figure 3 we show the expected change of the relative amplitude $\Delta I/I_1$ and of its $1/\sigma_1$ for a solar neutron event registered by a NM-64 at 6.3 GV, as a function of X and θ. The attenuation length $\lambda_1(X)$ of the detected multiplicity 1 was taken from /7/; K(X) is found to increase with altitude because $\lambda_1(X) > \lambda(X)$.
When only the events with detected multiplicity 1 are registered, it is convenient to increase the probability of detect-

ing the locally produced neutrons; this could be obtained by adding some BF_3-counters to the standard geometry without increasing the amount of lead; for instance, if the detection probability is increased by a factor 2, the signal to noise ratio $[\Delta I_4/I_4].\sigma_4^{-1}$ will increase by a factor 1.5-2.0.
Moreover the background cosmic ray intensity can be largely decreased, at least at middle latitudes, by shielding the monitor with an appropriate structure able to reduce the flux of cosmic ray particles which approach the monitor from the portion of the sky never scanned by the Sun. For instance at 42N geographic latitude we might shield the monitor from ~20S to 90N. If the background intensity is reduced by a factor ~2 the signal to noise ratio increases by a factor~1.4. This effect can be improved remarkably if the monitor is mounted on a platform which rotates with the Sun; in this case the shielding structure may also cover the lateral sides of the monitor; a possible geometry of this solar neutron telescope is given in Figure 5. With this telescope the cosmic ray background can be reduced by a factor 10. In Figure 6 we show, for a proper network of 9 near-equatorial solar neutron telescopes, located at mountain altitude, measuring the intensity of the detected multiplicity 1 and with increased (by a factor 2) probability of detecting the locally produced neutrons, the contour-lines of $(\Delta I_4/I_4).\sigma_4^{-1}$ = A, 2A and 4A respectively, as a function of time (day and hour); the value of A given in Figure 6 was computed for an event with observed relative amplitude $\Delta I/I = 0.5$ % for $P_T = 6.3$GV, $X = 1010$ g/cm², $\theta = 20°$.

References.

/1/ H. DEBRUNNER et al.: 18th I.C.R. Conf. 4,75,1983.
/2/ G.E. KOCHAROV: 8th E.C.R. Symp. Tecnoprint, p.51,1983.
/3/ F. BACHELET et al.: Nuovo Cimento 35, 23,1965.
/4/ M. BERCOVITCH et al.: Phys. Rev. 119, 412, 1960.
/5/ E.B. HUGHES and P.L. MARSDEN:J.Geophys.Res.71,1435,1966.
/6/ E.L. CHUPP et al.: 18th I.C.R. Conf. 10,334,1983.
/7/ N. IUCCI et al.: Nuovo Cimento 6B,111,1971.

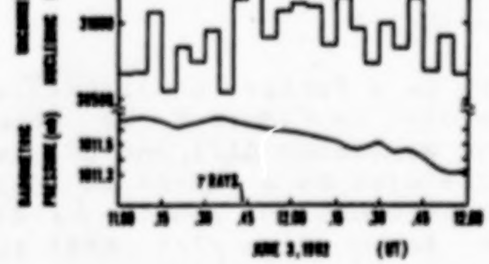

Figure 1

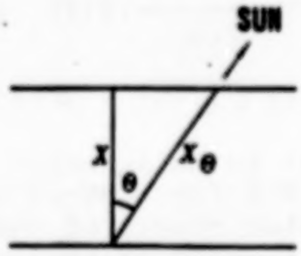

Figure 2

34765

ORIGINAL PAGE IS
OF POOR QUALITY

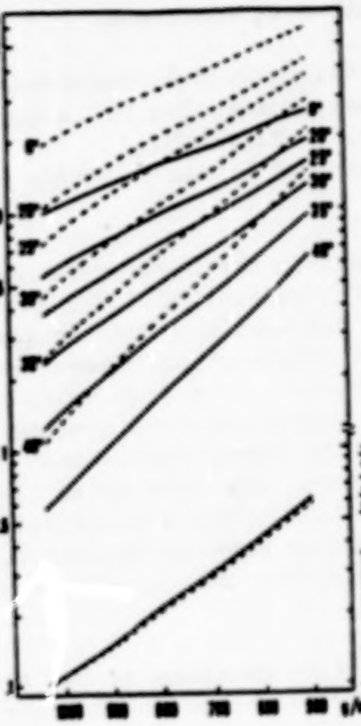

Figure 3: Changes of the observed relative amplitude and of the inverse of its standard error, for a solar neutron event registered by a neuton monitor located at R_T = 6.3 GV vs. atmospheric depth for different Sun zenith angles (total counts registered: full lines; multiplicity 1 counts registered: broken lines).

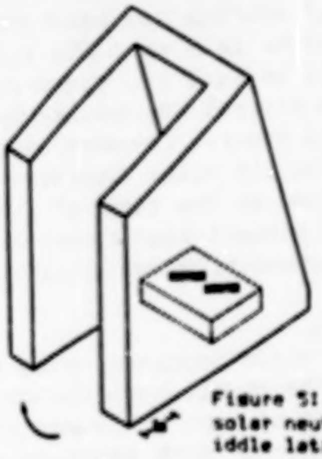

Figure 5: Sketch of a possible solar neutron telescope for middle latitudes (≈40°).

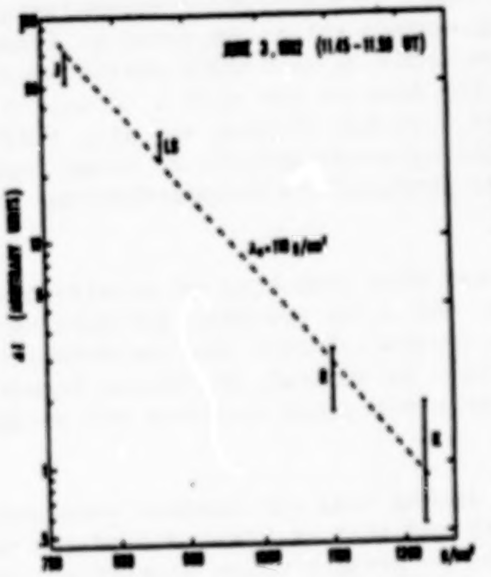

Figure 4: The absolute amplitude ΔI of the June 3, 1982 event for the Jungfraujoch(J), Lomnicky Stit(LS), Rome(R) and Kiel (K) stations vs. atmospheric depth to Sun X⊙. The I are computed from the ΔI/I by applying the latitude and altitude changes of I.

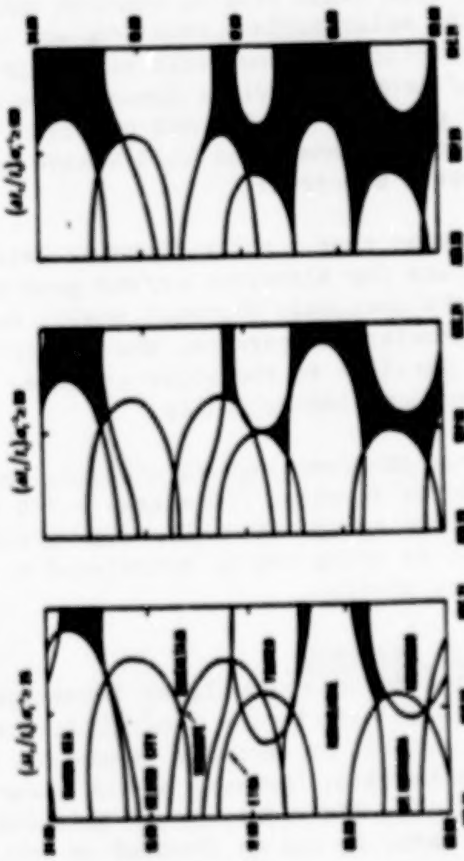

Figure 6

SEARCH FOR SOLAR NEUTRONS USING NM-64 EQUIPMENT

N.J. Martinic, A. Reguerín, E. Palenque, M.A. Taquichiri
Chacaltaya Cosmic Ray Laboratory, University of La Paz
M. Wada, A. Inoue, K. Takahashi
Institute of Physical and Chemical Research, Tokyo

ABSTRACT

Two years (1980-1982) neutron monitor data from the Chacaltaya (geographic coordinates: N16.32°, W68.15°; cutoff rigidity: 13.1 GV; altitude: 5,300 m a.s.l.) station has been scanned; the sampling time of the 12NM-64 neutron monitor is 5 min. The nucleonic component increases have been correlated with 66 hard X-, gamma-rays satellite data from solar origin, as reported by several groups. We present typical neutron monitor time profiles of the events. Chree-analysis was performed discriminating the events according its solar coordinates. Ground data from solar limb locii are more enhanced at the time of the onset than other geometrically visible flares. We present also Chree histograms of neutron monitor out-put profiles from geometrically invisible events from the Chacaltaya station.

1. Introduction

The search for solar neutrons using evaporation neutrons of the nucleonic components of the cosmic rays detected by ground based instruments has led to scan out-puts of high altitude, high cutoff rigidity stations. The low attenuation length of such stations makes it possible to recognize additional, from solar origin, neutron enhancements one is expected to identify. On the solar surface neutrons are available as secondary particles of the interactions of energetic nuclei in the base of the corona; also, ^{1}H capture of neutrons radiate gamma lines of 2.22 MeV (Prince et. al., 1983). Other photons: the 0.5 MeV positron annihilation and the Π^0 decay furnishes the other gammas; the hard X-rays are produced via bremmsstrahlung from the enrgetic electrons.

We assume that a solar flare is related with some kind of acceleration mechanisms for electrons or/and protons and other species; and that neutrons (or the energetic photons) shall, in general, follow the trajectories of the accelerated parents. The latter has, in general, preferred directions, say, parallel to the solar surface. Less energetic neutrons and X-rays may be produced isotropically.

In this phenomenological analysis we assume that the neutron generationis impulsive (typical life-time: ≈ 100 s) and that at least 0.5 of the neutrons can escape the solar atmosphere. We present below statistical analyses of 66 solar events correlated to the ground based 12 NM-64 of the Chacaltaya station.

2. Data treatment

From the 66 solar events we investigate, we show in Fig. 1 a typical time profile as seen by the 5-min Chacaltaya monitor. The short sample of 3 hours exhibit an increase synchronic with the onset time of the reported satellite data; however, notice other increases more important than the former one. The sigma, σ, of this short sample is 0.3 % taken during 6 hours data. As can be checked on Table III, the parent flare was a limb one and the onset was on 21:15 of Dec. 23th 1980. It was a short lived

ORIGINAL PAGE IS
OF POOR QUALITY

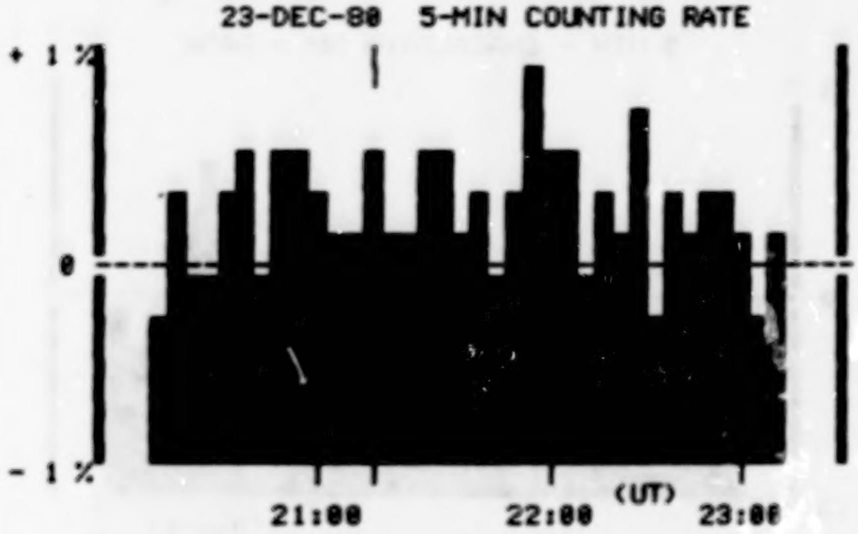

Fig.1: Nucleonic component NM-64 time profile.
The solar gamma ray event is shown with a dash.

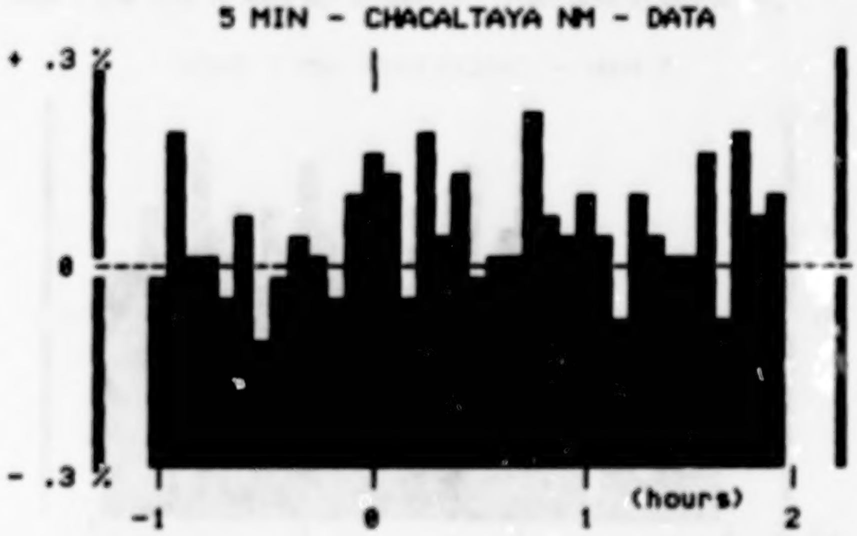

Fig.2: Chree Analysis of 11 visible gamma or X- flares (see Table III). The ordinates are given in % of 6-hour mean value. The total length of the plotted data is three hours. The onset of the event is shown with a dash.

flare (15 s) with a peak emission above 0.3 MeV photons according to the SMM data; the GOES classification is M3. A special feature of this profile is that it appears en enhancement more or less continuous of the monitor data one hour before and one hour after the flare onset.

Fig. 2 illustrates a Chree analysis of 11 solar events when the sun is above the horizon (see Table III); the flare location is correlated with the limb of the sun. The criterion: If the solar longitudes are larger than 70°, then they belong to this group. The increases associated with these flares can be seen clearly on the onset of the event, above the statistical fluctuations. In Fig. 3 we present a superposed epoch analysis centered on the onset of the parent flares with coordinate positions on the disk

ORIGINAL PAGE IS
OF POOR QUALITY

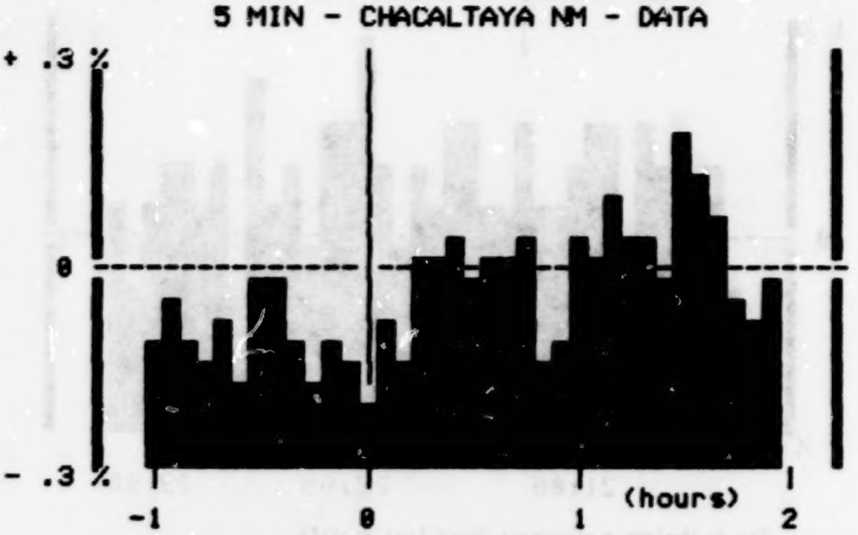

Fig.3: Chree Analysis of 21 visibles gamma or X- flares (see Table II). The ordinates are given in % of 6-hour mean value. The total length of the plotted data is three hours. The onset of the event is shown with a dash.

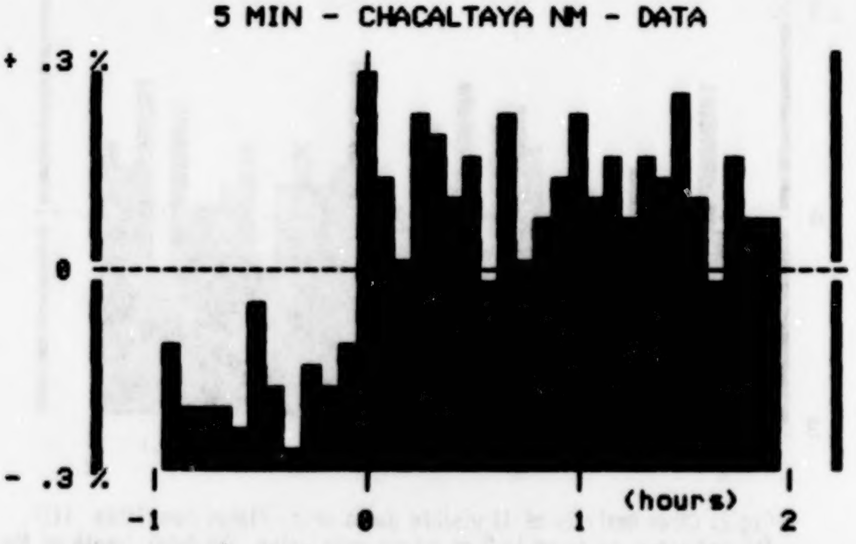

Fig.4: Chree Analysis of 16 invisible gamma or X- flares (see Table I). The ordinates are given in % of 6-hour mean value. The total length of the plotted data is three hours. The onset of the event is shown with a dash.

when the sun is above the Chacaltaya horizon. (Cf. Table II). The short plotted sample illustrates a smooth increase, starting at the onset time; no peaks can be observed. Among these events no discrimination was taken into account with the solar zenith angle as seen by Chacaltaya. Finally, Fig. 4 illustrates the histogram of a superposed epoch analysis of 16 solar events with coordinates on the solar disk (their solar longitudes are less than 70°) when the sun is below the Chacaltaya horizon and shows a step-like behaviour, well above the statistical fluctuations, of the mean value before and after the onset of the events. Other 'nocturnal' events, not shown here, do not present any special feature and its analysis shall be omited.

N85-34766 141

ORIGINAL PAGE IS
OF POOR QUALITY

TABLE I

List of 16 Invisible Solar Flares with Solar Longitudes in the Disk

Date	Solar Coord.	Onset Time	Ref
06/04/80	S14E38	00:54	¥
07/31/81	S12W35	05:55	¥
08/10/81	S13W15	06:50	¥
09/07/81	N08E47	00:00	¥
11/05/81	S10W11	00:32	¥
06/15/82	N13E32	00:30	¥
06/15/82	N13E47	10:19	¥
06/25/82	N17W61	21:33	¥
07/09/82	N09E38	22:50	¥
07/10/82	N16E69	03:16	¥
07/10/82	N16E69	04:08	¥
07/10/82	N16E69	00:30	¥
07/11/82	- -	00:34	¥
07/20/82	N11W69	04:17	¥
08/08/82	S09W65	02:03	¥
12/10/82	S10W20	00:21	¥

TABLE II

List of 21 Visible Solar Flares with Solar Longitudes in the Disk

Date	Solar Coord.	Onset Time	Ref
04/26/80	S17E61	20:31	¥
05/21/80	S14W15	20:54	¥
07/01/80	S12W37	16:26	¥
10/09/80	S17E50	11:23	¥
11/02/80	S20W50	14:10	¥
11/08/80	S08E57	14:52	¥
11/11/80	S11W71	17:43	¥
12/18/80	N07W11	19:21	¥
17/02/81	N20W20	21:46	¥
02/26/81	S12E53	14:24	¥
03/23/81	- -	16:13	♦
04/10/81	N11E53	11:09	‡
04/24/81	N18W50	14:00	‡
05/05/81	N17W01	14:09	♦
07/26/81	S15E27	13:53	¥
07/28/81	S10W18	20:05	¥
10/16/81	S19W36	12:48	♦
02/15/82	N08E27	13:21	♦
06/15/82	S22E66	15:11	¥
12/15/82	S10E15	16:30	¥
12/17/82	S08W21	10:56	¥

TABLE III

List of 11 Visible Solar Flares with Solar Longitudes in the Limb

Date	Solar Coord.	Onset Time	Ref
04/28/80	S14W89	20:30	¥
12/23/80	S13E90	21:15	¥
04/26/81	N12W74	11:44	¥
04/26/81	N13W79	17:39	¥
09/07/81	S13W83	20:05	♦
09/15/81	N10W78	21:13	¥
10/14/81	S06E86	17:05	¥
12/07/81	S04E90	14:50	¥
02/08/82	S13W88	12:49	¥
07/21/82	N23W80	18:22	¥
12/08/82	N07E88	14:37	¥

(¥) SMM satellite
(♦) HINOTORI satellite
(‡) Other sources

3. Discussion

Althought satellite data is not available in order to discriminate solar sources of neutrons visible from the Chacaltaya neutron monitor, say according to its integral neutron intensity (which is model dependent), type of photon emission, and the like, we have presented a preliminary superposed epoch analysis of 66 events pint-pointed mainly via satellite flare survey. We concentrated on solar events of disk or limb parent flares location, and when the sun is above or below the Chacaltaya horizon. The search of solar neutrons via neutron monitor by other authors and known to us (Debruenner et al., 1983; Iucci et al., 1984) show positive identification of solar effects.

We summarize our work: The limb flares, when the sun is above or below the Chacaltaya horizon a) for local nocturnal flares no feature can be noticed and b) for diurnal ones the histogram may produce a peak. For parent flares located on the disk they produce an enhancement of the neutron monitor intensity before and after the onset times, when the sun is below the Chacaltaya horizon; otherwise no particular features can be seen.

References

Prince et al., 1983, 18th ICRC, Bangalore, 4, 79
Debruenner et al,, Chupp et al., 1983, 18th ICRC, Bangalore, 4, 75
Iucci et al., 1984, Rome, IFSI-report

A SEARCH FOR SOLAR NEUTRONS ON A LONG DURATION BALLOON FLIGHT

R. Koga
Space Sciences Laboratory, The Aerospace Corporation
El Segundo, CA 90245, USA

G. M. Frye, Jr. and A. Owens
Physics Department, Case Western Reserve University
Clevelend, OH 44106, USA

B. V. Denehy, O. Mace, and J. Thomas
RAAF Physics Department, Melbourne University
Parkville, Victoria, Australia

ABSTRACT

The EOSCOR III detector, designed to measure the flux of solar neutrons, was flown on a long duration RACOON balloon flight from Australia during Jan - Feb, 1983. The circum-global flight lasted 22 days. No major solar activity occurred during the flight and thus only an upper limit to the solar flare neutron flux is given. The atmospheric neutron response is compared with that obtained on earlier flights from Palestine, Texas.

1. Introduction. A solar neutron detector, EOSCOR III, (1) was launched from Alice Springs, Australia (23.5° S) at 2040 UT Jan. 19, 1983 on a 0.44 x 10^6 m^3 zero pressure polyethylene balloon. As first pointed out by Lally (2), during the summer months at low latitudes, a zero pressure balloon will descend to a stable float altitude after sunset without any ballast drop and then return to its original float altitude after sunrise. Because the magnitude of the day-night altitude excursion is determined primarily by the difference in the radiation seen by the balloon in the day and night environments, Lally (2) has christened this the RACOON (Radiation-controlled balloon) technique. Since we are interested only in a solar observation, the RACOON method is admirably suited to achieving a multi-day observing period at a few mbar altitude with a standard balloon (3).

2. The Flight Characteristics. The circum-global flight was scheduled for the summer to take advantage of the zonal winds which are characteristically uniform both in bearing and velocity, during the three summer months at mid-latitudes. The flight path is shown in Figure 1. The day and night altitudes were initially about 130 and 70 k ft, respectively. The night altitudes remained nearly constant during the flight except when over a very cold cloud deck near Tahiti. The day altitude, however, gradually decreased, reaching approximately 110 k ft one day before termination. The ambient air temperature varied between -20° and -75°C during the flight.

Power for the detector instrumentation was provided by silicad batteries, continuously charged during the day by an array of solar panels. Processed data from the experiment were telemetered to the

ORIGINAL PAGE IS
OF POOR QUALITY

ground through the METEOSAT and GOES satellites and the position of the balloon continuously monitored by the ARGOS satellite network.

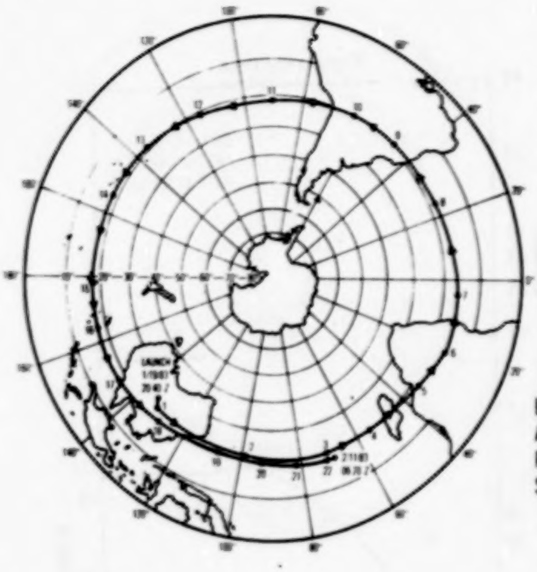

Fig. 1. RACOON Flight Trajectory.

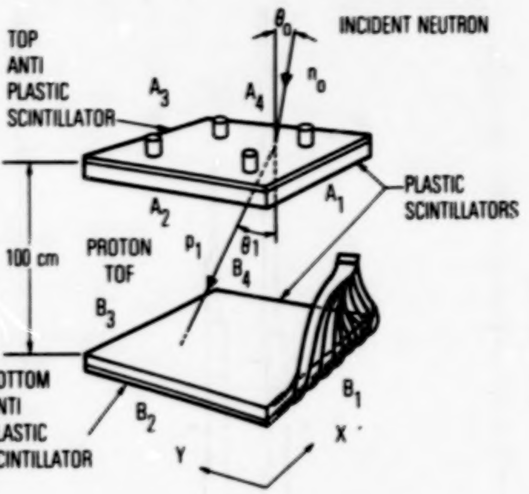

Fig. 2. The EOSCOR III Detector. Adiabatic, Isochronous Light Pipes with 7.8 cm PMT's View the Edges $A_1 \ldots B_4$. (only B_1 shown).

3. Experimental. The detector was designed to measure solar flare neutrons in the energy range 20 to 150 MeV (4). It consisted of two 1 m^2 scintillators separated by a 1 m time-of-flight (TOF) path, as shown in Figure 2. Proton energies from n-p scatters and $^{12}C(n,pX)$ interactions in the upper scintillator were determined by pulse height and TOF measurements. TOF is also used to discriminate the slower moving protons from the more numerous, downward moving Compton electrons. This is shown in Figure 3 where pu, eu, ed, and pd denote upward moving (albedo) protons and electrons, and downward moving electrons and protons, respectively. The separation of these components was made possible by use of a light time compensation technique (1) carried out by an on-board computer. The FWHM of the electron peak was 2.2 ns, which was very close to that obtained during the earlier calibration run at the Indiana University Cyclotron Facility. Raw data related to events within the pd group are telemetered for further analysis.

Solar neutron events are identified by an increase in the neutron counting rate over the atmospheric background, correlated in time with the solar flare. From the gondola position and orientation, the angle θ_o between the vertical detector axis and the neutron arrival direction is known and therefore the neutron energy is given by $E_n = E_p/\cos^2\theta_o$, where E_n and E_p are the incident neutron and the measured proton energies, respectively.

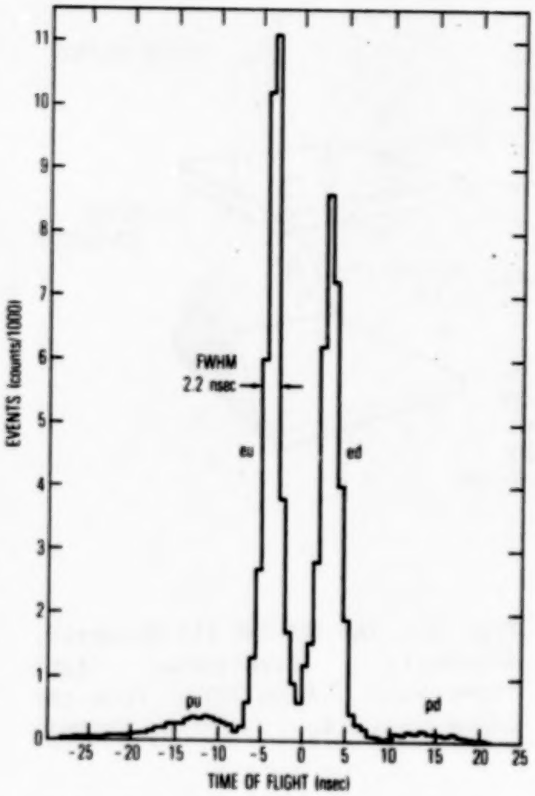

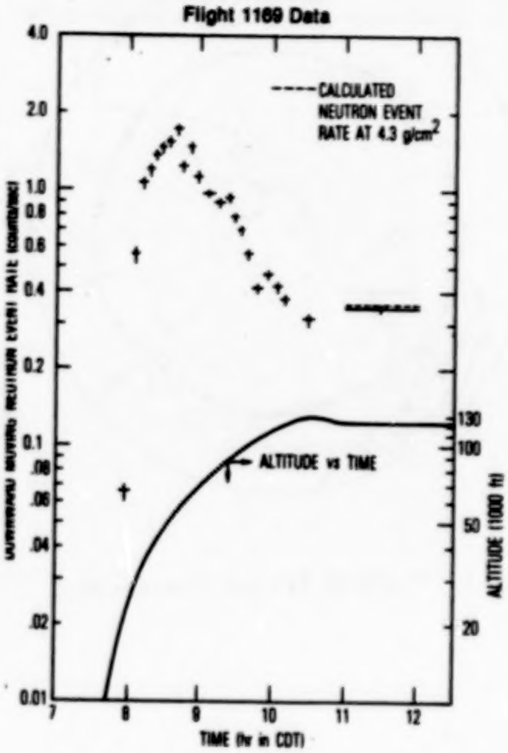

Fig. 3. TOF Spectrum at 3.1 g/cm^2 above Alice Springs.

Fig. 4. Event rates of downward moving neutrons at Palestine, Texas (September 25, 1979).

4. Atmospheric Neutrons. Because the atmospheric neutrons are omnidirectional the proton spectrum cannot be unfolded to yield the atmospheric neutron spectrum. However, the counting rates as a function of altitude and geomagnetic cutoff give a measure of the variation of the atmospheric neutron intensity with these parameters. The rate of downward moving neutrons is obtained from group pd in Figure 3. Measurements of high energy neutrons near the top of the atmosphere have been reported for geomagnetic cutoffs 0.4 GV (Thompson, Manitoba), 4.5 GV (Palestine, Texas), and 11.6 (Parana, Argentina) (5,6). The downward moving neutron flux measured by Preszler et al. (6) was used to calculate the expected counting rates for the EOSCOR III detector. The expected rate is shown in Figure 4 along with the measured rates. For comparison the downward moving neutron rates from several previous flights are also listed in Table 1.

Table 1. EOSCOR III Downward Moving Neutron Event Rates

LOCATION	DATE	ALTITUDE (g/cm^2)	RATE (event/sec)
Palestine	25 Sept 1979	4.3	0.34 ± .02
Palestine	17 Oct 1979	9.0	0.61 ± .03
Palestine*		4.6	0.35
Alice Springs	19 Jan 1983	3.1	0.16 ± .01
Alice Springs	19 Jan 1983	4.3	0.22 ± .01

*Calculated from the measured 1971 neutron flux of Preszler et al. (6).

5. Solar Neutrons.

The sun was quiet during the observational period of the flight (7) with the exception of normal sporadic C class flares. On January 20, 1983, for instance, there were a few such flares. From our derived neutron counting rates we place a 3σ limit on the solar neutron flux of 3×10^{-3} neutrons cm^{-2} s^{-1}.

6. Acknowledgments.

This work was supported by NSF grant ATM 82-06044, the Australian Research Grants Committee, and the RAAF. The work of one of the authors (R.K.) was supported by The Aerospace Corporation-sponsored Research Program.

References

1. Koga, R., et al.; Proc. of the 17 ICRC, 9 (1981) 328.
2. Lally, V.; Proc. XXIV COSPAR conf. Ottawa, I.1.4 (1982).
3. Frye, G. M., Jr.; Adv. Space Sci., 3, no. 6 (1983) 117.
4. Koga, R., et al.; Nuc. Instr. and Meth., 165 (1979) 47.
5. Nazaretz, M. A.: PhD thesis CWRU (1976).
6. Preszler, A. M., et al.; J. Geophys. Res., 81 (1976) 4715.
7. Solar-Geophysical Data, 467B, Boulder, Colorado (1983).

N85-34767

SH 1.4-7

NEUTRAL PION PRODUCTION IN SOLAR FLARES

Forrest, D. J., Vestrand, W. T., Chupp, E. L.
University of New Hampshire, Durham, NH 03824 USA

Rieger, E., Cooper, J.
Max-Planck-Institut fur extraterrestriche Physik, 8046 Garching, FRG

Share, G.
E.O. Hulburt Center for Space Research, Naval Research Laboratory, USA

ABSTRACT

The Gamma-Ray Spectrometer (GRS) on SMM has detected more than 130 flares with emission >300 keV. More than 10 of these flares were detected at photon energies >10 MeV (1). Although the majority of the emission at 10 MeV must be from electron bremsstrahlung, at least two of the flares have spectral properties >40 MeV that require gamma rays from the decay of neutral pions. We find that pion production can occur early in the impulsive phase as defined by hard X-rays near 100 keV. We also find in one of these flares that a significant portion of this high-energy emission is produced well after the impulsive phase. This extended production phase, most clearly observed at high energies, may be a signature of the acceleration process which produces solar energetic particles (SEP's) in space.

1. Introduction. Gamma-ray production in solar flares at energies >10 MeV is only expected from a few mechanisms. These are bremsstrahlung by primary accelerated electrons, bremsstrahlung by positrons and electrons from the decay of charged pions, and directly from the decay of neutral pions. Each process has secondary characteristics other than it's spectrum at energies >10 MeV. These include intense low-energy X-ray emission from any continuous spectrum of primary electrons, emission of the 0.511 MeV gamma-ray line for charged pions, and the emission of high-energy neutrons for neutral pions. These secondary signatures can be used to confirm a spectral interpretation and they can also be used to extract more information concerning the primary particle spectra at the Sun. In particular we note that while the spectral shape of the pionic gamma rays does not depend strongly on the details of the accelerated particle spectrum, it's intensity is a strong indicator of the nuclear reaction rate which must produce both neutrons and pions (2, 3). Hence, combined measurements of both pions and neutrons will yield information on both the directivity and spectra of the very high-energy accelerated ions.

2. The High-Energy Monitor on GRS. The high-energy monitor on the SMM GRS (4) consists of 2 separate sensors. The top or sunward sensor consists of seven 7.6 cm X 7.6 cm NaI detectors and the bottom sensor consists of a 24 cm X 7.5 cm CsI back detector. Neutral events producing energy losses between (10-100) MeV are recorded in 4 energy bands in each of the sensors for three different cases. These are events which occur only in the NaI, only in the CsI, and events which occur in both (called "mixed" events). By appropriately summing these energy-loss bands we can define a five-channel energy-loss spectrum. The nominal energy edges of these channels are 10,25,40,65,100 and 140 MeV. The effective area for both gamma rays and neutrons have been calculated by Cooper et al. (5). These calculations have also shown that only gamma rays are effective in producing "mixed" events. Hence, the ratio of the "mixed" to the NaI only and/or CsI only events is an effective separator of neutrons and gamma rays. We note that events in the (100-140) MeV band, which only uses "mixed" events, requires gamma rays with energies greater than 100 MeV.

3. Flare Observations. The high-energy neutron observations from the flare at 01:18:20 UT on 21 June 1980 have been presented earlier (6,7) and have been reanalyzed with improved neutron efficiencies in a companion paper (8). The basic high-energy observations shows strong emission >10 MeV in the 65 s impulsive phase, followed by a low-intensity excess lasting to the end of the orbit (see Figure 1; ref. 8). Figure 1 shows the photon spectrum measured during the impulsive phase of this flare. The solid curves in this figure are the best-fit photon spectrum, determined by combining both power-law and pion gamma-ray spectra. The power-law spectrum is (5.0 ± 0.1) $(E/10\ \mathrm{MeV})^{(2.7 \pm 0.1)}$ photons MeV^{-1} cm^{-2} and the integral of the neutral pion spectrum is 0.6 photons cm^{-2}. The statistical test used to determine these values shows that while the overall fit is better with the pion spectra, the improvement is not sufficiently large to require it. Hence, the above pion flux must be considered an upper limit. The only way to get a larger pion flux would be to introduce a spectral break in the power law near 40 MeV. Note however, that the data do require photons >100 MeV. In the extended emission phase we find that neither the spectral properties nor the observed ratio of "mixed" to CsI counts (8) is consistent with gamma rays. We find that only 13±6% of the observed counts in this phase can be due to photons with a resulting upper limit neutral pion photon flux of 0.5 ± 0.2 cm^{-2}.

The time history in several energy bands for the flare of 3 June 1982 is shown in Figure 3 by Chupp et al. (8). Again the high-energy observations show strong emission in a 65 s impulsive phase. However, in this event the impulsive phase is followed by a stronger extended emission phase. Figure 2 shows the photon spectrum observed during the 65 s impulsive phases. Again, these data indicate an intense power-law continuum but in this case the data show a strong hardening at energies >40 MeV which is described by a neutral pion photon spectrum with a integrated flux of 12 photons cm^{-2}. Figure 3 shows a 65 s spectrum from the beginning of the extended phase. As can be seen all of the data in this interval can be fit with a combined charged and neutral pion photon spectra. We have used these data to experimentally determine the charged-to-neutral pion ratio and find it to be 3.1±0.2.

Finally, in Figure 4 we show a 65 s spectrum further into the extended phase. In this case an attempt was made to fit the data, under the assumption that all the counts are due to photons. The data in Figure 4 show that a pion-photon spectrum is a good fit in the lowest and the highest channel but the observations exceed the pion-photon model in the three middle channels. Both the spectral shape and the time dependence of this mid-energy excess is what is expected from the high energy neutrons which must accompany any pion emission. It is just this process which allows us to separate the gamma-ray and neutron components versus time within the GRS data. Chupp et al. (8) have used these separated data to study the high-energy neutron production from this flare.

As a confirmation of the pion intensities deduced from gamma-ray spectral shape arguments, we note that these intensities are a predictor of the 0.511 MeV line flux from charged pions. As an example we use the spectrum shown in Figure 3, which requires an integrated neutral pion-photon flux of 7.8±0.4 cm^{-2}. With our observed charged-to-neutral pion ratio of 3.1±1, and a positive-to-total charged pion ratio of 0.70, our predicted 0.511 MeV flux, during this interval, from charged pions is 0.12±0.02 [f(0.511)] photons cm^{-2} s^{-1}. Here, f(0.511) is the 0.511-to-positron ratio (3). Share et al. (9) found that the total flux at this time 0.35±0.05 photons cm^{-2} s^{-1}. Murphy et al. (3) found that only 0.15 photons cm^{-2} s^{-1} could be accounted for by the radioactive positron emitters produced mainly in the impulsive phase. The difference between the measured value and Murphy's values is 0.20 photons cm^{-2} s^{-1}, which is in agreement with our predictions for charged pions produced well after the impulsive phase for a f(0.511) = 1.6±0.2.

Our analysis shows a integrated flux of 45 cm^{-2} neutral pion photons measured after 11:46:00 UT. When compared to the 12 cm^{-2} measured in the impulsive phase, we find that >80% of the pion emission was observed in the extended phase.

4. Discussion. We have presented spectral evidence for pion production in 2 flares. During the impulsive phase this emission is always accompanied by intense primary electron bremsstrahlung. In the larger of these two flares, 3 June 1982, the pion production continued well after the impulsive phase. The properties of this extended phase are distinctly different from the impulsive phase. Specifically, the extended phase seems to be ion enriched and spectrally hardened.

It is interesting to speculate that this newly discovered phase is associated with the acceleration process that generates SEP's in space. Surprisingly, there is poor correlation between the nuclear gamma-ray intensity and the size of the well-connected SEP's (10). This argues against a close link between impulsive phase acceleration and SEP acceleration. McDonald et al. (11) have shown that the cosmic-ray event associated with the 3 June 1982 flare had an unusually hard spectrum. It is intriguing that the spectrum associated with the extended gamma-ray phase is also unusually hard.

5. Acknowledgements. We wish to thank Mary Chupp and Robin Tuttle for preparation of this manuscript; Karen Dowd and Sabrina Kirwan for data analysis assistance. This work was in part supported by contract NAS5-28609 at the University of New Hampshire; NASA contract S.70926A at the NRL; contract 010K017ZA/WS/WRK 0275:4 at the MPI, FRG; and the Swiss National Science Foundation Grant 2.876.80 at the University of Bern.

References

1. Rieger, E., et al., (1983) Proc. 18th ICRC 10, 338.
2. Ramaty, R., et al., (1975) Space Sci. Rev. 18, 341.
3. Murphy, R. J. and Ramaty R., (1985) Advances in Space Research 4, 127.
4. Forrest, D. J., et al., ([illegible]) Solar Physics 65, 15.
5. Cooper, J. F., et al., ([illegible]) This Conference, SH 9.1, 1.
6. Chupp, E. L., et al., ([illegible]) Ap. J. 263, L95.
7. Ramaty, R., et al., (1983) Ap. J. (Letters) 273, L41.
8. Chupp, E. L., et al., (1985) This Conference, SH 1.4-1.
9. Share, G., et al., (1983) Positron-Electron Pairs in Astrophysics, eds. M. Burns, A. Harding, and R. Ramaty, (American Institute of Physics: New York) p. 15.
10. Cliver, E., et al., (1983) Proc. 18th ICRC 10, 342.
11. McDonald, F. B. and Van Hollebeke, M., (1985) Ap. J. (Letters) 290, L67.

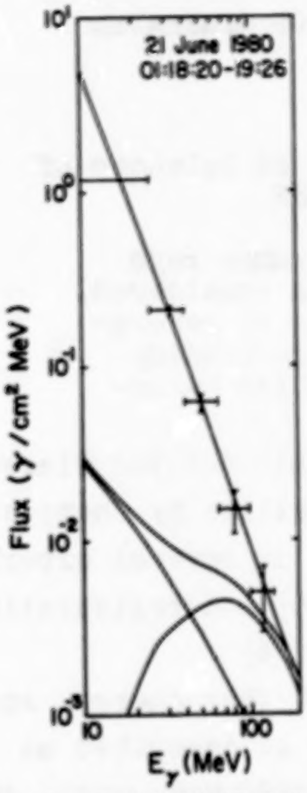

Fig. 1. The (10-140) MeV photon spectrum for the impulsive phase of the 21 June 1980 flare.

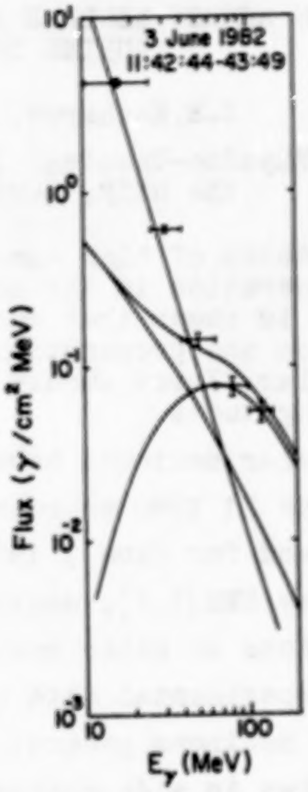

Fig. 2. The (10-140) MeV photon spectrum for the impulsive phase of the 3 June 1982 flare.

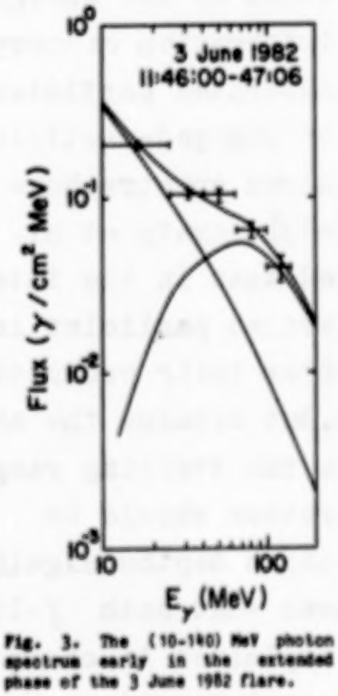

Fig. 3. The (10-140) MeV photon spectrum early in the extended phase of the 3 June 1982 flare.

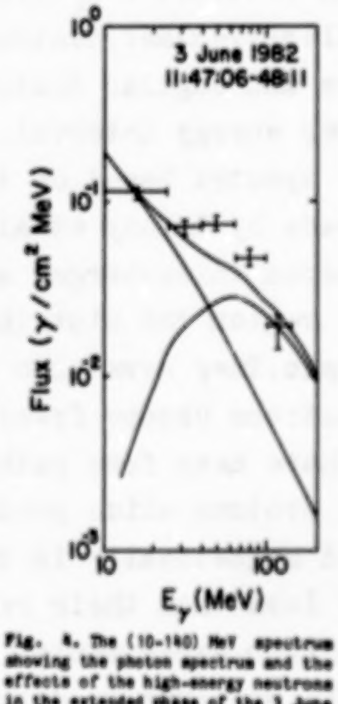

Fig. 4. The (10-140) MeV spectrum showing the photon spectrum and the effects of the high-energy neutrons in the extended phase of the 3 June 1982 flare.

N85-34768

SH-1.4-8

HIGH ENERGY NEUTRON AND GAMMA-RADIATION GENERATED DURING THE SOLAR FLARES

G.E.Kocharov, N.Z.Mandzhavidze

Ioffe Physico-Tecnical Institute Academy of Sciences of the USSR, Leningrad, 194021,USSR

Problem of high energy neutrons and gamma rays generation in the solar conditions is considered. It is shown that due to a peculiarity of generation and propagation of neutrons corresponding solar flares should be localized at high heliolongitudes.

Solar neutrons have been detected only for two flares: for June 21 1980 on board of the SMM satellite by Chupp et al. [1] and for June 3 1982 simultaneously in several experiments by SMM [1,2], neutron monitors [3,4,5] and registration of protons of solar neutron decay origin [6] .

Experimental data allow to establish that energy spectra of neutrons generated in a flare may be described as power law in wide energy interval 50 to 1000 MeV with the spectral indexes 3 and 3.5 for the flares 21.06.80 and 3.06.82 accordingly.

In contrast to γ-lines which are formed by low energy particles(10-30MeV)neutrons contain an information on energy spectra and angular distributions of accelerated particles in wider energy interval. Calculations of charged-particle energy spectra based on the observed neutron spectra have been made by Ramaty et al. and by us [7-13].Ramaty et al. considered thick-target model and assumed that in the interaction region the distribution of accelerated particles is isotropic.They have also assumed that after their production the neutrons escape freely from the Sun.But because the neutrons have mean free paths comparable to the stopping range of the protons which produce them,the protons should be trapped magnetically in the region at column depths significantly less than their ranges.It was shown that both γ-line and neutron experimental data might be explained if charged particle spectrum is described by the Bessel function.

In our calculations we tried to refuse the assumption on magnetic trap and considered a beam configuration of accelerated particles. In this case for any direction of beam the flux of solar neutrons increases with an increase of a flare heliolongitude. It can be easy shown for the beam directed to the observer. Really, the thickness of matter traversed by accelerated particles in the solar atmosphere into Earth's direction for limb flare is higher than for disc flare about $(\pi R_0/2h_0)^{1/2} \simeq$ 30-100 times (h_0 - is the scale height, R_0 - is the solar radius). If the accelerated particles move to the Sun the neutrons which are scattered on 90° for the limb flare and on 180° for the disc flare are detected. The probability of backscattering is less relative to the scattering on 90°. However, as in this case nuclear reactions occur in deep regions of the solar atmosphere an absorption of neutrons may be essential. This effect was considered by us and it is shown that the limb retains an advantage.

All calculations of neutron generation and their escape from the Sun were made using Monte-Carlo method taking into account the angular and energy characteristics of (PP) and (pHe) reactions which are the main source of high energy (>50 MeV) neutrons. The beams with different angles relative to solar radius were considered. Particle spectra were presented as power law with different spectral indexes. For different heliolongitudes total yield of neutrons and their energy spectrum have been calculated. Fig. 1 shows the dependence of the fluxes of the neutrons (>50 MeV) on flare heliolongitude for 3 cases. It is seen that for all cases the neutron fluxes are decreased strongly from the limb to the disk. If we consider the beam directed to the Sun the experimental spectra for the flares 21.06.80 and 3.06.82 may be explained if γ_p = 3-3.5 for E_p>100 MeV. In this case using experimental figures for total flux of neutrons: $2.8\cdot10^{28}$ and $2.5\cdot10^{29}$ we obtain for the total number of accelerated particles the following values: $N_p(>30)=7\cdot10^{32}$ and $7,5\cdot10^{33}$,

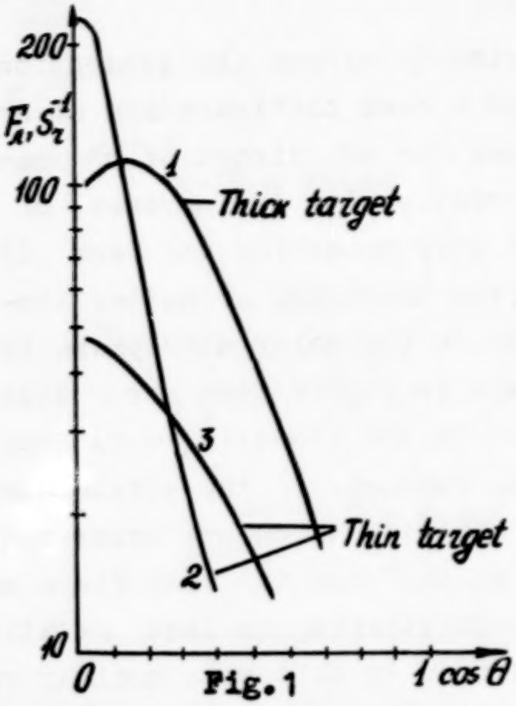

Fig.1

Dependence of neutron fluxes on flare heliolongitude for the beams with different angles relative to solar radius.
1.α=0, γ_p=3,5, N_p(>30MeV)=10^6
2.α=90°. 3.Isotropic yield to upper hemisphere γ_p= 2.5, $n N_p$(>30 MeV)$h_o^{1/2}$ = $1.5 \cdot 10^{23}$, n is number density in an interaction region.

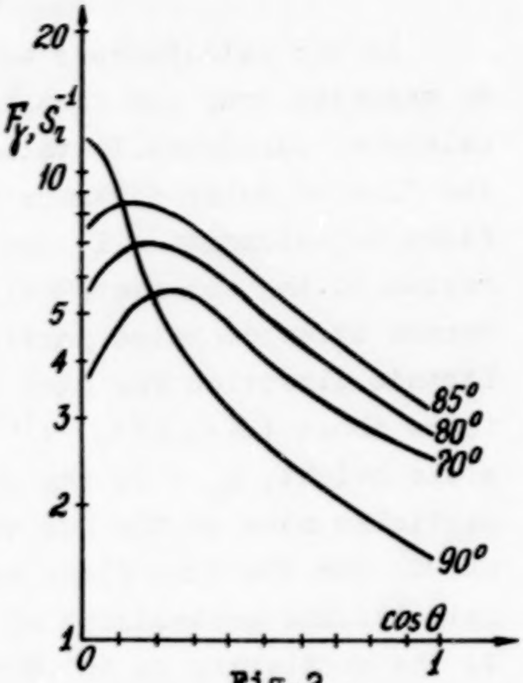

Fig.2

Dependence of gamma-ray flux on flare heliolongitude for beams with different angles relative to solar radius.

accordingly.These figures are in good agreement with the total number of accelerated particles obtained by using γ-line data (see [13] and references therein).So, supposing a beam configuration it is possible to explain particle spectrum as power law from 10 MeV to 1000 MeV with single spectral index. Definitive conclusion can be made after obtaining of experimental distribution on heliolongitude for flares with measurable neutron fluxes.

Now we concern with the problem of high energy γ-rays. At the present time 14 solar flares with high-energy (> 10 MeV) γ-rays are registered [14].These events have a strong solar limb preference with 13 of 14 occurring in flares with a heliocentric angle >72° [14].

If high energy gamma-rays are generated by ultrarelativistic electrons then the radiation is directed along of electron velocity and above considered arguments are correct. Let us consider the case when the source of high energy gamma-rays are π^0-mesons,which are generated in the same reactions as energetic solar neutrons.

It is seen (Fig.2)that the dependence for $\alpha < 90^0$ is weaker than for the neutrons.For tangent beams an advantage of limb is obvious.But in this case the flare should occur in dense region $n \geqslant 10^{13} cm^{-3}$.According to [14] all high energy γ-ray flares are characterized by fast impulses ($\leqslant$ 2s)which is in favour of high density of interaction region. Thus we cannot exclude a nuclear origin of high energy γ-rays.To made a definitive conclusion on the source of high-energy γ-rays it is very important to measure an energy spectrum of gamma-radiation.

References.

1. Chupp E.L. et al.Astrophys.J.Letts.,1982,v.263,p.135.
2. Chupp E.L. et al.Proc.18-th ICRC,Bangalore,1983,v.4,p.97.
3. Efimov Yu.E. et al.,ibid.,v.13,p.240.
4. Debrunner H.et al.,ibid.,v.4,p.75.
5. Iucci N. et al.,1984,Preprint,IFSI,Italio,N 84-1.
6. Evenson P. et al.Astrophys.J.,1983,v.274,p.875.
7. Ramaty R. et al. Astrophys.J.,1983,v.273,p.L41.
8. Ramaty R. et al.,Solar Phys.,1983,v.86.
9. Lingenfelter R.E. et al.Proc.18-th ICRC,Bangalore,1983, v.4,p.101.
10. Ramaty R.,Murthy R.J.,Proc.of the Plasma Astrophys.School and Workshop,Varenna,1984,p.83.
11. Kocharov G.E.,Mandshavidse N.Z.Izv.AN SSSR,ser.fiz.,1984, v.48,N.11,p.2212.
12. Kocharov G.E.,Mandshavidse N.Z.,Pis'ma v Astron.Journ., 1984,v.10,p.771.
13. Kocharov G.E.,Proc.of the Plasma Astrophys.School and Workshop,Varenna,1984,p.65.
14. Rieger E. et al. Proc.18-th ICRC,Bangalore,1983,v.4,p.83, paper presented at 164-th AAS Meeting,Baltimore,Maryland, 1984.

N85-34769

SH-1.4-9

ON THE ANGULAR AND ENERGY DISTRIBUTION OF SOLAR NEUTRONS GENERATED IN P-P REACTIONS

Yu.E.Efimov, G.E.Kocharov

Ioffe Physico-Technical Institute Academy
of Sciences of the USSR,194021,Leningrad
U S S R

Problem of high energy neutron generation in P-P reactions in the solar atmosphere is reconsidered.It is shown that the angular distribution of emitted neutrons is anisotropic and the energy spectrum of neutrons depends on the angle of neutron emission.

Solar neutrons have been detected for two flares June 21 1980 and June 3 1982 in direct experiments on board of the SMM satellite [1,2]. P.Evenson et al. [3] have observed fluxes of energetic protons in interplanetary space which they interpret as the decay products of neutrons generated in a solar flare on June 3 1982. High energy neutrons from this flare have been observed by high mountain neutron monitors at Jungranjoch(Switzerland) and Lomnitsky Stit (Czechoslovakia) and by ground-based station in Roma [4-7] .

The problem of neutrons generation and their escape from the solar atmosphere have been considered by R.Lingenfelter et al. [8] .They assumed that an angular distribution of the neutrons is isotropic and the probability of neutron generation in proton-nucleus collisions does not depend on energy.However this assumption for the energies higher than 100 MeV is not valid for P-P and p-He collisions.For example, generated in p-p reactions neutrons with a kinetic energy 500 MeV are concentrated in apex angle of cone of 30°.As at the experiments solar neutrons are registered up to 1000 MeV we reconsider a problem of neutron generation taking into account available data on the differential cross sections of corresponding nuclear reactions.Here we consider only the results of the calculations for P-P interaction with one pion generation. Neutron escape from solar atmosphere was calculated using Monte-Carlo method. Total and differential cross-sections for elastic and inelastic P-P-interactions were approximated by polynoms based on the available data. Details of calculations are given in [9] .Results of calculations are shown in Fig.1 and 2.

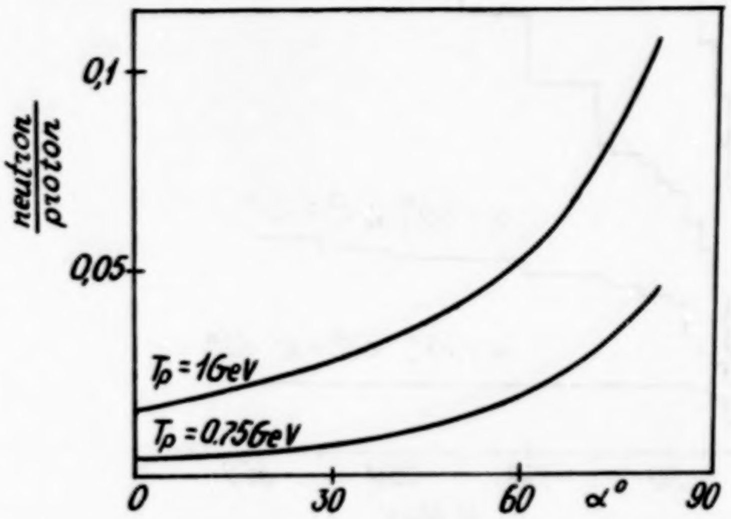

Fig.1. Dependence of neutron yield from the Sun (for energy interval 1-350 MeV) on angle of incidence α -is the angle between the Sun outward and proton velocity direction). T_p-is kinetic energy of protons.

It is seen that neutron emission is anisotropic and their energy spectrum depends on neutron emission angle. Neutrons with energy ≥100 MeV are emitted only at angles 60°and more. It is natural that only neutrons generated by protons with high α can escape the solar atmosphere without collision or with one or two collisions.

Based on the obtained data one can show that very few neutrons emmit at the angles $\Delta\theta = 0^\circ - 15^\circ$ to solar normal and there is no neutrons with the energies ≥100 MeV. This fact helps to clarify that the neutrons were discovered in the flares with high heliolongitudes. The protons moving to the upper hemisphere practically have not ionization losses and the products of their reactions do not interact. Neutrons yield in this case depends on the thickness of the matter

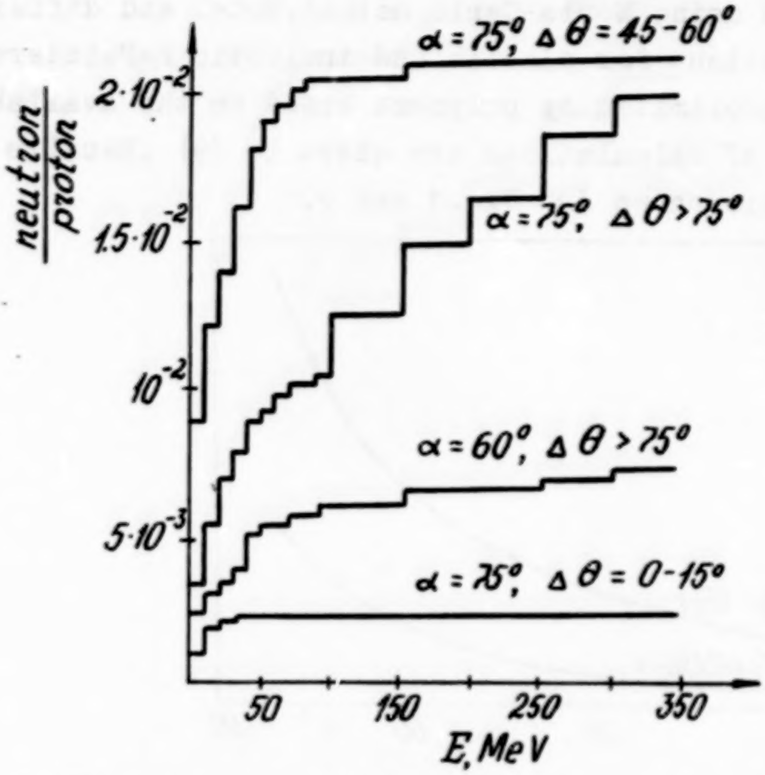

Fig.2. Energy spectrum of neutrons escaping into interplanetary medium(normalized to one proton).T_p=1 GeV

and for the given point of observation on angular distribution of neutrons.The difference of neutron fluxes from the protons moving at 0° to solar surface and at large angle to it,will be mainly connected with different path of protons in the outer atmosphere of the Sun.Considering in first approximation that passing thickness of matter $\sim 1/\cos\alpha$ we obtain that for protons moving at the angle 72°, the neutron flux should be 3.2 times higher than for the protons at the angle 0°.Protons with the angles up to 15-20° take part in generation of neutron flux for disc flare (0°),and for the flare E72°-protons with angles less 72° are the main source of neutrons.So the difference in neutron fluxes from two such type of flares is not substantial (although, spectrum for the flare E72 will be more rigid).But the possibilities of observation of neutrons generated by protons moving to the lower hemisphere are substantially different for consisphere are substantially different for considered two flares. Based on these facts, one may conclude that in flare 3.06.82(E72) the neutrons are generated by protons moving to the lower hemisphere. If in the acceleration region number density is $10^{12}cm^{-3}$, the relative yield of neutrons for 72° in the case of thin target will be 10^{-2}-10^{-3} from the yield for the thick target.

We can conclude also (not taking into consideration magnetic field), that in the flare of 3.06.82, accelerated particles did not form sufficiently narrow beam, directed bottom at the angles 0-30°.

The fact that the fluxes of neutrons with the energies >100 MeV and the energy spectra depend on the direction of motion of accelerated particles allow to obtain the information on angular distribution of accelerated high energy particles by the registration of high energy neutrons.

References.

1. E.L.Chupp et al. Astrophys.J.Lett.263,L95,1982.
2. E.L.Chupp et al. Proc.ICRC Bangalore,v.4,p.74,1983.
3. H.Debrunner et al. Proc.ICRC,Bangalore,v.4,p.75,1983.
4. Yu.E.Efimov et al.,Proc.18-th ICRC, Bangalore,v.13,p.185, 1983.
5. P.Evenson et al. Proc.18-th ICRC,Bangalore, v.4,p.97, 1983.
6. R.E.Lingenfelter et al.,Journ.Geophys.Res.,v.70,p.4077, 1965.
7. R.E.Lingenfelter, R.Ramaty in High Energy Nuclear Reactions in Astrophys.,ed.B.S.Shen,New York, W.A.Benjamin, 1967, p.99.
8. G.V.Voskresenskaya et al.,Preprint FTI,N.896,1984, Leningrad.

SH 1.4-10

N85-34770

POSSIBLE DETECTION OF FLARE-GENERATED POSITRONS BY HELIOS 1 ON 3 JUNE 1982

E. Kirsch, E. Keppler, K. Richter
Max-Planck-Institut für Aeronomie,
D-3411 Katlenburg-Lindau, FRG

1. Introduction. The production of neutrons and γ-ray lines by solar particles in the photosphere has been studied by (1,2,3) and others. In the meantime γ-line measurements were reported (4,5,6,7). The principal positron emitters which lead to the 0.51 MeV γ-line are ^{11}C, ^{14}O, ^{15}O, ^{13}N, ^{19}Ne. The energies of the positrons from radioactive nuclei are of the order of few hundred keV. Positrons resulting from the π^+ decay have energies of ∿ 10-100 MeV and cannot be measured by the MPAe-detector.

Most of the positrons annihilate in the photosphere. A fraction however should be able to escape into the interplanetary space (2). It is the purpose of this paper to present proton, electron and, for the first time, positron measurements (E = 152-546 keV) obtained by the MPAe-particle detector on board of Helios 1.

2. Experiment description and method of detection. The MPAe-detector was designed to measure ions (E ⩾ 80 keV), electrons (E ⩾ 20 keV) and positrons (E = 152-546 keV) with high energy (16 channels) and angular (16 sectors) resolution (8,9). Ions, electrons and positrons are separated by a inhomogeneous magnetic field and then detected by several semiconductor detectors. S_7 (125 mm² area, 322 μ thickness) is the ion detector and S_8 (300 mm², 274 μ) its anticoincidence detector. The positron detector S_6 (200 mm², 1000 μ) is anticoincidence shielded by S_9 (300 mm², 322 μ). A fully anticoincidence shield was not possible due to weight limitations. Various coincidence conditions lead to the following channels: $S_{6.1} \cdot \overline{S_{6.2}} \cdot \overline{S_9} = e^+$ (152-546 keV); $S_{6.1} \cdot S_{6.2} \cdot \overline{S_9} = e^+$ (>546 keV), $S_7 \cdot \overline{S_8} = p$ (> 80 keV) and x,γ rays, $S_7 \cdot S_8 = p,e$ (⩾ 6 MeV); $S_9 = p,e$ ⩾30 MeV) and x,γ-rays; $S_{1,2,3,4} = e^-$ (⩾ 20 keV) and x,γ rays. The x and γ-ray sensitivity results from the Compton scattering process of photons in the detectors. In interplanetary space positrons must be identified in the presence of relativistic particles, x and γ-rays and high energy neutrons produced by the same flare.

3. Observations. The 2B white light flare (S 09°, E 72°) on 3 June had its optical emission from 11:41 - 13:26 UT (Hα max = 11:48 UT) and produced X rays (Solar Geophysical Data, June 1982), γ-rays and neutrons (6). Helios 1 was at a distance of 0.57 AU from the sun and at ∿99° heliographic longitude i.e. well connected to the flare region. The time resolution of the measurements was 107 sec. Fig. 1 shows from top to bottom ⩾30 MeV protons and electrons (S_9), ⩾ 6 MeV protons, electrons ($S_7 \cdot S_8$) and measurements of the 2 positron channels. It can be seen that the positron channels are disturbed by particles which penetrate the shielding of the instrument and cannot be eliminated by the anticoincidence detector S_9. Thus the only chance to separate positrons against the background exists before the main increase. The low energy positron channel has a small premaximum followed by a short minimum (Fig. 1). The increase phase is shown in Fig. 2 with 107 sec time resolution. The main event starts to increase in intervals 4, 5 and 6 and only interval 4 may be suitable for a possible positron identification. If we take the maximum of the radio burst (Solar Geophysical Data, June, 1982) 11:43:20 UT at earth (minus 500 sec at the sun) as the start of the nuclear interaction and the production of the positron emitters the first positrons of 150-550 keV will be expected ∿ 425-310 sec later at Helios, i.e. 11:40:10 - 11:42:05 UT which is interval 4 of Fig. 2.

From other observations it is known that the event starts with a γ and x-ray peak (6) which is in time coincidence with interval 3 of Fig. 2. About 100 sec later (corresponding to interval 4 and 5 of Fig. 2 the x ray and 4.1-6.4 MeV γ-line flux is smaller by approximately a factor of 10. However the delayed γ-ray lines (2.2 MeV see (10 their Fig. 1) and 0.51 MeV see (11 their Fig. 6)) contribute to the background of interval 4 and 5 of Fig. 2 and must be eliminated. The curves 1 and 2 (Fig. 2) present measurements of the electron detectors for the solar (1) and antisolar (2) direction. Different operation modes of the ion detector ($S_7 \cdot \overline{S_8}$) are shown in curves 3-6 for the solar (3,5) and antisolar (4,6) direction which measure the x and γ-ray background in this early phase. Curve 7 presents protons, electrons and γ-rays measured by the single detector S_9 whereas curve 8 (S_7 S_8) shows the increase phase of charged particles. Thus charged particles and γ-rays contribute to the count rate of the positron channels also in interval 4 (curves 9,10). In comparison to the pre-event intervals (I_o, I_1, I_2) the interval 4 shows the following increases

1) p, γ, ($S_7 \cdot \bar{S}_8$, $\Delta E \geqslant 80$ keV), curve 5 and 6

$$I_4/(I_1+ I_2)/2 = \frac{182}{133} = 1.368$$

2) p,e,γ, (S_9, $\Delta E \geqslant 80$ keV), curve 7

$$I_4/(I_o+ I_1+ I_2)/3 = \frac{816}{645.33} = 1.264$$

3) e^+,p,γ ($S_{6.1} \cdot \overline{S_{6.2}} \cdot \overline{S_9}$, $\Delta E = 152 - 546$ keV), curve 9

$$I_4/(I_o+ I_1+ I_2)/3 = \frac{106}{65} = 1.63$$

The second positron channel (curve 10, $\Delta E \geqslant 546$ keV) will not be considered since the magnetic system of the experiment does not quantitatively deflect the positrons of such energies.

By comparing the proton (5+6) and the positron channel (9) it follows that 1.368/1.63 = 0.839 of the positron count rates results from background radiation. The positron count rate in interval 4 would then be

$$106 - 0.839 \quad 106 = 17 \pm 14$$

(14 = statistical error calculated after quadratic error propagation). The flux above the statistical error may be considered as positrons. It follows for a geometric factor of G = 3.2 10^{-2} cm² sterad and 107 sec measuring time

$$\frac{3}{107 \quad 3.2 \quad 10^{-2}} = 0.876\ e^+/\text{cm}^2 \text{ sec ster}$$

or extrapolated to 1 AU distance = 0,28 e^+/cm^2 sec ster. It is assumed that positrons are confined by the interplanetary magnetic field to, say ∿1 sterad. The same flux distributed over 2 π steradian would then be 4.4 10^{-2} e^+/cm^2 sec ster. Model calculations (3; their fig. 5) reveal that about 40 % of the positron emitters have decayed in ∿100 sec. The totally emitted positron flux is therefore ∿ 11 e^+/cm^2.

4. Discussion and conclusion. The flare of 3 June 1982 has been investigated by (6,10, 11). It is of interest to compare the flux of the emitted positrons with the flux of totally generated positrons. After Share and Rieger (private communication) the time integrated flux of the 0.51 MeV line was ∿100 γ/cm^2. According to (11, their fig. 6) the flare of 3 June 1982 has a high $\alpha \cdot T$ value (α = stochastic acceleration efficiency of the flare region, T = particle residence time in the acceleration region) namely $\alpha \cdot T = 0.04$. For such an $\alpha \cdot T$ a ratio of the generated positrons to the 4-7 MeV γ flux of

$$\frac{e^+}{4\text{-}7\ \text{MeV}} \sim 0.7$$

can be derived from (3, their fig. 4). From the 4-7 MeV flux of 305 photons/cm² (11) follows then 213 e^+/cm^2 have been generated.

A further possibility to calculate the flux of the positrons is to compare the total proton flux ⩾ 30 MeV of $3 \cdot 10^{33}$ protons (11) with model calculations of (3, their fig. 5). It follows $\sim 5.5 \cdot 10^{-32}$ $3 \cdot 10^{33}$ = 165 photons/cm² (when $\alpha\tau = 0.02$) and more than 165 would be expected for $\alpha\tau = 0.04$.

Thus assuming the "thick target" interaction model and the here derived positron flux (11 e^+/cm^2) it can be concluded that ⩽ 10 % of the positrons can escape into the interplanetary space.

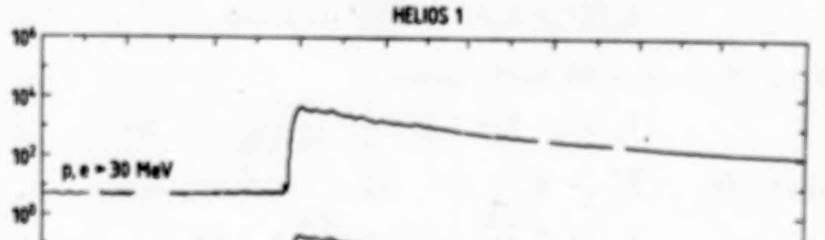

Fig. 1 Proton, electron and positron measurements on June 3, 1982, 06:00 - 24:00 UT.

ORIGINAL PAGE IS
OF POOR QUALITY

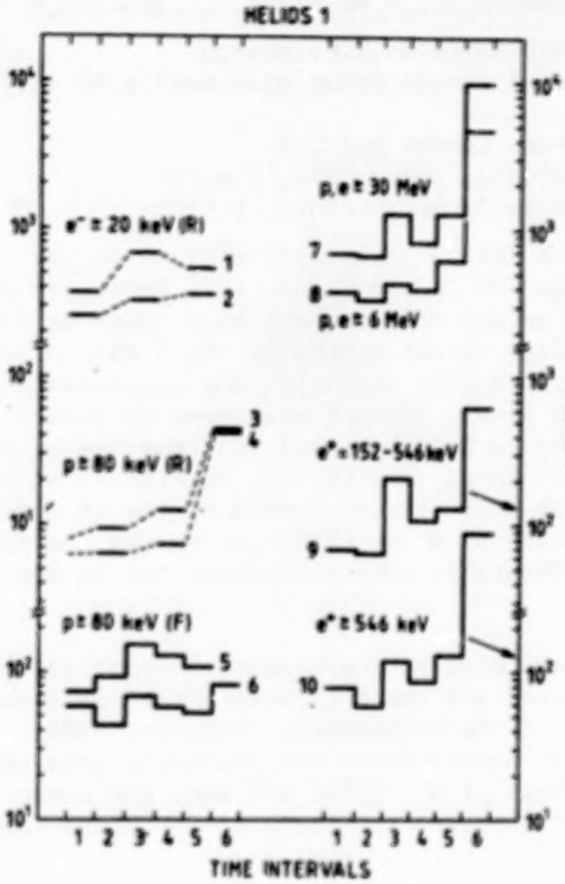

Fig. 2 Increase phase of the June 3, 1982 particle event.

Interval 1 = 11:35:24 UT
2 = 11:37:11 UT
3 = 11:38:58 UT
4 = 11:40:45 UT
transmit time
5 = 11:42:32 UT

ΔT = 107 sec

References

1. Lingenfelter, R.E. and R. Ramaty, (1967), Ed. B.S.P. Shen, University of Pensylvenia, USA, pp.99
2. Ramaty, R., et al., (1975), Space Science Rev. 18, 341
3. Ramaty, R., et al.; (1983), Sol. Phys. 86, 395
4. Chupp, E.L., et al., (1973), Nature 241, 333
5. Chupp, E.L., et al., (1982), The Astrophysical Journal 263, L95
6. Chupp, E.L., et al., (1983), 18th International Cosmic Ray Conf., Bangalore 1983, Vol. 10, 334
7. Yoshimori, M., et al., (1983), 18th International Cosmic Ray Conf., Bangalore 1983, Vol. 4, 85
8. Keppler, E., et al., (1976), Bundesministerium für Forschung und Technologie, BMFT-FBW 76-14
9. Keppler, E., et al., (1977), J. Geophys. - Zeitschrift für Geophysik, 42, 633
10. Prince, T.A., et al., 18th International Cosmic Ray Conf., Bangalore 1983, Vol. 4, 79
11. Murphy, R.J. and R. Ramaty, (1984), Adv. Space Res., Vol. 4, No.7, 127

N85-34771

SH-1.5.1.

SHOCK AND STATISTICAL ACCELERATION OF ENERGETIC PARTICLES IN THE INTERPLANETARY MEDIUM

Valdés-Galicia,J.F.[1],Moussas,X.[2],Quenby,J.J.[3],Neubauer,F.[4],Schwenn,R.[5]

1. Instituto de Geofísica,UNAM,04510 Coyoacán,D.F.,México
2. Astrophysics Lab.,National Univ.of Athens,Panepistimiopolis,GR 15771 Athens, Grece.
3. The Blackett Lab.Imperial College, London SW7 G.B.
4. Inst. für Geophysik und Meteorologie, Univ. Köln, F.R.G.
5. Max Planck Inst. für Aeronomie, Katlenburg-Lindau, F.R.G.

1. Introduction. Definite evidence for particle acceleration in the solar wind came around a decade ago (Mc Donald et al, 1976,Barnes et al, 1976). Since then a considerable amount of data have been taken at different distances from the sun confirming and extending the first findings and it is now widely accepted that particles are accelerated in the Solar Wind (Quenby, 1983). Two likely sources are known to exist: particles may be accelerated by the turbulence resulting from the superposition of Alfvén and Magnetosonic waves (Statistical Acceleration) or they may be accelerated directly at shock fronts formed by the interaction of fast and slow solar wind (CIR's) or by traveling shocks due to sporadic coronal mass ejections. Naturally both mechanisms may be operative.

Shock acceleration has been widely investigated theoretically (Axford, 1981 and references therein) and there is substantial evidence of this as an operative mechanism in the Heliosphere (Scholer, 1984). However there are also experimental observations not obviously consistent with shock acceleration v.g.(Van Ness et al, 1984) and some ion enhancements only explained in terms of statistical acceleration (Richardson, 1984).

Previous treatments of statistical acceleration involved theoretical methods based on power spectral representations of the electromagnetic field (see Quenby, 1983 and references therein).

In this work the acceleration problem was tackled numerically using Helios 1 and 2 data to create a realistic representation of the Heliospheric plasma as will be described in the next section. Two 24 hour samples were used: one where there are only wave like fluctuations of the field (Day 90 Helios 1) and another with a shock present in it (Day 92 of Helios 2) both in 1976 during the STIP II interval. Transport coefficients in energy space have been calculated for particles injected in each sample and the effect of the shock studied in detail.

2. Interplanetary Medium Model. The magnetic field used is defined from $\underline{B}_i$ three dimensional vectors where each one corresponds to the 8 sec. measurements of Helios 1 or 2. Every point in space is also furnished with a solar wind velocity vector $\underline{V}_i$ where these are the corresponding velocities in the solar wind frame. Consequently because all parts of the solar wind are moving there is an electric field $\underline{E}_i = -\underline{V}_i \times \underline{B}_i$ associated to every point in space. For every sample we have divided the space in a series of layers where both the electric and magnetic fields are constant. Trajectories are integrated based on analytical solutions of the equations of motion for each layer. For more details see Moussas et al,(1982).

Because we require layers of roughly 1/20 of a cyclotron radius only 100 MeV protons have been used in this work, lower energies require smaller IMF sampling time to keep a reasonable number of layers per gyroradius.

3. Calculation of Transport Coefficients in Energy Space. First and second order coefficients (D_T and D_{TT}) were calculated in energy space by two different techniques. One is based upon the construction of a steady state distribution by injecting particles with a single energy T_0 (100 MeV in this case) and removing them when they reach any of the two preset boundaries "above" and "below" the injection point (see Moussas et al, 1982 for details).

Another method is based upon the time evolution of the energy distribution. D_T is calculated via a least square fit of succesive distributions first order momenta vs. time. If we take the diffusion equation in energy, integrate for injection at $T=T_0$, assume a first order Taylor expansion in energy for D_{TT}, and make a determination of the spread $\langle(T-\langle T\rangle)^2\rangle$ we arrive at

$$\langle(T-\langle T\rangle)^2\rangle = 2D_{TT}(T_0)t+2(D_T)^2$$

from where D_{TT} can be calculated.

Both methods are generalizations of those initially developed by Jones et al (1978) to study pitch angle scattering on a randomly generated IMF.

The effect of the shock is traced by counting every particle encounter with it and recording the resulting energy change. The average energy change is given by the ratio of the total gain and the number of shock encounters. Transport coefficients can be calculated using the time an average particle takes to get back to the shock $t_B = 2\lambda/v$ where λ = mean free path = 0.03 AU (see Valdés-Galicia et al, 1984) and v = particle velocity.

4. Shock Characteristics. The shock used in this study passed through Helios 2 on day 92 of 1976 when the spacecraft was at 0.45 AU from the Sun. It is a perpendicular shock $\Theta_{B\hat{n}} = 89°$ (Lepping et al, 1971) with a high Alfvén Mach number $M_A = 7.5$. The magnetic field overshoot is some 24 Gammas which is around 50% of the downstream field.

It was assumed to be a plane shock and data were transformed to a frame where the Y-Z plane coincides with that of the shock so that it is parallel to our layer planes.

5. Results and Discussion.

In figure 1 we present a result of a time stationary distribution of particles for an experiment carried out using data from day 90/Helios 1. It can be easily appreciated the asymetry of the distribution towards the "right" of the injection energy T_o showing strong acceleration by waves. Boundaries were put at $\pm$ 2 MeV from T_o = 100 MeV. It should be noted that the mean free path these particles is very small (λ = 0.006 AU, Valdés-Galicia et al, 1984).

Figure 2 shows an evolution diagram of the distribution function of particles in energy and time. Contours are drawn for different density levels. Areas with zero density within the distribution are shown black. Injection energy is at the middle of the figure and energy increases downwards. Full extension from top to bottom is 6 MeV. The horizontal scale covers 2000 sec. Balck diamonds represent first order momenta of particle distributions every 100 secs.

In table I we show the main results of this work. Transport coefficients are average values of the calculations done by the two different methods. Although not shown individually both values agree within 15%. The second row of table I shows results for all particles (85) used with Helios 2 day 92 sample including 79 shock crossings so they are representative of the two proccesses involved (shock and statistical acceleration).

We can apreccíate that even though average energy changes corresponding to statistical and statistical plus shock acceleration are greater than the shock produced average, transport coefficients for this process are greater by an order of magnitude. In the last column of the table we have calculated the the e-folding times (τ) corresponding to every experiment (Wibberenz et al, 1972). If we calculate the time for adiabatic deceleration at 0.45 asuming V_{sw} = 400 Km/sec and radial expansion we get τ_{ad} = 35.3 hours. Thus altough statistical acceleration can have an effect in reducing the adiabatic cooling only the shock accelerated particles are able to overcome it at these energies.

Unfortunately we were limited by the time resolution of the data and could not explore lower energies in a similar manner.

6. Conclusions.

a) The time evolution and time stationary methods to calculate transport coefficients agree quite well.

b) Statistical acceleration at particle energies of 100 MeV in the inner Heliosphere is not able to overcome the effects of adiabatic cooling.

c) Shock acceleration as opposed to statistical acceleration may be a source of particles at these places an energies.

N85-34772

d) Statistical acceleration may be a more efficient process at lower energies.

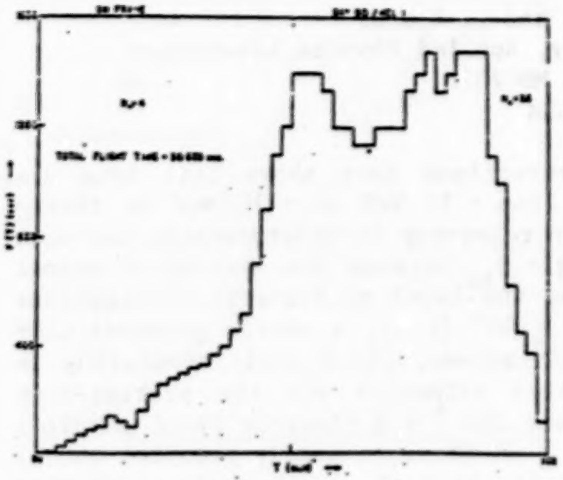

FIG. I

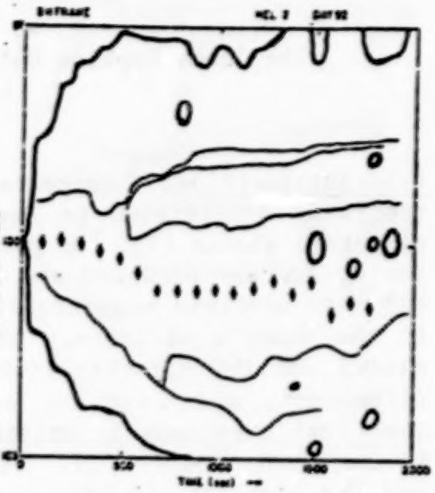

FIG. 2

TABLE I

DOY/SC	POSITION (AU)	ACCELERATION PROCESS	<ΔT> (MeV)	D_T (MeVs^{-1})	D_{TT} (MeVs^{-2})	τ (Hrs)
90/HEL 1	0.31	STATISTICAL	0.76	$(3.6\pm2.1)\times10^{-4}$	$(4\pm3)\times10^{-4}$	76.5
92/HEL 2	0.45	SHOCK+STATISTICAL	0.83	$(5.2\pm2)\times10^{-4}$	$(5\pm3.5)\times10^{-4}$	53.
92/HEL 2	0.45	SHOCK	0.26	$(3.4\pm1.5)\times10^{-3}$	$(1\pm.9)\times10^{-4}$	10.9

ORIGINAL PAGE IS
OF POOR QUALITY

REFERENCES

Axford I. (1981) Proc. XVII I.C.R.C., 12, 155.
Barnes J. et al. (1976) Astrophys. J. Lett, 210, L91.
Jones et al. (1978) Phys. Fluids, 21, 361.
Lepping et al. (1971) J.G.R., 76, 4349.
Mc. Donald F. et al. (1976) Astrophys. J. Lett., 203, L 149.
Moussas et al. (1982) Astrophys. Sp. Sci., 85, 99.
Quenby J. (1983) Sp. Sci. Rev., 34, 137.
Richardson I. (1984) Planet. Sp. Sci., 32, 1179
Scholer M. (1984) Proc. Int. Symp. on C.R. Mod., Morioka, Japan, 161.
Valdes-Galicia et al. (1984) Solar Phys. 91, 399.
Van Hess P. et al. (1984) J.G.R., 89, 2122.
Wibberenz et al. (1972) in Cosmic Plasma Physics (ed. K. Schindler) 399.

N85-34772

ENERGETIC ION ACCELERATION AT COLLISIONLESS SHOCKS

R. B. Decker and L. Vlahos
The Johns Hopkins University, Applied Physics Laboratory
Laurel, MD 20707
USA

1. Introduction. Spacecraft observations have shown that ions are routinely accelerated to energies from ~ 10 keV to ~ 10 MeV at interplanetary shocks (1). Of particular relevance in understanding how such ion events are produced are the angle $\overline{\Theta}_{Bn}$ between the mean shock normal and mean upstream magnetic field and the level of magnetic fluctuations in the shock's vicinity. When $\overline{\Theta}_{Bn} \lesssim 90°$ (i.e., a nearly perpendicular shock) and the magnetic field quasi-laminar, pitch angle scattering is infrequent, and ions are accelerated primarily via the scatter-free shock drift process by drifting along the $\vec{U} \times \vec{B}$ electric field parallel to the shock surface (2). When $\overline{\Theta}_{Bn} \gtrsim 0°$ (i.e., a nearly parallel shock) and the level of magnetic wave activity is high, pitch angle scattering is frequent, and ions are accelerated primarily via the diffusive shock acceleration process by being compressed between converging magnetic irregularities fixed in the upstream and downstream flows (3).

Although a small minority of ion events observed near 1 AU have features indicative of the acceleration process being predominantly either scatter-free shock drift or diffusive, most events are more complex, and are associated with shocks having intermediate values of Θ_{Bn} and various levels of wave activity. To model these cases, we have developed a test particle simulation that integrates along ion orbits in a system described below.

2. Model. Let K[X,Y,Z] denote a system fixed with the shock, with the shock lying in the Y-Z plane, and the unit vector $\hat{X} = -\hat{n}$ ($\hat{n}$ = shock normal), so that X < 0 upstream (subscript 1) and X > 0 downstream (subscript 2). The vectors $\vec{U}_1 = U_1 (\cos \delta_1, 0, \sin \delta_1)$ and $\vec{B}_{01} = B_{01}(\cos \theta_1, 0, \sin \theta_1)$ denote the upstream plasma velocity and mean magnetic field ($\theta_1 = \overline{\theta}_{Bn}$), respectively. In K the $\vec{U} \times \vec{B}_0$ electric field is along Y. Given in addition the upstream Alfvén Mach number M_{A1} and plasma beta β_1, the mean downstream conditions are obtained by solving the MHD jump equations (with a ratio of specific heats of 5/3).

We assume that the injected ions are true test particles (i.e., they are not coupled self-consistently to the shock and/or waves), and neglect shock structure by requiring (ion gyroradius) >> (shock transition). Pitch angle scattering is introduced by superposing upon $\vec{B}_{0i}$ (i = 1 or 2) a zero-mean, random magnetic field component $\vec{b}_i(z)$ which, in either the upstream or downstream plasma frame, varies only with coordinate z along $\vec{B}_{0i}$, is transverse to $\vec{B}_{0i}$, and is static (i.e., scattering is elastic in either plasma frame). The field $\vec{b}_i(z)$ is a superposition of N circularly polarized plane waves with wavevectors along $\vec{B}_{0i}$. The amplitude of each Fourier component with wavenumber k is derived from a power spectrum P(k) using a well-known technique (4).

ORIGINAL PAGE IS
OF POOR QUALITY

The simulation proceeds first by constructing the $\vec{b}_1(z)$, then by solving the Lorentz force equation for the particle orbit using the field $\vec{B}_1(z) = \vec{B}_{01} + \vec{b}_1(z)$ in the appropriate plasma frame, performing a Lorentz transformation between plasma frames at shock crossings, and continuing until pre-set spatial and/or temporal boundaries are crossed, whereupon the process is repeated for a new particle.

3. Results. Acceleration at interplanetary shocks was simulated using the form P(k) in Figure 1, which shows sample upstream spectra with $B_0 = B_{01} = 5$ nT. Wavenumber k in the solar wind or plasma frame (top and right axes) was related to frequency f in the spacecraft frame (bottom and left axes) via $k = 2\pi f/V_{SW}$ for a solar wind speed $V_{SW} = 4 \times 10^7$ cm/s. Spectrum A (correlation length 2×10^{11} cm) represents that of ambient transverse Alfvénic fluctuations in the interplanetary medium (5). Spectra B and C (correlation length 1.3×10^8 cm) represent transverse MHD waves presumably driven by ions streaming upstream from the shock (6,7). To model the observed spectra, we damped the upstream shock-associated field amplitude with the function $[1 + |X|/X_1{*}]^{-1}$, where $X_1{*} = D_1 \cos \Theta_1$, with D_1 measured along $\vec{B}_{01}$ from the shock. For $D_1 = 1.5 \times 10^{11}$ cm = 0.01 AU (>> 1.3×10^8 cm), the integrated power or variance σ^2 of C at $|X| = X_1{*}$ is $0.06\ B_{01}^2$, 1/4 that of spectrum B at X = 0, where $\sigma^2 = 0.25\ B_{01}^2$. Downstream spectra used were similar to those in Figure 1, except $D_2 = 1.5 \times 10^{13}$ cm = 1 AU, and $\sigma^2 = 0.36\ B_{02}^2$ to model the enhanced wave levels observed downstream of shocks. Realizations of spectra A and B for N = 4096 were superposed to form $\vec{b}_1(z)$, with linear interpolation used between grid points during orbit integrations. The upper scale in Figure 1 shows the resonant proton energy at which proton gyroradius $\rho \sim k^{-1}$.

Figures 2 and 3 show results for $\delta_1 = 0°$, $\Theta_1 = 60°$, $U_1 = 4 \times 10^7$ cm/s, $B_{01} = 5$ nT, $M_{A1} = 8$, $\beta_1 = 1$, and protons injected upstream with energy $E_0 = 10$ keV in the upstream plasma frame. For this case, $B_{02}/B_{01} = 3.2$ and the plasma density jump r = 3.7. We define the scale time $\tau_{01} = eB_{01}/m_0c = 13$ sec (upstream proton gyroperiod) and scale length $\rho_{01} = v_0\tau_{01}/2\pi = 2.8 \times 10^8$ cm (upstream gyroradius of a 10 keV proton with speed $v_0 = 1.3 \times 10^8$ cm/s).

In Figure 2(a) kinetic energy E/E_0 in the shock frame is shown versus distance X/ρ_{01} from the shock (upstream at left, downstream at right of X = 0). In 2(b) and 2(c) E/E_0 and X/ρ_{01} are shown versus time t/τ_{01} during the orbit. Periods A-H in 2(a) are marked atop 2(b). The largest and most rapid

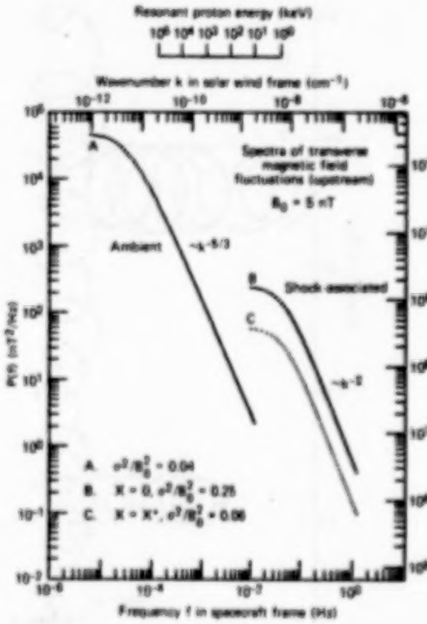

Fig. 1. Wave power spectra

ORIGINAL PAGE IS
OF POOR QUALITY

energy gains clearly occur during the shock drift phases of acceleration (e.g., t/τ_{01} = 8 to 9, 11 to 14, 24 to 30, and 40 to 42). In comparison, diffusive energy gains due to compression between the inflowing upstream plasma and the shock are relatively small (e.g., t/τ_{01} = 14 to 24 and 30 to 40). The particle in Figure 2 crossed the shock 42 times and was accelerated from 10 to 560 keV in 43 τ_{01} = 9.4 min. This orbit shows features typical of the case $\Theta_1 = 60°$.

In Figure 3 we show the energy spectra that result after an elapsed time of 300 τ_{01} = 66 min for 2900 injected protons. The quantity $\Delta f(E)/\Delta E$ is the fraction of particles with energy E within ΔE centered at the logarithmically-spaced plot points. The upstream (solid) and downstream (dashed) spectra denote sums over all particles with $X < 0$ and $X > 0$, respectively. Error bars are two statistical standard deviations in length.

4. Discussion. The most striking aspect of Figure 3 is that well-formed energy spectra spanning more than two decades in energy are produced within only one hour after injection and that these spectra bear remarkable qualitative and quantitative resemblance to observations. For example, the downstream spectrum from 10 keV to 1 MeV is well-described by a power law with spectral exponent ~ 2.2, which is quite close to some observed values (1). In addition, the upstream

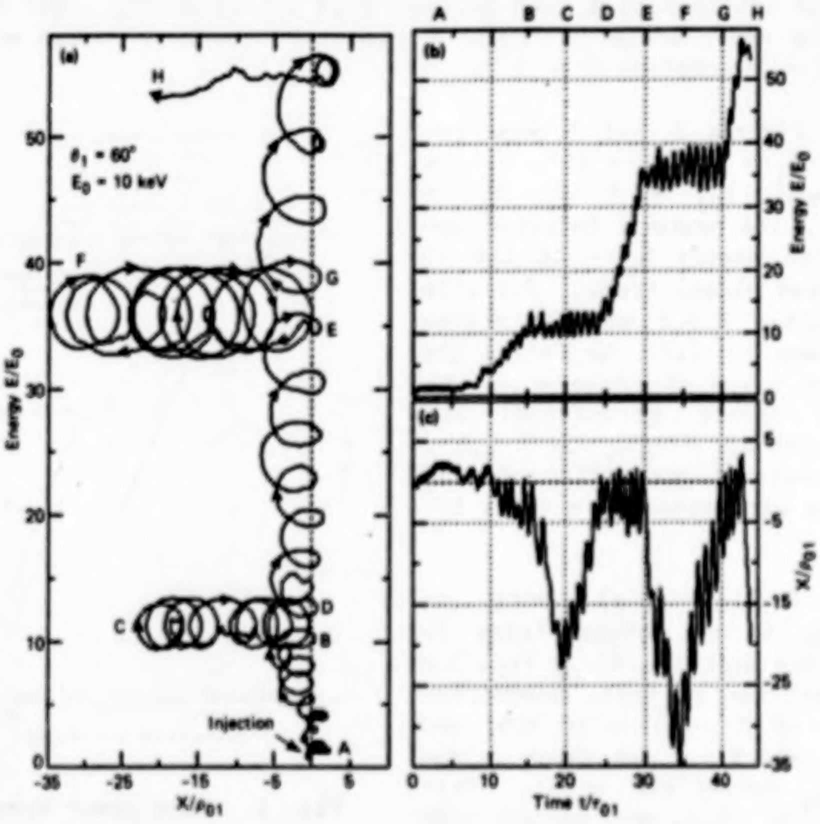

Fig. 2. Sample proton orbit

ORIGINAL PAGE IS
OF POOR QUALITY

spectrum folds over with decreasing energy, similar to observed events (8). The cutoff time as well as the upstream escape boundary at X = 0.5 AU produce the steepening of the upstream spectrum beyond ~ 1 MeV.

We emphasize that the spectra in Figure 3 are primarily the products of the shock drift acceleration process, with pitch angle scattering simply providing the means to return particles to the shock for multiple drift acceleration phases, as in Figure 2. Diffusive acceleration contributes little to acceleration in this case. To estimate the maximum effect expected from diffusive acceleration, we set $\theta_1 = 0°$, and keeping all other parameters fixed as in the $\theta_1 = 60°$ case, injected particles at 10 keV ($B_{02}/B_{01} = 1$ and $r = 3.85$ in this case). After 300 τ_{01} the spectra extended no further than $E/E_0 = 10$ or 100 keV, illustrating, as one might expect, that 300 gyroperiods is far too short a period for diffusive acceleration alone to produce an extended energy spectrum. Examples of energy spectra for various values of θ_1 from 0° to 75° are shown by reference 9.

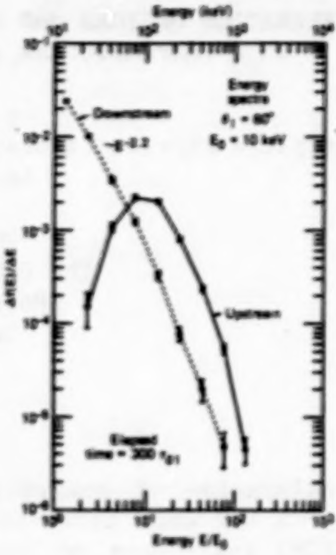

Fig. 3. Proton energy spectra

5. Conclusions. We have presented an example from a test particle simulation designed to study ion acceleration at oblique turbulent shocks. For conditions appropriate at interplanetary shocks near 1 AU, we have found that a shock with $\overline{\theta}_{Bn} = 60°$ is capable of producing an energy spectrum extending from 10 keV to ~ 1 MeV in ~ 1 hour. In this case total energy gains result primarily from several separate episodes of shock drift acceleration, each of which occurs when particles are scattered back to the shock by magnetic fluctuations in the shock vicinity.

6. Acknowledgements. This work was supported in part by the JHU/APL Independent Research and Development Program under Navy Contract N00024-83-C-5301 and in part by NSF Grant ATM-83-05537.

References

1. van Nes, P., et al.: 1984, JGR, 89, 2122.
2. Decker, R. B.: 1983, JGR, 88, 9959.
3. Lee, M. A.: 1983, JGR, 88, 6109.
4. Owens, A. J.: 1978, JGR, 83, 1673.
5. Hedgecock, P. C.: 1975, Solar Phys., 42, 497.
6. Tsurutani, B. T., et al.: 1983, JGR, 88, 5645.
7. Sanderson, T. R., et al.: 1985, JGR, 90, 3973.
8. Decker, R. B., et al.: 1981, JGR, 86, 8819.
9. Decker, R. B. and Vlahos, L.: 1985, paper SH 1.1-6, these proceedings.

N85-34773

SH-1.5-4

ACCELERATION OF IONS AND ELECTRONS TO NEAR-COSMIC RAY ENERGIES IN A PERPENDICULAR SHOCK:THE JANUARY 6, 1978 EVENT

S. M. Krimigis
Applied Physics Laboratory, The Johns Hopkins University
Laurel, MD 20707

E. T. Sarris
The University of Thrace
Polytechnic School
Xanthi, Greece

ABSTRACT

Acceleration of energetic ions to ~ 200 MeV and electrons to ~ 2 MeV were detected by the Low Energy Charged Particle (LECP) instrument on Voyager 2 in association with a quasi-perpendicular shock of $\theta_{Bn} = 87.5°$ at 1.9 AU. The measurements, obtained at a time resolution of ~ 1.2 sec, reveal structure of the energetic particle intensity enhancements down to a scale of the order of the particle gyroradius, and suggest that acceleration takes place within a gyrodiameter of the shock. The observations are consistent with the predictions of the shock drift acceleration (SDA) mechanism. The absence of any fluctuations in the magnetic field during the shock passage suggests that turbulence is not essential to the shock acceleration process in the interplanetary medium.

1. Introduction. It is a well documented observational fact that even weak ($M_A = 1.5$) quasi-perpendicular shocks readily accelerate ions to relatively high energies (up to ~ 50 MeV, Sarris et al., 1976), while quasi-parallel shocks rarely accelerate ions to rather modest (~ 200-300 keV maximum) energies, if such shocks are more or less supercritical ($M_A = 2.8$, Kennel et al., 1984). Surprisingly, theoretical work on shock acceleration of cosmic rays has concentrated on quasi-parallel shocks (Axford et al., 1977; Blandford and Ostriker, 1978), despite the fact that such shocks are demonstrably incapable of producing high energy particles in the interplanetary medium. In an earlier paper (Sarris and Krimigis, 1985) we reported the details of a high mach number shock ($M_A = 3.4$) observed by Voyager 2 at 1.9 AU. In this paper we examine further the development of the energy spectrum and the time variability of the intensity at the time of shock passage. For details of the detector system and instrument operation see Krimigis et al., 1977.

2. Results. Figure 1 shows the count rate profile of several channels from the LECP instrument from January 1 - 7, 1978, following a 2N flare at 2145 UT on January 1, 1978. The shock wave intercepted the Voyager 2 spacecraft on January 6, 1978 at 00:01:30 UT, as is evident from the intensity-time profile in the figure. The energy extent of the enhancement can be seen from the fact that the iron channel in the range ~ 2-12 MeV/nuc (i.e. a total energy > 112 MeV) increased in intensity by well

ORIGINAL PAGE IS
OF POOR QUALITY

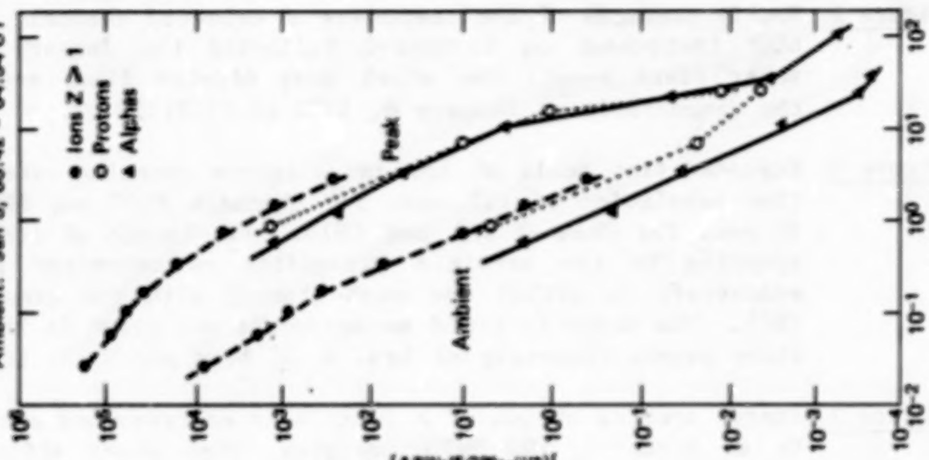

Fig. 3

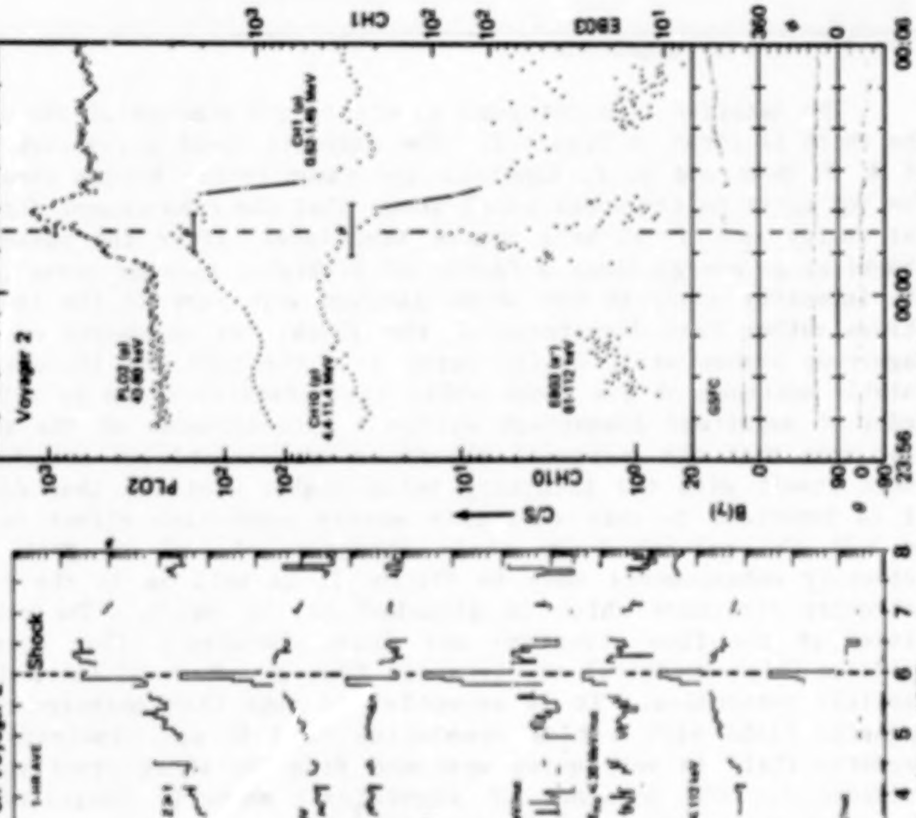

Fig. 2

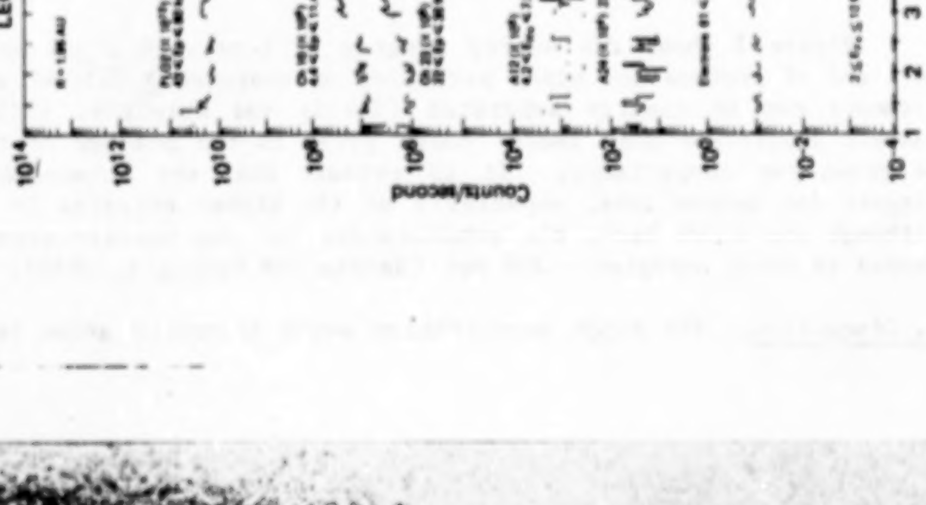

Fig. 1

Figure 1 Hourly averages of the responses of selected channels from the LECP instrument on Voyager-2 following the January 1, 1978 solar flare event; the shock wave (dashed line) encountered the spacecrarft on January 6, 1978 at 00:01:30 UT.

Figure 2 Expanded time scale of ion and electron counting rates with a time resolution of 1.2 sec. for channels PL02 and EB03 and ~ 10 sec. for Channel CH1 and CH10. The length of time corresponding to the particle gyroradius as convected past the spacecraft is marked for each channel with the exception of EB03. The magnetic field measurements are shown in the bottom three panels (Courtesy of Drs. N. F. Ness and R. P. Lepping).

Figure 3 Energy spectra of ions $Z > 1$ at lower energies and protons and He at higher ($\gtrsim 100$ MeV) energies, when shock effects were weak (ambient) and around the shock (peak).

---

over 2 orders of magnitude.

The detailed time interval to within ± 5 minutes of the passage of the shock is shown in Figure 2. The magnetic field parameters (courtesy of N. F. Ness and R. P. Lepping) are shown in the bottom three panels. The top curve in the upper panel shows that the enhancement for the lowest energy ions (~ 40 keV) occurs immediately after the passage of the shock; at an energy about a factor of 10 higher (second curve), however, the intensity peaks at the shock passage with more of the increase upstream rather than downstream of the shock. At an energy one order of magnitude higher still (third curve from the top) the increase is most notable upstream of the shock while the intensity drops by well over an order of magnitude downstream within a gyro-diameter of the shock. We also note that the energetic electrons are essentially attached to the shock itself with the intensity being higher upstream than downstream. It is important to note that this energy separation effect is distinct in both the general large scale structure of the energetic particle intensity enhancements seen in Figure 1, as well as in the fine scale intensity structure which is attached to the shock. The peak intensities of the fine structure are found downstream (low energies) or upstream (high energies) at distances from the shock of the order of the particle gyroradius. It is essential to note that measurements of the magnetic field with a time resolution of 1.92 sec. indicate that the magnetic field is very quiet upstream from the shock front and show no evidence for the presence of significant magnetic turbulence in the frequency range from ~ 0.2 Hz to ~ 10^{-3} Hz.

Figure 3 shows the energy spectra of ions with $Z \gtrsim 1$ up to ~ 3 MeV, and of protons and alpha particles at energies $\gtrsim 0.5$ MeV where the elements can be clearly separated (Sarris and Krimigis, 1985). The ambient population some twenty hours prior to the passage of the shock is shown for comparisons. It is evident that the enhancements were largest for helium ions, especially at the higher energies (~ 10 MeV). Although not shown here, the enhancements for the heavier elements extended to total energies ~ 200 MeV (Sarris and Krimigis, 1985).

3. Discussion. The shock acceleration event described above is remark-

able in that not only did it accelerate nuclei and electrons to almost cosmic ray energies, but that it did so in the absence of any discernible level of turbulence in the magnetic field. Further, the data demonstrate that all intensity enhancements and fine structure occur within a gyrodiameter of the shock from the lowest (~ 40 keV) to the highest ($\gtrsim$ 20 MeV) energies. This event and many other similar ones (Armstrong et al., 1985) demonstrate that turbulence is not a necessary condition for particle acceleration in shocks, to the highest energies observed in the interplanetary medium.

Recent simulation work on quasi-perpendicular and quasi-parallel shocks in the presence of turbulence (Decker and Vlahos, 1985) shows that magnetic fluctuations have a tendency to cause a test particle to encounter the shock more than once. In each of these encounters, however, the energy gain is mostly through drift acceleration along the shock surface, rather than compression. This result helps to explain the observation that maximum energies attained in quasi-parallel shocks are at most ~ 300 keV. The apparent maximum energy gain is likely due to the fact that the time during which the instantaneous magnetic field-shock normal geometry is near-perpendicular is rather small and consequently the energy gain through shock-drift is low. This energy gain "saturation" effect at relatively low energies suggests that the particle escapes the shock turbulence region after only a few encounters with the shock.

Similarly in the astrophysical case, quasi-perpendicular shocks would energize the ions to several hundred MeV. Such particles would then become the seed population; further energization would obtain through scattering in magnetic field fluctuations which may cause the ions to undergo additional encounters with the shock for further energy gains. At some point (relativistic energies?) compression may begin to become an appropriate description for the process.

4. Acknowledgements. We are grateful to Dr. A. Vinas of GSFC for providing us with the shock parameters. This work was supported by NASA under Task I of Contract N00024-83-E-5301.

5. References. Armstrong, T. P. et al., Shock Drift Acceleration, Proceedings of the Chapman Conference on Collisionless Shocks, AGU, 1985.

Axford, W. I. et al., The acceleration of cosmic rays by shock waves, Proceedings, International Conf. of Cosmic Rays 15th, 11, 132, 1977.

Blandford, R. D. and J. P. Ostriker, Particle acceleration by astrophysical shocks, Astrophys. J., 221, L29, 1978.

Decker, R. B. and L. Vlahos, Energetic ion acceleration at collisionless shocks, 19th ICRC Conference, SH 1.5-3, 1985.

Krimigis, S. M. et al. The Low Energy Charged Particle (LECP) experiment on the Voyager spacecraft, Space Sci. Rev., 21, 329, 1977.

Kennel, C. F., et al., Structure of the November 12, 1978 quasi-parallel interplanetary shock, J. Geophys. Res., 89, 5435, 1984.

Sarris, E. T. and S. M. Krimigis, Quasi-perpendicular shock acceleration of ions to ~ 200 MeV and electrons to ~ 2 MeV observed by Voyager 2, Astrophys. J., __, (in press) November 15, 1985.

Sarris, E. T. et al., Observations of a high-energy ion shock spike in interplanetary space, Geophys. Res. Lett. 3, 133, 1976.

N85-34774

SH 1.5-5

PARTICLE ACCELERATION DUE TO SHOCKS IN THE INTERPLANETARY FIELD: HIGH TIME RESOLUTION DATA AND SIMULATION RESULTS.

R.L. Kessel, T.P. Armstrong, R. Nuber, J. Bandle
University of Kansas, Lawrence, KS, 66045, U.S.A.

INTRODUCTION

In this study, data is examined from two experiments aboard the Explorer 50 (IMP 8) spacecraft. The Johns Hopkins University/Applied Physics Lab Charged Particle Measurement Experiment (CPME) provides 10.12 second resolution ion and electron count rates as well as 5.5 minute or longer averages of the same, with data sampled in the ecliptic plane. The Goddard Space Flight Center Magnetic Field Experiment provides the high time resolution magnetic field data (15.36 sec). IMP 8 spends about half its nearly circular (32 to 38 Re) orbit in the interplanetary field. The high time resolution of the data allows for an explicit, point by point, merging of the magnetic field and particle data and thus a close examination of the pre- and post-shock conditions and particle fluxes associated with large angle oblique shocks in the interplanetary field. A computer simulation has been developed wherein sample particle trajectories, taken from observed fluxes, are allowed to interact with a planar shock either forward or backward in time. Shock normals are determined from the single spacecraft method of Lepping and Argentiero (1) using the Imp 8 magnetic field data and OMNI plasma data (J.W. King, NSSDC). One event, the 1974 Day 312 shock, is examined in detail.

DETERMINATION OF THE SHOCK NORMAL

The method of Lepping and Argentiero is based on the coplanarity theorem (2) in which the normal is determined by the magnetic fields:

$$\hat{n} = \frac{\left(\vec{B}_2-\vec{B}_1\right)\times\left(\vec{B}_1\times\vec{B}_2\right)}{\left|\left(\vec{B}_2-\vec{B}_1\right)\times\left(\vec{B}_1\times\vec{B}_2\right)\right|}$$

Instead of using the average values calculated from the data, "best estimate" values are determined in a manner to be explained below. Two assumptions are necessary to use this method: first, that the Rankine-Hugoniot equations are valid for interplanetary shocks; second, that the shock is a step-function increase in all parameters, with superimposed noise. Figure 1 lends credibility to the second assumption. The first assumption is necessary because certain of the

Rankine-Hugoniot equations are used as a constraint on the shock normal. The equations in the shock rest frame are:

$$[\rho V_n]_1^2 = 0$$

$$\left[\rho V_n V_t - \frac{B_n B_t}{4\pi}\right]_1^2 = 0$$

$$[V_n B_t - V_t B_n]_1^2 = 0$$

$$[B_n]_1^2 = 0$$

Eleven variables can be identified from these equations:

$$\rho_1, \rho_2, \vec{W}\left(\vec{V_2} - \vec{V_1}\right), \vec{B}_1, \vec{B}_2$$

Three of these variables are isolated in terms of the other eight. In the Lepping and Argentiero study any three variables could be isolated. Their data consisted of 30 sec averaged magnetic field data and approximately 90 sec averaged plasma data. In this study 15 sec averaged magnetic field data was used along with 5 min averaged plasma data. Because of the large standard deviations associated with the solar wind data (Wx,Wy,Wz), partly due to the low resolution of the data, it was necessary to isolate these three variables. To use them in the Rankine-Hugoniot equations to solve for the other variables produced inconsistent results or no convergence.

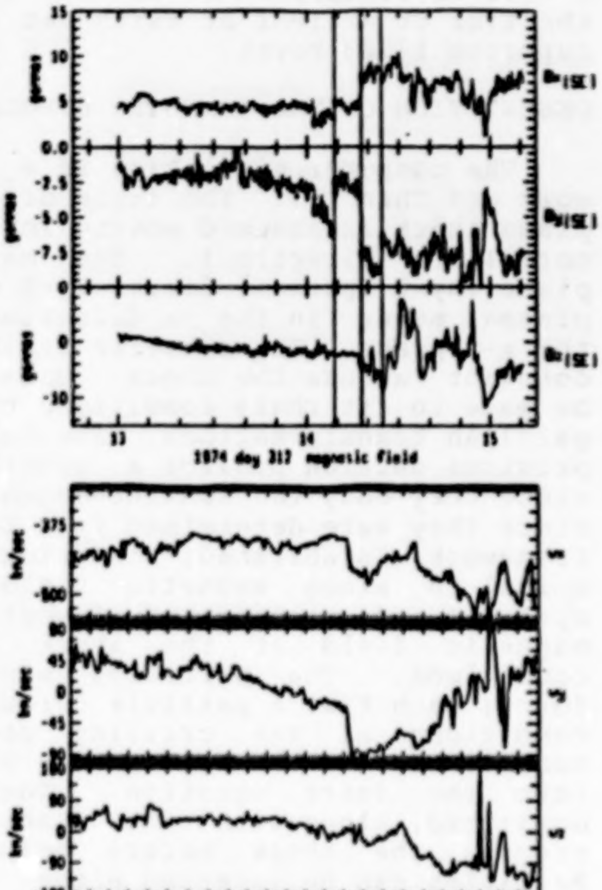

Fig. 1. a) Magnetic field in solar ecliptic coordinates. Vertical lines seperaete field into pre- and post- shock regions which were used in the shock normal determination. b) Solar wind in solar ecliptic coordinates. Shock occurs at 14.30 hours.

The method uses the eight "known" variables and the three variables calculated from the Rankine-Hugoniot equations in a type of least squares fit which is minimized by use of an iteration process. The solution should converge to the "best estimate" values relatively quickly. Many starting values should be used and these compared to assure convergence to the same minimum.

This normal determination method was tested in several ways. Multiple runs were made with different starting values (particularly, different numbers of plasma points were used from 15 min to 40 min of data), and these were checked against each other. Three events were used; one, the 1974 day 312 shock to be used in the remainder of this work, and two others which were checked against thetabn angles supplied by Tsurutani (private comm.)--thetabn being the angle between the magnetic field and the shock normal. The 1979 day 93 thetabn was calculated at 39° which is within 4° of that calculated by Tsurutani, and the 1979 day 95 thetabn is within 6° of the Tsurutani value. The 1974 day 312 shock was not included in the Tsurutani study. It was further checked by calculating the time of propagation of the shock from the spacecraft along the shock normal to the Earth and comparing against the reported SSC time. For a calculated thetabn of 60° and a shock speed of 470 km/sec, the time of arrival at Earth was 14.29 hours compared to the reported 14.23 hours.

DESCRIPTION OF THE COMPUTER SIMULATION

The computer simulation is a further development of the work of Chen (3). The frame of reference is as follows. A plane shock is assumed moving in the direction of the shock normal (x direction). The magnetic field is in the x-z plane (By=0 upstream forces By=0 downstream). The upstream plasma moves in the -x direction, the downstream plasma in the x-z plane. The electric field is in the y direction and constant across the shock. Data for a particular shock can be made to fit these conditions by suitable rotations and galilean transformations. The best estimate values from the previous section provide a consistent set for this work since they obey the Rankine-Hugoniot equations (as they must since they were determined from these equations). With this framework established, individual particles are allowed to spiral in along magnetic field lines and be reflected upstream or transmitted downstream due to the change in magnetic field at the shock surface and the initial conditions. The particles move according to the Lorentz force; each time a particle crosses the shock the final conditions at the crossing point become the new initial conditions, and the appropriate magnetic field is inserted into the force equation. The gain or loss in energy is monitored, along with the number of times the particle crosses the shock before being reflected or transmitted. Particles can be inserted either upstream or downstream from the shock and can move either forward or backward in time.

DISCUSSION

Figure 2 shows the CPME data used in the study. This is the 290 keV to 500 keV sectored proton data. It is highly structured on a short time scale particularly in the post shock region. Associated with each of the eight data channels is a direction consistent with the midpoint in the ecliptic plane of the 45 degree sampling angle. Plasma flow collected for each of these channels will be in the opposite direction. Magnetic field data is also available on this high resolution time scale. For several of the peaks the magnetic field is identified, and associated pitch angles are determined for each of the eight channels. Then, using a linear distribution of phase angles for each pitch, an ensemble of particles is sent backward in time to the shock surface.

The objective of this study is a quantitative determination of the particle kinematics in the vicinity of interplanetary shocks, in particular the 1974 day 312 shock. The anisotropy of the particle data at certain peaks together with the phase averaged energy changes, and comparisons, will be presented.

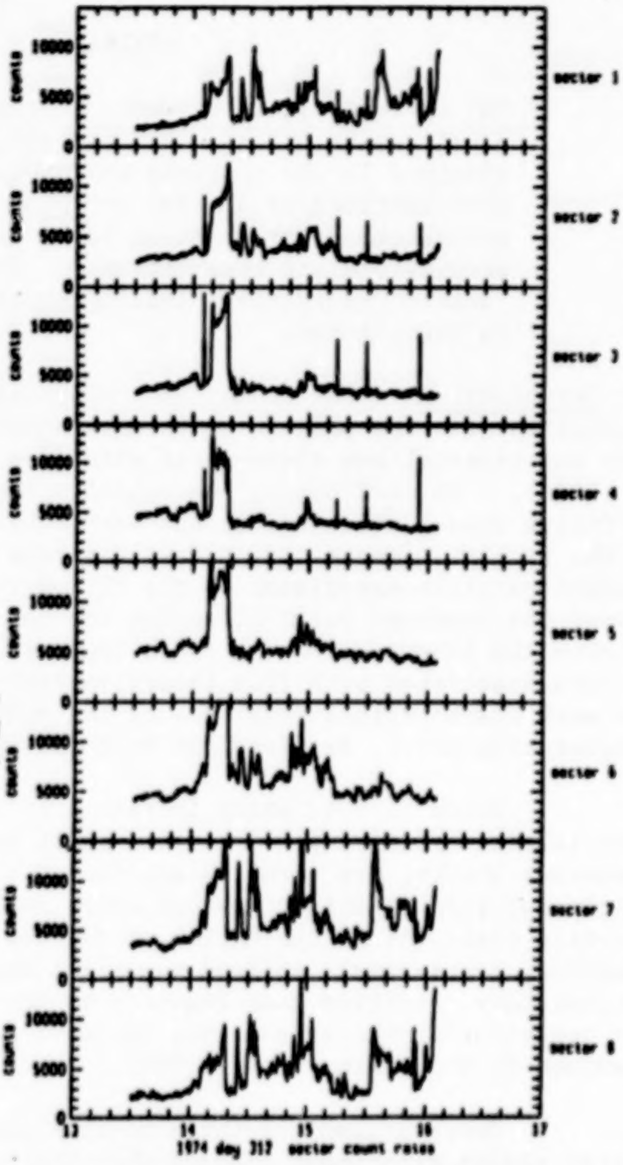

Fig. 2. 8 sectors in the ecliptic plane of 290 keV to 500 keV proton data from the JHU/APL Charged Particle Measurement Experiment (CPME). Shock occurs at 14.30 hrs.

ACKNOWLEDGEMENTS

The authors wish to thank Dr. P. R. Briggs for helpful suggestions and technical assistance. This work was supported in part by the NSF through grant ATM-7925987.

REFERENCES

1. R.P. Lepping and P.D. Argentiero, "Single Spacecraft Method of Estimating Shock Normals", J. Geophys Res., 76,19, 1971.

2. D.C. Colburn and C.P. Sonett, "Discontinuities in the Solar Wind", Space Sci. Rev., 5,439, 1966.

3. G. Chen, "Numerical Simulation of the Interaction of Charged Particles with Oblique Magnetohydrodynamic Shocks", PhD Thesis, University of Kansas, 1975.

N85-34775

SH 1.5-6

PITCH ANGLE DISTRIBUTIONS OF 35-1000 keV PROTONS AT QUASI-PERPENDICULAR INTERPLANETARY SHOCKS

A. Balogh
Physics Department
Imperial College, London, UK

and

G. Erdös
Central Research Institute for Physics
Budapest, Hungary

ABSTRACT

The characteristic features of the scatter-free acceleration process near perpendicular shocks are examined in the upstream and downstream pitch angle distributions of 35-1000 keV protons. Reasonable quantitative agreement is found between theoretical predictions and observations. The role played by "bottle" geometries, leading to enhanced acceleration, is highlighted.

1. Introduction. The mechanisms responsible for particle events associated with the passage of interplanetary shock waves have received much experimental and theoretical attention (Axford, 1981; Sanderson et al., 1985). In particular, the relative importance of scatter-free and diffusive acceleration models has been subjected to close scrutiny, much of the recent evidence coming from the observations made by the low energy charged particle experiment on the ISEE-3 (now ICE) spacecraft in orbit around the Lagrange point L1 during the period 1978-80. In this paper we examine the behaviour of the pitch angle distributions of 35-1000 keV protons associated with five interplanetary shocks which exhibited some of the most characteristic features of the scatter-free (gradient drift) acceleration model, as discussed by Sanderson et al. (1985).

Shock spikes, sharp increases in the intensity of low energy ions in close proximity to the passage of quasi-perpendicular interplanetary shocks, are normally attributed to particles accelerated in a single interaction with the shock wave, during which they drift along the electric field due to the motion of the shock in the frame of the plasma. Numerous, increasingly refined numerical simulations and analytical calculations have clarified many features of the process (see Decker, 1983). The behaviour of the anisotropy, in terms of spherical harmonics, was examined by Sanderson et al. (1985).

Observations presented in this paper were obtained with the low energy proton experiment onboard the ISEE-3 spacecraft (Balogh et al., 1978), which provides a 180-point measurement of the distribution function of 35-1000 keV protons every 16 seconds. The technique for describing the distribution function in terms of pitch angle distribution in the frame of the solar wind was worked out by Erdös (1981).

Time-reversed trajectory calculations for various shock parameters have been used to derive the qualitative features of the pitch angle distribution upstream and downstream of the shock. In Figure 1, results are shown for a shock of velocity $w_s = 200$ km/s, with an angle $\alpha = 80°$ between the shock normal and the upstream magnetic field, and therefore a transformation velocity into the electric field free frame (e.g. Axford, 1981) $w = w_s \sec \alpha = 1100$ km/s. We assumed a particle velocity $v = 3000$ km/s and an exponent of the differential power law spectrum $\gamma = 2.5$.

Peak intensities (in the solar wind frame) can be derived from adiabatic theory. The critical pitch angle for reflection upstream of the shock in the E-free frame is $\mu_c = \sqrt{1 - B_u/B_d}$, where B_u and B_d are the magnetic field strengths upstream and downstream of the shock, respectively. The transformation into the solar wind frame gives

$$\mu_u = \frac{\mu_c + w/v}{\sqrt{1 + 2\mu_c\, w/v + (w/v)^2}} \quad (1) \qquad \text{and} \qquad \mu_d = \frac{w/v}{\sqrt{1 + (w/v)^2}} \quad (2)$$

as the cosine of the pitch angle for which the maximum occurs in the distributions, respectively upstream and downstream of the shock. We note that the maxima in the distributions occur at pitch angles which depend on particle velocity. For oblique shocks and low energy particles the downstream distributions do not peak exactly at 90°, although as the particle energy increases, the peak of the distribution for given shock velocity and geometry moves to 90°, or $\mu = 0$.

For simple shock geometries, the gradient drift model predicts a sharp peak in the upstream pitch angle distribution at a value of μ given by (1) and the existence of a loss cone due to particles transmitted through the shock.

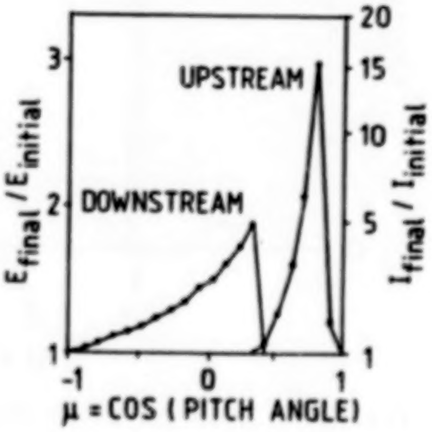

Fig. 1. Time-reversed calculation of upstream and downstream pitch angle distributions.

2. Observations. Pitch angle distributions upstream and downstream of five shock associated events are shown respectively in Figures 2 and 3. The energy dependence of upstream distributions is illustrated qualitatively in Figure 2, where pitch angle distributions are shown from two energy channels (35-56 keV and 91-147 keV, respectively).

The transformation velocity w can be estimated, using (2), from the position of the peak in the downstream pitch angle distributions, and compared to the value calculated from w_s and α as determined by Sanderson et al. (1985). The two sets of values, w(peak) and $w(w_s,\alpha)$ respectively, are shown in Figure 3.

The shift in the peak of the pitch angle distribution towards $\mu = 0$ for increasing energies was clearly identifiable on 26.7.79 and

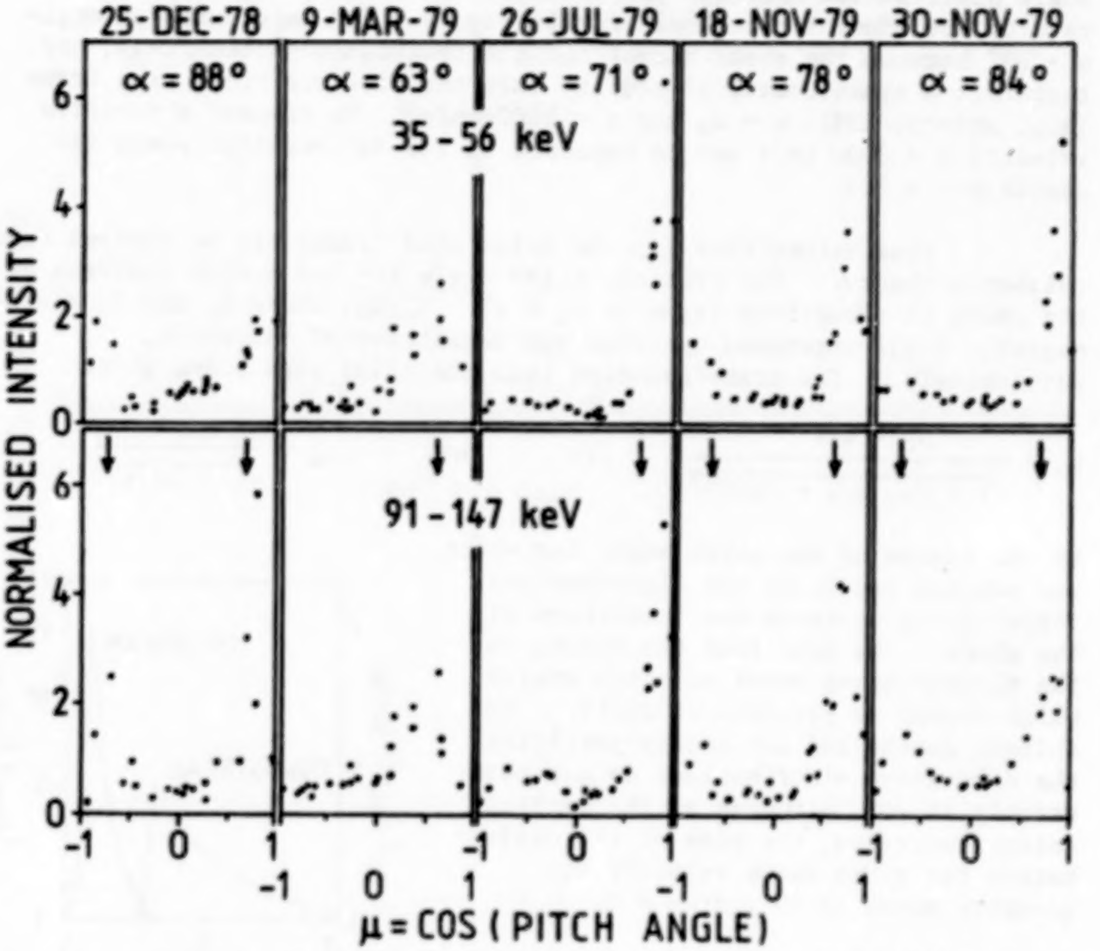

Fig. 2. Upstream pitch angle distributions in five shock-spike events. The arrows indicate the calculated values of μ_c.

μ_d	0.53	0.04	0.81	?	0.68
w(peak)	1800	100	4000	?	2700 km/s
$w(v_s,\alpha)$	3800	370	330	700	900 km/s

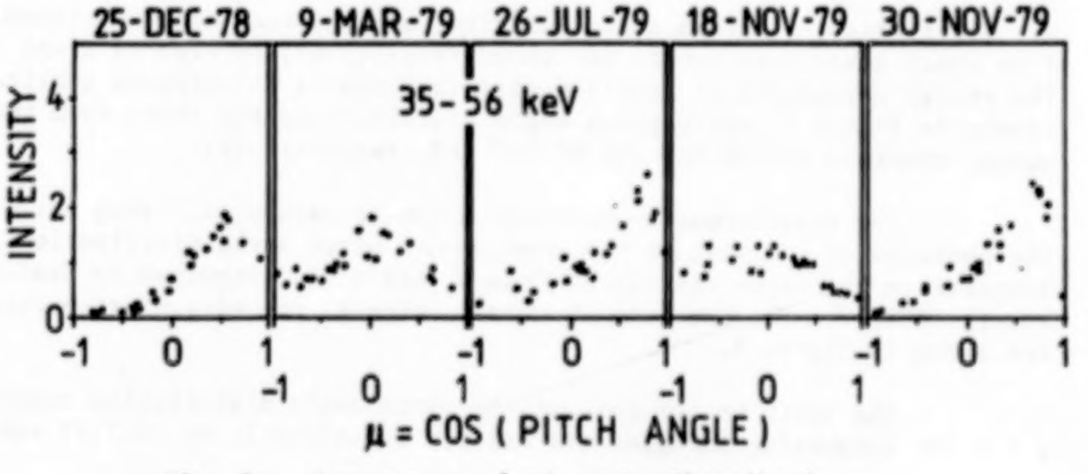

Fig. 3. Downstream pitch angle distributions.

30.11.79, illustrated in Figure 4 for the second of these events. On 9.3.79 and 18.11.79 the peak of the distribution was at $\mu = 0$ for all energies. On 25.12.78, the behaviour of the peak could not be ascertained due to poor statistics at high energies.

3. Discussion and Conclusions. For particles reflected upstream of the shock we observe a sharp cut-off in the pitch angle distribution, characteristic of a loss-cone in the distributions even at the lowest (∿ 35 keV) energies, corresponding to v = 3000 km/s. The existence of upstream reflected particles implies that the transformation velocity is in all cases less than about 3000 km/s.

The existence of a bi-directional loss cone as shown in Figure 2 at higher energies in at least two, possibly three events (25.12.78, 30.11.79, possibly 18.11.79), corresponding to the largest values of α, appears to indicate that the upstream magnetic field lines intersected the shock in such a way as to form a short-lived magnetic "bottle" as discussed by Balogh and Erdös (1983).

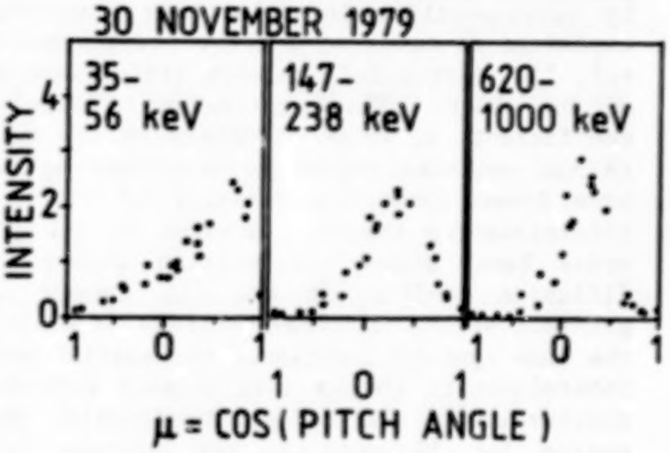

Fig. 4. Energy dependence of the downstream pitch angle distribution.

The effective shock velocity, determined from the position of the peak in the downstream pitch angle distribution, is different from that determined using w_s and the time-averaged value of the angle $\langle\alpha\rangle$ between the upstream magnetic field and the shock normal. This can be explained by either a small error (a few degrees) in the determination of the shock normal, or possibly by the sensitivity of pitch angle distribution to $w_s \langle \sec \alpha\rangle$ whereas the calculated velocity is $w_s \sec \langle\alpha\rangle$.

Overall, the shape and energy dependence of pitch angle distributions support the identification of these five events as examples of the gradient-drift acceleration process. However, the model should include the effect of fluctuations in the angle between the shock normal and the upstream field. Furthermore, at close-to-perpendicular shocks, the special geometry identified as a possibly short-lived magnetic "bottle" (as proposed by Balogh and Erdös, 1983) is likely to contribute significantly to the intensity of the shock spike.

References

Axford, W. I., (1981), 17th ICRC (Paris), 12, 155.
Balogh, A., et al., (1978), IEEE Trans. Geosci. Electronics GE-16, 176.
Balogh, A., and Erdös, G., (1983), Planet. Space Sci., 31, 1389.
Decker, R. B., (1983), J. Geophys. Res., 88, 9959.
Erdös, G., (1984), 17th ICRC (Paris), 8, 197.
Sanderson, T. R., et al., (1985), J. Geophys. Res., 90, 19.

N85-34776

SPATIAL DEPENDENCE OF THE LOCAL DIFFUSION COEFFICIENT MEASURED UPSTREAM OF THE NOVEMBER 12, 1978 INTERPLANETARY TRAVELING SHOCK

G. Gloeckler[1], F.M. Ipavich[1], B. Klecker[2], D. Hovestadt[2] and M. Scholer[2]

[1]Dept. of Physics & Astronomy, Univ. of MD, College Park, MD 20742 USA
[2]MPI für Extraterrestrische Physik, 8046 Garching, FRG

1. Introduction. Characteristics of suprathermal particles accelerated by quasi-parallel interplanetary traveling shocks have been generally explained in terms of a first order Fermi mechanism (e.g. see review in ref. 7). Such models require diffusive scattering of particles upstream of the shock. This scattering is characterized by a local diffusion coefficient, κ, which is determined by the local power density of waves in the upstream region as described by Lee (7). A number of studies have investigated the behavior of κ of $\lesssim 1$ MeV upstream ions close to interplanetary shocks. Scholer et al. (8) have used results of first order Fermi shock acceleration theory (e.g. ref. 1) to derive the diffusion coefficient and its energy dependence from the measured gradient of the upstream particle intensity. Van Nes et al. (9), using the same approach, obtained the spatial and energy dependence of κ for 3 interplanetary shocks over a more extended energy and distance range. Klecker et al. (6) deduced the spatial dependence of κ in the upstream region for 30 and 130 keV protons from the measured first-order anisotropies and intensity gradients.

In this paper we examine the dependence of the diffusion coefficient of suprathermal upstream protons on distance from the November 12, 1978 interplanetary traveling shock using a different approach. Unlike previous studies our method, which is based on measurements of particle streaming and intensity gradients, does not rely on predictions of shock acceleration theories or require first-order expansions. We have chosen to examine the local spatial variations of κ upstream of the November 12, 1978 shock because the characteristics of this quasi-parallel shock have been extensively studied (e.g. ref. 5), and also because of its favorable geometry (i.e. B field nearly radial). The initial results of this study have been reported by Gloeckler et al. (3).

2. Instrumentation and Method of Analysis. For this study we use the counting rate data from the University of Maryland/Max-Planck-Institut-Garching ULECA sensor (see ref. 4 for details) on ISEE-3 which was placed in a halo orbit at a radial distance of $\sim 230\ R_E$ upstream of the earth. Of relevance to the present discussion are the capabilities of the electrostatic deflection vs energy ULECA sensor to reliably separate protons from alpha particles and to determine their differential intensities in three energy bands centered on energies $\bar{E}$ of 33, 66 and 132 keV/e, and respective band widths $\Delta E/\bar{E}$ of 20, 27 and 37%. The sensor has a 60° fan-like acceptance aperature with its wide angle in a plane perpendicular to the ecliptic. The three proton counting rates are available every 128 sec in each of eight 45° sectors of the ecliptic plane.

For the present analysis we use the 33 and 66 keV sectored proton counting rate data to derive the proton distribution function, f, in the

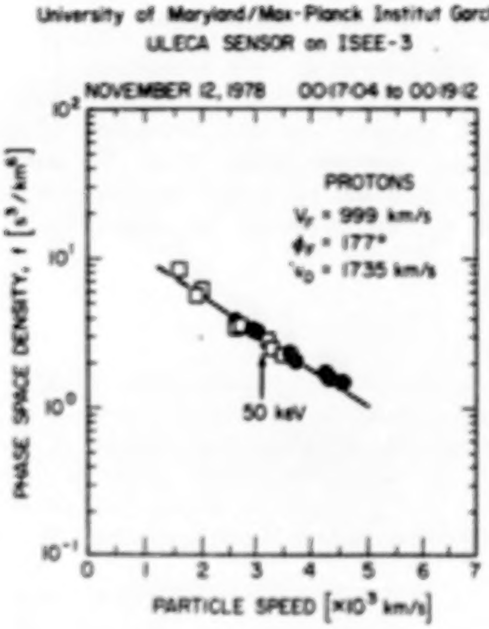

Figure 1. Rest frame proton phase space density, f(v). For $V_F = 999$ km/s and $\phi_F = 177^\circ$ segments of f(v) from the 33 keV proton rate channel (open squares) and the 66 keV channel (solid circles) join smoothly to form a common spectrum.

frame of reference (rest frame) in which f is assumed to be isotropic, and find the velocity, $\vec{V}_F$, of that rest frame relative to the spacecraft. We follow the technique of Gloeckler et al. (2) for mapping the sectored counting rate data into segments of the rest frame distribution function f(v), where v is the particle speed in the rest frame, making use of the invariance properties of f. When the proper rest frame velocity, $\vec{V}_F$, is chosen, the two segments of f(v) join up and the resulting spectrum becomes smooth, as shown in Figure 1. We note in particular that our method requires no prior knowledge of the shape of the rest frame energy spectrum nor need V_F/v be small.

3. Observations. Using a least-squares technique we derive for each available 128 sec interval the rest frame velocity and the rest frame distribution function (over a range of particle speeds from ~1000 to 5000 km/s). Figure 1 shows an example of a 128 sec averaged distribution function f(v) obtained ~ $4 \cdot 10^{10}$ cm upstream of the shock. We note that the shape of f(v) tends to be between that of a pure power law and an exponential, and that the spectrum becomes harder with distance from the shock (3). In the present analysis an exponential form is assumed and the e-folding speed, v_o, is computed from a linear fit to the data as shown in the figure.

In Figure 2 we plot the derived speed, V_F, (solid circles) and direction of motion, ϕ_F, (upper panel) of the suprathermal proton rest frame for each available 128 sec interval as a function of time as the shock is approached. Notice that the direction of $\vec{V}_F$ is generally within ~10° antisunward. Also shown is the sum of the solar wind, V_{SW}, and Alfvén, V_A, speeds taken (or derived) from data published in (5). While far ahead of the shock V_F exceeds $(V_{SW} + V_A)$ by as much as 1000 km/s, close to shock this difference is about a few hundred km/s, and behind the shock the two velocities are the same within experimental errors, implying pure convention at a speed equal to the sum of solar wind and Alfvén speeds. If we interpret the difference between the speeds V_F and $(V_{SW} + V_A)$ upstream of the shock to be the diffusive streaming of suprathermal ions along the magnetic field B (nearly radial for this shock) which results from the observed upstream particle density gradient, the local diffusion coefficient along B, $\kappa_{\parallel}(r_i,v)$ at a distance $r_i = (t_{sh}-t_i)V_{sh}$ from the shock (V_{sh} and t_{sh} are the shock speed and arrival times respectively) may be related to quantities measured at r_i as follows:

$$(1)\quad \vec{S} = 0 = [\frac{1}{3} v(\frac{\partial f}{\partial v})]*\vec{e}_B \cdot [\vec{V}_F(v)-(\vec{V}_{SW}+\vec{V}_A)] + \kappa_{\parallel}(r_i,v)*\vec{e}_B \cdot \vec{\nabla} f(v).$$

$\vec{S}$ is the differential streaming (which in zero is the particle rest frame), and $\vec{e}_B$ is the unit vector along $\vec{B}$. Since for the November 12, 1978 shock $\vec{B}$ and $\vec{V}_{SW}$ were nearly radial, and assuming that $\vec{V}_A$ was directed along $\vec{B}$ in the upstream region, and that f(v) has an exponential dependence on v with e-folding speed v_o, eq. (1) may be simplified to

$$(2)\quad \kappa_{\parallel}(r_i,v) = [\frac{v}{3v_o}]*[\frac{256\cdot 10^{10}}{\ln(f_{i+1}/f_{i-1})} V_{sh}]*[V_F-(V_A+V_{SW})].$$

To obtain κ at a distance r_i upstream of the shock values for v_o are obtained from the slope of the ith distribution function, and the particle density gradient is determined from the neighboring values of f at v = 3100 km/s (50 keV). V_F and $(V_A + V_{SW})$ are those plotted in Figure 1 at times t_i related to r_i by $r_i=(t_{sh}-t_i)V_{sh}$, where we used values for V_{sh} of 612 km/s and t_{sh} of 0:28:18 as given in (5).

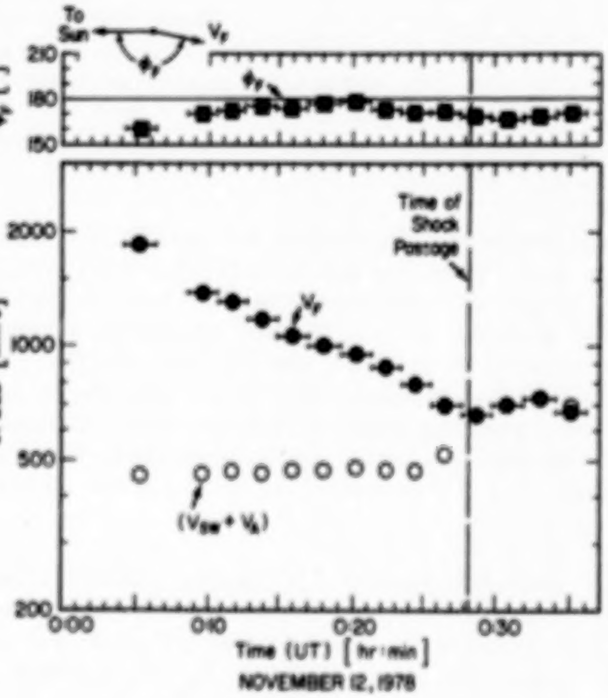

Figure 2. Speed and direction of motion of the rest frame (solid symbols) and the solar wind plus Alfvén speed $(V_{SW} + V_A)$ vs time before and immediately after shock passage. The difference between V_F and $(V_{SW} + V_A)$ is interpreted in terms of diffusive streaming. Behind the shock $V_F \simeq (V_{SW} + V_A)$ implying pure convection of 50 keV protons at that speed.

4. Spatial Dependence of $\kappa_{\parallel}$. In Figure 3 we show values of $\kappa_{\parallel}$ for ~ 50 keV protons as a function of distance from the shock, where $\kappa_{\parallel}$ is computed using eq. (2). The uncertainties shown come primarily from inaccuracies in determining the local density gradients. We note that there may be systematic errors (≲30%) in the values of κ resulting from using the simpler eq. (2) rather than eq. (1) which incorporates vector quantities. Consistent with expectations (7) we find that κ increases exponentially from a value of $\sim 7\cdot 10^{17}$ cm^2/s near the shock to $\sim 2.5\cdot 10^{18}$ cm^2/s at ~ $4.5\cdot 10^{10}$ cm from the shock with an e-folding distance of $3.4\cdot 10^{10}$ cm. What is surprising is the subsequent decrease (again exponential, with e-folding distance of $\sim 1.1\cdot 10^{10}$ cm) in

the value of κ with distance from the shock.

5. Discussion and Conclusions. The factor of ~ 4 increase in κ over a distance of ~ $4.5 \cdot 10^{10}$ cm is consistent with a comparable decrease in the power spectral density of waves at $2 \cdot 10^{-2}$ Hz (see Fig. 8 of ref. 7). The value of $7 \cdot 10^{10}$ cm^2/s of $\kappa_\parallel$ (50 keV) near the shock is in excellent agreement with prediction (for this shock) based on a self-consistent theory for wave excitation and particle acceleration upstream of interplanetary shocks (7). Our values of κ and its spatial dependence are also in qualitative agreement with those reported in (6,9). What is puzzling is the decrease of $\kappa_\parallel$ (50 keV) at larger distances which is not predicted by current theory. To pursue this point further we computed $\kappa_\parallel$ (100 keV) following the procedure outlined above but now using the 66 and 132 keV proton counting rate data. We found that the rest frame speeds V_F characteristic of ~100 keV protons are smaller than those shown in Figure 1 for 50 keV protons. Ratios of κ_{100}/κ_{50} were determined to be ~3.0, 1.2 and 1.8 near the shock, at $r = 4 \cdot 10^{10}$ cm and $8 \cdot 10^{10}$ cm respectively. Assuming a simple power law dependence of κ on particle energy these values correspond to $\kappa \propto E^{+1.6}$, $E^{+0.26}$, $E^{+0.85}$ respectively. We therefore conclude in agreement with (9) that one cannot characterize the energy dependence (or the spatial dependence) of κ in a simple way. Our results indicate an increase in the wave power density beyond $r \sim 5 \cdot 10^{10}$ cm and in general a more effective scattering of 50 keV protons compared to 100 keV protons. This hypothesis can be checked using local wave power spectrum measurements as a function of distance from the November 12, 1978 interplanetary traveling shock.

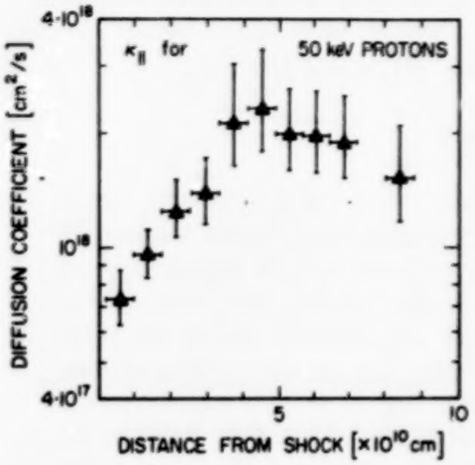

Figure 3. Spatial dependence of $\kappa_\parallel$ on upstream distance from the shock.

Acknowledgements. We are grateful for helpful discussions with Dr. M.A. Lee, and to the many individuals at UMD and MPE who made our ISEE experiments a success. This work was supported by NASA under contract NAS5-28704 and grants NAGW-101, NGR 21-002-224/316, and by the BMFT contract RV 14-B8/74 in West Germany.

References

1. Axford, W.I. et al. 1977, Plovdiv ICRC, 11, 132.
2. Gloeckler, G. et al. 1984, Geophys. Res. Letters, 11, 603.
3. Gloeckler, G. et al. 1984, Trans. Am. Geophys. U. (EOS), 65, 1035.
4. Hovestadt, D. et al. 1978, IEEE Trans. Geo. El., GE-16, 166.
5. Kennell, C.F. et al. 1984, J. Geophys. Res., 89, 5436.
6. Klecker, B. et al. 1984, private communication.
7. Lee, M.A. 1983, J. Geophys. Res., 88, 6109.
8. Scholer, M. et al. 1983, J. Geophys. Res., 88, 1977.
9. van Nes, P. et al. 1984, Adv. Space Res., 4, 315.

N85-34777
SH1.5-14

LATITUDE DEPENDENCE OF CO-ROTATING SHOCK ACCELERATION

R. E. Gold,[1] L. J. Lanzerotti,[2], C. G. Maclennan,[2] S. M. Krimigis[1]

[1] The Johns Hopkins University Applied Physics Laboratory, Laurel, MD, 20707 USA

[2] AT&T Bell Laboratories, Murray Hill, NJ, 07974 USA

ABSTRACT

We briefly discuss energetic particle observations in the outer heliosphere ($\geq$12 A.U.) by the LECP instruments on the Voyager 1 and Voyager 2 spacecraft that show a definite latitude dependence of the number and intensity of particle enhancements produced by corotating interplanetary regions during an interval when no solar energetic particle events were observed. The particle enhancements are fewer in number and less intense at higher ($\sim$20°) heliolatitudes. However, the similar spectral shapes of the accelerated particles at the two spacecraft indicate that the acceleration process is the same at the two latitudes, but less intense at the higher latitude.

1. Introduction. Particles accelerated in various regions of the heliosphere -- e.g., planetary bow shocks and magnetospheres, interplanetary traveling shocks, corotating interaction regions -- have been studied extensively near Earth (1 A.U.) [e.g., review by Gloeckler, 1984]. The progression of the two Voyager spacecraft deep into the outer heliosphere, beyond the orbit of Saturn, at nearly the same heliolongitude provides the opportunity to study interplanetary shock acceleration processes in the outer heliosphere as well as to search for heliolatitude dependences of the acceleration processes.

This brief note presents the results of some initial analyses of Voyager data during the period when the Voyager 1 (V1) spacecraft was at high heliolatitudes. The data used are from the Low Energy Charged Particle (LECP) instrument flown on both Voyager spacecraft [Krimigis et al., 1967]. Ion and proton data from selected sub-systems of the instrument are used.

2. Observations. Plotted in Figure 1 are the daily average fluxes of low energy ions and higher energy protons for the interval 1981 to mid-1984. The higher energy fluxes shown provide information on the occurrences of solar energetic particle events. The lower energy fluxes provide information on the occurrences of corotating interplanetary regions which can accelerate particles. The enhanced corotating particle fluxes are seen to occur sporadically at each spacecraft.

While there are a number of interesting intervals in the data (see Gold et al., 1985 for discussions of other aspects of these data), we concentrate specifically on the $\sim$200 days of data between day 243, 1983, and day 75, 1984. During this interval of 1983-84 the two Voyager spacecraft were at approximately the same heliolongitude, with Voyager 1 increasing in heliolatitude from $\sim$20.5 to $\sim$22.5° and in distance from $\sim$17.2 to $\sim$19 A.U. while Voyager 2 remained approximately in

ORIGINAL PAGE IS
OF POOR QUALITY

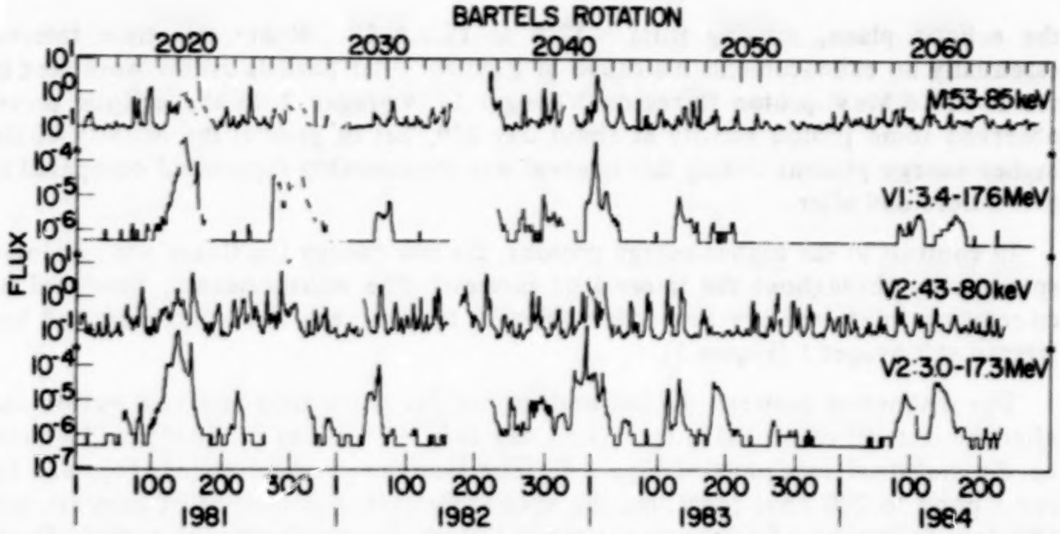

Fig. 1 Plot of daily average fluxes in ion and proton channels from LECP experiment on Voyager 1 and Voyager 2 spacecraft, 1981 to mid-1984.

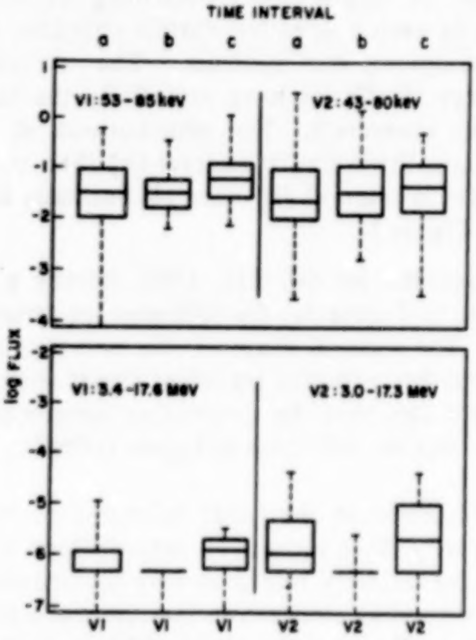

Fig. 2 Statistical distributions (represented as box plots) of fluxes in ion and proton channels on the two Voyager spacecraft for three time intervals. The interval (b) corresponds to day 243, 1983, to day 75, 1984. Intervals (a) and (c) correspond to a 200 day period preceding and a 150 day period following interval (b).

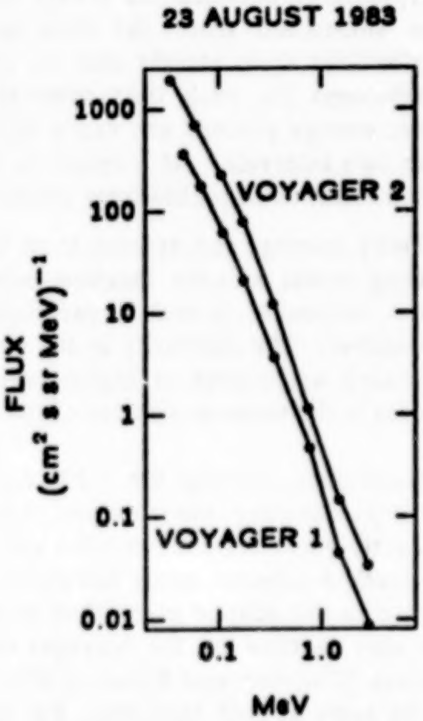

Fig. 3 Daily average ion spectra from Voyager 1 and Voyager 2 on day 235, 1983.

the ecliptic plane, moving from ~12.3 to 13.7 A.U. Within this time interval essentially no enhancements indicative of transient solar particle events were seen in the 3.4-17.6 MeV proton fluxes on Voyager 1. Voyager 2, in the ecliptic plane, observed some proton activity at about day 270, but in general the activity of the higher energy protons during this interval was considerably suppressed compared to that before and after.

In contrast to the higher energy protons, the low energy ion fluxes are enhanced sporadically throughout the interval of interest. The enhancements, produced by co-rotating interplanetary interaction (shock) regions, are less numerous and less intense at Voyager 1 (Figure 1).

The distinction between the ion and proton fluxes for time intervals before and after the interval of special interest (i.e., day 243, 1983 to day 75, 1984) is illustrated by the statistical box plots of Figure 2. The intervals denoted as (a), (b), and (c) correspond to 200 days preceding the special interval, the interval of interest, and 150 days following. Each box represents 50% of the distribution of particle fluxes during each time interval, with the median indicated by the line across the middle or lower edge of the box. The "error bars" indicate the distributions of fluxes for the upper 25% and lower 25% of the fluxes. A background, consisting of linear interpolations between the lowest flux rate in each respective Bartels rotation, has been subtracted from the data before compiling the statistics. The statistical distributions show clearly that the low energy ion fluxes have essentially the same distributions for each time interval at each spacecraft. The distributions of the higher energy protons are vastly different, quantitatively, in interval (b) than in the other two intervals. At Voyager 1, the fluxes in interval (b) were all basically near background, as is qualitatively evident from Figure 1.

Daily average ion spectra from both spacecraft on day 235, 1983, during a co-rotating event at each location, are shown in Figure 3. (A different co-rotating region, of course, is seen at each location.) The spectral shapes at the two locations are similar. The similarity in the spectra together with the statistical result showing decreased amplitudes at higher latitudes indicates that the co-rotating acceleration process is the same in and out of the ecliptic, but less effective at higher latitudes.

3. Discussion. During the ~200 days of quiescence in the outer heliosphere, when the interplanetary environment was essentially undisturbed by intermittent solar energetic particle events and the accompanying transient interplanetary disturbances, the particle enhancements associated with co-rotating interaction regions were more intense in the ecliptic plane than at latitudes ~20° above the plane. This conclusion was also reached by the Voyager cosmic ray instrument team studying >0.5 MeV protons [Christon and Stone, 1985]. The acceleration process, however, appears to be the same at both locations. For the ~200 days, the medium may have resembled the prediction of Burlaga [1983], who speculated that beyond ~10 A.U. the large scale dynamics of the interplanetary medium could be dominated by pressure waves; the originating coronal signatures would be lost. The solar wind would therefore be more homogeneous on a large scale [see also Smith et al., 1985, and Whang and Burlaga 1985]. Finally, Lanzerotti et al. [1985] suggested that the undisturbed (by transient events) outer heliosphere during this interval facilitated the detection of the enhanced levels of 3 kHz plasma waves that Kurth et al. [1984] attributed to plasma processes produced at the heliosphere boundary between the interaction of the solar wind with the interstellar medium.

4. Acknowledgements. **The work at The Johns Hopkins University Applied Physics Laboratory was supported by NASA under Contract N00024-83-C-5301.**

5. References

Burlaga, L. F., (1983), *J. Geophys. Res.*, *88*, 6085-6094.
Christon, S. E., and Stone, E. C., (1985), *Geophys. Res. Lett.*, *12*, 109-112.
Gloeckler, G., (1984), *Adv. Space Res.*, *4*, 127-137.
Gold, R. E., et al. (1985), in preparation.
Krimigis, S. M., et al. (1977), *Space Sci. Rev.*, *21*, 329-354.
Kurth, W. S., et al. (1984), *Nature*, *312*, 27-31.
Lanzerotti, L. J., et al. (1985), *Nature*, submitted.
Smith, Z. K., et al. (1985), *J. Geophys. Res.*, *90*, 217-220.
Whang, Y. C., and Burlaga, L. F., (1985), *J. Geophys. Res.*, *90*, 221-232.

N85-34778

ELEMENTAL ABUNDANCES IN COROTATING EVENTS

T. T. von Rosenvinge and R. E. McGuire*
NASA/Goddard Space Flight Center, Greenbelt, MD 20771, U.S.A.

1. Introduction. Large, persistent solar-wind streams in 1973 and 1974 produced corotating interaction regions which accelerated particles to energies of a few MeV/nucleon. The proton to helium ratio (H/He) reported in reference (1) was remarkably constant at a value (22 ± 5) equal to that in the solar wind (21 ± 3), suggesting that particles were being accelerated directly out of the solar wind. In this paper we report on preliminary results from a similar study approximately 11 years (i.e., one solar cycle) later. Corotating events have been identified by surveying the solar wind data, energetic particle time-histories and anisotropies. This data was all obtained from the ISEE-3/ICE spacecraft. These events also show H/He ratios similar to that in the solar wind. In addition, we have examined other corotating events at times when solar flare events could have injected particles into the corresponding corotating interaction regions. We find that in these cases there is evidence for H/He ratios which are significantly different from that of the solar wind but which are consistent with the range of values found in solar flare events.

2. Results. In Figure 1 we present a 27-day recurrence plot of the solar wind speed obtained from the Los Alamos National Laboratory Solar Wind Experiment on the ISEE-3 spacecraft (now renamed ICE); this data was processed by a simplified algorithm adequate for this purpose and is not to be considered definitive. ICE at this time was near 1 AU, leading the Earth in its orbit. Figure 1 shows the formation of two recurrent solar wind streams. A similar plot for the interplanetary magnetic field direction shows that these two streams are in opposite portions of a two sector magnetic field pattern. Using Figure 1 and particle time-history plots, we identified eight different time intervals as candidate corotating events. Low energy electron rates and high energy proton rates were scanned for any evidence of impulsive (solar) origin. In addition, anisotropy data was examined for apparent flow from the east. (Corotating events typically have particle flow from the east. This results from the vector sum of the radial Compton-Getting anisotropy due to the outward flow of the solar wind and the backward flow along the interplanetary magnetic field lines from the presumed acceleration region at several AU from the Sun.) The H/He ratio was evaluated for each interval in the energy range 4.5-6.5 MeV/nucleon. Also the C/O ratio was evaluated in the energy range 1.8-2.8 MeV/nucleon. Averaged over all eight intervals we find H/He = 20 ± 8 and C/O = .8 ± .2 (to be compared with H/He = 22 ± 5 and C/O = .8 ± .2 in reference (1)).

Other time periods since the launch of ISEE-3 in 1978 have been examined in a similar manner. A long-lived high-speed stream gave rise to a brief but apparently clean corotating event August 1-4, 1979. The

---

* Also Department of Physics and Astronomy, University of Maryland College Park, MD 20742, U.S.A.

ELEMENTAL ABUNDANCES IN COROTATING EVENTS

T. T. von Rosenvinge and R. E. McGuire*
NASA/Goddard Space Flight Center, Greenbelt, MD 20771, U.S.A.

1. Introduction. Large, persistent solar-wind streams in 1973 and 1974 produced corotating interaction regions which accelerated particles to energies of a few MeV/nucleon. The proton to helium ratio (H/He) reported in reference (1) was remarkably constant at a value (22 ± 5) equal to that in the solar wind (21 ± 3), suggesting that particles were being accelerated directly out of the solar wind. In this paper we report on preliminary results from a similar study approximately 11 years (i.e., one solar cycle) later. Corotating events have been identified by surveying the solar wind data, energetic particle time-histories and anisotropies. This data was all obtained from the ISEE-3/ICE spacecraft. These events also show H/He ratios similar to that in the solar wind. In addition, we have examined other corotating events at times when solar flare events could have injected particles into the corresponding corotating interaction regions. We find that in these cases there is evidence for H/He ratios which are significantly different from that of the solar wind but which are consistent with the range of values found in solar flare events.

2. Results. In Figure 1 we present a 27-day recurrence plot of the solar wind speed obtained from the Los Alamos National Laboratory Solar Wind Experiment on the ISEE-3 spacecraft (now renamed ICE); this data was processed by a simplified algorithm adequate for this purpose and is not to be considered definitive. ICE at this time was near 1 AU, leading the Earth in its orbit. Figure 1 shows the formation of two recurrent solar wind streams. A similar plot for the interplanetary magnetic field direction shows that these two streams are in opposite portions of a two sector magnetic field pattern. Using Figure 1 and particle time-history plots, we identified eight different time intervals as candidate corotating events. Low energy electron rates and high energy proton rates were scanned for any evidence of impulsive (solar) origin. In addition, anisotropy data was examined for apparent flow from the east. (Corotating events typically have particle flow from the east. This results from the vector sum of the radial Compton-Getting anisotropy due to the outward flow of the solar wind and the backward flow along the interplanetary magnetic field lines from the presumed acceleration region at several AU from the Sun.) The H/He ratio was evaluated for each interval in the energy range 4.5-6.5 MeV/nucleon. Also the C/O ratio was evaluated in the energy range 1.8-2.8 MeV/nucleon. Averaged over all eight intervals we find H/He = 20 ± 8 and C/O = .8 ± .2 (to be compared with H/He = 22 ± 5 and C/O = .8 ± .2 in reference (1)).

Other time periods since the launch of ISEE-3 in 1978 have been examined in a similar manner. A long-lived high-speed stream gave rise to a brief but apparently clean corotating event August 1-4, 1979. The

---

* Also Department of Physics and Astronomy, University of Maryland College Park, MD 20742, U.S.A.

N85-34779

SOLAR AND INTERPLANETARY PARTICLES AT 2 TO 4 MEV DURING SOLAR CYCLES 21, SOLAR CYCLE VARIATIONS OF EVENT SIZES, AND COMPOSITIONS

T.P. Armstrong, J.C. Shields, P.R. Briggs and S. Eckes
University of Kansas, Lawrence, Kansas 66045 U.S.A.

I. INTRODUCTION

In this paper we study 2-4 MeV/nucleon protons, alpha particles, and medium (CNO) nuclei in the near-Earth interplanetary medium during the years 1974-1981. Since this period contains both the solar activity minimum in 1976, and the very active onset phase of Solar Cycle 21, we have searched for characteristic compositional differences between the solar minimum and solar maximum ion populations.

Previous studies of interplanetary particle composition at these energies have concentrated on well-defined samples of the heliospheric medium. During flare particle events, the ambient plasma is dominated by ions accelerated in specific regions of the solar atmosphere; observation of the proton/alpha and alpha/medium ratios for flare events shows that there is marked compositional variability both during an event [1] and from event to event [2,3], suggesting the complicated nature of flare particle production and transport. Longer-term studies of non-flare activity have uncovered non-impulsive flux increases that recur with the same frequency as the Sun's 27-day rotational period; indeed, there appears to be a strong spatial relationship between these particle populations and the global structure of the interplanetary magnetic field [4,5]. The unusual spectral and compositional features of these non-flare events may point toward an interplanetary acceleration mechanism [6].

Beneath this overlying activity is a substrate of low-level flux which can be examined during so-called "quiet" periods. The characterization of quiet-time plasma carries some of the same difficulties as any null measurement, i.e. the need to remove ALL external effects; however, a continuous outflow of suprathermal solar particles has been observed and analyzed during less-active portions of the previous Solar Cycle [7].

Our aim is to examine the compositional characteristics of these separate particle populations at Solar Minimum, and to track the evolution of those characteristics during the transition to the Solar Active phase.

II. TECHNIQUE

The observations for this paper come from the Charged Particle Measurement Experiment aboard the Explorer 50 (a.k.a. IMP-8) satellite. The CPME is a telescope stack of solid-state detectors, with fixed descriminator voltages on each detector and on-board channel logic; the raw data is in the form of passbands in dE-vs-E space, and these passbands have been structured to provide for very "pure" single-species channels in the 2-4 MeV/nucleon range: channel P4 for protons, channel A3 for alphas, and channels Z1 and Z2 for medium nuclei. A complete description of the CPME has been presented elsewhere [8].

Daily-average count rates for the four channels mentioned above are used to produce values of the proton/alpha and alpha/medium ratios at 2-4 MeV/nucleon [8]. At this temporal resolution, data coverage is essentially complete from IMP-8 launch in 1973 up to the present; from examination of the entire data set, we have selected two continuous intervals: day 300 1974 to day 200 1977 (Solar Minimum), and day 1 1978 to day 365 1981 (Solar Active).

These two intervals have been subdivided into three categories of solar activity: 1) FLARE days, when the observed flux can be traced to a solar particle event or events; 2) QUIET time, when the daily-averaged flux is below a specified upper limit; and 3) non-flare, non-quiet (NFNQ) periods, when non-flare acceleration mechanisms may be operating. We have taken considerable care to identify flare-related flux enhancements, using earlier catalogues of particle flare observations [9,10] and extending these techniques for the identification of flares in the 1978-81 "Solar Active" period. The criterion for labeling daily-averaged flux as QUIET was a count rate in channel A3 (1.8 - 4.2 MeV/nucleon) less than 4 x 10**(-4) counts/sec; this threshold lies well above the instrumental background level, but below the typical level of activity observed by the CPME.

III. RESULTS

The sampling statistics for the Solar Minimum and Solar Active intervals appear in Table 1. As expected, the percentage of "quiet" days decreases when the Solar Active phase commences (from 53% to 8%), and the number of flare-dominated days increases (from 14% to 24%). However, our analysis also shows that the average flux increases for both flare and non-flare days during the Solar Active period. Median FLARE proton flux at Solar Active time is 4.20 protons/(cm**2 sec sr MeV), about 250 times as large as at Solar Minimum (0.017 protons/(cm**2 sec sr MeV)); the median alpha particle flux increases by a factor of 144, and the medium nuclei flux increases by a factor of 138. Even for non-flare periods, the average intensity increases from Solar Minimum to Solar Active intervals: by a factor of 80 for protons (from 0.00098 to 0.081 protons/(cm**2 sec sr MeV)) and by a factor of 25 for alphas and medium nuclei. Clearly, the active onset of a new Solar Cycle is very broad-based for medium-energy solar ions; the general level of particle production rises, while the number and intensity of solar particle flares increases.

Composition ratios of FLARE, NFNQ, and QUIET intervals for Solar Minimum and Solar Active periods appear in figures 1 and 2. We have formed histograms of the logarithm of H/He and He/CNO for these sets, and indicate the median of each distribution by an arrow. These median values are displayed in the figures, along with uncertainties representing the limits of two-thirds of the total range of values.

At Solar Minimum, the distributions are obviously distinct, with the QUIET flux having a relatively higher content of $Z > 1$ ions. Notice that the FLARE and NFNQ are also distinct, with the FLARE composition ratios showing wide variations. Apparently, the products of non-flare acceleration processes have different compositional signatures from flare particles, though the greatest differences exist between quiet and non-quiet flux.

The situation changes at the Solar Active period, with the H/He ratios increasing for all classes of activity. The NFNQ distribution is now almost identical with the FLARE distribution. Since the sheer number of samples makes it extremely unlikely that the NFNQ set is dominated by undocumented flare events, we suggest that the majority of NFNQ particles in the Solar Active phase may have their origin in flare acceleration processes.

ACKNOWLEDGMENTS

This work was supported in part by the NSF through grant ATM-83-05537 to the Johns Hopkins University Applied Physics Laboratory and the University of Kansas, and by a University of Kansas Undergraduate Research Award.

REFERENCES

1. Armstrong, T.P. et al,"Variations in the Charge Composition of the July 2-12, 1974 Solar Particle Event", Proceedings XIV Int. Cosmic Ray Conf., Munich, 1975, p. 1592
2. Lanzerotti, L.J. et al,"Abundance of solar cosmic ray alpha particles", J. Geophys. Res., 78, 1973, p. 3935
3. Mason, G.M. et al,"A survey of 1 MeV/nucleon solar flare particle abundances, $1<Z<26$, during the 1973-1977 solar minimum period", Ap. J., 239, 1980, p. 1070
4. Pesses, M.E. et al,"Energetic protons associated with interplanetary active regions 1-5 AU from the Sun", J. Geophys. Res., 83, 1978, p. 553
5. Briggs, P.R. et al,"Observations of interplanetary energetic ion enhancements near magnetic sector boundaries", GRL, 11, 1984, p. 27
6. Gloeckler, G. et al,"Observed distribution functions of H, He, C, O, and Fe in corotating energetic particle streams ...", Ap. J. (Lett.), 230, 1979, p. L191
7. Krimigis, S.M. et al,"Measurements of the quiet time low energy proton, alpha, and M nuclei component in cosmic rays", Proceedings XIII Int. Cosmic Ray Conf., Denver, 1973, p. 1656

N85-34780

ORIGINAL PAGE IS
OF POOR QUALITY

8. Armstrong, T.P.,"Handbook and reference manual for Charged Particle Measurement Experiment data from Explorer 47 and 50", Rep. JHU/APL 76-02, Appl. Phys. Lab., Johns Hopkins Univ., Laurel, Md., 1976
9. Briggs, P.R.,"Solar and interplanetary ions near Earth", dissertation, University of Kansas, 1981
10. Nonnast, J.H. et al,"A study of solar flare soft X-rays and their relation to particle events observed with IMP 8", J. Geophys. Res., 87, 1982, p. 4327

TABLE 1. Sampling Statistics

	Solar Minimum	Solar Active
QUIET	493	116
NFNQ	401	948
FLARE	132	346

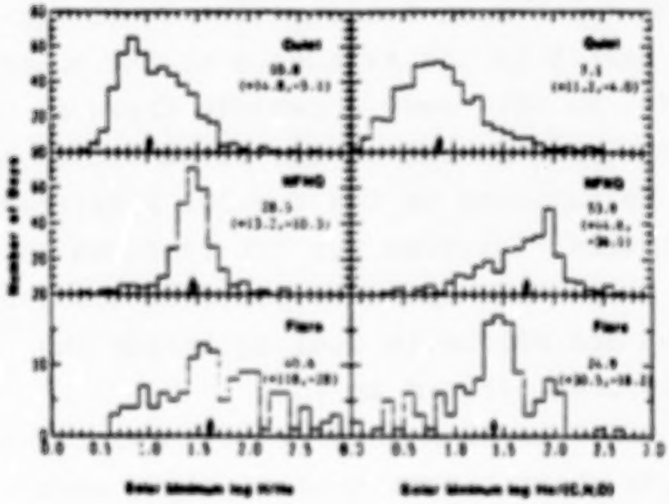

Figure 1

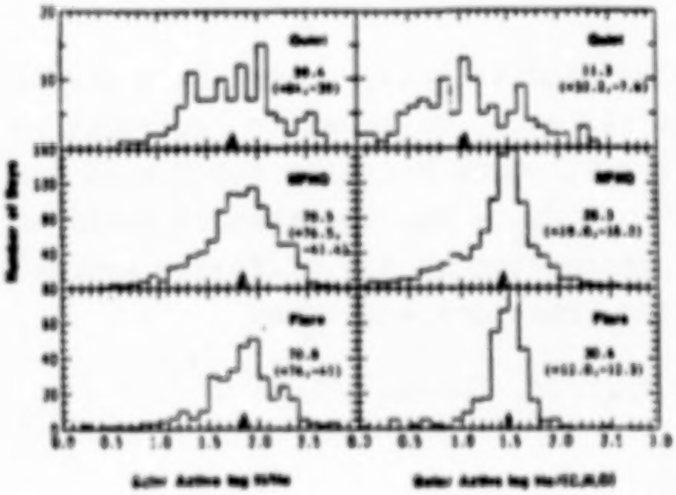

Figure 2

N85-34780

SH 1.5-17

COSMIC RAY ACCELERATION BY STELLAR WIND. SIMULATION FOR HELIOSPHERE

S.I.Petukhov, A.A.Turpanov, V.S.Nikolaev
Institute of Cosmophysical Research and Aeronomy,
Lenin Ave., 31, 677891 Yakutsk, USSR

ABSTRACT

It is shown that the acceleration of the solar wind particles at the solar wind terminal shock is capable of providing the total flux, spectrum and radial gradients of the low-energy protons close to ones observed in the interplanetary space.

__1. Introduction.__ The solar wind deceleration by the interstellar medium may result in the existence of the solar wind terminal shock [1]. In this case a certain fraction of thermal particles after being heated at the shock would obtain enough energy to be injected to the regular acceleration process [2-5]. An analytical solution for the spectrum in the frame of a simplified model that includes particle acceleration at the shock front and adiabatic cooling inside the stellar wind cavity has been derived in [6].

A more realistic model is discussed in the present paper in order to estimate whether this process might occur the main source of the low-energy cosmic rays in the heliosphere.

__2. Model.__ Let the solar wind velocity u(r) in a steady state spherically symmetric model be equal to u_1=const at $r < R$ and $u_2(R/r)^2$ at $r > R$, where R is the solar wind terminal shock radius, $\sigma = u_1/u_2$ - the compression ratio of the shock. Cosmic ray propagation in the diffusive approximation is governed by the transport equation:

$$\frac{1}{r^2}\frac{\partial}{\partial r}\left(r^2\varkappa\frac{\partial n}{\partial r}\right)-\frac{1}{r^2}\frac{\partial}{\partial r}(r^2un)+\frac{1}{3r^2}\frac{\partial}{\partial r}(r^2u)\frac{\partial}{\partial p}(np)=0 \qquad (1)$$

where n(r,p) is the particle number density per unit interval of momentum p, $\varkappa(r,p)$ - cosmic ray diffusion coefficient. At $r < R$ and $r > R$ (subscripts 1 and 2, respectively) it is given by

$$\varkappa_{1,2} = \mathcal{D}_{1,2}(p)\cdot(r/R)^{\beta_{1,2}}$$

The matching conditions are that the particles current and the number density should be continious at the shock. The other conditions are the absence of source or sink at r=0 ($r\cdot n(r,p) \to 0$ as $r \to 0$) and a given spectrum at infinity ($n(r,p) \to N_\infty(p)$ as $r \to \infty$).

Integrating (1) with respect to r from 0 to R-0 and using the analytical solution to (1) at $r > R$, the matching condition might be reduced to the following:

$$\frac{\sigma-1}{3\sigma}\cdot\frac{\partial}{\partial p}\left[p\cdot n(R,p)\right] + \frac{n(R,p)}{\sigma\cdot[1-\varphi(p)]} = \tag{2}$$

$$= \frac{1}{u_1 R^2}\int\limits_0^{R-0}\frac{1}{3r^2}\cdot\frac{\partial}{\partial r}(r^2 u_1)\frac{\partial}{\partial p}\left[p\cdot n(r,p)\right]r^2 dr + \frac{\varphi(p)\,N_\infty(p)}{\sigma[1-\varphi(p)]}$$

where $\varphi(p) = \exp\left[-u_2 R/(1+\beta_2)\,\mathcal{D}_2(p)\right]$.

Hence, the problem is to solve the equation (1) at $r \leqslant R$ with respect to the boundary condition (2). The equation (1) is valid at particle momentum p higher than some limiting value, say p_0. One more condition is necessary to make the system (1),(2) being completed, namely $n(R,p_0)=n_0$. This condition relates the injection rate to the spectrum amplitude $p=p_0$.

It has been shown [7-9], that the shock acceleration is efficient enough to transfer a significant fraction (~ 50%) of the inflowing plasma kinetic energy to the accelerated particles. The accelerated particles spectrum takes on the power law form with the index equal to that one given by the linear theory at particles velocity $v \simeq 3\,u_1$ [9]. The corresponding values for the solar wind particles are $T \simeq 10$ keV or $p_0 \simeq 3\cdot 10^{-3}\,m_p c$. Particles of energy corresponding to the cutoff velocity diffuse far upstream and suffer catastrophic adiabatic cooling.

3. Results and Discussion. The results of the numerical calculations are presented in Figure in comparison with the observational data [10]. The curve labelled "1" is the differential proton flux near the shock, "2" - that one at the orbit of the Earth. The following parameters were used: $u_1=5\cdot10^7$ cm/s, $R=7{,}5\cdot10^{14}$ cm, $\sigma=4$. The solar wind energy density near the shock E_k has been taken equal to 5 eV/cm^3. The value of n_o has been defined so, that accelerated particles ($T \gtrsim 10$ keV) contain 10% of the kinetic energy density E_k. The diffusion coefficients are $\varkappa_1=6{,}5\cdot10^{22}(p/m_pc)^{0,3}\,(r/R)^{0,2}$ cm$^2\cdot$s^{-1}, $\varkappa_2 \ll \varkappa_1$. The diffusion coefficient in the outside vicinity of the shock might be significantly reduced due to the magnetic field compression and convection of the turbulence excited by the accelerated particles. This leads to the strong modulation of the galactic proton flux at $T \lesssim 10$ MeV. Radial gradient $n^{-1}\partial n/\partial r$ takes on a value of 15%/AU at T=10 keV and 5%/AU at $T \simeq (1-10)$MeV.

The comparison of the results with the observations shows that under the above assumptions the acceleration rate (source Q_1) is capable of providing the

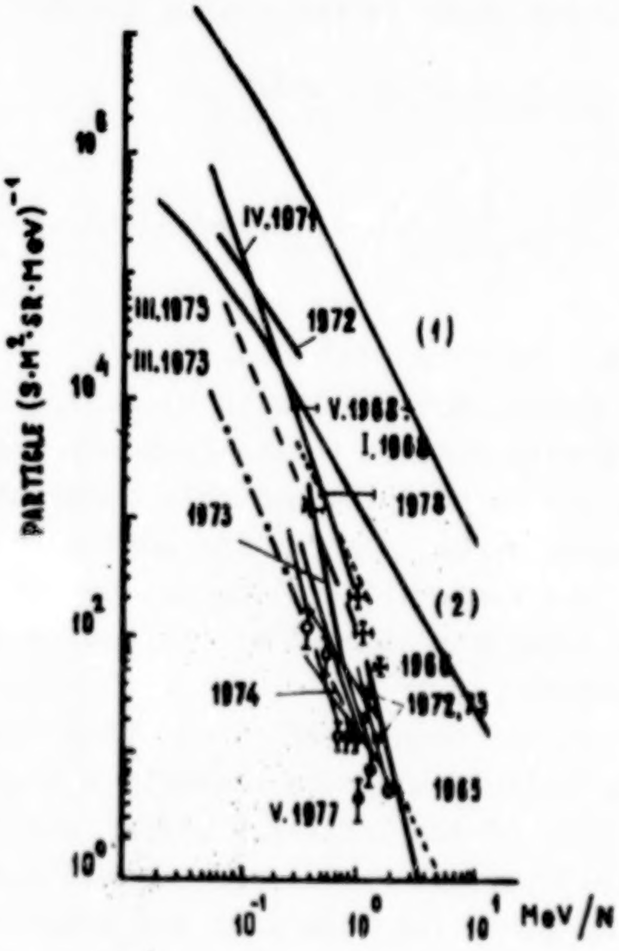

registered intensity of the low-energy particles in the interplanetary space. In the energy range $T < 100$ KeV the solar cosmic rays might contribute significantly to the total intensity, especially during the maximum of solar activity [11]. This would cause the complicated variations of the low-energy cosmic ray intensity: in the energy range $T < 100$ KeV the intensity is correlated with the solar activity level [10]; at the energy $T=6$ MeV/nucl. the anticorrelation takes place [11]. The relative contribution of the source Q_1 increases with the heliocentric distance r.

The cutoff energy for the accelerated particles spectrum is determined by $\varkappa_1 (T_{max}) \simeq Ru_1$; on the other hand, $T_{max} \simeq 10$ MeV/nucl. as is observed for different nuclear species. That shpuld be consistent with our model if $\varkappa$ is a function of T per nucleon only. The verification of this suggestion should be based on the treatment of the cosmic ray chemical composition.

4. Acknowledgements. The authors are grateful to Dr.E.G.Berezhko for useful discussions.

References

1. Baranov, V.B., Krasnobayev, K.V., (1977), Gidrodinamicheskaya Teoriya Kosmicheskoi Plasmy, Moskva, Nauka.
2. Krymsky, G.F., (1977), Dokl. AN SSSR, 234, 1306.
3. Axford, W.I. et al., (1977), Proc.15-th ICRC, Plovdiv, 11, 132.
4. Bell, A.R., (1978), Mon.Not.Royal Astron.Soc., 182, 147.
5. Blandford, R.D., Ostriker, J.P., (1978), Ap.J., 221, 29.
6. Webb, G.M. et al., (1983), Proc.18-th ICRC, Bangalore, 2, 263.
7. Eichler, D., (1979), Ap.J., 229, 419.
8. Krymsky, G.F., (1981), Izv. AN SSSR, Ser.fiz., 45, 450
9. Berezhko, E.G. et al., (1983), Proc.18-th ICRC, Bangalore, 2, 259.
10. Zeldovich, M.A., Logachev, Yu.I., (1983), Kosmicheskiye Issledovaniya, 21, No.5, 803.
11. Zamow, R., (1975), Ap.J., 197, 167.

N85-34781

SH 1.5-18

The Energy Spectrum of Jovian Electrons in Interplanetary Space

S. P. Christon, A. C. Cummings, and E. C. Stone

California Institute of Technology, Pasadena, CA 91125 USA

W. R. Webber

University of New Hampshire, Durham, NH 03824 USA

In this paper we report on the energy spectrum of electrons with energies ~10 to ~180 MeV measured with the electron telescope on the Voyager 1 and 2 spacecraft [*Stone et al.*, 1977] in interplanetary space from 1978 to 1983. The kinetic energy of electrons is determined by double dE/dx measurements from the first two detectors (D_1, D_2) of a stack of eight solid state detectors and by the range of particle penetration into the remaining six detectors (D_3 to D_8) which are interleaved with tungsten absorbers.

From 1978 to 1983 (radial range ~2 to ~12 AU) electrons of jovian origin were clearly observable for electrons stopping in D_3 ($E \gtrsim 4$ MeV) and in D_4 ($E \gtrsim 8$ MeV). For electrons stopping in D_5 ($E \gtrsim 12$ MeV), the jovian flux dominated the galactic electron flux for a period of approximately one year near the encounter with Jupiter [*Christon et al.*, 1985]. Jovian electrons were also observed in D_6 ($E \gtrsim 21$ MeV) but not in D_7 ($E \gtrsim 28$ MeV). A detailed interpretation of the electron variations in all energy channels depends on an accurate subtraction of background induced by energetic protons of a few 100 MeV. This subtraction is facilitated by laboratory calibration results at several energies. Further results on the differential energy spectrum of jovian electrons and limits on the maximum detected energies will be reported.

This work was supported in part by NASA under contract NAS 7-918 and grant NGR 05-002-160.

References.

Christon, S. P., A. C. Cummings, E. C. Stone, and W. R. Webber, *19th Internat. Cosmic-Ray Conf., La Jolla*, paper SH4.7-4, 1985.

Stone, E. C., R. E. Vogt, F. B. McDonald, B. J. Teegarden, J. H. Trainor, J. R. Jokipii, and W. R. Webber, *Space Sci. Rev.*, *21*, 355, 1977.

N85-34782

SH 1.5-19

THE JOVIAN ELECTRON SPECTRUM: 1978-1984[*]

Paul Evenson[+], Peter Meyer[x], and Dan Moses[x]

[+]Bartol Research Foundation, University of Delaware
Newark, Delaware 19716 USA

[x]Enrico Fermi Institute and Department of Physics
University of Chicago, Chicago, Illinois 60637 USA

ABSTRACT. Observations of Jovian electrons through six consecutive 13-month Jovian synodic periods from 1978 to 1984 have been made by the University of Chicago electron spectrometer onboard the ISEE-3 (ICE) spacecraft. The Jovian electron spectrum was determined from 5 to 30 MeV and was found to have a shape which is not a power law in kinetic energy, but cuts off at approximately 20 MeV. The average shape of the spectrum over each of the six intervals of best magnetic connection remains the same for all intervals within uncertainties.

1. **INTRODUCTION**. Observation of interplanetary electrons of Jovian origin at 1 AU provides a unique opportunity to study the propagation of charged particles in the inner heliosphere. Jupiter is a point source of particles imbedded in the solar cavity which sweeps through a range of magnetic connection to the earth with a well defined period. Previous investigators of Jovian electrons at 1 AU during the period of solar minimum (1,2) successfully applied a convection-diffusion model of propagation, determined the value of the "cross-field" diffusion coefficient, and demonstrated the modulation properties of corotating interaction regions. The study presented in this paper goes beyond the previous work into the time of solar maximum with observations by the University of Chicago spectrometer onboard the ISEE-3 spacecraft.

2. **METHOD**. A detailed description of the University of Chicago electron spectrometer onboard ISEE-3 is given in reference (3). The observations from ISEE-3 are unique in two aspects: the large change in the level of solar activity during the active life of the spacecraft and the absence of magnetospheric effects as the spacecraft was positioned at the inner Lagrangian point during most of the flight. Also, the instrument was very stable over the six years of observations. The single factor restricting continuous coverage of Jovian electrons is contamination by solar flare electrons. Elimination of solar flare contamination periods is handled by monitoring the spectral index of electrons observed on IMP-8 at lower energy (1-3 MeV). A better solar flare monitor is being developed using data from the Max-Planck-Institute ULEWAT instrument on ISEE-3 which is also free from magnetospheric effects.

The question of instrument stability in time is critical for solar modulation studies. The solid state detectors and plastic anticoincidence detectors show stability at the 3% level in all calibration and consistency checks over the duration of the flight. The ethylene gas Cerenkov detector used for proton rejection has a small gas leak, and loses approximately 1 atm of pressure per year from an initial pressure of 18 atm. The change in Cerenkov threshold is continually measured by a change in the pulse height distribution of the Cerenkov signal. The CsI calorimeter also exhibits a drift due to gain changes in the photomultiplier tube for which a correction is made using pulse height analysis of the signal from minimum ionizing protons.

---

[*]Supported, in part, by NASA contract NAS5-26680 and NASA grant NGL-14-01-005

Excellent background rejection is obtained with the requirement of a Cerenkov signal coincident with a stopping particle. The modulation of the flux of Jovian electrons at 1 AU due to changes in the degree of magnetic connection of the spacecraft to Jupiter can be used to further improve background rejection of particles which are not electrons, as well as electrons which are not Jovian in origin. The 10 MeV energy bin was chosen to monitor the Jovian modulation because it is the bin with the highest background rejection efficiency and because solar flares only rarely emit electrons at 10 MeV. A regression of daily rates of each energy bin relative to the 10 MeV bin determines the spectral shape of the Jovian component.

3. RESULTS. An example of a Jovian electron energy spectrum determined by the regression technique during the first epoch of best connection (Oct. 27, 1978 to Feb. 24, 1979) is shown in Figure 1. The spectrum is normalized by the average flux in the 10 MeV bin with the assumption that the flux in that bin is totally free of background. One characteristic of the Jovian electron spectral shape of particular interest is the roll off at energies above 20 MeV. The existence of a high energy limit to the Jovian interplanetary emission was first suggested in (4) and has implications for the acceleration of Jovian electrons, as will be discussed in a separate paper.

The form of the energy spectrum of Jovian electrons determined by the regression technique is found to be the same for each epoch of best connection. Therefore, within statistical errors, the average spectral shape of the Jovian quiet-time increases is constant over the period of observation covering six Jovian seasons. Further, the correlation of the daily rates of each energy bin with the reference 10 MeV bin is better fit by a linear regression than by any higher order polynomial during any one epoch of best connection, implying that the spectral shape is constant over a time scale as short as one day. The chi-square goodness of fit parameter degrades with the separation in mean energy of a bin from the reference 10 MeV bin. Because of limited statistics, the interpretation of this uniform scatter about the regression fit line as fluctuations of the spectral shape about an average shape cannot be quantified. Specifically, 10 hour variations in

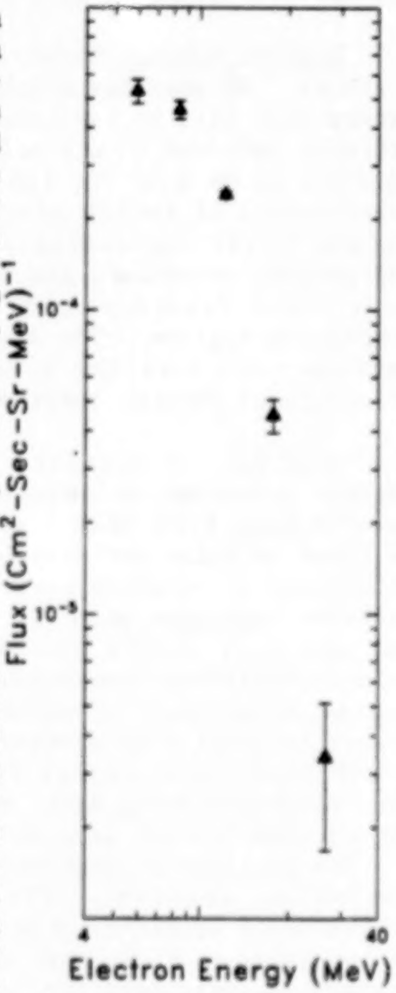

Fig. 1: Jovian electron spectrum determined by regression fit technique during Dec. 1978 epoch.

the spectral shape were searched for using several techniques and none were found.

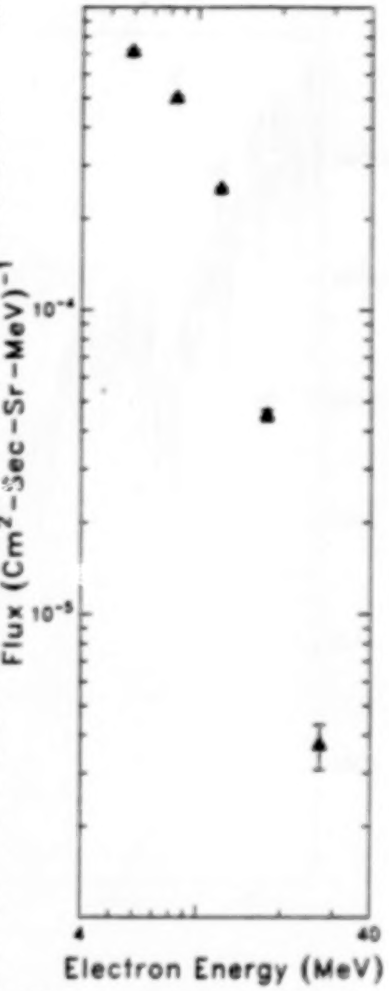

Fig. 2: Spectrum of all electrons during December 1978 epoch.

4. DISCUSSION. The spectral shape of Jovian electrons below 10 MeV presented in this paper is flatter than the kinetic energy power law index of 1.5 reported in (5). However, the spectral index reported at lower energies (.2-1 MeV) of -1.3 or less (6) coupled with the observed roll off above 20 MeV demonstrates that a power law spectrum is a poor approximation in this energy regime. Relying on the background rejection efficiency of the instrument, an average spectrum over the same time interval can be generated which includes the electron component not modulated by the change in the magnetic connection of the spacecraft to Jupiter (and therefore excluded from the spectrum obtained by the regression technique) (Figure 2). This spectrum more closely matches that of Eraker and Simpson (5) and, in comparison with the spectrum obtained by the regression technique, suggests the existence of a significant non-Jovian component at lower energies which would probably be of solar origin. A low energy solar electron component could also explain the degradation of the goodness of fit parameter at these energies.

The constancy of the spectral shape from epoch to epoch during the onset of solar maximum activity demonstrates the lack of solar cycle modulation of the Jovian electron spectrum. This lack of solar modulation is consistent with the conclusions from the radial gradient measurements of cosmic rays (7) that during solar maximum activity 99% of modulation occurs at a solar distance >31 AU. The difference in solar modulation of galactic particles and the relatively local Jovian particles is very clearly seen in the intensity-time plots in Figure 3. While galactic relativistic protons of significantly higher rigidity undergo an obvious solar cycle intensity variation, the Jovian electrons continue with the same 13-month cycles fit by the same convection-diffusion model envelope as observed during solar minimum activity. The only solar cycle effect in the Jovian electrons noted to date is a more impulsive rise and fall of individual increases.

REFERENCES

1. Conlon, T. 1978, JGR 83, 541.
2. Chenette, D. 1980, JGR 85, 2243.
3. Meyer, P. and Evenson, P. 1978, IEEE Trans. GE16, 180.
4. L'Heureux, J. and Meyer, P. 1976, Ap.J. 209, 955.
5. Eraker, J. and Simpson, J. 1979, Ap.J 232, L131.
6. Mewaldt, R., Stone, E. and Vogt, R. 1975, Proc. of 14th ICRC, 2, 758.
7. McKibben, B., Pyle, R. and Simpson, J. 1985, Ap.J 289, L35.

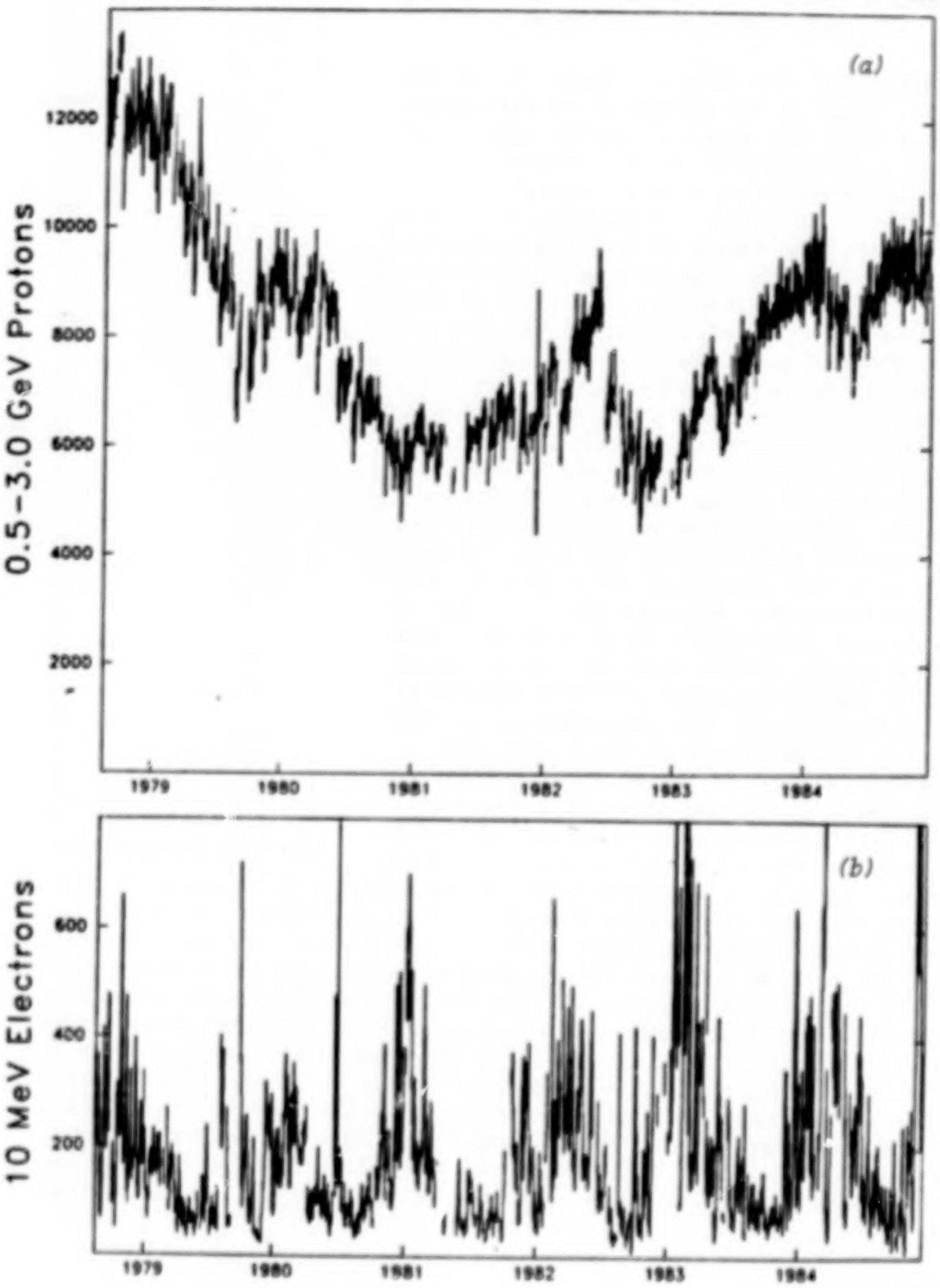

Fig. 3: Daily rates of protons (a) and electrons (b) observed by ISEE-3. No flare subtraction has been made in these plots.

N85-34783

SH 2.I-I

OBSERVATION OF THE FLUXES OF NUCLEI WITH ENERGIES IO-20 MEV PER NUCLEON DURING THE SOLAR FLARE OF APRIL 26, I984

Bobrovskaya V.V., Grigorov N.L., Zhuravlev D.A., Kondratyeva M.A.,
Nymmik R.A., Tretyakova Ch.A., Alekseev N.V., Vakulov P.V.,
Sechinov V.P.

Institute of Nuclear Physics, Moscow State University,
Moscow, USSR

ABSTRACT

Observations of the fluxes of low energy nuclei in the Earth's magnetosphere are reported. The energy distribution and the composition of the nuclear component of cosmic rays observed during the Solar flare of April 26, I984 are presented.

I. Introduction. The nuclei (C,N,O) with energies 5÷IO MeV per nucleon at altitudes 350÷450 km within $-52^0 < \lambda < 52^0$ were observed on the Skylab (I973-I974) and Salyut-6 (I98I) scientific orbital stations [I, 2] . The question now is what is the origin of these particles.

Indeed, the magnetic rigidity of the nuclei is so small that the Earth's magnetic field inhibits the access of these nuclei to the noted latitude from the interplanetary space. The assumption [I] that the observed particles are the singly charged ions which are "stripped" at the altitudes of hundreds of kms and trapped by the earth magnetic field seems to us unsound because the carbon ion C^+ with an energy of 5 MeV per nucleon will have the rigidity I.2 GV and can be trapped on the shell with $L \geqslant 3.5$ only. At the altitudes 350÷450 km within the latitudes $\pm 52^0$ there are no regions where the particles trapped at $L \geqslant 3.5$ could be observed.

The assumption that the observed particles are the nuclei accelerated in the magnetosphere and accumulated in the internal Earth radiation belt [3] is not obvious either. The fact is that at the noted altitudes the maximum of the intensity of the trapped particles corresponds to $L = I.2 \div I.5$. If the particles are accelerated while radial drifting from the more removed L-shells to L=I.2÷I.5, they will fail to reach the observing level, because of the low drift velocity they lose the total energy to ionization in the residual atmosphere at heights of 400--700 km. The assumption that the particles are accelerated at the observed altitudes would imply the existence of an unknown acceleration mechanism.

The consideration of the situation led us to the assumption that there are short-time periods when the radial drift velocity is by several orders of magnitude higher than that of mean one typical for small L. During these short-time periods the particles could jump from L = 2 to L = I.2 without energy losses. This assumption leads inevitably to the consequence on strong intensity variations of the flux of low energy nuclei observed at low altitudes near the Earth.

2. Methods. To obtain the information on the stability of the fluxes we regularly exposed small stacks of solid detectors to the near-earth space. The stacks consisted of several I00 mkm cellulose nitrate sheets. The area of the stacks was I0÷20 cm^2. The stacks were wrapped about with two Al mylar layers, each 5 mkm in thickness.

3. Results and discussion. The results of observations during the I984 year are presented in Table I.

Table I.

No. of the stack	Exposure time	Angle of inclination of orbit	Mean height	Flux of nuclei (C,N,O) $cm^{-2}day^{-I}$	Notes
I	April-Mai I984	72.9^0	400 km	~2000	Solar flare
2	June I984	72.8^0	400 km	I.3±0.I	
3	June-Julay I984	62^0	260 km	2.4±0.2	
4	September-Oktober I984	70^0	400 km	I5±I.0	
"Salyut-6"	Mai I98I	52^0	350 km	~200	Solar flare

C-4

The fluxes of nuclei in the 9th column refer to the particles coming to rest in the upper layer of the stacks. The I98I-year data are given in the last line of the Table. It is seen from the Table that during the I98I-I984 year period the flux of nuclei at the Earth magnetosphere at heights of ~ 300 km changed by a factor of $\sim 10^2$. During the I984 year the flux also varied (the data from the stacks No. 2, 3, and 4).

We failed to identify the charges of nuclei registered in the stack No.2 and No.3 because their paths were small. The spectra of particles stopping in the top sheet of these stacks were, therefore, identified from their total ranges on the assumption that all the nuclei registered are the oxygen ones. The obtained spectra are presented in Fig. I and 2. Typical is a very "soft" spectrum such as $I(E) \sim E^{-\gamma}$ with $\gamma \simeq 6$. It is similar in shape to the spectrum of the particles observed in the Earth's magnetosphere on the Salyut-6 station, but the flux intensities differ sharply. The bending of the

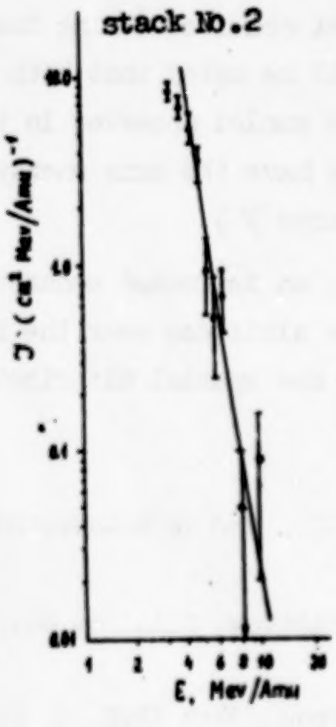

Fig. I

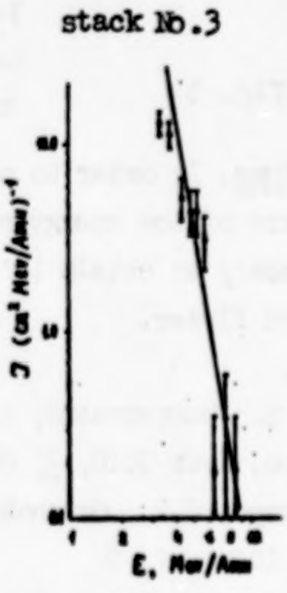

Fig. 2

spectrum at E < 4 MeV per nucleon is due to the threshold effect.

In April I984 the exposure time of the stack No.I coincided with a powerful solar flare. The particles observed in the stack No. I are seemingly the particles from the flare detected during the short-time periods when the satellite (Inclination to the equatorial plane ~ 73°) arrived into the region with a low rigidity of the magnetic cut-off. The charge identification was made from the dependence of the etched cone length on the residual range. The energy of the nuclei with a known charge was determined from the total path in the stack. Fig. 3 presents the energy spectrum of C and O nuclei observed during the flare. It will be noted that both flare particles and nuclei observed in the magnetosphere have the same energy distribution (large γ).

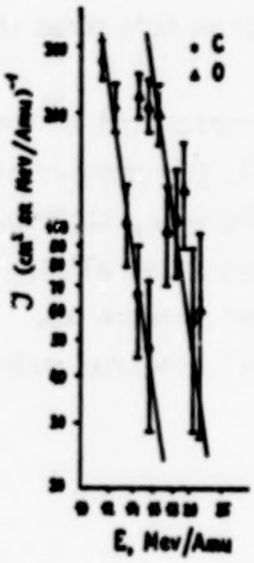

Fig. 3

4. Conclusions. In order to contribute to an increased understanding of the nature of low energy nuclei at low altitudes near the Earth it is necessary to obtain information on the spatial distribution of the observed fluxes.

References.

I. Biswas, S., Durgaprasad, N., Nevatia, J., and Venkatavaradan, V.S., (I975), Proc. I4th ICRC, 2, 8I6.

2. Bobrovskaya, V.V., Gorchakov, E.V., Grigorov, N.L. et al.,(I983), Proc. I8th ICRC, 2, 2.

3. Chan, J.H., and Price, P.B., (I975), Proc. I4th ICRC, 2, 83I.

ENERGETIC PARTICLE OBSERVATIONS OF THE SOLAR-GAMMA RAY/NEUTRON FLARE EVENTS OF 3 JUNE 1982 AND 21 JUNE 1980 ISOTOPIC AND CHEMICAL COMPOSITION

M.A.I.Van Hollebeke, Musee National des Sciences, Technique et Industrie
PARC de La Villette, Paris, France
Frank B. McDonald, NASA Headquarters/Code P, Washington, DC 20546
James H. Trainor, NASA/GSFC, Code 600, Greenbelt, MD 20770

ABSTRACT

Studies of the charge composition of two solar gamma-ray/neutron-flare events reveal a striking enrichment of Iron relative to Oxygen with a smaller enrichment of intermediate nuclei. He/O is also enhanced and moderate amounts of ^{3}He are detected but there is no evidence for ^{2}H or ^{3}H.

1. Introduction. The extensive studies of the charge composition of flare-associated energetic particles (McGuire et al., 1979, 1985; Cook et al., 1980, 1984; Mason et al., 1980) have shown there are large changes in the relative abundances of the various elements from event-to-event. J.P. Meyer (1985) has established that this data can be organized to first order by the assumption that there is a basic composition pattern (that differs from the photospheric composition by a simple bias related to an elements first ionization potential) with a superimposed additional bias which is a monotonic function of Z for $Z = 6 - 26$ and which varies from event-to-event.

It is of interest to compare these basic patterns with the charge and isotopic composition measured for the flare events of 3 June 1982 and 21 June 1980. Both of these events produced nuclear gamma-rays and solar neutrons that were detected by the Solar Max Mission gamma-ray experiment (Chupp 1984). These observations of nuclear gamma-rays and energetic neutrons require that a significant fraction of the solar energetic ions accelerated in conjunction with the flare event must have undergone nuclear interactions as they traversed the region of the lower corona and solar photosphere. It is especially useful to examine the isotopic composition of hydrogen and helium for the presence of the generally rare isotopes ^{2}H, ^{3}H and ^{3}He that could have been produced by spallation processes. Furthermore, the near simultaneity of the x-ray and γ-ray emission (Forrest & Chupp 1984) characterize these as very impulsive events that place stringent constraints on the particle acceleration time.

As reported previously (McDonald & Van Hollebeke, 1985a, b) the observed characteristic of the energetic protons and electrons accelerated in these events differ in several important aspects from typical solar particle increases. They had flat energy spectra ($\gamma = 1.22$ from 3-200 MeV for 3 June 1982 and $\gamma = 2.7$ for 21 June 1980), are electron rich ($P/e = 1$ at 4 MeV for 3 June 1980) and both have small but well-defined precursor events that begin some 3 hours before the impulse flare increase.

The principal detector used in these composition studies was the Low Energy Telescope (LET-1) of the Goddard Helios I cosmic-ray experiment. This 4 element multi-parameter system (two 150 micron Si dE/dx detectors, one 0.25 cm total energy solid-state detector and an anti-coincidence element) has a geometric factor of 0.13 cm^2-sr and is identical to that flown on Pioneer 10/11 except that the gain settings and priority selection system on Helios were modified to provide full scale coverage from $Z = 1-26$. Webber et al., 1975 has discussed in detail the excellent charge resolution of this telescope.

On 3 June 1981, Helios I was at a heliocentric distance of 0.57 AU and ∿3° in heliolongitude from the nominal interplanetary field-line connecting to the region above the flare site (S09, E72). On 21 June 1980 the spacecraft was ∿33° from the nominal field line joining the flare site (N20, W88) at a heliocentric distance of 0.54 AU.

2. Isotopic Composition. The detection of nuclear gamma-rays and neutrons from these two flare events indicate that nuclear interactions are occurring in the solar atmosphere and photosphere. At higher particle energies, nuclear spallation processes should result in the production of ^2H, ^3H and ^3He. The presence of these otherwise rare isotopes would provide additional information on the acceleration and transport of these energetic particles. From Table 1, it is seen that no ^2H or ^3H was detected except for one candidate ^2H on 3 June 1982. The upper limits in Table 1 are comparable to those of Mewaldt and Stone 1983 and McGuire et al., 1985 for single solar events but are substantially larger than their upper limits obtained by averaging over many events.

TABLE 1

	$^2H/H$ 3.3-39 MeV/nuc	$^3H/H$	$^3He/^4He$ 30-50 MeV/nuc
3 June 1982	$<4\times10^{-4}$	$<4\times10^{-4}$	$.02\pm.014$
21 June 1980	$<5\times10^{-4}$	$<4.5\times10^{-4}$	$.03\pm.013$

From the thin-target calculation of Ramaty and Kozlovsky, 1974, with $\gamma = 1.3$, an upper limit of ∿0.25 g/cm^2 is obtained for the solar material traversed by 30 MeV ions. There is a small but finite amount of ^3He detected for both of these events suggesting preferential injection and/or acceleration of this component rather than production by nuclear spallation processes.

3. Charge Composition. As in other studies of the elemental abundances, it is necessary to extend the analysis period beyond the time of peak intensity. However, because of the impulsive nature of the events, unusually short integration periods have been used (6.5 hrs for 6/3/82 and 10.5 hrs for 6/21/81). The resulting energy spectra for the more abundant species are shown in Fig 1. The H, He, C, O and Mg have a spectral index, $\gamma = 1.4$ for 3 June 1982 event and $\gamma = 2.0 \pm .1$ for Fe. For 21 June 1980 the corresponding γ values are 2.2 and 2.75. This steepening may result from the fact that the Iron spectra extends to higher energies (the H data is in agreement with this interpretation).

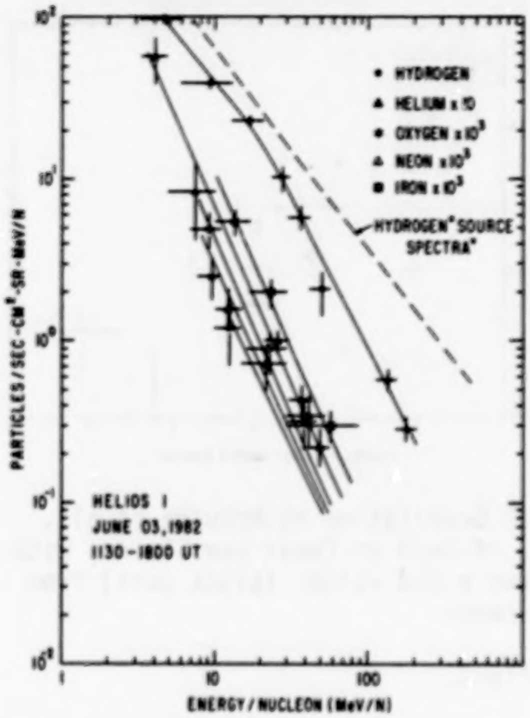

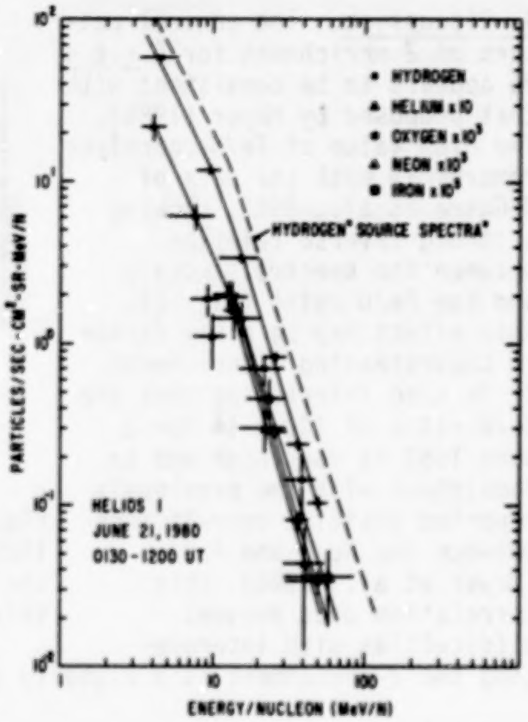

The details of the charge composition (Table 1) reveal a striking over abundance of Fe. The Fe/O of 2.5 ± .5 for the 3 June 1982 event is a factor of 34 above the baseline SEP value of McGuire et al., while the value of 0.91 for the 21 June 1982 increase is 14x the SEP baseline. The final line in Table 2 is an enhancement factor using the GSFC solar energetic particle baseline which is an average of events with little or no Fe enrichment. J. P. Meyer has derived a "mass-unbiased" baseline using a different criteria for selecting events. By either measure these events display a remarkable Fe/O enrichment. The Ne/O, Mg/O are enhanced by more modest amounts. The Si/O ratio is substantially less than would be expected but the poor statistics for this element do not permit any definite conclusions.

TABLE 2

SOLAR ENERGETIC PARTICLE ABUNDANCES: 10-47 MeV/nuc

	H/He	He/O	C/O	N/O	O/O	Ne/O	Mg/O	Si/O	Fe/O
3 June 1982 1130-1800	132	102±14	0.38±1	-------	1	0.87±.2	0.62±.18	0.2±.08	2.5±.5
21 June 1980 0130-1200	29	79±10	0.53±1	.16±.06	1	0.46±.13	0.19±.06	0.4±.1	0.91±.02
McGuire et al. SEP Baseline	66	53±5	0.45±.02	.13±.01	1	0.13±.01	0.18±.01	0.15±.01	0.066±.006
Enrichment Factor 3 June 1980	2	1.9±.27	0.84±.2	-------	1	6.7 ±1.5	3.4 ±1	1.3±.5	38±7.6

4. Discussion. The general pattern of Z enrichment for $6 \leq Z \leq 26$ appears to be consistent with that proposed by Meyer (1985). The high value of Fe/O correlate remarkably with the data of McGuire et al., 1985, showing a strong inverse relation between the spectral index γ and the Fe/O ratio (Fig. 2). This effect may be a key factor in understanding Z enrichment. It is also interesting that the He/O ratio of 102 ± 14 for 2 June 1982 is very high and is consistent with the previously reported positive correlations between the He/O and Fe/O (Meyer et al., 1985). This correlation does present difficulties with interpreting the Z-enrichment as a rigidity effect.

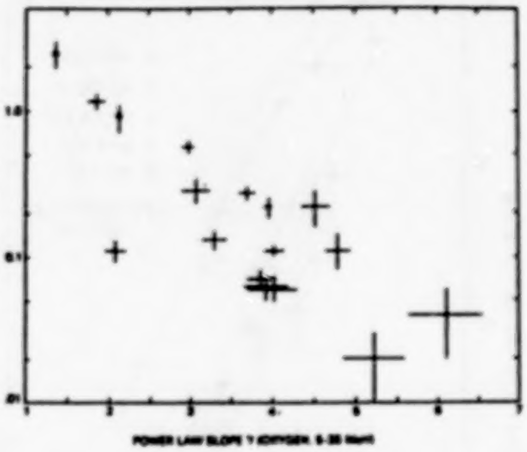

Fig. 2 Compilation by McGuire et al., 1985, of Fe/O vs Power Law Slope γ with the two added values (black dots) from this paper.

Solar neutrons are probably produced mainly by the spallation of He nuclei, but the large overabundance of Iron means Fe nuclei will make a substantial contribution to these events. Further studies are now underway to determine this relative role of He and Fe.

References

1. Chupp, E.L., (1984), Ann. Rev. Astron. Astrophysics, 22, 359
2. Cook, W.R., Stone, E.C., and Vogt, R.E., (1980), Ap.J., 238, L97; (1984), Ap. J. 279, 827
3. Forrest, D.J., and Chupp, E.L., (1984), Nature, 305, 291
4. Mason, G.M., Fisk, L.A., Hovestadt, D., and Gloeckler, G., (1980), Ap.J. 239, 1970
5. McDonald, F.B., and Van Hollebeke, M.A.I., (1985a), Ap.J., 290, L67; (1985b), Proc. 19th ICRC, Paper # SH1.3-8
6. McGuire, R.E., von Rosenvinge, T.T., and McDonald, F.B., (1979), Proc. 16th ICRC, Kyoto, 5, 61; (1985) submitted for publication to Ap.J.
7. Mewaldt, R.A. and Stone, E.C., (1983), Proc. 18th ICRC, Bangalore, 4, 52
8. Meyer, J.P., (1985), Ap.J. Supplement, 57, 1515.
9. Ramaty, R, and Kozlovsky, B., (1974), Ap.J., 193, 1974
10. Ramaty, R., Lingenfelter, R.E., and Kozlovsky, B., (1982), Gamma Ray Transients and Related Phenomena, Ed. R.E. Lingenfelter, et al., (N.Y. AIP) P211
11. Webber, W.R., Roelof, E.C., McDonald, F.B., Teegarden, B.J., and Trainor, J.H., (1975), Ap.J., 199, 482.

N85-34785 SH 2.1-4

Precision Measurements of Solar Energetic Particle Elemental Composition

H. Breneman and E. C. Stone

California Institute of Technology
Pasadena, California 91125 USA

1. Introduction

Using data from the Cosmic Ray Subsystem (CRS) aboard the Voyager 1 and 2 spacecraft (Stone et al. 1977), we have determined solar energetic particle abundances or upper limits for all elements with $3 \le Z \le 30$ from a combined set of 10 solar flares during the 1977-1982 time period. Statistically meaningful abundances have been determined for the first time for several rare elements including P, Cl, K, Ti and Mn, while the precision of the mean abundances for the more abundant elements has been improved by typically a factor of ~3 over previously reported values. When compared to solar photospheric spectroscopic abundances, these new SEP abundances more clearly exhibit the step-function dependence on first ionization potential previously reported by Cook et al. (1979, 1984) and Meyer (1981, 1985).

2. Observations

Each CRS includes four Low Energy Telescopes (LET) and two High Energy Telescopes (HET) employing silicon solid-state detectors and covering a combined incident energy range for oxygen of 3.5 - 50 MeV/nucleon. A scatterplot of LET data from the Z = 14 - 20 charge range is shown in Fig. 1. Even relatively rare elements such as Ar and Ca are clearly resolved. For the rarer elements (e.g., P, Cl, K), the abundances were determined by performing maximum-likelihood fits to the rare element peak and its two usually more abundant neighbors. For the most abundant elements (C, N, O, Ne, Na, Mg, Al, Si, S, Ar, Ca, Cr, Fe), the abundances could be determined in each of the flares; these values were averaged to obtain mean abundances using a weighting technique that takes into account both statistical variations and real abundance variations from flare to flare.

3. Results

The average SEP abundances relative to silicon for elements with $3 \le Z \le 30$ are listed in Table I. In Fig. 2, these results for the more abundant elements are compared to those obtained by other recent investigations. It can be seen that the new abundances agree well with the previously determined values but have about a factor of three higher precision.

4. Discussion

An ordering by first ionization potential (FIP) of SEP composition relative to "solar system" or photospheric composition has been noted in the past (Hovestadt 1974; Webber 1975; McGuire et al. 1979). In particular, Cook et al. (1979, 1984) found a step-function dependence on FIP, with elements with FIP > 10 eV depleted by a factor of ~5 in SEPs and elements with FIP < 8 eV approximately equally abundant in SEPs and the photosphere. This behavior may be expected on the basis of

N85-34785

ORIGINAL PAGE IS
OF POOR QUALITY

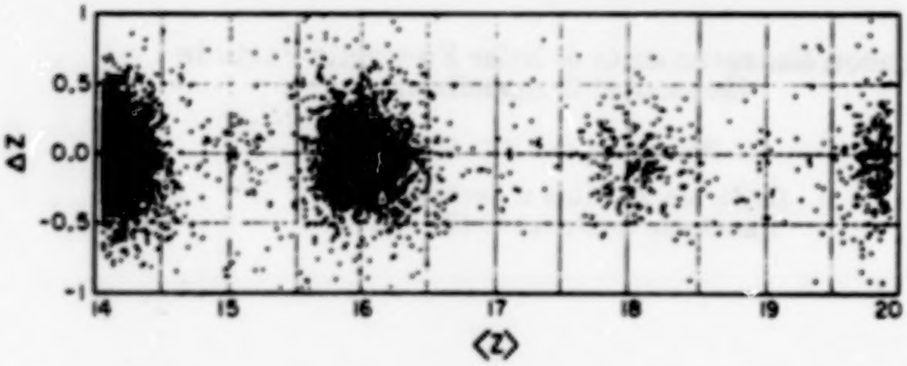

Fig. 1. Scatterplot of SEP data from LET in the Z = 14 - 20 charge range. ⟨Z⟩ is the average, and ΔZ the difference, of two essentially independent charge determinations obtained from the LET data for each analyzed particle.

dynamical ionization models such as that of Geiss and Bochsler (1984) for the formation of the corona. Fig. 3 shows that the step-function ordering by FIP is more clearly defined in the new data, including the elements P, Cl, K, Ti, and Mn. However, Fig. 3 also discloses statistically significant enhancements and depletions of several elements such as Na, Fe and Ni, which are discussed by Breneman and Stone (1985) in the context of an acceleration/propagation fractionation of SEPs based on the ionic charge-to-mass ratio of the species making up the SEPs.

In Fig. 4, the SEP abundances are compared to galactic cosmic ray source (GCRS) abundances (Lund 1984). The absence of a FIP-dependence in the SEP/GCRS ratio indicates that the GCRS may have a FIP-dependent step-function fractionation like that of the SEPs (Cook et al. 1979, Meyer 1981, Lund 1984). Both may exhibit a depletion of elements with FIP greater than ~10 eV because of the smaller flux of ionizing photons with energies greater than that of Ly-α (10.2 eV). Both C and N appear to be distinctly different in SEPs and the GCRS.

Table I. SEP average elemental abundances (Si = 1000).

Z	abundance	Z	abundance	Z	abundance	Z	abundance
3	< 1.33	10	887. [illegible]	17	2.01 [illegible]	24	14.3 [illegible]
4	< 0.17	11	73.3 [illegible]	18	20.7 [illegible]	25	5.0 [illegible]
5	< 0.34	12	1206. [illegible]	19	2.95 [illegible]	26	959.$^{+105}_{-94}$
6	2710. [illegible]	13	87.4 [illegible]	20	68.$^{+18}_{-16}$	27	< 13.5
7	775. [illegible]	14	1000.	21	(0.22 [illegible])*	28	33.6 [illegible]
8	6230. [illegible]	15	4.78 [illegible]	22	3.5$^{+1.4}_{-1.1}$	29	(0.40 [illegible])*
9	(0.29 [illegible])*	16	222. [illegible]	23	(0.34 [illegible])*	30	1.09 [illegible]

* Abundances for these elements are based on fewer than 5 particles and are highly uncertain.

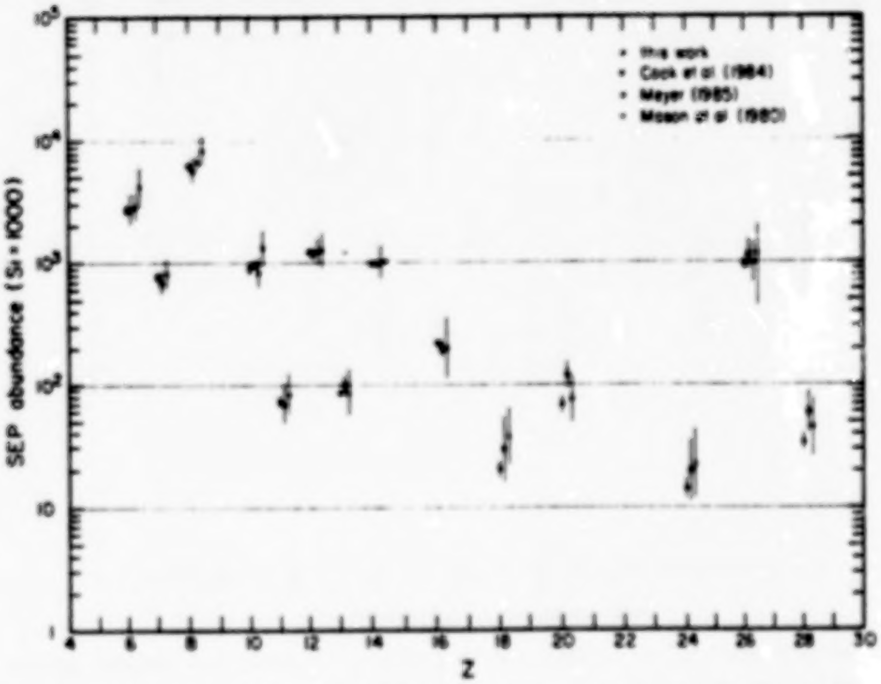

Fig. 2. Comparison of the new SEP abundances with other recent SEP abundance measurements.

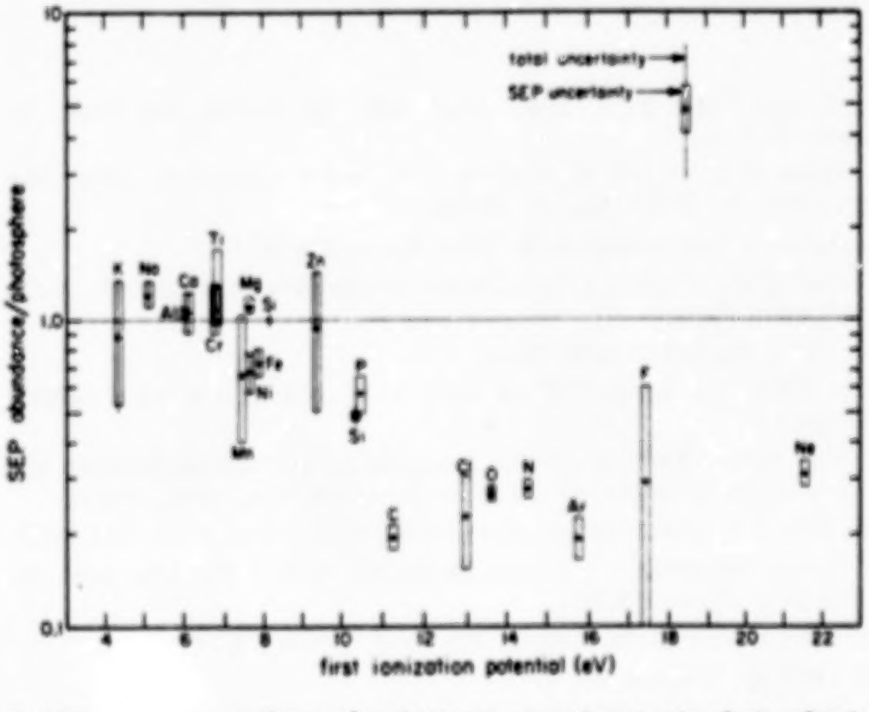

Fig. 3. SEP abundances (Si = 1) relative to spectroscopic photospheric abundances (Grevesse 1984), plotted vs. FIP.

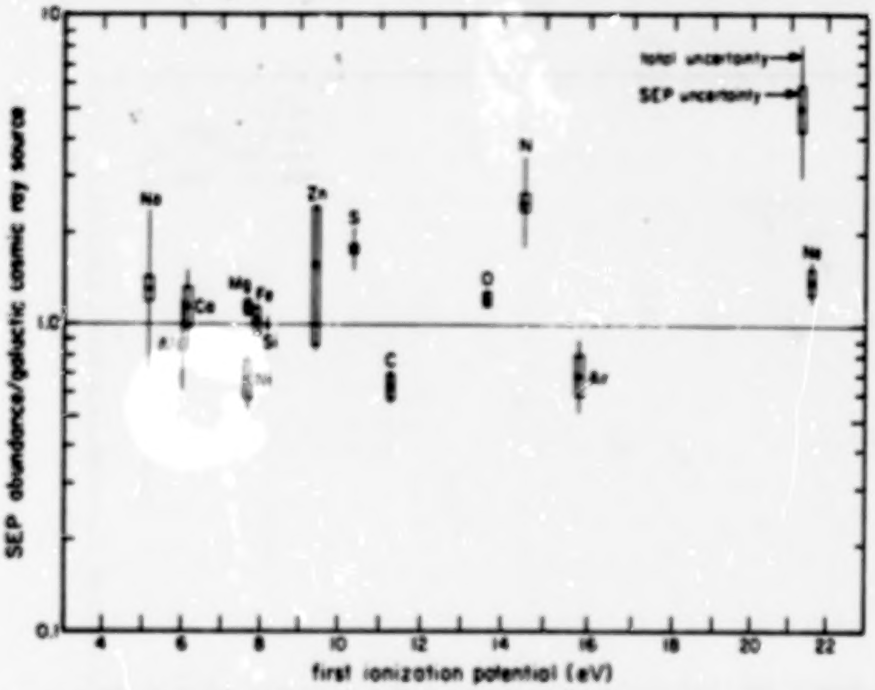

Fig. 4. SEP abundances (Si = 1) relative to galactic cosmic ray source abundances (Lund 1984), plotted vs. FIP.

5. Acknowledgements

This work has been supported in part by the National Aeronautics and Space Administration under contract NAS7-918 and grant NGR 05-002-160.

References

Breneman, H., and Stone, E. C. 1985, *Proc. 19th Int. Cosmic Ray Conf.* (La Jolla), paper SH 2.1-5.

Cook, W. R., Stone, E. C., Vogt, R. E., Trainor, J. H., and Webber, W. R. 1979, *Proc. 16th Int. Cosmic Ray Conf.* (Kyoto), **12**, 265.

Cook, W. R., Stone, E. C., and Vogt, R. E. 1984, *Ap. J.* **279**, 827.

Geiss, J., and Bochsler, P. 1984, International Conference on Isotopic Ratios in the Solar System, Paris.

Grevesse, N. 1984, *Physica Scripta* **T8**, 49.

Hovestadt, D. 1974, in *Solar Wind III*, ed. by C. T. Russell, University of California, Los Angeles.

Lund, N. 1984, Invited Lecture at the Symposium on Nucleosynthesis and Acceleration of Cosmic Rays, XXV COSPAR Plenary Meeting, Graz, Austria.

Mason, G. M., Fisk, L. A., Hovestadt, D., and Gloeckler, G. 1980, *Ap. J.* **239**, 1070.

McGuire, R. E., von Rosenvinge, T. T., and McDonald, F. B. 1979, *Proc. 16th Int. Cosmic Ray Conf.* (Kyoto), **5**, 61.

Meyer, J.-P. 1981, *Proc. 17th Int. Cosmic Ray Conf.* (Paris), **3**, 145.

Meyer, J.-P. 1985, *Ap. J. Suppl.* **57**, 151.

Stone, E. C., Vogt, R. E., McDonald, F. B., Teegarden, B. J., Trainor, J. H., Jokipii, J. R., and Webber, W. R. 1977, *Sp. Sci. Rev.* **21**, 355.

Webber, W. R. 1975, *Proc. 14th Int. Cosmic Ray Conf.* (Munich), **5**, 1597.

N85-34786

Solar Coronal and Photospheric Abundances from Solar Energetic Particle Measurements

H. Breneman and E. C. Stone

California Institute of Technology
Pasadena, California 91125 USA

1. Introduction

Solar energetic particle (SEP) elemental abundance data from the Cosmic Ray Subsystem (CRS) aboard the Voyager 1 and 2 spacecraft (Breneman and Stone 1985) are used to derive unfractionated coronal and photospheric abundances for elements with $3 \le Z \le 30$. We find that the ionic charge-to-mass ratio (Q/M) is the principal organizing parameter for the fractionation of SEPs by acceleration and propagation processes and for flare-to-flare variability, making possible a single-parameter Q/M-dependent correction to the average SEP abundances to obtain unfractionated coronal abundances. A further correction based on first ionization potential allows the determination of unfractionated photospheric abundances.

2. Results

The composition of individual flares relative to the average SEP composition can be described by a function that is roughly monotonic in Z but variable in magnitude from flare to flare (Cook et al. 1979, 1984; McGuire et al. 1979; Meyer 1981,

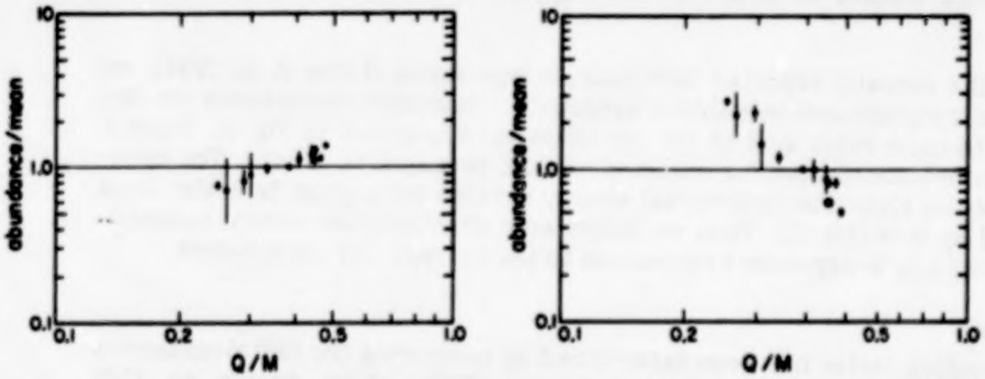

Fig. 1. Abundances relative to the mean SEP abundance for two typical flares, plotted vs. Q/M.

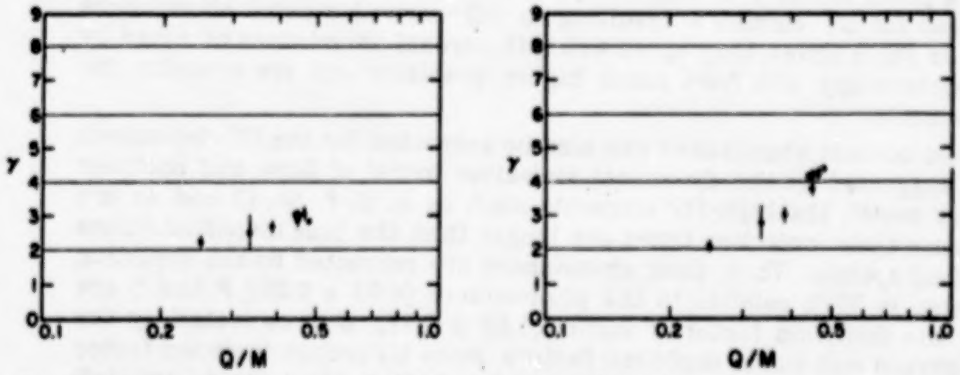

Fig. 2. Spectral index γ vs. Q/M for two typical flares.

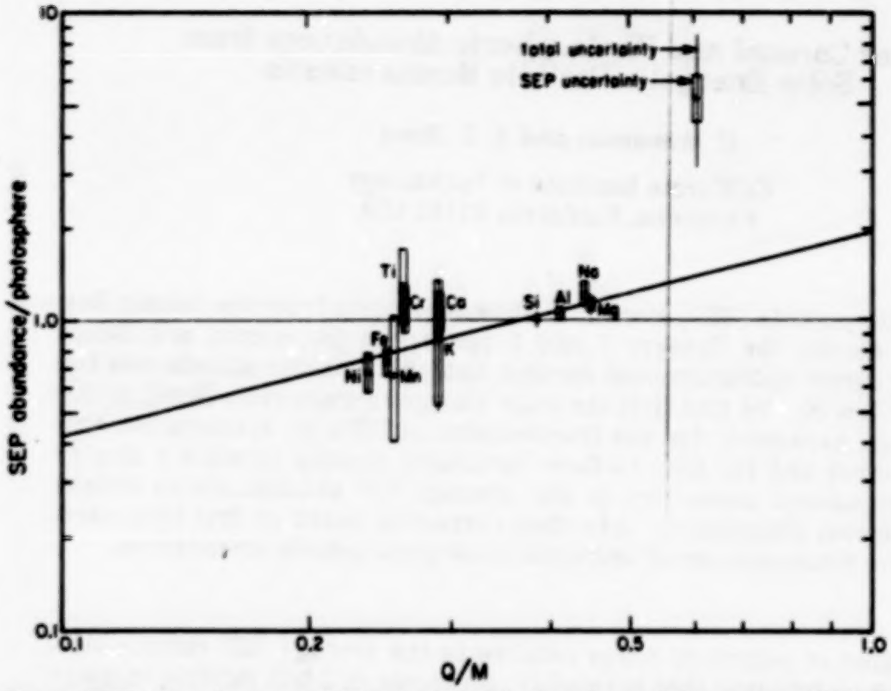

Fig. 3. Mean SEP abundance relative to the photosphere (Grevesse 1984) for the low-FIP elements, plotted vs. Q/M. The best-fit power-law has a reduced χ^2 of 1.0.

1985). Using the recently reported SEP ionic charge states (Luhn et al. 1984), we find that this compositional variability exhibits a monotonic dependence on the ionic charge-to-mass ratio Q/M of the particles, as illustrated in Fig. 1. Such a dependence is not unexpected for acceleration and propagation effects. The spectral indices of the elemental differential energy spectra for a given flare also tend to be ordered by Q/M (Fig. 2). Thus we derive an unfractionated coronal composition by applying a Q/M-dependent correction to the average SEP abundances.

3. Discussion

The correction factor has been determined by comparing the SEP abundances of elements with low first ionization potential (FIP), which display no FIP-dependent fractionation (Breneman and Stone 1985), to the photospheric spectroscopic abundances (Grevesse 1984) (see Fig. 3). The derived correction function, which is a power-law in Q/M with a slope of 0.66 ± 0.17, may be applied to the SEP abundances for *all* elements, resulting in SEP-derived coronal abundances (see Table I). As Fig. 4 shows, they agree well with coronal abundances obtained by XUV/X-ray spectroscopy, but have much higher precision and are available for many more elements.

The derived coronal abundances can also be corrected for the FIP-dependent fractionation suggested by the dynamical ionization model of Geiss and Bochsler (1984). In this model, the high-FIP elements such as N, O, F, Ne, Cl and Ar are depleted because their ionization times are longer than the time individual atoms spend in a rising spicule. Thus, their abundances are corrected by the depletion factor of oxygen in SEPs relative to the photosphere (4.03 ± 0.26); P and S are corrected by the depletion factor of sulfur (1.89 ± 0.17); C is corrected by the mean of the oxygen and sulfur depletion factors, since its proper depletion factor is uncertain; and the low-FIP elements, which are quickly ionized, are left

Table I. SEP-derived coronal and photospheric abundances relative to silicon.

Z	SEP-derived corona	SEP-derived photosphere	Z	SEP-derived corona	SEP-derived photosphere
6	$2350.^{+[illegible]}_{-[illegible]}$	$6490.^{+[illegible]}_{-[illegible]}$	19	$3.9^{+2.1}_{-1.6}$	$3.9^{+2.1}_{-1.6}$
7	$700.^{+[illegible]}_{-[illegible]}$	$2775.^{+[illegible]}_{-[illegible]}$	20	$82.^{+14}_{-12}$	$82.^{+14}_{-12}$
8	$5680.^{+[illegible]}_{-[illegible]}$	22900.	21	$(0.31^{+0.65}_{-0.31})$*	$(0.31^{+0.65}_{-0.31})$*
9	$(0.28^{+[illegible]}_{-[illegible]})$*	$(1.1^{+1.8}_{-1.1})$*	22	$4.9^{+1.9}_{-1.3}$	$4.9^{+1.9}_{-1.3}$
10	$783.^{+84}_{-77}$	$3140.^{+[illegible]}_{-165}$	23	$(0.48^{+[illegible]}_{-0.48})$*	$(0.48^{+[illegible]}_{-0.48})$*
11	$67.0^{+[illegible]}_{-[illegible]}$	$67.0^{+[illegible]}_{-[illegible]}$	24	$18.3^{+3.9}_{-3.3}$	$18.3^{+3.9}_{-3.3}$
12	$1089.^{+[illegible]}_{-[illegible]}$	$1089.^{+[illegible]}_{-[illegible]}$	25	$6.8^{+2.9}_{-2.7}$	$6.8^{+2.9}_{-2.7}$
13	$83.7^{+4.8}_{-4.6}$	$83.7^{+4.8}_{-4.6}$	26	$1270.^{+170}_{-150}$	$1270.^{+170}_{-150}$
14	1000.	1000.	27	< 18.1	< 18.1
15	$4.69^{+[illegible]}_{-0.72}$	$9.24^{+1.48}_{-1.34}$	28	$46.5^{+8.1}_{-7.4}$	$46.5^{+8.1}_{-7.4}$
16	$242.^{+10}_{-8}$	$460.^{+42}_{-36}$	29	$(0.57^{+0.87}_{-0.57})$*	$(0.57^{+0.87}_{-0.57})$*
17	$2.38^{+0.84}_{-0.66}$	$9.6^{+3.5}_{-3.5}$	30	$1.61^{+0.87}_{-0.76}$	$1.61^{+0.87}_{-0.76}$
18	$24.1^{+4.8}_{-3.6}$	$102.^{+20}_{-17}$			

* Based on fewer than 5 particles and highly uncertain.

unchanged. The resulting SEP-derived photospheric abundances (Table I) involve fewer modeling parameters than spectroscopic determinations and are available for some elements (e.g., C, N, Ne, Ar) that cannot be observed spectroscopically. The main differences (Fig. 5) are a significantly higher abundance of Cr (and possi-

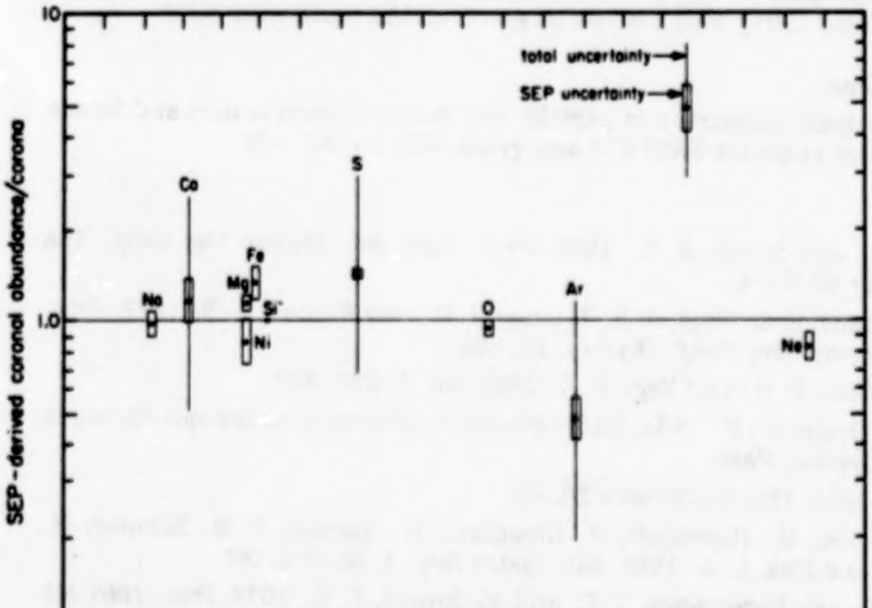

Fig. 4. SEP-derived coronal abundances relative to spectroscopically-derived coronal abundances (Veck and Parkinson 1981), plotted vs. FIP.

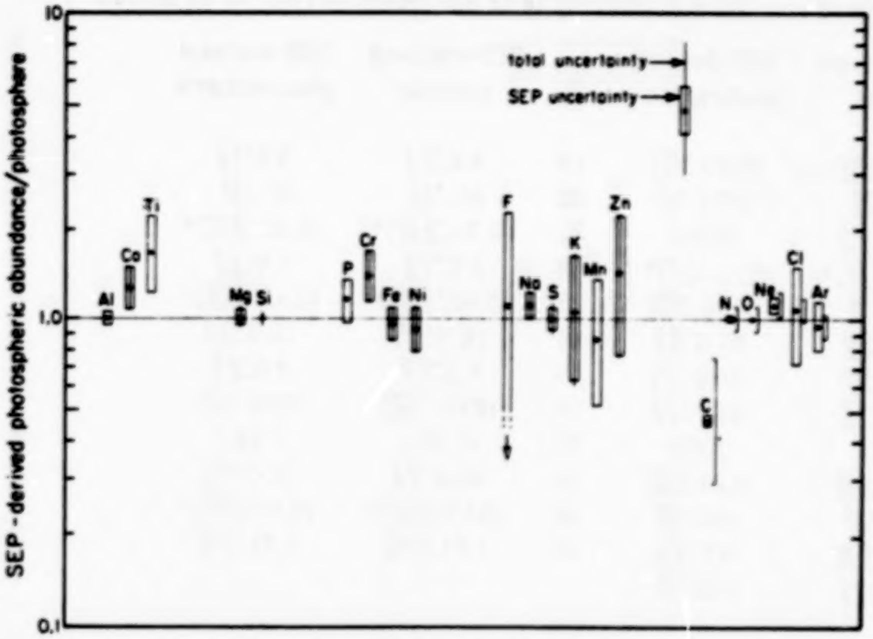

Fig. 5. SEP-derived photospheric abundances relative to spectroscopically-derived photospheric abundances (Grevesse 1984). The estimated uncertainty in the FIP fractionation correction is indicated by the vertical brackets.

bly Ca and Ti) and a C abundance that is about half of the commonly assumed solar abundance. The SEP-derived Fe/Si ratio is in agreement with the recent photospheric value (Grevesse 1984), which is 50% larger than the meteoritic value.

4. Acknowledgements

This work has been supported in part by the National Aeronautics and Space Administration under contract NAS7-918 and grant NGR 05-002-160.

References

Breneman, H., and Stone, E. C. 1985, *Proc. 19th Int. Cosmic Ray Conf.* (La Jolla), paper SH 2.1-4.

Cook, W. R., Stone, E. C., Vogt, R. E., Trainor, J. H., and Webber, W. R. 1979, *Proc. 16th Int. Cosmic Ray Conf.* (Kyoto), **12**, 265.

Cook, W. R., Stone, E. C., and Vogt, R. E. 1984, *Ap. J.* **279**, 827.

Geiss, J., and Bochsler, P. 1984, International Conference on Isotopic Ratios in the Solar System, Paris.

Grevesse, N. 1984, *Physica Scripta* **T8**, 49.

Luhn, A., Klecker, B., Hovestadt, D., Gloeckler, G., Ipavich, F. M., Scholer, M., Fan, C. Y., and Fisk, L. A. 1984, *Adv. Space Res.* **4**, No. 2-3, 161.

McGuire, R. E., von Rosenvinge, T. T., and McDonald, F. B. 1979, *Proc. 16th Int. Cosmic Ray Conf.* (Kyoto), **5**, 61.

Meyer, J.-P. 1981, *Proc. 17th Int. Cosmic Ray Conf.* (Paris), **3**, 145.

Meyer, J.-P. 1985, *Ap. J. Suppl.* **57**, 151.

SILICON TO IRON ABUNDANCES IN SOLAR COSMIC RAYS AND IN THE SUN

M.N. Vahia, S. Biswas and N. Durgaprasad
Tata Institute of Fundamental Research, Bombay 400005
INDIA

ABSTRACT

Differential spectra of even charged nuclei between Si and Fe in the August 4, 1972 event are made in the energy region of 10 to 40 MeV/n-1 using rocket borne plastic detectors. The resultant relative abundances of elements and low energy (E < 25 MeV n-1) enhancements are obtained. Comparison with spectroscopically determined photospheric abundances is also made. The implications of these relative abundances on the acceleration mechanisms is discussed.

1. Introduction. With rocket flights and solid state nuclear track detectors, large flares have been studied in great details and it has been shown that at the higher energies (E > 25 MeV/amu) the relative abundances tend to match the photospheric abundances (Bertsch et al 1974; Biswas et al., 1983; Crawford et al.,1975). August 4, 1972 was amongst the largest events with large heavy ion fluxes. Data of good statistics on relative abundances for even charged nuclei between Z = 14 to 26, were obtained in this flare. The results are discussed in this paper.

2. Experimental Method. The study of the August 4, 1972 event was done with a stack of 23 sheets of Lexan polycarbonate flown on a sounding rocket in NASA's SPICE programme from Ft. Churchill, Canada at 1916 UT to study the emission from an optical flare of 0617 UT the same day. The rocket was spin stabilised and reached an altitude of 160 kms above earth. The rocket nose cone was opened at an altitude of 60kms on ascent and closed at 85 kms on descent giving a total of 245 seconds of exposure (see Durgaprasad et al.,1982).

The plastics were recovered and processed in 6.25 N NaOH solution at (40 ± 0.1°C) for 4 hours to reveal the tracks of Z > 12 elements. A total area of 30 sq. cms. was studied at different depths to determine the spectra. The details of the technique are discussed elsewhere (Vahia, 1983).

Fractional charges were assigned to the tracks using the constant energy contours. The Gaussian of all charge values for all the events had FWHM for Si as 0.24 and for Fe as 0.33 charge units. From this the differential spectra were determined. The differential spectrum of Fe obtained by us was compared with that obtained by other investigators on the same flight and good agreement was found. The oxygen spectra were taken from the measurements by Bertsch et al (1974) made in the same flight. The relative abundances are plotted in Fig. 1

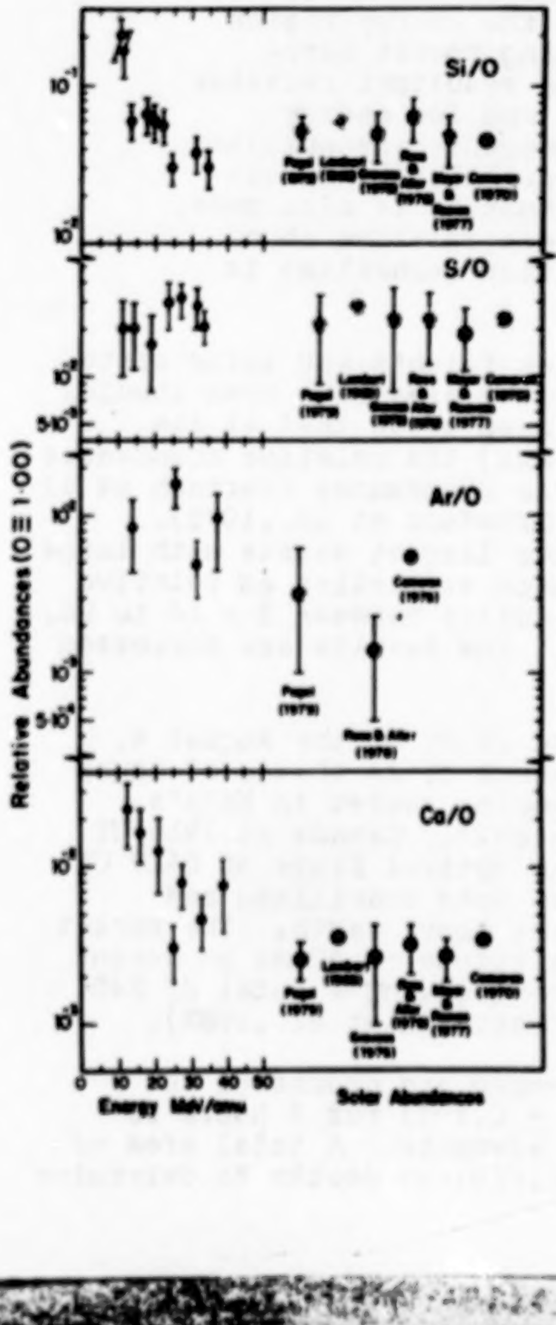

3. Results. In the case of odd charges, only 13 Al, 15 P, 17 Cl, 23 V and 25 Mn have observable flux values. It should however be noted that since the processing of the sheets was done to study Z > 14 elements, the aluminium events are subject to detection efficiency and its relative abundances need not be considered for the present study.

Fig. 1a Variation of relative abundances as compared to oxygen of Si, S, Ar and Ca nuclei with energy and comparison with photospheric value.

As for other observed elements, with the notable exception of Mn, they are seen in very small numbers and no definite flux measurements can be attempted. The Mn fluxes can be determined only approximately by the method of histogram subtraction. In the entire energy range Mn/O ratio is about 0.10. This is a factor of about 10 above the spectroscopic determination of 0.008 ± 0.005. In our study we observed a high Mn/Fe ratio of 0.15 (~20 events) in sheets 2 and 3 (energy 10-25 MeV/amu). In the sheets 4-5 and 8-9 we saw no appreciable flux of Mn implying Mn/Fe < 0.01. Hence it seems that Mn must be having a steeply falling spectrum. This would result in a steeply falling enhancement between 10 and 40 MeV/amu. Therefore the Mn observations seem to be consistent with the photospheric determinations within experimental approximations. The elements Si, S, Ar, Ca, Ti, Cr and Fe are seen in sufficiently large numbers to help in determining detailed spectra of these elements. Their charge histograms are also distinct and devoid of possible contaminations. Hence flux determination can be made accurately and with a high degree of confidence.

At low energy, the more abundant elements for which detailed study is possible show varying degrees of enhancements.(Figure 1)

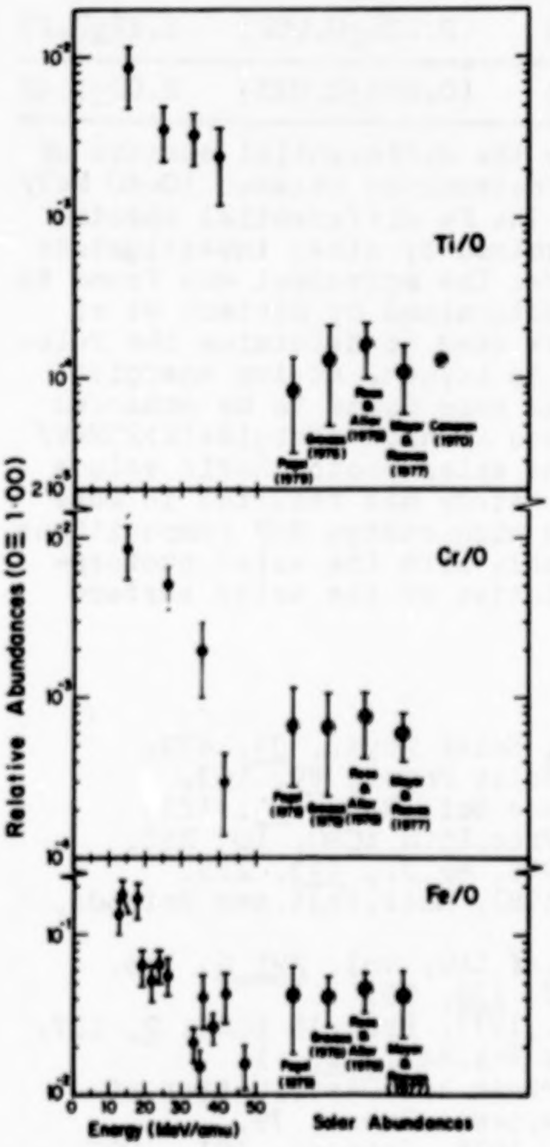

Fig.1b Variation of relative abundances as compared to oxygen of Ti, Cr and Fe nuclei with energy and comparison with photospheric value.

This is given in Table 1 for E between 10 and 20 MeV/amu.

Table 1 : Enhancement factors of Si-Fe elements in August 4, 1972 event

Element	Solar abundance Pagel (1979)	Energy Interval	Abundance relative to oxygen	Enhancement factor
Si	(0.052±0.013)	10-16	(0.12±0.05)	2.31±1.12
		16-20	(0.058±0.024)	1.12±0.54
S	(0.021±0.012)	10-20	(0.020±0.009)	0.95±0.69
Ar	0.0031	10-20	(0.0097±0.0055)	3.06±1.25*
Ca	(0.0026±0.0007)	10-20	(0.020±0.009)	7.69±4.03
Fe	(0.042±0.024)	10-20	(0.131±0.052)	3.12±2.17
		20-25	(0.085±0.035)	2.02±1.42

4. Conclusions. In this study the differential spectra of Si,S,Ar,Ca,Ti,Cr and Fe were determined between 10-40 MeV/amu during Aug.4,1972 event. The Fe differential spectra were checked with those determined by other investigators using the same flight exposure. The agreement was found to be good. The oxygen spectra determined by Bertsch et al (1974) in the same flight were used to determine the relative abundances with respect to oxygen. At low energies (10-20 MeV/amu) the abundances were found to be enhanced over the photospheric value and at high energies(E>25MeV/amu) the values agree with the solar photospheric values in general. In most casesthis study has resulted in more accurate determination of the high energy SEP compositions which may be used interchangably with the solar photospheric abundances as representative of the solar surface matter.

References

1. Bertsch, D.L. et al.,1974, Solar Phys., 39, 479.
2. Biswas, S. et al., 1983, Solar Phys., 89, 163.
3. Cameron, A.G.W., 1970, Space Sci. Rev., 15, 121.
4. Cook, W.R. et al., 1979, Proc.16th ICRC, 10, 265.
5. Crawford, H.J., et al., 1975, Ap.J., 195, 213.
6. Durgaprasad, N., et al., 1982, Nucl.Inst.and Methods, 199, 573.
7. Grevessi, N., 1976, Trans.of IAU, vol. XVI B, 116.
8. Lambert, D.L., 1968, MNRAS, 138, 79.
9. Meyer, J.P. and Reeves, H.,1977, Proc.15 ICRC, 2, 137.
10. Pagel, B.E.J., 1973, Space Sci.Rev., 15, 1.
11. Pagel, [illegible].J., 1979, in Origin and Distribution of Elements, Ed. L.H. Ahrens, Pergamon Press, 79.
12. Ross, J.E. and Aller, L.H.,1976, Science, 191, 1223
13. Vahia, M.N., Thesis submitted to the Bombay University.

N85-34788

VARIATIONS IN ELEMENTAL COMPOSITION OF SEVERAL MEV/NUCLEON IONS OBSERVED IN INTERPLANETARY SPACE

R.E. McGuire[†], T.T. von Rosenvinge, and D.V. Reames
NASA/Goddard Space Flight Center,
Greenbelt, MD 20771 USA

ABSTRACT

We have surveyed six years of accumulated ISEE-3 and IMP-8 data to study variations in elemental relative abundances among the different populations of energetic (1.5 to >10 MeV/nuc) ions seen in interplanetary space. We present evidence suggestive that heavy ion enrichments may be organized (with substantial scatter) by a rigidity scaling factor A/Z* over the range H to Fe. We also show some data to support the hypothesis that shock-associated particles are probably accelerated from ambient energetic fluxes.

1. Introduction. The elemental composition of solar energetic particle (SEP) events has been the subject of a number of recent studies [1,2,3,4,5,6]. This paper is a report of results from a new, ongoing study of low energy (1-10 MeV/nucleon) elemental composition with combined data from the Goddard particle experiments on ISEE-3 and IMP-8.

2. Abundance Distributions. We have identified nearly 150 separate events, which occurred between 1978 and 1983, with >50 Oxygen counts in the ISEE-3 energy band 1.9 to 2.8 MeV/nucleon. Of these events, we can associate about one-half with solar flares. The other periods are either shock-associated or of unknown origin. Figure 1 contains histograms of the abundance ratios H/O, He/O, C/O, Si/O and Fe/O constructed from event averages of the flare events. The arrows indicate median values in the distributions. Data for He and heavier ions comes from the ISEE-3 experiment, data for H and again He comes from IMP-8. We note that the He/O, C/O and Si/O distributions are narrow compared to H/O or Fe/O and that there is a high abundance tail in the Si/O distribution. Histograms constructed using our identified shock events or from those increases that are of unknown origin tend to follow the same

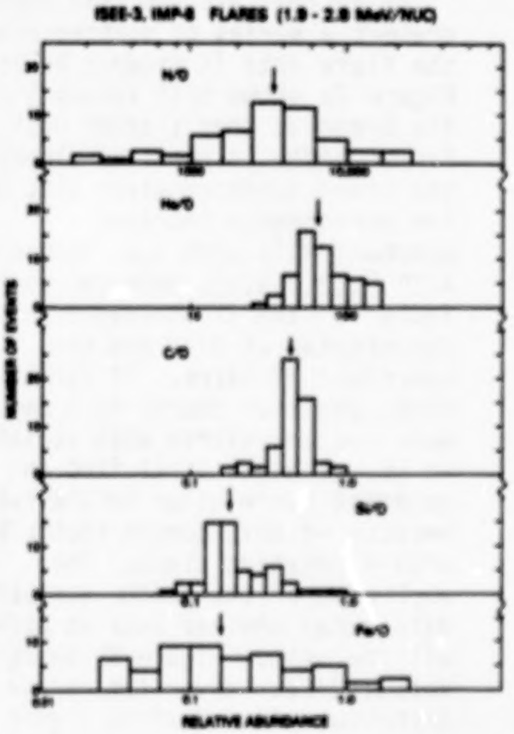

Fig. 1. Abundances in flare events.

[†] Also Dept. of Physics and Astr., U. of MD, College Park, MD 20742 USA

general range and distribution of values as the flare events in Figure 1, except that there are fewer Fe-enriched events.

3. Abundance Correlations. An important question in the interpretation of heavy-ion enrichments is whether atomic number (Z), atomic mass (A) or the rigidity-scaling factor mass divided by effective charge (A/Z*) best organizes the enrichment factors for different elements. Note that A/Z* for H:He:O:Si:Fe fall in the approximate ratios 1.0:2.0:2.2:2.6:4.0, using the charge state measurements of [7]. Thus the relative histogram widths in Figure 1 are consistent with A/Z* as the organizing parameter, in that largest differences in A/Z* give rise to the widest distributions.

To further explore this idea, we present a series of scatter plots of the flare data in Figures 2a-2c. Figure 2a shows O/Si versus Si/Fe. The trend as seen (larger O/Si imply larger Si/Fe, a positive slope) is the trend expected given that heavy ion enrichments increase monotonically with e.g. increasing A/Z* [1,2,3,4,6]. Note the common factor of the Si abundance in the denominator of O/Si and the numerator of Si/Fe. If variations (from whatever cause) in O and Fe were not correlated with variations in Si, we might still find an apparent correlation in the ratios because of this common factor but with a negative slope. The amplitude of the random variations determines whether such an effect will be seen. Figure 2b shows He/O versus O/Fe. Given the narrow distribution of He/O in Figure 1, it is not surprising that we find,

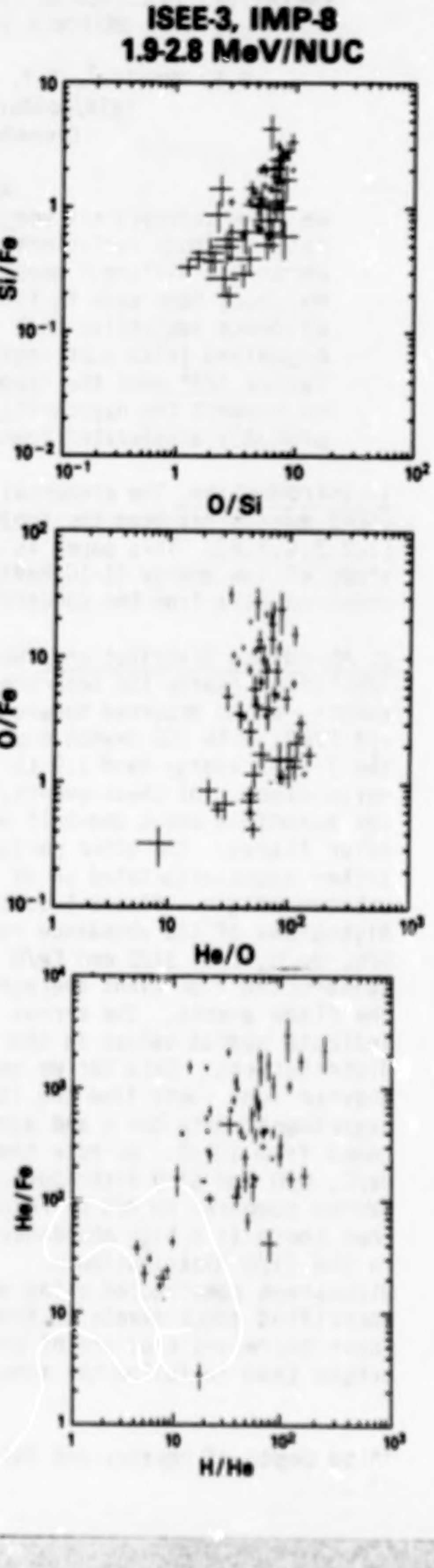

Fig. 2. Scatter plots of flare abundance ratios: (a) O/Si vs Si/Fe, (b) He/O vs O/Fe, and (c) H/He vs He/Fe.

ORIGINAL PAGE IS
OF POOR QUALITY

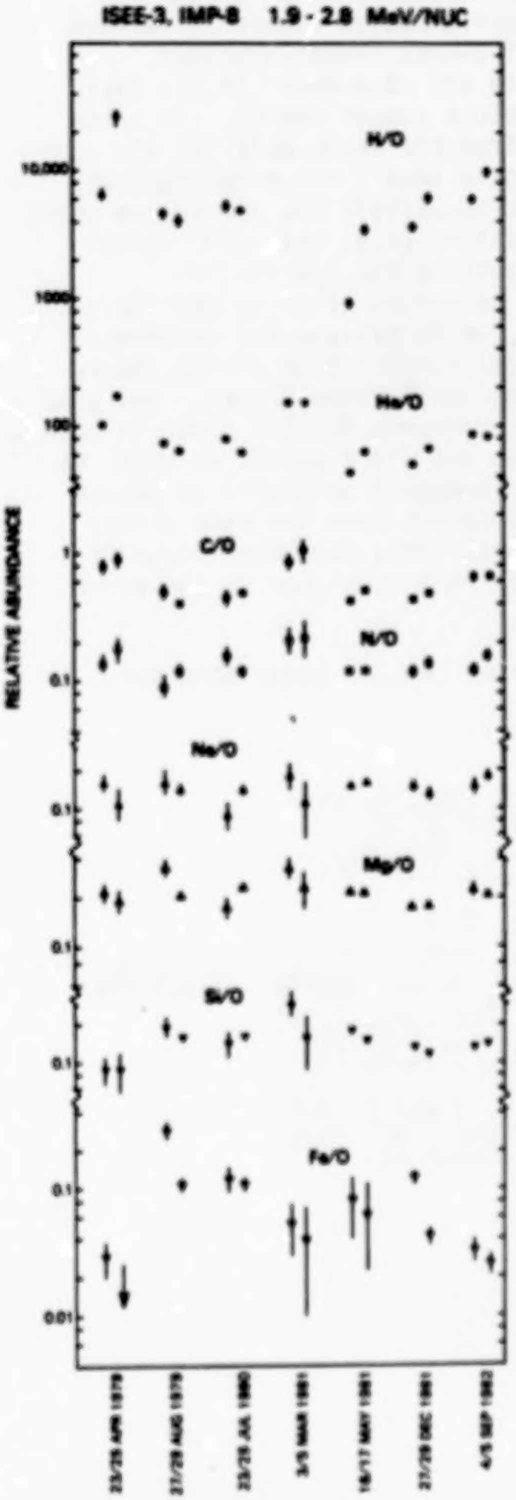

Fig. 3. Abundances for 7 pairs of events (ambient energetic flare particles and shock-associated particles).

at best, only a slight positive slope to the correlation. This plot is also consistent with A/Z* organization since the scaling factors for He and O are similar. It is not easily understood in terms of organization by Z or A separately. Random variations would again give a negative slope, if any, to the plot.

A plot of higher energy (7.2-12.5 MeV/nucleon) He/O to O/Fe in fact shows such a negative slope. This higher energy data is consistent with the published ratios of McGuire et al. (1979,1985) but we emphasize that such a negative slope is ambiguous because of the common factor in the ratios. That the nature of these plots changes with energy may be only a consequence of the increased scatter in the relative fluxes at the higher energies.

Figure 2c shows H/He versus He/Fe. Here too there is a suggestion of positive slope (possibly larger in magnitude than that of He/O versus O/Fe) but the trend is obscured by the overall scatter in the data. If A/Z* organizes the data overall, we would expect H/He to be positively correlated with He/Fe or O/Fe. We note that H and He spectral slopes are generally not equal [2,8,9]; the unequal spectral slopes may be largely responsible for the scatter. Other explanations for a general coincidence of low H/He ratios with higher Fe abundances (for instance, special plasma conditions required in the source region for an Fe enrichment to take place [10]) are also clearly possible.

4. A Source Population for Shock-associated Particles. A quite different question of concern to us is that of the source population in shock-associated energetic particle

flux increases. In particular, if these particles are locally accelerated, then we might expect the shock particles to mirror the abundances of ambient energetic particle fluxes. In Figure 3, we have plotted elemental abundances as pairs of events (event-averaged abundances preceeding the shock particles and abundances in the flux peak associated with the shock) for a select set of events. In these events, the ambient peak was separable from the shock peak (at the energy range of the composition data, again from 1.8-2.8 MeV/nucleon) and both averaged fluxes were sufficient to satisfy the >50 Oxygen count limit. Those events with unusual composition (e.g. high C/O ratios) were expected to be the most useful in testing the hypothesis. Unfortunately, few events satisfied the selection criteria and these had mostly average composition. In general, we do believe the abundance pairs as plotted are consistent with local acceleration of the shock-associated particles from the ambient energetic populations. The plot does not however provide strong positive evidence for the idea. We note that variation in H/O between the ambient and shock particles might be expected because the energy spectra are steepened generally at shocks and because the ambient H and He spectra do not have the same slope. Fe/O is complicated by the kind of temporal variations that occur in many events [6,11,12], specifically where Fe/O is higher at the event onset than near the shock arrival time.

5. Acknowledgments. This work was supported in part under NASA Grant NGR 21-002-316.

References.

1. McGuire, R.E. et al., 1979, Proc. 16th ICRC, 5, 61.
2. McGuire, R.E. et al., 1985, submitted to Ap. J..
3. Cook, W.R. et al., 1980, Ap. J. (Lett.), 238, L97.
4. Cook, W.R. et al., 1984, Ap. J., 279, 827.
5. Mason, G.M. et al., 1980, Ap. J., 239, 1070.
6. Reames, D.V. and T.T. von Rosenvinge, 1981, Proc. 17th ICRC, 3, 162.
7. Luhn, A. et al., 1984, Adv. Space Res., (Graz, COSPAR Proceedings).
8. McGuire, R.E. et al., 1981,. Proc. 17th ICRC, 3, 65.
9. McGuire, R.E. et al., 1984, Adv. Space Res., 4, 117.
10. Fisk, L.A., 1978, Ap. J., 224, 1048.
11. O'Gallagher, J.J. et al., 1976, Ap. J. (Lett.), 209, L97.
12. Scholer, M. et al.,1978, J. Geophys. Res., 83, 3349.

N85-34789

SH 2.1-8

ON THE RETENTION OF HIGH-ENERGY PROTONS AND NUCLEI WITH CHARGES $Z >$ OR EOUAL TO 2 IN LARGE SOLAR FLARES AFTER THE PROCESS OF TNEIR ACCELERATION

N.N. Volodichev, B.M. Kuzhevsky, O.Yu. Nechaev, I.A. Savenko

Institute of Nuclear Physics, Moscow State University;
Moscow 119899, USSR

Abstract. The available experimental data obtained from ground-based neutron monitors and from satellites suggest that the protons with energies of up to several GeV should be retained on the Sun after the process of their acceleration. The protons are on the average retained for 15 min, irrespectively of the solar flare heliolatitude and of the accelerated particle energy ranging from 100 MeV to several GeV. One of the explanation for the phenomenon is that the particles are retained in a magnetic trap formed in a solar active region. However, there does not exist information on how the nuclei with charges $Z \geqslant 2$, whose fraction in the Sun's atmosphere is $\sim 10\%$, bihave during the retention time. The Prognoz experiments failed to find any $Z \geqslant 2$ nuclei of solar origin during large solar flares. The upper limit of the number of such nuclei does not exceed 1% of the number of $\geqslant 500$ MeV solar protons and may be accounted for by the features of the experimental methods. The absence of the $\geqslant 500$ MeV/nucleon nuclei with $Z \geqslant 2$ may be due to their retention in the magnetic trap which also retains the high-energy protons. During the trapping time (15 min on the average) the $\geqslant 500$ MeV/nucleon nuclei with $Z \geqslant 2$ may escape due to nuclear interactions and ionization loss. In this case the H concentration should be $\sim 10^{12}$ cm^{-3}, which is observed in the lower chromosphere.

1. Introduction. The period between the moments of generation of particles in a flare and their emergence in interplanetary space is understood here to be the time of particle retention by the flare. The particle generation moment is meant to be onset time of the radio, X-ray, and gamma-ray emissions. If a particular event is rapid, the time of electromagnetic radiation maximum is taken to be the particle generation moment.

The time of accelerated-particle runaway to the interplanetary space was determined in /1, 2/ using the information concerning the time of the first arrival of the $\geqslant 100$ MeV and $\geqslant 500$ MeV protons at the Earth. Considering that the diffusive mode of particle propagation does not get stationary as yet and making the natural assumptions that the $\geqslant 100$ MeV and $\geqslant 500$ MeV particles are injected to the interplanetary space simultaneously and traverse the same path by the moment of their detection, we may find the moment of particle runaway to interplanetary space using the known time of the initial detection of the $\geqslant 500$ MeV and $\geqslant 100$ MeV protons.

2. Results and discussion. The table below presents the various data for the events detected on board Prognoz satellites. The main conclusion following from the data is that the moment of particle injection to the interplanetary space is delayed relative to the particle generation moment, irrespectively of whether the microwave radio, X-ray, or gamma-ray emission maximum times are taken to be the particle generation moment. The delays vary from several minutes to several tens of minutes for different events.

Fig. 1 shows the results of analyzing the dependence of the delay on the flare heliolatitude. The dark circles show the measurement results of /3/, the light circles are the Prognoz measurements. It may be concluded that in case of the Sun's western hemisphere the delay is independent of flare longitude. The delays for most of the events range from 10 to 20 min. The comparison between the delays inferred from the satellite and neutron monitors data shous that the delay is also independent of particle energy in the 100 MeV – 2 GeV range.

Table

The delays of the $\geqslant 100$ MeV and $\geqslant 500$ MeV solar protons injections to interplanetary space relative to the maxima of the microwave radio, X-ray, and gamma-ray emissions

N	$E_p \geqslant 100$ MeV, $\geqslant 500$ MeV							$E_p \sim 2$ GeV
	Ref.	Date	Region Mc Math	Helio-coordinates	Flare class	Satellite	Delay, min	Delay, min /3/
1	/1/	July 7, 1966	8362		2B	Proton-3	≲20	24±5
2	/1/	July 22, 1972	11976 ?	Post-limb flare	–	Prognoz-2	0÷12	–
3	/1/	Aug. 4, 1972	11976		3B	Prognoz-2	17±4	–
4	/1/	Aug. 7, 1972	11976		3B	Prognoz-2	≃6	9±3
5	/1/	April 29, 1973	12322		2B	Prognoz-3	≃40	40±3
6	/1/	Sept. 24, 1977	14942 or ? 14943	Post-limb flare	–	Prognoz-6	4÷8	10±3
7	/1/	Nov. 22, 1977	15031		2B	Prognoz-6	24±5	9±3
8	/2/	April 1, 1981	17539		2B-3B	Prognoz-8	60±10	–
9	/2/	April 4, 1981	17539		3B	Prognoz-8	22±2	–
10		April 10, 1981	17568		2B-3B	Prognoz-8	13±3	–

3. Discussion. Two reasons for the particle delays may be indicated. The first is the particle retention in closed magnitic fields of solar active regions /4/. The second reason is that the

ORIGINAL PAGE IS
OF POOR QUALITY

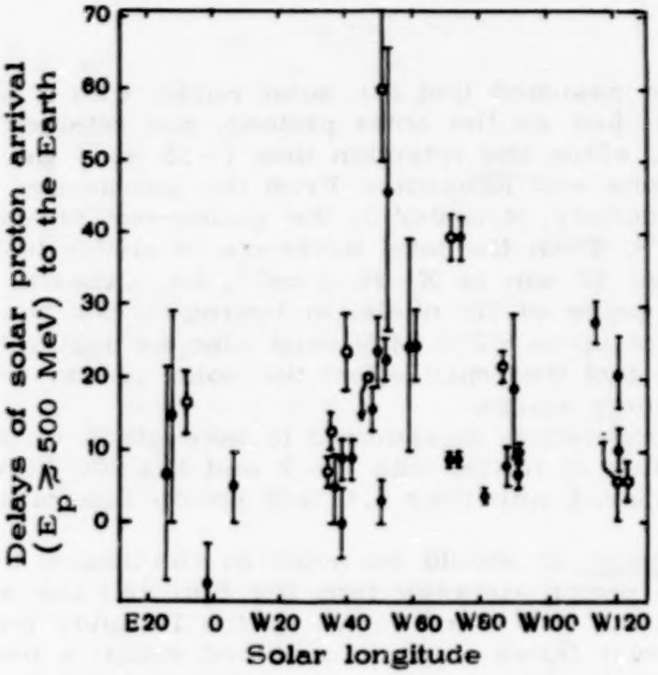

• - /3/ ; ∘ - the present work

Fig. 1. The high-energy solar proton delays versus flare heliolongitude

delay may correspond to the time interval between the accelerations from low to high-energies. The gamma-ray line emission and the X-rays from the flares are generated by particles with energies of several MeV /5/, whereas the particle delays were determined for the ≥100 MeV and ≥500 MeV protons. In case of neutron monitors, the mean effective energy is some 1 GeV. The entire solar cosmic ray spectrum was found in a flare region, whereas the time intervals between the moments of the emergence of low-energy protons and the associate gamma-ray line emission and high-energy protons are determined by the rate of energy gain. The ≥30 MeV gamma-ray data and the flare-generated neutron detection /6/ indicate that the period within which the particles are accelerated up to hundreds and thousands of MeV may not exceed a minute.

It is not excluded, however, that the particles are accelerated in the solar corona or even in the interplanetary medium by the moving shocks. In such cases the time interval between the electromagnetic radiation generation and the high-energy particle generation may reach tens of minutes.

It should be noted that the solar nuclei $Z \geq 2$ and energies ≥500 MeV/nucleon were not in practice detected in large solar flares. The upper limit for the number of such nuclei relative to the ≥500 MeV protons was found to be a fraction of one percent in the Prognoz data, and this level may well be accounted for by the methodical features of the experimental design.

It may be assumed that the solar nuclei with $Z \geqslant 2$ (mainly the He nuclei), just as the solar protons, are retained in a magnetic trap and, within the retention time (~ 15 min) are lost for nuclear collisions and ionization. From the gamma-ray data it follows that the density of matter in the gamma-ray prodaction region is $n \sim 10^{12}$ cm^{-3}. Then the total thickness of matter traversed by He nuclei within 15 min is $X \sim 20$ g cm^{-2}, i.e. exceeds the nuclear and ionization paths of He nuclei in hydrogen. But the protons with energies of up to ~ 200 MeV must also be lost within the same period, the fact that must affect the solar proton energy spectrum in this energy range.

If the acceleration is assumed to take place up to the same rigidities, the flux of nuclei with $Z \geqslant 2$ and $E \geqslant 500$ MeV/nucleon should be compared with the $\geqslant 1{,}4$ GeV proton flux of the same rigidity.

4. Conclusion. It should be noted in conclusion that the delay of high-energy proton runaway from the Sun and the absence of high-energy nuclei with $Z \geqslant 2$ found by the Prognoz measurements during large solar flures may be combined within a umfied model relevant to particle retention in a magnetic trap located in an active region on the Sun. In this case, however, the solar proton energy spectrum should exhibit a feature at ~ 200 MeV. At the same time, if the charged particles are accelerated in large flares up to a certain rigidity, one must compare between the fluxes of protons and heavier nuclei of the same rigidity. If in this case the solar particle flux ratio replicates the solar atmospheric composition, the delay of the particle runaway from the Sun may be explained by, for example, a durable acceleration mechanism.

References

1. Volodichev N.N., Savenko I.A. Proc. 17-th ICRC, Paris, 1981, v. 3, p. 45.
2. Volodichev N.N. Kosmich. Issl., 1983, v. 21, p. 731.
3. Cliver E.W., et al. Astroph. J., 1982, v. 260, p. 362.
4. Mullan D.J. Astrophys. J., 1983, v. 269, p. 765.
5. Kuzhevsky B.M. Uspekhi Fiz. Nauk, 1982, v. 137, No 2, p. 235.
6. Chupp E.L. Conference proceedings U.S. - Japan Seminar on "Recent Advances in the Understanding of Solar Flares", 1982, Tokijo, Japan.

SH 2.1-9

DIFFUSION IN THE CHROMOSPHERE , AND THE COMPOSITION OF THE SOLAR CORONA AND ENERGETIC PARTICLES

N85-34790

Sylvie VAUCLAIR
Observatoire du Pic-du-Midi et de Toulouse, France
Jean-Paul MEYER
Service d'Astrophysique, Centre d'Etudes Nucléaires de Saclay, France

1. Introduction. Composition observations, (i) in the Solar Photosphere, and (ii) in the upper Transition Region (TR) and Corona (as well as in Solar Wind, SW, and Solar Energetic Particles, SEP) imply a change of composition of the solar atmosphere somewhere between the Photosphere and the upper TR ($T > 70000$ K) /7,8,25,26,46/. Heavy elements with First Ionization Potential (FIP) > 9 eV (hereafter "high-FIP elements") are ~4 times less abundant in the TR and Corona than in the Photosphere, as compared to both Hydrogen and heavy elements with lower FIP ("low-FIP elements").

These observations suggest a separation between neutral and ionized elements in a region where the high-FIP elements are mostly neutral, and the low-FIP elements ionized /25,26/. This occurs in the Chromosphere at altitudes above 600 km and below 2000 km above Photosphere (in the average quiet chromospheric model VAL C of /43/, used throughout this paper; fig. in /13/). Here we shall investigate whether diffusion processes can explain the observed change in composition.

2. The diffusion equation - Possible processes. When a gas mixture is subject to pressure, temperature or concentration gradients, or to selective forces, the gas components diffuse with respect to one another. This process, believed to be the reason for chemically peculiar A and B stars /e.g.28, 29,27,45/, has already been invoked to explain the He depletion in the Solar Wind /19,27,12,13/. Thermal diffusion in the TR has also been studied by /9,30,42,36,33,34,35,12,13/. The diffusion velocity for a gas with negligible abundance in a gas mixture may be written /6,10/

$$v_D = D\,(\nabla \ln c - k_p \nabla \ln p - k_T \nabla \ln T + F/kT)$$

where D is the diffusion coefficient, k_p the pressure diffusion factor (the $\nabla \ln p$ term is equivalent to the gravitational settling), k_T the thermal diffusion factor, F any selective forces (e.g. the radiative force), and c the concentration of the element.

In solar-type stars, the radiative acceleration is never large enough to compete with gravitational settling /28/ : the last term is negligible. In the chromospheric plateau, the temperature gradient is small, and the thermal term is also negligible. In the TR this term is large. However, all elements become 100 % ionized as T increases and the neutral-ionized element separation therefore cannot work there. As the concentration gradient is also generally small the diffusion velocity reduces to

$$v_D = D\,k_p \nabla \ln p \qquad \text{(gravitational settling term)}$$

In case of partial ionization of an element, the atoms spend part of their time in the various ionization states, and the resulting velocity may be written, in first approximation /29,1/, as $v_D = \eta_k v_{Dk}$, where η_k is the fraction of atoms in the ionization state k, and v_{Dk} the corresponding diffusion velocity.

If the elements have to diffuse across a magnetic field, the tansverse diffusion velocities of the ions are reduced by a factor of $(1+\omega^2 t_{col}^2)^{-1}$, where ω is the Larmor pulsation and t_{col} the characteristic time between two collisions /44,1/. If this factor is large, the transverse diffusion of ions is stopped, while the diffusion velocity of neutrals is unchanged. Thus the

ORIGINAL PAGE IS
OF POOR QUALITY

diffusion velocity of any element reduces to $v_D = \eta_n v_{Dn}$, where the index n refers to the neutral fraction.

Now, a large fraction of the solar surface is always covered with horizontal magnetic fields anchored in the network, from altitudes of ~700 km /3,11,47,14,20,15/ up to above the Hα emitting region (>1500 km)/22,23/. Their typical intensity is ~5 to 25 G. At a typical chromospheric temperature of ~6000 K, the factor $\omega^2 t_{col}^2 \approx (4.6\cdot 10^{13}/n_H)^2$ for ions becomes > 1 for altitudes above ~950 km, reaching values of ~10 and ~100 at ~1100 and ~1300 km. Above these altitudes, ions are effectively prevented from settling gravitationally, while neutrals are not.

3. The diffusion coefficient for neutral heavies. The diffusion coefficient D for neutral heavy nuclei of mass A on the dominant neutral H gas of the chromosphere can be expressed as /6,10/

$$D = 3\sqrt{2\pi}/16 \cdot 1/(n_H \cdot \sigma_{eff}) \cdot \sqrt{kT/m^*}$$

$$D = 4.287\cdot 10^{18} \cdot 1/(n_H \cdot \sigma_{15}) \cdot \sqrt{T} \cdot \sqrt{1+1/A} \qquad (\mathrm{cm}^2\ \mathrm{s}^{-1})$$

where n_H is the neutral H number density, T the temperature, $m^* = m_H A/(A+1) \approx m_H$ the effective mass of the interaction, σ_{eff} an "effective" collision cross section to be discussed below, and $\sigma_{15} = \sigma_{eff}$ in units of 10^{-15} cm^2. (The diffusion coefficient in ionized H is not very different; a small admixture of H^+ therefore does not affect the picture). The effective cross-section σ_{eff} can conveniently be expressed as $\sigma_{eff} = \pi r^{*2} \Omega^{(1,1)*}$, where r^* is some typical range of the interaction potential, and $\Omega^{(1,1)*}$ is the reduced collision integral describing the collision kinematics in the actual potential /6,10,32,41,31/.

The noble gas-H interaction potentials are characterized by a steep repulsive part and a tiny Van der Waals attractive well, whose depth $\epsilon \sim 10^{-3}$ eV is extremely small as compared to the mean thermal energy kT = 0.52 eV of the atoms in the ~6000 K chromospheric gas (fig.1). So, only the repulsive part is important. The key information on these potentials comes from /5/, whose results have been by and large confirmed by more recent work /4,39,40,17,38/. The repulsive part of the potential is most realistically fitted by a modified Buckingham-type potential /21,5,6,10/, and we have adopted the potential parameters of /5/. On this basis the collision integrals $\Omega^{(1,1)*}$ have been interpolated from the tables of /21/ (reproduced in /6,10/), yielding the effective cross-sections σ_{eff} given in Table 1 (or the effective collision radii r_{eff} such that $\sigma_{eff} = \pi r_{eff}^2$ shown in fig.1).

In reactive element-H potentials, the tiny Van der Waals minimum is completely swamped out by a ~4 eV attractive well associated with the covalent bond (fig.1). The characteristics of these potentials have been derived from the data tabulated in /18/, using the formalism of /16/. They can be reasonably well fitted with Morse-type potentials /16,10/. The collision integrals $\Omega^{(1,1)*}$ have been interpolated from the tables of /37/ (reproduced in /10/), yielding the values of r_{eff} and σ_{eff} given in fig.1 and Table 1, the latter being ~2.4 times as large as the σ_{eff}'s for noble gases.

Table 1	Interaction	He-H	Ne-H	Ar-H	C-H	N-H	O-H	S-H
	σ_{eff} (10^{-15} cm^2)	0.89	1.05	1.45	2.84	2.17	2.35	3.27

4. The neutral element diffusion velocity and time scale. The diffusion velocity due to the gravitational force for neutral elements is /6,10/

$$v_D = D \cdot (A-1) \cdot \nabla(\ln p) \cdot \eta_n$$

$$v_D = 3.70\cdot 10^{18} \cdot \sqrt{T} \cdot (A-1)\sqrt{1+1/A} \,/\, \sigma_{15} \cdot 1/n_H \cdot \nabla(\ln p) \cdot \eta_n \qquad (\mathrm{km/day})$$

where we have inserted D and n_H is in cm^{-3} and $\nabla(\ln p)$ in cm^{-1}. This velocity has been evaluated in the framework of model VAL C /43/. η_n is close to 1 for most high-FIP elements up to $x \approx 1900$ km (see fig. in /13/), except for C (and probably S) for which ionization reduces the diffusion velocity by factors up to ~2.5 within the chromospheric plateau. Fig.2 shows the calculated v_D's vs.

ORIGINAL PAGE IS
OF POOR QUALITY

altitude x, for the two extreme elements Ar and C. All other high-FIP elements have intermediate diffusion velocities.

From these velocities, we derive for each element A diffusion time scales $t_{D,A}(x) = N_H/(S_{\odot} \cdot v_{D,A}(x) \cdot n_H(x))$ /2/. This time is the time needed for a mass of N_H H-atoms above an altitude x, assumed completely mixed, to be depleted in atoms A by a factor of 1/e by downward diffusion at its base x ($S_{\odot}$ = solar surface area). These diffusion times t_D are plotted vs. altitude x in fig.3, for Ar and C.

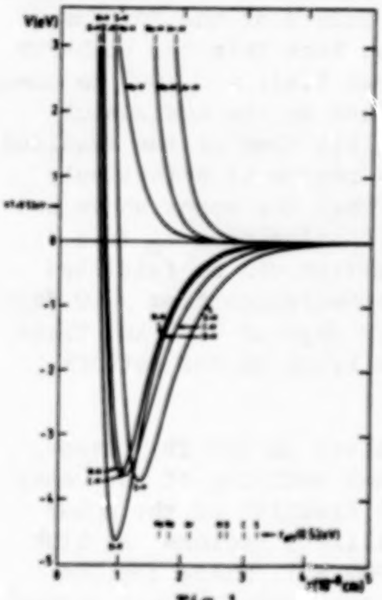

Fig.1

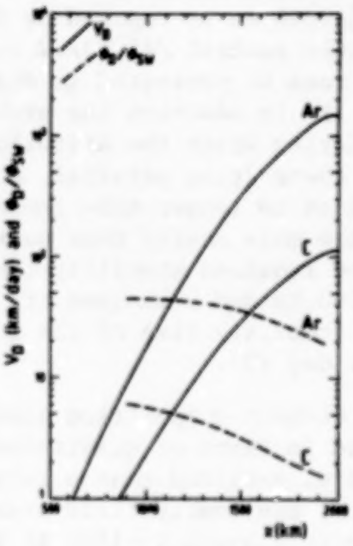

Fig.2

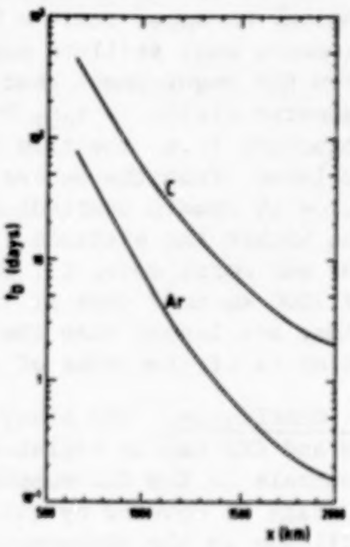

Fig.3

5. Discussion - A tentative scheme. The surface of the quiet Sun at altitudes of ~700 to 2000 km is believed to be largely covered, above the Supergranulation (SG) cells, by horizontal magnetic fields of intensity ~5 to 25 G, whose energy density exceeds that of the gas above ~1000 km (fig.4) /3,11,47, 14,20,15,22,23/. Above ~1000 km, the gas may therefore be stabilized by the field, and we may have in the chromospheric plateau a "diffusion region" with an horizontal field, which remains stable, isolated from lower lying material, over some unknown time scale τ . Gravitational settlement of heavy neutrals takes place there, but the horizontal field acts as a filter against ions. Starting in the upper Chromosphere above the network (SG boundaries), spicules are probably the major upward carrier of material from Chromosphere into Corona. Almost all the material they lift later falls back, either in the spicule itself, or as a rain along the more vertical configuration of the field at higher altitudes (fig.4). Only 0.7 % of it leaves the system in the form of SW /above ref./. Above the quiet "diffusion region" at altitude x, we therefore have an apparently fully "mixed region" comprizing the entire TR and Corona (fig.4). The material leaving the "mixed zone" as SW (flux $\phi_{SW,H}$) is treated as constantly replenished by fresh matter from the undelying "diffusion region" at an average effective velocity $U(x) = \phi_{SW,H}/n_H(x)$, in a steady state fashion lasting over the stability time τ of the "diffusion region".

By and large, the abundance of an element A in the "diffusion zone" (and hence in the "mixed zone") can be kept low if its downward diffusion velocity $v_{D,A}(x)$ relative to the bulk H gas is larger than the effective upward velocity U(x) of this bulk gas : $v_{D,A}(x)/U(x) = n_H(x) \cdot v_{D,A}(x)/\phi_{SW,H} = \phi_{D,A}(x)/\phi_{SW,A} \gtrsim 1$ (since n_A/n_H = cst throughout the "mixed zone"). Fig. 2 shows that this ratio is indeed >1 (~30 for Ar, and ~3 for C, our worst case), and does not depend much on the altitude x of the interface between the quiet and the mixed-up zones. This strong constraint is thus satisfied.

ORIGINAL PAGE IS
OF POOR QUALITY

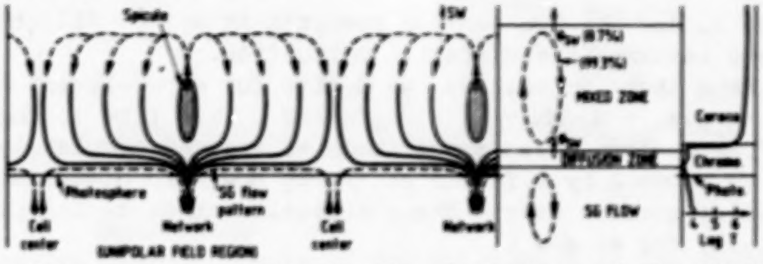

Fig.4

Other constraints lead to limits to the altitude x of the "diffusion region". An upper limit $x \lesssim 2000$ km is imposed by the fact that the high-FIP elements must still be mostly neutral /43,13/. A lower limit $x \gtrsim 1000$ km comes from the requirement that ions be prevented to diffuse by the horizontal magnetic fields $(\omega^2 t_{col}^2 \gg 1)$. In addition the stability time of the required structure (i.e. the time during which the diffusion region is effectively isolated from the denser lower lying material, so that the zones above and below it remain unmixed) must be longer than the diffusion time t_D (fig.3). The higher the altitude, the more easily this constraint can be fulfilled. For our worst case, C , the required stability time decreases from ~ 60 days at 1000 km to 7 days at 1500 km and a minimum of ~ 2 days at 2000 km. These times are longer than the stability time of the low lying SG and network, which is of the order of 1 day /3/.

6. Conclusion. The heavy element composition anomalies in the TR, Corona, SW and SEP can be explained in terms of gravitational settling of the heavy neutrals in the Chromosphere, provided that a large fraction of the solar surface is covered by quiet, presumably field stabilized, regions at high altitude in the chromospheric plateau (~ 1500 to 2000 km). These regions must effectively shield the coronal reservoir from the denser, lower chromospheric gas. They must be stable over at least a few days, and must therefore not be strongly perturbed by the daily changes of the SG pattern at lower altitude. Unless a different scheme is found to explain it, the odd coronal composition therefore permits to set stringent limits to the degree of chaos of the Chromosphere, to the turbulent exchange of matter between the lower and the upper chromospheric layers.

Acknowledgements. We wish to thank Pierre Mein, Georges Michaud and Bernard Sayer for important discussions.

References

1. Alecian,G. et al 1983,Fund Cosmic Phys.8,369
2. Aller,L.H. et al 1960,Ap.J.132,461
3. Athay,R.G. 1976,The Solar Chromosphere and Corona:Quiet Sun (Reidel)
4. Bassi,D. et al 1976,Phys.Rev.A 13,584
5. Bickes,R.W. et al 1973,Faraday Disc.Chem.Soc.55,167
6. Chapman,S. et al 1970,The Mathematical Theory of Non-Uniform Gases (Cambridge U. Press)
7. Cook,W.R. et al 1980,Ap.J.Letters 238,L97
8. Cook,W.R. et al 1984,Ap.J. 279, 827
9. Delache,P.1967,Ann.d'Ap.30,827
10. Ferziger,J.H. et al 1972,Mathematical Theory of Transport Processes in Gases (North Holland)
11. Gabriel,A.H. 1976, Phil.Trans.R.Soc.Lond.A81,339
12. Geiss,J. 1982,Space Sci.Rev.33,201
13. Geiss,J. et al 1984, in Isotopic Ratios in the Solar System,Paris,(CNES),in press
14. Giovanelli,R.G. 1980, Solar Phys.68,49
15. Giovanelli,R.G. et al 1982,Solar Phys. 79,267
16. Herzberg,G. 1950,Spectra of Diatomic Molecules (Van Nostrand)
17. Nishinuma,N. 1981,J.Chem.Phys.75,4960
18. Huber,K.P.et al 1979, Constants of Diatomic Molecules (Van Nostrand)
19. Jokipii, J.R.1966,in The Solar Wind, ed. R.J.Macklin et al (Pergamon),p.215
20. Jones,H.P. et al 1983,Solar Phys.87,37
21. Mason,E.A. 1954,J.Chem.Phys.22,169
22. Mein,P. et al 1982, Astr.Ap.111,136
23. Mein,P. et al 1984,Preprint
24. Meyer,A. et al 1979,Astr.Ap.78,33
25. Meyer J.P. 1981,17thICRC,Paris,3,149
26. Meyer,J.P. 1985,Ap.J.Suppl.57,173
27. Michaud,G. 1980,Astron.J.85,589
28. Michaud,G. et al,1976,Ap.J.210,447
29. Montmerle,T. et al 1976,Ap.J.Suppl.31,489
30. Nakada,M.P. 1969,Solar Phys.7,302
31. Pauly,H. 1979,in Atom-Molecule Collision Theory,R.B. Bernstein ed. (Plenum Press).
32. Pauly,H. et al,1965, in Advances in Atomic and Molecular Physics, vol.1,D.R.Bates ed. (Academic)
33. Roussel-Dupré,R. 1980,Ap.J.241,402
34. Roussel-Dupré,R. 1981,Ap.J.243,329
35. Roussel-Dupré,R. 1981, Ap.J. 252,393
36. Shine,R. et al 1975,Ap.J.Letters 202,L101
37. Smith,F.J. et al 1964,J.Chem.Phys.41,3560
38. Theodorakopoulos,G. et al 1984,J.Phys.B 17,1453
39. Toennies,J.P. et al 1976,Chem.Phys.Letters 44,5
40. Toennies,J.P. et al 1979,J.Chem.Phys. 71,614
41. Torrens,I.M. 1972,Interatomic Potentials (Academic)
42. Tworkowski,A.S. 1975, Ap.Letters 17,27
43. Vernazza,J.E. et al 1981,Ap.J.Suppl.45,635
44. Vauclair,S. et al 1979,Ap.J.227,526
45. Vauclair,S. et al 1982,Ann.Rev.Astr.Ap.20,37
46. Webber,W.R.1982,Ap.J.255,329
47. Withbroe,G.L. et al 1977,Ann.Rev.Astr.Ap.15,363

N85-34791

ANOMALOUS ABUNDANCES OF SOLAR ENERGETIC PARTICLES AND CORONAL GAS: COULOMB EFFECTS AND FIRST IONIZATION POTENTIAL (FIP) ORDERING

D. J. Mullan
Bartol Research Foundation
University of Delaware
Newark, DE 19716
USA

ABSTRACT

We argue that FIP ordering of elemental abundances in solar energetic particles and in the corona can both be explained Coulomb effects.

1. Introduction. Solar energetic particles (SEP) and coronal gas have anomalous abundances relative to the photosphere (1). The anomalies are similar in both cases: this led Meyer (1) to conclude that SEP acceleration is not selective, but merely preserves the source abundances (in the corona). Here, we argue that SEP acceleration can be selective, because identical selectivity operates to determine the coronal abundances.

The abundance anomalies are ordered by first ionization potential (FIP). Meyer (1) claims that this requires source temperatures of $T=8000$ K. However, we find that FIP ordering occurs even if $T > 10^6$K.

2. Coulomb effects in SEP. SEP pre-acceleration in magnetic reconnection (e.g. in a solar flare) favors ions with low Coulomb losses (2) (hereafter ML). Pre-acceleration selects ions with charge $Z < R A^{0.5}$. (A is atomic weight, R is a critical number.) ML argued that in a hydrogen dominated corona, where coronal heating itself depends on reconnection, R should lie close to the proton value, R=1.0. Then the pre-acceleration time scale t_B would be marginally shorter than the proton Coulomb loss time t_p. With R=1, pre-acceleration of (e.g.) iron ions will favor ions with $Z \leq 7$. This selection of certain (low) charge states gives rise to abundance anomalies in SEP (see (2)).

ML discussed two cases of reconnection in a coronal magnetic loop. Case A had $t_B < t_p$ only at the top of the loop; case B had $t_B < t_p$ at all points in the loop. Abundance anomalies in Case A were found to be quite large in some cases: to agree with observations, the anomalies would require dilution with non-processed material. Meyer (1) criticizes Case A because different flares would apparently require rather similar dilution factors. However, Case B yields anomalies which are much closer to the observed values. Dilution is irrelevant in Case B. In this paper, we refer only to Case B.

ML predicted that Na/Si, Mg/Si, Ca/Fe, and Ni/Fe should be less in flares than in the photosphere by factors of 2-3. Meyer (1) claims that SEP data do not support these predictions. However, the observed ratios have a large scatter in different flares (see Fig. 3 in (1)). The scatter is such that the lower limit on the above ratios can be smaller than photospheric by factors of 2-3 (as Case B predicts) except for Na/Si. Thus, the Na/Si ratios might present a problem for Case B: perhaps the ionization equilibrium of Na are incorrect. Apart from Na, however, the data can be reconciled with Case B predictions, contrary to the claim in (1) that the ML scenario disagrees with the data. (Meyer (1) did not discuss Case B of ML).

As an indication of how the ML scenario succeeds, both qualitatively and quantitatively, in reproducing the observed elemental anomalies in energetic particles, we show Case B predictions and data in Fig. 1, as a function of FIP. (Both cases are normalized to Si). Experimental points in Fig. 1 are taken mainly from (1), but in the case of elements which have not yet been detected in solar cosmic rays, we took data from (3) for the galactic cosmic rays. (Elemental anomalies are quite similar in solar and galactic cosmic rays (1).) As regards the ML predictions plotted in Fig. 1, we note that no specific values were predicted in Case B for H and He. The nature of the ML scenario (marginal heating of H) is such that the amount of hydrogen selected for pre-acceleration depends in detail on the extent to which the margin is exceeded. This is not known: however, a firm prediction is that, since H and He in the corona have identical values of Z^2/A, the abundances of both H and He (whatever they are) should be identical. To show this in Fig. 1, we join the H and He predictions by a horizontal dashed line. The vertical placing of this line cannot be determined at the present level of detail: we have chosen to plot it so as to overlap with the error bars of the data for H and He.

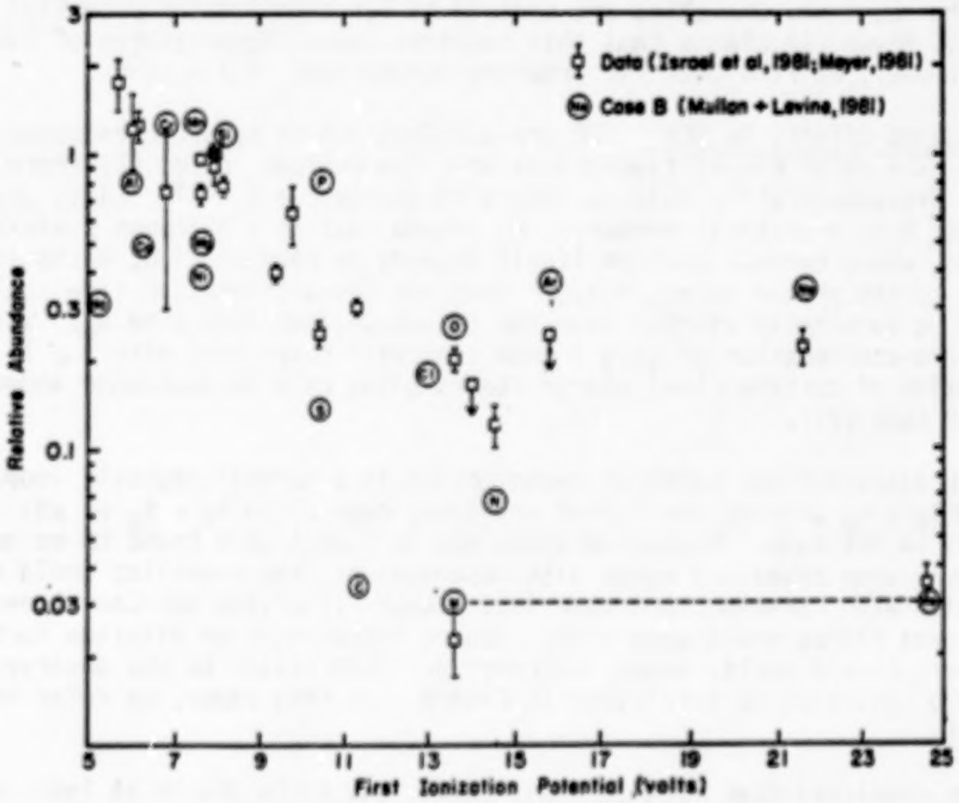

Fig. 1. Relative abundances of elements as a function of FIP.

The agreement between Case B predictions and data in Fig. 1 is quite good. Thus, both show maximum values of the abundance anomalies (around values of 1) at low FIP (except for Na), and both show a pronounced "step" down to lower values at about 10 volts. The lower abundances at large FIP are down for both by factors of 3-10 relative to those at low FIP. The "step" is well-defined in the Case B predictions: for the elements P, S, and C, the FIP values differ by < 10%, but their abundances differ by factors of ~ 1000%. The H and He data can be reconciled with the prediction of equal abundances: H need not be regarded as an exception in the Case B scenario. Note that the only free parameter in Case B is the loop thermal structure.

Since the ML predictions in Fig. 1 were obtained for coronal loops with $T \gtrsim 10^6$K, an important conclusion from Fig. 1 is that FIP ordering of elemental abundances does not require a chromospheric phenomenon: it may occur even in the corona.

We stress that the predicted anomalies in Fig. 1 arise from a selection of ions with Z^2/A less than a critical ratio, viz. $R = 1.0$. Abundance anomalies similar to those shown in Fig. 1 are expected to occur in any loop where ions with $Z < A^{0.5}$ are preferentially selected. This will be important to keep in mind when we consider the accumulation of minor ions in the solar corona due to solar wind outflow.

3. Solar Wind: Minor Ions. The solar wind consists mainly of protons, but minor ions are dragged along by Coulomb effects if the proton flux is sufficiently large. In order that ions of atomic weight A and charge Z be dragged out of the sun, the proton flux must exceed the minimum value

$$F_{min} = 3.4 \times 10^8 \, (T/10^6)^{3/2} \, G(A,Z) \text{ cm}^{-2}\text{s}^{-1} \text{ (cgs)}. \qquad [1]$$

Coronal temperature T will be taken to be 10^6 K here. G is a function of A, Z, and T (see (4)): in the limit of heavy ions, $G \simeq A/Z^2$.

The actual solar wind flux is not infinitely large: therefore, some ions will not be dragged out by the protons, but will instead be left behind to accumulate in the corona. Which ions are left behind? To answer this, we refer to the actual value of the solar wind flux. During the years 1962-1975, in low speed solar wind, the flux was 3.9×10^8 cgs on average; in high speed wind, it was 2.7×10^8 cgs on average; in a long term average, it was 3.8×10^8 cgs (5). As mentioned in (5), these fluxes are uncertain by factors of order 30%, and there is a rather large spread in the fluxes: the standard deviation in the long term average is 2.4×10^8 cgs (5). In a sample of solar wind recorded near solar maximum (August 1978 to February 1980) by ISEE-3, we have examined a series of 2117 "snapshots" of the solar wind, each lasting 3 seconds, with one "snapshot" every 5-6 hours throughout a 550-day interval. The mean flux we found was 3.2×10^8 cgs. This lies within the 30% uncertainty of the long term average in (5). It appears safe to adopt a mean solar wind flux of $(3\text{-}4) \times 10^8$ cgs.

The interesting aspect of these fluxes for our purposes can be seen from eq. [1]. The mean flux apparently suffices to drag out only those ions which have $G < (3\text{-}4)/3.4 = 0.9\text{-}1.2$, i.e. ions with $Z > (0.92\text{-}1.06)A^{0.5}$. The remaining ions, those with $Z \lesssim (0.92\text{-}1.06)A^{0.5}$, are left behind to enrich the corona.

There is no a priori reason why the solar wind flux should have any relationship whatever to the coefficient in eq. [1]. Thus, the mean value of the upper limit on the ratio $R = Z^2/A$ of the ions which would enrich the corona could be arbitrary, in principle. We draw attention to the fact that, in practice, however, the upper limit on R in the enriched coronal gas is equal to unity (within the uncertainties of the solar wind measurements). Thus, ions of (e.g.) iron with $Z \leq 7$ will accumulate in the solar corona.

4. Discussion. We have found that ions which are selectively preaccelerated in SEP (i.e. those with $R < 1$) are the same as those which enrich the coronal gas because the average solar wind leaves them behind. Therefore, abundance anomalies which appear in SEP because of the Coulomb selectivity are also expected to appear in the coronal gas. Thus, the predictions in Fig. 1 should also be relevant for abundances in the coronal gas, provided thermal structures are not too different. (Note that Case B predictions, which appear in Fig. 1, are insensitive to source temperature, as long as $T \gtrsim 10^6$ K; see Fig. 8 of (2). Hence, differences in temperature between a solar flare site and the source region of the solar wind will not affect the predictions in Fig. 1, since both temperatures in all likelihood are $\gtrsim 10^6$K.) We suggest that coronal abundances are anomalous relative to the photosphere because of Coulomb losses in the solar wind, while SEP anomalies are due to Coulomb losses at a flare site. Hence, SEP acceleration can be selective: but since it enhances the selection which has already occurred in the corona, the anomalies appear similar. Different classes of Fe-richness in SEP may reflect situations in the sun where SEP selectivity and/or solar wind selectivity have operated and reinforced each other to varying extents.

The enrichment of the solar corona will not proceed indefinitely: at times, the solar wind flux becomes considerably larger than average. Thus, in the data set discussed in (5), the 5-95% range limit on the solar wind flux is $(1.5\text{-}7.8) \times 10^8$ cgs. In 550 days of ISEE-3 data, we found 9 samples (out of 2117) with fluxes of $(9.0\text{-}9.9) \times 10^8$ cgs. each separated by an average interval of about 60 days. At such times, the accumulated enrichment of 60 days is flushed out, such that only ions with very small Z are left behind ($Z < (0.5\text{-}0.6)A^{0.5}$). But on the average, enrichments of coronal gas will build up with abundance anomalies as shown in Fig. 1.

5. Conclusions. Elemental abundances are observed to be anomalous (relative to the photosphere) in both SEP and in coronal gas. Here we propose that Coulomb effects can explain both sets of anomalies. The Coulomb loss scenario makes predictions of elemental anomalies as a function of FIP and these predictions agree well both qualitatively and quantitatively with the observed data for energetic particles (see Fig. 1). FIP ordering is not a sign that the source material is at $T = 8000$ K: we find that the source material can have $T \gtrsim 10^6$K, and still preserve FIP ordering.

References

1. Meyer, J. P., (1985), Ap. J. Suppl., 57, 151.
2. Mullan, D. J. and Levine, R. H., (1981), Ap. J. Suppl. 47, 87 (ML).
3. Israel, M. et al., (1981), Proc. 17th ICRC, 2, 36.
4. Hollweg, J., (1981), J. Geophys. Res., 86, 8899.
5. Feldman, W. et al., (1977), in: The Solar Output and Its Variations ed. O. R. White (Colorado Univ. Press), p. 357.

THE MEAN IONIC CHARGES OF N, NE, MG, SI, AND S IN SOLAR ENERGETIC PARTICLE EVENTS

N85-34792

A. LUHN, D. HOVESTADT, B. KLECKER, M. SCHOLER
Max-Planck-Institut für extraterrestrische Physik, 8046 Garching, F.R.G.
G. GLOECKLER, F. M. IPAVICH, A. B. GALVIN
University of Maryland, College Park, MD 20742, U.S.A.
C. Y. FAN
University of Arizona, Tucson, AZ 85721, U.S.A.
L. A. FISK
Universty of New Hampshire, Durham, NH 03824, U.S.A.

ABSTRACT

The mean ionic charges of Nitrogen, Neon, Magnesium, Silicon, and Sulfur in solar flare particle events have been determined for 12 flares during the time interval from September 1978 to September 1979. The observations were carried out with the MPI/UoMd ULEZEQ Sensor on the ISEE-3 satellite. Comparing the results with mean charge states established in a hot coronal plasma under equilibrium conditions, we derive different temperatures for different elements. These range from approx. $2\cdot10^6$K to $7\cdot10^6$K in a single flare. From flare to flare the variation in temperature for each element is less than the variation between different ion species.

1. Introduction. The ionic charge state distributions of solar energetic particles provide important information about both the conditions at the source region and the nature of acceleration, coronal, and interplanetary propagation processes. The processes involved in general depend on the particle's rigidity; thus, a knowledge of the particles mass to charge ratio A/Q is essential for comparing observations of solar energetic particles with theoretical models of acceleration and propagation processes. Since charge states are not altered during the passage of the ions to earth[1], measurement of the charge state distributions can be used to diagnose the conditions of the plasma at the source region of the energetic particles.

We report measurements of the mean ionic charges for the elements C, N, O, Ne, Mg, Si, S, and Fe in 12 flare associated solar energetic particle events in the time period from September 1978 to September 1979. Mean ionic charges of C, O, and Fe have been published before for all but two of the flares considered here[2,3]. In [4] the other elements have been analysed for three of the flare events. For completeness these results are included in this work.

2. Instrument and Data Analysis. The data presented in this paper have been obtained with the Max-Planck-Institut / University of Maryland ULEZEQ Sensor onboard the ISEE-3 spacecraft. During the period of the measurements from September 1978 to October 1979 this satellite was positioned at the Lagrangian point L_1 between the Earth and the Sun, at a distance of about 230 R_E from the Earth. By combining an electrostatic deflection system with a position sensitive solid state detector and a proportional counter, the ULEZEQ sensor is capable of determining seperately the energy E and nuclear charge Z of an incoming ion in the energy range from ~0.3 to ~4 MeV/nucleon as well as measuring it's ionic charge Q. Because of the poor counting statistics, especially for the rarer elements (N, Ne, Mg, Si, and S) and the limited charge resolution of the sensor, we present only the mean values of the charge state distributions. The determination of the ionic charge is, apart from statistical errors, subject to a systematic uncertainty of less than 5%. The resolution of the sensor with respect to elemental species is such that within the iron group, individual elements cannot be seperated. However, since most particles in this group are in fact iron, we stay with the common practice to designate them by "Fe". For a detailed description of the sensor and data analysis see Hovestadt et al.[5].

For our analysis we selected 12 well identified flare associated solar energetic particle events from September 1978 to September 1979 (see Table 1). The start and end times for the accumulation periods were chosen as to maximize the counting statistics, that is from the onset of the energetic particle flux well into the declining phase. We assume here that the charge states are not affected by post-acceleration of the flare generated shock wave during the passage to earth. The energy ranges for the accumulation of the different elements represent a compromise between charge resolution and counting statistics. They are 0.45-2.34 MeV/N for C, 0.45-2.62 MeV/N for N, 0.54-2.64 MeV/N for O, 0.56-3.14 MeV/N for Ne, 0.56-3.37 MeV/N for Mg, 0.55-2.97 MeV/N for Si, 0.55-3.17 MeV/N for S, and 0.34-1.78 MeV/N for Fe.

Table 1: *Selected SEP events.*

ID		Accumulation period
1	1978	doy 266,12:00- 271,00:00
2		doy 314,06:00- 321,00:00
3		doy 346,06:00- 355,00:00
4	1979	doy 48,18:00- 55,06:00
5		doy 87,06:00- 90,00:00
6		doy 93,12:00- 98,00:00
7		doy 113,06:00- 117,12:00
8		doy 147,12:00- 152,12:00
9		doy 157,06:00- 165,00:00
10		doy 213,06:00- 218,00:00
11		doy 231,12:00- 239,00:00
12		doy 258,06:00- 272,00:00

3. Results and Discussion. In Table 2 we summarize the results for the mean charges in all of the observed flares. We also give the weighed average of the 12 periods. From the measured mean charge and ionization equilibrium tables[6,7,8,9] one can derive for each ion the electron temperature of the source plasma of these ions. This should give consistent results if the following assumptions hold: 1) Conditions are such that charge equilibrium can be established, 2) the distribution function of the plasma electron is a Maxwellian (this is asumed in the calculation of the tables), and 3) charge exchange processes are negligible during acceleration and propagation. As an example we show in Fig. 1 mean equilibrium charge states as a function of temperature for O, Ne, Mg, Si, and S. The values of the mean charge for accumulation period 1 are indicated by heavy lines. For the elements shown as well as for C and N there is no difference in the mean values of the charge state distributions as calculated from the tables of Jordan (6,7) and Shull and van Steenberg (8,9) above temperatures of $\lesssim 10^6$K. We do not show Iron, because for this ion the difference in the inferred temperatures for the two tabulations is significant. We attribute this to the inherent difficulties in estimating the ionization and recombination rates for a many electron system (as Iron in this temperature range) and the errors introduced in the simple analytical interpolation formulæ for the rate coefficients used in [8]. In Fig. 2 we compile

the inferred equilibrium temperatures for all of the 12 periods. It is evident that 1) different elements aperently reflect different equilibrium temperatures and 2) these values remain fairly constant from flare to flare. This is a strong indication that at least one of the above three assumptions is not applicable.

Recently calculations have been performed to allow for 1) non steady state charge states and 2) a non-Maxwellian tail of the electron distribution function determining the charge state distributions ([10]), as well as 3) for charge states by interactions of fast ions with a hot coronal plasma ([11]). Neither of these relaxations from the original assumption of charge equilibrium can explain the observed variations in the mean charge states for the different elements. To resolve this discrepancy one possibly has to invoke a combination of the above three effects and also take into account the x-ray radiation field, which is neglibible in the quiet solar corona, but might not be in solar flares [12].

Table 2: *Mean charges in solar energetic particle events.*

period ID	mean charge C	N	O	Ne	Mg	Si	S	Fe
1	5.76 ± 0.05*	6.31 ± 0.11	7.13 ± 0.04	9.23 ± 0.15	10.8 ± 0.16	11.1 ± 0.21	11.2 ± 0.42	14.4 ± 0.16
2	5.90 ± 0.06	6.59 ± 0.13	7.17 ± 0.05	9.20 ± 0.25	11.4 ± 0.20	12.0 ± 0.31	10.5 ± 0.47	16.3 ± 0.24
3	5.79 ± 0.09	6.53 ± 0.16	7.19 ± 0.06	9.53 ± 0.29	11.0 ± 0.28	11.9 ± 0.37	12.9 ± 1.31	15.7 ± 0.26
4	5.66 ± 0.13	6.74 ± 0.26	7.11 ± 0.11	9.74 ± 0.27	10.5 ± 0.38	11.5 ± 0.67	—	17.7 ± 0.62
5	5.81 ± 0.16	7.06 ± 0.41	6.76 ± 0.16	8.89 ± 0.88	11.2 ± 0.69	10.0 ± 0.82	—	12.2 ± 1.35
6	5.72 ± 0.05	6.37 ± 0.09	7.01 ± 0.04	9.06 ± 0.16	10.7 ± 0.16	11.4 ± 0.28	11.0 ± 0.82	15.1 ± 0.24
7	5.82 ± 0.07	6.79 ± 0.14	7.05 ± 0.10	9.14 ± 0.44	10.6 ± 0.36	11.7 ± 0.17	—	13.6 ± 0.86
8	5.80 ± 0.15	6.25 ± 0.34	6.89 ± 0.18	9.47 ± 0.48	9.72 ± 0.70	11.7 ± 1.41	—	16.3 ± 1.34
9	5.59 ± 0.04	6.19 ± 0.07	6.83 ± 0.04	8.77 ± 0.14	10.4 ± 0.15	9.83 ± 0.23	9.55 ± 0.90	14.2 ± 0.22
10	5.58 ± 0.16	6.65 ± 0.43	7.10 ± 0.20	8.46 ± 0.71	10.2 ± 0.67	—**	—	14.5 ± 0.51
11	5.62 ± 0.07	6.34 ± 0.17	6.84 ± 0.06	8.91 ± 0.21	10.5 ± 0.24	10.6 ± 0.33	11.2 ± 0.59	14.7 ± 0.26
12	5.40 ± 0.11	6.25 ± 0.22	6.71 ± 0.12	8.21 ± 0.48	10.8 ± 0.53	11.1 ± 0.57	8.97 ± 1.25	14.6 ± 0.74
average:	5.70 ± 0.02	6.37 ± 0.04	7.00 ± 0.02	9.05 ± 0.07	10.7 ± 0.07	11.0 ± 0.10	10.9 ± 0.24	14.9 ± 0.09

* Errors are 1σ statistical errors only. Additionally, the mean charges are subject to a systematic error of $\le$ 5%.

** No values are given if less than 3 counts are detected

5. Acknowledgements We are grateful to the many individuals at the Max-Planck-Institut für extraterrestrische Physik and the Space Physics group of the Department of Ph[illegible] and Astronomy at the University of Maryland, who developed the hardware and software for our ISEE experiments. This work is supported in part by NASA under contract NAS5-20062, grants NGR-21-002-224 and NGR-21-002-316, and by the Bundesministerium für Forschung und Technologie, contract RV 14B8/74 and 0101 017-ZA/WF/WRK 175/4.

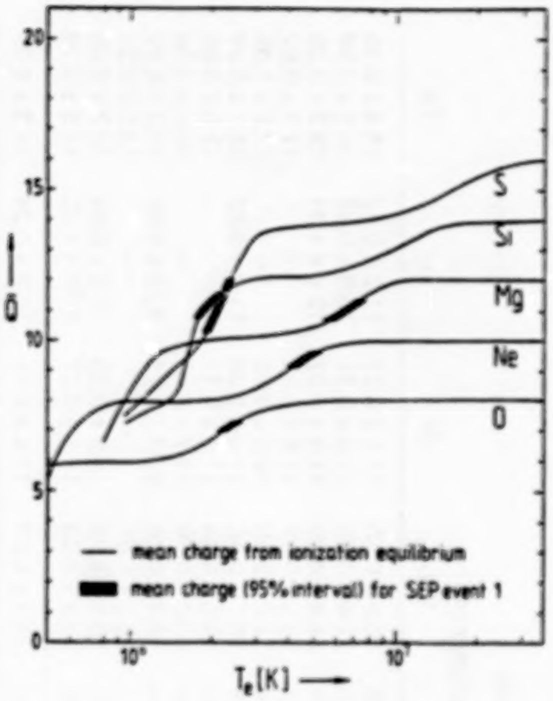

Fig. 1 ***Mean charge of O, Ne, Mg, Si, and S as a function of temperature as calculated from [8,9]. Heavy lines mark the temperature ranges compatible with the 95% confidence interval of the charge state measurements of solar energetic particle event 1.***

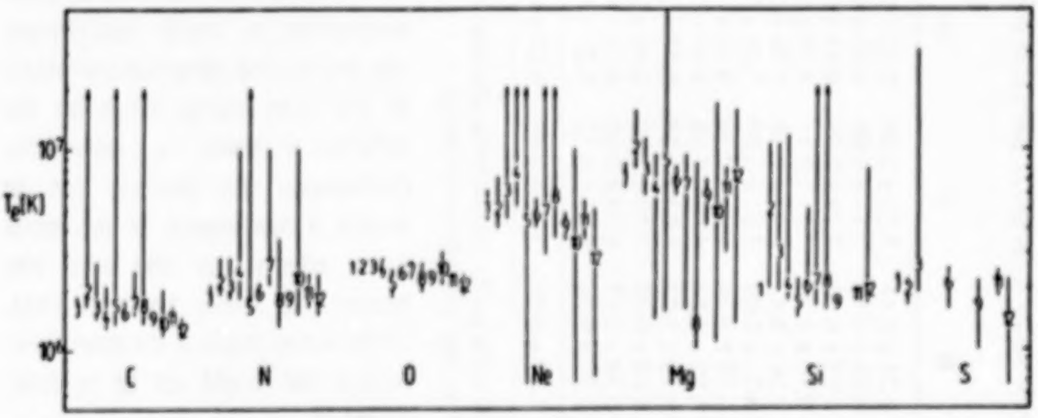

Fig. 2 ***Equilibrium temperatures (95% confidence intervals or lower limits) for the 12 SEP periods of Table 1, derived from [8,9].***

References

1. D. Hovestadt et al.: Ap. J. **281**, p.463 (1984)
2. G. Gloeckler et al.: Proc. 17th Int. Cosmic Ray Conf. (Paris), **3**, p.136 (1981)
3. D. Hovestadt et al.: Adv. Space Res. **1**, p.61 (1981)
4. A. Luhn et al.: Adv. Space Res. **4**, p.161 (1984)
5. D. Hovestadt et al.: IEEE Trans. Geos. Electr. **GE-16**, p.166 (1978)
6. C. Jordan: M.N.R.A.S. **142**, p.501 (1968)
7. C. Jordan: M.N.R.A.S. **148**, p.17 (1969)
8. M. J. Shull, M. v. Steenberg: Ap. J. Suppl. **48**, p.95 (1982)
9. M.J. Shull, M. v. Steenberg: Ap. J. Suppl. **49**, p.351 (1982)
10. A. Luhn, D. Hovestadt: paper SH 2.1-12 (this conference)
11. A. Luhn: Ph.D. Thesis, Technische Universität München (1985)
12. D.J. Mullan: priv. comm. (1985)

245 N85-34793

SH 2.1-12

CALCULATIONS OF HEAVY ION CHARGE STATE DISTRIBUTIONS FOR NONEQUILIBRIUM CONDITIONS

A. Luhn, D. Hovestadt
Max-Planck-Institut für extraterrestrische Physik
8046 Garching, F.R.G.

ABSTRACT

Numerical calculations of the charge state distributions of test ions in a hot plasma under nonequilibrium conditions are presented. In particular, we derive the mean ionic charges of heavy ions for finite residence times in an instantaneously heated plasma and for a non-Maxwellian electron distribution function. Comparing the results with measurements of the charge states of solar energetic particles, we find that neither of the two simple cases considered can explain the observations.

1. Introduction. Recent measurements of the charge states of heavy ions in solar energetic particle events[1] indicate that nonequilibrium conditions at the source of the solar energetic particles (presumably an active region in the lower corona) are likeley to play a key role in establishing the charge state distribution observed at earth. In particular, the temperature as derived from the equilibrium tables of charge state distributions [2,3,4] differed significantly for different ion species. Calculations of equilibration times for impurity ions in a fusion plasma [5] indicate that, as a function of plasma temperature, the time for initially neutral atoms to reach their equilibrium charge state distribution can vary by approximately two orders of magnitude. We have therefore calculated the mean ionic charges for elements of relevance to solar flare studies which are expected a) for a finite residence time of the ions after an instantaneous heating of the plasma, and b) for a non-Maxwellian distribution function for the electrons in the plasma.

2. Methods. The rate of change of the abundances n_i of the ionization states i of an ion with nuclear charge Z is given by the following system of equations:

$$\begin{aligned} \dot{n}_1 &= n_e(-n_1 S_1 + n_2 \alpha_2); \\ \dot{n}_i &= n_e(n_{i-1} S_{i-1} + n_{i+1} \alpha_{i+1} - n_i(S_i + \alpha_i)), \quad (i=2 \dots Z); \qquad (1) \\ \dot{n}_{Z+1} &= n_e(n_Z S_Z - n_{Z+1} \alpha_{Z+1}). \end{aligned}$$

For vanishing time dependence this becomes

$$n_i S_i = n_{i+1} \alpha_{i+1}, \quad (i = 1 \dots Z). \qquad (2)$$

S_i denotes the total ionization rate coefficient from ionization state i to i+1, α_i the total recombination rate coefficient from i to i-1, and n_e is the electron density. The rate coefficients are obtained by multiplication of the relevent cross sections with the electron velocity, averaged over the electron distribution function. For the time dependent calculations with a Maxwellian electron distribution we use the fit parameters for the rate coefficients given in [2] and [3]. These are calculated using the corona aproximation, i.e. neglecting any density dependent terms in the cross sections and photoionization by the radiation field, which is valid for the parameter range considered here. The processes included are collisional ionization and radiative and dielectronic recombination together with corrections taking into account autoionization after collisional excitation and dielectronic recombination. For the calculation of the charge states produced by a non-Maxwellian distribution, however, we need the cross sections σ as a function of electron impact velocity. To obtain these, we use the analytical forms of the rate coefficients for a Maxwellian distribution given by [6] and solve numerically for the parameters of the cross sections by comparing them with the rate coefficients given by [2,3]. We then can find the rate coefficients for an arbitrary electron distribution f_e by calculating $\int v\sigma(v) f_e(v) dv$, were v denotes the electron velocity.

The equations (1) are solved by numerical integration with an algorithm suited for the widely differing time scales of the abundance changes for the different ionization states. The initial charge distributions and the equilibrium distributions for a non-Maxwellian electron distribution function are calculated using the equilibrium equations (2). In view of the accuracy of the parameters given by [2] for the interpolation formulæ for the rate coefficients, conclusions based on the values of specific ionization ratios have to be made with caution. However, the mean values of the charge distributions, which are used for this work, are much less affected.

3. Results and Discussion. We first discuss the time development of the mean ionic charge of different ions after an instantaneous heating of the plasma. This is motivated by the observation that in the initial phase of a solar flare the temperature rises by a factor of approx. 10 over the ambient coronal temperature of about 10^6 K within a time of the order of 1 second (see for instance [7] and [8]). The subsequent acceleration of protons, alpha particles, and heavier ions may remove the ions in a timescale comparable to the equilibration time for the ionic charge. In Fig. 1 we plot the mean charge as a function of $n_e t$ for the case of a temperature rise from 10^6K to 10^7K. Note that the time for Neon and Magnesium to reach their new equilibrium charge state distribution is a factor of ten larger than that for e.g. Oxygen: if one assumes a typical electron density of 10^9 cm^{-3}, it is of the order of 100 s.

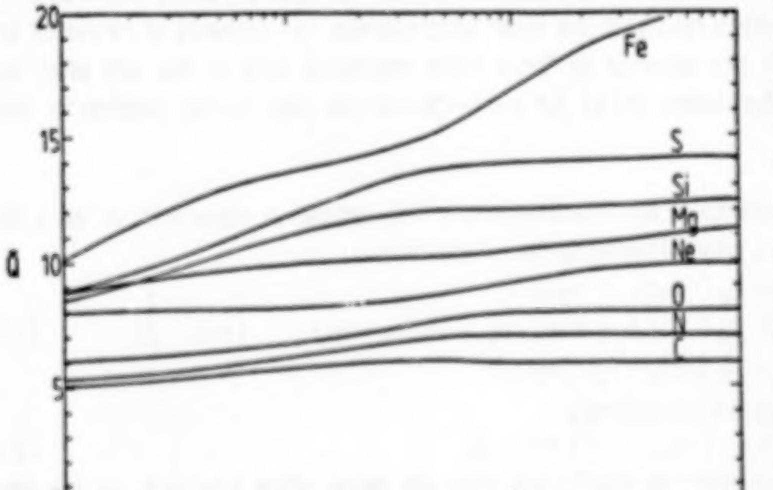

Fig. 1 *Time development of mean charges after an instantaneous heating of the plasma from 10^6 K to 10^7 K at time t=0*

This is a consequence of the high ionization potential for the K shell electrons of these elements, which in this temperature range cannot be removed for ions with a higher atomic number Z. The differences in the equilibration times contrast with the observation of rather high charge states for Ne and Mg [1], which on the basis of the notion sketched above would be expected for elements with short equilibration times. For different initial and final temperatures the equilibration times change. However, their ratios for the different ions remain approximately the same. We can therefore conclude, that the simple model of the freezing in of nonequilibrium charge states due to the escape of the particles from the heated coronal material cannot explain the ionic charges of solar energetic particles.

The second case considered is the calculation of equilibrium charge distributions for a non-Maxwellian electron distribution function of the coronal plasma. The existence of a non-thermal tail of electrons in the transition zone and the lower corona is supported both by theoretical calculations for the quiet sun (e.g. [9,10]) and observations in flaring regions (e.g. [11,12]). Owocki and Scudder (6) have considered this case and derived the ionization ratios O^{+6}/O^{+7} and Fe^{+11}/Fe^{+12}. They find that an estimation of the temperature based on these ratios overestimates or underestimates the true temperature of the plasma depending on the ratio $k_B T_m/I$, were k_B is the Boltzmann constant, T_m the temperature inferred with a Maxwellian distribution, and I the ionization potential of the state considered. We follow [6] in employing the "kappa" (generalized Lorentzian) distribution as a convenient one parameter representation of a Maxwellian with a power law tail. Our result is that the mean charge changes in general by considerably less than the ionization state ratios, especially if states are compared which constitute the flanks of the charge distribution.

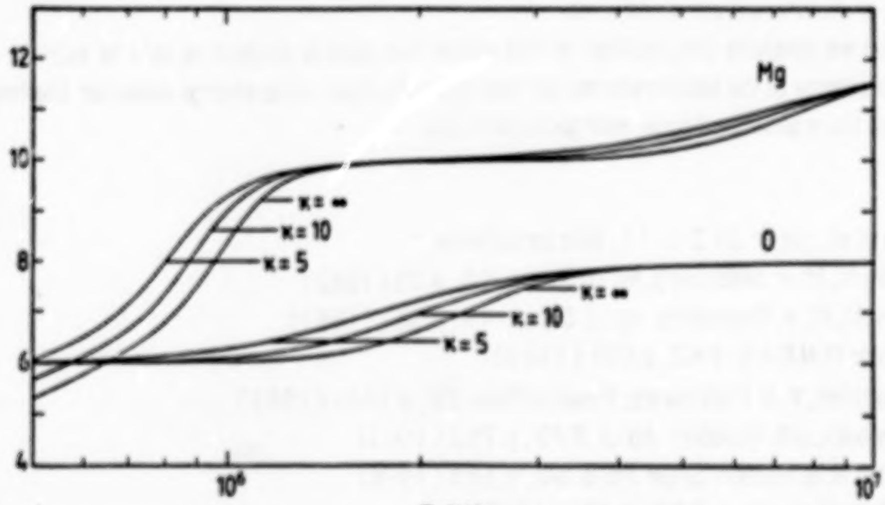

Fig. 2 *Mean equilibrium charges of O and Mg for a κ electron distribution function with κ=5 and 10 and a Maxwellian (κ=∞).*

In Fig. 2 we compare the mean equilibrium charges of O and Mg as a function of temperature (defined for the κ distribution as corresponding to the mean electron energy) for values of the parameter κ of 5, 10, and ∞ (corresponding to a strong and moderately pronounced electron tail and a purely Maxwellian distribution). Fig.3 shows the mean charges for various heavy ions for a κ distribution with κ=5. Although the effect of the energetic tail of the electron distribution is to raise the mean charge above that of a Maxwellian with the same temperature, the variation of this effect for the different ions is not pronounced enough to explain the variation of the temperature inferred for the different ions from a Maxwellian.

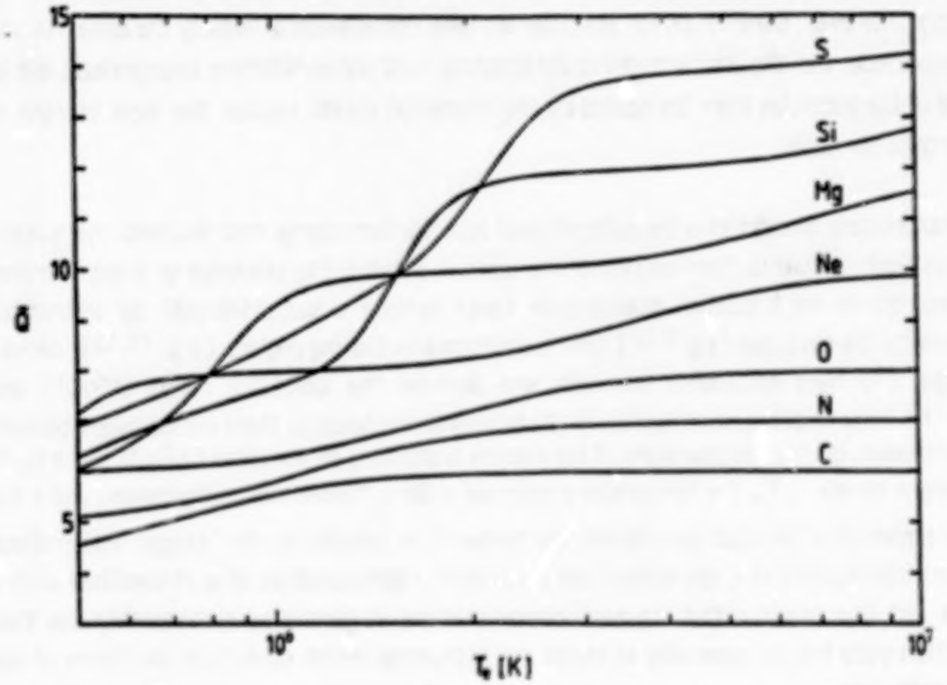

Fig.3 *Mean equilibrium charges as a function of electron temperature for a κ distribution with κ=5*

In closing we conclude that neither of the above two simple models is able to explain the observed discrepancy in the temperatures derived from the mean ionic charge states for the heavy constituents of flare generated solar energetic particles.

References

1 A.Luhn et al.: paper SH 2.1-11, this conference
2 M. J. Shull, M. v. Steenberg: Ap. J. Suppl. **48**, p.95 (1982)
3 M.J. Shull, M. v. Steenberg: Ap. J. Suppl. **49**, p.351 (1982)
4 C. Jordan: M.N.R.A.S. **142**, p.501 (1969)
5 P. G. Carolan, V. A: Piotrowicz: Plasma Phys. **25**, p.1086 (1983)
6 S. P. Owocki, J.D. Scudder: Ap. J. **270**, p.758 (1983)
7 R. P. Lin, H. S. Hudson: Solar Phys. **50**, p.153 (1976)
8 D. M. Rust et al.: Ap. J. **288**, p.401 (1985)
9 R. Roussel-Dupré: Sol. Phys. **68**, p. 243 and p. 265 (1980)
10 E. C. Shoub: Ap. J. **266**, p.339 (1983)
11 S. F. Smerd, in AAS-NASA Symposion on Solar Flares, NASA SP-50 (1964)
12 P. L. Dufton, A. E. Kingston, F. P. Keenan: Ap. J. **280**, L35 (1984)

N85-34794

SH 2.1-13

ABUNDANCES FROM SOLAR-FLARE GAMMA-RAY LINE SPECTROSCOPY

R. J. Murphy
University of Maryland
College Park, MD 20742

R. Ramaty
NASA/GSFC
Greenbelt, MD 20771

D. J. Forrest
University of New Hampshire
Durham, NH 03824

B. Kozlovsky
Tel Aviv University
Tel Aviv, ISRAEL

ABSTRACT

Elemental abundances of the ambient gas at the site of gamma-ray line production in the solar atmosphere are deduced using gamma-ray line observations from a solar flare. The resultant abundances are different from local galactic abundances which are thought to be similar to photospheric abundances.

1. INTRODUCTION. Gamma-ray emission from solar flares consists of lines from nuclear reactions and continuum primarily from relativistic electron bremsstrahlung (1,2). These gamma rays are produced in thick-target (3) interactions of energetic particles with ambient gas, most likely in the chromosphere or the transition region. A particularly good gamma-ray spectrum has been observed (4) by the gamma-ray spectrometer (GRS) on SMM from the April 27, 1981 flare. This spectrum shows several narrow lines: at 6.13, 4.44, 1.78, 1.63, 1.37 and 0.85 MeV from deexcitations of ^{16}O, ^{12}C, ^{28}Si, ^{20}Ne, ^{24}Mg and ^{56}Fe, respectively, at 2.22 MeV from neutron capture, at 0.51 MeV from positron annihilation and at ~0.45 MeV from α-α fusion. While earlier work (5,6) predicted that these should be the strongest lines, the observed line ratios are inconsistent (4) with our calculations which assume local galactic (7) abundances for the ambient gas (see Table 1). These local galactic abundances are believed (7) to be similar to photospheric abundances.

2. ANALYSIS. We have calculated deexcitation spectra resulting from thick-target nuclear reactions. These spectra, binned into photon energy channels j defined in ref.(6), can be expressed as $\sum_{\ell} n(\ell)A(j,\ell)$, where $n(\ell)$ is the abundance of element ℓ (with ℓ defined in Table 1) and $n(\ell)A(j,\ell)$ is the contribution of interactions of all the energetic particles with this element. To these spectra we add bremsstrahlung, the neutron capture line and positron annihilation radiation. For the bremsstrahlung we assume a power law with adjustable index, for the neutron capture we take an infinitely-narrow line at 2.223 MeV and for the

annihilation radiation we assume an infinitely-narrow line at 0.511 MeV along with the orthopositronium continuum corresponding to 67% of the positrons annihilating via positronium. We transform the photon spectra into pulse-height spectra using a numerical model of the detector response which will be presented elsewhere. The total pulse-height spectrum can then be written as $\rho(i) = \sum_\ell n(\ell)\mathcal{A}(i,\ell) + \mathcal{A}b(i) + \mathcal{A}n(i) + \mathcal{A}p(i)$, where i denotes pulse-height channel number, $\mathcal{A}(i,\ell)$ is the partial pulse-height spectrum of element ℓ, and $\mathcal{A}b(i)$, $\mathcal{A}n(i)$ and $\mathcal{A}p(i)$ are the bremsstrahlung, neutron capture and positron annihilation pulse-height spectra. We derive the abundances by comparing $\rho(i)$ to the observed pulse-height spectrum and varying the $n(\ell)$'s and $\mathcal{A}b$, $\mathcal{A}n$ and $\mathcal{A}p$ until a best fit is obtained. We only consider one isotope for each element except for C, Ne and Mg, for which we include the contributions of ^{13}C, ^{22}Ne and ^{26}Mg but with fixed isotopic ratios (8).

The partial spectra $\mathcal{A}(i,\ell)$ depend on the energetic-particle composition, spectrum and angular distribution. The particle composition that we use is given in Table 1. Because in the solar atmosphere interactions amongst nuclei heavier than He are expected to be negligible and because no gamma-ray lines are produced in p-p or p-α interactions, the $\mathcal{A}(i,\ell)$'s for $\ell>2$ depend only on the energetic protons and α-particles and consist mostly of narrow lines. For the same reason, $\mathcal{A}(i,1)$ depends only on the energetic C and heavier nuclei and consists mostly of broad lines. $\mathcal{A}(i,2)$ depends on the energetic α-particles and heavier nuclei and consists of the narrow feature at ~0.45 MeV in addition to broad lines. The dominant contribution to the total pulse-height spectrum is from the $\mathcal{A}$'s with $\ell>2$. The contributions of $\mathcal{A}$ with $\ell=1$ and 2 are relatively small, since in a thick target the interactions of the heavier nuclei are supressed by the Z^2/A dependence of the Coulomb energy loss. In addition, a good fit of the calculated pulse-height spectrum to the observed spectrum can only be achieved if the observed narrow lines are adequately accounted for. As just mentioned, the narrow lines are produced mostly by the energetic protons and α-particles. Thus, uncertainties in the abundances of the energetic heavy nuclei relative to each other and relative to the protons do not significantly affect the determination of ambient C and heavier element abundances. The ambient H abundance, however, does depend on the ratio of energetic heavy nuclei to protons and therefore cannot be determined reliably. Information on the ambient He abundance is obtained primarily by fitting the ~0.45 MeV feature and therefore depends on the α/p ratio which is also very uncertain. This uncertainty, however, does not significantly affect the heavy element abundance determinations as long as the α/p ratio is not much larger than ~0.1.

For the energy spectrum of the April 27, 1981 flare we use a Bessel function with $\alpha T = 0.02$, a value close to the average αT determined (3) for several flares using the 2.22 to 4-7 MeV fluence ratio or the high-energy neutron arrival-time profile. We cannot use either method for this flare because the 2.22 MeV line was strongly attenuated owing to the location of the flare on the solar limb and no neutrons were observed. Our calculations, however, indicate that variations in the spectrum do not affect the abundance determinations significantly. The angular distribution of the energetic particles affects the shapes and central energies of the lines, but since the Doppler shifts of the narrow lines are not expected to exceed the energy resolution of the SMM/GRS detector, we assume that the energetic particles are isotropic.

3. RESULTS. The abundances deduced by optimizing the fit of the calculated spectrum to the data are given in Table 1. This optimization method is discussed in the accompanying paper. Here we derive values of reduced χ^2, χ^2_ν, from the comparison of the gamma-ray abundances shown in Table 1 with both the local galactic and coronal abundances. We have renormalized the gamma-ray abundances using multiplicative factors determined by minimizing χ^2_ν. For the local galactic case, this factor is 1.4, leading to $\chi^2_\nu = 3.6$ ($\nu = 11$). This implies that the gamma-ray abundances are different from the local galactic abundances. For the coronal case, the factor is 1.1 and $\chi^2_\nu = 1.1$ implying that the gamma-ray and coronal abundances are consistent within the errors. The closed circles in Figures 1 and 2 show the ratios of the renormalized gamma-ray abundances to the mean local galactic and coronal abundances. The error bars reflect the 1-σ errors of the gamma-ray abundances. The open boxes represent the errors in the local galactic and coronal abundances.

With the renormalization that we have adopted, the principal difference between the gamma-ray and the local galactic abundances is the underabundance of C and O in the gamma-ray sample. The Fe, Si, Mg and Ne abundances in the two samples are in good agreement, but the statistical errors for Ca, S, Al and N and the systematic error for He (due to the uncertain α/p ratio) are too large to permit a quantitative conclusion. As discussed above, the gamma-ray determination of the H abundance is also subject to a large systematic error. A similar supression of C and O has been found (7) in the coronal abundances relative to the local galactic abundances (which are thought to be similar to photospheric abundances). It has been pointed out that this supression may be caused by charge-dependent mass transport from the photosphere to the corona. Since the photosphere is collisionally ionized at a relatively low temperature, the transport could depend on the first ionization potentials of the elements. While the gamma-ray sample probably pertains to the chromosphere or transition region, similar fractionation effects could be influencing these sites as well. However, if the Ne abundance in the photosphere (where it cannot be measured) is the same as in the local galactic sample, then the difference between the gamma-ray and photospheric abundances must be due to additional processes, because correlation with first ionization potential alone would predict a lower Ne abundance than that derived here.

4. REFERENCES

1. Ramaty, R. et al., 1983, Solar Physics, 86, 395.
2. Chupp, E. L., 1984, Ann. Rev. Astron. Astrophys., 22, 359.
3. Murphy, R. J. and Ramaty, R., 1985, Adv. in Space Res., 4, 127.
4. Forrest, D.J.,1983, in Posi.-Elec. Pairs in Astrop., AIP, NY, p.3.
5. Lingenfelter, R. E. and Ramaty, R., 1967, in High-Energy Nuclear Reactions in Astrophysics, Benjamin, NY, p.99.
6. Ramaty, R., et al., 1979, Ap. J. (Supp), 40, 487.
7. Meyer, J. P., 1985, Ap. J. (Supp), 57, 173.
8. Cameron, A. G. W., 1982, in Essays in Nuc. Astrop., Cambridge, p.23.

5. ACKNOWLEDGEMENTS. We would like to acknowledge discussions with E. L. Chupp and the rest of the GRS team, as well as with R. E. Lingenfelter. The work of DJF was supported by NASA, contract NAS 5-28609.

TABLE 1

Elemental Abundances

ℓ	Element	Local Galactic	Corona	Energetic Particles	Abundances from Gamma Rays
1	H	2.71×10^6 (1.1)	2.55×10^6 (1.4)	8.66×10^5	$(5.61\pm3.49)\times10^5$
2	He	2.60×10^5 (1.25)	2.50×10^5 (3.0)	5.86×10^4	$(1.92\pm0.25)\times10^5$
3	C	1260(1.26)	600(3.0)	270	288±50
4	N	225(1.41)	100(1.7)	75	117±91
5	O	2250(1.25)	630(1.6)	600	422±62
6	Ne	325(1.50)	90(1.6)	85	199±27
7	Mg	105(1.03)	95(1.3)	144	68±25
8	Al	8.4(1.05)	7(1.7)	8	-15±52
9	Si	100(1.03)	100(1.3)	100	100±28
10	S	43(1.35)	22(1.7)	19	48±83
11	Ca	6.2(1.14)	7.5(1.5)	7	17±15
12	Fe	88(1.07)	100(1.5)	99	76±18

Local galactic and coronal abundances from ref.(7). The quantities in parantheses are multiplicative errors, f. We take m(f-1) as an estimate for a 1-σ error about the mean value m. For the energetic particles, p/α and p/O are the same as those of ref.(8) and C through Fe relative to O or Si are similar to the mass-unbiased solar energetic particle abundances of ref.(7). The gamma-ray abundance errors are 1 σ.

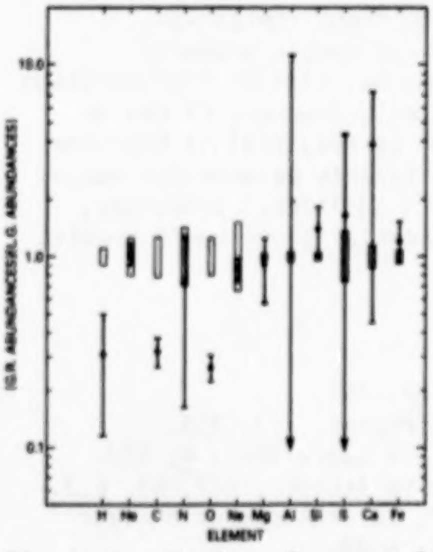

Figure 1. Ratios of renormalized gamma-ray abundances to local galactic abundances (closed circles).

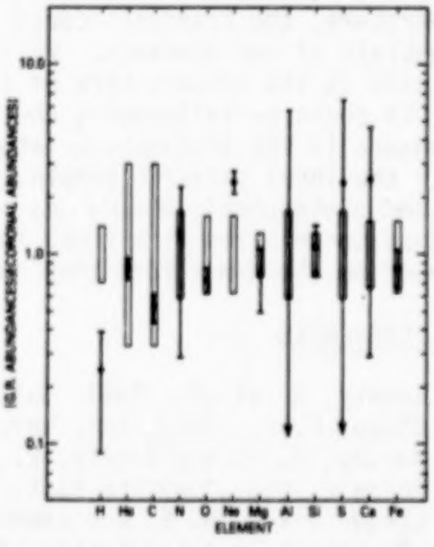

Figure 2. Ratios of renormalized gamma-ray abundances to coronal abundances (closed circles).

N85-34795

SH 2.1-14

SOLAR FLARE GAMMA-RAY LINE SPECTROSCOPY

R. J. Murphy
University of Maryland
College Park, MD 20742

D. J. Forrest
University of New Hampshire
Durham, NH 03824

R. Ramaty
NASA/Goddard Space Flight Center
Greenbelt, MD 20771

B. Kozlovsky
Tel Aviv University
Tel Aviv, ISRAEL

1. INTRODUCTION. In a previous paper (1), we have outlined the techniques and presented the results of solar elemental abundance determinations using observations of gamma-ray lines from the April 27, 1981 solar flare. Here, we elaborate on these techniques, present the observed and the best-fitting theoretical spectra, present numerical values for the photon fluences and derive the total number of protons involved in the thick-target production of these gamma rays.

2. DETECTOR RESPONSE. The gamma-ray spectrometer (GRS) on SMM is an actively-shielded, 7-crystal NaI scintillation detector (2) with 476 pulse-height channels. Its pulse-height resolution corresponds to an energy resolution of ~7% at 662 keV and its effective area is energy-dependent, varying from ~20 to ~200 cm^2. Using a numerical model for the detector response, a photon spectrum $a(j)$ incident on the detector can be transformed into a pulse-height spectrum $\rho(i) = \sum_j D(i,j)\, a(j)$, where $D(i,j)$ represents the detector response, and i and j are the pulse-height and photon energy channel numbers, respectively. This numerical model takes into account the effective area, the pulse-height resolution and the photopeak, first escape peak and Compton continuum fractions. In particular, the Compton continuum includes an edge feature resulting from the escape of photons through its unshielded aperture. The details of this model will be published elsewhere.

3. ANALYSIS. We have calculated deexcitation spectra resulting from thick-target nuclear reactions and combined them with spectra expected from bremsstrahlung, neutron capture and positron annihilation. The total spectrum, binned into photon energy channels j defined in ref. (3), can be expressed as $a(j) = \sum_\ell n(\ell)A(j,\ell)$, where, for $1<\ell<12$, $n(\ell)$ is the abundance of element ℓ and $n(\ell)A(j,\ell)$ is the contribution of interactions of all the energetic particles with this element (see ref.(1)), $n(13)A(j,13)$ is the bremsstrahlung spectrum, $n(14)A(j,14)$ is the neutron capture spectrum taken to be a delta-function at 2.223 MeV and $n(15)A(j,15)$ is the positron-annihilation spectrum assumed to be the sum of a delta-function at 0.511 MeV and the orthopositronium annihilation function normalized such that 67% of the positrons annihilate via positronium. For a power-law bremsstrahlung spectrum, we

find that a good fit to the data is obtained with an index equal to 2.1. Using the detector response, we obtain the pulse-height spectrum, $\rho(i) = \sum_\ell n(\ell)\,\mathcal{A}(i,\ell)$, where $\mathcal{A}(i,\ell)$ are partial pulse-height spectra.

To obtain the best fit between the calculated pulse-height spectrum, $\rho(i)$, and the observed spectrum, $c(i)$, we minimize χ^2_ν by varying the $n(\ell)$'s. Here, $\chi^2_\nu = \sum_i \omega(i)[c(i)-\rho(i)]^2/\nu$, where ν is the number of degrees of freedom (450 usable detector channels less the 15 free variables $n(\ell)$), $\omega(i)$ is the statistical weight of channel i and $c(i) = O(i)-fB(i)$, where $O(i)$ is the number of counts accumulated during the flare integration time, $B(i)$ is the number of counts accumulated during the background integration time and f is a factor adjusting background integration time to flare integration time. We take $\omega(i)$ to be $1/\sigma^2(i)$, where $\sigma^2(i)$ is the mean-square error for channel i. For the Poisson statistics assumed here, $\sigma^2(i) = O(i) + f^2B(i)$.

The values of $n(\ell)$ which minimize χ^2_ν are obtained by solving the set of equations resulting from taking partial derivatives of χ^2_ν with respect to each of the $n(\ell)$'s and setting them to zero. The solutions of these equations can be written as $\vec{n} = E\,\mathcal{A}^+\,W\,\vec{c}$, where $\vec{n}$ is a vector whose elements are the $n(\ell)$, $\mathcal{A}$ is a matrix whose elements are $\mathcal{A}(i,\ell)$, $\mathcal{A}^+$ is its transpose, W is a diagonal matrix whose elements are the statistical weights $\omega(i)$, $\vec{c}$ is the vector of the observed pulse-height spectrum and $E = (\mathcal{A}^+ W \mathcal{A})^{-1}$ is the error matrix. If the only source of error is observational counting statistics (i.e., fluctuations in $c(i)$), then the mean-square errors of the $n(\ell)$'s are the diagonal elements of E multiplied by χ^2_ν (4,5).

The off-diagonal elements of E give information on the interference between the partial spectra. Interference arises when two partial spectra contribute significantly to an observed spectral feature. The interference coefficient is $F(k,\ell) = [E(k,\ell)]^2/[E(k,k)E(\ell,\ell)]$. When $F(k,\ell)$ is much less than 1, the interference is negligible. However, when $F(k,\ell)$ is large, $n(k)$ and $n(\ell)$ cannot be determined independently. Their sum can be determined with an error $[E(k,k)+E(\ell,\ell)]\,\chi^2_\nu$, but the overall fit will remain just as good if either $n(k)$ or $n(\ell)$ is varied by a factor $F(k,\ell)$ while keeping the sum $n(k)+n(\ell)$ constant.

4. RESULTS. The resultant $n(\ell)$'s for $1<\ell<12$, together with their respective mean-square errors, are given in the last column of Table 1 of ref.(1). As discussed there, the statistical errors in the derived abundances of C, O, Ne, Mg, Si and Fe are sufficiently small to allow meaningful comparisons with the local galactic and coronal abundances, but the statistical errors for N, Al, S and Ca, as well as the systematic errors for H and He, preclude such comparisons. In addition to these 12 elements, the fit of the calculations to the data also provides information on the bremsstrahlung and the neutron-capture and positron-annihilation radiation. We present this information in terms of photon fluences incident on the detector. We find that the >0.3 MeV bremsstrahlung fluence is (1060±14) photons/cm^2 for the power law index of 2.1, the neutron capture line fluence is (4.3±2.9) photons/cm^2 and the 0.51 MeV line fluence is (25.8±2.6) photons/cm^2. In comparison, the fluences resulting from interactions with ambient H, He, C, N, O, Ne, Mg, Al, Si, S, Ca and Fe are 27, 59, 15, 6.7, 30, 62, 35, <1.3, 56,

4.2, 1.9 and 56 photons/cm^2, respectively, with the same relative errors as given in ref.(1).

We have also considered the interference coefficients between the 15 components given above. We find that between the six reliably determined elements (C, O, Ne, Mg, Si, Fe) these coefficients are all less than 0.1. Interference, therefore, should introduce little additional uncertainty in the determination of the abundances of these elements. However, we find interference between S and neutron capture (F=0.3), and He and positron annihilation (F=0.21), resulting from the detector's inability to adequately resolve the 2.22 MeV line from the 2.23 MeV line of ^{32}S and the 0.511 MeV line from the α-α feature at ~0.45 MeV, respectively. There is also interference between C and N (F=0.27), resulting from contributions to the 4.44 MeV line from C and N spallation. But, as already discussed, the abundances of S, N and He are not well determined. Also, the 2.22 MeV line fluence cannot be adequately determined because, for the April 27, 1981 flare, this line is strongly attenuated by Compton scattering in the photosphere.

The observed spectrum of the April 27, 1981 flare is compared to the calculated spectrum in Figure 1. Here, the lines of ^{16}O, ^{12}C, ^{20}Ne, ^{24}Mg and ^{56}Fe can be clearly seen. The feature marked n is due to the 2.22 MeV line, with additional contributions from ^{14}N (at 2.31 MeV) and ^{32}S. The lack of significant interference between the 2.22 and 2.31 MeV lines indicates that adequate detector resolution is available to distinguish between them. Even though the ^{28}Si line at 1.78 MeV is not clearly visible, the Si abundance can nevertheless be well determined since in the calculation the bulk of the photons above the line center energy are produced by interactions with Si. The dip just below the second ^{56}Fe line is probably due to the effects of a calibration line of ^{60}Co at 1.17 MeV.

From the fluences for the various components given above, the total nuclear radiation (including the 2.22 MeV line and all the positron annihilation radiation) is 372 photons/cm^2 and its ratio to the total observed bremsstrahlung above 0.3 MeV is 0.35. This value is of considerable importance for studies of the angular distribution of gamma rays from solar flares (6). Likewise, we find that in the 4-7 MeV band, 77 photons/cm^2 are from nuclear interactions and 28 photons/cm^2 are from bremsstrahlung. The fractional contributions of the various ambient elements to this 4-7 MeV nuclear radiation are the following: 0.1, 0.08, 0.18, 0.03, 0.30, 0.13, 0.06, 0.0, 0.08, 0.0, 0.0, 0.04 for the 12 elements from H through Fe. Thus, about 1/2 of the nuclear emission in the 4-7 MeV band is from interactions with ambient C, N and O.

To determine the total number of protons involved in the gamma-ray production, we must assume a ratio of H to the heavier elements in the ambient medium. Using the abundances deduced from the gamma rays in ref.(1), we obtain Np(>30 MeV) = 3.8x10^{32} protons, where Np(>30 MeV) is the number of protons with kinetic energy greater than 30 MeV. But, as we have discussed, the H abundance in this sample is uncertain. Assuming abundances similar to the local galactic abundances (for which the ratio of H to heavier nuclei is higher than for the gamma-ray sample (1)), Np(>30 MeV) = 6.7x10^{32}.

5. REFERENCES

1. Murphy, R. J. et al., this publication.
2. Forrest, D. J. et al., 1980, Solar Phys., 65, 15.
3. Ramaty, R., Kozlovsky, B. and Lingenfelter, R. E., 1979, Ap. J. (Supp.), 40, 487.
4. Trombka, J. I. and Schmadebeck, R. L., "A Numerical Least-Square Method for Resolving Complex Pulse Height Spectra", NASA SP-3044, 1968.
5. Bevington, P. R., "Data Reduction and Error Analysis for the Physical Sciences", McGraw Hill, NY, 1969.
6. Dermer, C. D. and Ramaty. R., 1985, submitted to Ap. J.

6. ACKNOWLEDGEMENTS. We would like to acknowledge discussions with E. L. Chupp and the rest of the GRS team, as well as with R. E. Lingenfelter. The work of DJF was supported by NASA, contract NAS 5-28609.

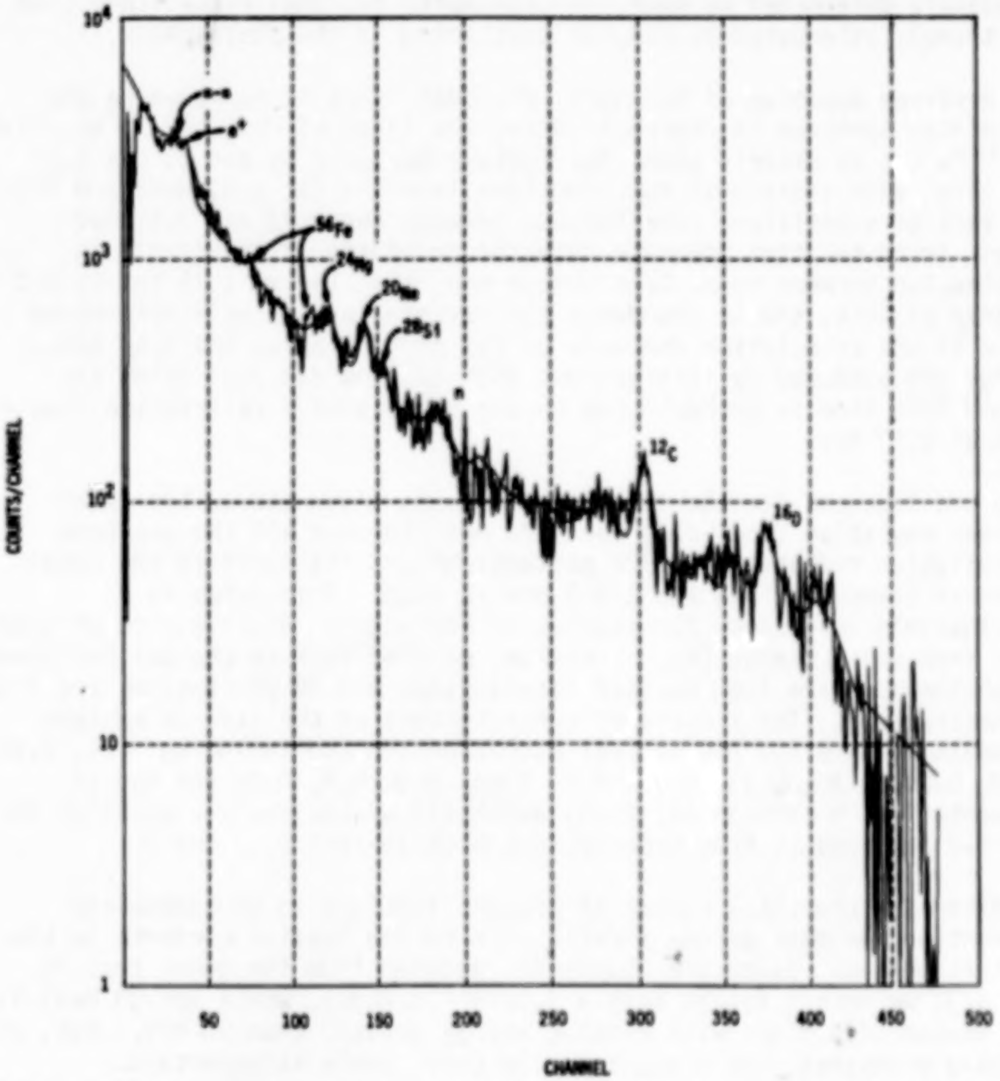

Figure 1. Observed and calculated (smooth curve) spectra of the April 27, 1981 solar flare.

N85-34796

ISOTOPIC OVERABUNDANCES AND THE ENERGETIC PARTICLE MODEL OF SOLAR FLARES

R. Pérez-Enríquez and S. Bravo
Instituto de Geofísica, UNAM, Ciudad Universitaria
México D.F., 04510, MEXICO

ABSTRACT

According to the energetic particle model of solar flares particles are efficiently accelerated in the magnetic field loop of an active region (AR) by hydromagnetic turbulence. Based on this picture, we shall demonstrate that the isotopic overabundances observed in some flares are not a consequence of the flare itself but they are characteristic of the plasma in the AR. Only in the event of a flare releasing the plasma into the interplanetary space it is posible to observe this anomalous composition at spacecraft locations.

1. Introduction. The observation of an anomalous composition of solar flare particles from some events began as early as 1962 when Schaeffer and Zahringer measured a ratio of ^{3}He/^{4}He ~ 0.2 for the Nov. 12, 1960 event, compared to the normal ratios in the solar atmosphere and in the solar wind of about 10^{-4} (Geiss and Reeves,1972). Since then, ratios of about one have been measured for these isotopes and substantial overabundances of Fe and another heavy elements have also been observed in the solar energetic particle flux. The characteristics features of the "rich" events have been reviewed by Ramaty et al. (1980), and Kocharov and Kocharov (1984).

Several models have been proposed for the explanation of such overabundances. The most successful are those in which the anomalous composition observed is the result of the acceleration of a preferentially preheated population at the time of the flare, the selective heating been caused by various instabilities generated in the plasma. There are two such plasma instabilities that seem to explain both the ^{3}He, and heavier ions overabundances observed: the Fisk's (1978) model which assumes that a current electrostatic instability leads to ion cyclotron waves which heat the ions by a resonant process, and the Ibragimov and Kocharov (1978) model which assumes that a high level of turbulence is present in the flare plasma giving rise to the production of ion sound waves with the consequent heating of the isotopes. The physical characteristics of the plasma assumed in both models are somewhat similar: They both requiered that the relative abundance of ^{4}He to H is already larger than normal -so the characteristic frequency of the plasma is closer to the gyrofrequency of the isotopes to be preferentially heated- and a value of β (the plasma to magnetic pressure ratio) smaller than one -to assure that the plasma remains confined to the magnetic field. There is, however, an important difference in the ratio of electron to ion temperatures (T_e/T_i) requiered by each mechanism to operate: ion cyclotron waves in Fisk's model requiere a value of about 10, while for the ion soun waves in the Ibragimov and Kocharov's model this ratio should be about 100.

Some observations seem to present problems to the requirements of these models. On the one hand, the X-ray emission detected by the SMM and Hinotori satellites (see reviews by Yoshimori et al., 1983; Chupp, 1983; Svestka and Shadee, 1983) seems to indicate that the β value of the plasma before and at the time of the flash of the flare is very near to one and not as low as requiered by both models. On the other hand, the coexistence of two different isotopes of Fe ($Fe^{11,12}$ and Fe^{17-20}) has been observed in the flare particle flux by MaSung et al. (1981), and Klecker et al. (1984), (see Table I), thus implying two different temperatures at the flare site. We shall show in the following sections that for the energetic particle model (EPM) no such difficulties exist, and that it can give an overall explanation of the observations.

TABLE I

Event	Overabundant Isotopes	Underabundant Isotopes
14-15 May,1974 (MaSung et al.1981)	^{3}He,Ne,Mg,Si, O,S,$Fe^{11,12}$ and $Fe^{16,17,18}$	C
Average of five events during 1978 and 1979 (Klecker et al.1984)	^{3}He,$Fe^{19\pm1}$	

__2. The Plasma in AR's According to the Energetic Particle Model of Solar Flares__. Here we shall limit ourselves to describe the characteristics of the energetic particle model (EPM) which are relevant to the problem of the production of the overabundances of ^{3}He and heavier nuclei in an AR;(for a more detailed discussion of the model see Pérez-Enríquez, 1985). In this model, particles from the coronal plasma are efficiently accelerated by hydromagnetic waves from the convective zone, as discussed by Hollweg (1984) in the contex of coronal heating, while they remain trapped in the intense bipolar magnetic field of an AR. Hence both the density and temperature of the plasma increase with time since the very appearence of the magnetic loop. In other words, the trapped plasma undergoes a dynamic evolution which may eventually lead to the ocurrence of a flare, in contrast with those models which assume that the plasma plays a pasive role in the generation of the flare and remains undisturbed until the flash.

Since the electrons move faster than the protons by a factor of ~43 at the same energy, a Fermi type of acceleration within the theory of Kulsrud and Ferrara (1971) will be efficient only for the ions and the electron population will gain its energy mainly from its interaction with the ions. Now, according to the theory of Kennel and Petschek (1966), the stable trapping of the particles can be mainteined as long as their energy E is below $E_c = B^2/8\pi n$, where B is the magnetic field, and n is the electron number density. As a consecuence of the Fermi acceleration there are everytime more ions beyond E_c which try to escape and as they do they generate their own resonant waves. The wave instability so produced will depend on the physical characteristics of the plasma in the AR such as the T_e/T_i ratio, the β of the plasma and the relative abundance of ^{4}He to H.

a) The T_e/T_i, and β values: As the energy of the electrons is "purely" of thermal nature, and the energy of the ions is mainly convective there will be a relative streaming between them, and thus, as described by Pérez-Enríquez (1985), a Buneman instability will take place with a growth rate $\gamma_B = \sqrt{3}/2\,(m_e/m_i)^{1/3}\,\omega_{pe}$. Here $m_{e,i}$ are the electron and ion masses respectively, and $\omega_{pe} = (4\pi n_e e^2/m_e)^{1/2}$ is the electron plasma frequency. For a value of $n_e \approx 3\times10^{7}$ cm^{-3}, $\gamma_B \approx 2.1\times10^{8}$ s^{-1} and T_e grows very fast while T_i does it much slower; so T_e/T_i increases with time reaching values as high as several hundreds as observed. In a similar manner, as the number density of particles in the region also tends to increase, so it does β. In other words, both T_e/T_i and β are growing functions of time and their schematic evolution is shown in Fig. (1). Notice that these functions are quite arbitrary, but here we are only interested in showing the increase of T_e/T_i and β with time. In the figure, t_F and t_{IK} correspond to the times where Fisk's or Ibragimov and Kocharov's models operate, respectively.

b) The He to H ratio: Since ^{4}He is four times heavier than H, it is expected to be more abundant at the bottom of the AR. In fact, from simple thermodynamic considerations, we obtain that the relative abundance of ^{4}He to H at the feet of a typical AR can be greater than that at the top by a factor as high as 100. So, the value of the ^{4}He to H ratio can be of about 10 at lower parts of the AR.

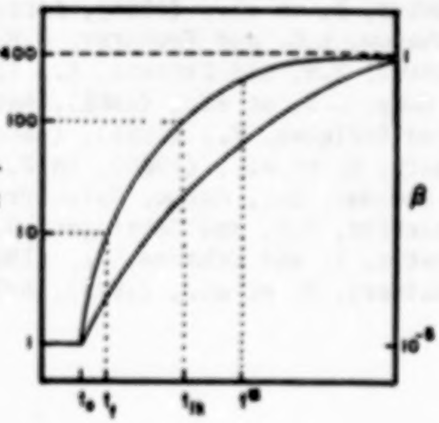

Fig.(1). Evolution of T_e/T_i and β in the active region(AR) from the initial time t_0 to a time t^*, the time of the flare.

3. Isotopic Overabundances and Conclusions. The picture that comes out from all this is the following: due to the dynamic evolution of the plasma in the AR as described by the EPM, the requirements of the overabundance model are fulfilled at times t_F (for Fisk's model), and t_{IK} (for Ibragimob and Kocharov's model) as a consequence of such evolution (see Fig. 1). That is, the composition of the plasma in AR's also presents an evolution and so the especific composition to be observed in the interplanetary space will depend on how late in the life of the AR the flare takes place. A flare happening in the early stages of the development of an AR will send out into the interplanetary medium energetic particles with normal composition for no time has been given to the plasma to grow an overabundance (t^* before t_F in the Figure), whereas if the flare happens later the energetic particles will present an anomalous composition. In other words, the overabundances observed are indeed a characteristic of the plasma in AR's and are not produced by the flare proper. The existence of two isotopes of iron (Table I) is also easily explained within the context of our model because different

temperatures are reached by the plasma at different stages of its evolution.

References.

Chupp, E.L., (1983), Solar Phys., 86, 383.
Fisk, L.A., (1978), Astrophys. J., 224, 1048.
Geiss, J. and Reeves, H., (1972), Astron. Astrophys., 18, 126.
Hollweg, J.V., (1984), Astrophys. J., 277, 392.
Ibragimov, I.A., Kocharov, G.E. and Kocharov, L.G., (1978), Joffe Phys. Techn. Inst., No. 588.
Kennel, C.F. and Petschek, H.E., (1966), J. Geophys. Res., 71, 1.
Klecker, B. et al., (1984), Astrophys. J., 281, 458.
Kocharov, L.G. and Kocharov, G.E., (1984), Space Science Rev., 35, 89.
Kulsrud, R.M. and Ferrara, A., (1971), Astrophys. Space Sci., 12, 302.
Ma Sung, L.S. et al., (1981), Astrophys. J. Lett. , 245, L45.
Pérez-Enríquez, R., (1985), (accepted for publication in Solar Phys.).
Ramaty, R. et al., (1980), in P.A. Sturrock (ed.), Solar Flares, Boulder, Co., Assoc. Univ. Press, p.117.
Schaeffer, O.A. and Zahringer, J., (1962), Phys. Rev. Letters, 8, 389.
Svestka, Z. and Schadee, A., (1983), Solar Phys., 86, 267.
Yoshimori, M. et al., (1983), Solar Phys., 86, 375.

N85-34797

SH 2.2-2

NUCLEOSYNTHESIS IN THE TERRESTRIAL AND SOLAR ATMOSPHERES

Chuanzan Yu Renming Zhou Shijie Zhan
Department of Physics, Yunnan University, Kunming
P.R.C.

ABSTRACT

Variations of δD, $\delta^{13}C$, $\Delta^{14}C$ and $\delta^{18}O$ with time have been measured by a lot of experiments. Many abnormalities of isotope abundances in cosmic rays have been found by balloons and satellites. We hold that these abnormalities are related to nucleosynthesis in the terrestrial and solar atmospheres and are closely related to solar activities.

1. Introduction. In recent years, radiative $\Delta^{14}C$ in annual rings of trees with different ages at different places[1], the contents of $\delta^{18}O$ in different ice-layers[2], the contents of $\delta^{13}C$ in organic layers at the bottom of the sea[3]. The ratios of (D/H) and the contents of ^{3}H at different altitudes of the terrestrial atmosphere[4] and the ratios of (D/H) in rain[5], snow[6] and tree[7] have been determined. Variations of the Earth's enviroment (Temperatures, the contents of CO_2 and the heights of the sea level) for several hundred thousand years can be inferred from there data. This kind of research has provided very important informations for meteorology, archaeology and enviromental science.

Recently high altitude balloon experiments have observed that the relative abundances of isotope D and ^{3}H[8], ^{15}N, ^{22}Ne and ^{26}Mg[9] increase greatly, each nucleus has energy of several hundred Mev and most of them come from the outside of the terrestrial atmosphere. At the same time, satellites have observed that the contents of ^{3}He, when solar flares burst, increase by $\sim 10^{4}$ times or even exceeds the contents of ^{4}He[10].

We hold that variations of isotopic contents mentioned above are related to nucleosynthesis in the terrestrial and solar atmospheres.

2. Nucleosynthesis in the Terrestrial Atmosphere. The main reactions are:

(1). The bombardment of cosmic rays with the terrestrial atmosphere and its secondary particles can cause many nuclear reactions and the intensity of cosmic rays is modulated by solar activities.

(2). High energy particles produced by solar flares can cause various nuclear reactions in the terrestrial atmosphere.

(3). Protons, in the inner radiative zone of the Earth, can be accelerated to 1--100Mev. They can interact with nuclei in the terrestrial atmosphere to bring about nucleosynthesis.

(4). All three processes mentioned above can produce secondary neutrons and will make neutrons to have a certain intensity, which will change with the

ORIGINAL PAGE IS
OF POOR QUALITY

period of solar activities and the terrestrial magnetic latitudes.

Radiative ^{14}C and ^{3}H are obviously the direct evidence of nucleosynthesis in the terrestrial atmosphere. They can be produced by following reactions:

$^{14}N(n,p)^{14}C$, (Q_m=0.6259Mev, σ_{therm}=1.81+0.05 b) (1)

$^{14}N(n,{}^{12}C)^{3}H$, (Q_m=-4.0151Mev), ~5% neutrons with E>4Mev (2)

The reaction rate in the terrestrial atmosphere is

$$r = N_N \ast \sigma \ast N_n \tag{3}$$

where N_N is the density of nitrogen-cylinder in the terrestrial atmosphere and N_n neutron flux. Near the equator, $N_n^{min}(1)$ = 0.110/$cm^2 \ast sec$ for the minimum solar activity years and $N_n^{max}(1)$=0.105/$cm^2 \ast sec$ for the maximum solar activity years. At regions with high latitude, $N_n^{min}(2)$=1.367/$cm^2 \ast sec$ for the minimum solar activity years and $N_n^{max}(2)$=0.709/$cm^2 \ast sec$ for the maximum solar activity years.

The amount of ^{14}C produced at high latitude region is usually 2--5 times as high as that at middle and low latitude regions. Therefore, the results of [1] can be reasonably explained.

By (1), (2) and (3) the average reaction rate forming ^{14}C in the terrestrial atmosphere at the sea level can be calculated to be ~6/$cm^2 \ast sec$ and the reaction rate for ^{3}H at stratosphere ~0.3/$cm^2 \ast sec$ (spallation products included).

The main composition of the terrestrial atmosphere are N and O. Their cross sections poroducing D, bombarded by incident protons with energy 40Mev, are measured to be 25mb and 30mb, respectively. The cross section producing ^{3}H is about 5 times smaller. The cross sections producing D and ^{3}H increase with energy of the incident protons.

^{13}C accounts for 1.1% of element C and ^{18}O 0.2% of element O. In the terrestrial atmosphere, reactions producing ^{13}C and ^{18}O are as follows:

$^{12}C(p,\gamma)^{13}N(\beta^{+},\nu)^{13}C$, ($s_o$=1.2Kev*b)

$^{12}C(n,\gamma)^{13}C$, (σ=3.4+0.3mb, Q_m=4.9464Mev) (4)

$^{14}N(n,d)^{13}C$, (Q_m=-5.3260Mev)

$^{16}O(n,\alpha)^{13}C$, (Q_m=-2.2156Mev)

$^{14}N(\alpha,\gamma)$ or $^{16}O(d,\gamma)$ $^{18}F(\beta^{+},\nu)^{18}O$, $^{17}O(n,\gamma)^{18}O$, (Q_m=8.0446Mev)

$^{15}N(\alpha,p)^{18}O$, (Q_m=-3.9796Mev)

$^{16}O(t,p)^{18}O$,(Q_m=3.7069Mev)

Only several Mev kinetic energy is needed for newly produced D and ^{3}H to penetrate the Coulomb barrier and to make nuclear reactions possible. The half-time of ^{3}H is $\tau_{\frac{1}{2}}$=12.25y and reaction $^{3}H(p,\gamma)^{4}He$ is easy to take place. Thus for different times there are different $\delta^{3}H$. It is easy for D in water vapour and newly produced D to react with protons, $D(p,\gamma)^{3}He$. Thus, D will decrease

ORIGINAL PAGE IS
OF POOR QUALITY

greatly and there are different D for different times and at different atmosphere heights. Combined with ions OH , D and ^3H fall on to the ground as rain and snow, and can be investigated as an index of precipitation and meteorology.

By same reason, the contents of ^{13}C, ^{14}C and ^{18}O in the terrestrial atmosphere, after nuclear interaction, will change. The main reactions are as follows;

$^{13}C(p,\gamma)^{14}N$, $(s_0=6.0+0.8Kev*b,\ Q_m=7.5506Mev)$

$^{13}C(n,\gamma)^{14}C$, $(\sigma=0.9+0.2mb, Q_m=8.1765Mev)$	$^{14}C(p,n)^{14}N$, $(Q_m=-0.6259Mev)$
$^{13}C(d,n)^{14}N$, $(Q_m= 5.3260Mev)$	$^{14}C(d,t)^{13}C$, $(Q_m=-1.3109Mev)$
$^{18}O(p,\alpha)^{15}N$, $(Q_m=3.9796Mev)$	$^{14}C(p,\gamma)^{15}N$, $(Q_m=10.2075Mev)$
$^{18}O(\alpha,\gamma)^{22}Ne$, $(Q_m=9.6675Mev)$	$^{14}C(p,d)^{13}C$, $(Q_m=-5.9519Mev)$
$^{18}O(p,t)^{16}O$, $(Q_m=-3.7069Mev)$	$^{14}C(\alpha,\gamma)^{18}O$, $(Q_m=6.2279Mev)$

Owing to different times of their production and destruction and different diffusion taking place in the atmospheric circulation, there are different δD, $\delta^{13}C$, $\Delta^{14}C$ and $\delta^{18}O$. By determining them, variations of solar activities and the Earth's enviroments for hundred thousand years can be inferred.

3.Nucleosynthesis in the Solar Atmosphere. Thermonuclear reactions in the interior of the Sun carry on in the "reactor" with $T=15*10^6 K$. The photospheric surfaces with $T<10^6$--6000 K are intense convective layers (photosphere), within which there are many kinds of processes of nucleosynthesis. The main processes are;

(1).n, D and ^3H leaked out from the "reactor" into the convective layers are no longer nuclear fuels. Passing through the chromosphere and corona, D and ^3H are accelerated by magnetic field to enter the terrestrial atmosphere. Passing through convective layers and chromosphere, reactions of n, D nd ^3H will take place, such as $p(n,\gamma)D$, $D(n,\gamma)^3H$, $D(D,p)^3H$, $D(p,\gamma)^3He$, $^3H(p,\gamma)^4He$, $^{14}N(n,\gamma)^{15}N$, $^{14}N(D,p)^{15}N$, $^{14}N(p,\gamma)^{15}O(\beta^+,\nu)^{15}N$, $^{20}Ne(D,\gamma)^{22}Na(\beta^+,\nu)^{22}Ne$, $^{20}Ne(^3H,p)^{22}Ne$. That is the reason why remarkable increases in D and ^3H have been observed[8] It has also been observed that the abundances of ^{15}N exceeds that of ^{14}N and the relative abundances of ^{22}Ne increase by 2.75 times[9]

(2).There is a good number of high energy particles jetted out at the bottom of the photosphere during solar flares. Thus they can cause many kinds of nucleosynthesis. IMP-8 recorded on May 7th-12th, 1974 that ^3He increases by 10^4 times and exceeds ^4He, Ne, Mg and Si increase by 10 times[10] They are caused by reactions $D(D,p)^3He$, $D(p,\gamma)^3He$, $^3H(p,n)^3He$ and $^{16}O(\alpha,\gamma)^{20}Ne$, $^{14}N(\alpha,\gamma)^{18}O(\alpha,\gamma)^{22}Ne$, $^{20}Ne(\alpha,\gamma)^{24}Mg$, $^{24}Mg(\alpha,\gamma)^{28}Si$, i.e. α-processes caused by temperature- rising at some solar flares. Owing to the fact that ^4He have been consumed greatly and ^3He have reached the low temperature regions, the abundances of ^3He exceeds that of ^4He and Ne, Mg and Si increase.

(3).There is so called "granulation" with diameter of 1500Km. Its magnetic field is about dozens of Gausses, by which protons in convection can be accelerated to knock out neutrons from CNO nucleus. Thus neutron rich isotopes increase to some extent.

4.Discussions.

(1).The counting rate recorded at the middle latitude sea level is 20% slower in the maxmum solar activity years than the minimum solar activity years. M.Stuiver and P.D.Quay[11], by determining ^{14}C, have found Maunder, spörer and Wolf minimums of solar activities. We hold that the rule of older solar activities might be found by comprehensive studies on δD, $\delta^{13}C$, $\Delta^{14}C$ and $\delta^{18}O$.

(2).Variations of δD, $\delta^{13}C$, $\Delta^{14}C$ and $\delta^{18}O$ are related to nucleosynthesis in the terrestrial atmosphere. In most cases, the experimental data give "-" values, i.e. the amounts of destruction are more than that of production. In order to find out their relations, experiments on the change of $\delta^{15}N$ and $\delta^{17}O$ contents should be carried on.

(3).^{22}Ne super-abundance experiments also observed large increasion in abundances of neutron rich isotopes, such as ^{15}N, ^{17}O, ^{18}O, ^{21}Ne, ^{25}Mg, ^{26}Mg, ^{29}Si, and ^{30}Si. They should be regarded as a whole and have same origin of non-thermal nucleosynthesis in the solar atmosphere.

(4).The abundance of ^{3}He increased by 10^{4} times is not a result of selective acceleration[10], but a result of large amounts of consumption of ^{4}He and ^{3}He jetted out to low temperature regions. Thus ^{3}He exceeds ^{4}He. Increasions in ^{3}H and D observed by balloons are results of nucleosynthesis in the solar atmosphere at different conditions.

5.Conclusions.

Following conclusions can be drawn from this paper:

(1).There are many kinds of nucleosynthetic processes in the terrestrial and solar atmospheres. They are different to each other.

(2).Variations of δD, $\delta^{13}C$, $\Delta^{14}C$ and $\delta^{18}O$ are related to solar activities.

(3).The super-abundance of ^{22}Ne has the solar origin.

(4).Abnormalities of abundances in cosmic rays observed in recent years are caused by nucleosynthesis of non-thermal nuclear reactions.

6.References.

[1].C.Y.Fan,et al.,18th ICRC, V3(1983)82-85
[2].P.I.Abell, Nature, 297(1982)321
[3].N.J.Shackleton,et al., Nature, 306(1983)319-322
[4].W.Pollock, et al., J.Geophys.Rev., V85,C10(1980)5555
[5].J.R.Lawrence, et al., Nature, 296(1982)638-640
[6].I.Friedman & G.I.Smith, Science, 176(1972)790
[7].J.R.Lawrence & J.W.C.White, Nature, 311(1984)558
[8].W.R.Webber & S.M.Yushak, Ap.J., 275(1983)391-404
[9].W.R.Webber, 17th ICRC, V2(1981)261-264
[10].E.Mobius & D.Hovestadt, IAU Symp. No.94,<<Origin of Cosmic Rays>>(1980)395
[11].M.Stuiver & P.D.Quay, Science, 207(1980)11

TYPE III SOLAR RADIO BURSTS AND ^{3}HE-RICH EVENTS

N85-34798

D. V. Reames and R. G. Stone
NASA/Goddard Space Flight Center,
Greenbelt, MD 20771 USA

ABSTRACT

We investigate the kilometric radio data for ^{3}He-rich events during the 1979-82 time period. Type III bursts are present for each event as expected from the previous electron/^{3}He-event association. A list of identified solar events is presented.

1. Introduction The association of solar ^{3}He-rich events and non-relativistic electron events by Reames, von Rosenvinge and Lin (RvL, 1985) allowed the precise timing and velocity dispersion of the electron data to be used to identify the solar events responsible for the acceleration of particles with such anomalous isotopic abundances. However, these non-relativistic electron data are only available for the first 15 months of the ISEE-3 mission while many of the larger and more interesting ^{3}He events occurred during the next several years of the mission. Fortunately, these same electrons are responsible for the rapidly drifting radio features called Type III bursts as they propagate at high velocity through the decreasing density of the interplanetary medium.

In this paper we show the relationship between the Type-III radio observations and the particle data in ^{3}He-rich events and then use this association to identify the source region for many of the events.

2. Observations and Analysis The helium observations described in this paper were obtained with the very-low-energy telescope (VLET) in the GSFC cosmic-ray experiment on ISEE-3. In a few events it was possible to observe energetic (0.25 to 2 MeV) electron increases in the high-energy telescope of the same experiment.

The kilometric radio data used to study the interplanetary portion of the Type III radio emissions were obtained from the Radio Astronomy Experiment aboard ISEE-3. These radio observations provide not only timing of the electron release at the sun but also directional information that can track the electron population in interplanetary space and locate the solar longitude of the source within 10 to 20 degrees.

A list of ^{3}He-rich time periods (Kahler et al., 1985) was re-examined for well-defined particle increases during the Dec. 1979 to Aug. 1982 study period. Dynamic radio spectra and single-frequency time histories were then examined during each of these events for the related Type III emission and the onset times and spectral characteristics of the events were determined.

In Figure 1 we show the particle and radio data for two ^{3}He time periods in 1982. Two events are seen in Fig. 1a, the Type III emission for the first event begins at 0533-0536 UT on June 25. There is no obvious increase in the energetic electrons from this event but the 2.2 - 3.4 MeV/AMU He nuclei begin to increase at 0745 and the 1.3 - 1.6 MeV/AMU nuclei arrive at 0830. The second event in Fig 1a begins in the radio data at 1945 and is seen minutes later (particle data are averaged in 15-min intervals) in the energetic electron data but He-nuclei from the event are not seen until after the data gap at about 2330.

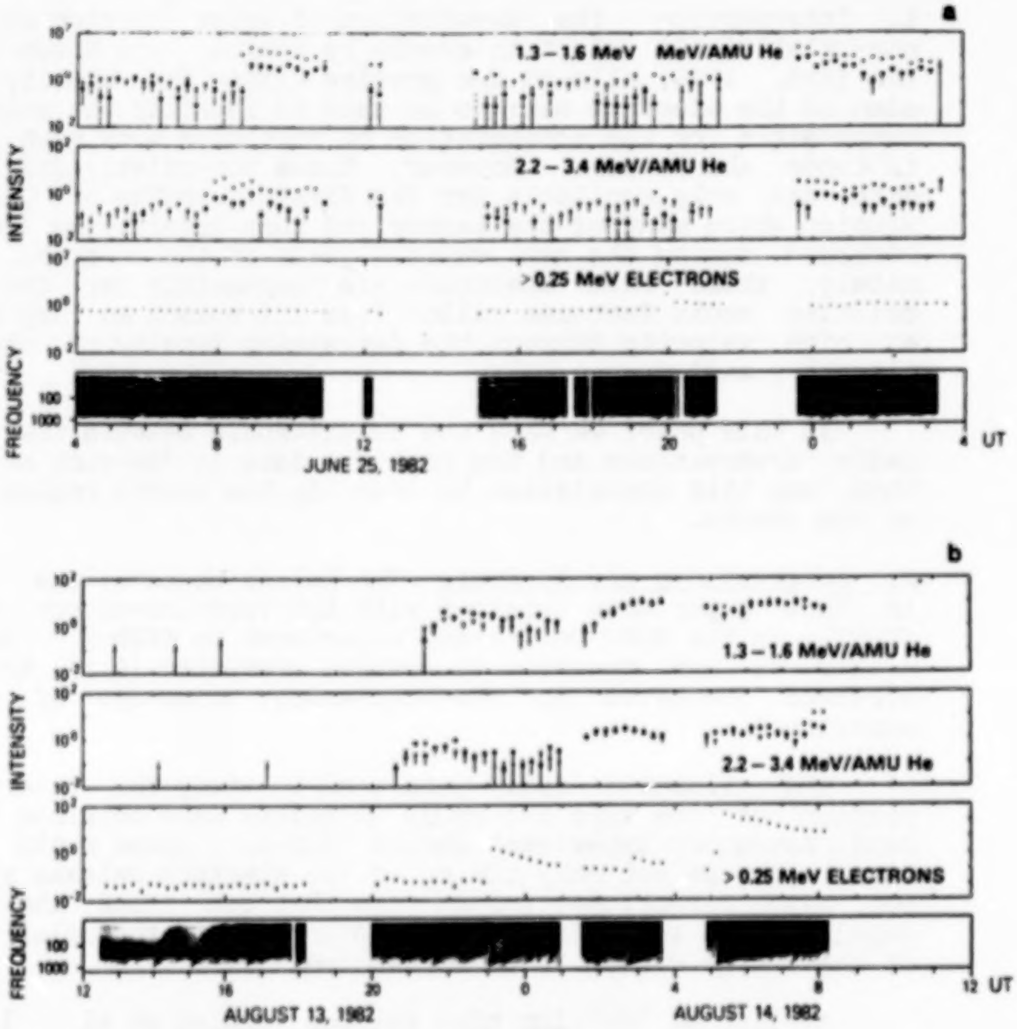

Fig. 1 Dynamic radio spectra and electron and He time histories for (a) Jun 25-26, 1982 and (b) Aug 13-14, 1982.

In Fig. 1b we show the striking series of ^{3}He-rich events on Aug 13 - 14, 1982 that include the gamma-ray event (also ^{3}He rich) at 0506 on Aug 14. The first Type-III event, is masked by the ubiquitous data gap at 1800-2000. Helium in the two energy intervals arrive at 2030 and 2115. The next three events beginning in the radio data at 2302, 0241 and 0509 each inject energetic electrons that are seen at 1 AU, and each inject fresh He nuclei that are observed after they propagate to 1 AU 2-3 hrs later as described by RvL (1985). Only the higher-energy He nuclei are seen from the large gamma-ray event before the data gap; all energies are seen again at 1200, just off the plot.

Note the difference in size and character of the Type III dynamic spectra in Fig. 1b for those events that contribute electrons and He at 1 AU and for those that do not. The other, weaker events in the same time period drift slowly to low frequencies because they lack sufficient intensities of faster, more-energetic electrons that would propagate outward more rapidly. Lacking energetic electrons, these events also lack measurable intensities of ^{3}He (see also Reames and Lin, 1985).

Note also the quiet conditions in the particle observations prior to the first Aug 13 event. During the first 6 hrs in Fig 1b (excluding data gaps seen as white areas in the radio data) only 5 ^{4}He particles enter the telescope in both energy bands. In fact, no ^{3}He particles enter the telescope in the 24-hr period prior to the first event.

The major ^{3}He-rich events in the Dec 1979 to Aug 1982 for which we can identify the likely radio onset time are shown in Table 1. Also shown are the metric-radio and H-alpha flare data for most of the events. Many of the events occur in groups from the same active region, a fact that greatly simplifies their identification. In a few cases, where other candidate events do exist, they are always smaller events from the same active region.

3. Conclusion In conclusion we have shown that the solar electron-^{3}He event association can be extended considerably by use of the kilometric radio data. Each ^{3}He-rich event we examined was found to have a candidate Type III event and in most cases an unambiguous identification could be made. Of course these data do not provide the continuous and direct extrapolation of the velocity dispersion provided by the direct observation of non- relativistic electrons. On the other hand, the directional capability of the radio experiment provides the added spatial information that was only partially exploited in this work.

The prevalence of multiple events, usually with different isotope ratios, from the same solar active region is, once again, a striking result of this study. Each event is itself composed of groups at much higher time resolution in the radio data.

Table 1. Type III and Flare Associations of ^{3}He-Rich Events

Date	1.3	He	2MHz	Metric		Flare		
	Onset	3/4	Time	Time		Time	Site	Imp.
1979 Dec 14	2000	1.5	1552 -1605	1550 -1559	2GG	1553 -1643	N10W51	1B
1980 Nov 9	1930	0.9	1621	1620 -1623	3G	1621 -1633	S14W44	-N
Nov 10	0000	1.4	2035	2033 -2035	2GV	2028 -2054	S12W48	-N
Nov 10	0830	1.8	0448	0448 -0449	2GV	0446 -0508	S09W51	-N
Dec 16	1830	0.5	1455					
1981 Sep 15	2315	1.2	1935	1933 -1937	3GGV			
Nov 20	1330	0.2	1045	1041 -1043	2GG	several		
1982 Mar 10	1615	>1.4	gap	1220 -1255	3GG	1213 -1308	S06W32	1B
Mar 10	2300	0.7	1845	1844 -1850	3GGV	1845 -1908	S06W34	2B
Jun 25	0830	0.3	0533 -0536	0530 -0535	3SIS	0528 -0615	N13W50	1B
Jun 25	2330	0.4	1945	1944 -1945	3GGV	1941 -2010	N17W56	2B
Jun 30	1315	>1.0	0915					
Aug 13	2130	2.0	gap	1813 -1820	2GG			
Aug 14	0200	0.8	2302	2259 -2303	3GV	2301 -2334	N13W59	-N
Aug 14	0600	1.2	0241 -0245	0238 -0244	2GV	0237 -0315	N11W60	1B
Aug 14	0800	0.2	0509	0506 -0515	3GV II	0507 -0525	N11W62 gamma-ray	1B

The event identifications begin to show a link between the impulsive electron-rich ^{3}He events and the impulsive electron-rich solar gamma-ray events with the Aug 14 event. ^{3}He has been observed in two other gamma-ray events by Van Hollebeke et al. (1985). The distinction between particle events with impulsive and long-duration X-ray events has been clearly demonstrated by Cane et al. (1985).

References

Cane, H. V., R. E. McGuire and T. T. von Rosenvinge, 1985, XIX ICRC paper SH 1.2-12 and Astrophys. J. (to be published).

Kahler, S. et al., 1985, Astrophys. J 290, 742.

Reames, D. V., and R. P. Lin, 1985, XIX ICRC paper SH 2.2-5.

Reames, D. V., T. T. von Rosenvinge and R. P. Lin, 1985, Astrophys. J. 292, 716.

Van Hollebeke, M. A. I., F. B. Mc Donald and J. H. Trainor, 1985, XIX ICRC paper 2.2-3.

SH 2.2-4

N85-34799

SOLAR SOURCE REGIONS OF ^{3}HE-RICH PARTICLE EVENTS

S.W. Kahler
Emmanuel College, Boston, Massachusetts 02115 USA

R.P. Lin
Space Sciences Laboratory, University of California
Berkeley, California 94720 USA

D.V. Reames
Laboratory for High Energy Astrophysics, Goddard Space Flight Center
Greenbelt, Maryland 20771 USA

R.G. Stone
Laboratory for Extraterrestrial Physics, Goddard Space Flight Center
Greenbelt, Maryland 20771 USA

M. Liggett
Big Bear Solar Observatory, California Institute of Technology
Pasadena, California 91125 USA

ABSTRACT

We use Hα, X-ray, and metric and kilometric radio data to examine the solar sources of energetic (~ 1 MeV/nucleon) ^{3}He-rich particle events observed near earth in association with impulsive 2 to 100 keV electron events. Each ^{3}He/electron event is associated with a kilometric type III burst belonging to a family of such bursts characterized by similar interplanetary propagation paths from the same solar active region. The ^{3}He/electron events correlate very well with the interplanetary low frequency (~ 188 kHz) radio brightnesses of these events, but progressively worse with signatures from regions closer to the Sun. When Hα brightenings can be associated with ^{3}He/electron events, they have onsets coinciding to within 1 min of that of the associated metric type III burst but are often too small to be reported. The data are consistent with the earlier idea that many type III bursts, and now, by implication, the ^{3}He/electron events, are due to particle acceleration in the corona, well above the associated Hα and X-ray flares.

1. Introduction. It is now clear that ^{3}He-rich energetic particle events are distinguished from the solar energetic particle (SEP) events of greater fluxes and energies not only by their anomalous He composition, but also by their lack of association with metric type II bursts and coronal mass ejections (Kahler et al. 1985). A comparison of 12 ^{3}He-rich events with impulsive 2 to 100 keV electron events suggests that ^{3}He ions are impulsively accelerated and injected into interplanetary space along with the electrons (Reames et al. 1985). The low fluxes and slow speeds of the E ~ 1 MeV/nucleon ^{3}He ions make injection times uncertain, but the close association of the particle events with fast-drift type III radio bursts provides the precision of timing needed to make the association of the particle events with solar phenomena.

To learn more about the sources of these events we examine the characteristics of the Hα flares and type III bursts associated with the 12 ^{3}He-rich events studied by Reames et al. (1985)

2. Observations and Analysis. The times of the 12 events are given in Table 1. Several of these events occurred on the same day and in these cases are associated with Hα flares in the same active region. In each case we give the time of the onset and the maximum reported burst size of the associated metric type III radio burst. The approximate flare sites and McMath region numbers, based on both reported Hα flares and inspection of Hα patrol films, are also listed. In three cases we give alternative suspected McMath regions in parentheses. All Hα events were subflares except for the November 8 1B flare.

Each ^{3}He/electron event was associated with a prominent kilometric type III burst observed with the Meudon/GSFC solar radio experiment on ISEE-3. An examination of the kilometric data during the few hours before and after the type III burst reveals that that burst is one of a family of such bursts, all of which show nearly identical solar elongation angles as a function of radio frequency. This suggests that the energetic electrons producing the bursts traverse similar paths from a single solar region through the interplanetary medium. Figure 1 shows an example of such bursts during a 6 hr interval on 1979 August 14. We have listed in Table 1 the number of prominent kilometric type III bursts in each such family during an 18 hr period around the time of the ^{3}He/electron burst. The last column gives the number of bursts possibly associated on the basis of the timings with listed Hα flares in the active region presumed to be the source of the ^{3}He/electron event. Numbers in parentheses are the numbers of bursts possibly associated with listed Hα flares in the alternative active regions for the three dates for which the active region is in some doubt.

TABLE 1

Date	Type III Start UT	Class[e]	Approx. Location	Hα Onset UT	McMath Region	Total km type III	Total with Hα flares
1978							
Nov 8	1751	3GG	N18 E12	1751	643	2	2
Nov 27	2056	3GG	N26 W47[a]	2055	672 (673)	6	0 (4)
Dec 26	1319[b]	-	S21 W41[a,d]	--	721	4	0
Dec 26	2122	WNG[c]	S21 W45[a]	2104	721		
1979							
Feb 10	1818	3GG	N13 W23[a]	< 1800	807 (808)	6	2 (1)
May 17	0558	2G	S35 W78[a]	0551	996 (010)	13	3 (0)
Aug 14	1728	3GG	S18 W45	1728	205	4	2
Aug 14	2048	3GG	S17 W48	2048	205		
Sept 6	0906	2GG	N20 W62	0906	252	10	5
Sept 6	1148	3GG	N18 W67	1148	252		
Sept 6	1332	3GG	N16 W63	1332	252		
Sept 6	1851	2GG	N16 W65[a]	1850	252		

[a] flare not listed in SGD, but found in visual inspection of Hα films.

[b] start time of 1980 kHz burst.

[c] weak intermittent group.

[d] no confirmation with optical data.

[e] GG: > 10 type III bursts; G: < 10 type III bursts.

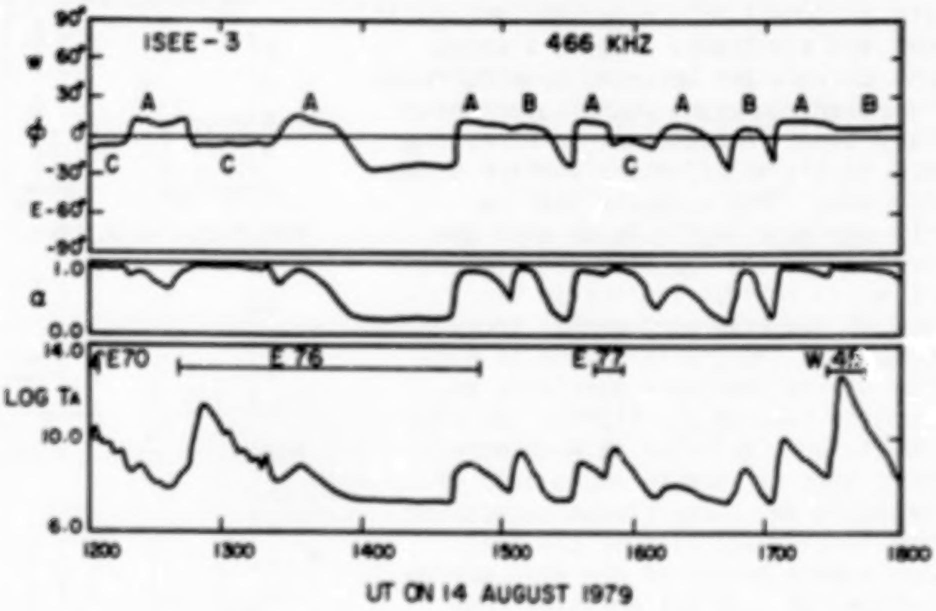

Figure 1. 466 kHz data from 1979 August 14. Three families of bursts labeled A,B, and C were present during the 6-hr interval. B events were associated with McMath 205. ϕ is the solar elongation angle; α a measure of the source size, with 1 being a point source; and T_A the antenna temperature. Associated Hα flare reports are also shown.

In two of the three events with questionable active region associations we see that the Hα flare associations of the alternative regions are worse than for the preferred active regions, although the statistics are limited. Using only these data, we could have selected the preferred region for all the ^{3}He/electron events except for the November 27 event and the two on December 26. In the latter case no choice could be made. On the other hand, by simply looking for listed Hα flares at well connected longitudes, we would have misidentified the source regions in two or three cases.

To get a better idea of the signatures of the ^{3}He/electron events, we have compared reported Hα flares, metric type III bursts, and antenna temperatures of the 1980 and 188 kHz bursts for the kilometric bursts with and without ^{3}He/electron events. We omit the large sample of events on May 17, few of which are associated with Hα flares or metric type III bursts. The results are shown in Figure 2. The contrast between the two groups increases as we consider first the Hα flares and then the progressively lower frequencies of the type III bursts. At 188 kHz the logs of T_A of all but one of the 12 ^{3}He/electron events exceeded 10.5. On the other hand, this value was exceeded by only 3 of the 21 kilometric type III burst group.

3. Discussion. Each kilometric burst family is characterized by the degree of its association with reported metric type III bursts and Hα flares as shown in Table 1. The families of November 8, August 14, and September 6 are well associated, while the others are not. This lack of observed associated Hα activity with several ^{3}He/electron events

suggests a coronal origin for the energetic ^{3}He ions and electrons. Figure 1 shows that the correlation between the occurrence of a ^{3}He/electron event and a solar/interplanetary event increases with increasing distance of the solar/interplanetary event from the sun. This suggests that Hα activity may have little to do with the acceleration of the ^{3}He ions and electrons other than to reflect indirectly the presence of the overlying event, presumably as a result of the precipitation of some fraction of the energized particles as suggested by Kane et al. (1974). We also found a close coincidence between onsets of metric type III bursts and onsets of associated Hα and X-ray flares suggesting that the initial activity of the ^{3}He/electron events begins in the high corona. Observations of type III emission from interplanetary electron beams are complicated by factors involving generation (Lin et al. 1981) and propagation of the bursts, so the situation may prove to be more complex.

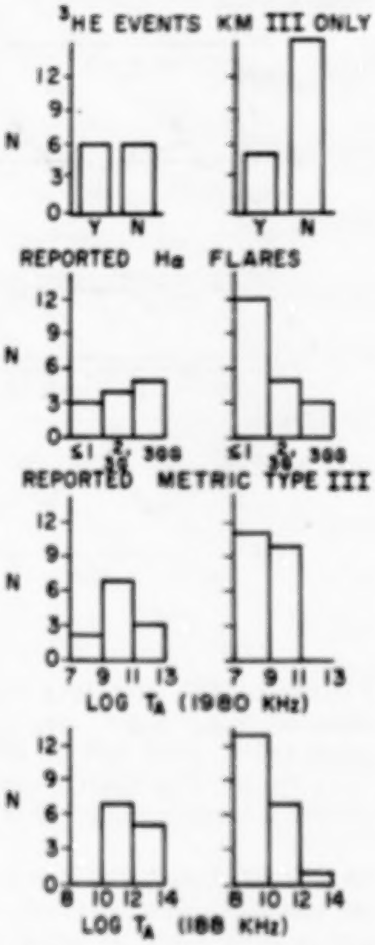

Figure 2. Histograms of Hα flares, metric type III bursts and log T_A for kilometric type III bursts with and without ^{3}He/electron events.

4. Conclusions. Each ^{3}He/electron event is associated with a kilometric type III burst which appears as a member of a family of bursts sharing similar interplanetary propagation paths. The members of each family differ from each other in their associated antenna temperatures at different frequencies and in their metric type III and Hα flare associations. In our study the best empirical indication of the occurrence of a ^{3}He/electron event proved to be a high antenna temperature at 188 kHz. Reported Hα flare observations are a poor guide to the occurrence or origin of these events and in some cases are misleading, perhaps because of inaccurate reporting. The poor association of the ^{3}He/electron events with Hα flares suggests a high coronal origin for at least some of the events.

Acknowledgements. This work was supported at Emmanuel College by AFGL Contract AF 19628-82 0039, at GSFC/University of Maryland by NASA grant NGR 21-002316, and at the University of California, Berkeley in part by NASA grant NAG 5-376.

REFERENCES

Kahler, S. et al. 1985, Ap. J., 290, 742.
Kane, S.R., et al. 1974, Solar Phys., 38, 483.
Lin, R.P., et al. 1981, Ap. J., 251, 364.
Reames, D.V., et al. 1985, Ap. J., in press.

^{3}HE IN SOLAR NON-RELATIVISTIC ELECTRON EVENTS

D. V. Reames
NASA/ Goddard Space Flight Center, Code 661,
Greenbelt, MD 20771 USA

and

R. P. Lin
Space Sciences Laboratory, University of California,
Berkeley, CA 94720 USA

ABSTRACT

We report on a systematic study of the presence of ^{3}He in 187 solar electron events observed on the ISEE-3 spacecraft during a 9-month period beginning in Aug 1978. ^{3}He is present in over half of the events and in 2/3 of events with 19 keV electrons, suggesting that ^{3}He would be found in all electron events given somewhat greater collection efficiency.

1. Introduction In a recent paper Reames, von Rosenvinge and Lin (RvL, 1985) suggested a common origin for solar ^{3}He-rich events and non-relativistic electron events. This association was based upon the close temporal relationship between the two species which share nearly scatter-free propagation from the sun and upon the observation of electrons in all of the ^{3}He-rich event periods.

In this paper we examine the inverse relationship by asking the extent to which all solar electron events are accompanied by ^{3}He. To this end, we have begun with a list of solar electron events observed by the Univ. of California experiment on the ISEE-3 spacecraft and, for each event, we have examined data from the very-low-energy telescope of the GSFC experiment on the same spacecraft for the presence of ^{3}He.

2. Observations and Results The solar electron event list used in this study gives the onset time of each event and the intensity of electrons at 2 and 19 keV. Of the 187 events during the study period, 103 (55%) had measurable fluxes of 19 keV electrons, the remainder being observed only at lower energies. Where possible, the source of the event has been identified by the metric Type III radio emission and/or the H-alpha flare characteristics using Solar-Geophysical Data.

The measurements in RvL (1985) showed the 1.34-1.63 MeV ^{3}He onset to occur 2-4 hrs after the electron onset and the ^{3}He maximum to occur 1-2 hrs later. We therefore scanned the hourly-averaged ^{3}He data during the 8-hr interval from 2 to 10 hrs after the electron onset and recorded the ^{3}He intensity. This technique allowed us to press for the maximum sensitivity to ^{3}He without introducing an unacceptable number of spurious events from ^{3}He background or from recounting multiple events. The ^{3}He background estimated at about one particle every 3-4 days would be expected to contribute 2 to 3 spurious events out of the 85 observed.

In 34 (18%) of the 187 events it was not possible either to observe or to set meaningful limits on the ^{3}He, usually because of a large particle event in progress but also occasionally because of data gaps. Of the subset of 103 events with 19-keV electrons, 17 were similarly excluded. The remaining events, 153 total and 86 with 19-keV electrons, are categorized by their ^{3}He content in Table 1. In Table 1 we see that over half (56%) of the electron events have ^{3}He and that fraction jumps to 2/3 (66%) for events with 19-keV electrons.

Table 1 ^{3}He in Electron Events

	^{3}He	no ^{3}He	total
All electron events	85(56%)	68(44%)	153
19-keV elect events	57(66%)	29(34%)	86

We explore the ^{3}He association as a function of electron intensity and spectral index in Tables 2 and 3. Here the highest electron intensities and flattest spectra show a high probability of ^{3}He association. Otherwise, the correlation with intensity is weak, especially for 2-keV electrons. For those events with ^{3}He, the ^{3}He intensity is plotted versus the electron intensities in Figure 1. There appears to be no correlation with 2-keV electrons in Fig. 1a , however, a broad correlation seems to exist with the 19-keV electrons in Fig. 1b but the limited dynamic range of the instruments makes its observation difficult.

Table 2 ^{3}He Observation vs. Electron Intensity

(a) 2-keV Electrons

Intensity (x1000)	^{3}He	no ^{3}He
>100	7(78%)	1
10-100	28(55%)	23
1-10	36(54%)	31
<1	14(52%)	13
Total	85(56%)	68

(b) 19-keV Electrons

Intensity	^{3}He	no ^{3}He
>10	9(78%)	1
1-10	26(65%)	14
0.1-1	22(61%)	14
Total	57(66%)	29
None(<0.3)	28(42%)	39

Table 3 ^{3}He Observation vs. Electron Spectral Index

Index	^{3}He	no ^{3}He
<2.0	1	0
2.0-2.9	9(69%)	4
3.0-3.9	22(59%)	15
4.0-4.9	15(68%)	7
>5.0	2(50%)	2

ORIGINAL PAGE IS
OF POOR QUALITY

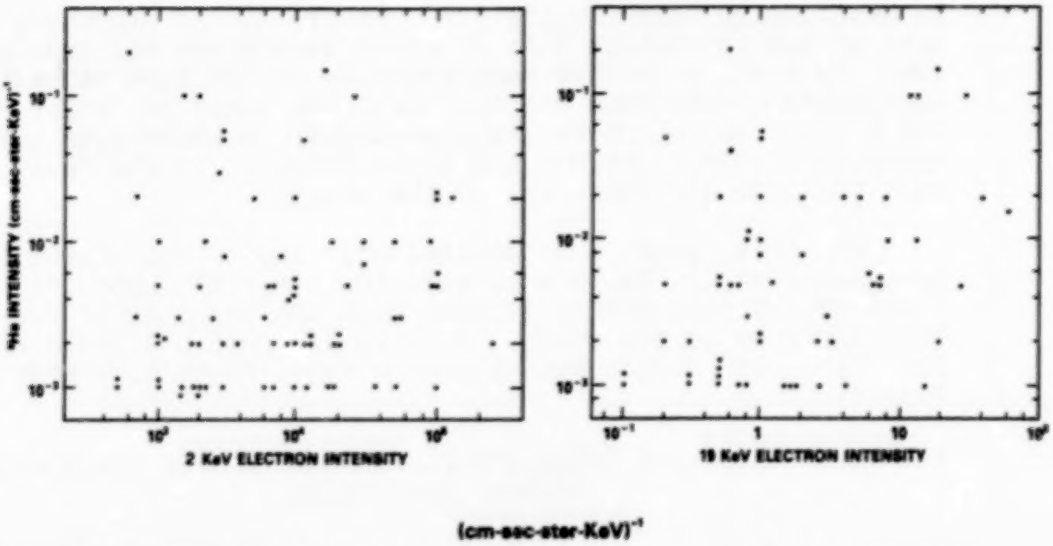

Fig. 1 ^{3}He vs. electron intensities for two electron energies.

With Figure 2 we address the question of the relative importance of electron intensity versus spectral index in determining the ^{3}He intensity. Symbols on the plot denote the most intense 13 ^{3}He events, other ^{3}He events, and events with no ^{3}He. The tendency of the more ^{3}He-rich events to lie toward the top of the plot (greater 19-keV intensity) is stronger than their tendency toward flatter spectra. Of the 23 events with 19-keV electron intensity above 3 (cm^2-ster-sec-MeV/AMU)$^{-1}$ (30% of plotted data), 19 (83%) exhibit ^{3}He and 8 (62%) of the 13 largest ^{3}He events are found in this region.

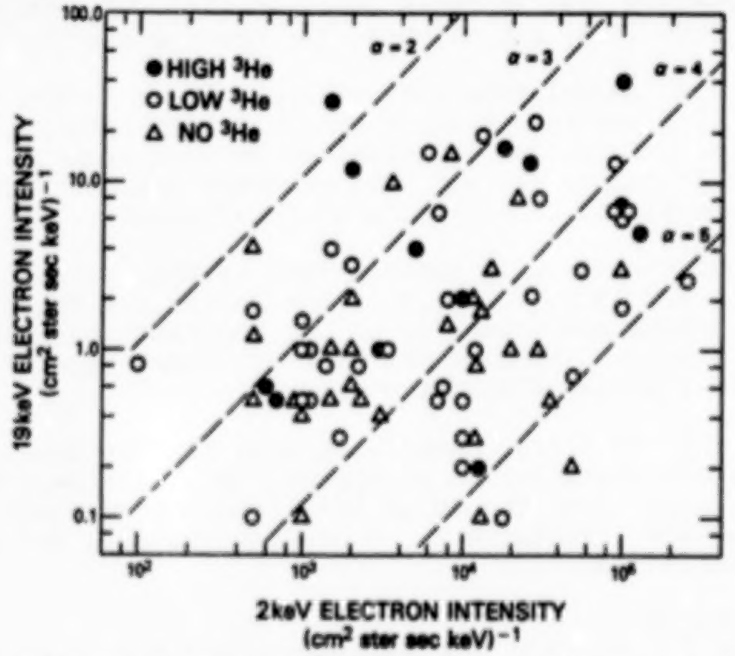

Fig. 2. Electron intensity cross-plot with ^{3}He content shown for each event. Electron power spectral indices are diagonal lines.

3. Relation to Solar Events The results of the preceding section lead to the conclusion that ^{3}He-rich events are not unusual, but are, in fact, a further manifestation of the same mechanism that accelerates electrons in the impulsive phase of solar events. Our ability to associate these particles in space with the corresponding radio, optical and X-ray features at the sun depends upon the size and character of the events.

We have used our preliminary radio and optical event associations in table 4 to show how the likelihood of identification of such events depends upon the presence of ^{3}He or 19-keV electrons in the event. We have included all radio events in the Type III column even though a small percentage of them are Type I.

Table 4 Number of Radio and Flare Associations for Events with Various Properties

	Type III	Flare	Total
^{3}He	61(72%)	40(47%)	85
No ^{3}He	41(61%)	18(26%)	68
Total	102(66%)	58(40%)	153
19-keV Electrons	84(82%)	60(58%)	103
No 19-keV Electrons	41(49%)	16(19%)	84
Total	125(67%)	76(41%)	187

Since metric Type III radio emission is a signature of electron ejection from the solar corona, it is not surprising to find a good correlation (67%) for all electron events. This correlation is improved substantially for events with 19-keV electrons (82%) and slightly for the ^{3}He events.

The correlation with H-alpha flares is not as good as with Type III events but again improves with both subsets of particle events. Particles accelerated on open magnetic field lines in the high corona may not have adequate access below the corona to produce significant H-alpha or X-ray events.

Of the 61 radio associations of the ^{3}He events, 6 are Type I events and 55 Type III; 8 of the latter are Type III, V. Most of the events are groups (G or GG) and about half have radio intensity 2 or 3. None of the 61 events show Type II or IV emission or other shock-related features.

The 40 flares associated with the ^{3}He events show the solar longitude distribution of typical impulsive well connected events with only 8 of the 40 in the eastern hemisphere. Two of the flares are importance 2, 6 are importance 1 and the remaining 32 are subflares.

REFERENCES

Reames, D.V., T.T. von Rosenvinge and R.P. Lin, 1985, Astrophys. J. 292, 716.

N85-34801

ELEMENTAL ABUNDANCE DIFFERENCES BETWEEN NUCLEI ACCELERATED IN CIR SHOCKS AND SOLAR FLARES

W.F. Dietrich and J.A. Simpson

Enrico Fermi Institute, University of Chicago,
Chicago, Illinois 60637, USA

ABSTRACT. By measuring the ratios of nuclear abundances H/He, CNO/Fe-group and the Fe-group/HE for 51 passages of Corotating Interaction Regions (CIRs) at 1 AU, and also by measuring these ratios from 620 solar flares in the energy range 0.6 to 4 MeV per nucleon, it is concluded that CIR shock acceleration alone does not change significantly these ratios from the values they have for solar system abundances or the solar wind. On the other hand, the solar flare ratios continue to reflect strong biases in the abundances, consistent with requirements for multi-stage acceleration processes at the Sun.

1. **Introduction**. It was discovered that hydrogen and helium nuclei are accelerated in the interplanetary medium in association with corotating interaction regions (CIRs) mainly beyond 1 AU (McDonald et al. 1976; Barnes and Simpson 1976) and that the corotating shocks associated with the CIRs are the site of the acceleration process (e.g. Barnes and Simpson 1976; Fesses et al. 1978). McGuire et al. (1978), Gloeckler et al.(1979) and Scholer et al. (1979) then showed that at 1 AU, CIRs accelerate nuclei over the element range of hydrogen to iron with relative abundances that tend to be different from typical abundance distributions observed at low energies in solar flare accelerated nuclei.

The evidence by Tsurutani et al. (1982) that CIR shock acceleration of ions is due to quasi-perpendicular shocks mainly beyond 1 AU now provides the opportunity to investigate further; 1) the origin of the local (interplanetary) "seed" ion population which is accelerated by CIRs, and; 2) the question of whether an interplanetary quasi-perpendicular shock can reproduce the kinds of preferential enhancements of abundances frequently observed for solar flare accelerated nuclei. This latter question has a strong bearing on whether, in solar flares, shocks alone can account for the observed enhancements, or whether, for example, the ions in the solar flare site undergo a preliminary stage of injection which biases the relative abundances. Our investigation includes the measurement of selected abundance ratios (e.g., H/He, CNO/Fe, and Fe/He) for 51 passages of CIRs at 1 AU during the period 1973-79. We also have determined these abundance ratios for 620 solar flares observed during 1973-84, of which a subset of 100 flares are observed to be ^{3}He-rich.

2. **Experimental Aspects**. Because the spectra of CIR accelerated nuclei have steep negative slopes and are restricted to energies below a few MeV per nucleon, their measurement by means of single dE/dx parameter analysis is difficult (e.g. McGuire et al. 1978). These difficulties are reduced in the case of the IMP 7 and IMP 8 Low Energy Telescope (LET; Simpson et al., 1974) which, in addition to a thin dE/dx detector has: a) a second yes/no detector providing particle range information, and; b) a 256 channel pulse height analyzer that spans the range H to Fe (which is in saturation). Pulse discriminator levels are set for fluxes of four

N85-34801

ORIGINAL PAGE IS
OF POOR QUALITY

major nuclear groups, mainly H, He, CNO and Mg-Fe. The latter group, dominated by the iron flux will be referred to as the Fe-group ("Fe") in this report. The pulse height analysis enables us: 1) to independently measure the energy spectrum of He nuclei; 2) to evaluate any contamination of low Z particles by higher Z nuclei (which is an insignificant factor for the CIR composition measurements) and; 3) to normalize the fluxes of H, He, CNO, and "Fe" to abundance ratios for the same energy per nucleon. For CIRs the principal source of error in the "Fe" group abundances is statistical fluctuations, however for the CNO group and He abundances, the largest errors are systematic (i.e. from uncertainties in the count rate discriminator levels, the spectral slope, and uncertainties of range-energy relations at these low energies). For solar flares the "Fe" contamination appearing in the CNO fluxes is the most significant factor. Since the same instrument and method of analysis are employed in obtaining both CIR and solar flare abundances, the systematic errors mostly cancel when determining the ratios of abundances. Further details on the analysis will be published elsewhere.

The identification of intervals for CIR passage were mainly based on CIRs identified in previous publications (see e.g., Christon and Simpson, 1979; Tsurutani et al., 1982) with the constraints that: 1) the flux for the He at low energy must reach a factor 6 above the prevailing background counting rate of 0.0015 He/s; 2) the magnetic field and solar wind measurements confirmed the presence of a CIR; and 3) a recurrence period of 27 days could be identified. Our investigations with IMP 7 and 8 at 1 AU assume, as do the reports of McGuire et al. (1978), Gloeckler et al. (1979), and Scholer et al. (1979) that the 1 AU observations of CIR abundances are the result of the inward flow of the ions (e.g. Marshall and Stone, 1977) from the CIRs beyond 1 AU.

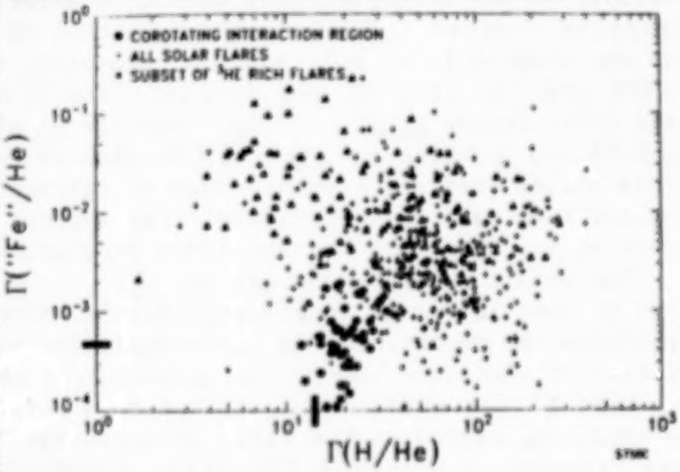

Figure 1

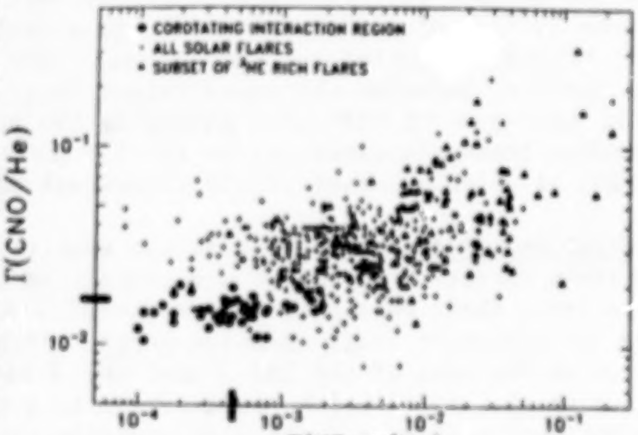

Figure 2

3. **Comparison of CIR and Solar Flare Accelerated Nuclei.** The abundance ratios of "Fe"/He versus H/He in the energy interval 0.6-4 MeV/n are plotted in Figure 1 for CIRs, all solar flares, and the subset ^{3}He-rich solar flares. Figure 2 is the corresponding plot for "Fe"/He versus CNO/He. The data from Figures 1 and 2 have been

ORIGINAL PAGE IS
OF POOR QUALITY

used to prepare the histograms in Figures 3 and 4. These plots reveal: 1) The range of variations for all 3 measured abundance ratios for CIRs (including experimental error) is seen in Figs. 1 and 2 to be small compared to that for the range of solar flare abundance ratios (i.e., the dynamic range of variation for CIRs is only a factor ~2 for H/He and CNO/He and factor 30 for "Fe"/He, whereas the dynamic ranges for solar flare abundance ratios are 3000, 40, and 3000 for H/He, CNO/He and "Fe"/He, respectively). From the number distributions of the CIR H/He and "Fe"/He ratios in Figs. 3 and 4 we note the narrower distribution for the CIRs compared with the corresponding solar flare distributions. Unlike the case for solar flares, we have found no examples of large deviations from the mean abundance ratios for CIRs; 2) the mean H/He, CNO/He and "Fe"/He ratios for CIRs are 20, 0.015, and 0.00048 respectively, while the corresponding H/He, CNO/He and "Fe"/He ratios for flares are 52, 0.030, and 0.0028, respectively. The CIR average abundance ratios are close to the universal abundance ratios (Cameron, 1982) (marked as bars on the axes of Figs. 1 and 2) except the H/He ratio which is in somewhat better agreement with fast solar wind values. Average solar flare "Fe"/He abundances at 2-4 MeV/n are seen to be enhanced by a factor of six to seven over photospheric abundances, and He is seen to be depleted in solar flares relative to both H and CNO. In Fig. 1 and 2, very few solar flares ratios appear in the plot area occupied by the CIR data.

We have compared our results for the H/He, CNO/He and Fe/He ratios of CIR accelerated particles with previously reported abundance ratios in Table 1. We have converted published He/O ratios to a CNO/He ratio by using the the published CIR C/O ratios. Clearly our survey, when averaged over many CIRS, confirms the earlier published work based on relatively few CIRs and flares.

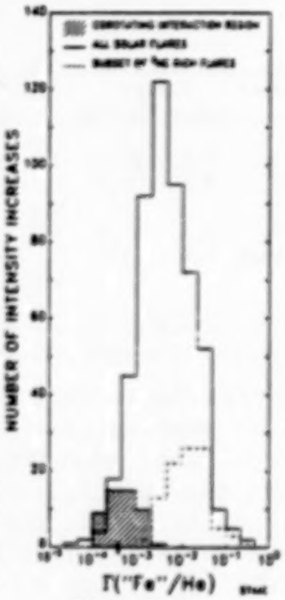

Figure 3

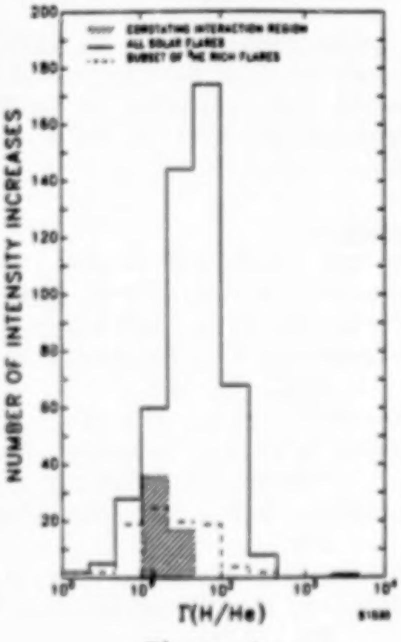

Figure 4

4. **Conclusions**. We find that: 1) for nuclei accelerated in corotating interaction region shocks the average values of the abundance ratios are close to the solar system abundances and are not inconsistent with the abundance ratios for the solar wind; 2) The variability of the abundance ratios for CIRs is more than an order of magnitude less than the variability observed in solar flares confirming McGuire et al. (1978); 3) there is no evidence for preferential enhancements of nuclear abundances in any CIR events.

From the above evidence we conclude that the "seed" nuclei for the CIR shock acceleration mechanism are ambient ions in the interplanetary medium with a composition which is similar to the solar system abundances. However, for solar flare nuclei we find, as reported by several

TABLE 1

Reference	Energy Range (MeV/n)	C/O	CNO/He x 100	Fe/He x 10000	p/He	Number of CIRs	Years
(7)	3.4 - 23.	0.8 ± .2	1.48 ± .45^{+}	NA	22. ± 5.*	6	1973-1976
(9)	0.6 - 1.0	0.91 ± .03	0.98 ± .045^{+}	7.1 ± .6	11.9 ± 0.2	4	1974
		0.90 ± .07	0.80 ± .084^{+}	1.8 ± .6	11.2 ± 0.2	5	1976
(4)	0.3 - 5.0	1.05 ± .19	1.25 ± .42^{+}	5.5 ± 2.	16.6 ± 3.5	9	1974,1976
This Work	0.6 - 4.0	NA	1.5 ± .25	5. ± 3.	20. ± 2.	51	1973-1979
(2)		0.60	1.67	4.7	14.		

+ Ratios and errors calculated from C/O and He/O ratios and errors quoted in each paper.
* Average of 17 events at 1.6-8.8 MeV/n

investigations, that the ambient source of nuclei reflects biases in the relative abundances of accelerated nuclei - i.e., preferential enhancements of some abundances. Thus, if shocks accelerate nuclei in solar flares, they probably represent the second stage of acceleration. The small variation in the CIR abundance ratios suggests that only shock acceleration is involved in the interplanetary medium, whereas the extreme variability of the solar flare ratios from solar flares points to a complex, multiple acceleration process.

5. Acknowledgements. We wish to acknowledge support of the staff in the Laboratory for Astrophysics and Space Research, particularly the aid given by S.P. Christon in identifying CIRs for this study. This work was supported in part by NASA Contract NAS 5-28422 and NSF Grant ATM 84-12382.

References

1. Barnes, C.W. and Simpson, J.A. 1976, Ap. J., 210, L91.
2. Cameron, A.G.W., 1982, Essays in Nucl. Astrophysics, 23.
3. Christon, S.P., and Simpson, J.A., 1979, Ap. J. (Letters), 227, L49.
4. Gloeckler, G., Hovestadt, D., Ipavich, F.V., and Mason, G.M. 1979, 16th ICRC, 5, 368.
5. Marshall, F.E., and Stone, E.C., 1978, J. Geophys. Res., 83, 3289.
6. McDonald, F.B., Teegarden, B.J., Trainor, J.H., Von Rosenvinge, T.T., and Webber, W.R. 1976, Ap. J. Lett., 203, L149.
7. McGuire, R.E., Von Rosenvinge, T.T., McDonald, F.B. 1978, Ap. J., 224, L87.
8. Pesses, M. E., Van Allen, J.A. and Goertz, C.K. 1978, JGR, 83, 553.
9. Scholer, M., Hovestadt, D., Klecker, B., and Gloeckler, G. 1979, Ap. J., 227, 323.
10. Simpson, J.A., Hamilton, D.C., McKibben, R.B., Mogro-Campero, A., Pyle, K.R., and Tuzzolino, A.J., 1974, JGR, 79, 3522.
11. Tsurutani, B.T., Smith, E.J., Pyle, K.R., and Simpson, J.A. 1982, JGR, 87, 7389.

SH2.2-7

N85-34802

THE HEAVY ION COMPOSITION IN ^{3}He-RICH SOLAR FLARES

G.M. Mason[1], D.V. Reames[2], D. Hovestadt[3] and T.T. von Rosenvinge[2]

[1]Dept. of Physics & Astronomy, Univ. of MD, College Park, MD 20742 USA
[2]NASA/Goddard Space Flight Center, Greenbelt, MD 20771 USA
[3]MPI fur Extraterrestrische Physik, 8046 Garching, FRG

1. Introduction. It has been known for some time that ^{3}He-rich flares show a tendency to be enriched in heavy ions (5), and that this enrichment covers the charge range through Fe (e.g. 3,8,10,14). The discovery of this association was responsible, in part, for the discarding of ^{3}He enrichment models which involved spallation or thermonuclear reactions, since such models were unable to produce heavy nuclei enhancements (e.g. review in ref. 12). More attractive appeared to be plasma resonance models which offered the possibility of producing ^{3}He and also heavy nucleus enrichments (e.g. 2,7). Previous studies of heavy nucleus enrichments in ^{3}He-rich flares (8,10) have covered only a few, isolated cases, thereby precluding the identification of systematic features of these enrichments. In order to investigate this association more thoroughly, we present here results of a survey of heavy nucleus abundances observed in 66 ^{3}He-rich flares which occurred over the period October 1978-June 1982.

2. Observations. The measurements were carried out in interplanetary space using instruments on the ISEE-3 spacecraft. ^{3}He and ^{4}He data are from the Goddard VLET sensors (13), and the heavy nuclei abundances are from the MPI/UMD ULEWAT sensor (4). The flares studied, and their method of selection, have been described in reference 6. In the present study, considerable care was exercised to insure that the two instruments were properly intercalibrated (9).

Figure 1 shows the enhancements relative to large flare abundances (from ref. 8) for 32 ^{3}He-rich flares in which there were ^{4}He flux increases. The energy ranges are 1.3-1.6 MeV/nuc for ^{4}He, and 1.0-1.8 MeV/nuc for heavier ions. Although the enhancements are normalized to O, the choice is arbitrary, and it can be seen from the figure that the enrichment increases with A or Z over the entire range ^{4}He through Fe. Figure 1 includes data for three "carbon-poor" flares (8) and for a survey of 17 flares (10). Note the striking similarity of the enhancements reported in the three separate studies. Note also that the measurements in the figure cover the range 1-17 MeV/nuc, and that there is no evidence of an energy dependence in the abundance pattern--thus the composition appears to be a measure of the abundances in the pre-injection plasma, e.g. as in the model of Fisk (2).

The error bars for the new results in Figure 1 are not obtained from the averaging (as is the case in the earlier studies), but rather they show the range of values observed in 2/3 of the cases centered about the mean. Thus, the "1-sigma" errors in the present work give an idea of the spread of values observed over a number of flares.

In view of the large range of ^{3}He/^{4}He enrichments (from ~10^3 to >10^4 times coronal values), one of the most surprising results of this survey was the discovery of a relatively narrow range of heavy nuclei enrichments. This can be seen from Figure 2, which shows histograms formed by least-squares fitting of each of 44 flares to the

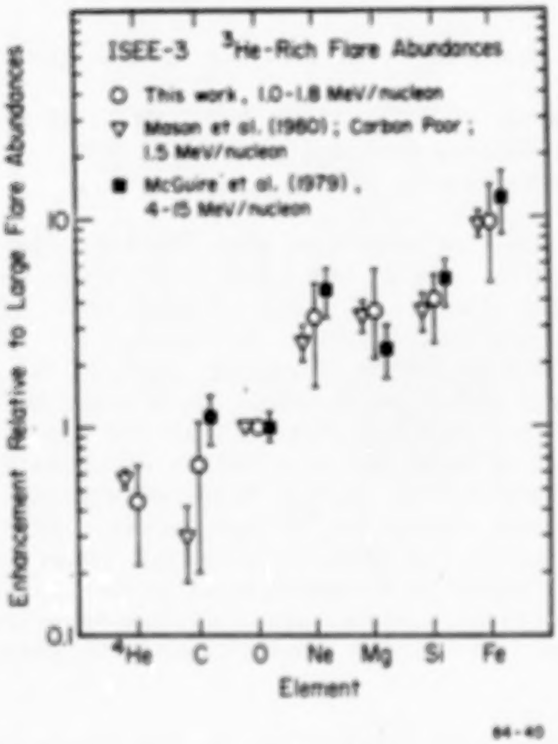

Figure 1

the abundance pattern shown in Fig. 1, and tallying the fractional deviations from the average values for each element. This fitting process results in histograms centered at 1.0, whose width is a measure of the deviations of individual elements from the average pattern (Fig. 1). Over the range C-Fe (left histogram) over 90% of the points fall within a factor of 2 of the mean, that is, between 0.5 and 2.0. Most of the large deviation points are from the element C, as can be seen from the right histogram, which shows fits over the range O-Fe, where 93% of the points fall within a factor of 2 of the mean.

If the heavy nucleus enrichment is caused by the same mechanism which causes the ^{3}He enrichments, then we might expect a ratio such as Fe/O to correlate with the ^{3}He/^{4}He ratio. Figure 3 shows that this is not the case: even though the Fe/O ratio is very large in these flares, the heavy least squares fit line in the figure has a slope of 0.02±0.06, and thus we find no statistically significant correlation between the degree of Fe enrichment and the degree of ^{3}He enrichment.

Flares showing extreme deviations from the average pattern may yield information about the acceleration mechanism(s). Therefore all the flares were examined for large χ^2 deviations from the average pattern. Only 4 of the 66 flares had significant deviations. The abundances in each of these is shown in Figure 4, where they are compared with large flare abundances (8) and the pattern from Fig. 1. Considering case (a) in the figure, the abundance anomaly is an enrichment of C by about 3 standard deviations compared with the ^{3}He-rich flare pattern. This is the most

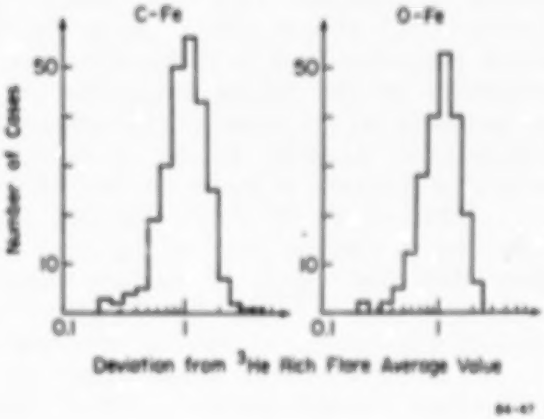

Figure 2

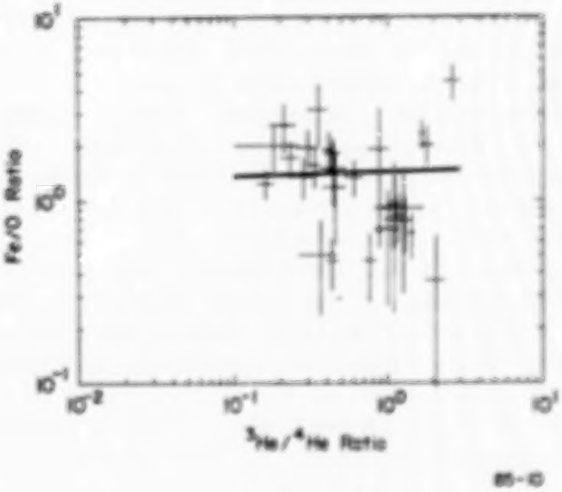

Figure 3

puzzling of the cases, and might be due to a statistical fluctuation. Case (b) appears to be an extreme example of the usual enhancement pattern. Cases (c) and (d) appear to show normal flare abundances for a range of lighter elements, and the ^{3}He-rich flare pattern for the remaining heavier elements. These latter cases are similar to the pattern seen in the 1977 Oct. 12-13 flare (8). Perhaps the most important comments to be made about the search for deviations from the average pattern are: (1) such deviations are rather rare, and (2) when they occur, there is no trend for very large enhancements for single elements or limited ranges of elements.

3. Discussion. Figure 5 compares the heavy nucleus enrichment pattern observed here with predictions from several models. Panel (a) compares the present results with the calculations of ref. 7 for short (solid line) and long (dashed line) heating times. The fit is not particularly good, although a different set of model parameters might well improve it. Panel (b) shows a fit using a simple model (9) based on the Fisk mechanism. Although the fit in panel (b) is acceptable, it depends on a particular choice of plasma parameters which if varied slightly will produce an enhancement pattern quite different from the result in our survey. In general, the plasma resonance models appear to need a very special set of parameter choices to yield the observed enrichments, and this is unsatisfying in view of the fact that virtually the same pattern appears from one flare to the next.

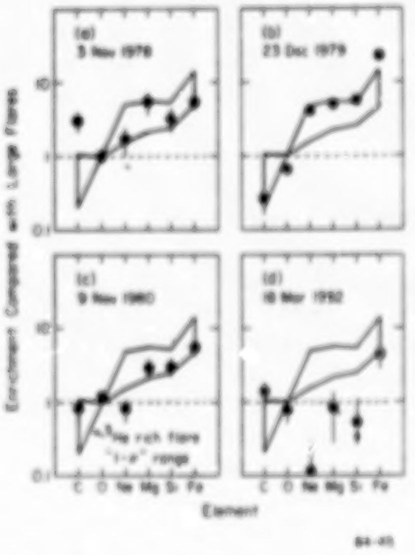

Figure 4

Figure 5(c) shows an enrichment pattern taken from the detailed calculations of Nakada (11) concerning the transport of heavy ions in the lower corona. Nakada's calculation includes effects of gravitational settling and thermal diffusion, assuming a temperature gradient of 1 K/cm at $T = 10^5$ K. The line in Fig. 5(c) shows the range of enrichments (compared with the baseline photospheric composition) for the range 5-9 x 10^5 K. The pattern is a surprisingly good fit to our results, and is all the more interesting because the mechanism in this case appears to produce basically the same result over a broad temperature range.

We interpret the observations presented here, along with previously reported work, to show that while a plasma resonance mechanism may account for the ^{3}He enrichments observed in these flares, this mechanism does not appear to be an attractive one for explaining the heavy nuclei enrichments that are associated with these events. Rather, we suggest that the heavy nuclei enrichments are due to heavy ion enrichments in the ambient plasma at the sites where the ^{3}He rich flares occur. We note that in plasma resonance models such as that of Fisk (2), a relatively high ^{4}He/H ratio is required, and the same mechanism which produces this enhancement might also produce the heavy nucleus enrichments. Model calculations by Nakada (11) indicate that sites with such enrichments may routinely occur in the corona.

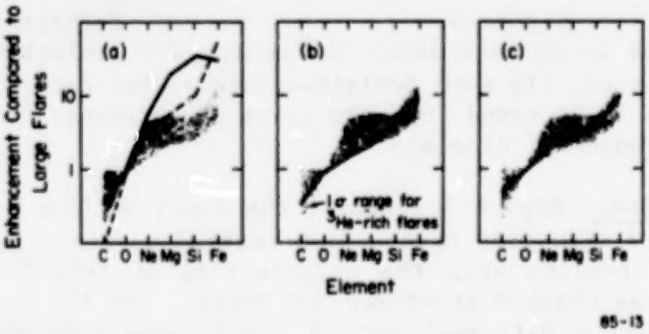

Figure 5. ^{3}He-rich flare heavy nuclei enhancements (shaded areas) vs. model calculations: (a) Kocharov and Orishchenko, (b) "Fisk", (c) lower coronal enhancements from Nakada (1969).

4. Acknowledgements. We are grateful to the many individuals at GSFC, MPI and UMD who were responsible for the success of the ISEE-3 instruments. This work was supported by NASA under contract NAS5-28704, grants NGR 21-002-224/316 and NAGW-101, by the NSF under grant ATM-84-07546, and by the Bundesministerium fur Forschung und Technologie, contract RV 14-B8/74.

References

1. Anglin, J.D. et al. 1977, Plovdiv ICRC, 5,43.
2. Fisk, L.A. 1978, Ap.J., 224, 1048.
3. Gloeckler, G. et al. 1975, Ap.J. (Letters), 200, L45.
4. Hovestadt, D. et al. 1978, IEEE Trans. Geo. El., GE-16, 166.
5. Hurford, G.J. et al. 1975, Ap.J. (Letters), 201, L95.
6. Kahler, S. et al. 1985, Ap.J., 290, 742.
7. Kocharov, L.G. and Orishchenko, A.V. 1983, Bangalore ICRC, 4, 37.
8. Mason, G.M. et al. 1980, Ap.J., 239, 1070.
9. Mason, G.M. et al. 1985, Ap.J. (submitted).
10. McGuire, R.E. et al. 1979, Kyoto ICRC, 5, 90.
11. Nakada, M.P. 1969, Solar Phys., 7, 302.
12. Ramaty, R. et al. 1980, in "Solar Flares" (ed. P. Sturrock), 117.
13. von Rosenvinge, T.T. et al. 1978, IEEE Trans. Geo. El., GE-16, 208.
14. Zwickl, R.D. et al. 1978, Ap.J., 225, 281.

C-5

SH 2.2-8

N85-34803

THE MEAN IONIC CHARGE OF SILICON IN ^{3}HE-RICH SOLAR FLARES

A. Luhn, B. Klecker, D. Hovestadt, E. Möbius
Max-Planck-Institut für extraterrestrische Physik
8046 Garching, F.R.G.

ABSTRACT

In addition to the previously reported mean ionic charge of Iron in ^{3}He-rich solar flares we have for the first time determined the average mean charge of Silicon for 22 ^{3}He-rich periods during the time interval from September 1978 to October 1979. The results indicate that the value of the mean charge state of Silicon is higher than the normal flare average by approximately 3 units and in particular it is higher than the value predicted by resonant heating models for ^{3}He-rich solar flares.

1. Introduction. The ^{3}He isotope was first measured as a constituent of solar energetic particle events in 1970 by Hsieh and Simpson [1]. Following this discovery, it has been firmly established by now that there exists a class of generally small solar flare events in which the abundance of the ^{3}He isotope relative to ^{4}He in solar cosmic rays is greatly enhanced relative to the normal solar abundance ratios. Enrichments of more than four orders of magnitude have been observed, leading to a ^{3}He/^{4}He ratio of $\gtrsim$ 1. These unusually high enrichment factors can best be explained by a two-stage acceleration process with a first step highly selective in mass per charge and a second step acting only upon particles above a certain threshold in rigidity or velocity. Several plasma heating processes have been proposed as the first stage ([2,3,4,5]), which preferentially heat certain minor ion species like ^{3}He. The effect of the preferential heating will be most pronounced in the tail of the ion distribution function. The second stage acceleration process will then (apart from introducing additional abundance changes, see [6]) mainly reflect the abundance ratios in the tails of the ion distribution functions. In all of the proposed heating processes the ionic charge states play a critical role for the largest attainable particle velocity and/or the heating rate. Measurements of the charge states of energetic ions in ^{3}He-rich events are therefore crucial in understanding the nature of the enrichment process. For recent reviews of observational and theoretical aspects of ^{3}He-rich flares see e.g. [7,8].

2. Instrument and Data Analysis. The data presented in this paper have been obtained during the period from September 1978 to October 1979 with the Max-Planck-Institut / University of Maryland ULEZEQ Sensor onboard the ISEE-3 spacecraft. (see also [9]). The instrument is described in more detail by Hovestadt et al. [10]. We performed the charge analysis of Fe and Si for 22 periods rich in ^{3}He as determined from a systematic study of the composition of solar energetic particles with our wide angle particle telescope (ULEWAT) on the same spacecraft. We selected periods with a ^{3}He/^{4}He ratio of $\geq$ 0.1, lasting more than one day. The average ^{3}He/^{4}He ratio of all 22 periods is 0.227. The energy range for which the charge analysis for Si and Fe is performed, is 0.55-3.0 and 0.34-1.8 MeV/N respectively. This represents a compromise between elemental and charge resolution and counting statistics.

N85-31803

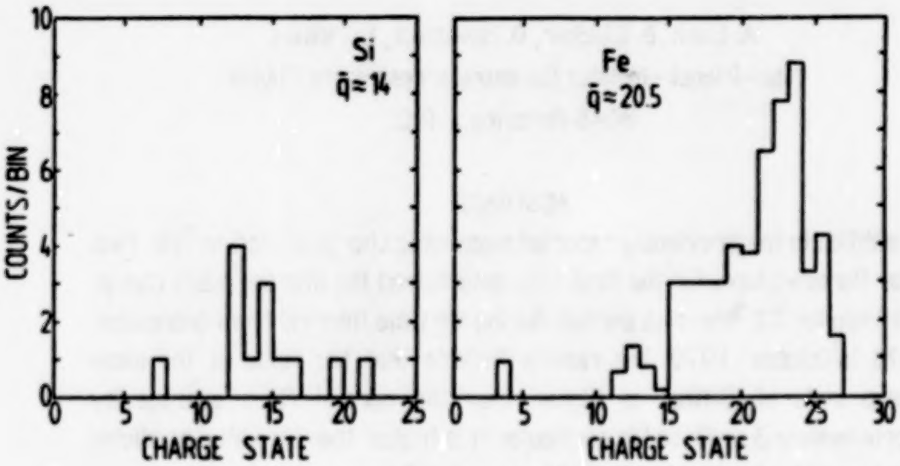

Fig. 1 ***Measured charge state distributions of Si and Fe for ^{3}He-rich energetic particle events***

3. Results. Because of the poor counting statistics for heavy ions in the ^{3}He-rich energetic particle events, it is impossible to give mean charge states for individual events. Instead, we have to accumulate the pulse height data for all of the observed events and derive an average charge state distribution. Still, we have only registered a total of 13 Silicon and 56 Iron ions. Fig.1. shows the resulting charge state histograms. The mean charge for Fe is 20.6±1.2 (95% confidence level). Compared to the average charge of 14.9±0.2 for normal solar energetic particle events[9], it is significantly higher for this class of flares, confirming the result of Klecker et al.[11,12] for a subset of ^{3}He-rich periods. The mean charge of Si is much less well determined. The value calculated from the measured distribution is compatible with fully ionized Si ions. In order to find lower bounderies for the mean charge, we performed a t test and obtain values of 12.6 and 11.7 for confidence levels of 95% and 99% respectively. Again this has to be compared with a value of 11.0 ± 0.2 for normal flares. Although the statistical significance is less then in the case of Fe, one can conlude that also

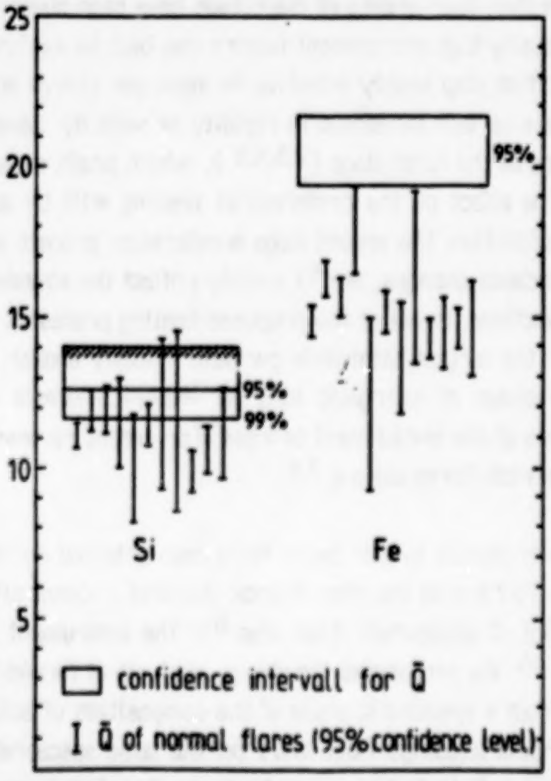

Fig. 2 ***Confidence levels for the average charge in ^{3}He-rich periods compared with results for normal flares (9).***

Si shows higher charge states in ^{3}He-rich flares. Fig. 2 gives the confidence intervals of the mean charges for Si and Fe together with results from normal flares. It should be noted that in addition to the statistical errors quoted above, the mean charges are subject to a systematic error of 5%. However this does not affect the comparison between this result and the mean charges of normal flares, since both measurements have the same systematic error.

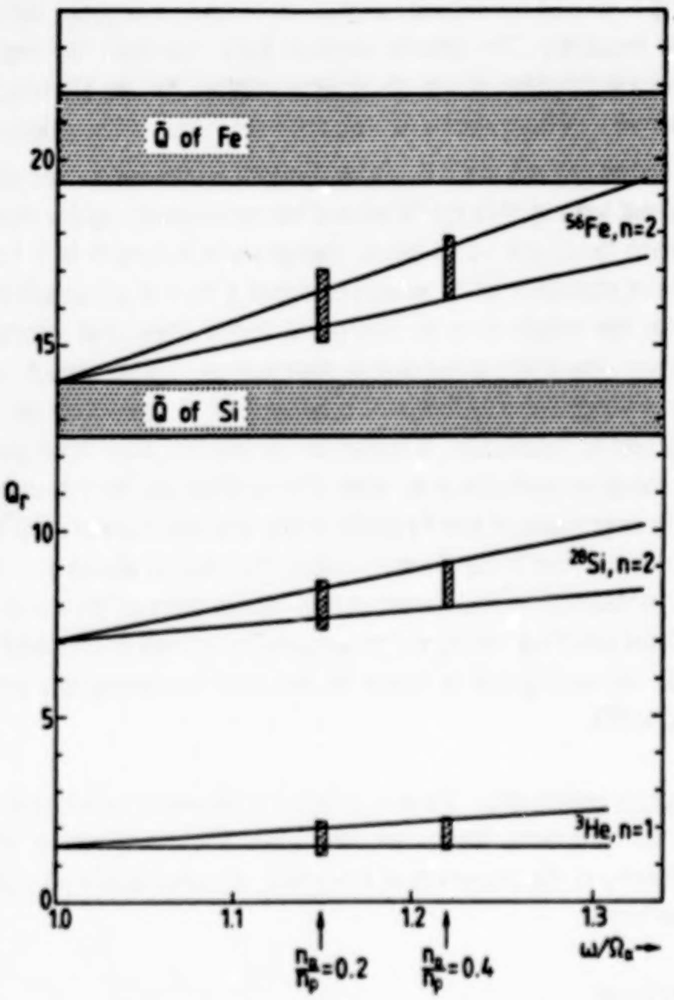

Fig. 3 *Allowed ranges of the ionic charge for resonant heating by He-cyclotron waves as a function of the wave frequency* ω/Ω_α

4. Discussion. We will concentrate on the comparison of the measurements with the implications of Fisk's [3] model for the preferential heating of ^{3}He. For a discussion of the other processes see [12]. Fisk employs resonant heating by electrostatic ion cyclotron waves in connection with a second stage acceleration process as described in the introduction to account for the ^{3}He enrichment factors observed. The condition for resonant interaction of an ion (mass m_i, charge q_i, velocity $v_\parallel$ parallel to the magnetic field B, gyrofrequency $\Omega=q_iB/m_ic$) with a wave of frequency ω and parallel wavenumber $k_\parallel$ is given by

$$|(\omega-n\Omega)/(k_\parallel v_\parallel)|=1 \qquad (1)$$

n is the number of the harmonic of the interaction. To be in resonance with the first harmonic of the gyrofrequency of ^{3}He requires He-cyclotron waves with a frequency $\omega \sim 1.2\ \Omega_\alpha$, Ω_α being the gyrofrequency of ^{4}He. To determine the charge states of heavy ions which interact resonantly with the wave, we follow Mason et al.[13] in setting $v_\parallel=(k_BT/3m_i)^{1/2}$ and requiring a value of $k_\parallel$ such that the bulk of the wave-supporting ^{4}He distribution does not fulfill the resonance condition (1). We then obtain the following expression for the resonant Q/A ratio (Q=charge in units of e, A=atomic mass number of the ion):

$$2\frac{\omega}{\Omega_\alpha}\left[1-\frac{2}{\sqrt{A}}\left(1-\frac{1}{4\omega/\Omega_\alpha}\right)\right] < n\frac{Q}{A} < 2\frac{\omega}{\Omega_\alpha}\left[1+\frac{2}{\sqrt{A}}\left(1-\frac{1}{4\omega/\Omega_\alpha}\right)\right] \qquad (2)$$

In Fig 3. we plot the allowed range of the resonant charge Q_r, satisfying (2), as a function of the wave frequency. The hatched vertical bars represent the regions of Q_r calculated from a numerical solution of the dispersion relation for an electrostatic ion cyclotron wave in a Hydrogen - Helium plasma for two different values of the relative Helium concentration n_α/n_p [14]. Shaded regions mark the 95% confidence interval for the observed average mean charges. Resonant heating of Fe via the second harmonic would require charge states of approx. 16 to 18, whereas for Si one would expect charge states around 8 to 9 (see also [13]). Despite the poor counting statistics for Si, a mean charge of 8 to 9 is not compatible with the observations. For Fe too the measured mean charge is higher than that required for resonant interaction. However, the width of the charge distribution is wide enough to extend down to the resonant charge states. One may therefore conclude that if indeed the Fisk mechanism is acting as a first stage heating mechanism, it cannot be the only one. Significant portions of the source plasma of the energetic particles must stem from a different, as yet unspecified injection process. The high charge states of both Fe and Si imply a temperature of ~10^7K in the source region of ^{3}He-rich flares. This is significantly higher than temperatures of ~$3 \cdot 10^6$K derived from Si and Fe charge states in normal flares[9]. A high temperature at the source region of ^{3}He-rich flares also excludes selective heating by ion acoustic turbulence as proposed by Kocharov[4], because in this model the heating site is located at the upper chromosphere with an ambient temperature of ~10^5K ([8]).

5. Acknowledgements. We are grateful to the many individuals at the Max-Planck-Institut für extraterrestrische Physik and the Space Physics group of the Department of Physics and Astronomy at the University of Maryland, who developed the hardware and software for our ISEE experiments.

References.

1. K.C. Hsieh, J.A. Simpson: Ap. J. Lett. **162**, L191 (1970)
2. J.A. Ibragimov, G.E. Kocharov: Proc. 15th Int. Cosmic Ray Conf. (Plovdiv), **12**, p.221 (1977)
3. L.A. Fisk: Ap. J. **224**, p.1048 (1978)
4. L.G. Kocharov: Proc. 17th Int. Cosmic Ray Conf. (Paris), **3**, p.175 (1981)
5. H. Vervoglis, K. Papadopoulos: Ap. J. Lett. **270**, L95 (1983)
6. E. Möbius et al.: Ap. J. **238**, p.768 (1980)
7. C.Y. Fan et al.: Space Science Rev. **38**, p.143 (1984)
8. L.G. Kocharov, G.E. Kocharov: Space Science Rev. **38**, p.89 (1984)
9. A. Luhn et al.: paper SH 2.1-11 (this conference)
10. D. Hovestadt et al.: IEEE Trans. Geos. Electr. **GE-16**, p.166 (1978)
11. B. Klecker et al.: Ap. J. **281**, p.458 (1984)
12. B. Klecker et al.: Proc. 18th Int. Cosmic Ray Conf. (Bangalore), **4**, p.65 (1983)
13. G. Mason et al.: Ap. J. **239**, p.1070 (1980)
14. A. Luhn, Ph.D. Thesis, Technische Universität München (1985)

N85-34804

SH 2.2-9

ON THE CONNECTION BETWEEN THE ^{3}He-ENRICHMENT AND SPECTRAL INDEX OF SOLAR ENERGETIC PARTICLES

L.G.Kocharov

Leningrad Polytechnical Institute, Leningrad, 195251, USSR

Ya.V.Dvoryanchikov

Ioffe Physico-Technical Institute of the Academy of Sciences of the USSR, Leningrad 194021, USSR

A model is presented which can explain the observed tendency of events with large ^{3}He/^{4}He ratios to have steeper spectra [1]. In this model preferential injection of ^{3}He, acceleration by Alfven waves and Coulomb deceleration of ions are considered simultaneously. The observed tendency may be obtained as a result of competition between injection and acceleration processes.

1. Introduction

It was shown that preferential injection (preacceleration) of ^{3}He by plasma waves can provide high ^{3}He-enrichment levels observed in some solar energetic particle events (see [2] and references therein). All proposed theoretical models for ^{3}He enrichment consider a two-stage acceleration process: a preacceleration (injection) stage due to wave-particle interaction at low energies and an acceleration process requiring a threshold injection velocity such as Fermi type acceleration by Alfven waves. The high ^{3}He/^{4}He ratio is proposed to arise at the first (preacceleration) stage, at the second stage the observed spectra are formed. Up to now these two stages were investigated separately [2,3]. Recently the tendency of events with large ^{3}He/^{4}He ratios to have steeper spectra was found [1]. It is possible only if injection and acceleration processes are connected by some way. The model taking into consideration such connection will be presented here.

2. The Model.

The equation for the ion distribution function has the form:

$$\frac{\partial f}{\partial t} = \frac{1}{V^2}\frac{\partial}{\partial V}\mathcal{D}V^2\frac{\partial f}{\partial V} - \frac{f}{T(V)} + \frac{1}{V^2}\frac{\partial}{\partial V}(FV^2 f). \qquad (1)$$

Here the diffusion coefficient $D = D^{(A)} + D^{(C)} + D^{(in)}$, where $D^{(A)}$ describes the acceleration by Alfven waves, $D^{(C)}$ is due to Coulomb collision, $D^{(in)}$ is the injection diffusion coefficient due to wave-particle interaction at low energies. The second term in right-hand side of equation (1) describes diffusive escaping of particles; it plays role only at high velocities $V \gg V_A$, where $T(V) = 3L^2\mathcal{D}^{(A)}/V_A^2V^2$

N85-34804

V_A is the Alfven velocity and L is a typical length scale of the acceleration region. The last term in (1) describes the deceleration of particles by Coulomb collisions. If we are interested in the injection problem the velocities from thermal up to observed in the interplanetary space should be considered. That is why we will use the diffusion coefficient $D^{(A)}$ in the form [4] which is valid for arbitrary velocity of test particle:

$$\mathcal{D}^{(A)} = \frac{4\pi Z^2 e^2 V_A^2}{V(1+V_A^2/C^2)C^2 A^2 m_p^2} \int_{K_0}^{K_{max}} dK \frac{W_K}{K} \Phi(\alpha,\beta); \tag{2}$$

$$\Phi(\alpha,\beta) = \int_0^{\infty} du \int_0^1 dx \cos(\alpha u x) \left\{ \left[s^2 \cos u - 3(1-x^2)\sin^2 u \right] \times \left(\frac{\sin(\beta s)}{\beta^2 s^5} - \frac{\cos(\beta s)}{\beta s^4} \right) + \frac{\sin(\beta s)}{s^3}(1-x^2)\sin^2 u \right\}; \tag{3}$$

$$s = \sqrt{4(1-x^2)\sin^2\frac{u}{2} + u^2 x^2}; \quad \alpha = \frac{KV_A}{\omega_H}; \quad \beta = \frac{KV}{\omega_H};$$

Here Ze and Am are the charge and the mass of accelerated ion, K is the wave number, $\omega_H = ZeH/Am_pc$, H is the magnetic field strength, $W_K \propto K^{-\nu}$ is spectral density of Alfven waves, K_0 and K_{max} are the minimum and maximum wave numbers of wave spectrum. The diffusion coefficient $D^{(C)}$ and deceleration coefficient F due to Coulomb collisions are given by expressions [5]:

$$\mathcal{D}^{(C)} = \frac{Z^2 e^2 \omega_{pe}^2 m_e \ln\Lambda}{A^2 m_p^2 V} \left[G(u) + \frac{T_e}{T_p} G(\mu u) \right]; \tag{4}$$

$$F = 2\frac{Z^2 e^2 \omega_{pe}^2 \ln\Lambda}{A m_p^2 V_e^2} \left[G(u) + \frac{T_e}{T_p} G(\mu u) \right];$$

$$u = V/V_e; \quad \mu = \sqrt{m_p T_e / m_e T_p}; \quad G(u) = \frac{erf(u) - u^2 \frac{d}{du} erf(u)}{2u^2};$$

$$erf(u) = \frac{2}{\sqrt{\pi}} \int_0^u e^{-x^2} dx. \tag{5}$$

Here $V_e = \sqrt{2k_B T_e / m_e}$ is the thermal velocity of electrons, T_e and T_p - electron and proton temperatures, ω_{pe} is electron plasma frequency. For simplicity at thermal velocities the injection diffusion coefficient was proposed to be constant

To obtain preferential injection of ^{3}He the diffusion coefficient $D^{(in)}$ for it must be greater: $\mathcal{D}^{(in)}_{^3He}/\mathcal{D}^{(in)}_{^4He}=3$. At higher energies it was proposed that $\mathcal{D}^{(in)}$ increases sharply and then it decreases as V^{-3} (Fig.1).

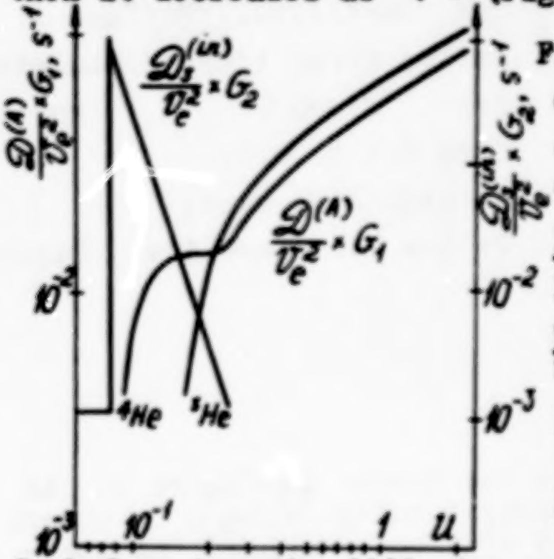

Fig.1. The diffusion coefficients $D^{(in)}_{^3He}$ and $D^{(A)}$ used in calculations. $K_{max}=0.35\frac{\omega_{Hp}}{V_A}$

$T = 6\cdot10^6$K, $\nu=1.5$

Low loss case: $n=4\cdot10^{10}cm^{-3}$, $L=5\cdot10^8$cm, $H=70$ Gs, $\nu_0=1$Hz, $\frac{W}{nK_BT_e}=0.35$, $G_1=2$, $G_2=3.3$

High loss case: $n=5\cdot10^{11}cm^{-3}$, $L=2\cdot10^9$cm, $H=260$ Gs, $\nu_0=1$Hz. $\frac{W}{nK_BT_e}=0.35$, $G_1=1$, $G_2=0.1$

Such form has the diffusion coefficient for ion-sound turbulence used earlier in ^{3}He-enrichment problem [4].
The solution of equation (1) has been found by the method described in [6] ,but at high energies we have obtained quasistationary solution. Theoretical parameters has been selected basing on observational data (for details see [7]).

3. Results and discussion

Calculations show that high ^{3}He/^{4}He ratio is formed at the energies from 100 eV up to 10 keV due to injection and the ratio changes slowly at higher energies where the acceleration mechanism works. As can be seen from experimental data [3] for some ^{3}He-rich solar particle events ^{3}He/^{4}He ratio decreases with increasing of energy at $E \geq 2$ MeV/N. For another events such decrease is not seen. To explain the ^{3}He/^{4}He decrease at $E \gtrsim 2$MeV/N we have proposed that the plasma density in the acceleration region is high. In this case higher Coulomb losses for ^{3}He leads to steeper spectra of this helium isotope. As a result ^{3}He/^{4}He ratio decrease with increasing of energy. For this high loss case the obtained parameters of acceleration region are: density $n \approx 10^{12}$ cm^{-3}, $L \approx 10^9$cm, $H \approx 250$ Gs, $T \approx 6\cdot10^6$ K and if the lowest frequency of Alfven wave spectrum $\nu_0=1$Hz the wave energy density $W/nK_BT_e \approx 0.2$. For events without ^{3}He/^{4}He decrease at $E \gtrsim 2$MeV/N lower values of n and H have been obtained (low loss case): $n \approx 3\cdot10^{10}$ cm , $H \approx 70$ Gs.

Calculations show that the higher turbulent energy density W/nK_BT_e (shorter acceleration time) is, the lower energy particles may be accelerated. But at lower energies the ^{3}He/^{4}He ratio is lower too (due to the injection mechanism). On the other hand, the shorter is the acceleration

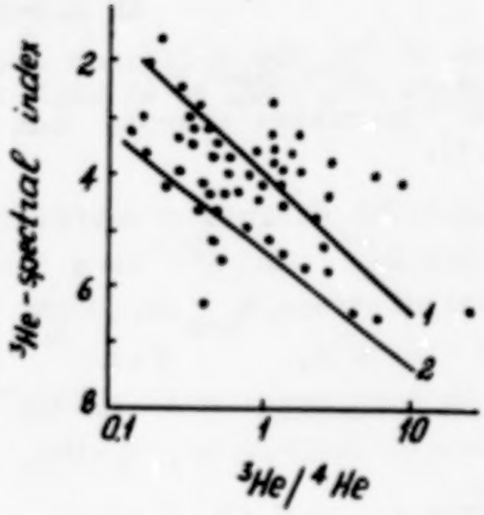

Fig.2. ^{3}He-spectral index (at 2MeV/N)vs. ^{3}He/^{4}He ratio; solid lines-calculated for $W/n\kappa_B T_e$ varied from 0.1 to 0.5;
1- high loss case;
2- low loss case (see Fig.1).

time, the smaller is the power low index. In figure 2 the result of varying of wave energy density $W/n\kappa_B T_e$, is shown. The experimental scatter plot of event-averaged ^{3}He-spectral index versus ^{3}He/^{4}He ratio is shown too [1]. It is seen that the experimental tendency conforms the tendency obtained by varying the acceleration time.Thus the observed tendency may be explained as a result of competition between injection and acceleration processes at the intermediate energy region ($U \approx 0.3$ in figure 1).

References

1.D.V.Reames,T.T. von Rosenvinge, 1983, 18-th ICRC,4 ,48.
2.L.G.Kocharov, G.E.Kocharov,1984, Space Sci.Rev.,38, 89.
3.E.Möbius et al.,1982, Astrophys.J.,259, 397.
4.V.N.Tsytovich, A.S.Tchyghachov, 1969, in "Fisika plasmy", v.2, Atomizdat, Moscow, p.87.
5.A.G.Sitenko, Tsyan-Yu-Tay, 1962, J.Tech.Fiz.,32,1324.
6.A.V.Gurevich,1960, J.Exp.Teor.Fiz.,38, 1597.
7.L.G.Kocharov, Ya.V.Dvoryanchikov, 1984, in "Energichnie tchastitsy i fotony solnechnigh vspishek",Leningrad,p.63.

THE PLASMA MECHANISM FOR PREFERENTIAL ACCELERATION OF HEAVY IONS

L.G. Kocharov
Leningrad Polytechnical Institute, Leningrad, 195251
U S S R
A.V. Orishchenko
Ioffe Physico-Technical Institute, Leningrad, 194021,
U S S R

The induced scattering of ion-acoustic waves on ions is considered for preferential preacceleration of heavy elements. The reconsidered diffusion coefficient in velocity space is used. If the threshold velocity for the main acceleration is linear in charge-to-mass ratio, the induced scattering can account for the observed heavy element abundances in solar cosmic rays.

1. Introduction.

In the paper [1] induced scattering of Langmuir waves on ions was considered as a mechanism by which heavy ion enrichment could be produced in solar cosmic rays. It was proposed that the threshold velocity for the main acceleration is linear in charge-to-mass ratio ($V_{th}=(Z/A)V_1$) and the diffusion coefficient in the velocity space due to induced scattering of Langmuir waves on ions $D_L \propto Z^4/A^2$. Recently the dependence of diffusion coefficient of ions D_L on charge Z and mass A has been reconsidered by L.Kocharov [2] and J.Weatherall [3]. It was shown that for Langmuir waves the factor Z^4/A^2 taken from [4] (expressions 5.107-5.109) should be replaced by factor Z^2/A^2. For ion-acoustic waves more complicated dependence on Z and A takes place (see below). As a result of this reconsideration J.Weatherall [3] concluded that induced scattering cannot lead to enrichment of ^{3}He and heavy elements. For ion-acoustic waves this conclusion was based on examination of diffusion coefficient D_{ia} at thermal velocity for a very high ratio of the number of helium nuclei to protons in solar plasma: $n(He)/n(H)=0.2$ (according to [5] $n(He)/n(H)=0.07$). On the contrary in the paper [2] the attention was drawn to the fact that in the significant for ^{3}He-enrichment problem nearest superthermal region and for moderate n(He)/n(H) ratio the diffusion coefficient D_{ia} is greater for the lighter helium isotope. Thus the preferential acceleration of helium-3 can be explained on the base of the ion-acoustic heating as it was proposed earlier (see [4]). Here we will show that the induced scattering of ion-acoustic waves can produce observed enrichment of heavy ions too, while Lengmuir heating leads to a normal abundances of elements.

2. The model.

We propose the ion-acoustic turbulence to be excited in a region with coronal temperature for a short time. As a result of interaction between waves and particles velocity distribution function of ions $f(\vec{V})$ is altered. The change of $f(\vec{V})$ is described by the diffusion equation in velocity space. At low velocities where the induced scattering of waves plays the main role the diffusion coefficient has the form:

$$\mathcal{D}_{ia} = \frac{\hbar^2}{A^2 m_p^2} \int w_{\vec{V}}(\vec{K}_1,\vec{K}_2) N_{K_1} N_{K_2} \frac{(\vec{K}_-\cdot\vec{V})^2}{V^2} \frac{d\vec{K}_1\, d\vec{K}_2}{(2\pi)^6} \qquad (1)$$

where $\vec{K}$ is a wavevector, $\vec{K}_- = \vec{K}_1 - \vec{K}_2$, N_K is a wave occupation number, (Am_p) is ion mass, $\vec{V}$ is ion velocity, $w_{\vec{V}}(\vec{K}_1,\vec{K}_2)$ is probability for scattering a wavevector $\vec{K}$ into a wavevector $\vec{K}_2$ by a particle with velocity $\vec{V}$ [2]:

$$w_{\vec{V}}(\vec{K}_1,\vec{K}_2) = \frac{Z^2 e^4 (2\pi)^3}{m_p^2 \omega_{pp}^4} \frac{(\vec{K}_1\cdot\vec{K}_2)^2}{K_1^2 K_2^2} \left[\frac{Z}{A}\left(1 - \frac{\vec{K}_-\cdot\vec{V}}{\omega_{K_1}}\right)^{-2} - 1\right]^2 \delta(\omega_- - \vec{K}_-\cdot\vec{V}). \qquad (2)$$

Here (Ze) is ion charge, ω_K is a frequency of wave with wavevector $\vec{K}$, $\omega_- = \omega_{K_1} - \omega_{K_2}$, ω_{pp} is proton plasma frequency. At low velocities $V \ll V_S$ ($V_S = \sqrt{T_e/m_p}$ is ion sound velocity):

$$\mathcal{D}_{ia} \approx \left[\frac{Z}{A}\left(1 - \frac{Z}{A}\right)\right]^2 \mathcal{D}_0; \qquad \mathcal{D}_0 = \left(\frac{W_{ia}}{nT_e}\right)^2 \frac{K}{\Delta K} \frac{V_S^2}{2} \omega_{pp}. \qquad (3)$$

Here W_{ia}/nT_e is a ratio of wave energy to thermal one, $\Delta K/K$ is relative width of wave spectrum, T_e is electron temperature. Similar to [1,4] the distribution function of ion species "i" at time t can be found as:

$$f_i(\vec{V},t) = (\pi b_i^2)^{-\frac{3}{2}} exp(-V^2/b_i^2); \quad b_i^2 = V_{Tp}^2\left\{\frac{1}{A_i} + \varkappa_0^{-2}\left[\frac{Z}{A}\left(1-\frac{Z}{A}\right)\right]^2\right\} \quad (4)$$

where $V_{Tp} = \sqrt{2T_p/m_p}$ is proton thermal velocity, $\varkappa_0^2 = V_{Tp}^2(4\mathcal{D}_0 t)^{-1}$, T_p is initial proton temperature. If the threshold velocity for the main acceleration is linear in charge-to-mass ratio ($V_{th}^i = \frac{Z_i}{A_i} V_1$), then the enrichment factor of ion species "i" relative to ion species "j" can be found:

$$Q_{ij} = \int_{V_{th}^i}^{\infty} v^2 f_i(\vec{V},t)\, dV \Big/ \int_{V_{th}^j}^{\infty} v^2 f_j(\vec{V},t)\, dV. \quad (5)$$

3. Discussion and summary.

From calculations of enrichment coefficients using different values of $\varkappa_0$, V_1 and ion ionization state it is seen that good accordance with experiment is possible when $\varkappa_0 = 0.2-0.3$, $V_1 \approx 6\ V_{Tp}$ and ionization state is equilibrium conforming to temperature $T_* \approx 5 \cdot 10^6$K. Calculated and observed enrichment factors for different elements relative to oxygen are shown in figure. The coincidence seems to be satisfactory.

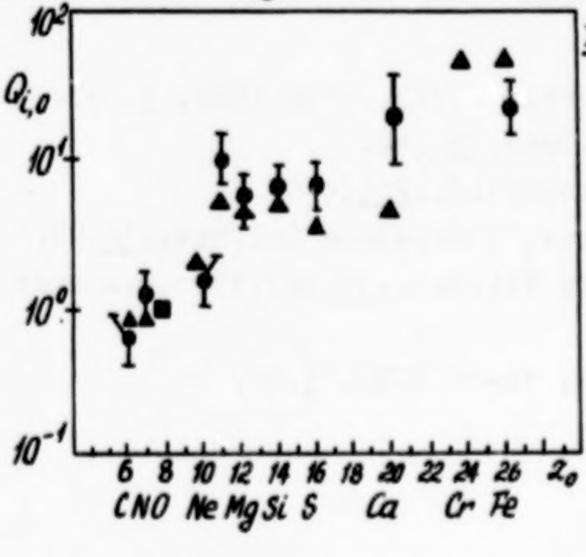

Figure. Enrichment factors relative to oxygen. Circles-observed for Sept.24,1977 event [6]. Triangles -calculated for $\varkappa_0 = 0.25$, $V_1/V_{Tp} = 6$, $T_* = 5 \cdot 10^6$K.

Thus the reconsideration of scattering probability [2,3] is not crucial for induced-scattering mechanism of heavy ion enrichment. Comparing to our previous model [1] now better agreement of theory and experiment is attained. In present model enrichment of heavy elements is a result of two reasons: (1) the induced scattering heats heavy ions up to a greater temperature ($T \propto \frac{Z^2}{A}(1-\frac{Z}{A})^2$); (2) the threshold velocity V_{th} is lower for heavier ions.

Note that induced scattering of Langmuir waves used in [1] combining with $V_{th} = \frac{Z}{A} V_1$ leads to the normal abundances of elements even when the portion of accelerated particles is small (while equilibrium Maxwellian distribution at coronal temperature leads to a great depletion of heavy ions). Thus the model [1] is suitable for events with normal abundances of ions.

In conclusion, the mechanism of preacceleration by induced scattering has the sensitivity to ion charge and mass needed to account for observed solar cosmic-ray abundances. The contrast conclusion made by J. Weatherall [3] probably derives from an incorrect application of plasma theory to solar cosmic-ray problems.

References.

1. L.G. Kocharov, A.V. Orishchenko. 1983. 18th ICRC, 4, 37.
2. L.G. Kocharov, 1983, Soln.Dann. 9, 60.
3. J. Weatherall, 1984, Astrophys.J., 281, 468.
4. L.G. Kocharov, G.E. Kocharov, 1984, Space Sci.Rev., 38, 89.
5. A.G.W. Cameron, 1973, Space Sci.Rev., 15, 121; 1981, preprint N.1357.
6. R.E. Mc Guire et al., 1979, 16-th ICRC, 5, 61.

ORIGINAL PAGE IS
OF POOR QUALITY

N85-34806

SH 3.1-1

OBSERVATIONS OF SOLAR ENERGETIC PARTICLES AT A SYNCHRONOUS ORBIT

T.Takenaka (a), Y.Ohi (b), T.Yanagimachi (b),
K.Ito (b), T.Kohno (c), and K.Sakurai (d)
(a) Science and Engineering Research Laboratory,
Waseda University, Shinju-ku, Tokyo 162, Japan
(b) Department of Physics, Rikkyo University,
Toshima-ku, Tokyo 171, Japan
(c) The Institute of Physical and Chemical Research,
Itabashi, Tokyo 173, Japan
(d) Institute of Physics, Kanagawa University,
Rokkakubashi, Yokohama 221, Japan

1. INTRODUCTION The Space Environment Monitors (SEM) on board the Japanese geostationary meteorological satellites (GMS-1 and GMS-2) observed energetic protons, alpha particles and electrons continuously for February 1978 to September 1984. The satellites were at 6.6 earth radii above 140°E equator. Observational items are shown in Table 1 [1].

In the propagation studies of solar energetic particles, statistical analyses for many events revealed on averaged picture of the propagation such as was reported by Reinhard et al.[2] and Van Hollebeke et al.[3]. They showed the existence of the fast propagation region (FPR:45°W ±~60°, on an average) or the preferred connection region (PCR:20° W - 80° W) in the heliolongitude. We tried to study some characteristics of the propagation process of solar energetic particles by using the data provided by the GMS/SEM's for February 1978 to February 1983. Some preliminary results of the data analyses are reported in the present paper.

2. DISTRIBUTION OF THE SEP EVENTS Sometimes, the GMS/SEM's observed the solar energetic particle (SEP) events at their synchronous orbits. Two examples of the SEP events are shown in Fig.1(a) and 1(b). As seen in the figures, there was apparent increase in each channel, except for the P1 and EL channels. These two channels are omitted from our analyses because they are contaminated dominantly by the geomagnetically trapped or quasi-trapped particles.

About 50 SEP events were observed by the GMS/SEM's for the period (Fig.2). Hourly plots of the SEM data, first, indicate that the time profiles of flux intensities of the SEP events are different from event to event. It seems, however, that they are able to be classified roughly into two groups. One of them is the short rise time (SRT) event group. The rise time of

Table 1. Observational items of the GMS/SEM's.

GMS-1/SEM			GMS-2/SEM		
Channel Name	Particle Type	Energy Range (MeV)	Channel Name	Particle Type	Energy Range (MeV)
P1	protons	1.2 - 4	P1	protons	0.8 - 4
P2	protons	4 - 8	P2	protons	4 - 8
P3	protons	8 - 16	P3	protons	8 - 16
P4	protons	16 - 34	P4	protons	16 - 30
P5	protons	34 - 80	P5	protons	30 - 60
P6	protons	80 - 200	P6	protons	60 - 100
P7	protons	200 - 500	-	-	-
A1	alphas	9 - 70	A1	alphas	8 - 66
A2	alphas	30 - 70	A2	alphas	32 - 66
A3	alphas	65 - 170	A3	alphas	64 - 120
A4	alphas	130 - 250	A4	alphas	120 - 240
A5	alphas	320 - 370	A5	alphas	270 - 370
EL	electrons	> 2	EL	electrons	> 2

The data were obtained by the GMS-1/SEM for Feb.1978 to Dec.1981 and by the GMS-2/SEM for Dec.1981 to Feb.1983.

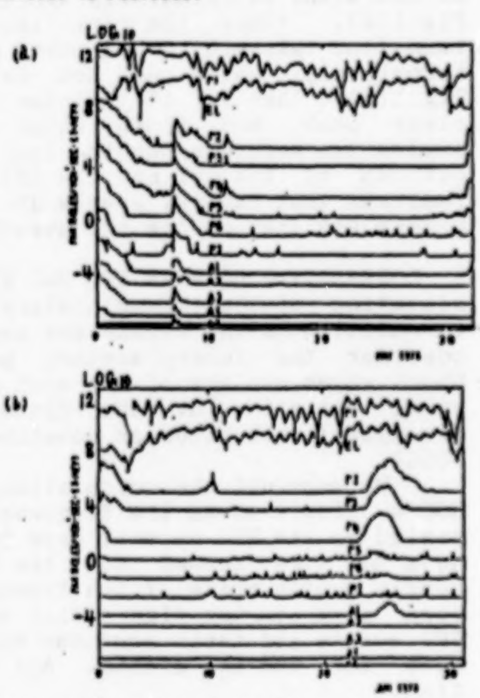

Fig.1. Two examples of the SEP events. Hourly averaged SEM data are plotted for May 1978 (a) and Jun.1978 (b). The event of May 7,1978 is classified as an SRT event, and Jun.23,1978 event as an LRT event. Each channel is separated from others by multiplying factor 10.

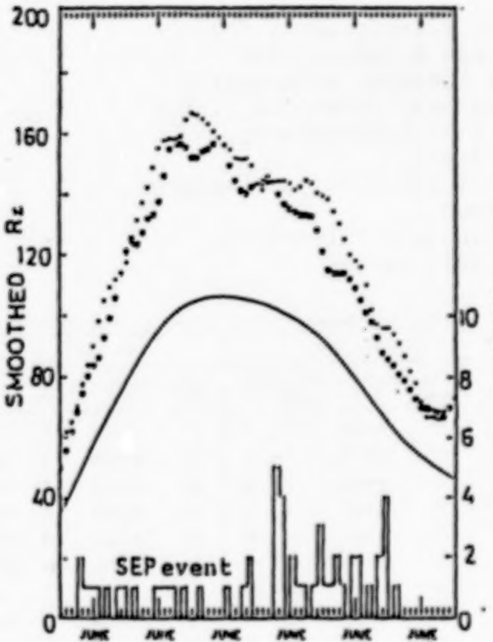

Fig.2. Distribution of the SEP events observed by the GMS/SEM's for the period of Feb.1978 to Feb.1983. This period just coincides with the maximum phase of solar activity cycle 21. (Sun spot data were taken from the SOLAR-GEOPHYSICAL DATA.)

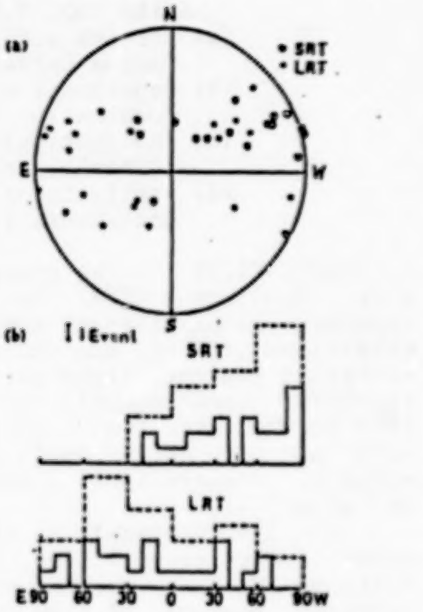

Fig.3. Distribution of the SEP events in the helioiongitude. The parent flares are plotted on the solar disk (a). In the figure (b), helioiongitudinal bin is taken by 10°(solid line) or 30°(broken line).

an SRT event is relatively short. It has a clear peak, as shown in Fig.1(a). (Here the rise time is defined as the time from onset to maximum flux intensity.) The other group is composed of several events, alternatively, which do not belong to the SRT event group (such as in Fig.1(b)), that is, it includes long rise time events, those which have no clear peak, and those which have somewhat complex time profiles. We called the second group the long rise time (LRT) event group. The distributions of the SRT and the LRT events are shown in Fig.3. These figures indicate that the SRT events distribute dominantly on the western hemisphere and many of the LRT events on the eastern.

3. CORRELATION BETWEEN THE SRT EVENTS AND THE PRECEDING SSC's Temporal situation of the interplanetary space will become a very important factor in addition to the steady and averaged configuration of the space, when we consider the interplanetary propagation of solar energetic particles. Shock waves are one of the most dominant sources which affects the temporal situation of the space such as the IMF. Shocks also disturb the geomagnetic situation as sometimes observed as storm sudden commencement (SSC).

We examined the correlation between the SEP events and preceding SSC's. Fig.4 shows the frequency distribution of events which were accompanied by the SSC several days prior to onset of event. In the figure, τ_0 is the time needed for the sun to rotate 180°; it is considered to be nearly double scale of the broadness of interplanetary shocks [5]. It can been seen in the figure that a reasonable correlation exists between the SRT events and their accompanied preceding SSC's, while no correlation exists for the LRT events. And τ is considered as a limit of the correlation.

4. TIME VARIATION OF P/α-RATIO It would be interesting to find tendencies of time variation of the proton-alpha ratio in the context of propagation study, because it is expected that there are some qualitative differences in the effects suffered during the propagation. We plotted

ORIGINAL PAGE IS
OF POOR QUALITY

three ratios corresponding to three energy (per nucleon) ranges, R(L), R(M) and R(H) defined as

$$R(L;t) = [P2(t)+P3(t)]/A1(t),$$
$$R(M;t) = P4(t)/A3(t),$$
$$\text{and } R(H;t) = P5(t)/A4(t).$$

Examples of these plots for an SRT and an LRT events are shown in Fig.5. In the figure, plots of R(H), which is the one of highest energy, fluctuate significantly, because of poor statistics on P5 and A4. From the plots of many events, we may be able to say that R(L) has a constancy in its value during a event for both the SRT and the LRT events but the values are different from event to event. And, for the SRT events, R(M) and R(H) have a tendency to decrease with time, while they were nearly constant for the LRT events. These tentatively identified tendencies are represented in Fig.5 by broken lines.

5.DISCUSSION

5.1 Coronal Propagation: The SEM data are hourly averaged ones and can not provide any information about anisotropy. Hence, it is not possible to discuss coronal propagation in detail. However, we can draw some suggestions about coronal propagation from the data. It is not natural that the mechanism of solar flare responsible for particle acceleration and release would change depending on the heliolongitude of flare position. Therefore, Fig.3 suggests as follows. The differences between the SRT and the LRT events are attributed to the differences of the propagation effects suffered during the propagation between the sun and the earth for each group. As is well known, the region of good connection is 40° - 50° W in the heliolongitude. According to Reinhard et al., the predominantly well guided region is not so narrow, in fact, it is rather more wide; that is the FPR has a size of ~100°. In section 2, we found that the width of distribution of the SRT event was about 100°. This may imply that the solar energetic particles, generated by the flare at a heliolongitude λ, fill up the region with a center of λ and radius of ~50° in heliolongitude, and when the root of the IMF passing the earth is lying in this region, that event will be observed as an SRT event at 1AU. Fig.3 is an evidence of the existence of the FPR. Thus, we would be able to state that the SRT events are distributing in the FPR and many of the LRT events are far from this region. We should, here,

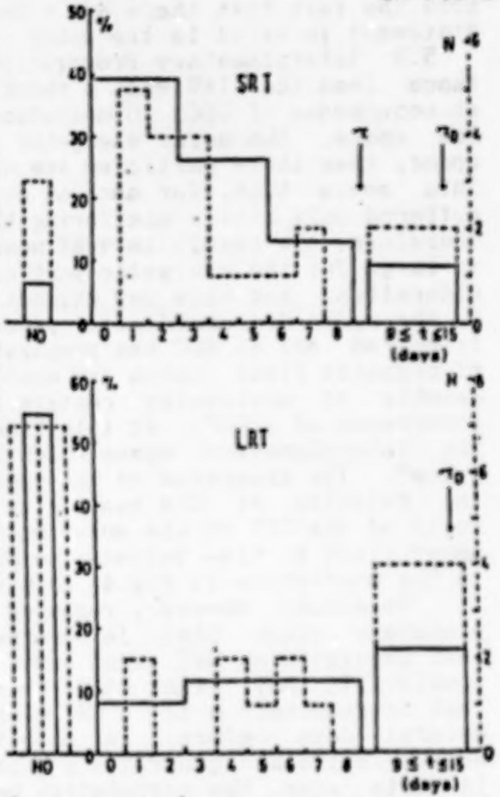

Fig.4. Correlation between the SEP events and their accompanied preceding SSC's. The frequency distribution is shown. The abscissa in the figure represents how many days does occur SSC prior to SEP event. And τ is a limit of the correlation. Diagram indicated by broken line with right hand side ordinate represents the distribution of event number.

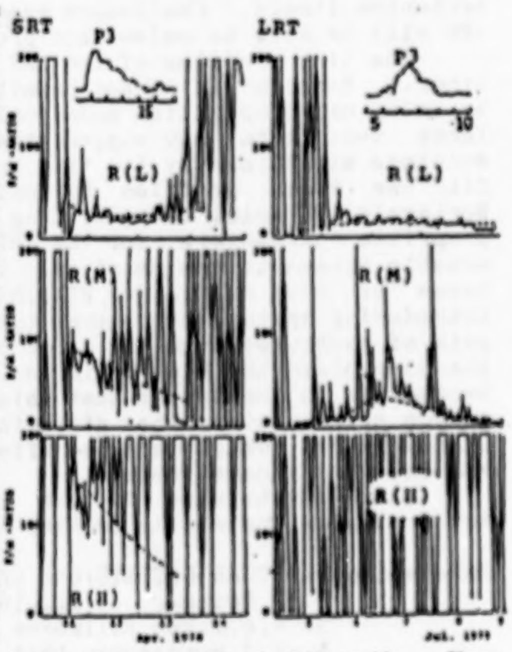

Fig.5. Time variation of P/d -ratio. Three ratios corresponding to three energy ranges are plotted. Tentatively identified tendencies are drawn by hand as broken lines.

note the fact that there are a few exceptions for both groups, and the statement is valid in the sense of averaged picture.

5.2 Interplanetary Propagation: Let us consider the space with distance less than 1AU when a shock has just passed, i.e., immediately after an occurrence of SSC. Observations show that, when a shock has passed in the space, the solar energetic particles propagate in the interplanetary space; then these particles are observed predominantly as an SRT event. This means that, for such an event, most of the energetic particles have suffered only little scattering through their propagation in the space. Therefore, the result is that mean free path, hence diffusion coefficient, is large for the energetic particles with energy (or rigidity) under consideration. And this may suggest the number density of scattering centers in the space decreased after passage of shock. When a shock wave that triggered off an SSC has propagated through the space, the irregularities of magnetic field which are scattering centers were swept out. Thus the density of scattering centers is minimized within several days after an occurrence of a SSC. At this time, it is considered that some region of the interplanetary space which has been swept out by a shock is a "clean space". The cleanness of the space will decay in two ways. One is due to the rotation of the sun . The other is due to the random motion of the roots of the IMF on the solar surface. Therefore, it is inferred that an upper limit in time between the SRT events and preceding SSC's. According to the statistics in Fig.4, this upper limit is 7-10 days.

We should, however, remember the following argument. If the interplanetary shock that is observed as a preceding SSC and the solar flare that generates an SRT event occur in the same active region, then another possibility may exist other than the above mentioned. The active region that is responsible for a SRT event has been in the eastern hemisphere several days before. At this time, it is possible to imagine that such active region has generated a shock wave that is responsible for a SSC. In this case, the correlation between a western hemisphere event and its preceding SSC necessarily exists. Then, the essential condition of the occurrence of SRT events is that the parent flare occurs in the western hemisphere; and the correlation between SRT events and their preceding SSC's is not the cause but a result. If it were a result, it becomes more interested because subsequent occurrences of shock ejection and flare provides informations of prediction of an occurrence of flare and of flare mechanism itself. Continuous measurements of the power spectrum of the IMF will be able to solve this problem.

The time profiles of the LRT events significantly differ from each other. Moreover it is not possible that the LRT events can be understood by using one propagation model only (e.g., anisotropic diffusion model). These two facts may suggest that the interplanetary propagation effects modulate significantly the time profile. For example, when we tried to fit the time profiles by using an anisotropic diffusion model (e.g., Burlaga's ADB model [5]), fitting curve was in good agreement with the appropriate parameters for the SRT events, but for the LRT events, no reasonable agreement was obtained. In the case of the SRT event, time variations of P/α -ratio for R(L),R(M) and R(H) are able to be understood by introducing appropriate energy (or rigidity) dependence of the mean free path of particles. On the other hand, for the LRT event, it is not possible to explain the time variation of P/α by using diffusion theory only because it is considered that this kind of events was suffered the propagation effects other than diffusion effect. Though, it seems that constancy in P/α restricts these effects such as that protons and alphas were modulated in a same manner.

The SEM data used in the present study were provided from the Meteorological Satellite Center, the Japanese Meteorological Agency.

References 1. SOLAR-GEOPHYSICAL DATA,1978.
2. R.Reinhard et al.,1974,Solar Phys.,36,473-494.
3. M.A.I.Van Hollebeke et al.,1975,Solar Phys.,41,189-223.
4. A.J.Hundhausen,1974,'Coronal Expansion and Solar Wind', Springer-Verlag,Berlin.Heidelberg.
5. L.F.Burlaga,1967,J.Geophys.Res.,72,4449-4460.

CORONAL PROPAGATION OF SOLAR FLARE PARTICLES OBSERVED BY SATELLITE

Tsuyoshi KOHNO, Nariaki NITTA, Masami WADA and Tomoshige SUDA*

Institute of Physical and Chemical Research
7-13, Kaga-1, Itabashi, Tokyo 173, Japan

Meteorological Research Institute*
1, Nagamine-1, Yatabe, Tsukuba, Ibaraki 305, Japan

Abstract

Propagation of solar flare particles in corona was studied using the satellite data at the geostationary orbit. By selecting very fast rise time events only, the interplanetary propagation were assumed to be scatter free arrival. The results show that the propagation in corona does not depend on particle energy in 4 - 500 MeV protons, and the time delays from optical flare do not depend on the distance between the flare site and the base of the interplanetary magnetic field which connects to the earth.

1. Introduction

Energetic particles accelerated in a solar flare play an important role in the flare energetics. Because of the propagation effects, however, it is very difficult to know the total energy of all particles in a flare using particle data observed at interplanetary space. There are two propagation effects ; one is coronal propagation from the flare site to the point where they are released from the sun to the interplanetary space , and the other is interplanetary propagation from that point to the earth. Many studies have been done for both propagation processes (Ma Sung et. al. 1975, Schatten and Mullan 1977, Mullan 1983 for coronal propagation and Jokippi 1971, Earl 1976, Ma Sung and Earl 1978, Owens 1983 for interplanetary propagation). Using 80 solar flare data, Ma Sung et. al. showed that particle propagation is independent of both rigidity and energy. This is very hard to understand with normal diffusion processes such as proposed earlier by Reid 1964. Schatten and Mullan proposed a magnetic bottle model to interpret the fast non diffusive propagation in the corona.

2. Observation and data presentation

The solar proton data were obtained from Japanese Geostationary Meteorological Satellite (GMS-1,GMS-2). The continuous data are available from February 1978. GMS-1 was switched to GMS-2 on December 21, 1981. The energy range of data used here is 4 - 500 MeV and 4 - 100 MeV for GMS-1 and -2, respectively. The differentially divided energy channels are seven and five for each.

We assumed that the coronal propagation effect can be separated from interplanetary one by selecting very fast rise time event only, which can be considered as scatter free propagation in the interplanetary space. We have chosen 18 events in the period from September 1977 to December 1982. The criterion of "fast rise" is not so severe but we selected having a rise time (from start of increase to the maximum) of less than a few hours. We assume the time profiles at the base of the garden hose lines of interplanetary magnetic field which connect to the earth can be seen from these so-called scatter free events which means the modulation during the propagation in space can be neglected.

Table 1. Scatter free arrival events observed by GMS-1, -2.

Date	G	Hα flare			SID		SWV	IMF	ρ
		onset	location	imp	onset	imp	km/sec	deg	deg
Sep.19 77	G	0955	N08 W57	3B	1028	3	330	W69	12
Sep.24 77	G	0539?							
Apr.11 78		1334+8	N22 W56	3	1401	3	505	45	30
Sep.23 78	G	1944+3	N35 W50	3B	0945	2+	340	66	32
Feb.17 79		1905	N16 W28	SB	1905	1-	310	73	50
Aug.21 79	G	0550	N17 W40	2B	0607	1-	600	38	10
Apr.10 81	G	1632	N08 W36	2B	1642	3	380	59	27
Apr.24 81		1346	N20 W50	2B	1348	2+	780	29	32
May 10 81		0715	N06 W73	1B	0717	1	340	66	11
Jul.20 81		1310	S26 W75	1B	1310	1	410	55	37
Jan.31 82		0020E	S13 E08	2N	2329)	3	(380)	59	66
Mar. 7 82		0308E	N17 W53	2B	0303	2	370	61	25
Jul.22 82		1648	N16 W89	1F	1645	2+		55	35
Nov.22 82		1741	S11 W36	1N	1742	2		55	23
Nov.26 82		0230	S11 W86	2B	0235	2		55	33
Dec.17 82		1820	S07 W20	3B	1820	3		55	35

G: Ground level enhancement, SWV: Solar Wind Velocity
ρ: angular distance between flare site and the base of IMF

Fig.1 gives intensity time profiles of typical example of a flare of August 21, 1979. Time A means the Hα flare start. The two lines in the each energy channel indicate the time delay band from optical flare observation assuming the travelling distance of 1.2 AU with the particle speed corresponding to each energy band. In the bottom of Fig.1, we can see that the intensity time profiles and the onset times of increase of all channels nearly coincide after correction of the propagation time. For the other events, nearly the same tendency can be seen with two exceptions (May 7, 1978 and Dec.7, 1981), although the average shape of time profiles and the onset time delays from the optical flare are different from flare to flare. These 16 flare characteristics are summarized in Table 1. We understand the two exceptions are special cases which can be interpreted by some interplanetary modulation as already reported by Kohno and Wada 1979.

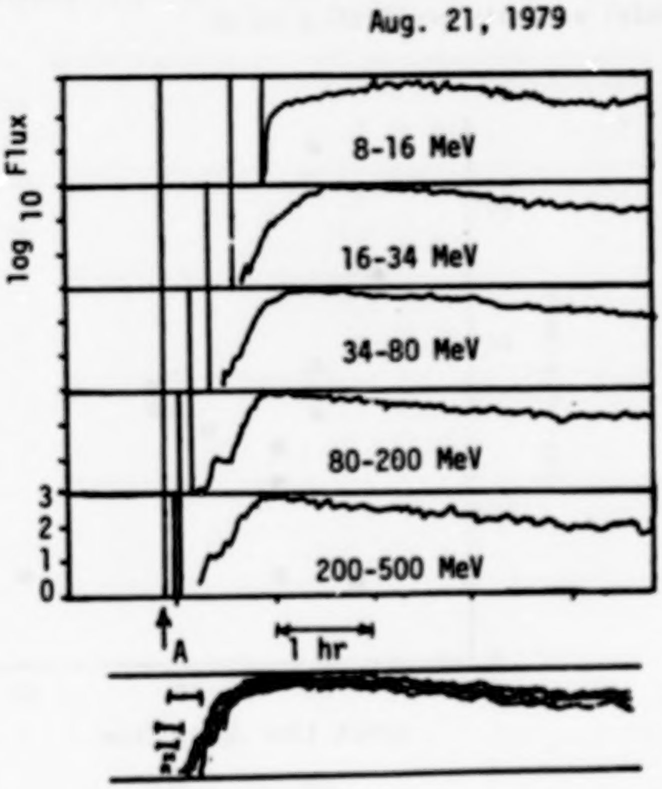
Aug. 21, 1979

Fig. 1 Examples of time profiles of two minutes averaged data normalized to the maximum flux. Time A shows the Hα start. two vertical lines in each channel indicate the time delay from optical observation depending on particles velocity of each channel

In order to see the dependence of the onset time delays from the optical flare on the distance between the flare site and the base of IMF which connects to the earth, we used the observed solar wind velocity data (King 1977, 1979) if available and mean value of 410 km/sec if not available. These distances thus obtained are shown in the last column of Table 1. In Fig.2, the relation of this distance vs the onset time delay from optical flare is plotted. It is clear that there is completely no relation between the two parameters. The mean value of the onset time delay from optical flare is about 30 minutes.

3. Discussion and conclusion

What we have shown here can be summarized as : i) When the travel times between the sun and the earth are adjusted, the intensity time profiles and the onset times of 4 - 500 MeV protons are almost same in a flare. ii) Distribution of onset time delays from optical flare has a mean value of 30 minutes and there is completely no relation with the distance between the flare site and the base of the IMF. This is another proof of energy-rigidity independent propagation in corona in addition to the results of Ma Sung et. al. 1975. Schatten and Mullan have proposed the magnetic bottle model to interpret the rigidity-energy independent propagation in corona. The bottles produced by flares serve as temporary traps of particles. They may have the dimension of half angle near 60° , which result in fast azimuthal propagation inside, and rather slow leakage from the bottle. The present results of analysis may match to this model. Our mean time scale of particle release from that bottle is 30 minutes while their model suggests about 60 minutes.

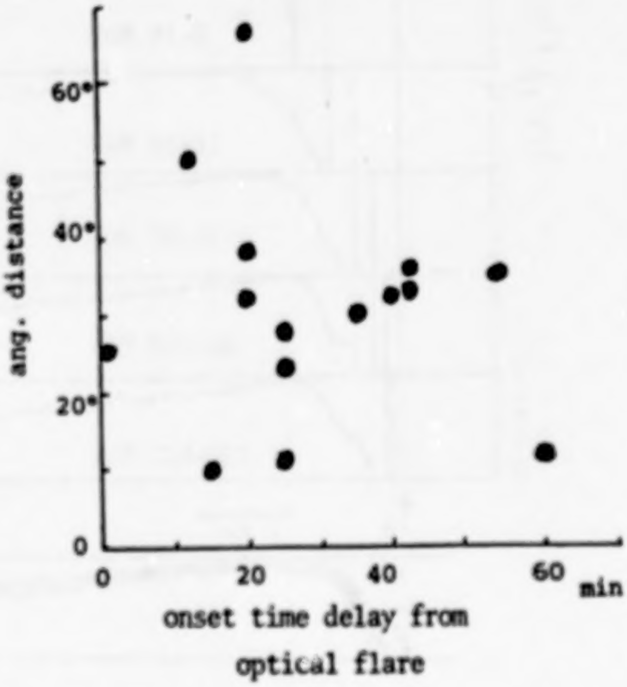

Fig.2
Relation of particle increase onset time delays from optical flare vs the distance between the flare site and the base of IMF. As shown in Table 2, no appropriate flare was found for one sample out of 16.

Mason et. al. (1984) also showed that there is no correlation between the relative abundances and separation angle, nor is there a significant correlation between the sizes of the relative abundance fluctuations. They proposed from this results the possible large scale shock acceleration model. Our results also support their assumption.

We acknowledge the Meteorological Satellite Center for providing the data.

References

Earl, J.A., *Ap.J.*, 208, 301, 1976.
Jokipii, J.R, *Rev. Geophys. Space Phys.*, 9 ,27, 1971.
King, J.H. NSSDC/WDCA-R&S 77-04, 77-04a, 79-08, 1977, 1979.
Kohno, T. and M. Wada, *Geophys. Res. Lett.*, 6, 421, 1979.
Mason, G.M., G. Gloeckler and D. Hovestadt, Ap. J., 280, 902, 1984.
Ma Sung, M.A.I. Van Hollebeke and F.B. McDonald, 14th ICRC, 5, 305, 1975.
Ma Sung and J.A.Earl, *Ap.J.*, 222, 1080, 1978.
Mullan, D.J., Ap.J., 269, 765, 1983.
Owens, A.J., *J. Geophys. Res.*, 84, 4451, 1979.
Schatten, K.H. and D.j. Mullan, *J. Geophys. Res.*, 82, 5609, 1977.

N85-34808

SH 3.1-3

CORONAL PROPAGATION OF FLARE ASSOCIATED ELECTRONS AND PROTONS

Schellert, G., Wibberenz, G., Kunow, H.
Institut für Reine und Angewandte Kernphysik, Universität Kiel
Olshausenstr. 40-60, 2300 Kiel, FR Germany

ABSTRACT

A statistical study of characteristic times and intensities of 36 solar particle events observed between 1977 and 1979 by the Kiel Cosmic Ray Experiment on board HELIOS-1 and -2 has been carried out. For ∿ 0.5 MeV electrons we order the times of maximum and the absolute intensities with respect to angular distance from the parent flare. Discussion of coronal parameters in terms of Reid's model leads to typical time constants for coronal diffusion and escape.

1. Introduction. Particle intensities observed in interplanetary space are a superposition of coronal and interplanetary propagation effects which are difficult to separate. In this paper we use statistical studies of a large number of events to investigate the properties of solar transport of flare particles.

2. Coronal angular dependence of maximum times. Assuming only diffusive propagation in interplanetary space it can be shown that the maximum times of solar particle events can be approximated by (1)

$$T_{max} = t_{max}^{ipl} + c_m \qquad (2.1)$$

in good agreement with the full numerical solution of the convolutional integral. C_m is the time-to-maximum of the coronal injection and t_{max}^{ipl} would describe the interplanetary propagation for δ-function injection.

Using the model of Reid (2) for solar particle transport and a simple model for interplanetary diffusion leads for sufficiently large angular distances ϕ to

$$T_{max} = t_{max}^{ipl} + \frac{\phi}{2} \sqrt{t_c t_L} \qquad (2.2)$$

In this case c_m increases linearly with angular distance ϕ.

Maximum times versus ϕ for ∿ 0.5 MeV electrons with diffusive time intensity and time anisotropy profiles are shown in Figure 1. Only events were selected for which the coronal magnetic connection point of the spacecraft is west of the corresponding flare. The H_α-onset has been chosen as acceleration time. Apparently the nearly constant propagation times for small angular distances ϕ are described by a fast propagation region (3) with a mean extension of ∿ 26°. The time constants seem to increase linearly for larger angular distances as predicted in (2.2). A least squares fit to the data results in a geometrical mean of the two time constants for coronal diffusion and escape of

$$\sqrt{t_c t_L} \approx 7.5 \text{ h}$$

Coronal transport effects can be neglected within the fast propagation region, so that measured maximum times would only be determined by interplanetary propagation. For a radially independent diffusion coefficient K we obtain with

$$t_{max}^{ipl} = \frac{r^2}{6K}$$

an upper limit for the mean free path parallel to the average interplanetary field of ~0.12 AU for r = 1 AU in good agreement with earlier work (4).

3. Coronal angular dependence of maximum intensities. In the 1977 - 1979 period we were able to obtain maximum intensities from both spacecraft HELIOS-1 and -2 for 12 events. Differences due to interplanetary propagation are corrected by assuming an r^{-2} dependence of the absolute intensities. Although the actual radial dependence can be derived only if coronal and interplanetary effects are taken into account in a combined propagation model, our statistical analysis shows that the coronal distance dependence is much stronger than the effects of different normalization factors $(r/r_E)^n$ for $2 \leq n \leq 3$. Radially normalized maximum intensities are therefore a measure of the number of particles at the injection maximum I_{max} for the respective angular distance. Using Reid's model in the range of large ϕ I_{max} is controlled only by the ratio of the time constants for coronal diffusion and escape:

$$I_{max} = I(c_m) \sim \frac{1}{\phi} \exp\left\{ -\sqrt{\frac{t_c}{t_L}}\,\phi \right\} \tag{3.1}$$

Since the exponential term will dominate the ϕ^{-1}-dependence, this leads to

$$I_{max} \sim \exp\left\{ -\sqrt{\frac{t_c}{t_L}}\,\phi \right\} \tag{3.2}$$

Comparing the normalized maximum intensities for the same event as observed by two spacecraft at different coronal connection distances from the flare allows to determine the ratio t_c/t_L:

$$\frac{I_{max}\,(\phi_2)}{I_{max}\,(\phi_1)} = \exp\left\{ -\sqrt{\frac{t_c}{t_L}}\,(\phi_2 - \phi_1)\right\} \tag{3.3}$$

Figure 2 shows the amplitude variations with coronal angular distance for ~0.5 MeV electrons. In order to disregard the different event sizes we normalize the respective maximum amplitudes to obtain $I_{max} = 1$ for $\phi = 0°$.

The slope varies considerably, apart from a group of four events with similar behaviour. It is not useful to describe this amplitude variation with angular distance by an average value of t_c/t_L. Regarding individual events observed by at least two spacecraft at different solar longitude we always find intensity variations larger for protons than for electrons. Figure 3 shows an example for the event of April 11, 1978, as observed by HELIOS-1 and -2. The large difference in temporal delays for protons as compared to electrons is immediately evident. In general the difference in amplitude variation between the two particles is more pronounced than in this example (see e.g. 1).

4. Conclusions. For non-relativistic protons Ng and Gleeson (5) found $t_c = 50 - 100$ h and $t_L = 10 - 15$ h between 1 - 50 Mev. Mc Guire et al. (6) derived $t_c \gtrsim 90$ h and $t_L \gtrsim 9$ h for 3 - 60 MeV protons taking into account a typical extension of the fast propagation region of ~25°.

The value from (6) for protons $t_c t_L \gtrsim 810\ h^2$ in contrast to our value $t_c t_L \gtrsim 55\ h^2$ quoted above for electrons shows that coronal transport occurs much faster for electrons for which the average rate of increase $\Delta T_m/\Delta\phi$ is almost a factor of 4 smaller. From the coronal transport models we can exclude electric field drift. This process proposed in (7) was based on (a) a linear rate of increase $\Delta T_m/\Delta\phi$ with ϕ and (b) the suggested independence of coronal transport from particle type (8). The simple Reid model leads to the observed linear dependence, based on the combination of coronal diffusion and escape, whereas diffusion alone would lead to $T_{max} \sim \phi^2$. We also find clear evidence that electrons are transported faster through the corona.

Any other process leading to coronal transport independent of particle type is also excluded by our observation (bird cage model (9) and coronal shock).

The considerable spread in the amplitude variation (Figure 2) precludes any simple classification scheme with coronal distance only. There is no apparent association of the size of the variation with the location of the coronal connection point inside or outside the fast propagation region. The observations suggest that we have no universal process for coronal diffusion as e.g. inherent in the Fisk and Schatten (10) model, but a process which varies highly with individual coronal magnetic field structures.

5. Acknowledgements. The authors appreciate the collaboration and support from the other members of the HELIOS-team from the Kiel University. This work was partly supported by the German Bundesminister für Forschung und Technologie.

References

1. Wibberenz, G., K. Kecskeméty, H. Kunow, A. Somogyi, B. Iwers, Y.I. Logachev, V.G. Stolpovskii, (1985), Coronal and interplanetary transport of solar energetic protons and electrons, to be published
2. Reid, G.C., (1964), J. Geophys. Res. 69, 2659 - 2667
3. Reinhard, R. and G. Wibberenz, (1974), Solar Phys. 36, 473 - 494
4. Palmer, I.D., (1982), Rev. Geophys. Space Phys. 20, 335 - 351
5. Ng, C.K. and L.J. Gleeson, (1975), Solar Phys. 46, 347 - 375
6. Mc Guire, R.E. et al., (1983), 18th Int. Cosmic Ray Conf. 10, 353 - 360
7. Reinhard, R. and E.C. Roelof, (1973), 13th Int. Cosmic Ray Conf. 2, 1378 - 1383
8. Ma Sung, L.S. et al., (1975), 14th Int. Cosmic Ray Conf. 5, 1767 - 1772
9. Newkirk, G. and D.G. Wentzel, (1978), J. Geophys. Res. 83, 2009 - 2015
10. Fisk, L.A. and K.H. Schatten, (1972), Solar Phys. 23, 204 - 210

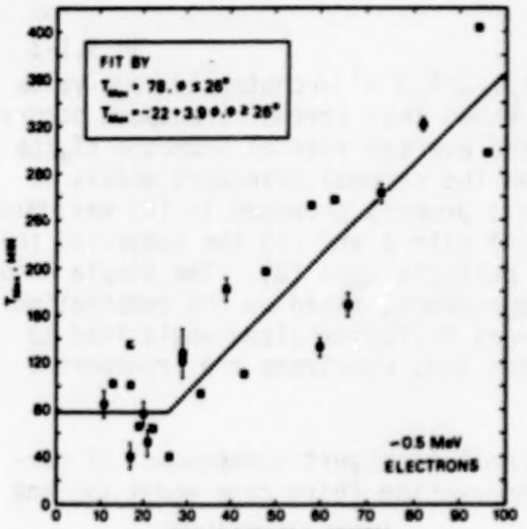

Fig. 1: Times to maximum of ~0.5 MeV electrons versus coronal angular distance for events with magnetic connection west of the flare. Separate least square fits are given inside and outside the mean fast propagation region.

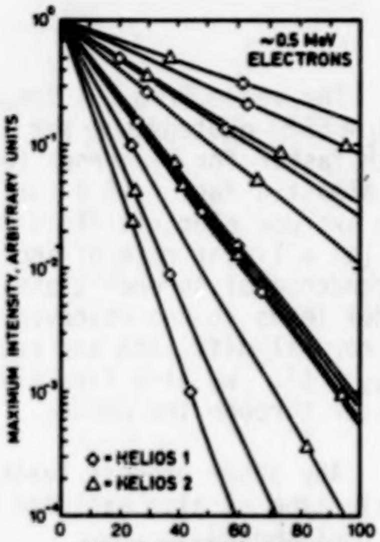

Fig. 2: Normalized maximum intensities for 1977 - 1979 ~0.5 MeV electron events measured on 2 separate spacecraft versus coronal angular distance.

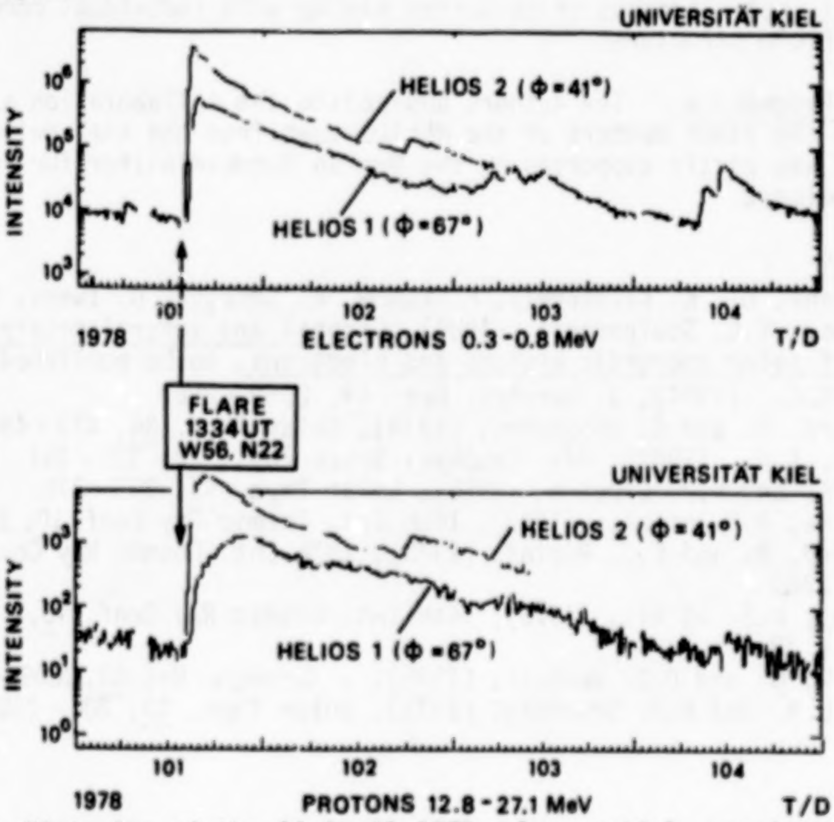

Fig. 3: Histories of the 11 April 1978 solar particle event are shown for protons and electrons as measured by HELIOS-1 and -2 at different coronal angular distances from the flare.

N85-34809

SH 3.1-5

GEOMETRY OF THE DIFFUSIVE PROPAGATION REGION IN THE AUGUST 14, 1982, SOLAR ELECTRON EVENT

Paul Evenson
Bartol Research Foundation of the Franklin Institute
University of Delaware
Newark, Delaware 19716 USA

ABSTRACT On August 14, 1982, relativistic electrons arrived promptly after an impulsive gamma-ray flare, indicating that very little scattering was taking place in interplanetary space. By ignoring anisotropy data the time profile of the event is well described by interplanetary diffusion except for the derived particle injection time. This discrepancy provides independent evidence that the particles are diffusing in a volume close to the sun rather than in interplanetary space. The flux at maximum method of determining the number of particles produced is still a good approximation when appropriately applied.

1. **INTRODUCTION** With the recent availability of high resolution gamma ray data from the solar maximum mission accurate counting of particles emitted by solar flares has assumed a new importance. Gamma ray fluences yield estimates for the number of particles interacting in the target which have been used to calculate the fraction of particles escaping the target by comparison with interplanetary observations (Von Rosenvinge et al. 1983, Evenson et al. 1984). To date these comparisons have been made using the time to maximum method (Parker, 1963) to estimate the number of escaping particles. It is well recognised that this method removes most sensitivity to the interplanetary diffusion coefficient but depends explicitly on the assumption that the particles are diffusing isotropically in interplanetary space and that the distance from the source to the observer is known.

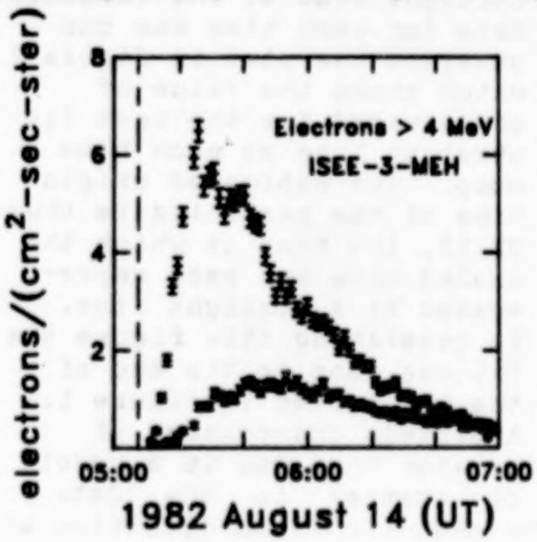

FIGURE 1

2. **THE 1982 AUGUST 14 ELECTRON EVENT** On the 14th of August, 1982, a solar flare located at a longitude of W66 produced an intense, highly impulsive burst of radiation (x-rays through MeV gamma rays) at 05:07:30 earth received time (Kane et al. 1985). The time profile of a relativistic electron event which followed this flare is shown in figure 1, where the dashed line gives the time of the photon impulse. A large anisotropy is evident -- the

upper trace gives the flux from the direction of the sun along the interplanetary magnetic field line and the lower trace gives the flux back toward the sun. When the observed anisotropy is considered it is obvious that isotropic diffusion in the interplanetary medium cannot be the source of the shape of the time profile. Kane et al. (1985) conclude that the time profile of this event can be explained by impulsive production of all electrons at the time of the photon impulse, followed by coronal diffusion (Reid, 1964) and interplanetary focused diffusion (Bieber et al., 1980).

3. VOLUME OF THE DIFFUSION REGION The combination of two dimensional diffusion with escape in the Reid model is in fact similar to three dimensional diffusion (Ford et al., 1977). Therefore if one ignores the anisotropy and models the average electron flux as a function of time by interplanetary isotropic diffusion a very good fit is obtained with an estimated mean free path of 0.15 AU. It is interesting to note that one can deduce that the particles have not in fact diffused in interplanetary space without reference to the anisotropy information. This conclusion is reached by considering plots of

$$\ln(I\cdot(t-t_0)^{3/2}) \text{ versus } 1/(t-t_0)$$

(e.g. Cline and McDonald, 1968). Data scaled in this manner lie on a straight line if and only if the correct choice for the origin time (t_0) of the particles is made. The slope of the line then gives the diffusion coefficient and the intercept gives the total number of particles released. determining the particle number in this manner is exactly equivalent to using the time of maximum method. By stepping the assumed origin time in small increments and fitting a straight line to the rescaled data for each time one can generate the plot in figure 2 which shows the value of chi-squared for the best fit straight line at each time step. The estimated origin time of the particles is thus 05:15, the time at which the scaled data are best represented by a straight line. In generating this figure the fit was done to the sum of the two curves in figure 1. A minimum chi-squared of greater than one is a result of scatter in the data introduced by fluctuations in the magnetic field direction at the spacecraft rather than a systematic deviation from a diffusive shape.

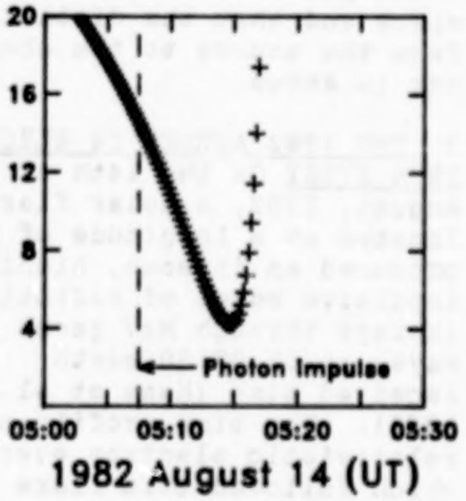

FIGURE 2

The time axis of figure 2 has been adjusted to correspond to the arrival time at the spacecraft of a photon emitted from the sun at the time of the supposed acceleration of the particles. The time of the photon impulse is indicated with a vertical line. Not only is the time derived from the diffusion fit much later than the gamma ray flash, it actually is later than the arrival of the first electrons at the spacecraft. This seemingly absurd finding is actually the desired result; it indicates that the observer is not embedded in the diffusion volume but rather is seeing the diffusion process as reflected in the continuous escape of a small fraction of the diffusing particles which then propagate to the spacecraft nearly unimpeded by scattering in the interplanetary medium.

The error in the acceleration time estimate immediately provides a limit on the volume of the diffusion region. Since the transit time of an electron along the Parker field is eleven minutes it can be shown that an eight minute error implies that the radius of the diffusion region cannot be larger than 0.3 AU. Actually the situation is more complex than this because interplanetary scattering is influencing the shape of the time profile. Using the profile of the outward flux (upper trace of figure 1) yields a larger time error whereas a fit only to the backward flux interestingly gives an origin time very much closer to the gamma ray flash. This backward flux profile of course is produced predominantly by interplanetary scattering. In conjunction with other work (Bieber et al., 1985) I have done a detailed fit to this event with the conclusion that the time evolution is consistent with diffusion in the solar corona, although a diffusion region with dimensions as large as 0.1 AU probably can not be excluded.

4. NUMBER OF PARTICLES ACCELERATED The pitch angle distribution of the electrons at the spacecraft can be determined from the data, integrated over time, and projected in the radial direction to obtain the electron fluence at the spacecraft, 25200 electrons per square centimeter. Reid (1964) shows that the net outflow from any point on the surface can be determined analytically given the distance from the flare to the foot of the field line, the loss time constant and the diffusion coefficient. Using the solar wind speed (Bame, private communication) of 280 km/sec I estimate that the flare occured 25 degrees from the best connection field line and then obtain a loss time constant of 1/hr and a mean free path of 500 km from the fit to the data. Scaling the spacecraft fluence to the solar surface by the square of the distance to the center of the sun and using the Reid expression for the fluence from the solar surface implies the production of $3.1x10^{31}$ electrons. This may be compared with an estimate of $6.2x10^{31}$ obtained using the directionally averaged flux and the time of maximum method.

The closeness of these two numbers is not completely fortuitous. As Reid (1964) points out, the fluence of particles leaving the sun is not nearly so strong a function of distance from the flare as is the maximum intensity. In the limit of slow escape the escaping fluence becomes independent of position. With the parameters derived for this event the fluence at a point 25 degrees removed from the flare site is only a factor of three more than the fluence obtained by dividing the total number of particles by the surface area of the sun. (The two fluences are approximately equal 55 degrees from the flare site.) If the subsequent diffusion in interplanetary space produces a time profile which is long compared to the duration of the injection then the time of maximum method can still yield reliable results even though the diffusion in connection longitude is taking place on the sun. In the 1982 August 14 event effects of interplanetary and coronal diffusion on the time profile are comparable. Therefore the two methods give consistent results. A good rule of thumb for counting particles from a flare would be that if the net fluence is easy to determine, i.e the event is very anisotropic, use the fluence and the Reid model. On the other hand, when an event is sufficiently isotropic that the fluence is statistically difficult to determine it is likely that the conditions for the validity of the time of maximum method are satisfied.

5. ACKNOWLEDGEMENTS I would like to thank Drs. J.A. Earl and J.W. Bieber for many helpful discussions. This work was supported in part by NASA grant NAG-374.

6. REFERENCES.

Bieber, J.W. et al., J. Geophys. Res., 85, 2313, 1980.
Bieber, J.W. et al., 19th ICRC paper SH 4.2-23, 1985.
Cline T. and F.B. McDonald, Solar Phys., 5, 507, 1968.
Evenson, P., et al., Astrophys. J., 283, 439, 1984.
Ford, T. et al., J. Geophys. Res., 82, 4704, 1977.
Kane, S.R., P. Evenson and P. Meyer, submitted, 1985.
Parker, E., Interplanetary Dynamical Processes, ed. R.E. Marshak, (New York: Wiley) 1963.
Reid G., J. Geophys. Res., 69, 2659, 1964.
Von Rosenvinge, T.T., et al., 17th ICRC, 3, 28, 1981.

N85-34810

PECULIARITIES OF PROPAGATION OF CHARGED PARTICLES IN SOLAR CORONA

E.I.Morozova, N.F.Pisarenko, N.A.Mikryukova
Space Research Institute, 117810 Moscow, USSR

V.V.Klimenko, V.E.Timofeev, Yu.G.Shafer
Institute of Cosmophysical Research & Aeronomy
Lenin Ave., 31, 677891 Yakutsk, USSR

ABSTRACT

The influence of boundaries of the large-scale unipolar magnetic regions (UMR) on the Sun upon the charged particle propagation in the solar corona and interplanetary space is investigated. Increases of the charged particle fluxes from solar flares on November 4 and 20, 1978 detected by "Venera-11" and "Prognoz-7" and on December 7, 1982 by "Venera-13" and "GMS-2" were analyzed.

1. The investigations of a large number of solar flares located at various heliolongitudes revealed some regularity in dependence of time of the coronal particle transfer from the flare heliolongitude [1,2]. It was shown that out of the region of fast propagation of particles the speed of coronal transfer of particles is 17 - 40°/hr [2]. However, it is still unclear where the deceleration of a flux of particles propagating in corona occurs and with what the decrease of transfer speed is associated.

2. To estimate the influence of boundaries of the large-scale UMR upon temporal and spectral characteristics of charged particle fluxes the increases of fluxes associated with November 4 and 20, 1978 and December 7, 1982 solar flares were investigated (Figure). Each event was observed simultaneously at two spacecraft located at various azimuthal and radial distances from the Sun. In Figure the synoptical maps of photospheric magnetic fields are shown where ■F are places of the flares [3]. Here the projections of force line bases (injection points) associated with spacecraft are shown. The points of connection on the Sun are calculated taking into account the average speed of solar wind on Prognoz-7 and IMP-8 data.

The injection moment of particles into the force tube connected with spacecraft was determined on [5]. On difference between moments of injection and generation of particles (maximum in H_α) the speed of particle flux transfer in the corona is estimated.

For 4.11.78 event the fast arrival of particles to the point of connection with Prognoz-7 (flare and point of connection are in one UMR) is observed and the transfer speed

ORIGINAL PAGE IS
OF POOR QUALITY

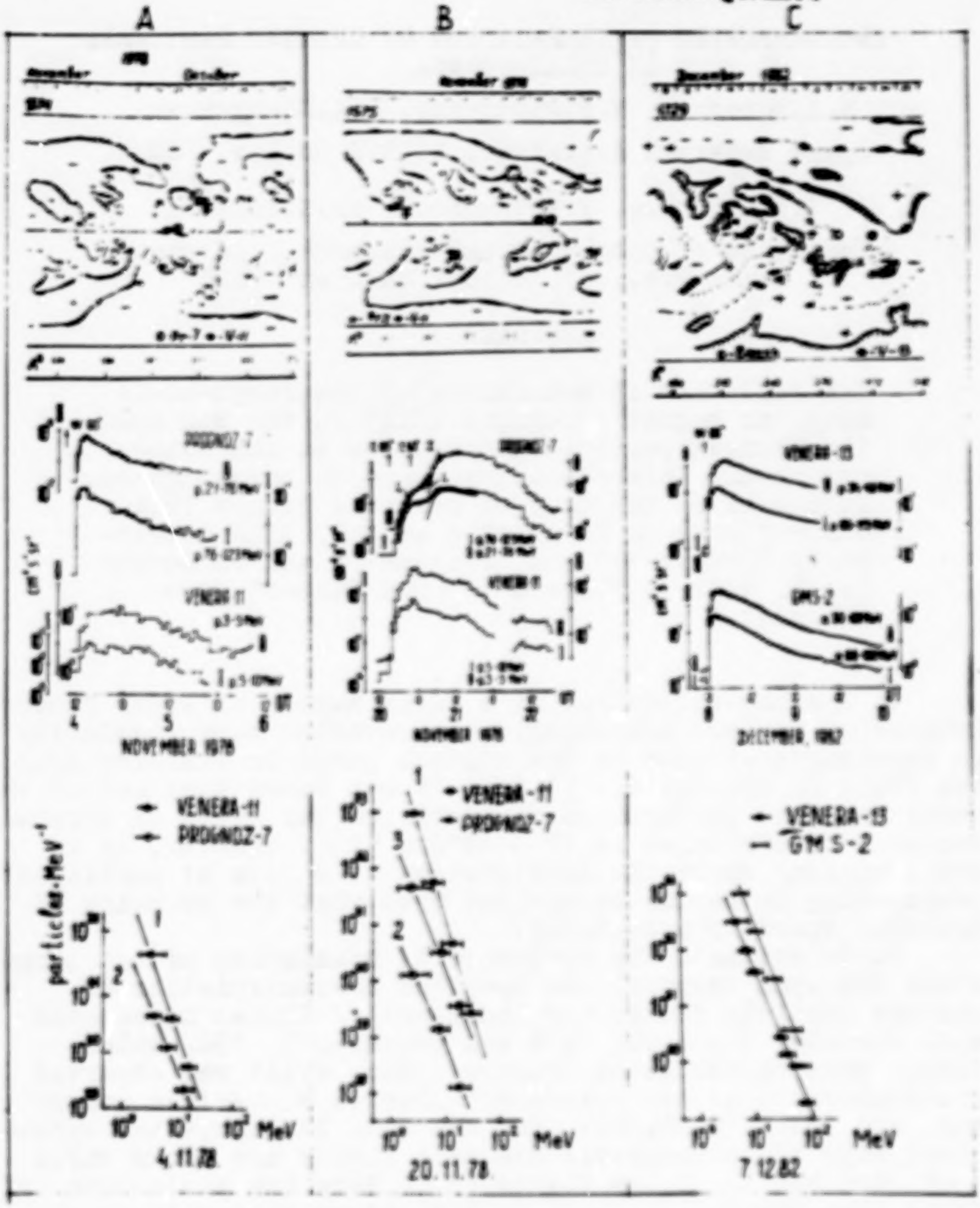

is ~ 145°/hr. At the injection point Venera-11 (a connection point) a significant delay of particles is observed and an average particle transfer speed in the corona to the connection point with Venera-11 is only ~ 12°/hr. It is obvious that such a decrease of the average speed is caused by the particle propagation across the UMR boundary. Since the azimuthal distance between injection points Prognoz-7 and Venera-11 is ~ 8° the estimated transfer speed of particles across the UMR boundary is ~ 5°/hr.

In 20.11.78 event (Figure,B) for Venera-11 the moments of injection and generation of particles coincide. The injection point Venera-11 is at one UMR with the flare and the fast transfer of particles inside UMR is realized. The particles from the flare into the force tube connected with Prognoz-7 are injected twice. The first moment of the injection (1525 UT) is delayed with respect to the moment of generation by ~33 min which yields the speed of particle transfer in the corona to the injection point Prognoz-7 ~ 135°/hr. The second injection (the arrival of the main "mass" of particle flux) occured at 1725 UT and the average speed particle transfer in the corona to the injection point Prognoz-7 is ~30°/hr. Since the azimuthal distance between injection points Venera-11 and Prognoz-7 is ~ 6° and they are located at various UMR near the boundary then the estimations of speed of particle flux transfer across the boundary yield ~ 2.5°/hr [4] . In 7.12.82 event (Figure, C) the place of the flare and the injection point for Venera-13 and GMS-2 are located in one UMR. The moments of generation and injection of particles within measurement errors coincide, i.e. the fast particle transfer in the corona is realized.

3. To determine a total number of particles at the injection point and to estimate the efficiency of the UMR boundary consider the propagation character of charged particles in the interplanetary medium. The location of force line bases connected with Venera-11 and Prognoz-7 (Figure,A,B) near UMR boundary determined significantly a complicated structure of temporal profiles of particle fluxes. UMR boundaries influence not only upon particle propagation in the solar corona but indirectly upon the character of particle propagation in the interplanetary medium. For instance, more complicated than in Prognoz-7 temporal structure of particle flux increase on Venera-11 was caused by a prolonged particle injection (for 4.11.78) into the force tube connected with Venera-11 and by a presence of large-scale interplanetary magnetic field structures near the UMR boundary (for 20.11.78). For illustration the temporal profiles of intensities only at two energy ranges (the average graphs of Figure,A,B,C) were chosen.

Temporal profiles of intensity were approximated by a solution of the diffusion equation [6] . The differential energy spectra of particles at injection points are presented in Figure, A,B,C, bottom. In Figure,A,B the curves 1 show spectra at injection point located in one UMR with flare (the fast particle transfer in the corona). The curves 2 are the spectra at injection point observed behind UMR boundary (the curve 3 transfer across the boundary). The curve 3 is the spectrum of particles propagating fastly across the UMR boundary.

A comparison of a total number of particles before and after the boundary allows to estimate its "transparency". For proton energies E_p ~ 5 MeV only ~15% (4.11.78) and ~8% (20.11.78) of a total particle flux penetrated across the boundary, for E_p ~ 20 MeV this value is ~ 25% (4.11.78) and

~ 20% (20.11.78). It is interesting to compare the absolute particle fluxes detected at injection points of Venera-11 and Prognoz-7 20.11.78 propagating fastly in the corona (curves 1 and 2, Figure, B). The ratio of these fluxes determines actually the efficiency of fast particle transfer across the UMR boundary. For $E_p \sim 5$ MeV only ~ 0.3% of particles is observed behind the boundary, for $E_p \sim 20$ MeV energies this value is ~ 0.7%.

In the event of 7.12.82 (Figure, C) the absolute particle fluxes on GMS-2 are by an order of magnitude larger than on Venera-11. Here there are no influences of UMR boundaries upon charged particle transfer in the corona. Such a difference in a value of flux confirms the earlier found experimental fact [7] that on closed force lines of geomagnetic field (L ~ 6.6) the measured particle flux is larger than its values beyond the Earth's magnetosphere due to the isotropization effect.

4. Thus, the boundary of the UMR decreases significantly the effective speed of particle transfer in the corona. Within the UMR boundary the speed of particle transfer is 2 ÷ 5°/hr. Only insignificant portion of flare particle flux propagates across the boundary without the change of the speed and density. At estimation of absolute values of particle fluxes from the flare it is necessary to take into account the influence of not only boundaries of large-scale UMR on the Sun but also the peculiarities of processes of interaction of particles with interplanetary and geomagnetic fields.

The authors are grateful to Dr.M.Wada for the kindly presented GMS-2 data.

References

1. Reinhard,R., Wibberentz, G.,(1974),Solar Phys., vol.36, p.473.
2. Ma Sung, L.S., Van Hollebeke,M.A., McDonald,F.B., (1975),Proc.14-th ICRC, vol.5, 1979.
3. Solar Geophys.Data,(1978),No.412, Part 1;(1979), No.417, Part II;(1983),No.461, Part I;(1983),No.462, Part I.
4. Klimenko,V.V., i dr.,(1982),Izv.AN SSSR, Ser.fiz., 46, No.9, 1702.
5. Walnichek, B.I. i dr.,(1980),Geomagnetizm i aeronomiya, 20, No.5, 777.
6. Krimigis, S.,(1965),J.Geophys.Res., 78, 1007.
7. Bezrodnykh, I.P. et al.,(1981),Proc.17-th ICRC, Paris, 3, 401.

N85-34811

SOME CHARACTERISTICS OF THE SOLAR FLARE EVENT OF FEBRUARY 16, 1984

H. Debrunner and E. Flückiger
Physikalisches Institut, University of Bern,
3012, Bern, Switzerland

J. A. Lockwood
Space Science Center, University of New Hampshire
Durham, New Hampshire 03824 USA

R. E. McGuire
NASA Goddard Space Flight Center
Greenbelt, Maryland 20771 USA

1. Introduction In the morning of February 16, 1984 a solar cosmic ray event (GLE) was recorded by the world-wide network of neutron monitors (NM). In Fig. 1 we show the counting rate vs. time profile of the Goose Bay NM (geog. lat. = 53.3°N, geog. long. = 299.6°E) where the increase is expressed as percent of the counting rate of an equatorial sea level NM. The Goose Bay NM was observed to have the maximum response to the solar particles. Its counting rate vs. time profile exhibits a rapid increase to maximum , has a large amplitude (∿ 170%) and decays rapidly to background in ∿ 90 min. In Fig. 1 we also show the counting rate vs. time profile for the Tixie Bay NM (71.6°, 128.9°) which recorded an increase of only a few percent. Since the NMs at Goose Bay and Tixie Bay have asymptotic viewing directions ∿ 180° apart in longitude, we can deduce the anisotropy of the solar particle flux at earth from these stations using the expression:

$$A = \frac{\Delta N_{GB} - \Delta N_{TB}}{\Delta N_{GB} + \Delta N_{TB}} .$$

The anisotropy shown in the lower part of Fig. 1 is ∿ 1 for the first 45 min. of the event.

The signature of the GLE on February 16, 1984 is similar to that of the GLE on May 7, 1978 for which it has been shown that:

a) the propagation of the solar particles was nearly scatter-free between the sun and the earth [1];
b) the flare particles at the sun had relatively easy access to the footpoint of the magnetic field line connecting the sun and the earth [2].

2. Source of the Solar Flare Particles We have inspected the Hα and solar magnetic field synoptic charts and the radio observations in order to locate the active region responsible for the solar flare in which the particles producing the GLS on February 16, 1984, were accelerated. The solar synoptic charts show three major active regions at heliocentric longitudes between 40°W and 150°W: Regions 4413 at ∿ 50°W, 4410 at ∿ 95°W and 4408 at ∿ 130°W [3]. No Hα flare was reported from the observations before or during the time of the GLE. We, therefore, conclude that the source of the particles was not on the visible disk of the sun.

On February 16, 1984 at 0858 UT a type III G, a type II metric and a microwave burst started. Since the microwave spectrum showed the spectral maximum below 3.2 GHZ, the corresponding active region must have been behind the limb of the sun. An analysis of the Nançay radio heliograph data [4] and the highest frequencies at which the burst was observed, excludes a flare position at 40° beyond the west limb of the sun corresponding to active region 4408.

The possibility that the active region 4408 was the source of the solar particles can also be excluded on the basis of the intensity-time (IT) profile of the GLE observed at earth. From an analysis of the fine-time resolution data from the cosmic-ray telescopes on IMP7 and Helios A for the May 7, 1978 GLE we have shown that the acceleration of the energetic flare protons can be described by a δ-like process at the flare site and that the coronal propagation of the flare particles can be approximated by 2-dimensional diffusion with losses. We can write for the (IT) profile of the injection of the solar particles into the interplanetary medium [2]:

$$I^E(b,t) = \frac{A(E)}{t} \exp\left\{ - \frac{b^2}{4D_S^E t} - \beta^E t \right\} \qquad (1),$$

where:

b = longitudinal component of the position vector on the surface of the sun with respect to the flare site;
D_S^E = the solar diffusion coefficient for protons of energy E;
β^E = loss rate for protons of energy E;
A(E) = constant factor.

In the interval $20 < E \leq 500$ MeV the diffusion coefficient was found to be $D_S^E[\mathrm{cm}^2/\mathrm{s}] \sim 4.4 \times 10^{15} \{E[\mathrm{MeV}]\}^{-1}$. The loss rate for $90 < E < 500$ MeV was $\beta^E \sim (2.9 \pm 0.5)\mathrm{hr}^{-1}$. Using the results of this model for the flare particle propagation at the sun we calculated the expected (IT) profiles of the solar particles at earth for the GLE on February 16, 1984 assuming the flare position at 95°W in one case and 130°W in the other case. The diffusion of the solar particles in the interplanetary magnetic field (IMF) between the sun and the earth has been neglected because the high anisotropy of the GLE indicates scatter-free propagation. D_S^E was evaluated by extrapolating the energy dependence to 2 GeV. β^E was taken as $\sim 2.9\ \mathrm{hr}^{-1}$, which is probably too small because there is evidence that β is increasing with energy [2]. The position parameter b depends on the position of the footpoint at the sun of the IMF line connecting the earth to the sun. Unfortunately, no solar wind speed (V_{SW}) data were available to us to determine this footpoint. We, therefore, evaluated V_{SW} from the time delay of the sudden commencement observed on February 10, 1984, most probably produced by the shock front of the solar flare on February 16, 1984. For the deduced value of $V_{SW} \sim 400$ km/s, the footpoint of the IMF to earth was ∼ 33° from an assumed flare site at 95°W and ∼ 68° from a site at 130°W.

The theoretical (IT) profiles of the solar particles at earth are shown in Fig. 2 along with the NM count rate profile at Goose Bay. From an inspection of Fig. 2 we conclude that a source location of 130°W can be excluded. The only possible source is located at 95°W. Furthermore, the agreement between the observed and the theoretical (IT) profiles is very good if we consider that D_S^E was extrapolated, the value of β^E used for $E \sim 2$ GeV was determined for lower energy protons and both these parameters may vary from event to event [2].

3. Energy Spectrum and Pitch Angle Distribution of the Solar Particles

We recognize that the GLE of February 16, 1984 shows a normal signature for a flare event in which the particles at the sun have relatively easy access to the footpoint of the IMF line connecting the earth to the sun and the IMF conditions are quiet so that the flare particle propagation from the sun to the earth is essentially scatter-free. In order to determine the rigidity spectrum and pitch angle distribution of the relativistic solar protons at earth we followed the method given by [5]. The response of a neutron monitor to the anisotropic solar proton flux as a function of time, $\Delta N(t)$, can be expressed [6]:

$$\Delta N(t) = \sum_{P_c}^{\infty} S(P) \cdot I(P,t) \cdot F(\delta[P],t)$$

where P_c is the effective cutoff rigidity, $S(P)$ is the specific yield as a function of rigidity, I is the solar proton rigidity spectrum, and F is the pitch angle distribution assumed here to be independent of rigidity. The angle $\delta(P)$ represents the angular distance between the asymptotic direction of vertically incident particles at the NM and the direction of the IMF near the earth. By a trial and error procedure we can determine the apparent source position and I and F which give the best fit of the calculated to the observed data. We used NM data from Akad. Kurchatov, Alert, Alma Ata, Deep River, Durham, Goose Bay, Hermanus, Inuvik, Irkutsk, Jungfraujoch, Kerguelen, Kiel, Kiev, Leeds, Magadan, McMurdo, Moscow, Mt. Washington, Potchefstrom, Rome, Sanae, Terre Adelie, Tixie Bay, and Tsumeb and data from [7]. First results of the analysis give the apparent source direction in a region centered at the geographic coordinates ∿ 5°S, ∿ 5°E, which is 45°W of the earth-sun line.

The deduced pitch angle distribution $F(\delta)$ at the time of maximum intensity, is plotted in Fig. 3. Clearly $F(\delta)$ is very narrow, demonstrating that the propagation of the relativistic solar protons in the IMF from the sun to the earth was practically scatter-free (m.f.p. for pitch-angle scattering > 1 AU). At the time of maximum intensity the rigidity spectrum is given by $I(P)$ $[p/m^2 \text{ ster s GV}] \sim 7.25 \times 10^4 \{P[GV]\}^{-4.25}$ for $1 < P < 10$ GV, where $I(P)$ is the flux averaged over 4π. The corresponding energy spectrum is shown in Fig. 4 along with the spectrum at lower energies deduced from the cosmic-ray telescope onboard IMP8. The agreement between the two spectra is very good. Unfortunately IMP8 was in the earth's magnetotail so that no direct anisotropy measurements are available for E < 500 MeV.

4. Conclusion If we compare the pitch angle distribution and the energy spectrum of the GLE on February 16, 1984, with those of the GLE on May 7, 1978, we recognize that the two events had similar signatures. Therefore, the NM and spacecraft data for this event are again a key to study the acceleration of solar flare protons, their coronal propagation and their injection into the interplanetary medium.

5. Acknowledgements This research was supported by the Swiss NF (2.206-0.84) and the U.S./NSF (ATM-8324486 and INT-8118555). We thank all the principal investigators of neutron monitor stations who made data available to us. We are indebted to Drs. G. Trottet, K. L. Klein, and A. Magun for radio and microwave data and stimulating discussions. We gratefully acknowledge essential information on Hα observations by Dr. Prokakis and we thank H. Grädel for assistance in the data analysis.

6. References

1. Debrunner, H., et al., 1984, J. Geophys. Res., 89, 769.
2. Lockwood, J.A., and H. Debrunner, 1985, to be pub. J. Geophys. Res.

3. Solar Geophys. Data, 1984, 476, Part 1.
4. Klein, K.L., and G. Trottet, 1985, private communication.
5. Debrunner, H., and J.A. Lockwood, 1980, J. Geophys. Res., 85, 6853.
6. Smart, D., et al., 1971, Proc. ICRC 12th, 2, 483.
7. Pomerantz, M.A., et al., 1985, Proc. IS/CRMH (Japan), 437.

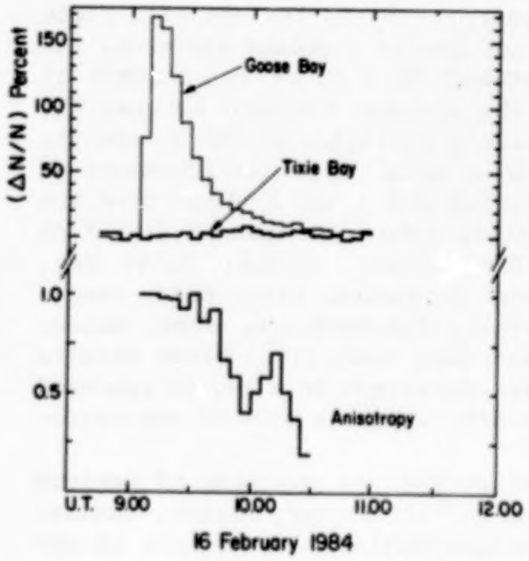

Fig. 1. Percent increase at Goose Bay and Tixie Bay NMs and anisotropy-time profile.

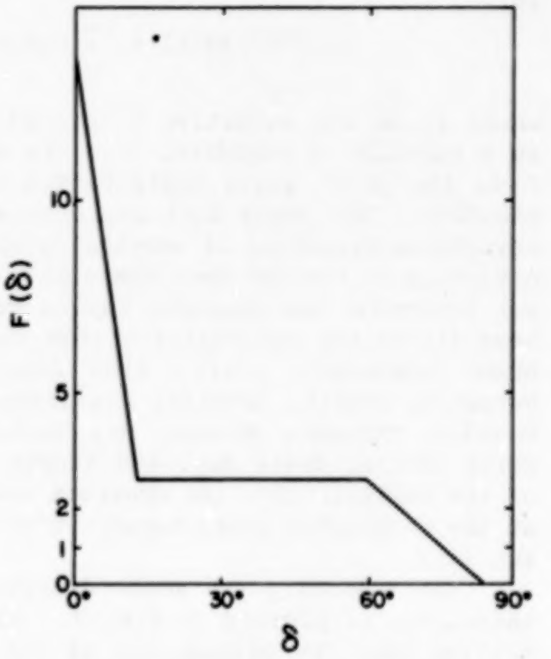

Fig. 3 Pitch angle distribution at time of maximum intensity.

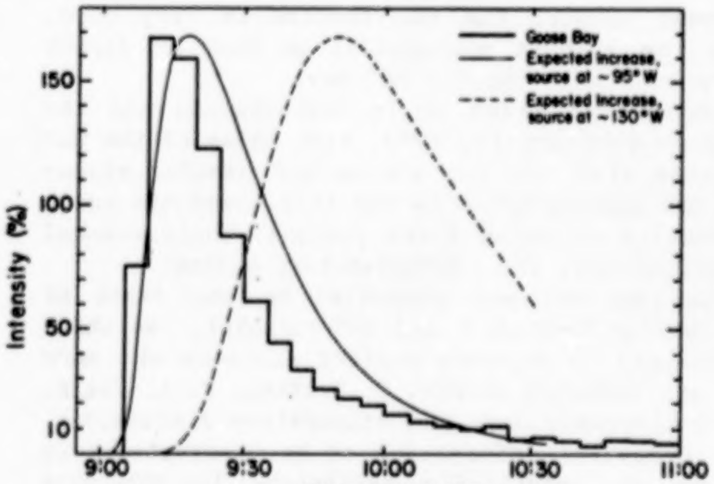

Fig. 2. Intensity-time profile at Goose Bay compared with expected increases for the solar flare locations at 95°W and 130°W.

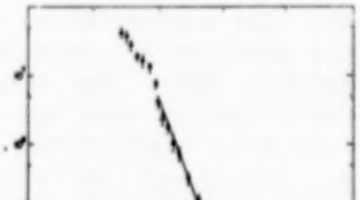

Fig. 4 Energy spectrum at the time of maximum intensity.

SH3.1-8

N85-34812

CONSTRAINTS ON SOLAR FLARE PARTICLE TRANSPORT MODELS FROM ANISOTROPY OBSERVATIONS AT VOYAGER 1

D.C. Hamilton, G.M. Mason and G. Gloeckler

Department of Physics & Astronomy
University of Maryland, College Park, MD 20742 USA

ABSTRACT

In general a particle transport model for energetic solar flare particles contains a number of free parameters which are determined by fitting various features of observed particle events. Frequently the parameter values are not uniquely determined. In order to place tighter constraints on the models, we have examined the anisotropy of 1 and 25 MeV/nuc protons and helium nuclei during the 22 November 1977 solar particle event using data from the LECP experiment on Voyager 1 at 1.6 AU. We have combined these observations with the time-intensity profiles at Voyager 1 and at 1 AU from ISEE-1 and IMP-8 to determine the magnitude and radial dependence of the interplanetary diffusion coefficient and the required injection duration at the sun. The first order anisotropy amplitudes for both 1 MeV and 25 MeV protons are observed to decrease from maximum values (~1) during event onset at Voyager 1 to values consistent with convection in the solar wind at about 3 days into the event decay phase. The intensity and anisotropy profiles at 1.6 AU are consistent with predictions of diffusive transport with a modest mean free path ($\lambda \sim 0.1$ AU). The radial dependence of K_r which was determined for low energy particles by Mason et al. (1) from the times-to-maximum intensity of 1 MeV/nuc helium at 1 AU and 1.6 AU ($K_r = K_0 r^{1.3}$) predicts too rapid an intensity decay for the 25 MeV protons at 1.6 AU. We are required to abandon a simple power law radial dependence for K_r in order to fit all the ISEE and Voyager observations.

Acknowledgements. This work was supported by NASA under [illegible] subcontract 601620 and contract NAS5-28704.

Reference

1. Mason, G.M. et al. 1985, 19th ICRC, La Jolla, paper SH3.2-5.

N85-34813

SH 3.1-9

LOW ENERGY PROTON BIDIRECTIONAL ANISOTROPIES AND THEIR RELATION TO TRANSIENT INTERPLANETARY MAGNETIC STRUCTURES : ISEE-3 OBSERVATIONS

R.G. Marsden, T.R. Sanderson, K.-P. Wenzel
Space Science Department of ESA
ESTEC, Noordwijk, The Netherlands
E.J. Smith
Jet Propulsion Lab., California Institute of Technology,
Pasadena, CA 91109, USA

1. Introduction. It is known that the interplanetary medium in the period approaching solar maximum is characterized by an enhancement in the occurrence of transient solar wind streams and shocks [1, 2] and that such systems are often associated with looplike magnetic structures or clouds [3, 4]. There is observational evidence that bidirectional, field-aligned flows of low-energy particles could be a signature of such looplike structures [5, 6, 11], although detailed models for the magnetic field configuration and injection mechanisms do not exist at the current time. In this paper we present preliminary results of a survey of low-energy proton bidirectional anisotropies measured on ISEE-3 in the interplanetary medium between August 1978 and May 1982, together with magnetic field data from the same spacecraft.

2. Instrumentation and Analysis. The particle measurements used in this analysis were obtained with the low-energy proton instrument on ISEE-3 [7], comprising three identical solid state detector telescopes oriented at 30°, 60° and 135° with respect to the spacecraft spin axis. Particles are counted in 8 logarithmically-spaced energy channels in the range 35 - 1600 keV, and with the exception of the highest energy channel (1000 - 1600 keV), data accumulated during each spacecraft revolution are sorted into 8 equal azimuthal sectors. Magnetic field measurements were obtained using the vector helium magnetometer [8] onboard ISEE-3.

In order to determine the anisotropy characteristics, the particle data in two channels (35-56 and 620-1000 keV) were first transformed into a frame of reference moving with the instantaneous solar wind velocity. These transformed data were then subjected to a spherical harmonic analysis in order to derive a series expansion of the 3-dimensional spatial distribution [9] from which the instantaneous particle intensity at 0°, 90°, and 180° relative to the positive B-field direction was calculated for each energy channel. The ratios of the harmonic components A_{10}'/A_0' and A_{20}'/A_0' where primed quantities refer to the solar wind frame, were used to define 1st and 2nd order anisotropies, respectively. A bidirectional flow (BDF) is seen as a reduction in the flux at 90° as compared to the fluxes at 0° and 180°, which remain approximately equal; in terms of the anisotropies, a BDF is characterised by a positive 2nd-order anisotropy, together with a 1st-order anisotropy which is close to zero. For the purpose of this study, since we are interested in relatively large scale phenomena, we have not considered BDFs of less than 3 hours duration.

We have examined plots of the magnetic field magnitude and direction for the same period for evidence of isolated, large-scale ($\gtrsim$ 0.1 AU) structures convecting past the spacecraft, in particular for signatures of magnetic clouds as defined in [3]. For those candidate structures having a rotational signature whereby the magnetic field vector rotates progressively in a plane, a minimum variance analysis has been performed to determine the degree of planarity.

3. Results and Discussion. From the 45-month data set used for this study, it was possible to identify 66 periods during which BDFs were present. In all cases, effects due to the bow shock have been excluded. By examining the magnetic field data corresponding to these periods, we have been able to group these BDF events into 5 classes as follows:

I. 19 events associated with a transient magnetic structure having a rotational signature characteristic of a magnetic cloud, which are also related to the passage of an interplanetary shock.

II. 12 events associated with a transient magnetic structure (non-rotational), which are also shock-related.

III. 8 events associated with a transient magnetic structure having a rotational signature, but no shock-association.

IV. 9 events associated with a transient magnetic structure having a non-rotational signature, but no shock-association.

V. 18 events for which no clear transient magnetic structure could be identified.

From the above it is apparent that the majority of the observed BDFs are associated with transient features in the magnetic field, although not all events are related to classical, shock-associated magnetic clouds. In addition, it should be noted that we have identified a number of examples of classical magnetic clouds which have no related BDF signature in the energy range covered by our instrument.

It is beyond the scope of this paper to present examples of all the above event classes in detail; however, in Figs. 1 and 2 we show the combined particle and magnetic field data for two 3-day periods containing a class I and a class III event, respectively. In the upper panels we have plotted the intensity of the 620 - 1000 keV channel (Fig. 1) and the 35 - 56 keV channel (Fig. 2) at 0°, 90° and 180° with respect to the magnetic field direction; the second panel shows the ratio of the second harmonic components A_{20}'/A_0' in the solar wind frame. The three lower panels show the magnitude, elevation and azimuth (in GSE coordinates) of the magnetic field, respectively.

The period containing the class I event starts at 0000 UT on Sep. 28, 1978. At this time, the fluxes seen in all channels are still elevated as a result of the large solar particle event which started 5 days earlier. The intensity in the 620 - 1000 keV channel shows an increase starting at 0700 UT, probably associated with a 2B flare, located at N27, W19 [10] with H_α maximum on Sep. 27, 1442 UT. An interplanetary shock was observed at the spacecraft at 2040 UT on Sep. 28; a second shock passed the earth at 0301 UT on Sep. 29, but was not seen at ISEE-3 due to a data gap. The particle intensity decreased sharply at 0830 UT, coincident with the arrival (presumably) of driver gas and an isolated magnetic structure possessing a clear rotational signature, which persisted until 0330 UT on Sep.30. Throughout this period, bidirectional particle fluxes were observed, as evidenced by the large positive 2nd harmonic

ORIGINAL PAGE IS
OF POOR QUALITY

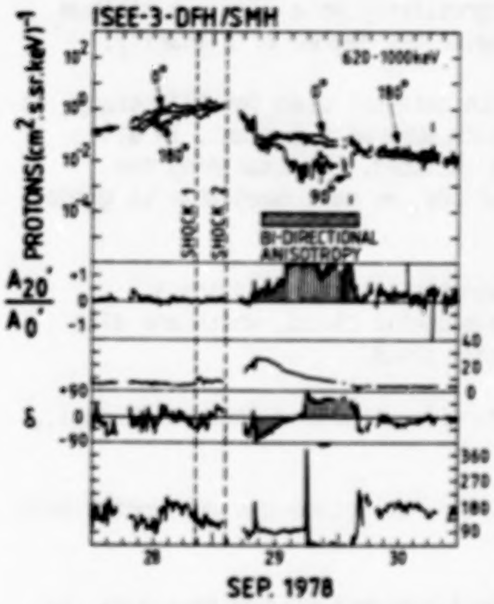

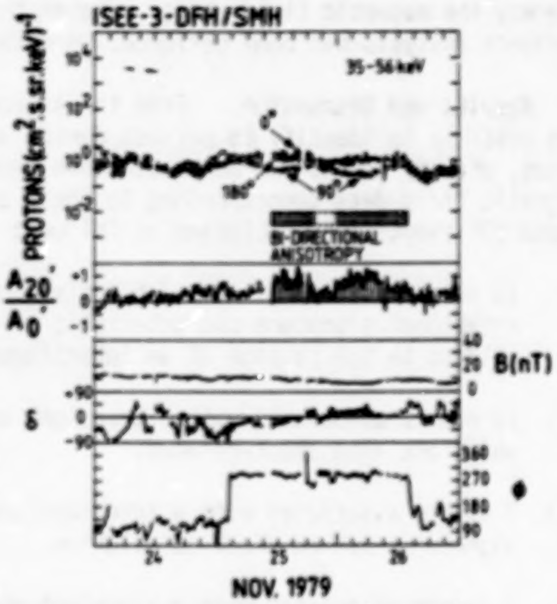

Fig.1. *(left) Proton intensity and anisotropy parameters, and magnetic data for the BDF event of 29 Sept. 1978.*

Fig.2 *(right) As for Fig. 1, for the BDF event of 25,26 Nov. 1979.*

which dominated the anisotropy signature, and the prominent decrease in the flux at 90° relative to the field-aligned component. The particle data at lower energies (not here) show evidence for two separate populations bounded by the discontinuity in the magnetic cloud signature occurring at 1720 UT on Sep. 29.

The 3-day period shown in Figure 2 starting at 0000 UT on Nov. 24, 1979 is characterised by the appearance of an isolated, stable magnetic structure at 0230 UT on Nov. 25, accompanied by bidirectional fluxes. In this example of a class III event, the magnetic signature is less rotational than in the class I event described above. As in the previous case, the bidirectional flow is not continuous at the same level throughout the event, but is interrupted, presumably by the passage of a flux tube separated from the cloud.

In addition to the classification described above, we have examined the statistical characteristics of the complete BDF event set, with the following results:

a) 48 events are associated with isolated, transient magnetic structures, of which 27 show a rotational signature and 10 show a constant field orientation normal to the nominal spiral direction; the remaining 11, while clearly separated from the ambient medium, show no specific directional features. In general, the r.m.s. noise in the field seems to be smaller when bidirectional fluxes are present.

b) The distribution of BDF event durations is presented in Fig. 3, the average duration being 15 hours. In 20% of the cases, the BDF persisted for more than 24 hours, and the longest event observed had a duration of 50 hours. In terms of the spatial extent of the structures supporting the flows, the above data imply an average scale size of ~0·15 AU, with a maximum of 0·5 AU if we assume a nominal solar wind velocity of 400 km/s.

N85-34814

c) 37 events followed the passage of an interplanetary shock, with a separation in time of, on average, 19 hours. This statistic should be treated with caution, however, since in several other events, the observed BDF may have been related to a shock which passed the spacecraft more than 40 hours previously.

d) For 41 events, the amplitude of the 2nd harmonic at 35 keV is comparable to, or greater than, that at 620 keV.

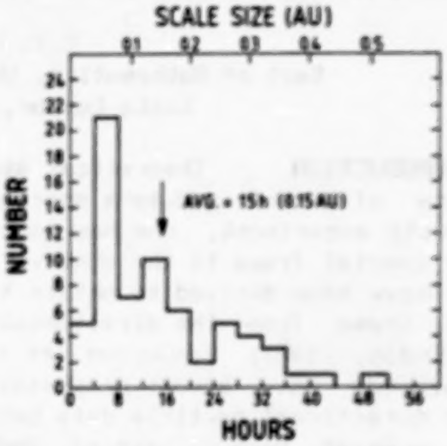

Fig.3. *Distribution of BDF event durations. Scale size shown for solar wind vel. = 400 km/s.*

Taking into account the relative propagation times for 35 and 620 keV particles together with point d) above, we suggest that, while undoubtedly fitting the data for a number of (in particular) class I events, the commonly proposed model (e.g. [11]) in which particles are confined in a simple, large-scale magnetic loop with mirroring occurring in the high-field regions close to the Sun cannot explain all our BDF observations. Given the uncertainty in the 3-dimensional field geometry within magnetic clouds which still exists, we cannot rule out effects of a more localised nature giving rise to the observed anisotropies, particularly for events having relatively short duration. The qualitative correlation between the degree of quietness of the magnetic field and the presence of bidirectional flows is clearly of importance, and will be addressed in a future paper.

4. Acknowledgment. Part of the research described in this paper was carried out by the Jet Propulsion Laboratory, under a contract with the National Aeronautics and Space Administration.

REFERENCES

1. Burlaga, L.F. et al., J.Geophys.Res., 89, 6579, 1984.
2. Smith, E.J., Sp.Sci.Rev., 34, 101, 1983.
3. Klein, L.W. and Burlaga, L.F., J.Geophys.Res., 87, 613, 1982.
4. Burlaga, L.F. et al., Geophys.Res.Lett., 9, 1317, 1982.
5. Sanderson, T.R. et al., Geophys.Res.Lett., 10, 916, 1983.
6. Palmer, I.D. et al., J.Geophys.Res., 83, 75, 1978.
7. Sanderson, T.R. et al., J.Geophys.Res., 86, 4425, 1981.
8. Frandsen, A.M.A. et al., IEEE Trans.Geosci.Electron., GE-16, 195, 1978.
9. Sanderson, T.R. et al., J.Geophys.Res., 90, 19, 1985.
10. Solar-Geophys. Data, 415-II, 29, 1979.
11. Kutchko, F.J. et al., J.Geophys.Res., 87, 1419, 1982.

N85-34814

SECOND-ORDER COMPTON-GETTING EFFECT ON ARBITRARY INTENSIY DISTRIBUTION

C.K. Ng
Dept of Mathematics, University of Malaya
Kuala Lumpur, Malaysia

1 INTRODUCTION Theoretical studies of energetic particles in space are often referred to a special frame of reference. To compare theory with experiment, one has to transform the particle distribution from the special frame to the observer's frame, or vice versa. Various methods have been derived to obtain the directional distribution in the comoving frame from the directional fluxes measured on a spacecraft (e.g., Erdös, 1981; Sanderson *et al.*, 1985, and references therein). These methods have become progressively complicated as increasingly detailed directional particle data become available.

We present here a set of 2nd order correct formulae for the transformation of an arbitrary differential intensity distribution, expressed as a series of spherical harmonics, between any two frames in constant relative motion. These formulae greatly simplify the complicated procedures currently in use for the determination of the differential intensity distribution in a comoving frame.

2. THE DESIRED FORM OF THE TRANSFORMATION In the observer's frame, let the particle differential intensity w.r.t. momentum (or rigidity) be expressed in terms of the spherical harmonics C_n^m, S_n^m as :

$$j_p^S(p_S,\theta_S,\phi_S) = \sum_{n=0}\sum_{m=0}^{n} \{A_{nm}^S(p_S)C_n^m(\theta_S,\phi_S)+B_{nm}^S(p_S)S_n^m(\theta_S,\phi_S)\}. \qquad (1)$$

We wish to transform this to the frame moving with velocity $\underline{W}$ relative to the observer, *also in terms of spherical harmonics* :

$$j_p(p,\theta,\phi) = \sum_n\sum_m \{A_{nm}(p)C_n^m(\theta,\phi) + B_{nm}(p)S_n^m(\theta,\phi)\}. \qquad (2)$$

Here $$C_n^m(\theta,\phi) = P_n^m(\cos\theta)\cos(m\phi),\ S_n^m(\theta,\phi) = P_n^m(\cos\theta)\sin(m\phi), \qquad (3)$$

$P_n^m(\ )$ = associated Legendre function, p = particle momentum, and θ, ϕ are the polar and azimuthal angles of the particle *arrival* direction. The superscript or subscript S indicates that the quantity is referred to the frame of the observer/spacecraft.

In short, our purpose is to find the relation between the coefficients A_{nm}, B_{nm} in the comoving frame and the coefficients A_{nm}^S, B_{nm}^S and their p-derivatives in the observer's frame, and *vice versa*.

We denote below the components of $\underline{W}$ along and normal to the magnetic field by $\underline{W}_\parallel$ and $\underline{W}_\perp$ respectively, and define $\hat{W}_\parallel = W_\parallel/W$, $\hat{W}_\perp = W_\perp/W$, and $\varepsilon = W/v$, with v the particle speed. We choose the polar coordinate axis to point along the magnetic field, and measure ϕ from the direction of $\underline{W}_\perp$. Hence, θ, ϕ denote the particle pitch-angle and gyrophase respectively. We will refer to this coordinate system as the standard one.

3. SOME CURRENT SOLUTIONS Gleeson and Axford (1968) and Forman (1970) obtained 1st order transformations from (2) to (1), for $j_p = A_{00}(p)$. Forman's elegant approach uses the Lorentz invariance of the phase-space distribution function. Balogh *et al.* (1973) obtained a 2nd order result for the isotropic case and a 1st order result for the anisotropic case that includes the $n=1$ terms. Ng (1984) obtained a 2nd order transformation for gyrotropic distributions ($j_p = \sum_n A_{no}(p)P_n(\cos\theta)$) valid for relativistic particles.

Another approach, taken by Sanderson *et al.* (1985), is based on a method by Ipavich (1974). This is outlined below. One may use eqn (12) of Ipavich (1974) to transform each term in the series (1), *provided one pays the price of using a non-standard coordinate system* in which the polar axis points along the velocity $\underline{W}$. Denote the non-standard polar and azimuthal angles by θ^*, ϕ^*. This allows any term $A^s_{nm}(p_s)C^m_n(\theta^*_s,\phi^*_s)$ *for the phase-space density* to be transformed to:

$$A^s_{nm}[p(1-2\varepsilon\cos\theta^*+\varepsilon^2)^{\frac{1}{2}}]C^m_n\{\tan^{-1}[\sin\theta^*/(\cos\theta^*-\varepsilon),\phi^*]\}, \tag{4}$$

and similarly for $B^s_{nm}(p_s)C^m_n(\theta^*_s,\phi^*_s)$. Following Ipavich and Sanderson *et al.*, one assumes a power-law spectrum $(p_s d/dp_s)\log A^s_{nm}(p_s) = -2r_n$, and obtains from (4),

$$(1-2\varepsilon\cos\theta^*+\varepsilon^2)^{-r_n-1}A^s_{nm}(p)C^m_n\{\tan^{-1}[\sin\theta^*/(\cos\theta^*-\varepsilon),\phi^*]\}. \tag{5}$$

Eqn (5) may be compared to Sanderson *et al.*'s eqn (A11). There remains the task of converting (5) to the form (2), including a change from θ^*,ϕ^* back to the standard angular coordinates θ,ϕ.

Sanderson *et al.* accomplish the above by *numerically integrating* the transformed intensity obtained from (5) (their eqns (A11) and (A12)) over each sector, each energy interval and each telescope to produce an *equivalent set of counts in the comoving frame*, and then *fitting* (2) to the equivalent set of counts.

Although the assumption of a power-law spectrum may be avoided by using (4), the numerical integration and the second fitting are time-consuming and unnecessary for say, >10 KeV protons, because we are able to obtain the transformation posed in Section 2, correct to $O(W/v)^2$ and for *arbitrary* direction of $\underline{W}$.

4. DERIVATION OF THE TRANSFORMATION FORMULAE

We begin with

$$j_p(p,\theta,\phi) = \sum_{n}\sum_{m}\left(\frac{vp^2}{v_s p_s^2}A^s_{nm}(p_s)C^m_n(\theta_s,\phi_s)+\frac{vp^2}{v_s p_s^2}B^s_{nm}(p_s)S^m_n(\theta_s,\phi_s)\right), \tag{6}$$

and consider each term in the series. First we transform the spherical harmonics $C^m_n(\theta_s,\phi_s)$. Galilean transformation of momentum gives

$$\cos\theta_s = \cos\theta - \varepsilon(\hat{W}_{\parallel}-\zeta\cos\theta) + \tfrac{1}{2}\varepsilon^2[(3\zeta^2-1)\cos\theta - 2\hat{W}_{\parallel}\zeta] + O(\varepsilon^3), \tag{7}$$

$$\begin{aligned}\sin^m\theta_s\cos m\phi_s &= \sin^m\theta\cos m\phi + m\varepsilon[\zeta\sin^m\theta\cos m\phi - \hat{W}_1\sin^{m-1}\theta\cos(m-1)\phi]+\\ &+ \tfrac{1}{2}\varepsilon^2\{[m(m+2)\zeta^2-m]\sin^m\theta\cos m\phi - 2m^2\hat{W}_1\zeta\sin^{m-1}\theta\cos(m-1)\phi +\\ &\quad + \hat{W}_1^2(m-1)m\sin^{m-2}\theta\cos(m-2)\phi\} + O(\varepsilon^3)\ ,\end{aligned} \tag{8}$$

where

$$\zeta = -\hat{\underline{v}}.\hat{\underline{W}} = \hat{W}_{\parallel}\cos\theta + \hat{W}_1\sin\theta\cos\phi, \tag{9}$$

$$\zeta\cos m\phi = \hat{W}_{\parallel}\cos\theta\cos m\phi + \tfrac{1}{2}\hat{W}_1\sin\theta[\cos(m-1)\phi + \cos(m+1)\phi], \tag{10}$$

$$\zeta^2\cos m\phi = (\hat{W}_{\parallel}^2\cos^2\theta + \tfrac{1}{2}\hat{W}_1^2\sin^2\theta)\cos m\phi + \hat{W}_{\parallel}\hat{W}_1\sin\theta\cos\theta\ \mathrm{x}$$

$$\times\ [\cos(m-1)\phi + \cos(m+1)\phi] + \tfrac{1}{4}\hat{W}_1^2 \sin^2\theta[\cos(m-2)\phi + \cos(m+2)\phi]. \qquad (11)$$

Using (7) - (10), and various properties of P_n^m, we obtain

$$C_n^m(\theta_s,\phi_s) = C_n^m(\theta,\phi)+\varepsilon(n+1)U_{n-1}^{mc}(\theta,\phi) +\varepsilon n V_{n+1}^{mc}(\theta,\phi) +\varepsilon^2(n-1)(n+1)X_{n-2}^{mc}(\theta,\phi)+$$
$$+ \varepsilon^2 n(n+1)Y_n^{mc}(\theta,\phi) + \varepsilon^2 n(n+2)Z_{n+2}^{mc}(\theta,\phi) + O(\varepsilon^3), \qquad (12)$$

where $(2n+1)U_{n-1}^{mc} = \tfrac{1}{2}\hat{W}_1(n+m-1)(n+m)C_{n-1}^{m-1} - \hat{W}_{\parallel}(n+m)C_{n-1}^{m} - \tfrac{1}{2}\hat{W}_1 C_{n-1}^{m+1}$, (13)

$$(2n+1)V_{n+1}^{mc} = \tfrac{1}{2}\hat{W}_1(n-m+1)(n-m+2)C_{n+1}^{m-1} + \hat{W}_{\parallel}(n-m+1)C_{n+1}^{m} - \tfrac{1}{2}\hat{W}_1 C_{n+1}^{m+1}\ , \qquad (14)$$

$$(2n-1)(2n+1)X_{n-2}^{mc} = \tfrac{1}{8}\hat{W}_1^2 \frac{(n+m)!}{(n+m-4)!}C_{n-2}^{m-2} - \tfrac{1}{2}\hat{W}_{\parallel}\hat{W}_1 \frac{(n+m)!}{(n+m-3)!}C_{n-2}^{m-1} +$$
$$+ \tfrac{1}{4}(2\hat{W}_{\parallel}^2 - \hat{W}_1^2)\frac{(n+m)!}{(n+m-2)!}C_{n-2}^{m} + \tfrac{1}{2}\hat{W}_{\parallel}\hat{W}_1(n+m)C_{n-2}^{m+1} + \tfrac{1}{8}\hat{W}_1^2 C_{n-2}^{m+2}, \qquad (15)$$

$$(2n-1)(2n+3)Y_n^{mc} = \tfrac{1}{4}\hat{W}_1^2 \frac{(n+m)!(n-m+2)!}{(n+m-2)!(n-m)!}C_n^{m-2} + \tfrac{1}{2}(2m-1)\hat{W}_{\parallel}\hat{W}_1(n-m+1)(n+m)C_n^{m-1}+$$
$$- \tfrac{1}{2}[(2n^2+2n-2m^2-1)\hat{W}_{\parallel}^2 + (n^2+n+m^2-1)\hat{W}_1^2]C_n^m + \tfrac{1}{2}(2m+1)\hat{W}_{\parallel}\hat{W}_1 C_n^{m+1} + \tfrac{1}{4}\hat{W}_1^2 C_n^{m+2}, \qquad (16)$$

$$(2n+1)(2n+3)Z_{n+2}^{mc} = \tfrac{1}{8}\hat{W}_1^2 \frac{(n-m+4)!}{(n-m)!}C_{n+2}^{m-2} + \tfrac{1}{2}\hat{W}_{\parallel}\hat{W}_1 \frac{(n-m+3)!}{(n-m)!}C_{n+2}^{m-1} +$$
$$+ \tfrac{1}{4}(2\hat{W}_{\parallel}^2 - \hat{W}_1^2)\frac{(n-m+2)!}{(n-m)!}C_{n+2}^{m} - \tfrac{1}{2}\hat{W}_{\parallel}\hat{W}_1(n-m+1)C_{n+2}^{m+1} + \tfrac{1}{8}\hat{W}_1^2 C_{n+2}^{m+2}\ . \qquad (17)$$

Note that the functions U, V, X, Y, and Z are all expressed in terms of the spherical harmonics C_n^m (θ,ϕ), and that

$$P_n^{-m}(\theta,\phi) = (-1)^m P_n^m(\theta,\phi)(n-m)!/(n+m)!, \qquad (18)$$

$$\zeta C_n^m = V_{n+1}^{mc} - U_{n-1}^{mc}\ , \qquad (19)$$

$$\zeta[(n-2)U_{n-1}^{mc} + (n+3)V_{n+1}^{mc}] - \frac{1}{2}C_n^m = (4-2n)X_{n-2}^{mc} - 3Y_n^{mc} + (2n+6)Z_{n+2}^{mc}. \qquad (20)$$

Secondly, we expand $A_{nm}^s(p_s)$ about $p = p_s$:

$$A_{nm}^s(p_s) = A_{nm}^s(p)+\varepsilon\zeta p A_{nm}'^{s}(p) + \tfrac{1}{2}\varepsilon^2[(1-\zeta^2)pA_{nm}'^{s}(p) + \zeta^2 p^2 A_{nm}''^{s}(p)]+O(\varepsilon^3). \quad (21)$$

Then we multiply (21) and (12), and use (10), (11), (19) and (20) to express $A_{nm}^s(p_s)C_n^m(\theta_s,\phi_s)$ in terms of a series of $C_n^m(\theta,\phi)$ correct to $O(\varepsilon^3)$. This expression actually applies to the transformation of phase-space distribution function, but will not be exhibited here.

Finally, multiplying

$$vp^2/(v_s p_s^2) = 1 + 3\varepsilon\zeta - (3\varepsilon^2/2)(1-5\zeta^2) + O(\varepsilon^3) \qquad (22)$$

into the above expression, and simplifying as before, we obtain

$$[vp^2/(v_s p_s^2)]A_{nm}^s(p_s)C_n^m(\theta_s,\phi_s) = A_{nm}^s C_n^m +\varepsilon[(n-2)A_{nm}^s + pA_{nm}'^{s}]U_{n-1}^{mc} +\varepsilon[(n+3)A_{nm}^s+$$
$$-pA_{nm}'^{s}]V_{n+1}^{mc} +\varepsilon^2[(n-4)(n-2)A_{nm}^s+(2n-5)pA_{nm}'^{\varepsilon}+p^2A_{nm}''^{s}]X_{n-2}^{mc}+\varepsilon^2[(n-2)(n+3)A_{nm}^s+$$
$$+4pA_{nm}'^{s}+p^2A_{nm}''^{s}]Y_n^{mc}+\varepsilon^2[(n+3)(n+5)A_{nm}^s-(2n+7)pA_{nm}'^{s}+p^2A_{nm}''^{s}]Z_{n+2}^{mc} + O(\varepsilon^3), \quad (23)$$

the right hand side being evaluated at (p,θ,ϕ). Eqns (8), (10) - (17), (19) - (20) and (23) hold when we replace all the cosines dependent on ϕ by sines, C_n^m by S_n^m, U_{n-1}^{mc} by U_{n-1}^{ms}, etc. Substituting (23) into (6), we obtain the desired result in the form (2), as well as the relation between A_{nm} and A_{nm}^S and their derivatives. These, however, are not exhibited here for lack of space. For the inverse transformation, we merely need to interchange quantities labelled and unlabelled with S, and reverse the signs of $\hat{W}_{\parallel}$ and $\hat{W}_{\perp}$ in the above.

5. SOME IMPLICATIONS For >10 KeV protons, once A_{nm}^S and their 1st and 2nd derivatives are experimentally determined, one need only substitute these into the formulae to obtain the relevant A_{nm} in the comoving frame, bypassing the complicated procedures mentioned in Section 3.

The formulae are useful in other regards. For example, we have

$$A_{n0}^S = A_{n0} + \varepsilon[(n+1)/(2n+3)][n-1+pd/dp][\tfrac{1}{2}\hat{W}_{\perp}(n+2)A_{n+1,1} - \hat{W}_{\parallel}(n+1)A_{n+1,0}] + \varepsilon[n/(2n-1)][n+2-pd/dp][\tfrac{1}{2}\hat{W}_{\perp}(n-1)A_{n-1,1} + \hat{W}_{\parallel}\,nA_{n-1,0}] + O(\varepsilon^2). \quad (24)$$

For highly anisotropic solar particles, the gyrotropic terms A_{n0} >> the non-gyrotropic term A_{n1}. The former may be eliminated in (24) by choosing the $\underline{E}\times\underline{B}$ drift frame $(W_{\parallel} = 0)$. If in addition, $A_{n-1,1}$ and $A_{n+1,1}$ are neglible, then $A_{n0} - A_{n0}^S = O(\varepsilon^2)$.

Next consider the 1st harmonic terms.

$$\begin{aligned} A_{10}^S &= A_{10} + \varepsilon\hat{W}_{\parallel}(3A_{00} - pA'_{00} - 2pA'_{20}/5) - \varepsilon\hat{W}_{\perp}pA'_{21} + O(\varepsilon^2)\,, \\ -A_{11}^S &= -A_{11} + \varepsilon\hat{W}_{\perp}(3A_{00} - pA'_{00} + pA'_{20}/5 - 6pA'_{22}/5) + 3\varepsilon\hat{W}_{\parallel}pA'_{21}/5 + O(\varepsilon^2)\,, \\ -B_{11}^S &= -B_{11} + 3\varepsilon\hat{W}_{\parallel}pB'_{21}/5 - 6\varepsilon\hat{W}_{\perp}pB'_{22}/5 + O(\varepsilon^2)\,. \end{aligned} \quad (25)$$

Even if all the non-gyrotropic terms vanish, if $pA'_{20} \neq 0$, the *1st order* 1st harmonic anisotropy vector is *not* aligned with $\underline{W}$!

6. REMARKS The new formulae are useful in the study of transverse anisotropies. The derivation in Section 4 is being extended to cover relativistic particles (see also Ng, 1984). These and other considerations and a more complete account of the present work will be presented elsewhere.

Acknowledgement. This work was initiated whilst I enjoyed the hospitality of Professor E. C. Stone and his colleagues at Caltech. I thank B. L. Ng for her help in preparing the manuscript.

References

Balogh, A., *et al.* (1973) *Planet. Space Sci., 21,* 1802.
Erdös, G. (1981) *17th ICRC, Paris,* Paper T5-14.
Forman, M.A. (1970) *Planet. Space Sci., 18,* 25.
Gleeson, L.J. & Axford, I.A. (1968) *Astrophys. Space Sci., 2,* 431.
Ipavich, F.M. (1974) *Geophys. Res. Lett., 1,* 149.
Ng, C.K. (1984) *Res. Report #15/84,* Dept. of Maths., U of Malaya.
Ng, C.K. (1985) This conference, Paper SH 3.1-11.
Sanderson, T.R., *et al.* (1985) *J. Geophys. Res., 90,* 19.

DETERMINATION OF THE PITCH-ANGLE DISTRIBUTION AND TRANSVERSE ANISOTROPY OF INTERPLANETARY PARTICLES

N85-34815

C. K. Ng
Dept of Mathematics, University of Malaya
Kuala Lumpur, Malaysia

1. INTRODUCTION We present a method to determine the directional differential intensity (d.d.i.), expressed in terms of spherical harmonics, from sectored particle data, concurrent interplanetary magnetic field (IMF) and solar-wind velocity. In Section 2, we show the relation between the d.d.i. and the mean sector count rates X_i. In Section 3, we show how to estimate the d.d.i. from the measured X_i and the associated errors due to Poisson statistics. In Section 4, using the above method, we determine the pitch-angle distribution and the transverse anisotropy of the d.d.i of low energy protons for the Day 118, 1978 solar particle event. In Section 5, we discuss an interesting correlation between the transverse anisotropy and the IMF direction.

2. RELATION BETWEEN DIRECTIONAL INTENSITY AND SECTOR RATES

We express the particle directional differential intensity as

$$j(p,\theta,\phi) = \sum_{n=0}^{\infty} \sum_{m=0}^{n} P_n^m(\cos\theta) \left\{ A_{nm}(p) \cos m\phi + B_{nm}(p) \sin m\phi \right\}, \quad (1)$$

where P_n^m = the associated Legendre functions, p = particle momentum, θ = pitch-angle and ϕ = gyrophase in the standard coordinate system (Ng, 1985). When the telescope points in the direction (γ,η), it measures the differential count rates

$$C(p,\gamma,\eta) = \int_{\Omega} j(p,\theta,\phi)\, S[\,\theta'(\gamma,\eta,\theta,\phi)\,] \sin\theta \, d\theta \, d\phi, \quad (2)$$

where, following Sentman and Baker (unpublished manuscript), we express the angular response function of the particle telescope as

$$S(\theta') = \sum_{k=0}^{\infty} S_k P_k(\cos\theta') = \sum_{k=0}^{\infty} S_k \Big\{ P_k(\cos\gamma) P_k(\cos\theta) + \\ + 2 \sum_{m=1}^{k} [(k-m)!/(k+m)!]\, P_k^m(\cos\gamma) P_k^m(\cos\theta) \cos m(\eta-\phi) \Big\} . \quad (3)$$

It follows from the orthogonality of the spherical harmonics that

$$C(p,\gamma,\eta) = 4\pi \sum_{n=0}^{\infty} [S_n/(2n+1)] \sum_{m=0}^{n} \left\{ A_{nm}(p) \cos m\eta + B_{nm}(p) \sin m\eta \right\} P_n^m(\cos\gamma). \quad (4)$$

As the telescope sweeps over sector i, we average (4) to obtain $X_i(p)$ the mean differential count rate over sector i,

$$X_i(p) = 4\pi \sum_{n=0}^{\infty} [\,S_n/(2n+1)\,] \sum_{m=0}^{n} \Big\{ A_{nm}(p) \langle P_n^m(\cos\gamma) \cos m\eta \rangle_i + \\ + B_{nm}(p) \langle P_n^m(\cos\gamma) \sin m\eta \rangle_i \Big\}, \quad (5)$$

where $\langle \; \rangle_i = (1/\Delta\psi) \int_{\psi_i}^{\psi_{i+1}} d\psi$, ψ = the spacecraft (s/c) spin-angle measured from the projection of the IMF onto the spin plane, and (ψ_i, ψ_{i+1}) defines sector i (see the 2nd coordinate system in Fig. 1). For multiple-telescope systems (Sanderson & Hynds, 1977), eqn (5) should be repeated for each telescope.

We now illustrate by specialising (1) and (5) to 8-sectored data for a telescope sweeping in the spacecraft's spin plane:

$$j(p,\theta,\emptyset) = \sum_{n=0}^{4} A_{n0}P_n(\cos\theta) + \sum_{n=1}^{3} A_{n1}P_n^1(\cos\theta)\cos\emptyset, \tag{6}$$

$$X_i = 4\pi \sum_{n=0}^{4} S_n A_{n0} Q_{n0}^i/(2n+1) + 4\pi \sum_{n=1}^{3} S_n A_{n1} Q_{n1}^i/(2n+1), \tag{7}$$

where $$Q_{n0}^i = \langle \sum_{j=0}^{n} a_j^n \sin^j\theta_B \cos^j\psi \rangle_i, \tag{8}$$

$$Q_{n1}^i = \langle (\hat{W}_{\perp 1}\cos\psi + \hat{W}_{\perp 2}\sin\psi) \sum_{j=0}^{n} b_j^n \sin^j\theta_B \cos^j\psi \rangle_i, \tag{9}$$

a_j^n = coefficient of x^j in $P_n(x)$, b_j^n = coefficient of x^j in $P_n^1(x)/(1-x^2)^{\frac{1}{2}}$ θ_B = angle between IMF and s/c spin-axis, and $(\hat{W}_{\perp 1}, \hat{W}_{\perp 2}, \hat{W}_{\perp 3})$ denotes a unit vector in the direction of $\underline{E}\times\underline{B}$ in the 2nd coordinate system (Fig. 1). Note that the integrations in (8) and (9) may be performed readily in closed form.

3. DETERMINATION OF j FROM MEASURED X_i To simplify notation in the following, let

$$D_n = A_{n0} \quad (n=0,4), \qquad D_n = A_{n-4,1} \quad (n=5,7), \tag{10}$$

$$R_n^i = Q_{n0}^i \quad (n=0,4), \qquad R_n^i = Q_{n-4,1}^i \quad (n=5,7). \tag{11}$$

We least-square fit $$X_i = \sum_{n=0}^{7} C_n R_n^i, \quad (i=0,7), \tag{12}$$

to the 8 measured sector rates $\bar{X}_i$. This yields

$$\sum_{j=0}^{7} H_{nj}C_j = \sum_{i=0}^{7} R_n^i \bar{X}_i, \qquad (n=0,7), \tag{13}$$

where $$H_{nj} = \sum_i R_n^i R_j^i, \qquad (n=0,7;\ j=0,7). \tag{14}$$

Inverting (13), we have

$$C_n = \sum_k H_{nk}^{-1} \sum_i R_k^i \bar{X}_i, \qquad (n=0,7), \tag{15}$$

and thence $$D_n = \sum_i M_{ni}\bar{X}_i, \qquad (n=0,7), \tag{16}$$

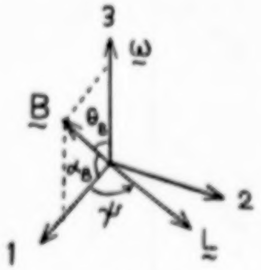

Fig. 1

where M_{ni} is ultimately expressed in terms of Q_{n0}^i, Q_{n1}^i, and S_n. Using (16), we may determine the coefficients A_{nm} in (6) by a matrix multiplication into the measured sector rates. When the IMF projection lies on a sector boundary, the symmetric matrix H_{nj} becomes singular. So we drop the A_{40} term in (6) whenever the IMF projection comes within 2° of a sector boundary.

Suppose that K_i counts are registered over the time interval t_c in sector i. Assuming Poisson statistics, we estimate

$$X_i = K_i/t_c, \quad \mathrm{var}(X_i) = K_i/t_c^2, \quad \mathrm{var}(D_n) = \sum_i M_{ni}^2 \mathrm{var}(X_i). \tag{17}$$

If we define the anisotropy $\xi_n = D_n/D_0$, then, providing the counts are not too low,

$$\mathrm{var}(\xi_n) \simeq (1/\bar{D}_0^2) \sum_i (M_{ni} - \bar{\xi}_n M_{0i})^2 \mathrm{var}(X_i). \tag{18}$$

Systematic errors are, of course, much harder to estimate.

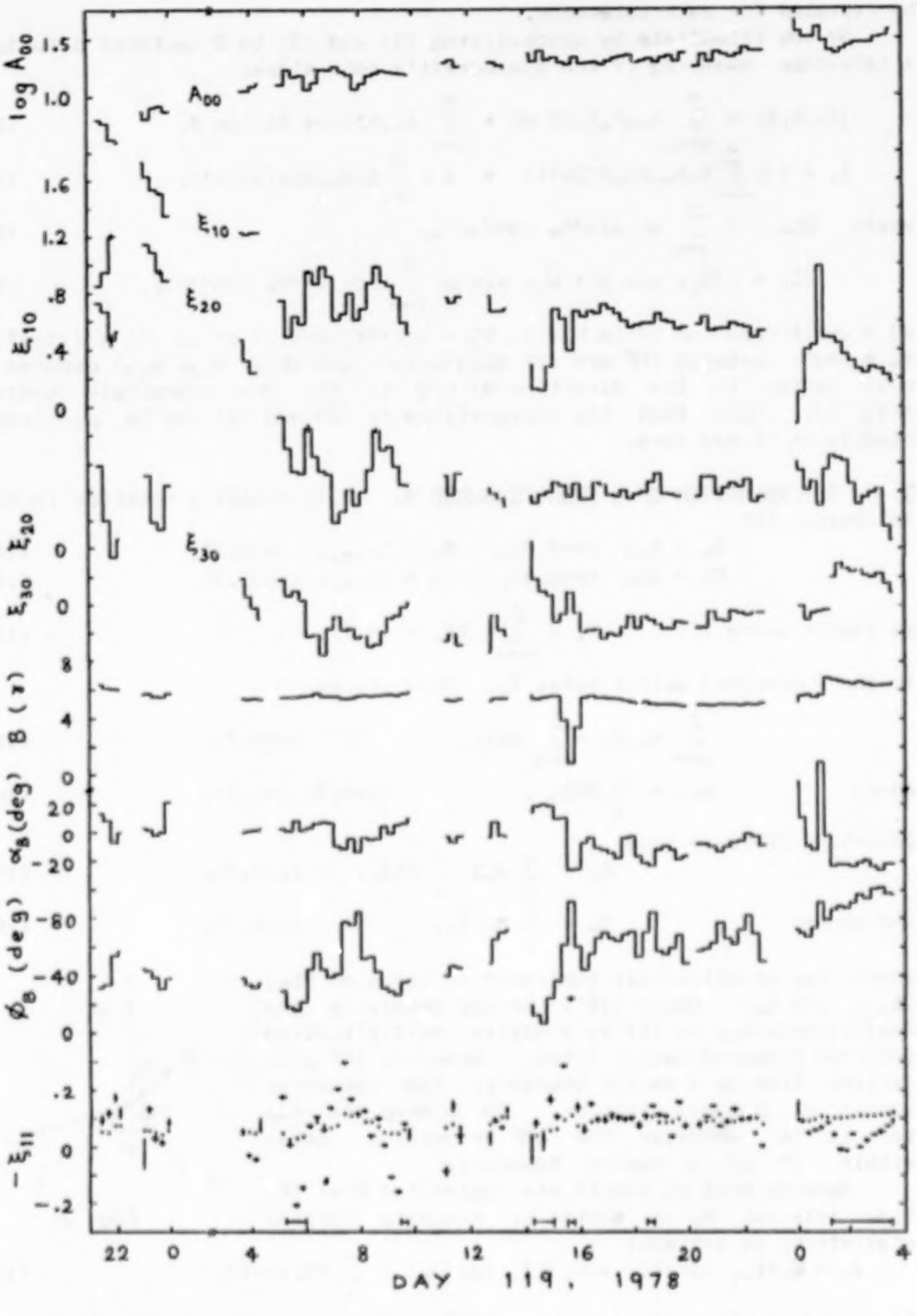

Fig. 2: 15-minute intensity and anisotropies of 1.4-2.5 MeV protons

4. **APPLICATION** As an example, we show in Fig. 2 the 15-min averages of A_{00}, ξ_{10}, ξ_{20}, ξ_{30}, and $-\xi_{11}$ for 1.4 - 2.5 MeV protons, determined

with the above method using 8-sectored particle data (P.I.: R.E. Vogt, CalTech), concurrent IMF (P.I.: N.F. Ness, GSFC), and hourly solar wind speed (P.I.: H. Bridge, MIT), measured aboard IMP-8 and accessed through NSSDC. Some typical standard errors due to Poisson statistics only are indicated by vertical bars.

Estimating the spectral slopes by using the corresponding results for 4-13 MeV protons, we have found the Compton-Getting corrections (Ng, 1985) for transformation to the $\underline{E}\times\underline{B}$ drift frame to be small, $<.002\ A_{00}$, $<.01$, $<.01$, $<.02$ for A_{00}, ξ_{10}, ξ_{20}, and ξ_{30} respectively. (For transformation to the solar wind frame, the corrections are of the order of $0.04\ A_{00}$, 0.1, 0.3, and 0.5 respectively). Thus A_{00}, ξ_{10}, ξ_{20}, ξ_{30} essentially characterise the pitch-angle distribution in the $\underline{E}\times\underline{B}$ drift frame.

5. DISCUSSION The Compton-Getting correction, $\varepsilon \dot{W}_\perp(3 - pA'_{00}/A_{00} + pA'_{20}/5A_{00})$ to the transverse anisotropy $-\xi_{11}$ is indicated by the dots in Fig. 2. The observed anisotropy varies in phase with this correction but is much larger in magnitude. The same feature, even more marked, is seen for 4-13 MeV protons. What is the cause of this large discrepancy?

For Fig. 2, IMP-8's GSE coordinates in R_E varies from (21.6, 21.5, 5.5) to (5.7, 29.5, 18.1). The times when the IMF is connected to the nominal bow shock (BS) are indicated by horizontal bars in Fig. 2 (Ng & Roelof, 1977). At ~1537 UT Day 119, some solar particles with guiding centres below the IMF through IMP-8 are probably shadowed by the nose of the BS, resulting in the observed peak value of $-\xi_{11} = 0.53$. However BS connection does not account for the general variation of $-\xi_{11}$ in Fig. 2.

Close inspection reveals that the sector plot of X_1 lags behind the IMF in directional changes. Hence a tentative explanation is that some observed 15-min averages contain a substantial fraction of non-gyrotropic distributions which reside a short distance (~1 gyroradius) beyond a 'kink' in the IMF. An alternative explanation is as follows. When ϕ_B swings rapidly in an averaging interval such that its average value is close to one end of the range of values, then a field-aligned anisoptropy ξ_{10} would "induce" a nonzero value of $-\xi_{11}$, i.e., the apparent value of $-\xi_{11}$ is not real. Further studies with smaller averaging intervals would clarify this matter.

6. CONCLUSION We have shown how to obtain the directional differential intensity referred to the standard coordinate system (Ng, 1985) from sectored particle data and concurrent IMF and solar wind data. The corrections for transformation to the $\underline{E}\times\underline{B}$ drift frame are explicitly calculated and found to be small for these ~1.5 MeV protons. However, the new correction formulae would be important for $\lesssim$ 500 KeV protons. It is tentatively suggested that the 'observed' transverse anisotropy may in large part be induced by a rapidly changing IMF in the presence of a field-aligned anisotropy.

Acknowledgement Prof E.C. Stone's hospitality and the advice of Drs. R.A. Mewaldt and T.G. Garrad on CalTech EIS experiment are gratefully acknowledged. I thank B.L. Ng for helping to prepare the manuscript.

References

Ng, C.K. (1985) Paper SH 3.1-10, this conference.
Sanderson, T.R. & Hynds, R.J. (1977) *Planet. Space Sci.*, *25*, 799.
Ng, C.K. & Roelof, E.C. (1977) *EOS Trans. A.G.U.*, *58*, 1205.

N85-34816

SH 3.1-13

PITCH ANGLE DISTRIBUTIONS OF SOLAR ENERGETIC PARTICLES AND THE LOCAL SCATTERING PROPERTIES OF THE INTERPLANETARY MAGNETIC FIELD

Beeck, J., and Wibberenz, G.
Institut für Reine und Angewandte Kernphysik, Universität Kiel
Olshausenstr. 40, D-2300 Kiel, FR Germany

ABSTRACT

We discuss an approximate solution of the Fokker-Planck equation containing pitch angle scattering and adiabatic focusing. For modest focusing effects the omnidirectional density obeys an ordinary diffusion equation with a modified diffusion coefficient. The anisotropic part of the distribution function is properly normalized and split into an even and an odd part. The even part is determined by the ratio between the scattering mean free path and the focusing length and by the degree of polarisation of the magnetic field fluctuations. The odd part is determined by the deviation of the pitch angle scattering from isotropic scattering $\kappa(\mu) \sim (1 - \mu^2)$. The method supplies a powerful tool to obtain the local characteristics of pitch angle scattering. It is insensitive to long-lasting solar injections and to moderate radial variations of the mean free path. The method is applied to solar particle events observed on Helios-1 and -2. We find marked differences from one event to the other. Results are presented for the solar particle events of March 28, 1976; Nov 22, 1977; April 8, 1978; April 11, 1978. In general, the pitch angle coefficient has a pronounced minimum for pitch angles near 90°. The first three events are characterized by a small local degree of scattering, with the mean free path ranging from 0.5 to 1.0 AU, whereas the April 11, 1978, event is of a more diffusive nature with $\lambda \approx 0.12$ AU.

EXPONENTIAL ANISOTROPY OF SOLAR COSMIC RAYS

J. W. Bieber, P. A. Evenson, and M. A. Pomerantz
Bartol Research Foundation of The Franklin Institute
University of Delaware, Newark, Delaware 19716

ABSTRACT

On 16 February 1984 a flare on the sun's invisible disk produced a large, highly anisotropic solar particle event. A novel technique, in which interplanetary scattering parameters are determined purely from the form of the particle anisotropy, is here applied to energetic particle data from neutron monitors and the ICE spacecraft.

1. Introduction. Recent theoretical investigations (Roelof, 1969; Kunstmann, 1979; Earl, 1981) indicate that the cosmic ray anisotropy may appropriately be expressed as an exponential function of pitch angle:

$$f = c_0 + c_1 B \exp\left\{\frac{(4-q)}{3}\frac{\lambda}{L}\,\mu|\mu|^{1-q}\right\} . \qquad (1)$$

Here, f is the phase space density, c_0 and c_1 are constants, μ is the cosine of pitch angle, B is the magnetic field magnitude, λ is the scattering mean free path, L is the magnetic field scale length, and q is a parameter which, according to quasilinear theory (Jokipii, 1971), is related to the slope of the power spectrum of magnetic field fluctuations. Provided that q and the ratio λ/L do not change with distance, (1) is an exact solution of the steady-state Boltzmann equation in arbitrary guiding field configurations, including the Parker field. Solar particle anisotropies are, of course, not precisely steady-state. Nonetheless, it might reasonably be expected that (1) constitutes a better approximation to actual anisotropies than the often utilized first-order anisotropy ($f = c_0' + c_1'\mu$) which is a solution of neither the steady-state nor the time-dependent Boltzmann equation.

On 16 February 1984, a flare on the invisible disk of the sun produced an unusual solar particle event that was recorded by neutron monitors on Earth (Pomerantz et al., 1984) and by the MEH instrument aboard ICE, which at that time was located on nearly the same nominal Parker field line as Earth at a distance of 0.07 AU upstream. The best timing of the parent flare is given by the sudden onset of radio emission at 0858 UT (Earth-received time) from beyond the western limb of the sun. This highly anisotropic event provides an ideal observational basis for testing which of the alternate forms of pitch angle distribution — first-order or exponential — best describes energetic solar particle anisotropies.

2. Neutron Monitor Observations. To determine the form of solar particle anisotropy in this event, the fractional increases recorded by 8 polar neutron monitors during the interval 0900-1000 UT were corrected to sea level pressure. An effective value of μ was calculated for each station. The data were then fitted to a first-order anisotropy and to the exponential anisotropy (1) with the parameter q set equal to unity. Separate determination of q from the available neutron monitor data was not feasible for this event.

Results of this analysis appear in Figure 1. It is immediately apparent that the exponential anisotropy provides a substantially better description of the data than the first-order anisotropy. The goodness-of-fit parameter, χ^2, is nearly 10 times larger for the first-order fit than for the exponential fit. Even this poor fit for the first-order case is accomplished only by resort to the unphysical artifice of assuming negative densities for μ less than -0.4. Changes in μ appear between the two fits because the best-fit symmetry axis differs slightly for the two assumptions.

The value of λ/L corresponding to the exponential plotted in Figure 1 is 2.8. However, comparable agreement was obtained for λ/L in the range 2-10. The value of L at this time, as calculated for a Parker magnetic field corresponding to the ICE-observed solar wind speed of 280 km/s, was 1.4 AU. Hence, at neutron monitor energies (> 400 MeV) the scattering mean free path in this event was 3 AU or larger.

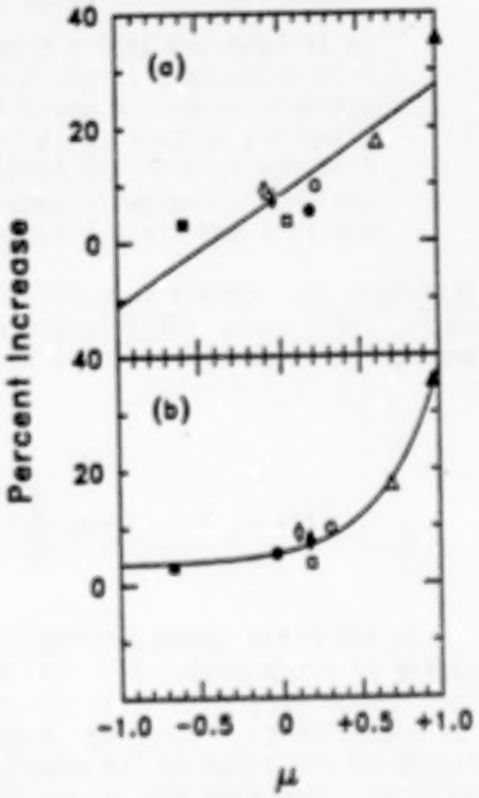

Fig. 1. Two alternate forms of pitch angle distribution are fitted to hourly-averaged neutron monitor data from Thule (○), McMurdo (●), Alert (□), Inuvik (■), Goose Bay (▲), Mawson (△), Apatity (⧫), Oulu (◊).

3. Spacecraft Observations. Measurements of the flux of protons with energies 35-145 MeV from eight equally spaced arrival directions are made every 97 seconds by the MEH instrument on the ICE (formerly ISEE-3) spacecraft (Meyer and Evenson 1978). Since the magnetic field is also measured at the spacecraft (E. Smith, private communication via ISEE common datapool tape), a representative pitch angle for each viewing direction can be computed directly by averaging the magnetic field observations over the period of the particle flux measurement. This is in contrast to the neutron monitor analysis wherein the direction of the field was a free parameter. Figure 2 shows the 35-145 MeV ICE data (10 minute average) at approximately 0955 UT on 16 February 1984, near the maximum of the event at these energies. The

sectored data obviously do not follow a straight line (first-order anisotropy) but the exponential (1), with a choice of $q=1.2$ and $\lambda/L=2.8$, provides an excellent fit, as shown by the plotted curve.

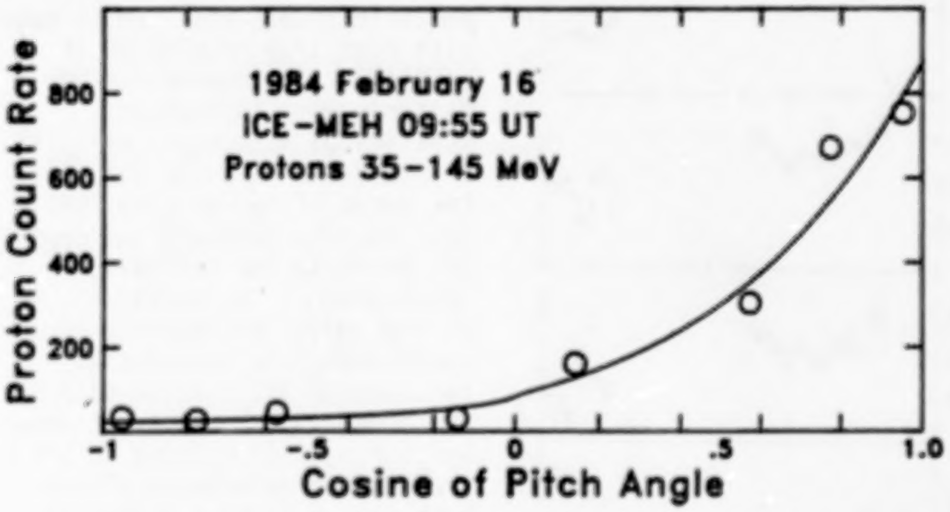

Fig. 2. Sectored ICE particle data (circles) are compared to an exponential anisotropy (curve) with $\lambda/L = 2.8$ and $q = 1.2$.

The persistent high anisotropy of the event and the long mean free path determined from the shape of the pitch angle distribution suggest that the entire time profile is a reflection of continued injection at or near the sun. We have modeled the time profile using coronal diffusion (Reid, 1964) and interplanetary focused diffusion (Bieber et al., 1980) and find excellent agreement. A key result of this analysis is that the flow at the position of the spacecraft is at all times approximately steady state. Changes with time are nearly all due to changes in the source strength at the sun.

Such a steady state flow may be used to look for changes in the scattering parameters which determine the shape of the pitch angle distribution. A related analysis conducted by Bieber and Pomerantz (1985) uses long term averages of neutron monitor data. The shape of the pitch angle distribution may be characterized many ways, one of which is to consider ratios of the amplitudes of harmonic components determined by Fourier analysis of the counting rate as a function of arrival direction. Figure 3 shows the average flux, ratio of second to first harmonic r_2/r_1, and ratio of third to first harmonic r_3/r_1 as a function of time. Note the distinctly different values of the harmonic ratios before and after the data gap. This jump implies a reduction in the mean free path for scattering by almost a factor of two, while q remains nearly unchanged. It is likely that this change is related to the change in the properties of the solar wind which is indicated by the increase in the magnetic field magnitude also shown in Figure 3.

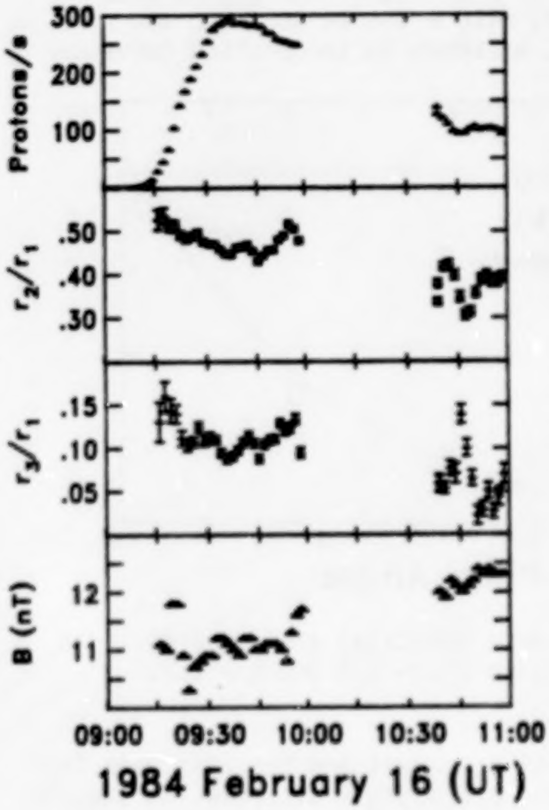

Fig. 3. Time profiles of average particle flux, harmonic ratios r_2/r_1 and r_3/r_1 (see text), and magnetic field B observed at ICE.

4. Conclusions. Local measurements of important parameters of interplanetary particle propagation can be made with high time resolution if particle anisotropies can be measured with sufficient statistical accuracy. Analysis of energetic particle data for the event of 16 February 1984 from neutron monitors and from ICE leads to the following conclusions: (1) Particle anisotropies are better described by an exponential function of pitch angle than by the commonly assumed first-order anisotropy. (2) Fitting to the exponential anisotropy allows both the scattering mean free path λ and the parameter q, which characterizes the dependence of the scattering rate upon pitch angle, to be determined. For this event, it is found that λ is greater than 3 AU and q is approximately 1.2. (3) An apparent change in the scattering mean free path occurred in connection with a small change in the magnitude of the interplanetary magnetic field.

5. Acknowledgments. This research was supported by the National Science Foundation under grants ATM-8303758 and DPP-8300544 and by NASA under grant NAG-5-374.

References

Bieber, J. W., and M. A. Pomerantz, (1985), paper SH 4.5-21, this conference.

Bieber, J. W. et al., (1980), J. Geophys. Res., 85, 2313.

Earl, J. A., (1981), Astrophys. J., 251, 739-755.

Jokipii, J. R., (1971), Rev. Geophys. Space Phys, 9, 27-87.

Kunstmann, J. E., (1979), Astrophys. J., 229, 812-820.

Meyer, P. and P. Evenson, (1978), IEEE Trans. Geosci. Electronics, GE-16, 180.

Pomerantz, M. A. et al., (1984), Proc. Intl. Symp. on C-R Modulation in the Heliosphere, pp. 437-443, Morioka, Japan.

Reid, G. C., (1964), J. Geophys. Res., 69, 2659.

Roelof, E. C., (1969), Lectures in High-Energy Astrophysics, NASA Spec. Publ. 199, pp. 111-135, NASA, Washington, D. C.

N85-34818

SH 3.2-2

ENERGETIC SOLAR PARTICLE EVENTS

K.B.Fenton, A.G.Fenton and J.E.Humble
Physics Department, University of Tasmania
Box 252C, G.P.O., Hobart, Tasmania, Australia, 7001

1. Introduction. Studies of the arrival directions of energetic solar particles during ground level enhancements (GLE's) observed by neutron monitors have shown that, in general, in the first hour of the event most of the particles arrive with a distribution of pitch angles peaked about the garden-hose field direction in the vicinity of Earth (e.g., McCracken, 1962, Maurer et al.,1973, Duggal,1979). During the first hour some of the particles arrive from the anti-solar direction, while in later stages of the event the intensity becomes more nearly isotropic as a result of scattering of particles in interplanetary space.

In this paper an attempt is made to determine the arrival directions of the particles during the early stages of the GLE of 16 February 1984 using the data currently available to us from high latitude neutron monitors near sea level where the cut-off is essentially atmospheric (∿1GV).

2. Data. In this event the first particles arrived at Earth during the interval 0905-0910 UT and the data we have used for this interval are listed in Table 1 together with the asymptotic viewing directions assumed for the neutron monitors for 2 GV particles (Shea and Smart, 1975). We also list the percentage increases observed in the next five minutes. These figures are expressed as the percentage above the level prevailing in the hour 0800-0900 UT.

TABLE 1 DATA FOR GLE OF 16 FEBRUARY 1984

STATION	ASYMPTOTIC DIRECTION AT 2GV LATITUDE	LONGITUDE,^{0}E	PERCENTAGE INCREASE 0905-0910	0910-0915
Goose Bay	-8	0	42.4	94.2
Deep River	-22	10	39.5	71.9
Mawson	-13	56	36.6	49.3
Kerguelen	26	152	5.5	11.0
Thule	68	324	0	8.4
Terre Adelie	-53	170	0	5.0
Inuvik	16	233	0	1.5
Alert	83	8	0	0
McMurdo	-67	275	0	0

3. Analysis. It was expected that during the first five minutes virtually all the particles would arrive from the garden-hose direction or from small angles relative to that direction, since the time would not be available for receiving scattered particles, except those scattered very close to Earth.

Following earlier authors, we use the symbol δ to represent the angle between the asymptotic mean direction of arrival of the particles and the asymptotic viewing direction of a neutron monitor, calculated in most instances for 2 GV particles.

In spite of the apparent simplicity of this event, we have so far been unable fully to understand the pattern of arrival directions. At 0910 UT on 16 February 1984, the Sun was overhead at $(-12^{0},42.5^{0})$, implying that if the solar wind speed were such that the garden-hose angle was 45^{0}W of the Earth-Sun line, the mean arrival direction of the particles should have been $(-12^{0},357.5^{0})$. However, the fact that the increases observed in the first five minutes at Goose Bay, Deep River and Mawson were so nearly the same would appear to require a near equality of the δ values for these stations instead of the 5^{0}, 16^{0} and 57^{0} calculated for this case. By trial, we have found that if, instead, the mean arrival direction were $(5^{0},25^{0})$ the δ values for Goose Bay, Deep River and Mawson would have been 28^{0}, 31^{0} and 36^{0} respectively, values consistent with the progression towards slightly smaller intensity increases for these stations. This arrival direction, however, implies a garden-hose angle of less than 20^{0}W of the Earth-Sun line which would appear to be unacceptably small.

There is the further problem that for a mean arrival direction of $(5^{0},25^{0})$ Kerguelen has a δ value for 2 GV particles of 120^{0} and would not therefore be expected to receive prompt particles. However, a 5.5% increase occurred in the first five minutes, and the profile has the appearance characteristic of prompt particles. If it is assumed that, say, 4 GV particles were responsible for the increase at Kerguelen, the δ value would be 74^{0}. Although less than 90^{0}, this value seems to be still too large for prompt particles. In any case Thule and Alert have δ values of 74^{0} and 78^{0} respectively but registered no increase in the first five minutes. At this stage, we have not found a satisfactory solution to these problems.

A similar analysis of the next five minute interval, during which scattered particles were received at several monitors, has also failed so far to yield an orderly progression of percentage increase versus δ. It is interesting to note that Pomerantz et al. (1984) found by analysing the hourly average data for this event that a smooth function of the percentage increase versus cos δ could be obtained. Whether this is due to the effect of smoothing fine structure is a matter to be investigated.

4. Comments. As with previous analyses which we have made of five minute data, e.g., the event of 7,8 December 1982 (Fenton et al., 1983), we believe that a more detailed treatment may be necessary in which the actual asymptotic directions at the time of the event are used and in which the over-simplification is eliminated of assuming that a single asymptotic direction can be used for each station. In a more detailed analysis, the responses of high altitude, as well as non-polar, monitors should also be taken into account. It should be possible to extend the analysis to one-minute data, at least for large GLE's for which accurately timed data are available, and thus obtain additional information on the scattering environment in the nearby interplanetary space.

5. Acknowledgements. We wish to thank the people responsible for the operation of the neutron monitors listed in Table 1 and their organizations for supplying us with their data. The project is supported in part by the Australian Research Grants Scheme.

References.

Duggal,S.P.,(1979), Rev. Geophys. and Space Phys., 17, 1021.

Fenton,K.B., Fenton,A.G. and Humble,J.E.,(1983), Proc.18th ICRC, 4, 189.

McCracken,K.G.,(1962), J. Geophys. Res., 67, 435.

Maurer,R.H., Duggal,S.P. and Pomerantz,M.A.,(1973), J. Geophys. Res.,78,29.

Pomerantz,M.A., Bieber,J.W. and Evenson,P.A.,(1984), Proc. Int. Symp. Cosmic Ray Modulation in the Heliosphere, Morioka, Japan, 437.

Shea,M.A. and Smart,D.F.,(1975), Air Force Cambridge Research Laboratories Environmental Research Papers, No. 502, AFCRL-TR-75-0177.

N85-34819

SH 3.2-3

CHANNELED PROPAGATION OF SOLAR PARTICLES

K. A. Anderson[*] and W. M. Dougherty

Space Sciences Laboratory
University of California, Berkeley, CA 94720
U.S.A.

1. Introduction. *Bartley et al.* (1966) and *McCracken and Ness* (1966) identified bundles of interplanetary magnetic field (IMF) lines that differed in direction from the interplanetary field lines in which they were imbedded. These bundles, called filaments by the authors, differed in direction by as much as several tens of degrees from the surrounding field. The filaments were first noticed due to the large and sudden change in flow direction of highly anisotropic solar flare protons in the energy range 1 to 13 MeV. Passage of the filaments over the spacecraft required a few hours, implying a diameter for the filaments of approximately 3×10^6 km at a distance of 1 AU from the Sun. In 1968, *Jokipii and Parker* used *Leighton's* hypothesis of random walk of magnetic field lines associated with granules and supergranules (1964) to develop a picture of an interplanetary medium composed of a tangle of field lines frozen into the solar wind, but whose feet were carried about by the random motions at the solar surface. *Jokipii and Parker* noted that using a correlation length of 15,000 km — about the radius of a supergranule — the magnetic structure would be 3×10^6 km in size at 1 AU. This is close to the size of the filaments as determined by *Bartley et al.* and *McCracken and Ness.* These workers did not find changes in the solar particle intensity, anisotropy ratio or energy spectrum as the spacecraft entered the filament.

In this paper we analyze further the phenomenon of interplanetary filamentary structure. We have identified about 50 such well-defined structures in 1978 and 1979, mainly on the basis of intensity changes in fluxes of solar electrons of energy 2 to 10 keV. Ion intensity changes are often found to accompany the changes in electron intensity. We have made use of simultaneous observations of solar wind plasma and magnetic field on the ISEE-3 spacecraft in order to further characterize interplanetary filament structure.

2. Discussion. Figure 1 shows a solar flare particle event as seen at 1 AU on the ISEE-3 spacecraft. After the impulsive phase, the electron intensity decays and the slower moving ions begin to appear at about 1800 UT. At 2000 UT the low energy electrons and the ions abruptly increase in intensity. About 6 hours later the particle intensity suddenly decreases. In this case, there are no well-defined changes in the solar wind or IMF parameters with which to associate the particle intensity changes. Of further interest is the small solar flare particle injection which begins at about 0100 UT on 21 May. From the observed velocity dispersion in the higher energy channels, we would expect the arrival of 2 keV electrons sometime after 0200 UT. The absence of a new injection of electrons at this time in the lowest energy channels could be simply due to the absence of low energy electrons in the flare. This seems unlikely to us since, in the many such flare events observed on ISEE-3, we almost always find a rising spectrum down to the lowest energies. We prefer to interpret the effect as being due to location of the small flare within the region of field lines which define the filament. After the filament passes over the spacecraft, electrons from the small flare can no longer reach the spacecraft. The presence of particles from the earlier flare for many hours before and after the passage of the filament implies that the particles from this flare were injected into a much larger spatial region than was the case for the smaller flare. Figure 2 shows that the angular distribution of the low energy electrons differs significantly from that in the surrounding IMF. Just before entry into the filament, the pitch angle distribution was nearly isotropic (I in Figure 2). Inside the filament, the percentage of the

---

[*] Also Department of Physics.

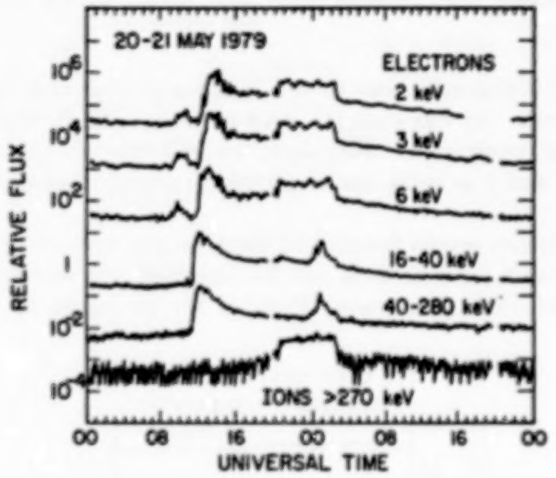

Figure 1. A broad filament interrupts the decay of a solar flare particle event for about 6 hours. The filament evidently connects the spacecraft to a place in the solar atmosphere where the emission of solar particles is greater than in the surrounding regions.

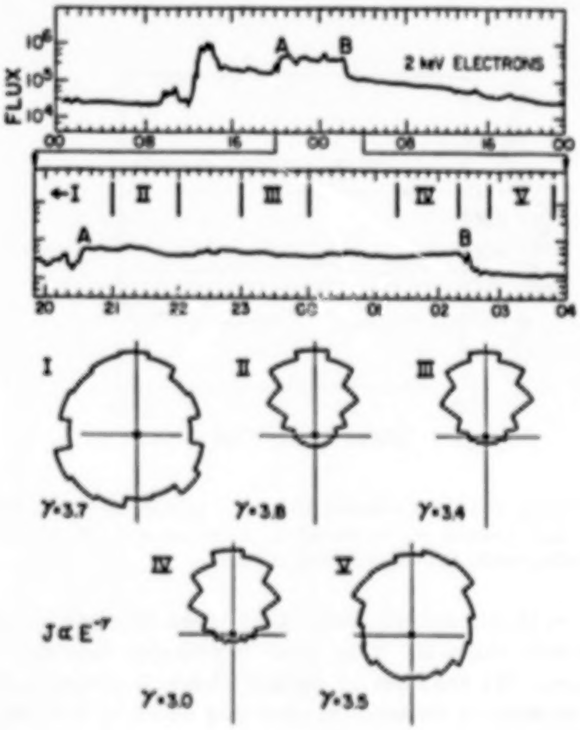

Figure 2. The pitch angle distribution of the low energy electrons in the filament shows a strong flow of particles away from the Sun. The energy spectrum of the electrons inside and outside the filament do not differ much, perhaps indicating the particles in the filament also come from the flare which began at 1107 UT.

electrons directed back toward the Sun is very small. After passage of the filament, the flow becomes much less anisotropic. The propagation conditions are very different for the low energy electrons inside the filament than for those in the surrounding interplanetary medium.

Figures 1 and 2 illustrate some of the features of filaments in the IMF as seen in low energy solar electrons. In this example, and in many others, there is little change in the solar wind and IMF parameters. Therefore, we will refer to particle effects such as those shown in Figures 1 and 2 as being due to particle propagation channels.

Figure 3 illustrates several features of these propagation channels. During the 24-hour interval shown, at least three of these can be identified. First, there are strong correlations with solar wind and IMF parameters. Perhaps the strongest of these is with solar wind number density.

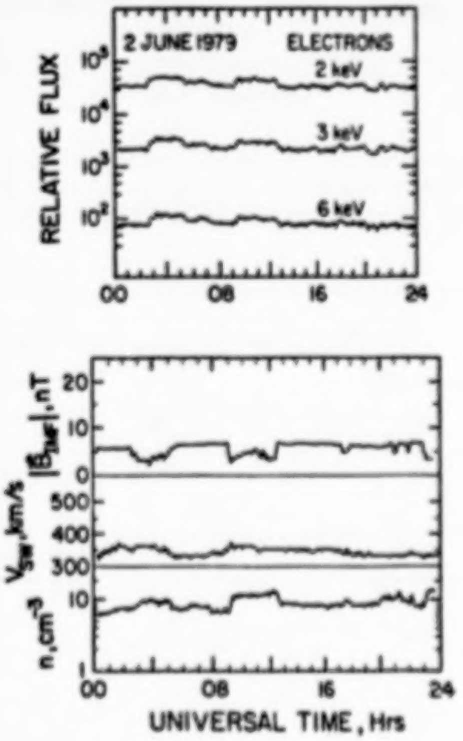

Figure 3. Particle propagation channels often occur in clusters. In this example at least three such channels can be identified. There are well-defined correlations with solar wind density and magnetic field changes.

Although not as clearly defined, solar wind speed changes appear to be spatially coincident with the particle channels. It is quite remarkable that the relative magnetic field decreases are so large. The sequence of particle channels shown in Figure 3 illustrates the tendency for them to come in clusters. Several may occur in one day, but then several days may go by without their appearance.

We have selected 37 of the most clearly defined examples of particle channels and, using solar wind velocity and IMF direction, calculated the spatial extent of each channel. The result is $3.7 \pm 2.3 \times 10^6$ km, where we have given the average and the average deviation. We have not attempted to correct these numbers for geometrical effects based on assumed cross-section shapes for the channels. Our average value is somewhat higher than that obtained by *Bartley et al.*, but the agreement is nonetheless good.

3. Conclusions. Finally, we summarise a few of the results obtained to date:

1) Particle propagation channels tend to come in clusters separated by a few hours. Intervals of days may elapse without the appearance of these features. There is a strong tendency for the particle channels to appear in populations of solar particles which are relatively young. Conversely, the channels are relatively rare near the end of long-lived streams of solar particles.

2) Particle propagation channels are defined by particle decreases as well as increases. The channels may contain ions as well as electrons. In some channels, the ions may show an increase while the electrons decrease, and *vice versa*.

3) The angular distribution of electrons inside the particle channels often differs greatly from the angular distributions outside the channel. This implies a considerable difference in the amount of magnetic turbulence in the frequency range 1 to 10 Hz, the frequencies most effective in scattering the pitch angles of low energy electrons.

4) We believe that particle channeling characterizes much of the interplanetary medium. While the average rate of occurrence of clearly defined ("square wave") particle channels may be on the order of only one per day, there appear to be many more channels which are less well-defined.

5) Correlation with solar wind and IMF parameters is highly variable. Sometimes the channel is distinctly defined by several of these parameters; at other times one parameter may mark the channel. In one case, a tangential discontinuity marks the edges of a particle channel (*Tsurutani, Personal Communication*, April, 1985).

6) The particle propagation channels consist of magnetic field lines which trace back to a distinctly different place in the solar particle source region, presumably in the solar atmosphere, than do field lines adjoined to the propagation channels.

4. Acknowledgements. This work was supported by NASA grant NAG5-376.

References.

Bartley, W. C., R. P. Bukata, K. G. McCracken and U. R. Rao, Anisotropic cosmic radiation fluxes of solar origin, *J. Geophys. Res.* **71**, 3297, 1966.

Jokipii, J. R. and E. N. Parker, Random walk of magnetic lines of force in astrophysics, *Phys. Rev. Lett.* **21**, 44, 1968.

Leighton, R. B., Transport of magnetic fields on the Sun, *Astrophys. J.* **140**, 1547, 1964.

McCracken, K. G. and N. F. Ness, The collimation of cosmic rays by the interplanetary magnetic field, *J. Geophys. Res.* **71**, 3315, 1966.

N85-34820

SH 3.2-4

THE PROPAGATION OF SOLAR ENERGETIC PARTICLES IN MAGNETIC CHANNELS

*F. B. McDonald
NASA Headquarters

L. F. Burlaga
NASA/Goddard Space Flight Center

The existence of interplanetary flow systems produced by the entrainment of interplanetary transients - consisting of flare-produced shocks, high-speed solar wind streams and coronal mass ejection - has been established by Burlaga and co-workers. This entrainment process produces enhanced regions of the interplanetary magnetic field that should be connected back to the solar corona. These compressed regions can provide a preferred magnetic channel for the propagation of solar cosmic rays. The characteristics of these events appear to be different from those previously reported by the NASA/University of New Hampshire team and the University of Chicago in their study of a large number of events in the region beyond 1 AU. These new events have a very flat energy spectra (with $\gamma \approx 1.5$) that frequently extend to energies above 100 MeV and have a significant enhancement of MeV electrons. The combined data of Pioneer 11 and Voyagers 1 and 2 make it possible to separate temporal and spatial variations. The particle anisotropies are modest (<10% at 12 MeV). Because of the field compression, adiabatic energy losses appear to be significantly reduced. This effect should be of general astrophysical significance since it provides a mechanism for injecting particles accelerated near a star into the interstellar region without large energy losses.

Frank B. McDonald
NASA Headquarters/Code P
Washington, DC 20546

*Presented by

N85-34821

RADIAL TRANSPORT OF ~1 MeV/nucleon IONS DURING THE 22 NOVEMBER 1977 SOLAR PARTICLE EVENT

G.M. Mason[1], D.C. Hamilton[1], G. Gloeckler[1] and B. Klecker[2]

[1]Dept. of Physics & Astronomy, Univ. of MD, College Park, MD 20742 USA
[2]Max-Planck-Institut fur Exterrestrische Physik, 8046 Garching, FRG

1. Introduction. Time-intensity profiles of solar flare energetic particle events carry information on the particle injection processes at the sun, as well as the transport of particles in interplanetary space. However, in order to help identify the individual processes of injection versus transport it is necessary to use observations taken at more than one radial location. We present here results of such a study concerning the 22 November 1977 solar particle event, observed with instruments at 1.0 and 1.55 AU. The observations are for particles of energies near 1 MeV/nucleon, considerably less than the ~10-20 MeV/nucleon energies typical of previous radial transport studies (e.g. 2,10). Thus, in the present work we are able to examine the validity of transport models to considerably lower energies than in previous work.

2. Observations. The 22 November 1977 event began at 0945 UT with a 2B flare at N24 W40. From this location it is reasonable to assume that particles had prompt access to the interplanetary magnetic field line connected to Earth. This solar particle event has been widely studied (e.g. references in 7). Figure 1 shows the time-intensity profiles for several species observed at 1 AU with the ISEE-1 ULEWAT sensor (5). Gaps in the profile are due to data removal around radiation belt passes. For He, the time of maximum (M) was about 36 hours after the flare (F), well before the passage of the flare-associated shock (S) late on November 25. Figure 2 shows time-intensity profiles for the same set of species observed at 1.55 AU (3) with the Voyager-2 LECP instrument (6). During this flare the Earth-Sun-Voyager angle was about 5°, and so this spacecraft was also well connected to the flare site. Although the Voyager profiles show some disturbance during the onset phase between 0000-1200 on November 23, it appears that the times to maximum can be identified, with a value of about 48 hours for He.

3. Model Fits. In modeling the time to maximum for low energy particles such as those in this study, it is essential to include the effects of convection and adiabatic deceleration (e.g. 9). Accordingly, we have used a model based on the spherically symmetric Fokker-Planck equation including diffusion, convection and adiabatic energy loss, numerically solved using the code of Hamilton (2). In the calculation we used a constant solar wind velocity typical for this period, an injection time at the H_α onset, and an assumed particle number density in the form of a power law in energy/nucleon with spectral index derived from the observed spectra at 1 and 1.55 AU. The interplanetary diffusion coefficient had the functional form typical in radial propagation studies: $\kappa = \kappa_o r^b = v_{particle} \lambda_r/3$. Finite injection time profiles used the form $I = I_o \exp(-t/\sigma_c)$. Following reference (7) it was assumed that κ_o scaled as $(A/Q)^{0.55}$ for this particle event.

With the model so specified, the adjustable parameters are λ_r, b,

ORIGINAL PAGE IS
OF POOR QUALITY

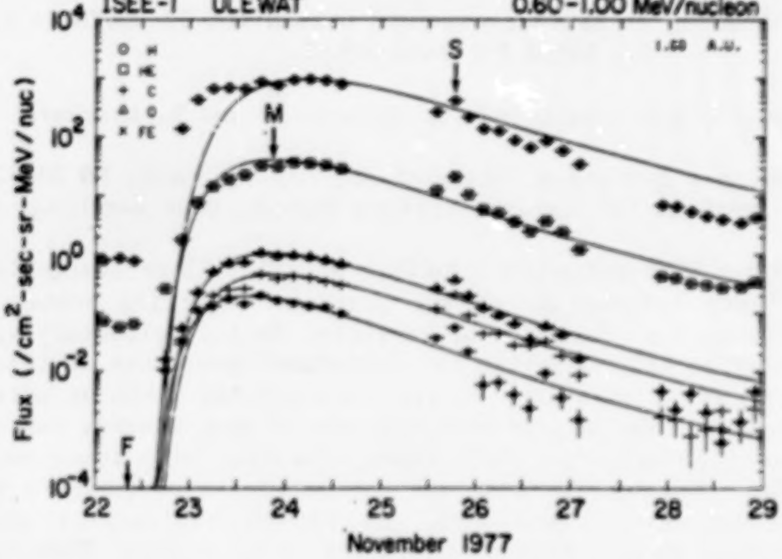

Figure 1

and σ_t; note that σ_t is a source characteristic while λ_r and b are properties of the interplanetary transport. Fitting the Helium time to maximum at 1 and 1.55 AU does not uniquely determine the 3 parameters: an additional observation was needed. This was chosen to be the time to 1% of maximum intensity at 1 AU (~10 hours) for Helium, thus fitting the early rise portion of the event.

Figures 3 and 4 show families of curves in the λ_r - b plane which provide the required T_{max} values at both sites: notice the wide range of values which are possible with an observation at 1 or 1.55 AU only. Overlaying Figures 3 and 4, an intersecting line is obtained, shown in Figure 5, which has the λ_r - b values which yield the observed T_{max} values at both 1 and 1.55 AU. The intersection of this line with the locus of values for $T_{1\% \text{ of } max}$ = 10 hours (Figure 5) yields a unique set of values for λ_r, b and σ_t, which are listed in Table 1. The uncertain-

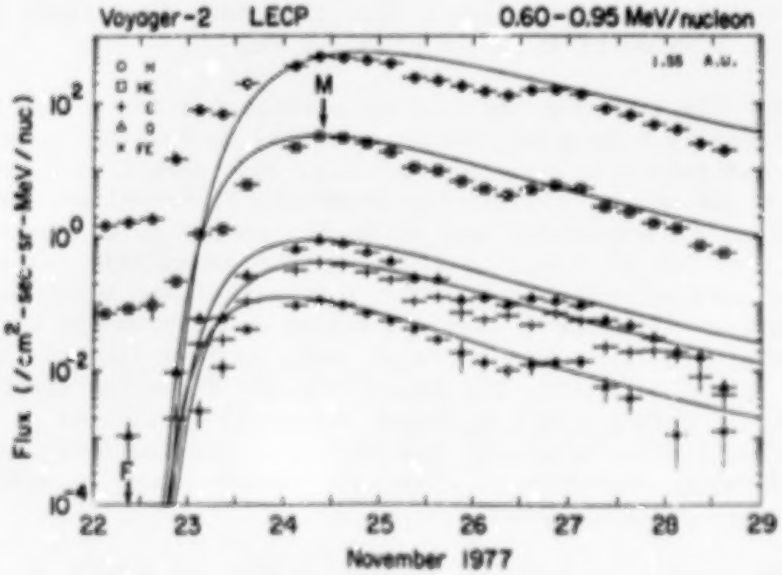

Figure 2

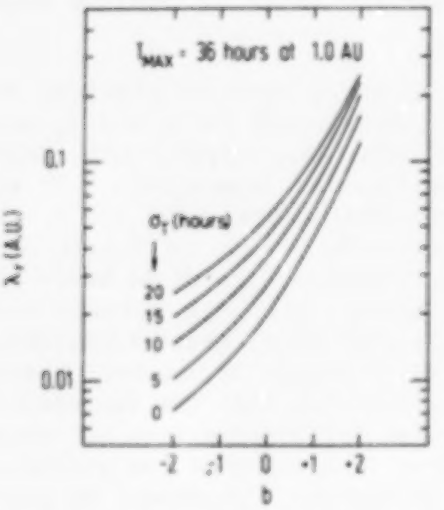

Figure 3

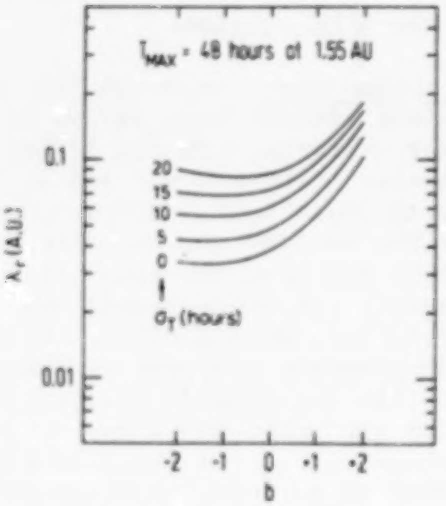

Figure 4

ties in the values are based on an estimated uncertainty of ± 20% in κ.

Table 1
Fit Parameters for 0.6-1.0 MeV/nuc Helium

λ_r = 0.10 ± 0.02 AU at 1 AU
b = 1.3 + 0.1
σ_t = 12 ± 3 hours

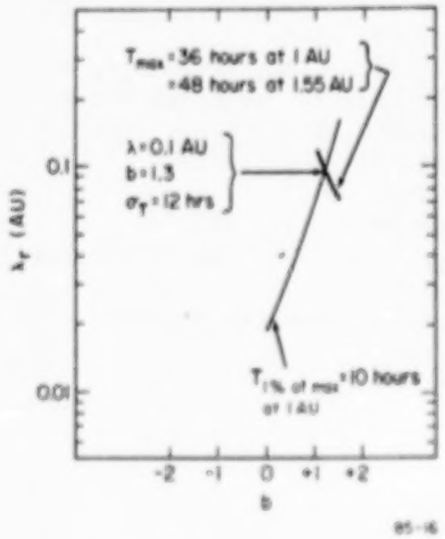

Figure 5

Time intensity profiles for all species using the Table 1 values for He, and assuming scaling in λ_r as $(A/Q)^{0.55}$, are shown in Figures 1 and 2. Considering the 1 AU data in Figure 1, the fits are generally satisfactory for He, C, O and Fe up through the early decay phase, and they reproduce the temporal variations of the heavy ion ratios such as Fe/O seen in this event (7). Protons, however, have a fast rise time which is not fitted by the assumed scaling. This may be indicative of interplanetary acceleration for the protons, which, as the lowest rigidity particles in the set would be expected to be the most susceptible to such effects. The 1.55 AU fits are reasonable for the times to maximum and the decay phases, although of course the model does not fit the previously noted distortions in the rise phase. As is the case at 1 AU, the protons observed at Voyager have a fast rise-time which does not follow the $(A/Q)^{0.55}$ scaling used for the $A/Z=2$ species.

4. Discussion. Although the value of λ_r found here is similiar to previous studies (e.g. review in 8), the values found for b and σ_t are rather different from the higher energy studies (e.g. 1,2), which have generally yielded $b \sim 0$ and $\sigma_t = 0$ (delta function injection). If we were to force such a choice on the present observations at 1 AU, it is possible to find the required λ_r value from the curves in Figure 3-- however the resulting value ($\lambda_r = 0.015$ AU) yields a T_{max} of 66 hours at Voyager: 18 hours beyond the observed value, and well outside the experimental uncertainties. It is possible that this result represents a disagreement with the previous work. More likely, it is due to the fact that the particle energies are lower, and also that the two spacecrafts are relatively close to 1 AU and thus the observations are more sensitive to σ_t and the behavior of λ_r out to 1 AU than the previous studies at generally much larger radial distances. It should be possible to resolve these uncertainties by considering additonal data such as anisotropies (4) and by analyzing additional particle events.

5. Acknowledgements. We are grateful to the MPE, UMD, Johns Hopkins/APL individuals responsible for the success of the ISEE and Voyager instruments. One of us (G.M.) wishes to thank the Max-Planck-Institut, Garching, for its hospitality during a visit when most of this study was carried out. This work was supported by NASA under contract NAS5-28704, grants NGR 21-002-224/316, and NAGW-101, by the NSF under grant ATM-84-07546, by NASA/APL subcontract 601620, and by the Bundesministerium fur Forschung und Technologie, contract RV 14-B8/74.

References

(1) Goeman, R. and Webber, W.R. 1983, 18th ICRC, Bangalore, 10, 385.
(2) Hamilton, D.C. 1977, J. Geophys. Res., 82, 2157.
(3) Hamilton, D.C. and Gloeckler, G. 1981, 17th ICRC, Paris, 10, 49.
(4) Hamilton, D.C. et al. 1985, 19th ICRC, LaJolla, paper SH 3.1-8.
(5) Hovestadt, D. et al. 1978, IEEE Trans. Geo. El., GE-16, 166.
(6) Krimigis, S.M. et al. 1977, Space Sci. Rev., 21, 329.
(7) Mason, G.M. et al. 1983, Ap.J., 267, 844.
(8) Palmer, I.D. 1982, Rev. Geophys. Space Phys., 20, 335.
(9) Scholer, M. 1981, Adv. Sp. Res., 1, 121; 1976, Ap.J. (Letters), 209, L101.
(10) Zwickl, R.D. and Webber, W.R. 1977, Solar Physics, 54, 457.

ENERGETIC SOLAR PARTICLE FLUXES OUT TO 3 AU DURING THE MAY 7, 1978 FLARE EVENT

Lockwood, J.A.
Space Science Center, University of New Hampshire, Durham, NH 03824, USA

Debrunner, H.
Physikalisches Institut, University of Bern, 3012 Bern, Switzerland

Simultaneous solar proton flux measurements on IMP 7 and by the world-wide neutron monitor network during the May 7, 1978 flare event led us to conclude that in the energy range from 50 MeV to 10 GeV: 1) the propagation of the flare particles in the interplanetary magnetic field (IMF) between the sun and the earth was nearly scatter-free; and 2) therefore, the intensity-time (IT) profiles of the solar proton fluxes observed at earth for about one hour after onset represent the solar injection profiles even to energies as low as 50 MeV (Debrunner et al., 1984). Observations of the IMF at Helios A indicate that the IMF was undisturbed between the sun and Helios A at the time of the May 7, 1978 flare event; and, therefore, we infer that the solar particle propagation was also scatter-free from the sun to Helios A. We then made a detailed study of the acceleration and coronal transport of the flare particles and their injection into the IMF using the fine-time resolution data from IMP 7 and Helios A (Lockwood and Debrunner, 1983, 1985). The relative positions of IMP 7 and Helios A spacecraft along with the solar flare location are shown in Fig. 1. The IMF lines are drawn for a solar wind speed V_{SW} = 480 km/s. As an example of the solar particle fluxes observed at IMP 7 and Helios A we show in Fig. 2 the responses of the energy channel with $E_{median} \sim 90$ MeV. The coronal transport was then analysed by assuming a δ-like acceleration of the protons at the flare site and by using the Reid (1964) and Axford (1965) model of two-dimensional diffusion with losses. Comparing the (IT) profiles from IMP 7 and Helios A, we found that the coronal diffusion coefficient D_S^E [cm^2/s] $\sim 4.4 \cdot 10^{15}$ (E [MeV])^2 for 20 MeV < E < 500 MeV and that the loss rate $\beta^E \sim (2.9 \pm 0.5)$ hr^{-1} for 90 MeV < E < 500 MeV. To test the validity of the model used and the deduced parameters we then calculated the ratios of the maximum solar proton fluxes at IMP 7 and Helios A for the energy channels $E_{median} \sim 90$ MeV and ∼ 350 MeV. The calculated ratios agree with the observed ones to within a factor of 2 which is good agreement. The constancy of the factor with energy further confirms the results of this analysis.

Here we apply the same model to interpret the solar proton fluxes observed on the Voyager (V) spacecraft, the locations of which are also given in Fig. 1. The solar particle fluxes for the two high energy telescopes (HET) from 70 MeV < E < 500 MeV ($E_{median} \sim 107$ MeV) at V1 and V2 are combined and shown in Fig. 3. The combination of the data is valid because the counting rates of the four HETs agreed within statistical fluctuations. In Fig. 3 we also show the (IT) profile (shaded area) expected at V according to our model of only coronal transport without IMF diffusion. Comparing the onset time and (IT) profile of the theoretical response (no IMF diffusion) with the observed ones it is clear that the propagation of the solar protons was diffusive beyond the orbit of the earth. In order to include the effects of the IMF diffusion we must determine the extent of the region over which the diffusion took place. We examined the plasma and magnetic field data on Helios A from April 25 to May 7, the Kp data at earth from April 29 to May 10, and magnetic field and solar wind data on V1 and V2 from May 7 to May 17. The shocks and/or disturbed regions found on May 7, 1978, at 0300 UT are indicated in Fig. 4. In this figure we have also shown the IMF lines to Voyager for $V_{SW} = 420$, 455, and 490 km/s. We infer that the propagation of the solar particles along the IMF lines to Voyager was scatter-free for $r < 1.6$ AU and diffusive for $r \geqslant 1.6$ AU.

To describe the diffusive propagation of the flare protons for $r \geqslant 1.6$ AU we assume as explained in Fig. 5 one-dimensional diffusion along the IMF lines with a constant mean free path λ, an "absorbing" barrier at $x = -2\lambda$, and a δ-like injection of N particles at $x = 0$, $t = 0$. The presence of an "absorbing" barrier at $x = -2\lambda$ is the equivalent physical description of the transition of the flare protons from the undisturbed to the disturbed region. The density of solar particles is then:

$$n(x,t) = \frac{N}{2(\pi Dt)^{1/2}} \left\{ \exp\left(- \frac{x^2}{4Dt} \right) - \exp\left(- \frac{[x+4\lambda]^2}{4Dt} \right) \right\} \quad (1),$$

where $D = \lambda v$, λ = mean free path for scattering and v is the particle velocity. If $x \gg \lambda$, then

$$n(x,t) = \frac{N}{(\pi Dt)^{1/2}} \cdot \frac{x}{vt} \cdot \exp\left(- \frac{x^2}{4Dt} \right) \quad (2),$$

which exhibits the same time dependence as 3-dimensional diffusion. The best fit of equation 2 to the Voyager data is found for $\lambda = 0.04$ AU in the range $1.6 \text{ AU} \leqslant r \leqslant 3.0$ AU. The theoretical data were normalized to the observations at the time of maximum and shown in Fig. 3. The agreement of the onset times and of the (IT) profiles over 3 days is excellent. From the solar transport model and the data from IMP 7 (Lockwood and Debrunner, 1985) we can estimate the value of N and predict the absolute maximum intensity at Voyager if we include the effect of the divergent IMF (Parker, 1963). The ratio of the observed to the predicted maximum fluxes at these large distances from the sun is strongly dependent upon the detailed structure of the IMF and V_{SW}. For example, we find that for $V_{SW} = 420$, 455 and 490 km/s the ratios are 1.5, 5 and 15 respectively. If we include the effect of solar particles escaping from the diffusive region into the undisturbed region ($r < 1.6$ AU), then being reflected in the undisturbed region, and later returning to the disturbed region, the ratios are reduced by about a factor of 3. The resulting ratios of 0.5, 1.7 and 3 respectively are in very good agreement using such a simple physical model.

We conclude that the coronal transport model developed in Lockwood and Debrunner (1985) and the description assumed here for the IMF diffusive propagation predict the observed solar proton fluxes at Helios A ($r = 0.35$ AU), near earth, and at the Voyager spacecraft ($r = 3$ AU) for the May 7, 1978 solar flare event.

Acknowledgements

This research was supported by grants from the US NSF (ATM-8324486 and INT-81-18555) and from the Swiss NF (2.811-0.83). We gratefully acknowledge the assistance of Dr. R.E. McGuire and Dr. N. Lal to interpret the IMP 7 and Helios A solar proton data. We thank Dr. F. McDonald for making available the Voyager data and Mrs. G. Sebor and Mrs. G. Sturzenegger for computational assistance and preparing the manuscript.

References

Axford, W.F., Planet. Space Sci. 13, 1301, 1965.
Debrunner, H., E. Fluckiger, J.A. Lockwood, and R.E. McGuire, J. Geophys. Res. 89, 769, 1984.
Lockwood, J.A., and H. Debrunner, to be published in J. Geophys. Res. 1985.
Lockwood, J.A., and H. Debrunner, Proc. 18th Int. CRC 4, 185, 1983.
Parker, E.N., Interscience Pub. (J. Wiley & Sons), 1963.
Reid, G.C., J. Geophys. Res. 69, 2659, 1964.

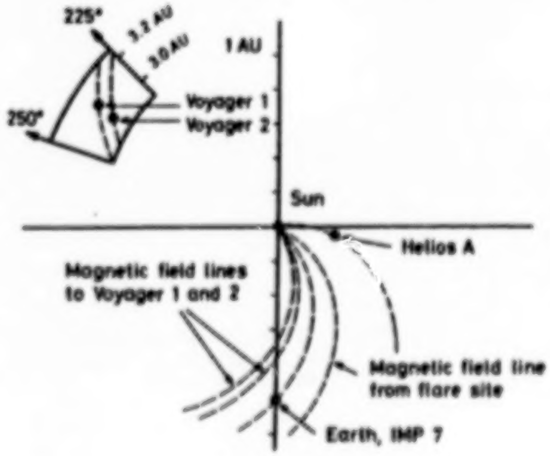
225°
3.2 AU
3.0 AU
1 AU
250°
Voyager 1
Voyager 2
Sun
Helios A
Magnetic field lines
to Voyager 1 and 2
Magnetic field line
from flare site
Earth, IMP 7

Fig. 1 Location of Helios A, the earth, IMP 7, V 1 and V 2 on May 7, 1978.

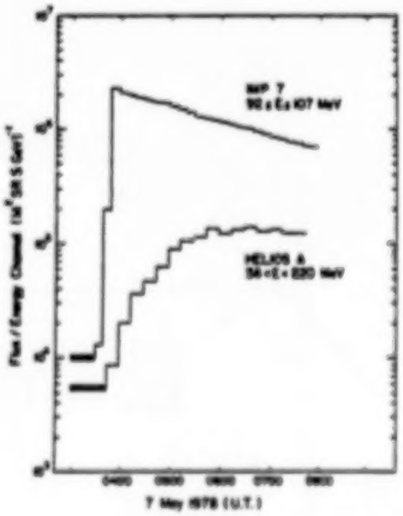

Fig. 2 Solar proton fluxes observed at Helios A and IMP 7 on May 7, 1978 for $E_{median} \sim 90$ MeV.

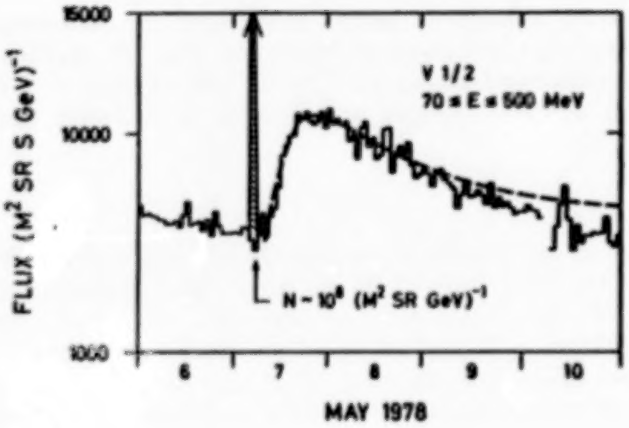

Fig. 3 Solar proton flux at V (—) compared with predicted flux (---). Shaded area is the expected solar proton flux with coronal transport only.

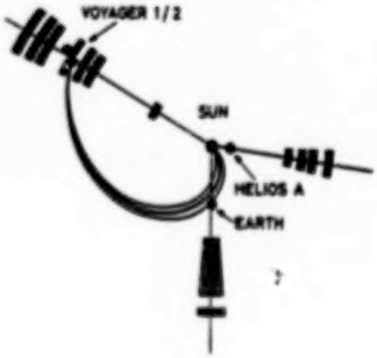
VOYAGER 1/2
SUN
HELIOS A
EARTH

Fig. 4 Locations of shocks and/ or disturbed regions at 0300 UT on May 7, 1978

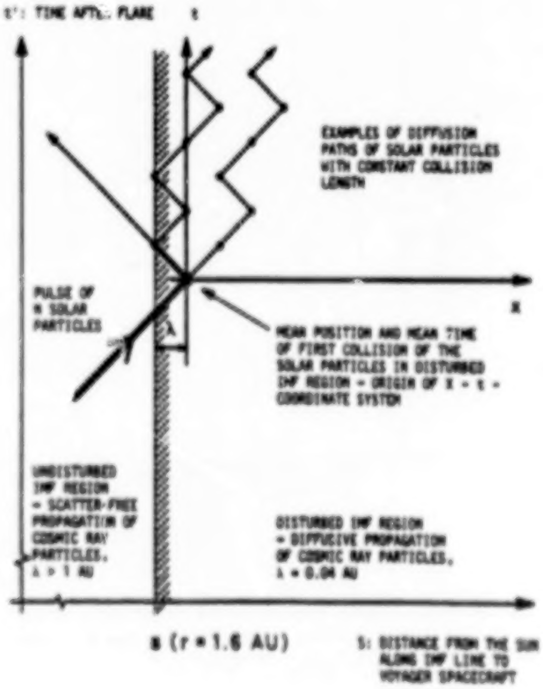
t': TIME AFTER FLARE
t
EXAMPLES OF DIFFUSION PATHS OF SOLAR PARTICLES WITH CONSTANT COLLISION LENGTH
x
PULSE OF N SOLAR PARTICLES
λ
MEAN POSITION AND MEAN TIME OF FIRST COLLISION OF THE SOLAR PARTICLES IN DISTURBED IMF REGION = ORIGIN OF X - t - COORDINATE SYSTEM
UNDISTURBED IMF REGION = SCATTER-FREE PROPAGATION OF COSMIC RAY PARTICLES, λ > 1 AU
DISTURBED IMF REGION = DIFFUSIVE PROPAGATION OF COSMIC RAY PARTICLES, λ = 0.04 AU
s (r = 1.6 AU)
S: DISTANCE FROM THE SUN ALONG IMF LINE TO VOYAGER SPACECRAFT

Fig. 5 Schematic representation of the assumed model for the IMF diffusion

N85-34823

SH 3.2-8

THE LOCAL CHARACTERISTIC FUNCTION OF INTERPLANETARY PARTICLE PROPAGATION

G. Green and W. Schlüter
Institut für Reine und Angewandte Kernphysik
Universität Kiel
Olshausenstr. 40
2300 Kiel, W-Germany

ABSTRACT

We define an easily measurable intensity function which characterizes the interplanetary propagation of charged solar flare particles. This function is nearly time invariant during a solar event despite the large variations of intensity and anisotropy, but varies from event to event. It characterizes the systematic and stochastic forces of the interplanetary magnetic field which focus and scatter the particles in pitch angle. The model of focused transport shows that this function is essentially determined by the local shape and amplitude of the pitch angle diffusion coefficient $\kappa(\mu)$ and by the local value of the focusing length. The time profile of the solar particle injection is typically of negligible influence. The local characteristic function may be used as a powerful new tool for a systematic analysis of flare particle angular distributions. Examples are given.

N85-34824

INVESTIGATION OF COSMIC RAY PROPAGATION IN INTERPLANETARY SPACE

Chebakova E.A., Kolomeets E.V., Sevast'yanov V.N.
Kazakh State University, Timiryazeva St. 46,
Alma-Ata 480121, USSR

It was established experimentally that propagation of solar cosmic rays (scr) in interplanetary space up to 1 A.U. in most cases was of diffusion character (Palmeira R.A.R., et al., 1971) .

In present paper we describe solar cosmic ray events on the basis of equation given in the paper of Dolginov A.Z., Toptygin I.N., 1966):

$$\frac{\partial n}{\partial t}=\frac{1}{r^2}\cdot\frac{\partial}{\partial r}\left[r^2\cdot\left(\varkappa_r\cdot\frac{\partial n}{\partial r}-n\cdot V\right)\right]+\frac{\partial}{\partial \varepsilon}\cdot\left\{\frac{2}{3}\cdot\frac{V}{r}\cdot\alpha\cdot\varepsilon\cdot n+D_\varepsilon\left[\frac{\partial n}{\partial \varepsilon}-\frac{n(E^2+P^2)}{E\cdot P^2}\right]\right\} \quad (1)$$

where n is density of particles in unit interval of kinetic energy ε ,r - heliocentric distance, E and P -total energy and momentum of particle correspondinly, V - speed of solar wind, $\varkappa_r$ - coefficient of radial diffusion, D_ε -coefficient of diffusion in space of energy, $\alpha=(2m_0c^2+\varepsilon)/(m_0c^2+\varepsilon)$, where m_0c^2 - energy at rest. Equation (1) describes process of diffusion propagation of charged component of solar cosmic rays including convecton, adiabatic cooling and statistical acceleration. Numerical solution of equation (1) was based on the grid technique (Krylov V.I., et al., 1977).

Boundary conditions were taken in the form: $n(r,\varepsilon,t)=0$; $CnV-\varkappa_r\frac{\partial n}{\partial r}=Q(\varepsilon,t)$ at $r=r_3$, where Q is function of source, C -Compton-Getting factor, $n(r_L,\varepsilon,t)=0$, $r\in[r_3,r_L]$; $n(r,\varepsilon_1,t)=0$, $n(r,\varepsilon_2,t)\sim\varepsilon^{-\gamma_0}$, $\varepsilon\in[\varepsilon_1,\varepsilon_2]$.

As a test problem we solved equation (1) by Monte Carlo technique using transit moments of the first and second orders of the equation (1) which is equation of Fokker-Planck type (Jokipii J.R., Levy E.H., 1977). Figure 1 shows calculated time-intensity profiles at 11 MeV at r=1 A.U.. Solid line represents the results of calculation by grid technique, histogram-Monte Carlo technique for the case of instantaneous injection of solar cosmic rays at point $r=0.01$ A.U. for $\gamma_0=3,5$, $r_L=6$ A.U., $\varepsilon_1=0,2$ MeV, $\varepsilon_2=50$ MeV, $\varkappa_r=\varkappa_0\varepsilon$[illegible], $\varkappa_0=$ =const(r), $\varkappa_r(\varepsilon=11\ \mathrm{MeV})=1,16\times10^{21}\ \mathrm{cm}^2/\mathrm{s}$, V=400 km/s.

Figure 2 shows calculated energy spectra I_{t_m} obtained on the basis of maximum intensity at r=1 A.U., when $t=t_m$ and histogram represents the results of Monte Carlo technique, solid line -calculations by grid technique, dotted line shows the form of energy spectrum at source. The solid line at the bottom of figure 2 represents dependence of exponent γ on ε ,when I_{t_m} is approximated with the function of the form $\sim\varepsilon^{-\gamma}$,dotted line is value of γ_0 . Hardening of scr energy spectrum at 1 A.U. is due to prevailing action of adiabatic cooling, when $D_\varepsilon=\alpha\cdot\frac{\varepsilon\cdot P^2}{r}\cdot\frac{\Delta U^2}{\varkappa}$ (Dolginov A.Z., Toptygin I.N., 1966), where $\Delta U=50$ km/s - speed of alfven waves in solar wind plasma at r=1 A.U..

The dotted line in figure 1 is a result of solution of the equation (1) for all similar parameters and conditions except suggestion that $\varkappa_r(\mathcal{E})$=const=1,16x10^{21} cm^2/s. This condition is equvalent to γ=const(t). Good agreement in behaviour of I(t) was obtained for $t>t_m$ when γ=const(t) for $\varkappa_r \neq$const($\mathcal{E}$).

Usually when propagation of cosmic rays is investigated it is suggested that $\varkappa_r(r,\mathcal{E})=f(r)\Psi(\mathcal{E})$. To study validity of this suggestion we described experimental solar cosmic ray time-intensity profile for 28.05.67 and 02.11.69 events. The data were taken from the paper of Lanzerotti L.J. ,1975. Description was carried out by minimization the difference between experimental value of I(t) and theoretical ones. Minimization was carried out for scr at given energies in suggestion of instantaneous injection of particles and r_1=20 A.U., when $\varkappa_r=\varkappa_0 r^b$ at ranges $\varkappa_r$(r=1 A.U.) $\in$ [3,75x10^{19} cm^2/s; 3,75x10^{21} cm^2/s], b $\in$ [-2,2] with steps $\Delta\varkappa_0 = 0.1\cdot\varkappa_0'$, Δb=0.5 , where $\varkappa_0'$-previous value of $\varkappa_0$. Figure 3 shows obtained by minimization dependences $\lambda_r(\mathcal{E})$, b($\mathcal{E}$) for 28.05.67 event and dependences λ_r(R), b(R) for 02.11.69 event, where λ_r -radial mean free path, R- rigidity of particle ($\lambda_r = 3\varkappa_r/V$, V -particle speed).

Figure 3a shows values of $\lambda_r(\mathcal{E})$ and $b(\mathcal{E})$ obtained by minimization of χ^2(circles) and by least square method (rectangles) for γ_0=3 for protons at energy $\mathcal{E}$: 1.2-2,4 MeV,2.5-4.3 MeV, 4.4-5.0 MeV; 5.0-9.4 MeV; 9.4-17.4 MeV; 16,5-19.7 MeV. Figure 3b shows λ_r(R) and b(R) for 02.11.69 obtained by mininmization using least square technique for electrons at energies: >0.35 MeV; >0.6 Mev; >1,1 MeV; for protons at energies: 1,1-2.5 MeV; 2.5-4.3 MeV; 5.0-8.8 MeV; 5.9-8.8 MeV, 8.8-16.7 MeV, 17.0-19,7 MeV; for alfa-particles at energies: 3.8-6.2 MeV; 6.2-8.5 MeV, 8.5-17.5 MeV, 17.5-24,5 MeV, 24.5-42.5 MeV, 42.5-83.5 MeV. Rhombs, circles and rectangles in the upper part of figure 3b are values of λ_r for electrons,protons and alfa-particles correspondingly.

Analysis of figure 3 reveals that $\lambda_r \sim R^\alpha$, α=0,6 , α=0,27 for events 28.05.67 and 02.11.69 correspondingly and $\partial b/\partial R>0$. Solid smooth curves in figure 4 show the results of description of time-intensity profile of scr protons for 28.05.67 for γ_0=2.3, $\varkappa_r = \varkappa_0 r^b \mathcal{E}^\alpha$, α=0.8, b=0.75$\cdot\lg\mathcal{E}$, [$\mathcal{E}$] = MeV. Coordinate axis for the given curve is shown with the help of arrow. Figures near curves are energy ranges of registration of solar cosmic rays. Solid line in figure 5 is description of energy spectrum of proton intensity $I_{t_m}(\mathcal{E})$ for the given event.

Pronounced softening of $I_{t_m}(\mathcal{E})$ at r=1A.U. ($I_{t_m}(\mathcal{E}) \sim \mathcal{E}^{-2.6}$) with respect to scr spectrum at source where $I(t=0;r=r_1) \sim \mathcal{E}^{-1,8}$ should be noted.

ORIGINAL PAGE IS
OF POOR QUALITY

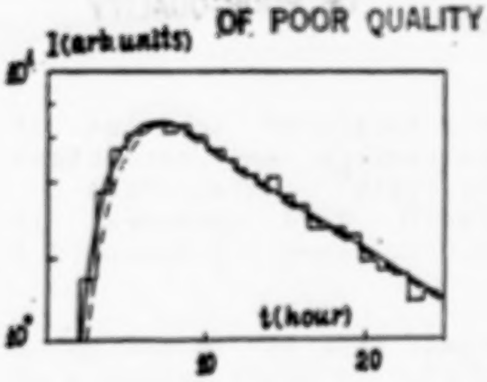

FIGURE 1.

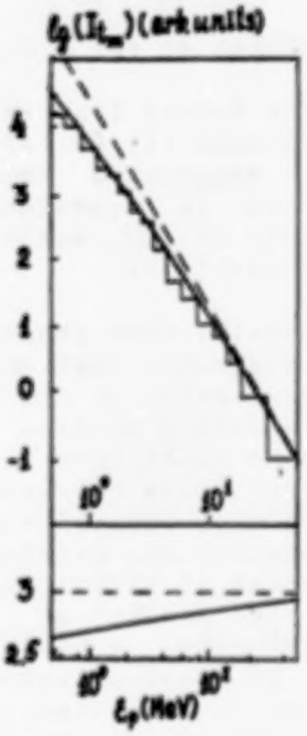

FIGURE 2.

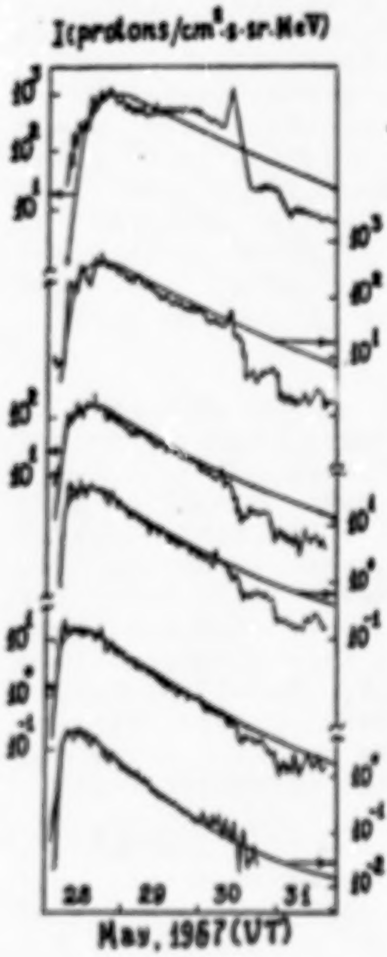

FIGURE 4.

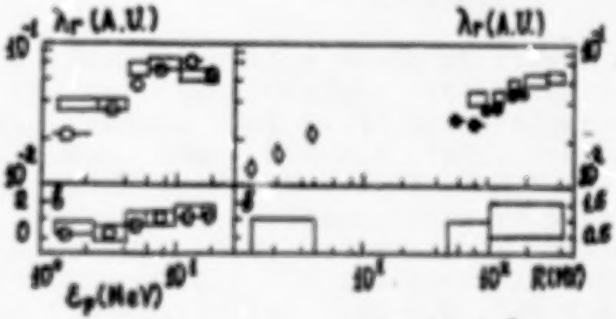

FIGURE 3.

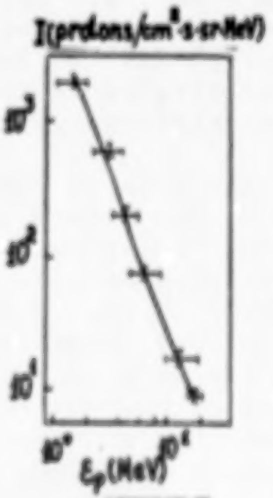

FIGURE 5.

Figure captions are given in the text.